PREMIER REFERENCE SOURCE

Dynamic Methods and Process Advancements in Mechanical, Manufacturing, and Materials Engineering



J. Paulo Davim

Dynamic Methods and Process Advancements in Mechanical, Manufacturing, and Materials Engineering

J. Paulo Davim
University of Aveiro, Portugal

ENGINEERING
SCIENCE REFERENCE

Managing Director: Lindsay Johnston
Senior Editorial Director: Heather A. Probst
Book Production Manager: Sean Woznicki
Development Manager: Joel Gamon
Assistant Acquisitions Editor: Kayla Wolfe
Typesetter: Adrienne Freeland
Cover Design: Nick Newcomer

Published in the United States of America by
Engineering Science Reference (an imprint of IGI Global)
701 E. Chocolate Avenue
Hershey PA 17033
Tel: 717-533-8845
Fax: 717-533-8661
E-mail: cust@igi-global.com
Web site: http://www.igi-global.com

Copyright © 2013 by IGI Global. All rights reserved. No part of this publication may be reproduced, stored or distributed in any form or by any means, electronic or mechanical, including photocopying, without written permission from the publisher. Product or company names used in this set are for identification purposes only. Inclusion of the names of the products or companies does not indicate a claim of ownership by IGI Global of the trademark or registered trademark.

Library of Congress Cataloging-in-Publication Data

Dynamic methods and process advancements in mechanical, manufacturing, and materials engineering / J. Paulo Davim, editor.
p. cm.
Includes bibliographical references and index.
ISBN 978-1-4666-1867-1 (hardcover) -- ISBN 978-1-4666-1868-8 (ebook) -- ISBN 978-1-4666-1869-5 (print & perpetual access) 1. Production engineering--Research. 2. Mechanical engineering--Research. 3. Materials engineering--Research. I. Davim, J. Paulo.
TS176.D986 2013
670--dc23

2012005370

British Cataloguing in Publication Data
A Cataloguing in Publication record for this book is available from the British Library.

The views expressed in this book are those of the authors, but not necessarily of the publisher.

Editorial Advisory Board

S. Arunachalam, *University of East London, UK*
Viktor P. Astakhov, *Michigan State University, USA*
Leonid Burstein, *Israel Institute of Technology, Israel*
Uday Shanker Dixit, *Indian Institute of Technology Guwahati, India*
Patricio Franco, *Technical University of Cartagena, Spain*
Han Huang, *The University of Queensland, Australia*
Mark J. Jackson, *Purdue University, USA*
L. Norberto López de Lacallle, *University of the Basque Country, Spain*
Dimitrios E. Manolakos, *National Technical University of Athens, Greece*
Paulo A. F. Martins, *Technical University of Lisbon, Portugal*
R. Venkata Rao, *S. V. National Institute of Technology, India*
Xipeng Xu, *Huaqiao University, China*
Liangchi Zhang, *The University of New South Wales, Australia*

List of Reviewers

S. Basavarajappa, *University BDT College of Engineering, India*
Nourredine Boubekry, *University of North Texas, USA*
Mohamed Bououdina, *University of Bahrain College of Science, Bahrain*
Juan C. Campos Rubio, *Federal University of Minas Gerais, Brazil*
Kevin Chou, *The University of Alabama, USA*
Mohammad A. Chowdhury, *Dhaka University of Engineering and Technology, Bangladesh*
José Maria Cirne, *University of Coimbra, Portugal*
António Completo, *University of Aveiro, Portugal*
Leonardo R. da Silva, *Federal Center for Technological Education, Brazil*
Teresa M. G. P. Duarte, *University of Porto, Portugal*
Jorge Ferreira, *University of Aveiro, Portugal*
Leandro Freitas, *Petróleo Brasileiro SA – PETROBRAS, Brazil*
V. N. Gaitonde, *B.V.B College of Engineering & Technology, India*
Lidia Gurau, *Transilvania University of Brasov, Romania*
Maki K. Habib, *The American University in Cairo, Egypt*
Zhengyi Jiang, *University of Wollongong, Australia*
Sihai Jiao, *Research Institute Baosteel, China*
Ana-Eva Jiménez-Ballesta, *Technical University of Cartagena, Spain*
Martin Jun, *University of Victoria, Canada*

S. R. Karnik, *B.V.B College of Engineering & Technology, India*
N. Muthu Krishnan, *Sri Venkateswara College of Engineering, India*
Harmesh Kumar, *Panjab University, India*
Aitzol Lamikiz, *University of the Basque Country, Spain*
Yajie Lei, *George Washington University, USA*
Shuting Lei, *Kansas State University,USA*
Altino Loureiro, *University of Coimbra, Portugal*
Alakesh Manna, *Punjab Engineering College, India*
Angelos P. Markopoulos, *National Technical University of Athens, Greece*
Louis Montebello, *STMicroelectronics, Malta*
Rui A. S. Moreira, *University of Aveiro, Portugal*
Fusaomi Nagata, *Tokyo University of Science, Japan*
Arup Kumar Nandi, *Central Mechanical Engineering Research Institute, India*
Alfonso H. W. Ngan, *University of Hong Kong, China*
Meng Ni, *The Hong Kong Polytechnic University, China*
K. Palanikumar, *Sri Sairam Institute of Technology, India*
Risto Poykio, *Environmental Manager of Kemi City, Finland*
Fabrizio Quadrini, *University of Rome "Tor Vergata", Italy*
Ramon Quiza, *University of Matanzas, Cuba*
Manish Roy, *Defence Metallurgical Research Laboratory, India*
Prasanta Sahoo, *Jadavpur University, India*
Loredana Santo, *University of Rome "Tor Vergata", Italy*
M. A. Shah, *King Abdul Aziz University, Saudi Arabia*
Vishal S. Sharma, *Ambedkar National Institute of Technology, India*
M. A. Sheikh, *The University of Manchester, UK*
Jamal Sheikh-Ahmad, *The Petroleum Institute, United Arab Emirates*
Kai Shen, *University of North Carolina, USA*
Jing Shi, *North Dakota State University, USA*
Mukul Shukla, *Motilal Nehru National Institute of Technology, India*
S. K. Shukla, *Banaras Hindu University, India*
Inderdeep Singh, *Indian Institute of Technology Roorke, India*
Sergiu-Dan Stan, *Technical University of Cluj-Napoca, Romania*
Murali M. Sundaram, *University of Cincinnati, USA*
Filipe Teixeira-Dias, *University of Aveiro, Portugal*
Robertt A. F. Valente, *University of Aveiro, Portugal*
N. M. Vaxevanidis, *School of Pedagogical & Technological Education (ASPETE), Greece*
Wenshou Wang, *University of Minnesota, USA*
Jun Wen, *Caterpillar Inc., USA*
Haitao Xu, *Finisar Corp., USA*
Jiwang Yan, *Tohoku University, Japan*
Jin Yang, *Intel Corporation, USA*
Bekir S. Yilbas, *King Fahd University of Petroleum and Minerals, Saudi Arabia*
Xiaohong Tina Zhang, *Seagate Technology LLC, USA*
Jack G. Zhou, *Drexel University, USA*

Table of Contents

Preface xvii

Acknowledgment xxiv

Section 1
General Aspects of Mechanical Engineering

Chapter 1
Development of an Optimization Framework for Parameter Identification and Shape Optimization Problems in Engineering 1
A. Andrade-Campos, Universidade de Aveiro, Portugal

Chapter 2
Large Amplitude Forced Vibration Analysis of Stiffened Plates under Harmonic Excitation 25
Anirban Mitra, Jadavpur University, India
Prasanta Sahoo, Jadavpur University, India
Kashinath Saha, Jadavpur University, India

Chapter 3
Design and Evaluation of Hydro-Pneumatic Friction Damper Suspension System 62
S.V. Gorabal, SKSVMA College of Engineering & Technology, India
S.N. Kurbet, Basaveshwar Engineering College, India
K.K. Appukuttan, National Institute of Technology Karnataka, India

Section 2
Manufacturing

Chapter 4
An Investigation into the Environmental Impact of Product Recovery Methods to Support Sustainable Manufacturing within Small and Medium-Sized Enterprises (SMEs) 73
Michaela R. Appleby, Lancaster University, UK
Chris G. Lambert, Lancaster University, UK
Allan E. W. Rennie, Lancaster University, UK
Adam B. Buckley, The Manufacturing Institute, UK

Chapter 5
Recycling of Waste Epoxy-Polyester Powders for Foam Production..... 91
Carmine Lucignano, University of Rome "Tor Vergata," Italy
Erica Anna Squeo, University of Rome "Tor Vergata," Italy
Alessandro Guglielmotti, University of Rome "Tor Vergata," Italy
Fabrizio Quadrini, University of Rome "Tor Vergata," Italy

Chapter 6
Feature Recognition and Datum Extraction for Setup Planning and Operation Sequencing for Prismatic Parts 102
T. Srikanth Reddy, Indian Institute of Technology Madras, India
M. S. Shunmugam, Indian Institute of Technology Madras, India

Chapter 7
Laser Sub-Micron Patterning of Rough Surfaces by Micro-Particle Lens Arrays 130
Ashfaq Khan, University of Manchester, UK
Zengbo Wang, University of Manchester, UK
Mohammad A Sheikh, University of Manchester, UK
Lin Li, University of Manchester, UK

Chapter 8
A Finite Element Study of Buckling and Upsetting Mechanisms in Laser Forming of Plates and Tubes 140
M. S. Che Jamil, The University of Manchester, UK
M. A. Sheikh, The University of Manchester, UK
L. Li, The University of Manchester, UK

Chapter 9
The Impact of FEM Modeling Parameters on the Computed Thermo-Mechanical Behavior of SLA Copper Shelled Electrodes..... 157
Vassilios Iakovakis, Technological Educational Institute of Larissa, Greece
John Kechagias, Technological Educational Institute of Larissa, Greece
George Petropoulos, University of Thessaly, Greece
Stergios Maropoulos, Technological Educational Institute of West Macedonia, Greece

Chapter 10
Micro Machining of Nonconductive Al_2O_3 Ceramic on Developed TW-ECSM Setup..... 167
Alakesh Manna, PEC University of Technology, India
Amandeep Kundal, PEC University of Technology, India

Chapter 11
3D Finite Element Modeling of High Speed Machining 178
A.P. Markopoulos, National Technical University of Athens, Greece
K. Kantzavelos, National Technical University of Athens, Greece
N.I. Galanis, National Technical University of Athens, Greece
D.E. Manolakos, National Technical University of Athens, Greece

Chapter 12
A Finite Element Study of Chip Formation Process in Orthogonal Machining 197
Amrita Priyadarshini, Indian Institute of Technology, Kharagpur, India
Surjya K. Pal, Indian Institute of Technology, Kharagpur, India
Arun K. Samantaray, Indian Institute of Technology, Kharagpur, India

Chapter 13
Cold End Forming of Welded Steel Tubes 226
L. M. Alves, Instituto Superior Tecnico, Portugal
J. G. Medeiros, MC Graça, Portugal
P. A. F. Martins, Instituto Superior Tecnico, Portugal

Chapter 14
Study on Oxidation of Stainless Steels During Hot Rolling 240
Z. Y. Jiang, University of Wollongong, Australia
D. B. Wei, University of Wollongong, Australia
K. Tieu, University of Wollongong, Australia
J. X. Huang, Baoshan Iron & Steel Co., Ltd., China
A. W. Zhang, Baoshan Iron & Steel Co., Ltd., China
X. Shi, Baoshan Iron & Steel Co., Ltd., China
S. H. Jiao, Baoshan Iron & Steel Co., Ltd., China

Section 3
Material Science and Engineering

Chapter 15
Material Selection Using a Novel Multiple Attribute Decision Making Method 252
R. V. Rao, S. V. National Institute of Technology, India
B. K. Patel, S. V. National Institute of Technology, India

Chapter 16
Attribute Based Selection of Thermoplastic Resin for Vacuum Infusion Process: A Decision Making Methodology 267
R. T. Durai Prabhakaran, Technical University of Denmark, Denmark
Aage Lystrup, Technical University of Denmark, Denmark
Tom Løgstrup Andersen, Technical University of Denmark, Denmark

Chapter 17
Reciprocating Wear Behaviour of Two Dimensionally Reinforced Carbon-Phenolic and Carbon-Epoxy Composites 289
Sourav Sarkar, Advanced System Laboratory, India
V.G. Sekaran, Advanced System Laboratory, India
E. Badisch, Austrian Center of Competence for Tribology, Austria
Manish Roy, Defence Metallurgical Research Laboratory, India
R. Mitra, Indian Institute of Technology, Kharagpur, India

Chapter 18
Roughness Optimization of Electroless Ni-B Coatings Using Taguchi Method 302
Suman Kalyan Das, Jadavpur University, India
Prasanta Sahoo, Jadavpur University, India

Chapter 19
Al_2O_3 Nanobricks via an Organic Free Route Using Water as Solvent 320
M. A. Shah, King Abdul Aziz University, Saudi Arabia

Chapter 20
Preparation of Copper Oxide (CuO) Nanoparticles and their Bactericidal Activity 326
F. M. Al-Marzouki, King Abdulaziz University, Saudi Arabia
O. A. Al-Hartomy, King Abdulaziz University, Saudi Arabia
M. A. Shah, King Abdulaziz University, Saudi Arabia

Compilation of References 333

About the Contributors 360

Index 368

Detailed Table of Contents

Preface xvii

Acknowledgment xxiv

Section 1
General Aspects of Mechanical Engineering

Chapter 1
Development of an Optimization Framework for Parameter Identification and Shape Optimization Problems in Engineering 1
A. Andrade-Campos, Universidade de Aveiro, Portugal

The use of optimization methods in engineering is increasing. Process and product optimization, inverse problems, shape optimization, and topology optimization are frequent problems both in industry and science communities. In this paper, an optimization framework for engineering inverse problems such as the parameter identification and the shape optimization problems is presented. It inherits the large experience gain in such problems by the SIDOLO code and adds the latest developments in direct search optimization algorithms. User subroutines in SDL allow the program to be customized for particular applications. Several applications in parameter identification and shape optimization topics using SDL Lab are presented. The use of commercial and non-commercial (in-house) Finite Element Method codes to evaluate the objective function can be achieved using the interfaces pre-developed in SDL Lab. The shape optimization problem of the determination of the initial geometry of a blank on a deep drawing square cup problem is analysed and discussed. The main goal of this problem is to determine the optimum shape of the initial blank in order to save latter trimming operations and costs.

Chapter 2
Large Amplitude Forced Vibration Analysis of Stiffened Plates under Harmonic Excitation 25
Anirban Mitra, Jadavpur University, India
Prasanta Sahoo, Jadavpur University, India
Kashinath Saha, Jadavpur University, India

Large amplitude forced vibration behaviour of stiffened plates under harmonic excitation is studied numerically incorporating the effect of geometric non-linearity. The forced vibration analysis is carried out in an indirect way in which the dynamic system is assumed to satisfy the force equilibrium condition at peak excitation amplitude. Large amplitude free vibration analysis of the same system is carried out separately to determine the backbone curves. The mathematical formulation is based on energy

principles and the set of governing equations for both forced and free vibration problems derived using Hamilton's principle. Appropriate sets of coordinate functions are formed by following the two dimensional Gram-Schmidt orthogonalization procedure to satisfy the corresponding boundary conditions of the plate. The problem is solved by employing an iterative direct substitution method with an appropriate relaxation technique and when the system becomes computationally stiff, Broyden's method is used. The results are furnished as frequency response curves along with the backbone curve in the dimensionless amplitude-frequency plane. Three dimensional operational deflection shape (ODS) plots and contour plots are provided in a few cases.

Chapter 3
Design and Evaluation of Hydro-Pneumatic Friction Damper Suspension System 62
S.V. Gorabal, SKSVMA College of Engineering & Technology, India
S.N. Kurbet, Basaveshwar Engineering College, India
K.K. Appukuttan, National Institute of Technology Karnataka, India

Perceived comfort level and ride stability are the two most important factors in the evaluation of suspension system in a mobile vehicle. It is extremely difficult to simultaneously maintain a high standard of vehicle ride, handling and body control in the vehicle by using conventional passive suspension system. However, the use of active suspensions would result in better comforts than the passive ones. This paper presents the design and analysis of a pneumatic friction damper and hydro-pneumatic friction damper. A non-linear quarter car model is developed, which includes pneumatic actuation by pressure regulation. The performance of the proposed model was assessed in terms of level of vibration reduction. Simulations on a prototype model show that the proposed system has good performance and robustness.

Section 2
Manufacturing

Chapter 4
An Investigation into the Environmental Impact of Product Recovery Methods to Support Sustainable Manufacturing within Small and Medium-Sized Enterprises (SMEs)..... 73
Michaela R. Appleby, Lancaster University, UK
Chris G. Lambert, Lancaster University, UK
Allan E. W. Rennie, Lancaster University, UK
Adam B. Buckley, The Manufacturing Institute, UK

The effects of climate change and government legislation has changed the way in which manufacturers can dispose of their waste, encouraging SMEs to source alternative disposal methods such as those indicated in the waste hierarchy. It is economically and environmentally beneficial to use product recovery methods to divert waste from landfill. The environmental impact of two product recovery methods, remanufacturing and repairing, has been compared via a carbon footprint calculation for a UK-based SME. The calculation has identified that repairing has a lower carbon footprint than remanufacturing, however this only extends the original life-cycle of the product, whereas remanufacturing provides a new life-cycle and warranty, and therefore seen as the most preferable method of product recovery to support sustainable manufacturing.

Chapter 5
Recycling of Waste Epoxy-Polyester Powders for Foam Production..... 91
Carmine Lucignano, University of Rome "Tor Vergata," Italy
Erica Anna Squeo, University of Rome "Tor Vergata," Italy
Alessandro Guglielmotti, University of Rome "Tor Vergata," Italy
Fabrizio Quadrini, University of Rome "Tor Vergata," Italy

This paper proposes a new foaming technology (solid-state foaming) to produce structural foams from waste thermosetting resins. The proposed technology is easy and does not require specific and expensive equipments. Solid tablets are produced by cold compaction of resin powder, and foam by heating in an oven. Composite foams can be produced by mixing fillers and resin powder before the cold compaction. In the experiment, an epoxy-polyester (EP-PE) resin powder, deriving from the waste of a manufacturer of domestic appliances, was used with montmorillonite (MMT) particles. Resulting foams with a filler content ranging from 0 to 10 wt% were characterized in terms of physical and mechanical properties (by compression tests). Although the effect of the MMT content seems to be negative for the adopted resin, the feasibility of producing composite foams by recycling waste industrial powders is shown. The properties of the unfilled foams are sufficient for many industrial applications.

Chapter 6
Feature Recognition and Datum Extraction for Setup Planning and Operation Sequencing for Prismatic Parts 102
T. Srikanth Reddy, Indian Institute of Technology Madras, India
M. S. Shunmugam, Indian Institute of Technology Madras, India

An automated planning system extracts data from design models and processes it efficiently for transfer to manufacturing activity. Researchers have used face adjacency graphs and volume decomposition approaches which make the feature recognition complex and give rise to multiple interpretations. The present work recognizes the features in prismatic parts considering Attributed Adjacency Matrix (AAM) for the faces of delta volume that lie on rawstock faces. Conceptually, intermediate shape of the work-piece is treated as rawstock for the next stage and tool approach direction is used to recognize minimum, yet practically feasible, set of feature interpretations. Edge-features like fillets/undercuts and rounded/chamfer edges are also recognized using a new concept of Attributed Connectivity Matrix (ACM). In the first module, STEP AP-203 format of a model is taken as the geometric data input. Datum information is extracted from Geometric Dimension and Tolerance (GD&T) data. The second module uses features and datum information to arrive at setup planning and operation sequencing on the basis of different criteria and priority rules.

Chapter 7
Laser Sub-Micron Patterning of Rough Surfaces by Micro-Particle Lens Arrays 130
Ashfaq Khan, University of Manchester, UK
Zengbo Wang, University of Manchester, UK
Mohammad A Sheikh, University of Manchester, UK
Lin Li, University of Manchester, UK

Laser surface patterning by Contact Particles Lens Arrays (CPLA) has been widely utilized for patterning of smooth surfaces but there is no technique developed by which CPLA can be deposited on a rough surface. For deposition of CPLA, conventional techniques require the surface to be flat, smooth and hydrophilic. In this study, a new method for the deposition of CPLA on a rough surface is proposed and utilized for patterning. In this method, a hexagonal closed pack monolayer of SiO2 spheres was first

formed by self-assembly on a flat glass surface. The formed monolayer of particles was picked up by a flexible sticky surface and then placed on the rough surface to be patterned. A Nd:YVO4 laser was used to irradiate the substrate with the laser passing through the sticky plastic and the particles. Experimental investigations have been carried out to determine the properties of the patterns.

Chapter 8

A Finite Element Study of Buckling and Upsetting Mechanisms in Laser Forming of Plates and Tubes 140

M. S. Che Jamil, The University of Manchester, UK
M. A. Sheikh, The University of Manchester, UK
L. Li, The University of Manchester, UK

Laser beam forming has emerged as a viable technique to form sheet metal by thermal residual stresses. Although it has been a subject of many studies, its full industrial application is not yet established. This article aims to complement the existing research in the area of laser forming in order to gain a better understanding of the process. A numerical investigation of laser forming of stainless steel sheets has been carried out and validated experimentally using a High Power Diode Laser (HPDL). Three processing parameters are tested; laser power, beam diameter and plate thickness. Also, laser bending of stainless steel tube is simulated and compared against the published experimental data. The main underlying mechanisms of laser forming are demonstrated through the simulations.

Chapter 9

The Impact of FEM Modeling Parameters on the Computed Thermo-Mechanical Behavior of SLA Copper Shelled Electrodes 157

Vassilios Iakovakis, Technological Educational Institute of Larissa, Greece
John Kechagias, Technological Educational Institute of Larissa, Greece
George Petropoulos, University of Thessaly, Greece
Stergios Maropoulos, Technological Educational Institute of West Macedonia, Greece

In this study, the authors use the finite element method to model and analyse a cylindrical copper shelled SLA electrode for EDM operations, which is investigated experimentally in literature. A uniform silver paint thickness and copper shell thickness is assumed around the SLA epoxy core. In the experiment, 2-D analysis was used due to the axissymmetric shape, and steady state and transient die sink EDMing simulations were followed. Modelling parameters are varied and their impact on the resulting temperature and stress fields is evaluated. The intermittent nature of the electrode thermal loading is also simulated with FEM transient analysis. It is shown that, using the finite element method, the influence of the copper shelled SLA electrode manufacturing and EDM-process parameters can be studied.

Chapter 10

Micro Machining of Nonconductive Al_2O_3 Ceramic on Developed TW-ECSM Setup 167

Alakesh Manna, PEC University of Technology, India
Amandeep Kundal, PEC University of Technology, India

Advanced ceramic materials are gradually becoming very important for their superior properties such as high hardness, wear resistance, chemical resistance, and high strength to weight ratio. But machining of advanced ceramic like Al2O3-ceramics is very difficult by any well known and common machining processes. Normally, cleavages and triangular fractures generate when machining of these materials is done by traditional machining methods. It is essential to develop an efficient and accurate machining method for processing advanced ceramic materials. For effective machining of Al2O3-ceramics, a

traveling wire electrochemical spark machining (TW-ECSM) setup has been developed. The developed TW-ECSM setup has been utilized to machine Al2O3 ceramic materials and subsequently test results are utilized to analyze the machining performance characteristic. Different SEM photographs show the actual condition of the micro machined surfaces. The practical research analysis and test results on the machining of Al2O3 ceramics by developed TWECSM setup will provide a new guideline to the researchers and manufacturing engineers.

Chapter 11
3D Finite Element Modeling of High Speed Machining 178
A.P. Markopoulos, National Technical University of Athens, Greece
K. Kantzavelos, National Technical University of Athens, Greece
N.I. Galanis, National Technical University of Athens, Greece
D.E. Manolakos, National Technical University of Athens, Greece

This paper presents simulation of High Speed Machining of steel with coated carbide tools. More specifically, Third Wave Systems AdvantEdge commercial Finite Element Method code is employed in order to present turning models, under various machining conditions. As a novelty, the proposed models for High Speed Machining of steel are three-dimensional and are able to provide predictions on cutting forces, tool and workpiece temperatures, chip formation, and chip morphology. Model validation is achieved through experimental work carried out under the same conditions as the ones used in modeling. For the experimental work, the principles for design of experiment were used in order to minimize the required amount of experiments and obtain useful results at the same time. Furthermore, a Taguchi analysis is carried out based on the results. The analysis indicates that there is a good agreement between experiment and modeling, and the proposed models can be further employed for the prediction of a range of machining parameters, under similar conditions.

Chapter 12
A Finite Element Study of Chip Formation Process in Orthogonal Machining 197
Amrita Priyadarshini, Indian Institute of Technology, Kharagpur, India
Surjya K. Pal, Indian Institute of Technology, Kharagpur, India
Arun K. Samantaray, Indian Institute of Technology, Kharagpur, India

This paper examines the plane strain 2D Finite Element (FE) modeling of segmented, as well as continuous chip formation while machining AISI 4340 with a negative rake carbide tool. The main objective is to simulate both the continuous and segmented chips from the same FE model based on FE code ABAQUS/Explicit. Both the adiabatic and coupled temperature displacement analysis has been performed to simulate the right kind of chip formation. It is observed that adiabatic hypothesis plays a critical role in the simulation of segmented chip formation based on adiabatic shearing. The numerical results dealing with distribution of stress, strain and temperature for segmented and continuous chip formations were compared and found to vary considerably from each other. The simulation results were also compared with other published results; thus validating the developed model.

Chapter 13
Cold End Forming of Welded Steel Tubes 226
L. M. Alves, Instituto Superior Tecnico, Portugal
J. G. Medeiros, MC Graça, Portugal
P. A. F. Martins, Instituto Superior Tecnico, Portugal

The production of custom and specific tube end shapes by cold end forming using a die is generally limited to seamless tubular parts. Current research work in the field follows the same trend as that of industry and, therefore, there is no accumulated experience, no practical design rules, and no information available in the specialized literature concerning the utilization of tube end forming for shaping the end of thin-walled welded tubes. This paper is concerned with the lack of knowledge and is a contribution towards the understanding of the mechanics of deformation of tube end forming applied to welded tubes. The presentation addresses the influence of major operating parameters on the formability limits of the process with the purpose of understanding feasibility and establishing design rules for the benefit of those who design tubular parts in daily practice. The authors effectively contribute to transferable technological knowledge opening new market opportunities that stimulate innovations among carbon and stainless steel tubular products.

Chapter 14
Study on Oxidation of Stainless Steels During Hot Rolling 240
Z. Y. Jiang, University of Wollongong, Australia
D. B. Wei, University of Wollongong, Australia
K. Tieu, University of Wollongong, Australia
J. X. Huang, Baoshan Iron & Steel Co., Ltd., China
A. W. Zhang, Baoshan Iron & Steel Co., Ltd., China
X. Shi, Baoshan Iron & Steel Co., Ltd., China
S. H. Jiao, Baoshan Iron & Steel Co., Ltd., China

The oxidation of stainless steels 304 and 304L during hot rolling is studied in this paper. Results show the oxide scale thickness decreases significantly with an increase of reduction, and the oxide scales of both 304 and 304L stainless steels were found more deformable than the steel substrate. Surface roughness shows a complicated transfer during the hot rolling process due to the complexity of oxide scale characteristics. Also, surface roughness decreases with an increase of reduction. The friction coefficient increases with reduction in all cases, and the increase is more significant in the case of the 304 stainless steel than that of 304L stainless steel.

Section 3
Material Science and Engineering

Chapter 15
Material Selection Using a Novel Multiple Attribute Decision Making Method 252
R. V. Rao, S. V. National Institute of Technology, India
B. K. Patel, S. V. National Institute of Technology, India

Selection of a most appropriate material is a very important task in design process of every product. There is a need for simple, systematic, and logical methods or mathematical tools to guide decision makers in considering a number of selection attributes and their interrelations and in making right decisions. This paper proposes a novel multiple attribute decision making (MADM) method for solving the material selection problem. The method considers the objective weights of importance of the attributes as well as the subjective preferences of the decision maker to decide the integrated weights of importance of the attributes. Furthermore, the method uses fuzzy logic to convert the qualitative attributes into the quantitative attributes. Two examples are presented to illustrate the potential of the proposed method.

Chapter 16
Attribute Based Selection of Thermoplastic Resin for Vacuum Infusion Process: A Decision Making Methodology 267
R. T. Durai Prabhakaran, Technical University of Denmark, Denmark
Aage Lystrup, Technical University of Denmark, Denmark
Tom Løgstrup Andersen, Technical University of Denmark, Denmark

The composite industry looks toward a new material system (resins) based on thermoplastic polymers for the vacuum infusion process, similar to the infusion process using thermosetting polymers. A large number of thermoplastics are available in the market with a variety of properties suitable for different engineering applications, and few of those are available in a not yet polymerised form suitable for resin infusion. The proper selection of a new resin system among these thermoplastic polymers is a concern for manufactures in the current scenario and a special mathematical tool would be beneficial. In this paper, the authors introduce a new decision making tool for resin selection based on significant attributes. This article provides a broad overview of suitable thermoplastic material systems for vacuum infusion process available in today's market. An illustrative example—resin selection for vacuum infused of a wind turbine blade—is shown to demonstrate the intricacies involved in the proposed methodology for resin selection.

Chapter 17
Reciprocating Wear Behaviour of Two Dimensionally Reinforced Carbon-Phenolic and Carbon-Epoxy Composites 289
Sourav Sarkar, Advanced System Laboratory, India
V.G. Sekaran, Advanced System Laboratory, India
E. Badisch, Austrian Center of Competence for Tribology, Austria
Manish Roy, Defence Metallurgical Research Laboratory, India
R. Mitra, Indian Institute of Technology, Kharagpur, India

A comparative study has been carried out on performance of two-dimensionally reinforced carbon/phenolic (C/P) and carbon/epoxy (C/E) composites, subjected to low amplitude reciprocating wear at different temperatures. The C/P composite has shown greater wear rate than the C/E composite, with the difference being modest at room temperature, and larger at 250 °C. The values of coefficient of friction, surface roughness, and depths of craters on worn surfaces have been measured, which along with surface morphologies examined by scanning electron microscope have been correlated to both amount of weight loss and mechanisms of damage by wear.

Chapter 18
Roughness Optimization of Electroless Ni-B Coatings Using Taguchi Method 302
Suman Kalyan Das, Jadavpur University, India
Prasanta Sahoo, Jadavpur University, India

In this paper, the authors present an experimental study of roughness characteristics of electroless Ni-B coatings and optimization of the coating process parameters based on L27 Taguchi orthogonal design. Three coating process parameters are considered viz. bath temperature, reducing agent concentration, and nickel source concentration. It is observed that concentration of reducing agent together with bath temperature play a vital role in controlling the roughness characteristics of the coatings. The analysis yields the optimum coating parameter combination for minimum roughness. A reduction of about 15% is observed in roughness at the optimal condition compared to the initial condition. The microstructure, composition, and the phase content of the coating are also studied with the help of scanning electron microscopes energy dispersive X-ray analysis, and X-ray diffraction analysis, respectively.

Chapter 19
Al_2O_3 Nanobricks via an Organic Free Route Using Water as Solvent 320
M. A. Shah, King Abdul Aziz University, Saudi Arabia

The chemical synthesis of nanomaterials has been studied by few researchers, but innumerable improvements and better methods have been reported in the past few years. This new approach of preparing aluminum oxide (Al2O3) nanobricks is based on a soft reaction of aluminum powder and de-ionized (DI) water at 200oC without use of any additives or surfactants. Powder X-ray diffraction studies reveal that the as prepared nanobricks are highly crystalline in nature and by morphological investigations using FESEM, it was revealed that the bricks are rectangular in shape having width of 90±15nm and breadth of ~200nm, which was confirmed by high resolution TEM. The technique could be extended and expanded to provide a general, simple, and convenient strategy for the synthesis of nanostructures of other functional materials with important scientific and technological applications. The prospects of the process are bright and promising.

Chapter 20
Preparation of Copper Oxide (CuO) Nanoparticles and their Bactericidal Activity 326
F. M. Al-Marzouki, King Abdulaziz University, Saudi Arabia
O. A. Al-Hartomy, King Abdulaziz University, Saudi Arabia
M. A. Shah, King Abdulaziz University, Saudi Arabia

Single crystalline nanoparticles of copper oxide (CuO) having almost uniform particle size of ~40±10nm have been synthesized by a facile and versatile route. The technique employed is free from toxic solvents, organics, and amines, and is based on a simple reaction of copper powder and de-ionized water (DI) at very low temperatures of 180oC. The morphology, chemical composition, and crystalline structure of the nanoparticles were carefully investigated by the various characterization techniques. Besides simplicity, the advantages of producing nanoparticles by this method are that it is easeful, flexible, fast, cost effective, and pollution free. The synthesized nanoparticles are under investigations for various applications including their antibacterial activity.

Compilation of References 333

About the Contributors 360

Index 368

Preface

Mechanical engineering is a discipline that applies the principles of physics and materials science for analysis, design, manufacturing, and maintenance of mechanical systems. Nowadays, the term *manufacturing* is commonly applied to industrial production, in which raw materials are transformed into finished goods on a large scale. Materials science and engineering is a multidisciplinary field concerned with the composition, structure, properties, and applications of the various materials, such as metals, ceramics, plastics, and composites that are employed in science and technology as well as in industry.

Recently, there has been increased interest in dynamic methods and process advancements in mechanical, manufacturing, and materials engineering. This book captured the latest research developments in this subject, providing a learning and application of these important matters.

The current research book is a collection of cutting-edge research chapters in the field of mechanical, manufacturing, and materials engineering contributed by leading researchers from across the globe.

This research book can be used as a support book for final undergraduate engineering course (for example, mechanical, manufacturing, etc.) or as a subject on mechanical, manufacturing, and materials engineering at the postgraduate level. But, in general, this research book can be used for teaching modern engineering.

Also, this book can serve as a useful reference for academics, manufacturing and materials researchers, mechanical, manufacturing and materials engineers, or professionals in related industries with mechanical engineering.

The purpose of this research book is to present a collection of twenty chapters illustrating the state-of-the-art and research developments to mechanical, manufacturing and materials science, and engineering. The main text of this book is organized into three sections. In first section three chapters are presented with emphasis in general aspects of mechanical engineering. In second section, eleven chapters are presented related to manufacturing. Finally, in the last section, six chapters are presented related to materials science and engineering.

To note, versions of these chapters were are also published in *International Journal of Manufacturing, Materials and Mechanical Engineering*, Volume 1, numbers 1-4, edited by J. Paulo Davim, published by IGI Global. They were published with appropriate modifications in an effort to encourage wider dissemination of research.

SECTION 1. GENERAL ASPECTS OF MECHANICAL ENGINEERING

A. Andrade-Campos (Chapter 1) describes development of an optimization framework for parameter identification and shape optimization problems in engineering. According to the author, the use of optimization methods in engineering is increasing. Process and product optimization, inverse problems, shape optimization, and topology optimization are frequent problems both in industry and science communities. In this paper, an optimization framework for engineering inverse problems such as the parameter identification and the shape optimization problems is presented. It inherits the large experience gain in such problems by the SiDoLo code and adds the latest developments in direct search optimization algorithms. User subroutines in Sdl allow the program to be customized for particular applications. Several applications in parameter identification and shape optimization topics using Sdl Lab are presented. The use of commercial and non-commercial (in-house) Finite Element Method codes to evaluate the objective function can be achieved using the interfaces pre-developed in Sdl Lab. The shape optimization problem of the determination of the initial geometry of a blank on a deep drawing square cup problem is analysed and discussed. The main goal of this problem is to determine the optimum shape of the initial blank in order to save latter trimming operations and costs.

Anirban Mitra *et al.* (Chapter 2) describe large amplitude forced vibration analysis of stiffened plates under harmonic excitation. According to the authors, large amplitude forced vibration behaviour of stiffened plates under harmonic excitation is studied numerically incorporating the effect of geometric non-linearity. The forced vibration analysis is carried out in an indirect way in which the dynamic system is assumed to satisfy the force equilibrium condition at peak excitation amplitude. Large amplitude free vibration analysis of the same system is carried out separately to determine the backbone curves. The mathematical formulation is based on energy principles and the set of governing equations for both forced and free vibration problems derived using Hamilton's principle. Appropriate sets of coordinate functions are formed by following the two dimensional Gram-Schmidt orthogonalization procedure to satisfy the corresponding boundary conditions of the plate. The problem is solved by employing an iterative direct substitution method with an appropriate relaxation technique and when the system becomes computationally stiff, Broyden's method is used. The results are furnished as frequency response curves along with the backbone curve in the dimensionless amplitude-frequency plane. Three dimensional operational deflection shape (ODS) plots and contour plots are provided in a few cases.

S. V. Gorabal *et al.* (Chapter 3) describe design and evaluation of hydro-pneumatic friction damper suspension system. According to the authors, perceived comfort level and ride stability are the two most important factors in the evaluation of suspension system in a mobile vehicle. It is extremely difficult to simultaneously maintain a high standard of vehicle ride, handling, and body control in the vehicle by using conventional passive suspension system. However, the use of active suspensions would result in better comforts than the passive ones. This paper presents the design and analysis of a pneumatic friction damper and hydro-pneumatic friction damper. A non-linear quarter car model is developed, which includes pneumatic actuation by pressure regulation. The performance of the proposed model was assessed in terms of level of vibration reduction. Simulations on a prototype model show that the proposed system has good performance and robustness.

SECTION 2. MANUFACTURING

Michaela R. Appleby *et al.* (Chapter 4) describe an investigation into the environmental impact of product recovery methods to support sustainable manufacturing within small and medium-sized enterprises (SMEs). According to the authors, the effects of climate change and government legislation has changed the way in which manufacturers can dispose of their waste, encouraging SMEs to source alternative disposal methods such as those indicated in the waste hierarchy. It is economically and environmentally beneficial to use product recovery methods to divert waste from landfills. The environmental impact of two product recovery methods, remanufacturing and repairing, has been compared via a carbon footprint calculation for a UK-based SME. The calculation identified that repairing has a lower carbon footprint than remanufacturing; however, this only extends the original life-cycle of the product, whereas remanufacturing provides a new life-cycle and warranty, and is therefore seen as the most preferable method of product recovery to support sustainable manufacturing.

Carmine Lucignano *et al.* (Chapter 5) describe recycling of waste epoxy-polyester powers for foam production. According to the authors, this chapter proposes a new foaming technology (solid-state foaming) to produce structural foams from waste thermosetting resins. The proposed technology is easy and does not require specific and expensive equipments. Solid tablets are produced by cold compaction of resin powder, and foam by heating in an oven. Composite foams can be produced by mixing fillers and resin powder before the cold compaction. In the experiment, an epoxy-polyester (EP-PE) resin powder, deriving from the waste of a manufacturer of domestic appliances, was used with montmorillonite (MMT) particles. Resulting foams with a filler content ranging from 0 to 10 wt% were characterized in terms of physical and mechanical properties (by compression tests). Although the effect of the MMT content seems to be negative for the adopted resin, the feasibility of producing composite foams by recycling waste industrial powders is shown. The properties of the unfilled foams are sufficient for many industrial applications.

T. Srikanth Reddy *et al.* (Chapter 6) describe application of particle swarm optimization for achieving desired surface roughness in tungsten-copper alloy machining. According to the authors, an automated planning system extracts data from design models and processes it efficiently for transfer to manufacturing activity. Researchers have used face adjacency graphs and volume decomposition approaches which make the feature recognition complex and give rise to multiple interpretations. The present work recognizes the features in prismatic parts considering Attributed Adjacency Matrix (AAM) for the faces of delta volume that lie on rawstock faces. Conceptually, intermediate shape of the workpiece is treated as rawstock for the next stage and tool approach direction is used to recognize minimum, yet practically feasible, set of feature interpretations. Edge-features like fillets/undercuts and rounded/chamfer edges are also recognized using a new concept of Attributed Connectivity Matrix (ACM). In the first module, STEP AP-203 format of a model is taken as the geometric data input. Datum information is extracted from Geometric Dimension and Tolerance (GD&T) data. The second module uses features and datum information to arrive at setup planning and operation sequencing on the basis of different criteria and priority rules.

Ashfaq Khan *et al.* (Chapter 7) describe Laser sub-micron patterning of rough surfaces by microparticle lens arrays. According to the authors, Laser surface patterning by Contact Particles Lens Arrays (CPLA) has been widely utilized for patterning of smooth surfaces, but there is no technique developed by which CPLA can be deposited on a rough surface. For deposition of CPLA, conventional techniques require the surface to be flat, smooth, and hydrophilic. In this study, a new method for the deposition

of CPLA on a rough surface is proposed and utilized for patterning. In this method, a hexagonal closed pack monolayer of SiO2 spheres was first formed by self-assembly on a flat glass surface. The formed monolayer of particles was picked up by a flexible sticky surface and then placed on the rough surface to be patterned. A Nd:YVO4 laser was used to irradiate the substrate with the laser passing through the sticky plastic and the particles. Experimental investigations have been carried out to determine the properties of the patterns.

M. S. Che Jamil *et al.* (Chapter 8) describe a finite element study of buckling and upsetting mechanisms in Laser forming of plates and tubes. According to the authors, Laser beam forming has emerged as a viable technique to form sheet metal by thermal residual stresses. Although it has been a subject of many studies, its full industrial application is not yet established. This article aims to complement the existing research in the area of laser forming in order to gain a better understanding of the process. A numerical investigation of laser forming of stainless steel sheets has been carried out and validated experimentally using a High Power Diode Laser (HPDL). Three processing parameters are tested: laser power, beam diameter, and plate thickness. Also, laser bending of stainless steel tube is simulated and compared against the published experimental data. The main underlying mechanisms of laser forming are demonstrated through the simulations.

Vassilios Iakovakis *et al.* (Chapter 9) describe the impact of FEM modeling parameters on the computed thermo-mechanical behavior of SLA copper shelled electrodes. According to the authors, in this study, the authors use the finite element method to model and analyse a cylindrical copper shelled SLA electrode for EDM operations, which is investigated experimentally in literature. A uniform silver paint thickness and copper shell thickness is assumed around the SLA epoxy core. In the experiment, 2-D analysis was used due to the axisymmetric shape, and steady state and transient die sink EDMing simulations were followed. Modelling parameters are varied and their impact on the resulting temperature and stress fields is evaluated. The intermittent nature of the electrode thermal loading is also simulated with FEM transient analysis. It is shown that, using the finite element method, the influence of the copper shelled SLA electrode manufacturing and EDM-process parameters can be studied.

Alakesh Manna and Amandeep Kundal (Chapter 10) describe micro machining of nonconductive Al2O3 ceramic on developed TW-ECSM setup. According to the authors, advanced ceramic materials are gradually becoming very important for their superior properties such as high hardness, wear resistance, chemical resistance, and high strength to weight ratio. However, machining of advanced ceramic like Al2O3-ceramics is very difficult by any well known and common machining processes. Normally, cleavages and triangular fractures generate when machining of these materials is done by traditional machining methods. It is essential to develop an efficient and accurate machining method for processing advanced ceramic materials. For effective machining of Al2O3-ceramics, a traveling wire electrochemical spark machining (TW-ECSM) setup has been developed. The developed TW-ECSM setup has been utilized to machine Al2O3 ceramic materials, and subsequently, test results are utilized to analyze the machining performance characteristic. Different SEM photographs show the actual condition of the micro machined surfaces. The practical research analysis and test results on the machining of Al2O3 ceramics by developed TWECSM setup will provide a new guideline to the researchers and manufacturing engineers.

A. P. Markopoulos *et al.* (Chapter 11) describe 3D finite element modeling of high speed machining. According to the authors, this paper presents simulation of high speed machining of steel with coated carbide tools. More specifically, Third Wave Systems AdvantEdge commercial Finite Element Method code is employed in order to present turning models, under various machining conditions. As a novelty,

the proposed models for High Speed Machining of steel are three-dimensional and are able to provide predictions on cutting forces, tool and workpiece temperatures, chip formation, and chip morphology. Model validation is achieved through experimental work carried out under the same conditions as the ones used in modeling. For the experimental work, the principles for design of experiment were used in order to minimize the required amount of experiments and obtain useful results at the same time. Furthermore, a Taguchi analysis is carried out based on the results. The analysis indicates that there is a good agreement between experiment and modeling, and the proposed models can be further employed for the prediction of a range of machining parameters, under similar conditions.

Amrita Piyadarshini *et al.* (Chapter 12) describe a finite element study of chip formation in orthogonal machining. According to the authors, this chapter examines the plane strain 2D Finite Element (FE) modeling of segmented, as well as continuous chip formation while machining AISI 4340 with a negative rake carbide tool. The main objective is to simulate both the continuous and segmented chips from the same FE model based on FE code ABAQUS/Explicit. Both the adiabatic and coupled temperature displacement analysis has been performed to simulate the right kind of chip formation. It is observed that adiabatic hypothesis plays a critical role in the simulation of segmented chip formation based on adiabatic shearing. The numerical results dealing with distribution of stress, strain, and temperature for segmented and continuous chip formations were compared and found to vary considerably from each other. The simulation results were also compared with other published results; thus validating the developed model.

L. M. Alves *et al.* (Chapter 13) describe cold end forming of welded steel tubes. According to the authors, the production of custom and specific tube end shapes by cold end forming using a die is generally limited to seamless tubular parts. Current research work in the field follows the same trend as that of industry and, therefore, there is no accumulated experience, no practical design rules, and no information available in the specialized literature concerning the utilization of tube end forming for shaping the end of thin-walled welded tubes. This paper is concerned with the lack of knowledge and is a contribution towards the understanding of the mechanics of deformation of tube end forming applied to welded tubes. The presentation addresses the influence of major operating parameters on the formability limits of the process with the purpose of understanding feasibility and establishing design rules for the benefit of those who design tubular parts in daily practice. The authors effectively contribute to transferable technological knowledge opening new market opportunities that stimulate innovations among carbon and stainless steel tubular products.

Z. Y. Jiang *et al.* (Chapter 14) describe their study on oxidation of stainless steels during hot rolling. The oxidation of stainless steels 304 and 304L during hot rolling is studied in this paper. Results show the oxide scale thickness decreases significantly with an increase of reduction, and the oxide scales of both 304 and 304L stainless steels were found more deformable than the steel substrate. Surface roughness shows a complicated transfer during the hot rolling process due to the complexity of oxide scale characteristics. Also, surface roughness decreases with an increase of reduction. The friction coefficient increases with reduction in all cases, and the increase is more significant in the case of the 304 stainless steel than that of 304L stainless steel.

SECTION 3. MATERIALS SCIENCE AND ENGINEERING

R. V. Rao (Chapter 15) describes material selection using a novel multiple attribute decision making method. According to the author, selection of a most appropriate material is a very important task in design process of every product. There is a need for simple, systematic, and logical methods or mathematical tools to guide decision makers in considering a number of selection attributes and their interrelations and in making right decisions. This paper proposes a novel multiple attribute decision making (MADM) method for solving the material selection problem. The method considers the objective weights of importance of the attributes as well as the subjective preferences of the decision maker to decide the integrated weights of importance of the attributes. Furthermore, the method uses fuzzy logic to convert the qualitative attributes into the quantitative attributes. Two examples are presented to illustrate the potential of the proposed method.

R. T. Durai Prabhakaran *et al.* (Chapter 16) describe attribute based selection of thermoplastic resin for vacuum infusion process (a decision making methodology). According to the authors, the composite industry looks toward a new material system (resins) based on thermoplastic polymers for the vacuum infusion process, similar to the infusion process using thermosetting polymers. A large number of thermoplastics are available in the market with a variety of properties suitable for different engineering applications, and few of those are available in a not yet polymerised form suitable for resin infusion. The proper selection of a new resin system among these thermoplastic polymers is a concern for manufactures in the current scenario, and a special mathematical tool would be beneficial. In this paper, the authors introduce a new decision making tool for resin selection based on significant attributes. This article provides a broad overview of suitable thermoplastic material systems for vacuum infusion process available in today's market. An illustrative example—resin selection for vacuum infused of a wind turbine blade—is shown to demonstrate the intricacies involved in the proposed methodology for resin selection.

Sourav Sarkar *et al.* (Chapter 17) describe reciprocating wear behaviour of two dimensionally reinforced carbon –phenolic and carbon-epoxy composites. According to the authors, a comparative study has been carried out on performance of two-dimensionally reinforced carbon/phenolic (C/P) and carbon/epoxy (C/E) composites, subjected to low amplitude reciprocating wear at different temperatures. The C/P composite has shown greater wear rate than the C/E composite, with the difference being modest at room temperature, and larger at 250 °C. The values of coefficient of friction, surface roughness, and depths of craters on worn surfaces have been measured, which along with surface morphologies examined by scanning electron microscope have been correlated to both amount of weight loss and mechanisms of damage by wear.

Suman Kalyan Das and Prasanta Sahoo (Chapter 18) describe a roughness optimization of electroless Ni-B coatings using Taguchi method. According to the authors, in this chapter, the authors present an experimental study of roughness characteristics of electroless Ni-B coatings and optimization of the coating process parameters based on L27 Taguchi orthogonal design. Three coating process parameters are considered viz. bath temperature, reducing agent concentration, and nickel source concentration. It is observed that concentration of reducing agent together with bath temperature play a vital role in controlling the roughness characteristics of the coatings. The analysis yields the optimum coating parameter combination for minimum roughness. A reduction of about 15% is observed in roughness at the optimal condition compared to the initial condition. The microstructure, composition, and the phase content of the coating are also studied with the help of scanning electron microscopes energy dispersive X-ray analysis, and X-ray diffraction analysis, respectively.

M. A. Shah (Chapter 19) describes Al2O3 nanobricks via an organic free route using water as solvent. According to the author, the chemical synthesis of nanomaterials has been studied by few researchers, but innumerable improvements and better methods have been reported in the past few years. This new approach of preparing aluminum oxide (Al2O3) nanobricks is based on a soft reaction of aluminum powder and de-ionized (DI) water at 200ºC without use of any additives or surfactants. Powder X-ray diffraction studies reveal that the as prepared nanobricks are highly crystalline in nature and by morphological investigations using FESEM, it was revealed that the bricks are rectangular in shape having width of 90±15nm and breadth of ~200nm, which was confirmed by high resolution TEM. The technique could be extended and expanded to provide a general, simple, and convenient strategy for the synthesis of nanostructures of other functional materials with important scientific and technological applications. The prospects of the process are bright and promising.

F. M. Al-Marzouki *et al.* (Chapter 20) describes preparation of copper oxide (CuO) nanoparticles and their bactericidal activity. According to the authors, single crystalline nanoparticles of copper oxide (CuO) having almost uniform particle size of ~40±10nm have been synthesized by a facile and versatile route. The technique employed is free from toxic solvents, organics, and amines, and is based on a simple reaction of copper powder and de-ionized water (DI) at very low temperatures of 180ºC. The morphology, chemical composition, and crystalline structure of the nanoparticles were carefully investigated by the various characterization techniques. Besides simplicity, the advantages of producing nanoparticles by this method are that it is easeful, flexible, fast, cost effective, and pollution free. The synthesized nanoparticles are under investigations for various applications including their antibacterial activity.

J. Paulo Davim
University of Aveiro, Portugal

Acknowledgment

The Editor acknowledges his gratitude to IGI Global and editorial team for their adequate and professional support throughout the preparation of this book. Finally, he would like to thank all the chapter authors, the reviewers, and the editorial advisory board members for their availability for work on this project.

J. Paulo Davim
University of Aveiro, Portugal

Section 1

General Aspects of Mechanical Engineering

Chapter 1
Development of an Optimization Framework for Parameter Identification and Shape Optimization Problems in Engineering

A. Andrade-Campos
Universidade de Aveiro, Portugal

ABSTRACT

The use of optimization methods in engineering is increasing. Process and product optimization, inverse problems, shape optimization, and topology optimization are frequent problems both in industry and science communities. In this paper, an optimization framework for engineering inverse problems such as the parameter identification and the shape optimization problems is presented. It inherits the large experience gain in such problems by the SiDoLo code and adds the latest developments in direct search optimization algorithms. User subroutines in Sdl allow the program to be customized for particular applications. Several applications in parameter identification and shape optimization topics using Sdl Lab are presented. The use of commercial and non-commercial (in-house) Finite Element Method codes to evaluate the objective function can be achieved using the interfaces pre-developed in Sdl Lab. The shape optimization problem of the determination of the initial geometry of a blank on a deep drawing square cup problem is analysed and discussed. The main goal of this problem is to determine the optimum shape of the initial blank in order to save latter trimming operations and costs.

INTRODUCTION

The use of optimization methods in engineering is increasing. Process and product optimization, inverse problems, shape optimization and topology optimization are frequent problems in both industry and scientific communities (Andrade-Campos et al., 2007; Ponthot & Kleinermann, 2006; Belegundu & Chandruptla, 1999; Ceretti et al., 2010).

To solve this kind of problems, general mathematical/technical computing software, such as MatLab (2007) and Mathematica (2009), or programming languages (such as C++, Fortran,

DOI: 10.4018/978-1-4666-1867-1.ch001

Copyright © 2013, IGI Global. Copying or distributing in print or electronic forms without written permission of IGI Global is prohibited.

java, etc.) are usually used. In these cases, as these approaches use general-purpose software environments, it is necessary to write and implement the whole optimization algorithm including the objective function, the optimization method, the input/output data, etc. Although computationally very efficient, this approach can be very time consuming and has the prerequisite of full knowledge of a programming language. On the other hand, commercial engineering optimization software packages start to be used by many researchers and technicians. ModeFrontier (2008), Knitro (2007), and Heeds (2009), among others, can be easily used for general-purpose optimization processes. However, these packages have the disadvantage of being a closed *black-box* where the user cannot change any detail in the optimization methodologies or cannot implement new optimization methods.

An engineering optimization framework that aims to contradict the previously mentioned disadvantages is presented in this paper. The SDL optimization lab is a non-commercial framework designed for specific engineering inverse problems such as the parameter identification (Cailletaud & Pilvin, 1994; Liu & Han, 2003 among others) and the shape optimization problems (e.g., Maniatty & Zabaras, 1994; Fourment et al., 1996). Parameter identification problems have emerged due to the increasing demanding of precision in the numerical results obtained by Finite Element Method (FEM) software. High result precision can only be obtained with confident input data and robust numerical techniques. Unfortunately, the large majority of the robust numerical techniques are inherently more complex. Constitutive material models developed to simulate with increasing accuracy the behaviour of different materials are an example of these techniques that became more complex (Andrade-Campos et al., 2009). However, the accuracy of the model is much dependent on the model input data (constitutive model parameters) given by the user. Generally, the number of parameters to be determined increases with the model complexity and, consequently, increases the difficulty of the parameter identification problem. The determination of parameters should always be performed confronting numerical and experimental results leading to the minimum difference between them (minimization of the cost function that is defined as the difference between experimental and numerical results). This problem could be reduced to a curve-fitting problem if physical constraints were not taken into account. However, most material constitutive models have physical constraints such as material parameter boundary values and mathematical relations between them, guaranteeing the physical meaning of the material parameters.

The aim of shape optimization problems is to find the shape which is optimal (minimizes a certain cost functional while satisfying given constraints) for a determined objective. However, frequently, the cost functional (objective function) cannot be evaluated without performing a time-consuming simulation analysis.

The shape optimization problem can be similar to the parameter identification problem if the shape to be optimized is defined by a finite number of parameters. Therefore, both problems can be solved by the same approach.

The minimization of the cost function, defined as the difference between experimental and numerical results, can be a hard task. The function of a set of arguments (the material parameters) may have many isolated local minima, non-isolated minimum hypersurfaces, or even more complex topologies. No finite minimization method can guarantee to locate the unique, global, minimum of the parameter set without supplying additional information about the cost function by the user (Birkinshaw, 1998).

There is no best algorithm for finding the minimum of a cost function. Several approaches and optimization methods can be used to solve the mentioned non-linear optimization problems

with small computational costs and to efficiently determine the best suited material parameter set (Ejday & Fourment, 2010). For many optimization problems there are techniques which will locate a local minimum which may be close enough to the global minimum and there are techniques which will find the global minimum in a large fraction of the time (in a probabilistic sense). The most common optimization methods are the gradient-based methods followed by the genetic, evolutionary and nature-inspired algorithms. The immune algorithms and the methods based in neural networks and artificial intelligence are also often used. Without doubt, the most effective methods are gradient-based but their performance is known to be dependent on the starting set of parameters. Nature-inspired techniques provide a different way to determine an optimized set of parameters. Therefore, the difficulty of choosing a starting set of parameters is minor for this process. However, these proved to be computationally more expensive than the gradient-based methods.

In general, the greatest guarantee that the correct minimum has been found in a particular process is a careful examination of the nature of the solution (e.g., by plotting a fitted function over data) and some confidence that the full region where the minimum may lie in has been well searched by the algorithm used.

In order to increase the result confidence the following rules can be followed (Birkinshaw, 1998): (i) the result of a minimization using a single optimization method should not be accepted; the minimum obtained should be tested using a different method; (ii) the parameters obtained by the end of the optimization process should not be at the edges of the parameter space. In this case, this specific process must be disregarded since the minimum lies outside the search space or the minimization process missed the minimum; (iii) it is important to have a sensibility of the cost function values and the stability of the solution by starting the minimization process from several different parameter values and (iv) the minimum obtained should be checked using a plotting tool.

In order to verify these rules, gradient-based and direct search methods should be used in co-operation. Generally, gradient based methods start from only one parameter set leading to a single result. However, direct search methods starts with more than one set of parameters (called population for the genetic and evolutionary algorithms, particles for the PSO, temperatures cycles for the simulated annealing, etc.) driving to multiple results.

The SDL optimization lab uses both types of methods for solving parameter identification and shape optimization problems. It inherits the large experience gain in such problems by the SIDOLO code (Cailletaud & Pilvin, 1994; Andrade-Campos et al., 2007) and adds the latest developments in direct search optimization algorithms.

The SDL Framework can also be used by researchers that wishes to control every step of the engineering optimization procedure or by users with no experience in programming languages that want to use an intuitive graphical interface with the optimization problem formulation already implemented and explained. The user subroutines in SDL allow the program to be customized for particular applications or to implement new optimization methods and strategies.

In this paper, the SDL optimization Lab is presented by means of a parameter identification and a shape optimization problems. Both problems use finite element programs to evaluate the objective function.

Problem Formulation

Both parameter identification and shape optimization problems belong to the inverse problems group. The goal of an inverse problem consists in providing information to the numerical simulation model from the full knowledge of the physical process.

Constitutive Model Parameter Identification

Consider a physical system whose behaviour can be described by a numerical model and on which experimental results are available. The identification process uses a set of measurable variables $\mathbf{Z}^{\mathrm{T}} = \left[z_1, z_2, \ldots, z_m\right]$ that can be experimentally determined. For simple mechanical tests, such as tensile or shear test, the measurable variables are the stresses or strains. With this information, the solution of the identification problem consists in the minimization of a function that measures the difference between theoretical predictions (obtained by the numerical model), $\mathbf{Z}^{\mathrm{num}}$, and the experimental data, $\mathbf{Z}^{\mathrm{exp}}$, for a given set of parameters. This function (cost functional), $\mathcal{L}(\mathbf{A})$, can be given by (Cailletaud & Pilvin, 1994; Andrade-Campos et al., 2007)

$$\mathcal{L}(\mathbf{A}) = \sum_{q=1}^{N} \mathcal{L}_q(\mathbf{A}), \tag{1}$$

with

$$\mathcal{L}_q(\mathbf{A}) = \frac{1}{(t_1 - t_0)} \int_{t_0}^{t_1} \left[\mathbf{Z}^{\mathrm{num}}(\mathbf{A}) - \mathbf{Z}^{\mathrm{exp}}\right]^{\mathrm{T}} \mathbf{D}_q \left[\mathbf{Z}^{\mathrm{num}}(\mathbf{A}) - \mathbf{Z}^{\mathrm{exp}}\right] \mathrm{d}t, \tag{2}$$

where $\mathbf{A} = \left[A_1, A_2, \ldots, A_r\right]^{\mathrm{T}}$ is the set of the $r \in \mathbb{N}$ constitutive model parameters and $\mathbf{Z}^{\mathrm{exp}}$ is a known experimental value of $\mathbf{Z}$ in N experimental tests. (t_0, t_1) is the time period of the generic test q. Also, $\mathbf{D}_q$ is a given weight matrix associated to the test q and can be defined by

$$\mathbf{D}_q = \frac{1}{W_q^{\mathrm{abs}} + W_q^{\mathrm{rel}} \mathbf{Z}^{\mathrm{exp}}}, \tag{3}$$

where W_q^{abs} and W_q^{rel} stand for absolute and relative weights for the q test, respectively. These coefficients are chosen taking into account the uncertain nature of observed variables and different magnitudes of the measured variables. Special care must be taken when choosing $W_q^{\mathrm{abs}} = 0$ and $W_q^{\mathrm{rel}} > 0$ for values of $\mathbf{Z}^{\mathrm{exp}}$ near zero. In that case $\mathbf{D}_q \to \infty$, leading to infeasible results.

The evaluation of the difference between the numerical and the experimental data, represented by $\mathbf{Z}^{\mathrm{num}}(\mathbf{A}) - \mathbf{Z}^{\mathrm{exp}}$, only accounts for the measurable variables that cannot be controlled when performing the experimental tests. Numerically, the integral in Equation 2 can be approximated by a finite sum where the difference between the model and the experimental values is only evaluated at the M_q instants of observation, leading to

$$\mathcal{L}_q(\mathbf{A}) = \frac{1}{M_q} \sum_{i=1}^{M_q} \left[\frac{\mathbf{Z}^{\mathrm{num}}(\mathbf{A}, t_i) - \mathbf{Z}^{\mathrm{exp}}(t_i)}{W_q^{\mathrm{abs}} + W_q^{\mathrm{rel}} \mathbf{Z}^{\mathrm{exp}}(t_i)}\right]^2. \tag{4}$$

The optimization problem that should be solved consists in finding the minima of

$\mathcal{L}(\mathbf{A})$, *i.e.*,

$$\begin{aligned} \min_{\mathbf{A}} \quad & \mathcal{L}(\mathbf{A}) \\ \text{s.t.:} \quad & g_m(\mathbf{A}) \leq 0, \qquad m = 1, \ldots, M \\ & h_l(\mathbf{A}) = 0, \qquad l = 1, \ldots, L \\ & A_i^{\min} < A_i < A_i^{\max}, \quad i = 1, \ldots, r, \end{aligned} \tag{5}$$

where the M inequalities $g_m(\mathbf{A})$ and the L equalities $h_l(\mathbf{A})$ define the model constraints (Polak, 1997). The optimization parameters should also be found in the search-space limited by the boundary of each parameter $A^{\min}$ and $A^{\max}$. For direct search optimization methods the use of each parameter boundary (optimization variable limit) can be made directly in the generation (randomly or not) for new parameters. For gradient-based

optimization methods, these conditions can be taken as constraints (if the optimization method is prepared to deal with constraints) or as interior penalties, if an unconstrained optimization method is used. In the latter, the parameter can be transformed as

$$A \Rightarrow A_0\left[1+\left(A_{\max}-1\right)\left(1-\mathrm{e}^{\frac{1-A}{A_{\max}-1}}\right)\right], \tag{6}$$

for $A_0 \geq 1$, where A_0 is the initial value of A for existing $A_{\max}$ and A normalized. A similar expression is applied for $A_0 < 1$ using $A_{\min}$.

Inequalities constraints can also be added to the objective function if the optimization method cannot handle directly constraint conditions. However, for that case, the modified objective function must also obey the conditions of continuity and existence of derivative in any point of its universe and for any direction. Thus, the problem leads to the minimization of the following function:

$$\mathcal{L}^p(\mathbf{A}) = \sum_{q=1}^{N}\mathcal{L}_q(\mathbf{A}) + \sum_{m=1}^{M}\left[\alpha'_m \max\left\{0, g_m(\mathbf{A})\right\}\right]^2 + \sum_{l=1}^{L}\left[\alpha''_l h_l(\mathbf{A})\right]^2. \tag{7}$$

The penalty coefficients, $\alpha \supseteq \left\{\alpha', \alpha''\right\}$, lead to the evolution of the optimization process itself if a balanced value is chosen. The choice of α is not easy considering that for large values of α the function $\mathcal{L}^p(\mathbf{A})$ can be very non-linear. The second and third terms of Equation 7 are called exterior penalty functions.

Shape Optimization

Other categories of inverse problems are the shape and/or process optimization problems. These approaches extend the concepts detailed above to beyond the constitutive model, and shows a great potential in helping engineers to efficiently solve design problems in actual mechanical processes. In most forming processes, such as in the deep drawing of a car fender, the aimed final geometry is known a-priori, and the initial shape of the blank and/or the tools are needed to be determined. Moreover, the forming process must be designed to ensure that, after deformation, the blank will reach the prescribed shape of the desired safe final part, within thigh geometrical tolerances.

Shape optimization problem formulation is not so different from the previous problems formulation. The major difference is that, in parameter identification, the variables can have different magnitudes due to their different physical or numerical meaning, while in shape optimization, all variables define geometrical shapes and contours, being all at the same magnitude (now $\mathbf{A}$ are called the design variables). In a general form, the objective function of these problems, $\mathcal{L}(\mathbf{A})$, can be written as in Equation 1. However, Equation 2 is now replaced by

$$\mathcal{L}_q(\mathbf{A}) = \frac{1}{M_q}\sum_{i=1}^{M_q}\left[F_i(\mathbf{A}, \sigma, \varepsilon, \ldots)\right]^2, \tag{8}$$

where F_i is the specific function that characterizes the geometric shape as a function of structural properties such as, for instance, the stress σ and strain ε fields. The general formulation of the shape optimization problem is similar to the formulation defined in 5.

Optimization Methods

From the moment when the number of experimental tests and parameters to be identified increases, it becomes impossible to identify the parameters analytically or in an exploratory way. In these cases, the inverse problems defined in the previous sections should be solved through the resolution of a non-linear optimization problem that is carried out through the aid of iterative numerical methods. The use of these methods is associated to theoreti-

cal and numerical difficulties, since there is no unique solution for a nonlinear inverse problem.

The nonlinear optimization methods based on the gradient function can find local minima through an iterative process guided by the Jacobian (first-order partial derivatives of the objective function vector). However, commonly these are not the absolute minimum values and the final solution is much dependent of the initial parameters set. This effect can be decreased if an all-inclusive set of experimental results is selected in order to discriminate the different obtained solutions or if several initial sets were selected.

The choice of the technique of resolution of the optimization problem is crucial because this technique controls the efficiency of the identification method. Nowadays, there are more than a hundred optimization methods and their variants. Nevertheless, it is impracticable to find a single general, and at the same time efficient and robust, optimization method to solve all classes of inverse problems. The three main families of optimization algorithms are the gradient-based methods, the nature-inspired algorithms and artificial intelligence algorithms. The two last families belong to the class of direct and exploratory methods.

Gradient-based and direct search methods should be used in cooperation. Generally, gradient-based methods start from only one parameter set leading to a single result. However, direct search methods starts with more than one set of parameters driving to multiple results. The choice of the optimization methods to be used (in sequential, parallel or hybrid strategies) depends specifically on the cost of the objective function evaluation. Although the computation effort is duplicating every two years (see Moore's law), it is unfeasible to use direct search methods when the objective function evaluation needs a finite element analysis that takes more than 10 minutes.

Objective Function Evaluation

Various objective functions have been formulated to assess the errors between the experimental and computed data (Lin et al., 2002; Cao & Lin, 2008, among others). The objective functions should be able to lead efficiently the optimisation process. An ideal objective function should have the following properties: (i) all the experimental data points on the curve and all experimental curves should have equal opportunity to be optimised and (ii) different units and/or the number of curves in each sub-objective should not affect the overall performance of the fitting. These two criteria should be achieved without manually choosing the weighting factors. However, for some non-analytical specific problems, this is very difficult in practise. In those cases, the weighting factors are chosen in order to balance the different data and units of the curves.

Besides the minimization of analytical functions, generally in computational mechanics, the objective function evaluation needs a simulation analysis. In the last years, the Finite Element Method (FEM) has become a well-known and reliable tool for structural analysis. This method can be applied to analyse stresses and strains in a structure, dynamic response, heat conduction, fluid flow and other phenomena. Therefore, it can be a tool mostly used as objective function in parameter identification and/or shape optimization problems. The large number of available finite element codes (commercial, non-commercial and open-source) allows choosing easily a FEM code to be integrated in these mentioned problems. The drawback of the use of a FEM analysis is the large CPU time required for each objective function evaluation and, consequently, for the overall optimization problem. Optimization problems involving finite elements in a *quasi*-static structural analysis can be generally expressed as

$$\begin{aligned} \min_{\mathbf{A}} \quad & \mathcal{L}(\mathbf{A},\mathbf{U}) \\ \text{s.t.}: \quad & g_m(\mathbf{A},\mathbf{U}) \le 0, \qquad m = 1,\ldots,M \\ & h_l(\mathbf{A},\mathbf{U}) = 0, \qquad l = 1,\ldots,L \\ & A_i^{\min} < A_i < A_i^{\max}, \quad i = 1,\ldots,r\,, \\ \text{and} \quad & \mathbf{K}(\mathbf{A})\mathbf{U} = \mathbf{F}(\mathbf{A}) \end{aligned} \tag{9}$$

where $\mathbf{U}$ is the nodal displacement vector from which the displacement field $\mathrm{u}(x,y,z)$ is readily determined, $\mathbf{K}$ is the stiffness matrix and $\mathbf{F}$ is the load vector. Note that functions $\mathcal{L}$, g and h are implicit functions of the design variables $\mathbf{A}$. They depend explicitly on $\mathbf{A}$ and also implicitly through $\mathbf{U}$ as given in the last term of Equation 9 (Belegundu & Chadrupatla, 1999).

The finite element-based optimization problem is better solved using gradient-based methods since both number of degrees of freedom and the number of design variables can be large. The main difficulty in using such optimization methods is the efficient computation of gradients $\nabla\mathcal{L}$ and ∇g, also called sensitivity analysis.

Analytically, there are two principal methods of evaluating the gradient of an implicit function: (i) the direct method and (ii) the adjoint method. The first method consists in the direct derivation of the FEM equilibrium equation in respect to the design variables. Therefore, this method needs an inverse finite element analysis for each optimization variable, being subsequently computationally very expensive. The second method avoids the calculation of $d\mathbf{U} / dA_i$ by the use of an adjoint vector and adjoint equations. This method can be more efficient than the direct method, considering that the number of inverse finite element analyses is independent of the optimization variable number. However, it does need a lot more memory savings.

Both previous mentioned analytical methods need a full knowledge and access to the stiffness matrix of the FEM. This information is not always available when using different FEM codes, including commercial ones. In those cases, the simplest way to obtain the derivatives is using the numerical difference method. Newton's forward difference formula is often used to obtain an approximate expression to $\nabla\mathcal{L}$ (and also for $\nabla^2\mathcal{L}$) at a given point $\mathbf{A}^0$. The formula is

$$\frac{\partial\mathcal{L}(\mathbf{A})}{\partial A_i} \approx \frac{\mathcal{L}(A_1^0, A_2^0, \ldots, A_i^0 + \varepsilon, \ldots, A_r^0) - \mathcal{L}(\mathbf{A}^0)}{\varepsilon}, \quad i = 1,\ldots,r\,, \tag{10}$$

where ε is the divided difference parameter. In Equation 10, each variable is perturbed one at a time and the operator $\mathcal{L}$ is then re-evaluated. Note that $r+1$ function evaluations are needed to compute $\nabla\mathcal{L}(\mathbf{A}^0)$. This scheme is not recommended in problems where each function evaluation is computationally time consuming but it is the only way for the case where the access to FEM matrix is not allowed. For greater accuracy at a higher CPU cost, the central difference formula is used, and given by

$$\frac{\partial\mathcal{L}(\mathbf{A})}{\partial A_i} \approx \frac{\mathcal{L}(A_1^0, A_2^0, \ldots, A_i^0 + \varepsilon/2, \ldots, A_r^0) - \mathcal{L}(A_1^0, A_2^0, \ldots, A_i^0 - \varepsilon/2, \ldots, A_r^0)}{\varepsilon}, \tag{11}$$

with $i = 1,\ldots,r$. Numerically, other methods, such as the Automatic differentiation (Rall, 1981), are also available.

Numerical Implementation

The previously presented formulations are implemented in a general framework called SDL Optimization Lab. This framework was developed and it is still being developed specifically for parameter identification and shape optimization problems and tries to overcome the disadvantages presented by commercial optimization programs and its limited access to the source code. SDL Optimization Lab intends to give no restrictions to the user in

the sense that it is possible to change almost all source code and different optimization methods and external programs could be used altogether.

General Structure

SDL Optimization Lab is composed by the graphical interface and by the problem creator. The two parts together allow defining the following components: (i) initial and problem data information; (ii) objective function definition; (iii) gradient calculations; (iv) core algorithm definition; (v) real time monitoring; and (vi) results. Several GUI components of SDL Optimization Lab can be seen in Figure 1.

The initial and problem data, such as optimization variables' names, initial values ($\mathbf{A}_0$) and boundaries ($\mathbf{A}_{\min}$ and $\mathbf{A}_{\max}$), can be defined through the graphical interface. The measurable variables number and names should also be defined. The definition of the problem is made through a code editor integrated in SDL Optimization Lab that allows the writing of the objective function equations. The variables names defined in the graphical interface (optimization and measurable variables) are directly used without the need for new definitions or attributions. For time dependent problems (such as tensile tests or technological processes), the evolution of at least one measurable variable (e.g., time) should be defined. This can be done by file importation. The experimental values $\mathbf{Z}^{\exp}$ should also be given.

After the creation of the problem, the executable file is created (process preparation). This executable file is self-sufficient and can be used in other platform, such as single computers or clusters, without any adjustment. Real time monitoring and result analysis are available in SDL Optimization Lab.

Explicit and Differential Problems

The creation of a new problem objective function (the new model) depends on the formulation type used to define the mathematical/numerical relations of the behaviour of the model. Three types of formulations can be defined: (i) explicit; (ii) differential and (iii) external models.

The explicit model is the most simple formulation of a model. In this model, the evaluation of $\mathbf{Z}(t)$ is done with the aid of explicit relations, *i.e.*

$$\mathbf{Z}(t) = \mathbf{H}(\mathbf{A}, t) \tag{12}$$

where t represents the time, the incremental evolution of an event, instants of observation or different points of observation (such as, for instance, points that define a shape). When minimizing mathematical analytical functions (or cost functionals), the explicit model with only one instant of observation is used.

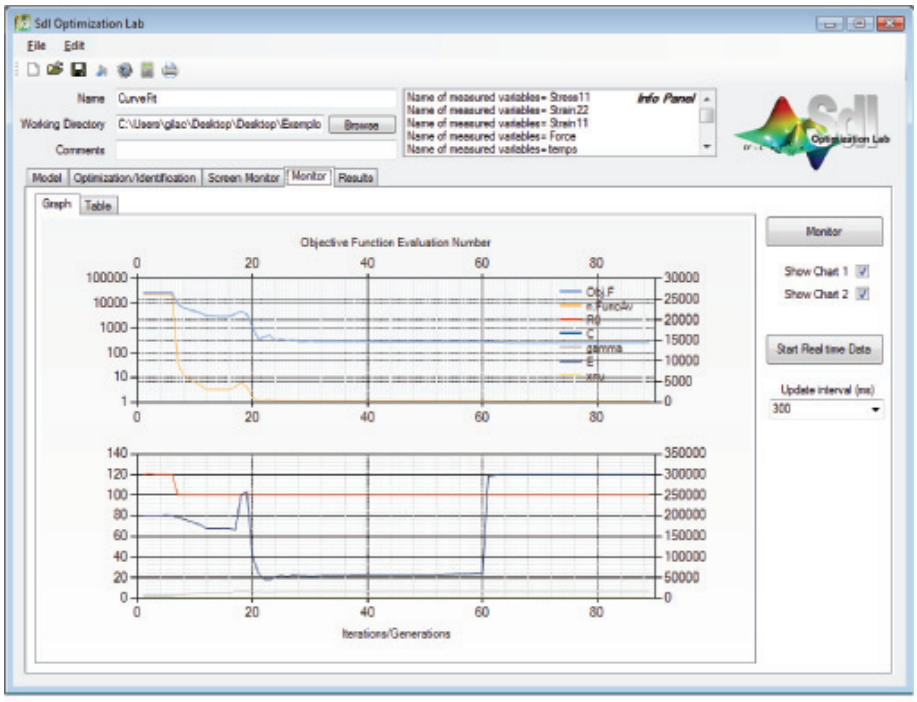
Differential problems, such as internal variable and viscoplastic constitutive models, are often formulated in the differential form. For this kind of problem the evaluation of $\mathbf{Z}(t)$ needs the solution of a first order partial derivatives equation. The evolution of a differential problem can be defined by a system of equations expressed by

$$\frac{\mathrm{d}\mathbf{Y}}{\mathrm{d}t} = \mathbf{F}\left(\mathbf{Z}_e, \mathbf{Y}; \mathbf{A}, t\right) \text{ with } \mathbf{Y}(t_0) = \mathbf{Y}_0, \tag{13}$$

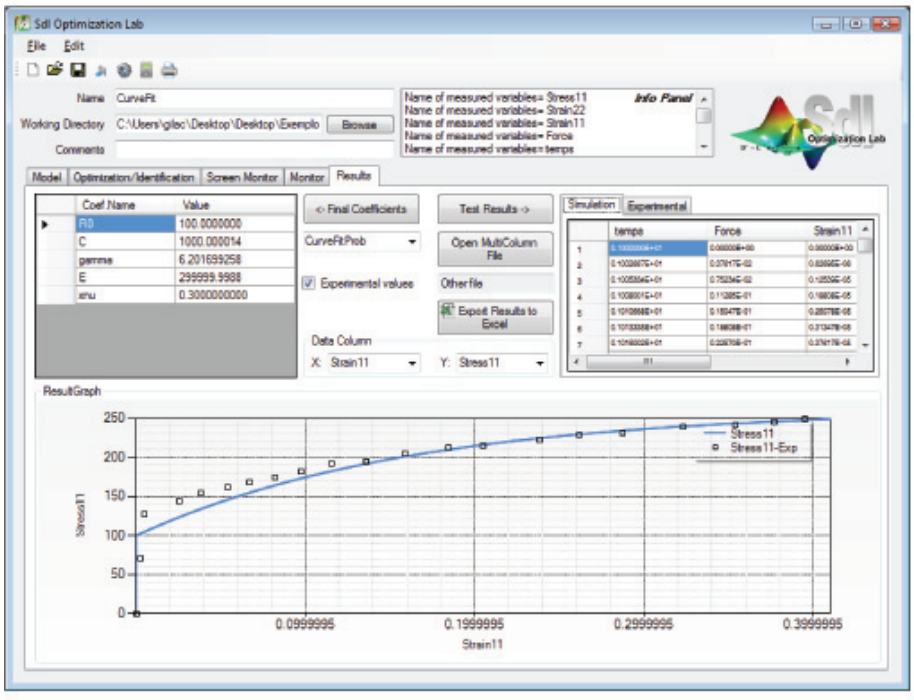
$$\mathbf{Z}(t) = \mathbf{G}(\mathbf{Y}; \mathbf{A}, t), \tag{14}$$

where $\mathbf{Y} = (y_1, y_2, ..., y_n)^{\mathrm{T}}$ represents the set of n variables defined in differential (or rate) form, necessary to evaluate the measurable quantities $\mathbf{Z}$. Constitutive material models, formulated to be implemented in finite element codes, are expressed in this type of formulation. Non-linear finite element analysis, especially in implicit codes

Figure 1. Sdl Optimization Lab GUI: (a) initial and problem data information, real time monitoring and (b) results



A



B

(e.g., ABAQUS standard), need incremental/rate form of its equations.

For this type of models the program SDL Optimization Lab uses direct numerical integration methods. The Runge-Kutta numerical integration methods proved to be sufficiently efficient. The efficiency of these methods is even more evident when using an adaptive time step algorithm (Cailletaud & Pilvin, 1994). The Runge-Kutta explicit integration methods of second (rk21), fourth (rk43) and fifth (rk54) degree are the ones used by the program SDL Optimization Lab to integrate the differential form of the rate equations (Equations 13 and 14). These methods use variable and adaptive time steps and proved to be numerically efficient.

An algorithm that accounts for large deformations is also implemented for the numerical evaluation of the constitutive models of these types. This algorithm calculates the strain gradient tensor $\mathbf{F}$ and the rotation tensor $\mathbf{R}$ by the polar decomposition method.

External Problems and Interfaces

When the evaluation of $\mathbf{Z}(t)$ is performed by an external program (not written in the model routine) the model is called external. This kind of model needs the development of an interface between the simulation program and the SDL Optimization Lab. For all kind of external simulation programs, a general interface is available. This interface requires little modifications in order to take in account specific characteristics of the program. For simulation programs widely spread (such as ABAQUS, Msc.Marc, DD3Imp, among others) pre-developed interfaces are available.

User Routines

The SDL Lab can be used by users non-familiarized with programming languages that want to use an intuitive graphical interface with the optimization problem formulation already implemented and by researchers that wishes to control every step of the engineering optimization procedures. Although part of SDL Optimization Lab is open source, user routines are available to easily implement new optimization methods, sensitivity analysis, etc. and allow the program to be customized for particular applications.

Besides the MODEL and the interface routines (see previous section), the following routines are examples of user routines available in the SDL Optimization Lab:

1. GRAD: this routine allows the user to implement new methods and algorithms to perform sensitivity analysis, i.e., to calculate the gradient (Jacobian) of the objective function. If used, this routine will calculate the gradient vector for all gradient-based methods already available in SDL Optimization Lab and in new optimization methods implemented by the user through user routines;
2. USEROPT: this user routine allows the user to employ new optimization methods (gradient-based or direct search methods) and strategies (sequential, parallel or hybrid). In the implementation of this routine, the user can call for unlimited times the evaluation of the objective function, the gradient, constraint functions, etc. In order to use real time monitoring, optimization process information can be send to the graphical component. Other subroutines, programmer methods and codes can be called by this user routine;
3. USER: this routine is called at many different occasions in SDL Optimization Lab allowing the user to add or retrieve additional information to the optimization process.

Other user subroutines include the customization of almost all SDL Lab environments.

Applications

In this section, several applications will be presented in order to demonstrate the potential of SDL Optimization Lab as a solver for parameter identification and shape optimization problems. The examples proposed here are not single and specific cases but represent a methodology and approach that can be generalised.

Although SDL Optimization Lab can use several optimization methods, from gradient-based to direct search methods, in a single run, sequentially or in parallel, only one optimization method will be used to exemplify the general methodology. However, it is important to notice that gradient-based and direct search methods should be used in cooperation. A direct search method is not used in the following applications due to the large time needed for a single objective function evaluation. For instance, in the last application (the determination of the initial blank geometry for the deep-drawing of a square cup), a single objective function evaluation needs ≈ 1500 s (25 minutes).

The first application shows the easiness in creating an explicit model in SDL Optimization Lab, such as an analytical function. The second application represents the parameter identification of a non-linear hardening model considering a multi-objective optimization task. The third application is a metal forming/large strains oriented example. It demonstrates the use of a framework in shape optimization problems using an external FEM programme to perform the metal forming simulation.

Creating an Analytical Function Model

An analytical function of multiple variables should be written as an explicit model where $\mathbf{Z} = \mathbf{H}(\mathbf{A})$. In this case, $\mathbf{Z}(1) = Z$ represents the final value of the analytical function. Considering the Rosenbrock function in the universe of dimension 10,

$$\begin{aligned} &\text{Function}: Z = \\ &H(\mathbf{A}) = \sum_{i=1}^{n-1}\left(1 - A_i\right)^2 + \\ &100\left(A_{i+1} - A_i^2\right)^2, \mathbf{x} \in \mathbb{R}^n, n = 10 \\ &\quad -5.12 \le A_i \le 5.12 \\ &H(\mathbf{A}^*) = 0,\ \mathbf{A}^* = \left[1,\ldots,1\right]^{\mathrm{T}}, \end{aligned} \tag{15}$$

where the global minimum value is given by $H(\mathbf{A}^*)$. A two-variable representation of the Rosenbrock's function can be seen at Figure 2. Although the Rosenbrock function is a unimodal function for two-dimensions, for higher dimensions ($n>3$) this function is not a unimodal and has two minima (Shang & Qiu, 2006).

The creation of an explicit model can be achieved with the definition of the observable variable (H) and the optimization variables (A). For this case, the model is written as

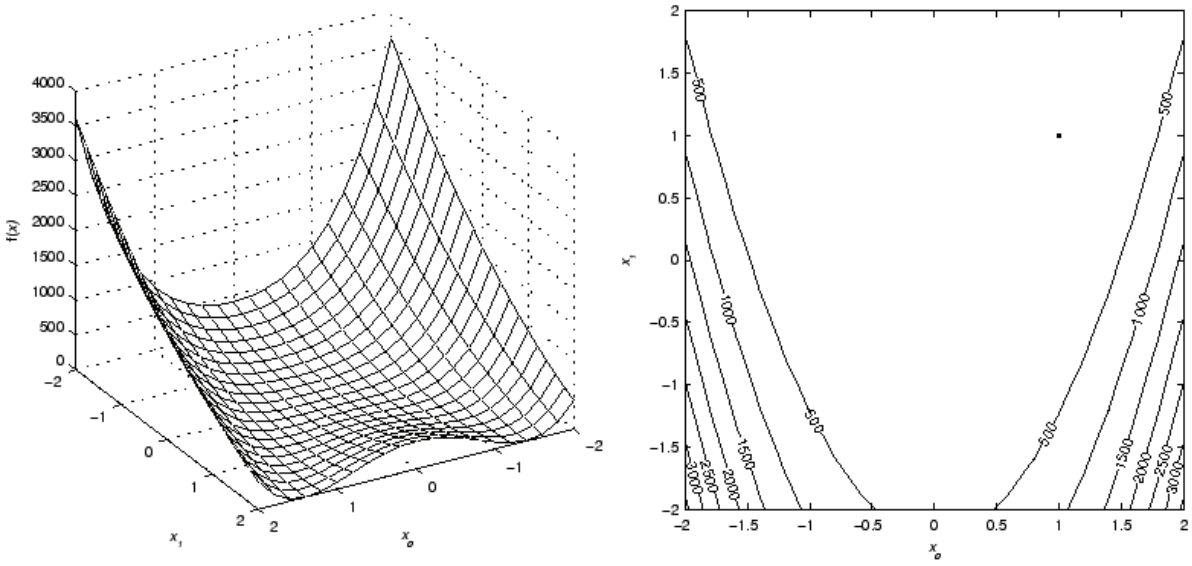
```
H=0
do i=1,9
H=H+100*(A(i+1)-A(i)**2)**2+(A(i)-1.)**2
enddo
```

considering the Fortran model routine.

Parameter Identification of a Non-Linear Hardening Model

In this example, the necking of a cylindrical bar is considered (Ponthot & Kleinermann, 2006). The initial geometry of the cylindrical specimen is of $\varnothing 12.826 \times 53.34$ [mm]. The model presents a geometric imperfection (the diameter in the middle of the bar is slightly smaller (1%) than at the end) in order to trigger necking at this specific zone. Deformation over the specimen is imposed by means of a prescribed axial displacement of 14 mm as in a tensile test. Experimental results (Norris et al., 1978) are used as reference

Figure 2. Three-dimensional representation of the Rosenbrock's function



for the calculation of the most suitable constitutive parameters to be used in the numerical simulation. The material, a special steel used in piping manufacture for nuclear industry (Ponthot & Kleinermann, 2006), is modeled following a non-linear hardening law in the following form (Simo, 1998):

$$\bar{\sigma}\left(\bar{\varepsilon}^{\mathrm{p}}\right) = \sigma^{0} + \left(\sigma^{\infty} - \sigma^{0}\right)\left(1 - \mathrm{e}^{-\delta\bar{\varepsilon}^{\mathrm{p}}}\right) + \zeta\bar{\varepsilon}^{\mathrm{p}} \tag{16}$$

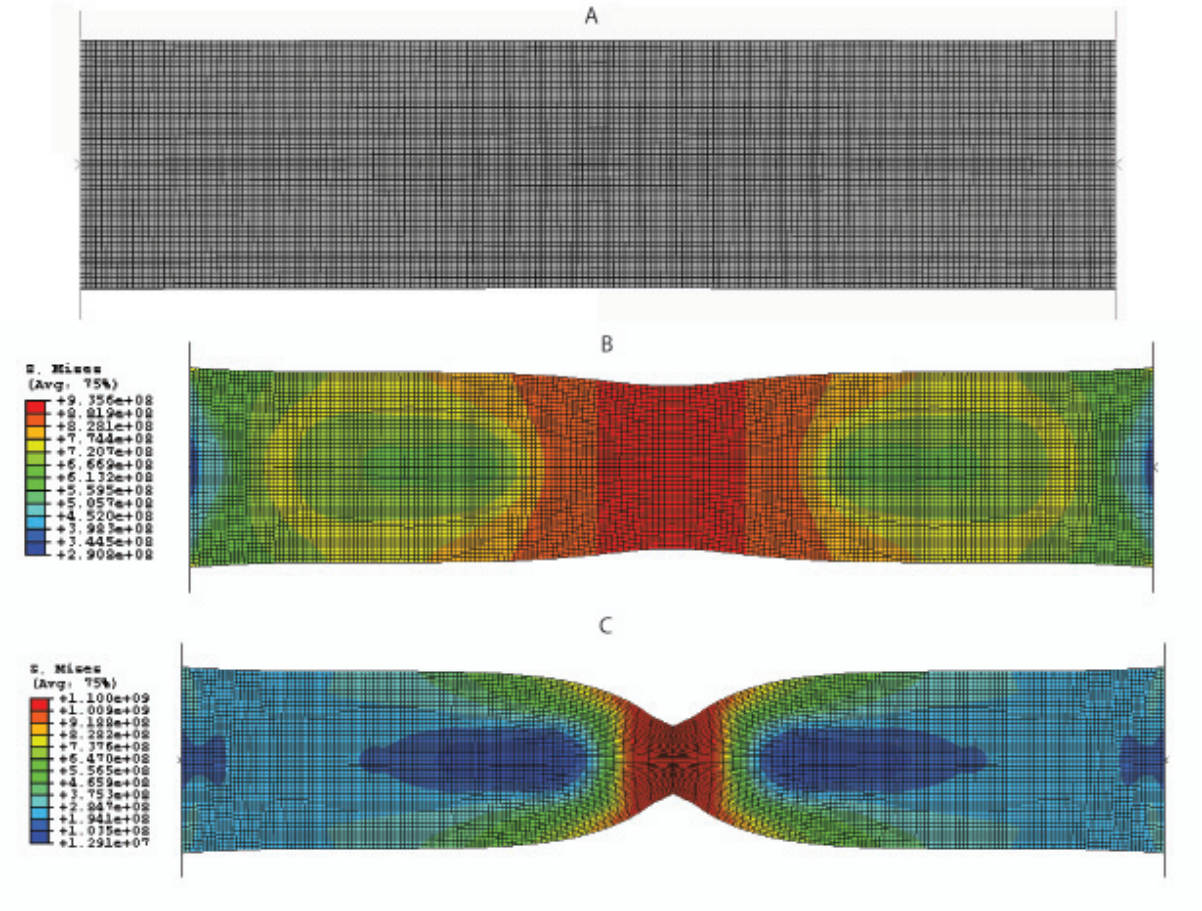
where the von Mises equivalent stress $\bar{\sigma}$ is a function of the equivalent plastic strain $\bar{\varepsilon}^{\mathrm{p}}$. The elastic parameters are considered known ($E = 206.9$ GPa and $\nu = 0.29$). Therefore, four constitutive parameters, from total of six, are unknown and need to be determined. These parameters are σ^{0}, σ^{∞}, δ and ζ and form the optimization variable vector $\mathbf{A}$. Due to the complex deformation pattern and non-homogeneous deformation in the necking region, seen in Figure 3, it is quite unattainable to fit a constitutive model onto an experimental curve (Ponthot & Kleinermann, 2006).

The objective function to minimize characterizes the gap between the results coming from the experimental curves (load *versus* elongation and necking radius evolution *versus* elongation) and the corresponding ones obtained from simulation. Considering Equation 4, the multi-objective function can then be expressed as

$$\mathcal{L}\left(\mathbf{A}\right) = \frac{1}{M_{\mathrm{L}}}\sum_{i=1}^{M_{\mathrm{L}}}\left(\frac{F_i^{\mathrm{fem}}\left(\mathbf{A}\right) - F_i^{\mathrm{exp}}}{\omega_{\mathrm{L}}^{\mathrm{abs}} + \omega_{\mathrm{L}}^{\mathrm{rel}}F_i^{\mathrm{exp}}}\right)^2 + \frac{1}{M_{\mathrm{N}}}\sum_{i=1}^{M_{\mathrm{N}}}\left(\frac{u_i^{\mathrm{fem}}\left(\mathbf{A}\right) - u_i^{\mathrm{exp}}}{\omega_{\mathrm{N}}^{\mathrm{abs}} + \omega_{\mathrm{N}}^{\mathrm{rel}}u_i^{\mathrm{exp}}}\right)^2. \tag{17}$$

where the subscript L and N stands for the load *vs* elongation and necking-radius *vs* elongation tests, respectively. In the first test, the measurable/observable variable is the Load (F). However, in the second test, the relative necking radius (u) is the measurable variable. Since the two measurable variables have different magnitudes and

Figure 3. Necking of a cylindrical bar. Deformation history of a 2376 element mesh corresponding to (a) initial configuration; (b) 8 and (c) 14 mm total elongation



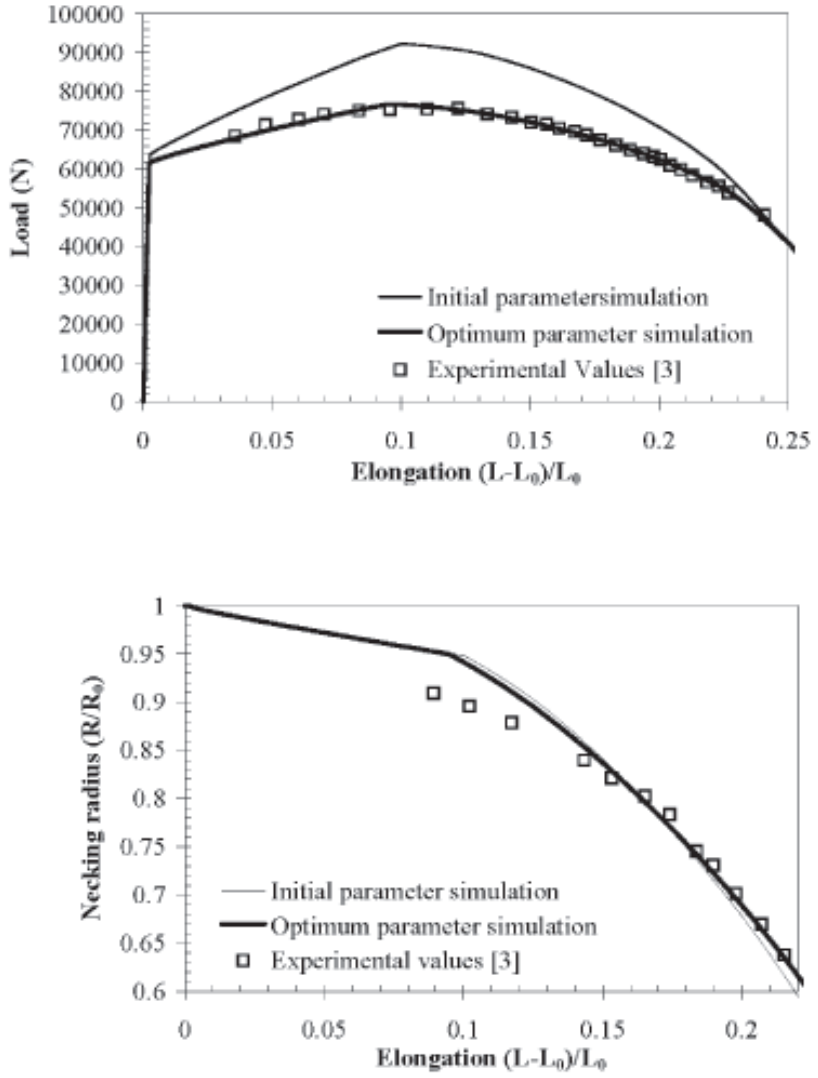
different physical interpretations, the absolute weights must balance numerically and physically both terms of Equation 17. These values should be chosen in order that the number of curves and different units in each sub-objective should not affect the overall performance of the fitting. As a result, the values of $\omega_{\mathrm{L}}^{\mathrm{abs}} = 1$ and $\omega_{\mathrm{N}}^{\mathrm{abs}} = 10^{-4}$ were taken.

The relative weights $\omega_{\mathrm{L}}^{\mathrm{rel}}$ and $\omega_{\mathrm{N}}^{\mathrm{rel}}$ were considered nulls. The numerical simulation is performed with the aid of the commercial FEM programme ABAQUS (2007) using axi-symmetric elements. For this application, the original gradient-based method of Levenberg-Marquardt (Marquardt, 1963) is employed.

The starting values and optimum parameter set are presented in Table 1. This table also shows the values obtained in Ponthot and Kleinermann (2006) or adopted by other authors (Simo, 1998). The simulation results obtained with the optimum parameters, compared to the experimental curves, are presented in Figure 4.

The values achieved for the optimum constitutive parameters, as shown in Table 1, are relatively close to those presented in the literature. It can be seen in Figure 4 that the bigger improve-

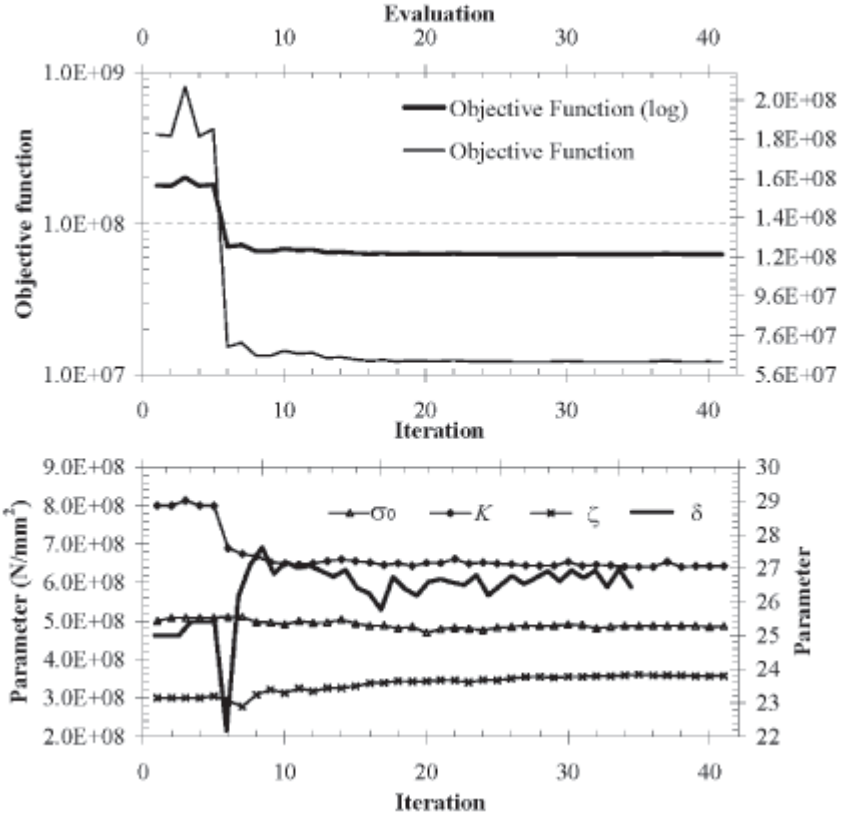
Figure 4. Comparison between experimental and simulation results for both (a) external load and (b) necking radius versus elongation



ment in the identification process was for the load-elongation curve, in which the initial parameters overrate the applied load. The necking radius evolution curve, that initially gave an acceptable approximation, nearly did not modify. The load-elongation numerical curve with the found parameters fits almost perfectly the experimental result. However, the necking radius curve only fits well the experimental curve for elongation values over 0.14 (Figure 5).

Figure 6 shows the objective function and parameters evolution during the optimization process. From this figure, it is possible to observe that almost all the optimization has taken place at the first ten iterations. Considering that the optimization method has used the first five iterations to evaluate the gradient through finite differences, the Levenberg-Marquardt method only needed five iterations to achieve an acceptable value for the objective function.

Figure 5. Objective function and parameter evolution during the optimization process for the parameter identification of a non-linear hardening model problem

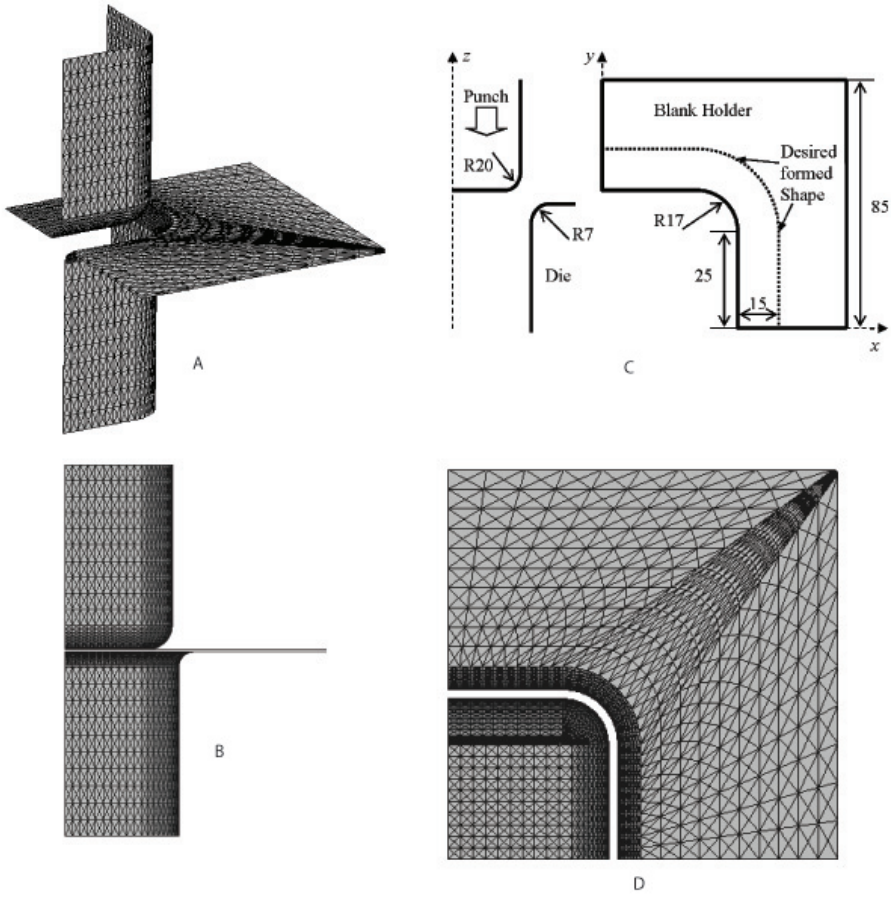


Determination of the Initial Blank Geometry for the Deep-Drawing of a Square Cup

Consider the deep-drawing forming process of a square cup using the dies with the geometry represented in Figure 6. Unfortunately, as show in Figure 7, the use of a square die leads to the formation of *ears* in the deformed square box, representing an excess of material. This phenomenon requires a posterior trim of the deformed square-box sheet in order to remove the excess of material and obtain the desired final box shape. In order to avoid the trim stage, the inverse problem of finding the geometry of the initial blank shape so that a final deep-drew form without the ears shape is obtained, similar to the shape obtained after the trim phase, is formulated. Therefore, the main goal of this problem is to determine the optimum shape of the initial blank (before forming) in order that the formed square cup would show a regular profile, without the onset of earing effects. In this case, it is possible to save initial material thus minimizing the material to be removed after the forming operation. While seeking for a regular final profile on the square cup edge (seen in the dashed lines represented in Figure 6), it is also of interest to redistribute and decrease the equivalent plastic strain levels affecting the final part, when compared to the original square cup.

In this application, the square-cup deep drawing simulations are carried out using the finite element code DD3IMP (contraction of Deep Drawing 3D Implicit code), developed by Mene-

Figure 6. Geometric representation of one quarter of the forming tools involved in the square cup problem



zes and Teodosiu (2000). DD3IMP is developed specifically to simulate sheet metal forming processes. The evolution of the deformation process is described by an updated Lagrangian scheme. An explicit approach is used to calculate an approximate first solution for the nodal displacements, the stress state and frictional contact forces. This first trial solution of the deformable

Table 1. Initially guessed and converged values for the constitutive parameters in the parameter identification of a non-linear hardening model problem

	σ^0 (MPa)	σ^∞ (MPa)	δ	ζ (MPa)
Boundaries (min, max)	(0, 10^3)	(0, 10^3)	(0, 30.0)	(0, 350.0)
Initial values	500.0	800.0	25.0	300.0
Optimum values	484.8	644.4	26.7	356.9
Ponthot and Kleinermann (2006)	458.5	657.7	18.87	311.4
Simo (1988)	450	715.0	16.93	129.2

body configuration is therefore iteratively corrected. This correction phase is done implicitly using a Newton-Raphson algorithm and finishes when a satisfactory equilibrium of the deformable body is achieved. It is then possible to update the blank sheet configuration at the end of time increment, as well as all the state variables, passing on to the calculation of the next increment until the end of the process. The Coulomb classical law is used to model the friction contact problem between the rigid bodies (tools) and the deformable body (blank). The contact with friction problem is treated by an augmented Lagrangian approach. The before mentioned fully implicit Newton-Raphson scheme is used to solve, in a single loop, all the non-linearities associated to the problem of contact with friction and the elastoplastic behaviour of the deformable body as described in

Figure 7. Final configuration of the formed square cup, with representation of the equivalent plastic strain levels

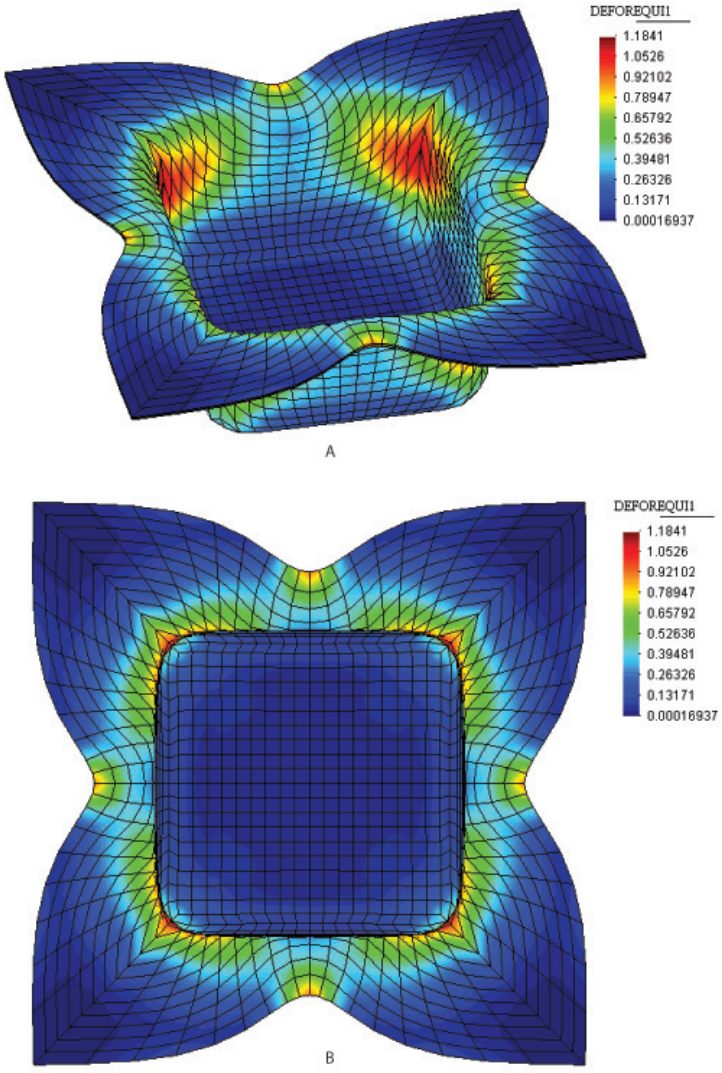


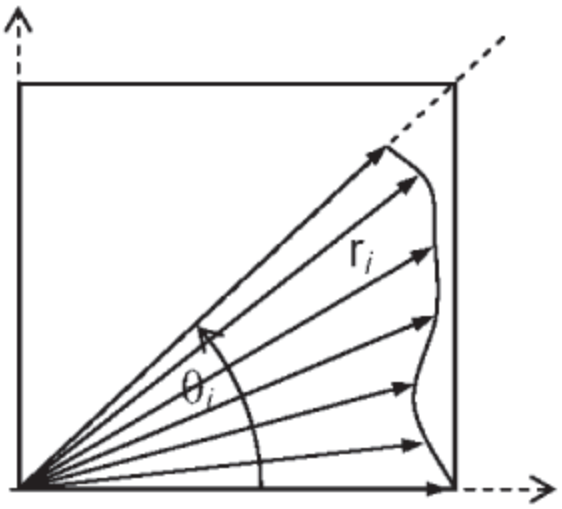
Table 2. Initial and final values of the optimization variables for the square-cup problem

A	r_1	r_2	r_3	r_4	r_5	r_6
Boundaries (min, max)	(65, 100)	(65, 100)	(65, 100)	(65, 100)	(65, 100)	(65, 110)
Initial value	75.0000	76.1569	79.8133	86.6025	97.9055	106.0660
Final value	80.6290	80.5700	80.2550	80.1043	79.6021	79.2011

Oliveira et al. (2007). The springback compensation phenomenon is also evaluated by a single-step approach (Finn, 1995) in DD3IMP and the rigid tools are handled by means of Bézier surfaces.

In order to optimize the geometry of the initial blank, one eight of its surface was covered and associated to 6 control points along its edge, as can be shown in Figure 8. Each one of the i control points to be parameterized along the edge of the representative area is geometrically characterized by the reference angle θ_i and the reference radius r_i, as represented in Figure 8. The external contour of the edge is defined as a fifth degree polynomial curve in polar coordinates and whose coefficients are found by a least-square approach. The six reference radius defines the design variable vector.

Figure 8. Parameterization of the edge (contour) points of one eight of the initial blank



The material considered in this example is a mild steel, with Young modulus of 206 GPa and Poisson coefficient of 0.3. An anisotropic yield criterion following the model of Hill (1948) was employed (Habraken, 2004), accounting for the following anisotropic coefficients:

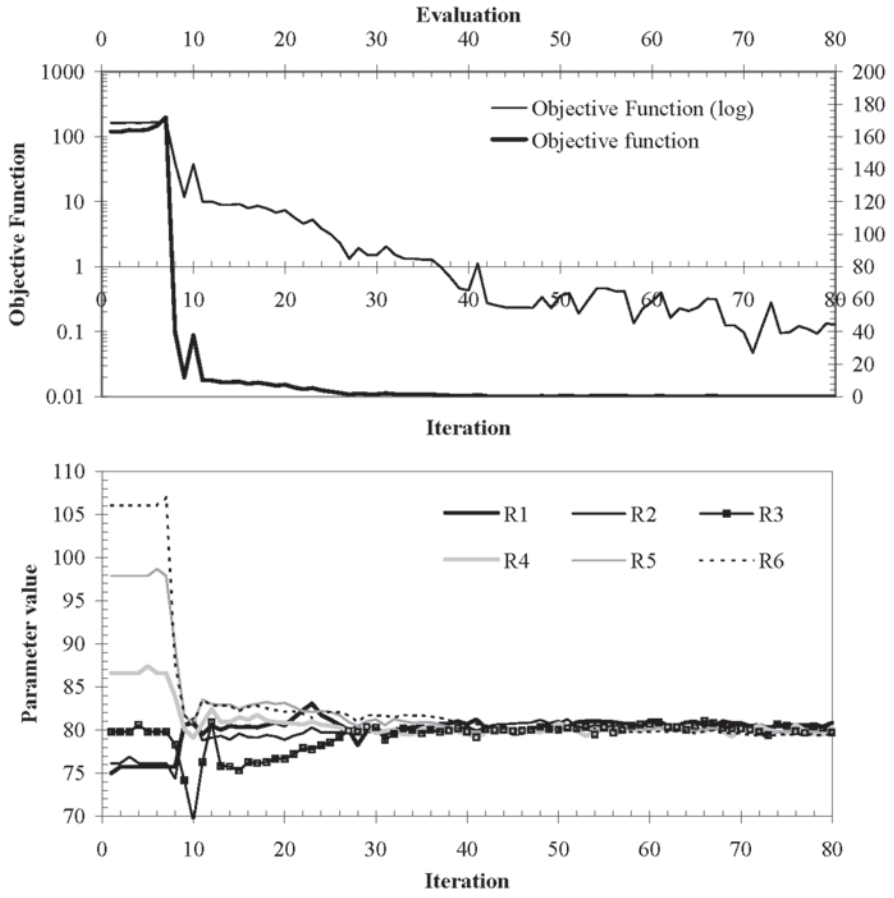
$$F = 0.2826; G = 03584; H = 0.6416; \\ L = 1.2885; M = 1.2885; N = 1.2885. \tag{18}$$

The friction coefficient considered for the contact between all involved parts is equal to 0.144. From the finite element discretization standpoint, two layers of hexahedral solid elements with 8 nodes and selective reduced integrated were considered.

The deep-drawing simulation of the square-box takes approximately 1500 s which is considered a high cost objective function evaluation. Therefore, a gradient-based algorithm must be used in this example. The original least-square Levenberg-Marquardt (Marquardt, 1963) is again employed. The forward finite-difference method with a perturbation of 0.01 is used to calculate the initial Jacobian. A stagnation value of 10^{-15} is taken for this optimization method. The initial values and boundaries for each design variable can be seen in Table 2.

Table 2 also lists the final optimized values for the design variables. The obtained values for the radius variables are similar and it nearly seems to form a circumference with the radius of 80. The evolution of the objective function and the progress of the design variables can be seen in Figure 9. In this figure, it is possible to observe that the optimization algorithm has only needed

Figure 9. Objective function and parameter evolution during the optimization process for the square-cup problem



10 iterations to reach an admissible value for the objective function. Considering that this algorithm has required the initial seven evaluations to compute the initial jacobian, it can be concluded that three effective iterations are needed to attain an acceptable result. Although the high efficiency and objectivity, the optimization algorithm continues to refine the solution through eighty iterations reaching a final value of the objective function of less than 0.1. From Figure 9, specifically in the design variable evolution curves, it is shown that all optimization variables converge approximately to the same value.

The evolution of the initial blank edge with successive simulations and optimization iterations can be seen in Figure 10. The configuration in subfigure 10(a) corresponds to the total initial square blank shape, and the corresponding simulation results for the fully formed part can be seen in figure (e), which relates to the original formed part with earing profile (Figure 7). After nine optimization iterations, the profile of the flat blank achieves the shape (b) in Figure 10, corresponding to the deformed shape of 10(f). It can be seen that the earing effect disappear totally after nine iterations.

The following subfigures in 10, corresponding to the 27th and 71st iteration (the best value), show the successive refinement accomplished by the optimization algorithm. A regular deformed

Figure 10. Evolution of the deformed shapes with iterative results coming from the optimization algorithm for the initial blank shape

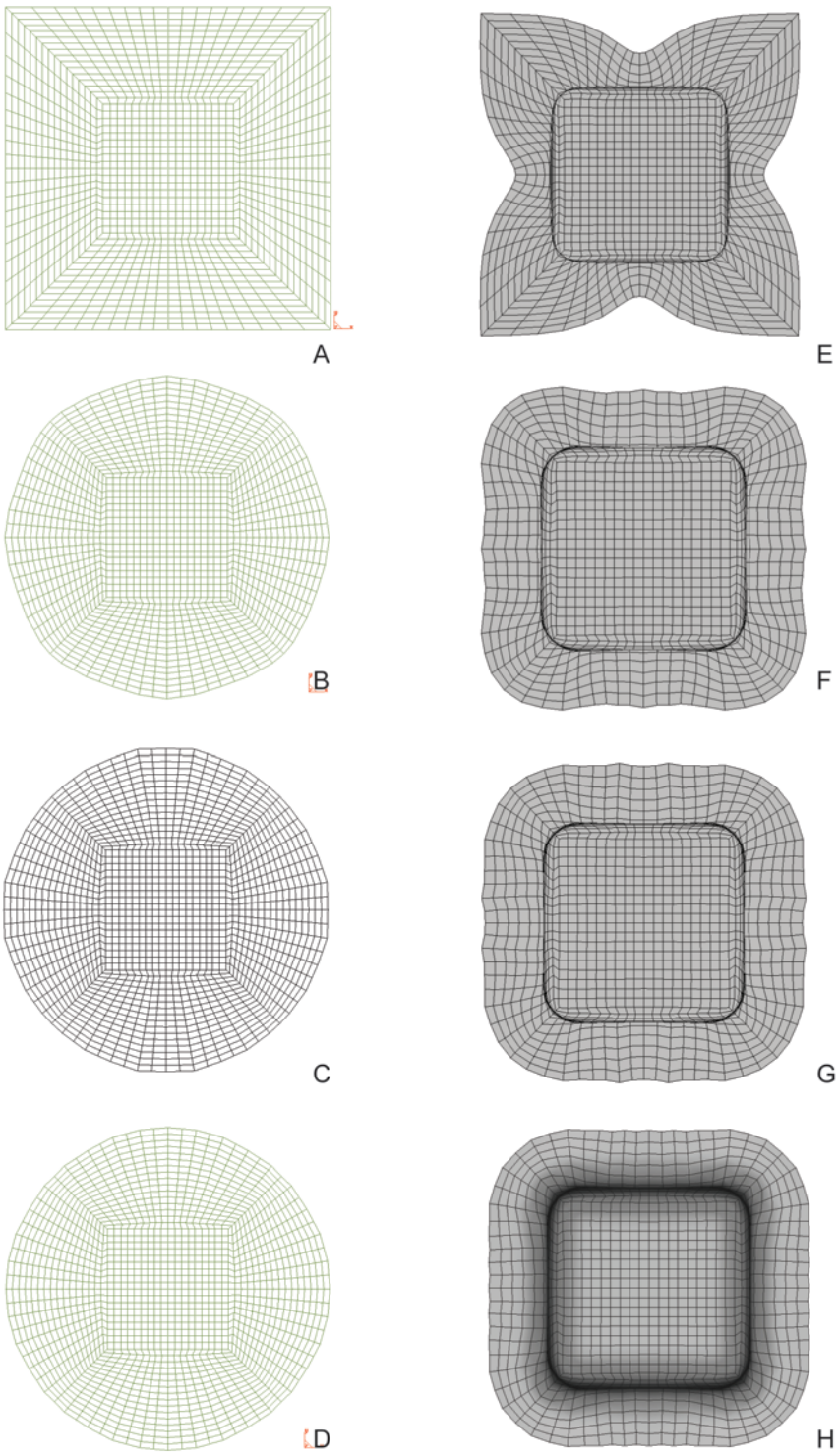
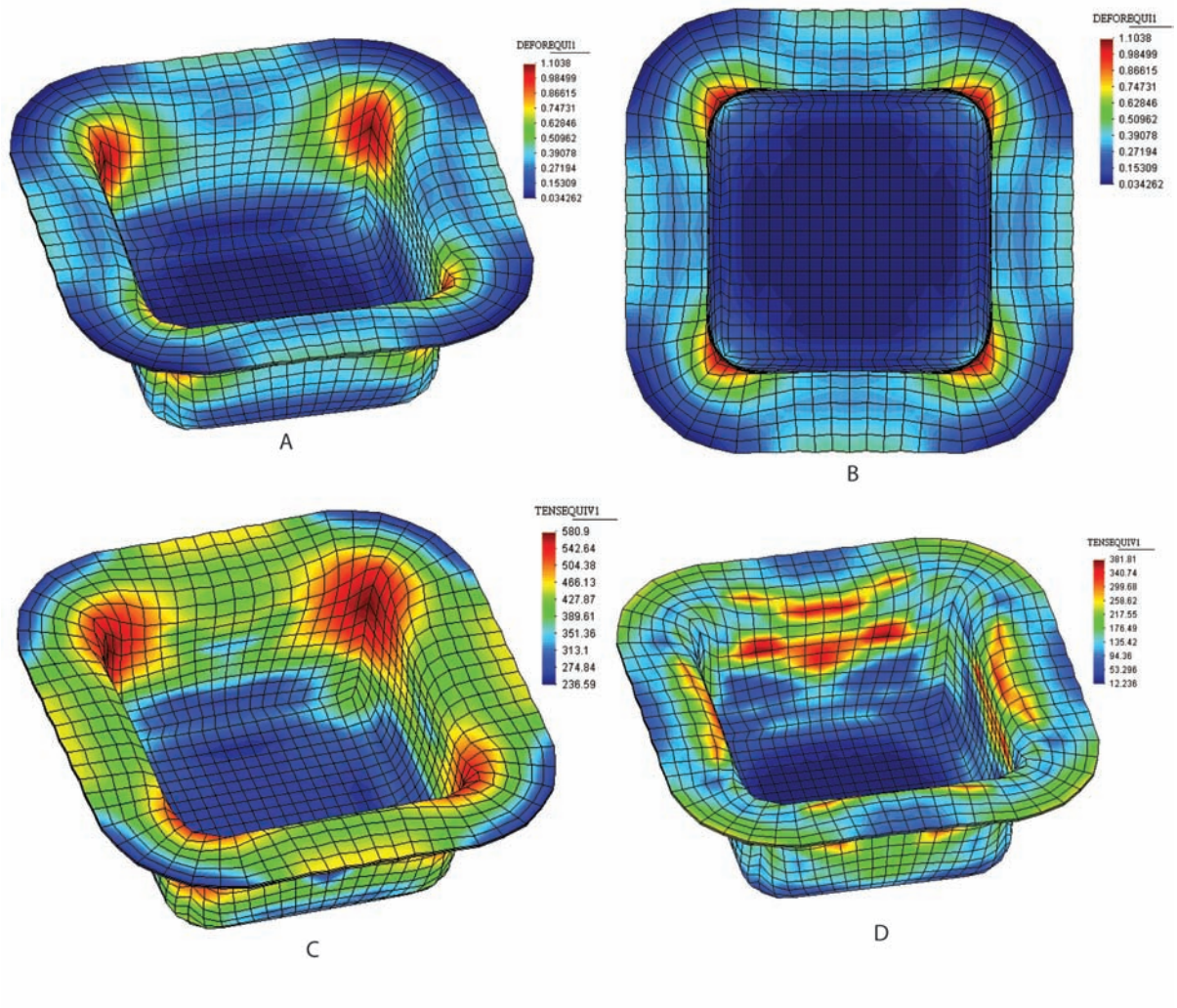


Figure 11. Deformed square cup shape, (a-b) coming from the optimum contour for initial blank. Equivalent von Mises stress contour (c) before and (d) after springback compensation



profile for the edge of the square cup, as shown in (h), is finally obtained from the optimized shape represented in picture (d) and the problem is then considered to be completed with the achievement of the optimized solution to the initial geometry of the blank.

The deformed configuration coming from the initial optimized blank shape, represented in picture (d) (Figure 10), can be seen in Figures 11(a-b), along with the equivalent plastic strain contours. It is clear the improvement of the optimized form in the figure when compared to the original square cup as coming from the initial blank shape. Although the higher values for the equivalent strain still take place at the corner of the square, the strain values of the lateral edges of the square cup have decreased. It is important to note that the results are coherent with those published by Kleinermann (2000).

Figures 11(c) and 11(d) show the von Mises equivalent stress contour before and after the springback compensation phase, respectively. It can be seen that a reduction of the stress levels is observed. Additionally, the zones with the higher

stresses are altered from the corners of the square cup to the inner lateral sides.

CONCLUSION

In this paper, an optimization framework designed for specific engineering inverse problems, such as the parameter identification and the shape optimization problems, is presented. The SDL Lab can be used by researchers that wishes to control every step of the engineering optimization procedures or by users that want to use an intuitive GUI. The numerical structures of an optimization framework and their implementation are discussed. The possibility of adding user routines in an optimization framework is highly important for researchers working in the engineering optimization field.

In order to show the capability of SDL Lab, several applications in parameter identification and shape optimization topics using SDL Lab were presented. The simplicity of creating a new optimization problem is shown through the problem of minimization of an analytical function. The use of commercial and non-commercial finite element methods codes to evaluate the objective function can be achieved using the interfaces pre-developed in SDL Lab. The shape optimization problem of the determination of the initial geometry of the blank on the deep drawing square cup problem is analysed and discussed. The main goal of this problem was to determine the optimum shape of the initial blank (before forming) in order that the formed square cup would show a regular profile, without the onset of earing effects. This objective was fulfilled showing the potentialities of the SDL optimization lab.

ACKNOWLEDGMENT

The author acknowledge the financial support given by the FCT - Fundação para a Ciência e Tecnologia and by the project PTDC/EME/PME/68975/2006. The author would also like to thanks M.C. Oliveira and L.F. Menezes for making available DD3IMP and their kind aid during the use of this code.

REFERENCES

Abaqus v6.7. (2007). Simulia Inc., Dassault Systémes.

Andrade-Campos, A., Pilvin, P., Simões, J., & Teixeira-Dias, F. (2009). *Software Development for Inverse determination of constitutive Model Parameters* (Software Engineering and Development, Chapter 4). Nova publishers. ISBN: 978-1-60692-146-3

Andrade-Campos, A., Thuiller, S., Pilvin, P., & Teixeira-Dias, F. (2007). On the determination of material parameters for internal variable thermoelastic-viscoplastic constitutive models. *International Journal of Plasticity*, *23*, 1349–1379. doi:10.1016/j.ijplas.2006.09.002

Belegundu, A. D., & Chandrupatla, T. R. (1999). *Optimization concepts and applications in engineering*. Upper Saddle River, NJ: Prentice-Hall.

Birkinshaw, M. (1998). *Some Advice on Minimization Routines (Internal Memo)*. AXAF Science Center.

Cailletaud, G., & Pilvin, P. (1994). Identification and inverse problems related to material behaviour. In *Proceedings of the International Seminar on Inverse Problems*, Clamart, France (pp. 79-86).

Cao, J., & Lin, J. (2008). A study on formulation of objective functions for determining material models. *International Journal of Mechanical Sciences*, *50*, 193–204. doi:10.1016/j.ijmecsci.2007.07.003

Ceretti, E., Braga, D., & Giardini, C. (2010). Optimization of process parameters and part geometry for high diameter tube hydroforming. In *Proceedings of the ESAFORM conference 2010 (CD-Rom)*, Brescia University, Italy (paper No. MS01-316).

Ejday, M., & Fourment, L. (2010). Metamodel assisted evolutionary algorithm for multi-objective optimization of non-steady metal forming problems. In *Proceedings of the ESAFORM conference 2010 (CD-Rom)*, Brescia University, Italy (paper No. MS01-017).

Finn, M. J., Galbraith, P. C., Wu, L., Hallquist, J. O., Lum, L., & Lin, T.-L. (1995). Use of a coupled explicit-implicit solver for calculating springback in automotive body panels. *Journal of Materials Processing Technology*, *50*, 395–406. doi:10.1016/0924-0136(94)01401-L

Fourment, L., Balan, T., & Chenot, J. L. (1996). Optimal design for non-steady-state metal forming processes. II. Application of shape optimization in forging. *International Journal for Numerical Methods in Engineering*, *39*, 51–65. doi:10.1002/(SICI)1097-0207(19960115)39:1<51::AID-NME845>3.0.CO;2-#

Habraken, A. M. (2004). Modelling the plastic anisotropy of metals. *Archives of Computational Methods in Engineering*, *11*, 3–96. doi:10.1007/BF02736210

Heeds. (2009). *Professional Design Optimization Software*. Red Cedar Technology, Inc.

Kleinermann, J.-P. (2000). *Identification Parametrique et Optimisation des Procédés de Mise a Forme par Problemes Inverses*. Unpublished doctoral dissertation, University of Liege, Liege, Belgium.

KNITRO Optimization software. (2007). Ziena Optimization Inc.

Lin, J., Cheong, B. H., & Yao, X. (2002). Universal multi-objective function for optimising superplastic-damage constitutive equations. *Journal of Materials Processing Technology*, *125-126*, 199–205. doi:10.1016/S0924-0136(02)00311-4

Liu, G. R., & Han, X. (2003). *Computational Inverse techniques in Nondestructible Evaluation*. Boca Raton, FL: CRC Press. doi:10.1201/9780203494486

Maniatty, A. M., & Zabaras, N. (1996). Investigation of regularization parameters and error estimating in inverse elasticity problems. *International Journal for Numerical Methods in Engineering*, *37*, 1039–1052. doi:10.1002/nme.1620370610

Marquardt, D. W. (1963). An algorithm for least-squares estimation of non-linear parameters. *Journal of the Society for Industrial and Applied Mathematics*, *11*, 431–441. doi:10.1137/0111030

Mathematica. (2009). *Wolfram Mathematica 7*. Wolfram Research, Inc.

Matlab. (2007). The Language of technical Computing. In *User Manual* (Vol. R2007). The Mathworks, Inc.

Menezes, L. F., & Teodosiu, C. (2000). Three-dimensional numerical simulation of the deep-drawing process using solid finite elements. *Journal of Materials Processing Technology*, *97*(1-3), 100–106. doi:10.1016/S0924-0136(99)00345-3

ModeFrontier. (2008). *ESTECO ModeFrontier - multi-objective optimization and design environment software* (Vol. 4.0). ESTECO.

Norris, D. M., Morran, J. R. B., Scudde, J. K., & Quinones, D. F. (1978). A computer simulation of the tension test. *Journal of the Mechanics and Physics of Solids*, *26*, 1–19. doi:10.1016/0022-5096(78)90010-8

Oliveira, M. C., Alves, J. L., Chaparro, B. M., & Menezes, L. F. (2007). Study on the influence of work-hardening modeling in springback prediction. *International Journal of Plasticity*, *23*, 516–543. doi:10.1016/j.ijplas.2006.07.003

Polak, E. (1997). *Optimization – Algorithms and Consistent Approximations*. New York: Springer Verlag.

Ponthot, J.-P., & Kleinermann, J.-P. (2006). A cascade optimization methodology for automatic parameter identification and shape/process optimization in metal forming. *Computer Methods in Applied Mechanics and Engineering*, *195*, 5472–5508. doi:10.1016/j.cma.2005.11.012

Rall, L. B. (1981). *Automatic Differentiation: Techniques and Applications (LNCS)*. New York: Springer Verlag.

Shang, Y. W., & Qiu, Y. H. (2006). A Note on the Extended Rosenbrock Function. *Evolutionary Computation*, *14*(1), 119–126. doi:10.1162/evco.2006.14.1.119

Simo, J. C. (1998). A framework for finite strain elastoplasticity based on maximum plastic dissipation and the multiplicative decomposition. *Computer Methods in Applied Mechanics and Engineering*, *66*, 199–219. doi:10.1016/0045-7825(88)90076-X

This work was previously published in the International Journal of Manufacturing, Materials, and Mechanical Engineering, Volume 1, Issue 1, edited by J. Paulo Davim, pp. 57-79, copyright 2011 by IGI Publishing (an imprint of IGI Global).

Chapter 2
Large Amplitude Forced Vibration Analysis of Stiffened Plates under Harmonic Excitation

Anirban Mitra
Jadavpur University, India

Prasanta Sahoo
Jadavpur University, India

Kashinath Saha
Jadavpur University, India

ABSTRACT

Large amplitude forced vibration behaviour of stiffened plates under harmonic excitation is studied numerically incorporating the effect of geometric non-linearity. The forced vibration analysis is carried out in an indirect way in which the dynamic system is assumed to satisfy the force equilibrium condition at peak excitation amplitude. Large amplitude free vibration analysis of the same system is carried out separately to determine the backbone curves. The mathematical formulation is based on energy principles and the set of governing equations for both forced and free vibration problems derived using Hamilton's principle. Appropriate sets of coordinate functions are formed by following the two dimensional Gram-Schmidt orthogonalization procedure to satisfy the corresponding boundary conditions of the plate. The problem is solved by employing an iterative direct substitution method with an appropriate relaxation technique and when the system becomes computationally stiff, Broyden's method is used. The results are furnished as frequency response curves along with the backbone curve in the dimensionless amplitude-frequency plane. Three dimensional operational deflection shape (ODS) plots and contour plots are provided in a few cases.

DOI: 10.4018/978-1-4666-1867-1.ch002

Copyright © 2013, IGI Global. Copying or distributing in print or electronic forms without written permission of IGI Global is prohibited.

INTRODUCTION

Stiffened plates are important structural elements due to their enhanced stiffness and stability characteristics with the advantage of light weight. So, it is no surprise that they are extensively used in many branches of modern civil, mechanical, and structural engineering. They have wide application in constructing marine structures like floors of bridges, bridge decks, ship hulls etc and aircraft structures. In these applications stiffened plates are regularly subjected to static and time varying loads. Hence, analysis of stiffened plates under different loading conditions has always been an area of immense interest to researches. Also when a system exhibits large amplitude vibration, the analysis no longer remains linear and therefore, a nonlinear analysis is required to investigate its dynamic behaviour.

Research work on nonlinear behaviour of stiffened plates has gone through different phases. Different researchers have employed different techniques and methodologies in carrying out nonlinear analysis of stiffened plates. In one of the earlier works Rossow and Ibrahimkhail (1978) applied the constraint method to finite element static analysis of concentrically and eccentrically stiffened plates. Koko and Olson (1991) developed a new numerical technique for large deflection elastoplastic analysis of stiffened plates using super finite elements. They derived the governing differential equations using the virtual work principle and solution was achieved by Newton-Raphson iteration technique. D. V. Rao, Sheikh and Mukhopadhyay (1993) presented a finite element analysis of large deflection behaviour of stiffened plates using the isoparametric quadratic bending element. Mukhopadhyay (1994) analyzed stiffened plates in bending through a semi-analytic finite difference method. Bedair (1997) put forward a methodology for the analysis of multi-stiffened plates under lateral loading based on energy formulation and sequential quadratic programming (SQP) technique. Sapountzakis and Katsikadelis (2000) investigated elastic deformation of ribbed plates subjected to static, transverse and in-plane loading using the analog equation method to solve nonlinearly coupled equations. Geometric non-linear analysis of stiffened plates was carried out by Sheikh and Mukhopadhyay (2000) utilizing spline finite strip method and von Karman non-linear plate theory. Ojeda, Prusty, Lawrence and Thomas (2007) introduced a new approach based on finite element analysis for large deflection analysis of isotropic and composite stiffened plates with arbitrarily oriented stiffeners. Bruback and Hellesland (2008) using semi-analytical large deflection analysis studied the strength criterion, both in local and global bending, of stiffened plates under in-plane loading. Wutzow and Paiva (2008) employed integral equations and boundary element method (BEM) to perform a linear analysis of stiffened plates.

The works on transverse and in-plane static loading and the corresponding static response of stiffened plates has been dealt with in the previous paragraph. Research work on dynamic behaviour of stiffened plates also evolved through different phases as nonlinear analysis of such structures was taken up by different researchers through different methodologies. An exhaustive idea about the techniques and methods involved in analyzing dynamic behaviour of stiffened plates can be obtained from two excellent review works (Mukherjee & Mukhopadhyay, 1986; Bedair, 1998). Aksu and Ali (1976) examined free vibration characteristic of rectangular stiffened plates having a single stiffener using the finite difference method. They minimized the total energy of the stiffened plate with respect to discretized displacement components through a variational technique and obtained natural frequencies and mode shapes as the solutions of a linear algebraic eigenvalue problem. Aksu (1982) later included the effect of in-plane inertia into free vibration analysis of stiffened plates. Pratap and Varadan (1978) dealt with the large amplitude, free flexural vibrations of clamped and simply supported stiffened plates

with two different in-plane edge conditions-movable and immovable. The solutions were obtained on the basis of a single term vibration mode shape by making use of Galerkin's method. Varadan and Pandalai (1979) investigated large amplitude free flexural vibrations of eccentrically stiffened elastic rectangular plates with clamped boundary conditions and movable in-plane edge conditions. They observed hardening type non-linearity for the system. Mukherjee and Mukhopadhyay (1988) introduced an isoparametric quadratic stiffened plate bending element for the free vibration analysis of eccentrically stiffened plates. They included the effect of shear deformation in the formulation and studied the effects of eccentricity, shape and torsional stiffness on the natural frequencies of the system. Koko and Olson (1992) carried out free vibration analysis of rectangular plates with discrete stiffener utilizing the super elements and including the effects of bending and in-plane effects as well as beam torsion and lateral bending motion. Rao, Sheikh, and Mukhopadhyay (1993) also studied large amplitude free flexural vibrations of stiffened and unstiffened plates using finite element method. Harik and Guo (1993) presented a compound finite element model based on small deflection theory to investigate free vibration of eccentrically stiffened plates. Chen, Liu, and Chern (1994) proposed a spline compound strip method for analyzing the free vibration problem of stiffened plates. Bedair and Troitsky (1997) studied the fundamental frequency characteristics of eccentrically and concentrically stiffened simply supported plates on the basis of energy formulation and Mathematical Programming technique. Bedair (1997) also presented a methodology for determination of the lowest natural frequency of stiffened plates, where the problem involving non-linear strain energy function was transformed into an unconstrained optimization problem. More recently, Peng, Liew, and Kitipornchai (2006) analyzed stability and free vibration problem of stiffened plates via the first-order shear deformable theory (FSDT) and mesh-free Galerkin method. Sapountzakis and Mokos (2008) developed an improved model presenting a general solution for the dynamic analysis of plates stiffened by arbitrarily placed parallel beams. Voros (2009) introduced a general solution method that takes into account the non-uniform torsional response of the stiffener for buckling and free vibration analysis of plates or shells stiffened by beams of arbitrary cross-section. A computationally efficient combined analytical-numerical method for prediction of modal characteristics of rectangular plates reinforced by a small number of light stiffeners was presented by Dozio and Ricciardi (2009). Xu, Du, and Li (2010) put forward an analytical method for the vibration analysis of plates stiffened by any number of beams of arbitrary lengths and placement angles.

Review of the existing literature indicates that studies are primarily focused on free vibration problem and forced vibration analysis of stiffened plates are rare. But some works on forced vibration response of thin unstiffened plates are available in literature. Leissa (1989) presented a method for determining the steady state vibratory response of continuous systems, including plates, subjected to distributed excitation forces. Kadiri and Benamar (2003) developed a semi-analytical model based on Hamilton's principle and spectral analysis, for determination of steady state periodic forced response of rectangular plates. Geometric nonlinear large amplitude forced vibration of plates was studied by Ribeiro (2004) using shooting, Newton and p-version hierarchical finite element methods. Amabili (2006) investigated, theoretically and experimentally, the large amplitude vibrations of rectangular plates with geometric imperfections subjected to harmonic excitation. In a recent work Efimtsov and Lazarev (2009) undertook forced vibration study of plates and cylindrical shells with regular orthogonal system of stiffeners.

The present paper undertakes a large amplitude forced vibration analysis of stiffened plates under harmonic excitation through a numerical method. The subsequent free vibration analysis of the sys-

tem is also presented for the sake of completeness of the study. The mathematical formulation is based on energy principle. To capture large amplitude dynamic behaviour, geometric nonlinearity of the system is considered in the formulation by incorporating nonlinear strain-displacement relations. A direct substitution method and a quasi-Newton method known as Broyden method are employed to solve the set of non-linear equations and the results are presented in the form of frequency-response curves in non-dimensional plane. Validity of the presented method is justified through comparison with existing results.

MATHEMATICAL FORMULATION

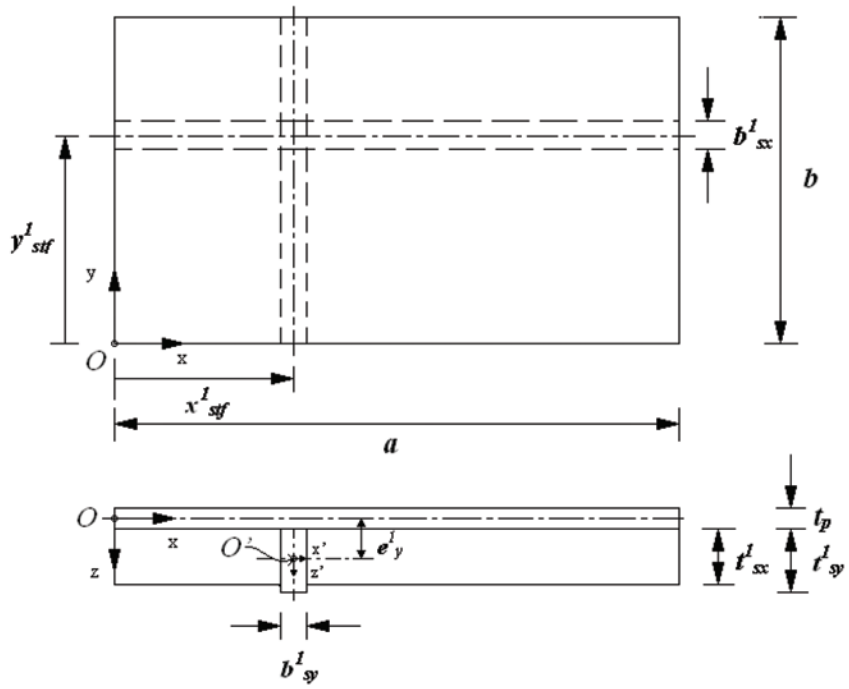
In the present study large amplitude forced vibration analysis and corresponding free vibration analysis of stiffened plates is carried out numerically. The forced vibration analysis determines the frequency response of the system in displacement amplitude versus external excitation frequency plane. A family of amplitude-frequency curves is generated for different amplitudes of external excitation, indicating functional relationship of the response amplitude with the frequency of excitation and this family of curves is termed as the frequency response of the system. The response curves are presented only in the neighbourhood of the first mode of vibration and correspond to primary resonance condition where the external excitation frequency becomes equal to the lowest fundamental frequency of the system. The mathematical formulation is based on variational form of energy principle and the set of governing equations is derived using Hamilton's principle.

The large amplitude free vibration problem is analyzed in two steps. The problem corresponding to a transverse static loading is solved first and subsequently the dynamic problem is taken up as an eigenvalue problem with the known displacement field. Both the static and dynamic problems are formulated through energy method and in both the case nonlinear strain-displacement relations are considered in deriving the governing equations, following the consideration of geometric nonlinearity. The solution is approximate in nature due to the assumption of the individual dynamic displacement fields as finite linear combinations of orthogonal admissible functions and unknown coefficients. The set of nonlinear equations obtained in case of free and forced vibration problem is solved by applying direct substitution technique with successive relaxation scheme. For forced vibration analysis in the vicinity of the backbone curve Broyden's method, which is a globally convergent solution algorithm, is employed separately to extend the response in the nonlinear zone. However, the present study only deals with steady-state dynamic response of stiffened plates under transverse harmonic excitation.

A stiffened plate with one stiffener parallel to each coordinate direction along with the significant dimensions and coordinate system used for the present analysis is shown in Figure 1. Although the figure shows only one stiffener along x- and y-axis, the formulation is carried out for stiffened plates with multiple stiffeners having generalized location and spacing in both direction. It is assumed that the stiffeners are always parallel to the edges of the plate and they are rigidly connected to the plate, which implies that there is no field discontinuity between the plate and the stiffeners. For the present study only rectangular cross-section of the stiffeners are considered. It is also assumed that the plate and stiffeners are of uniform thickness and the materials are isotropic, homogeneous and linearly elastic. Finally, the effect of shear deformation and rotary inertia and the interaction between two perpendicular stiffeners at their intersection has been neglected.

The formulation is generalized in nature to analyze problems for any classical boundary conditions and loading pattern. A complete set with 21 different boundary conditions may arise from the different combinations of clamped (C), simply supported (S) and free (F) end conditions

Figure 1. Stiffened plate with significant dimensions and coordinate system



of a plate. In order to keep the length of the paper within a reasonable limit, only the combinations of simply supported (S) and clamped (C) boundary conditions are considered for the present paper. Two of the most commonly encountered loading patterns in engineering applications namely, concentrated load and uniformly distributed load (UDL) are undertaken in the analysis. The expressions of these two harmonic loading patterns are given by,

$P = \bar{P}\, e^{i\omega\tau}$, for concentrated loading, and (1a)

$p = \bar{p}(x)\, e^{i\omega\tau}$, for uniformly distributed loading, (1b)

where, ω denotes the frequency of excitation and $i = \sqrt{-1}$. $\bar{P}$ and $\bar{p}$ represents the amplitude of harmonic excitation for concentrated and distributed loading.

Forced Vibration Analysis

In the present study forced vibration analysis under uniformly distributed harmonic excitation is carried out in an indirect way. The system response is assumed to have the same frequency as that of the external excitation as the damping in the system is considered negligible. To determine the frequency response of stiffened plate a frequency sweep is carried out at a particular amplitude of the external excitation. The sweep is started near zero value of the excitation frequency and steadily increased beyond resonance till the response amplitude falls to a sufficiently low level. Corresponding to each frequency of that particular excitation amplitude, the dynamic system is made to satisfy force equilibrium condition at the peak load value, *i.e.*, the sum of elastic and inertia forces equal the externally applied peak load level. Thus the dynamic system is reduced to an equivalent static system, whose response is dependent on

the excitation frequency and amplitude of the harmonic excitation.

The governing set of equations for the dynamic system is derived following Hamilton's principle, which states that,

$$\delta\left(\int_{\tau_1}^{\tau_2} L\, d\tau\right) = \delta\left(\int_{\tau_1}^{\tau_2} \left(T - U - V\right) d\tau\right) = 0. \qquad (2)$$

Here, T, U and V are the total kinetic energy of the system, total strain energy stored in the system and work function or potential of the external forces respectively. In the above equation L, δ and τ represent the Lagrangian, the variational operator and time coordinate respectively. The above mentioned energy functionals can be determined from the assumed transverse (w) and in-plane (u and v) dynamic displacement fields. It should be mentioned here that these dynamic displacements are defined at the neutral plane of the plate.

The total kinetic energy (T) is summation of plate kinetic energy (T_p) and stiffener kinetic energy (T_s). Hence,

$$T = T_p + T_s = T_p + \sum\nolimits_{p=1}^{ns_x} T_{sx}^p + \sum\nolimits_{q=1}^{ns_y} T_{sy}^q, \qquad (3)$$

where, T_{sx}^p, T_{sy}^q are kinetic energies of p-th stiffener along x-direction and q-th stiffener along y-direction, respectively and ns_x, ns_y are number of stiffeners in x- and y- direction. The expressions for the kinetic energies of plate and individual stiffeners are given below.

$$T_p = \frac{1}{2}\rho_p t_p (ab)\int_0^1\int_0^1 \left[\left(\frac{\partial w}{\partial \tau}\right)^2 + \left(\frac{\partial u}{\partial \tau}\right)^2 + \left(\frac{\partial v}{\partial \tau}\right)^2\right] d\xi\, d\eta$$

$$T_{sx}^p = \frac{1}{2}\rho_s t_{sx}^p (ab_{sx}^p)\int_0^1 \left[\left(\frac{\partial w}{\partial \tau}\right)^2 + \left(\frac{\partial u}{\partial \tau}\right)^2 + \left(\frac{\partial v}{\partial \tau}\right)^2\right] d\xi \qquad (4)$$

$$T_{sy}^q = \frac{1}{2}\rho_s t_{sy}^q (bb_{sy}^q)\int_0^1 \left[\left(\frac{\partial w}{\partial \tau}\right)^2 + \left(\frac{\partial u}{\partial \tau}\right)^2 + \left(\frac{\partial v}{\partial \tau}\right)^2\right] d\eta$$

where, ρ_p and ρ_s are density of the plate and stiffener materials.

Total strain energy (U) consists of two parts: strain energy stored in the plate (U_p) and total strain energy (U_s) stored in all the stiffeners. In case of large displacement analysis, both bending and stretching effects are taken into consideration. So, total strain energy stored in plate (U_p) is given by, $U_p = U_b + U_m$, where, U_b is the strain energy due to pure bending and U_m is the strain energy due to stretching of its mid-plane. The expressions of U_b and U_m have been mentioned in an earlier study (Saha, Mishra, Pohit, & Ghosal, 2004) for rectangular plates and are indicated here once again (see Box 1).

Where, E_p, υ and $D\left(= E_p\, t_p^3 \big/ 12(1-\upsilon^2)\right)$ are the elastic modulus, Poisson's ratio and the flexural rigidity of the plate respectively. u, v and w denote the displacements along x-, y- and z- directions, respectively. It is to be noted that u and v are deformation displacement whereas w is transverse displacement or deflection.

The strain energy stored in all the stiffeners can be expressed as, $U_s = \sum_{p=1}^{ns_x} U_{sx}^p + \sum_{q=1}^{ns_y} U_{sy}^q$, where U_{sx}^p, U_{sy}^q are strain energies stored in p-th stiffener along x-direction and q-th stiffener along y-direction and ns_x, ns_y are number of stiffeners in x- and y- direction respectively. These two strain energies can be calculated from the following expressions.

$$U_{sx}^p = \frac{E_s}{2}\iiint_{Vol} (\varepsilon_{xx}^s)^2\, dV \qquad (7a)$$

$$U_{sy}^q = \frac{E_s}{2}\iiint_{Vol} (\varepsilon_{yy}^s)^2\, dV \qquad (7b)$$

Table 1. Start functions for assumed displacement fields w, u and v

Boundary Condition	Start Function for w ($\varphi_1(\xi,\eta)$)
SCSS	$\{\sin(\pi\xi)\}.\{\eta^2(3-5\eta+2\eta^2)\}$
CCSS	$\{\xi^2(3-5\xi+2\xi^2)\}.\{\eta^2(3-5\eta+2\eta^2)\}$
CSCS	$\{\xi(1-\xi)\}^2.\{\sin(\pi\eta)\}$
CCCS	$\{\xi(1-\xi)\}^2.\{\eta^2(3-5\eta+2\eta^2)\}$

where, E_s is the elastic modulus of the stiffener material and ε^s_{xx} is the total axial strain of a stiffener along x-direction and it includes axial strain due to bending about the major axis, axial strain due to stretching of mid-plane and axial strain due to bending about the minor axis and can be expressed as,

$$\varepsilon^s_{xx} = \frac{du}{dx} + \frac{1}{2}\left(\frac{dw}{dx}\right)^2 - z_s\frac{d^2w}{dx^2} - y_s\frac{d^2v}{dx^2}. \tag{8}$$

Substituting (8) in (7a) the strain energy stored in a single x-direction stiffener is obtained as,

$$U^p_{sx} = \frac{E_s a}{2}\int_0^1 \left[I^p_y \frac{1}{a^4}\left(\frac{d^2w}{d\xi^2}\right)^2 + I^p_{yz}\frac{1}{a^4}\left(\frac{d^2v}{d\xi^2}\right)^2 - Q^p_y\left\{\frac{2}{a^3}\left(\frac{du}{d\xi}\right)\left(\frac{d^2w}{d\xi^2}\right)+\frac{1}{a^4}\left(\frac{d^2w}{d\xi^2}\right)\left(\frac{dw}{d\xi}\right)^2\right\}+ A^p_y\left\{\frac{1}{a^2}\left(\frac{du}{d\xi}\right)^2+\frac{1}{4a^4}\left(\frac{dw}{d\xi}\right)^4+\frac{1}{a^3}\left(\frac{du}{d\xi}\right)\left(\frac{dw}{d\xi}\right)^2\right\}\right] d\xi \tag{9}$$

Box 1.

$$U_b = \frac{D}{2}(ab)\int_0^1\int_0^1 \left[\left\{\frac{1}{a^2}\left(\frac{\partial^2 w}{\partial\xi^2}\right)+\frac{1}{b^2}\left(\frac{\partial^2 w}{\partial\eta^2}\right)\right\}^2 + 2\times(1-\upsilon)\frac{1}{a^2b^2}\left\{\left(\frac{\partial^2 w}{\partial\xi\,\partial\eta}\right)^2 - \left(\frac{\partial^2 w}{\partial\xi^2}\right)\left(\frac{\partial^2 w}{\partial\eta^2}\right)\right\}\right] d\xi\,d\eta \tag{5}$$

$$U_m = \frac{E_p t_p}{2(1-\upsilon^2)}(ab)\int_0^1\int_0^1 \left[\frac{1}{a^2}\left(\frac{\partial u}{\partial\xi}\right)^2+\frac{1}{a^3}\left(\frac{\partial u}{\partial\xi}\right)\left(\frac{\partial w}{\partial\xi}\right)^2+\frac{1}{b^2}\left(\frac{\partial v}{\partial\eta}\right)^2+\frac{1}{b^3}\left(\frac{\partial v}{\partial\eta}\right)\left(\frac{\partial w}{\partial\eta}\right)^2 + \frac{1}{4}\left\{\frac{1}{a^2}\left(\frac{\partial w}{\partial\xi}\right)^2+\frac{1}{b^2}\left(\frac{\partial w}{\partial\eta}\right)^2\right\}^2 + 2\upsilon\left\{\frac{1}{ab}\left(\frac{\partial u}{\partial\xi}\right)\left(\frac{\partial v}{\partial\eta}\right)+\frac{1}{2a^2b}\left(\frac{\partial v}{\partial\eta}\right)\left(\frac{\partial w}{\partial\xi}\right)^2 + \frac{1}{2ab^2}\left(\frac{\partial u}{\partial\xi}\right)\left(\frac{\partial w}{\partial\eta}\right)^2\right\} + \frac{1-\upsilon}{2}\left\{\frac{1}{b^2}\left(\frac{\partial u}{\partial\eta}\right)^2+\frac{2}{ab}\left(\frac{\partial u}{\partial\eta}\right)\left(\frac{\partial v}{\partial\xi}\right)+\frac{1}{a^2}\left(\frac{\partial v}{\partial\xi}\right)^2 + \frac{2}{ab^2}\left(\frac{\partial u}{\partial\eta}\right)\left(\frac{\partial w}{\partial\xi}\right)\left(\frac{\partial w}{\partial\eta}\right)+\frac{2}{a^2b}\left(\frac{\partial v}{\partial\xi}\right)\left(\frac{\partial w}{\partial\xi}\right)\left(\frac{\partial w}{\partial\eta}\right)\right\}\right] d\xi\,d\eta \tag{6}$$

Similarly, strain energy stored in a single y-direction stiffener is obtained as,

$$U_{sy}^{q} = \frac{E_s b}{2}\int_0^1 \left[I_x^q \frac{1}{b^4}\left(\frac{d^2w}{d\eta^2}\right)^2 + I_{xz}^q \frac{1}{b^4}\left(\frac{d^2u}{d\eta^2}\right)^2 - Q_x^q \left\{ \frac{2}{b^3}\left(\frac{dv}{d\eta}\right)\left(\frac{d^2w}{d\eta^2}\right) + \frac{1}{b^4}\left(\frac{d^2w}{d\eta^2}\right)\left(\frac{dw}{d\eta}\right)^2 \right\} + A_x^q \left\{ \frac{1}{b^2}\left(\frac{dv}{d\eta}\right)^2 + \frac{1}{4b^4}\left(\frac{dw}{d\eta}\right)^4 + \frac{1}{b^3}\left(\frac{dv}{d\eta}\right)\left(\frac{dw}{d\eta}\right)^2 \right\} \right] d\eta \tag{10}$$

where, E_s is the elastic modulus of the stiffener material. I_y^p, I_x^q and I_{yz}^p, I_{xz}^q are moment of inertia of the *p*-th (*x*-direction) and *q*-th (*y*-direction) stiffener cross-section about the coordinate axes of the plate. They can be determined by carrying out suitable transformation on the moment of inertia about the centroidal axes of the stiffener cross-section. For example, in case of a single *y*-direction stiffener, I_x^1 and I_{xz}^1 are determined by using following relations:

$I_x^1 = I_x^{1'} + A_x^1.e_y^{12}, I_{xz}^1 = I_{xz}^{1'} + A_x^1.(a\xi_{stf}^1)^2$ where, $I_x^{1'} (= b_{sy}^1 t_{sy}^{1\,3} \big/ 12)$ and $I_{xz}^{'} (= b_{sy}^{1\,3} t_{sy}^1 \big/ 12)$ are moment of inertia about the major and minor axis of the stiffenercross-sectionand $A_x^1 = b_{sy}^1 t_{sy}^1, , \xi_{stf}^1 = x_{stf}^1 \big/ a$, $e_y^1 = (t_p + t_{sy}^1)/2$. Q_y^p, Q_x^q are the first moment of area about the plate coordinate axes and A_y^p, A_x^q are the cross-sectional areas of the *p*-th *x*- and *q*-th *y*-direction stiffeners respectively. $Q_x^1 = A_x^1.e_y^1$ for a *y*-directional stiffener as shown in Figure 1. Similar transformations and nomenclatures have been used for *x*-directional stiffeners also.

The potential of the external forces is calculated corresponding to the peak load level. For a stiffened plate under uniform transverse pressure (*p*) and a concentrated load (*P*) total potential energy is given by,

$$V = -P\,w\,|_{\xi,\eta} - (ab)\int_0^1\int_0^1 (pw)\,d\xi\,d\eta \tag{11}$$

where, $w\,|_{\xi,\eta}$ is the deflection of the point of application of the concentrated load. In Equations (4), (5), (6), (9), (10) and (11) the mid-plane coordinates are expressed in dimensionless form as $\xi = x/a$, $\eta = y/b$, while the dimensions of all other physical quantities, such as load, deflection, elastic modulus etc., are retained as such. It is to be noted that the computations are carried out in normalized coordinate ξ and η.

Approximate Dynamic Displacement Fields

The dynamic displacements $w(\xi,\eta,\tau)$, $u(\xi,\eta,\tau)$ and $v(\xi,\eta,\tau)$ are assumed to be separable in space and time and can be approximately represented by finite linear combinations of orthogonal admissible functions and unknown coefficients d_i. They are expressed as shown below:

$$w\left(\xi,\eta,\tau\right) = \sum_{i=1}^{nw} d_i\,\varphi_i\left(\xi,\eta\right)\gamma_i\left(\tau\right)$$

$$u\left(\xi,\eta,\tau\right) = \sum_{i=nw+1}^{nw+nu} d_i\,\alpha_{i-nw}\left(\xi,\eta\right)\,\gamma_{i-nw}\left(\tau\right) \tag{12}$$

$$v\left(\xi,\eta,\tau\right) = \sum_{i=nw+nu+1}^{nw+nu+nv} d_i\,\beta_{i-nw-nu}\left(\xi,\eta\right)\gamma_{i-nw-nu}\left(\tau\right)$$

where, φ_i, α_i and β_i are sets of orthogonal functions for *w*, *u* and *v* and *nw*, *nu* and *nv* are the number of functions, respectively. The set of temporal function is expressed by $\gamma_i\left(\tau\right) = e^{i\omega\tau}$, where ω represents response frequency of the system under the specified loading. Appropriate start functions for these orthogonal sets are selected in such a way that they satisfy the flexural and membrane boundary conditions of the plate. The functions $\varphi_i(\xi,\eta)$ describe the displacements due to plate bending and the base function for this comes from the flexural boundary condition. The

start functions for stretching of the plate (u and v) come from the in-plane boundary conditions and zero displacement is assumed at the boundary edges *i.e.* $u = 0$ at $\xi = 0,1$ and $v = 0$ at $\eta = 0,1$. The higher-order functions are generated from the selected start functions following a two-dimensional implementation of the Gram-Schmidt orthogonalization scheme.

The displacement fields depicted in Equation (12) are two-dimensional and compatible with the plate. But the stiffeners are one-dimensional element and hence the chosen displacement fields require modification in order to be compatible with stiffeners. The justification of using the displacement fields of the plate is that the displacements at the junction of the plate and the stiffener are always equal. An interpolation function is used on the plate displacement values to transform the two-dimensional function into the one-dimensional displacement function at the location of the stiffener. For example, in case of the *y*-direction stiffener shown in Figure 1 the transverse displacement function is given by, $w(\xi,\eta)\,|_{\xi^1_{stf}} = w(\xi^1_{stf},\eta)$.

Governing System of Equations

Substitution of the complete expressions of the energy functionals and approximate displacement fields given in the previous section in Equation (2) gives the governing set of equations for the system under harmonic excitation in matrix form,

$$-\omega^2\left[M\right]\left\{d\right\}+\left[K\right]\left\{d\right\}=\left\{f\right\}. \qquad (13)$$

[K], [M] and *{f}* are stiffness matrix, mass matrix and load vector respectively. {d} is the vector of unknown coefficients. The total stiffness matrix [K] in (13) is given by, $\left[K\right]=\left[K_b\right]+\left[K_m\right]+\sum_{p=1}^{ns_x}\left[K_{sx}\right]^p+\sum_{q=1}^{ns_y}\left[K_{sy}\right]^q$, $\left[K_b\right]$ and $\left[K_m\right]$ being the contributions from bending and stretching action of the plate, whereas $\left[K_{sx}\right]^p$ and $\left[K_{sy}\right]^q$ are stiffness matrices of the p-th stiffener along x-direction and q-th stiffener along y-direction, respectively. The mass matrix is made up of contributions from the plate ($[M_p]$) and the x- and y-direction stiffeners ($[M_{sx}]$ and $[M_{sy}]$). These vectors as well as the total stiffness matrix and mass matrix have an order of (nw+nu+nv). The details of the stiffness matrices, mass matrices and load vector are furnished in the Appendix.

Solution Methodology for Forced Vibration Problem

Equation (13) represents the governing set of equations for the stiffened plate and can also be expressed as $\left[[K]-\omega^2[M]\ \right]\left\{d\right\}=\left\{f\right\}$. Here, the load vector {f} contains the amplitude of excitation ($\bar{P}$ or $\bar{p}$). The set of governing Equations (13) are nonlinear in nature as the stiffness matrix ($[K]$) is a function of the unknown coefficients (d_i), and hence cannot be solved directly. It can be said that the matrix $\left[\ [K]-\omega^2[M]\ \right]$ is an equivalent stiffness matrix, which represents the dynamic system stiffness and for a specified magnitude of loading, it depends on the frequency of loading as the forcing frequency appears explicitly in its expression. It is also important to note that with increase in the frequency of excitation, the dynamic stiffness may change its sign and usually it occurs when $\omega > \omega_1$, where, ω_1 is the first natural frequency of the stiffened plate.

Two different solution techniques, namely substitution method and Broyden's method, are utilised to solve the nonlinear system of equations. In substitution method the equations are solved through an iterative procedure utilizing the successive relaxation scheme. For a certain amplitude and frequency of harmonic excitation the values of the unknown coefficients are assumed and based on that, new values are calculated by matrix inversion. Calculated values are compared

with corresponding values in the previous iteration and convergence is achieved when the difference is below a predefined value of error limit (ε). Otherwise the values of $\{d\}$ are modified with a relaxation parameter and they are taken as the next approximation for the values of $\{d\}$. Broyden's method (Press, Teukolsky, Vetterling & Flannery, 2005) is a multidimensional quasi-Newton method for the numerical solution of a system of nonlinear equations. In this method an initial Jacobian of the system is calculated depending on the initial guess value and in the successive iterations an updated value of the Jacobian is used. Both these methods are dependent on the initial guess values. The solution procedure is elaborated for particular load and frequency value setting in the flow chart shown in Figure 2.

Free Vibration Analysis: Determination of Backbone Curve

In this section free vibration analysis is taken up under loaded condition to determine the backbone curve of the system, which is not achievable from forced vibration study. For a non-linear system, large amplitude free vibration analysis is essentially same as the free vibration analysis of the system subjected to a static load producing large amplitude deflection (Crandall, 1956) of same magnitude. Hence the present large amplitude free vibration analysis of stiffened plates is carried out in two steps. First, large displacement is statically imposed by applying transverse loading on the stiffened plate and then the free vibration analysis is performed as an eigen value problem to identify the loaded natural frequency. It can be said that static analysis yields the initial deflection profile used in the subsequent free vibration analysis. The variation of the natural frequency with the maximum amplitude of deflection yields the backbone curve of the system and graphically it represents the plot of non-dimensional frequency-amplitude relationship. For a physical system there exist different backbone curves for different modes of vibration. However, in the present scenario, only the first mode of vibration of the system is taken into consideration.

Static Analysis

The set of governing equations for the static problem is obtained by applying the principle of minimization of total potential energy of the system, which is given by,

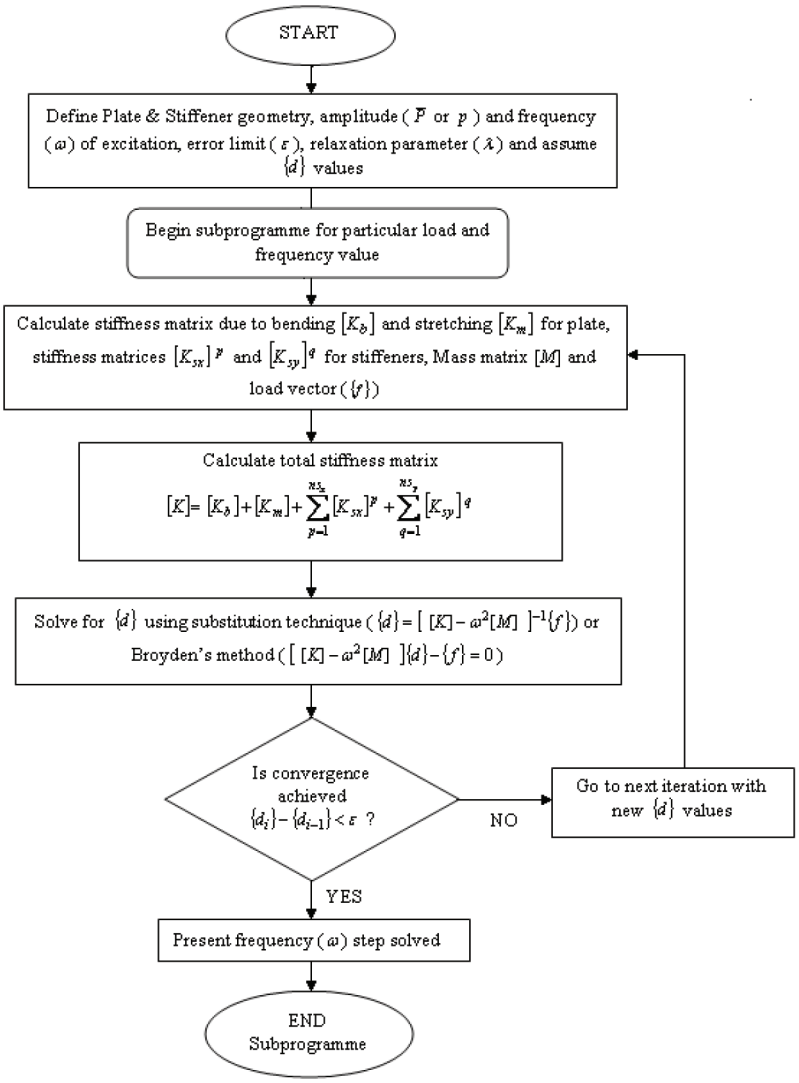
$$\delta\left(U+V\right)=0\,. \tag{14}$$

where, U is total strain energy stored in the system, V is work function or potential of the external forces and δ is the variational operator. The expressions of strain energies for plate and stiffeners are identical to those given by Equations (5), (6), (9) and (10), whereas the expression of V remains same as that given in Equation (11), except for the fact that the load becomes purely static. This implies that the expression for load does not contain any temporal or time varying function, unlike that given by Equation (1). The displacement fields assumed for the static problem are dependent on the axial coordinates x and y only and are independent of any time varying component. The assumed displacement fields are of the following form:

$$\begin{aligned} w\left(\xi,\eta\right) &= \sum_{i=1}^{nw} d_i\,\varphi_i\left(\xi,\eta\right), \\ u\left(\xi,\eta\right) &= \sum_{i=nw+1}^{nw+nu} d_i\,\alpha_{i-nw}\left(\xi,\eta\right), \\ v\left(\xi,\eta\right) &= \sum_{i=nw+nu+1}^{nw+nu+nv} d_i\,\beta_{i-nw-nu}\left(\xi,\eta\right) \end{aligned} \tag{15}$$

The sets of orthogonal admissible functions φ_i, α_i and β_i are essentially identical to those used in the forced vibration analysis. Substituting the expressions for strain energy and work function along with the assumed displacement fields given by Equation (15) in Equation (14) the set

Figure 2. Flow chart of the solution algorithm



of governing equations for the static problem is obtained in the form given below.

$$[K]\{d\}=\{f\} \tag{16}$$

where, $[K]$ and $\{f\}$ are stiffness matrix and load vector, respectively. The format and elements of $[K]$ and $\{f\}$ are identical to those mentioned for the forced vibration analysis in the previous section. In fact, as a special case if $\omega=0$ is substituted in Equation (13) it is reduced to the form given by Equation (16). This is due to the fact that both the equations describe the equilibrium of the system under transverse loading. In case of forced vibration the assumption of satisfying force equilibrium at the peak load value of external harmonic excitation contains inertia force as an additional term.

The nature of the governing set of equations given by (16) is nonlinear as the stiffness matrix $[K]$ is nonlinear. The set of nonlinear equations

are solved through a direct substitution method with successive relaxation technique, which has already been discussed in relation to the solution methodology of the forced vibration problem. The solution of the static analysis provides the statically imposed large displacement fields of the system, which serves as the starting point for the dynamic analysis, where the free vibration frequencies are determined at the deflected configuration.

Dynamic Analysis

The dynamic problem is formulated by applying Hamilton's principle as given by Equation (2). The expressions for these energy functionals T, U and V are identical to those provided for the forced vibration analysis. However, as the present analysis deals with a free vibration problem the potential of the external loading reduces to zero as the term V vanishes due to absence of external forces. The dynamic displacements $w(\xi,\eta,\tau), u(\xi,\eta,\tau)$ and $v(\xi,\eta,\tau)$ are assumed to be linear combination of space and time functions as shown previously in Equation (12). But for the free vibration analysis d_i is a different set of unknown coefficients, which represent the contribution of the individual space functions. The sets of admissible functions φ_i, α_i and β_i are same as used for the earlier forced vibration analysis and the set of temporal functions is expressed by $\gamma_i(\tau) = e^{i\omega\tau}$, where ω represents the natural frequency of the system.

After carrying out the necessary substitutions in Equation (2), the governing set of equations for the dynamic problem is obtained as

$$-\omega^2[M]\{d\} + [K]\{d\} = 0\,. \qquad (17)$$

Here, [K] and [M] are stiffness matrix and mass matrix, respectively and their forms and elements are same as that used for the forced vibration analysis. As mentioned earlier, the stiffness matrix [K] is nonlinear in nature. The nonlinear terms of the stiffness matrix for the eigen value problem is linearised using the solution of the static problem and thus the effect of statically imposed large amplitude of vibration is incorporated into the dynamic system. The standard eigen value problem of equation (17) is solved numerically by using IMSL routines. The square roots of the calculated eigen values represent the free vibration frequencies of the stiffened plate at the statically deflected configuration and are called the loaded natural frequencies. The amplitude of free vibration is provided by the displacement fields associated with the each of the eigen values. The plot of these frequencies against the corresponding amplitudes in non-dimensional plane represents the backbone curve, as stated earlier.

RESULTS AND DISCUSSIONS

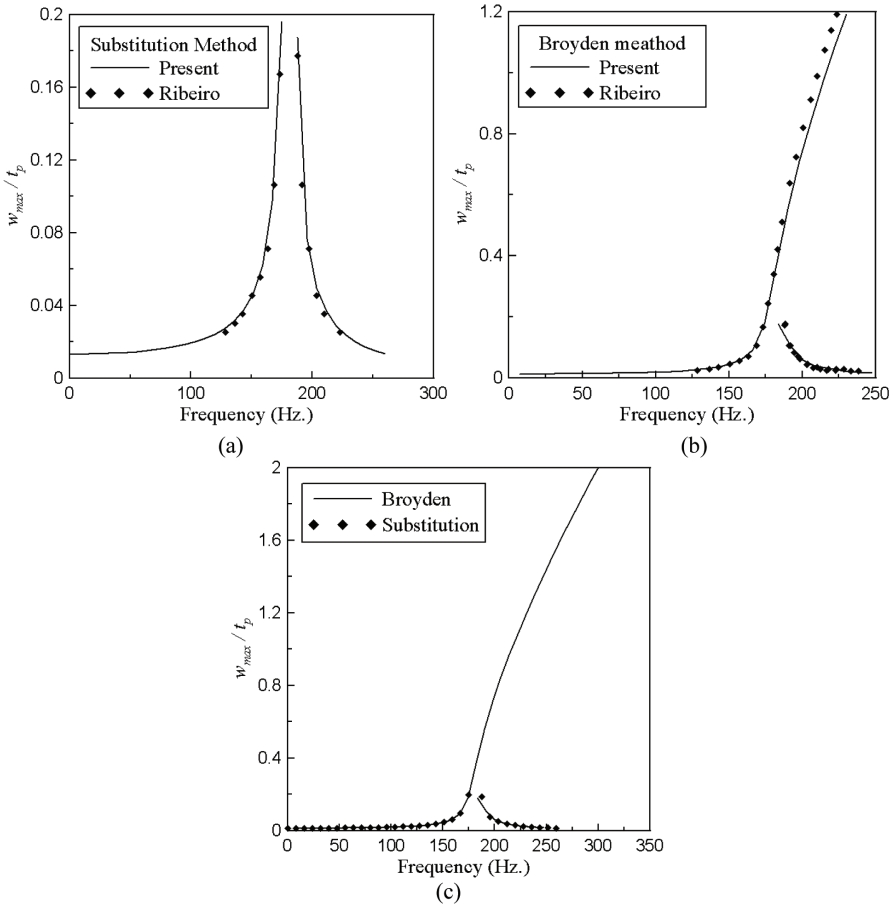
The objective of the present study is to investigate the large amplitude forced vibration behaviour of stiffened plates under harmonic excitation. The influence of stiffener position (ξ^i_{stf}), plate aspect ratio (a/b) and stiffener to plate thickness ratio (t_s/t_p) on the frequency response have been studied. The results are presented as frequency response curves in non-dimensional frequency-amplitude plane, where the ordinate represents normalized maximum amplitude of vibration (w_{max}/t_p) and the abscissa represents normalized excitation frequency (ω/ω_1). The normalization of the forcing frequency is done by the first natural frequency (ω_1), which is obtained from the free vibration analysis of the system. On the other hand, maximum amplitude of vibration is normalized by thickness of the plate.

The present analysis is carried out for a uniaxially single stiffened plate, classified according to number and orientation of the stiffener. For the above mentioned type of plate simply supported boundary condition at all the edges has been

considered. The start function for the definition of transverse deflection (w) comes from the simply supported ends and is given by $\varphi_1(\xi,\eta) = \sin(\pi\xi).\sin(\pi\eta)$. It should be pointed out here that due to the general nature of the formulation any other classical flexural boundary conditions can be handled through this method. In this regard some results pertaining to different boundary conditions arising out of the combinations of clamped (C) and simply supported (S) boundary are presented. These classical boundary conditions are namely, CCCS, CCSS, CSCS and SCSS. In this study, the nomenclature of the boundary conditions of the plate has been specified through its edge conditions (C or S) starting from the edge $x = 0$ and proceeding in counter-clockwise direction. The start functions selected for the mentioned boundary conditions are specified in Table 1.

The start functions for the stretching of the plate (u and v) are modeled as immovable by imposing zero in-plane displacements and they are given by, $\alpha_1(\xi,\eta) = \{\xi(1-\xi)\}.\{\eta(1-\eta)\}$ and $\beta_1(\xi,\eta) = \{\xi(1-\xi)\}.\{\eta(1-\eta)\}$. These selected start functions are used to generate the higher order functions with the help of two-dimensional Gram-Schmidt orthogonalisation principle. The number of functions for each of the plate displace-

Figure 3. Comparison of frequency response of an unstiffened clamped square plate under uniformly distributed harmonic excitation at 2000 Pa amplitude: (a) Substitution method and Ribeiro (2004), (b) Broyden method and Ribeiro (2004) and (c) Substitution and Broyden method



ments (u, v and w) is taken as 25 (5×5), i.e., 5 functions corresponding to two orthogonal directions. Any transverse loading pattern, mathematically expressible in terms of the coordinates, can be used for generating results using the present methodology. However, present study only considers uniformly distributed transverse excitation.

Validation Study

The forced vibration analysis is validated by comparing the results for an unstiffened clamped square plate analysed by Ribeiro. The geometric details of the plate are as follows: $a = b = 0.50$ m and $t_p = 0.005$ m and the material of the plate is steel with the following properties: $E_p = 210$ GPa, $\rho_p = 7800$ kg/m^3 and $\upsilon = 0.30$. The unstiffened plate is simulated in the present formulation by considering stiffener dimensions as zero. The frequency response curve under uniformly distributed harmonic excitation of amplitude 2000 Pa is compared with the results provided by Ribeiro and the comparison plots for substitution method and Broyden method are shown in Figure 3(a) and Figure 3(b) respectively. These figures exhibit good agreement with the existing results and establish the validity of present formulation and both the solution methodologies.

Figure 3(c) shows a comparison between solution domains of results generated through the two solution methodologies adapted in the present analysis. It is evident from the figure that the Broyden method is convergent over a wider range than the substitution method. But this method requires more time to achieve solution convergence. On the other hand, the substitution method is computationally efficient and requires much less processing time. But its domain of applicability is limited as it can capture only a part of the increasing branch of the response. However, it captures the two branches of the response curve while an ascending frequency sweep is performed. Broyden method captures the decreasing branch of frequency response when frequency sweeps in descending manner. It should be mentioned here that both the methods are dependent on the initial guess values. To minimize the computation time, first an ascending frequency sweep is performed through substitution method, which provides the

Table 2. Validation of the results for the first linear dimensional frequency parameters for a uni-axially single stiffened rectangular plate ($a = 0.60$ m, $b = 0.41$ m, $t_p = 0.00633$ m; $b^1_{sy} = 0.0127$ m, $t^1_{sy} = 0.02222$ m; $x^1_{stf} = 0.3$ m, $E_p = E_s = 211$ GPa, $\upsilon = 0.30$ and $\rho_p = \rho_s = 7830$ kg/m^3)

Boundary Condition	Research work by	First Natural Frequency (Hz.)
SSSS	Aksu	254.94
	Bedair	256.20
	Chen *et al*	245.17
	Harik & Guo	253.59
	Mukherjee & Mukhopadhyay	257.05
	Present	256.9694
SCSS	Chen *et al*	307.06
	Mukherjee & Mukhopadhyay	298.74
	Present	296.4808
CCCS	Chen *et al*	375.76
	Mukherjee & Mukhopadhyay	373.41
	Present	369.9907

starting frequency value and an initial guess for the Broyden method and then the Broyden method is employed to capture the rest of the response by sweeping the frequency from lower to higher values. The maximum value of dimensionless amplitude is taken as 2.0.

In order to validate the free vibration analysis the first natural frequency in Hz. for a rectangular plate with a centrally placed stiffener have been compared with the corresponding results presented by various authors in Table 2. The plate and stiffener dimensions along with the material properties considered for this comparative study are provided in the caption of the table. It is observed that the results of different researchers are at variance to some extent. However, it is found that the present results are very close to some of them and the slight variations may be ascribed to the difference in the solution methodologies adopted. The validation study establishes the methodologies of both the forced and free vibration analysis of the present method, albeit for different system with reduced complications. However, when both the methods are validated, it is surmised that their combination will also hold.

Figure 4. Normalized frequency response plots for uni-axially single stiffened rectangular plate with simply supported boundary conditions under two different amplitudes of uniformly distributed loading for various stiffener positions: (a) $\xi_{stf} = 0.5$*, (b)* $\xi_{stf} = 0.4$*, (c)* $\xi_{stf} = 0.3$ *and (d)* $\xi_{stf} = 0.25$.

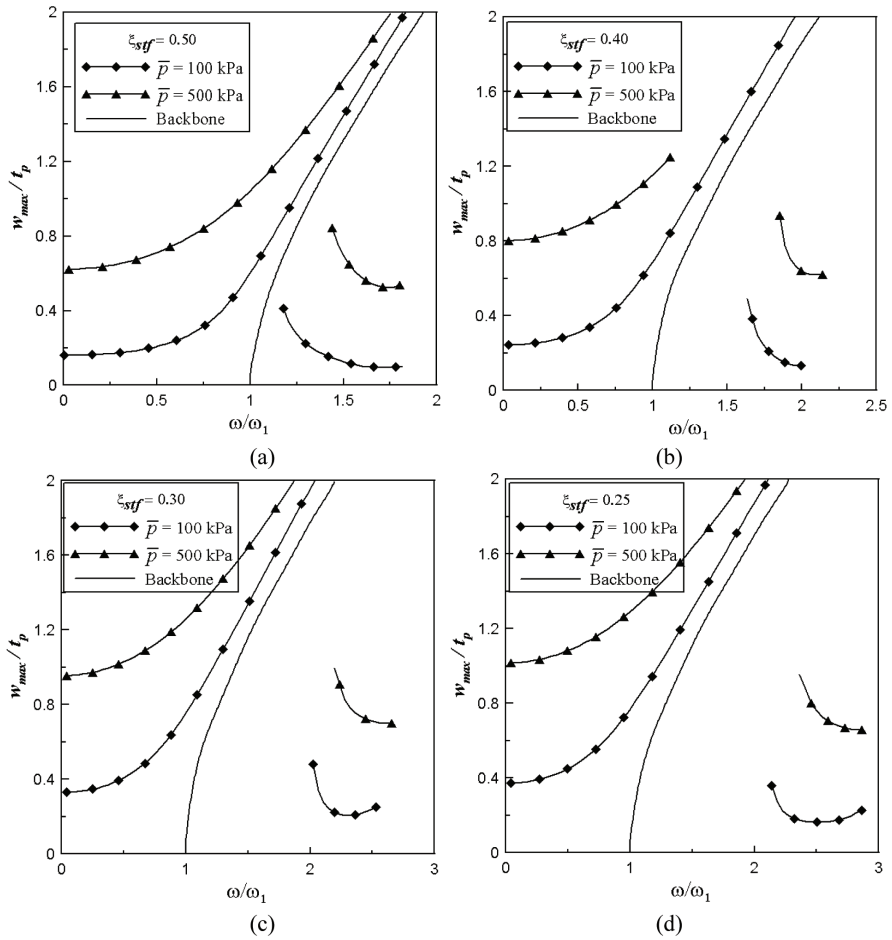
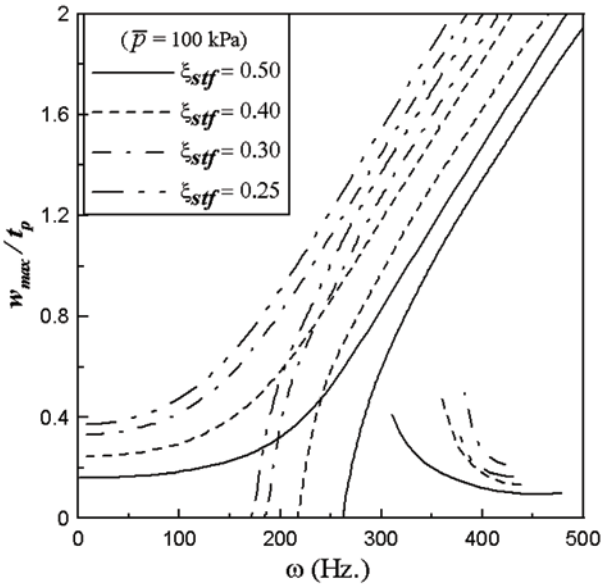


Figure 5. Frequency response plots for a uni-axially single stiffened rectangular plate with simply supported boundary conditions under UDL for different stiffener position

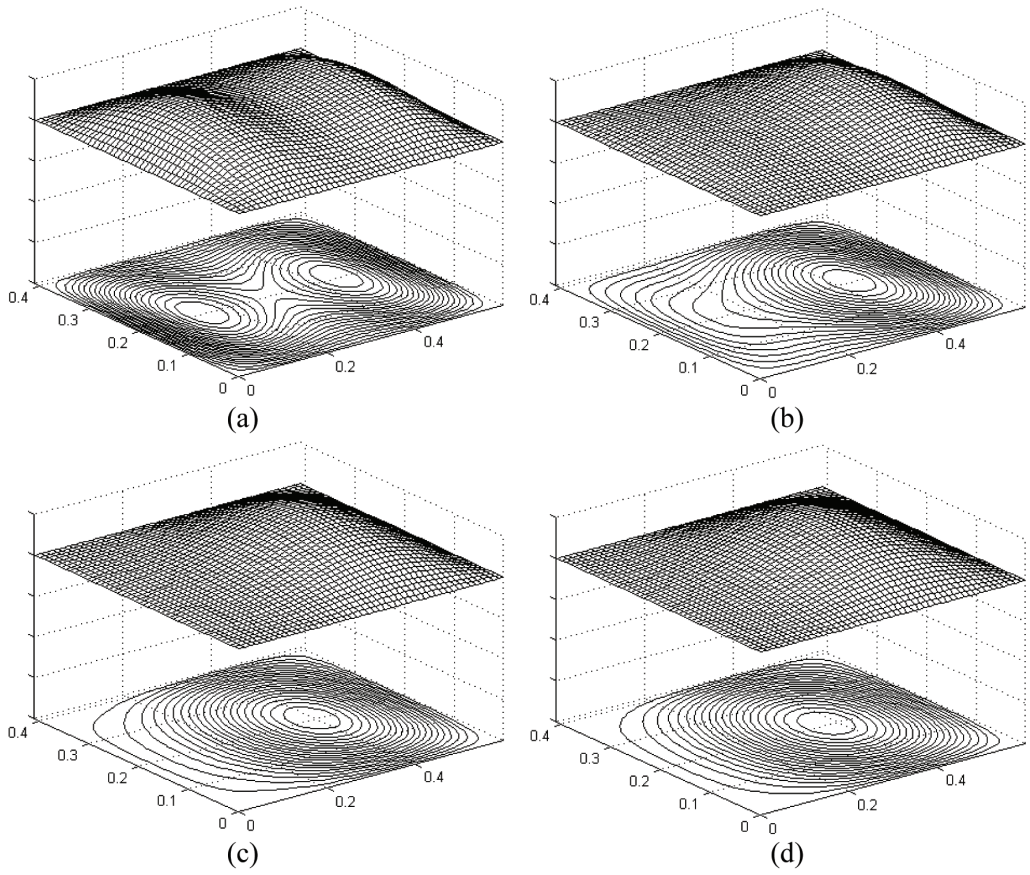


Effect of Stiffener Position on Frequency Response

The effect of the position of the stiffener on the system response under uniformly distributed excitation is studied and presented in Figures 4(a) through 4(d). The variations in the system response is shown for stiffener positions ξ_{stf} = 0.50, 0.40, 0.30 and 0.25 with a fixed value of aspect ratio (a/b) and thickness ratio (t_s/t_p). The plate and stiffener dimensions are taken identical to those mentioned in the caption of Table 1. In each of the plots of Figure 4, a family of curves is presented corresponding to different constant excitation amplitude as indicated in the legends of the figures. The backbone curve of the system determined through a separate dynamic analysis is also incorporated in these plots. It should be mentioned here that the response curves are presented only in the vicinity of the first mode of vibration and correspond to primary resonance condition where the excitation frequency becomes equal to the lowest fundamental frequency of the system.

From the set of figures it is clear that the system exhibits hardening type nonlinearity and the response curve for lower forcing amplitude tends towards the backbone curve of the system. All the response curves in Figure 4 show two distinct regions. The vibration amplitude increases monotonically with increase in excitation frequency when the excitation frequency is less than the natural frequency of the system. But after a certain frequency value two response amplitudes are obtained and there exists two branches of response for a certain frequency range. The higher branch continues to increase with excitation frequency from the single valued region, whereas in case of the lower branch a reverse trend is observed as the vibration amplitude decreases with increase in frequency. Theoretically the response curve for a nonlinear system under a harmonic excitation is made up of three regions, of which two are stable and experimentally obtainable. Actually, in the multi-valued interval of the response there are three steady state analytical solutions for a given excitation frequency. But the middle one

Figure 6. Deflected shape plots corresponding to increasing branches of response curves for different stiffener positions at $\omega = 0$ *Hz.: (a)* $\xi_{stf} = 0.5$, *(b)* $\xi_{stf} = 0.4$, *(c)* $\xi_{stf} = 0.3$ *and (d)* $\xi_{stf} = 0.25$

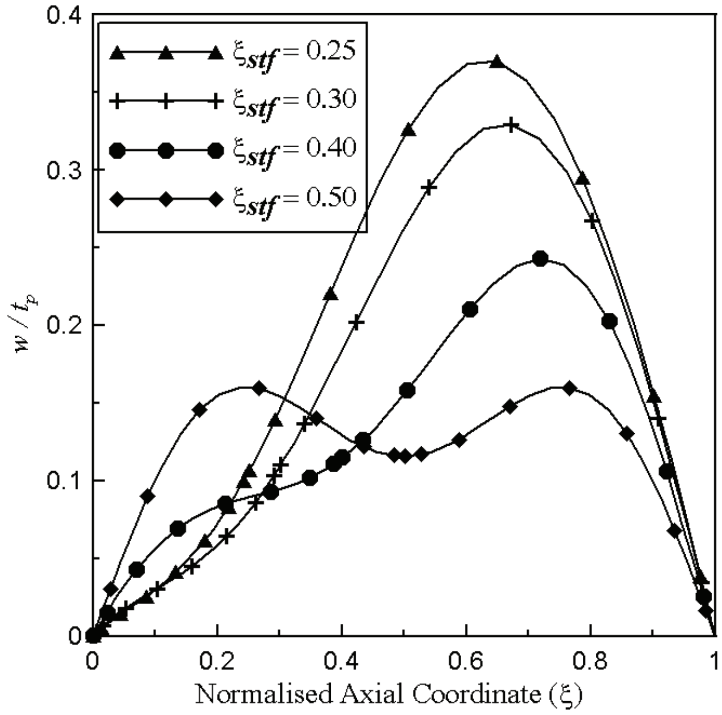


corresponds to an unstable response and hence cannot be captured experimentally. The present analysis captures the two stable regions but fails to capture the unstable region. The static deflection of the system can also be determined from the location where the response curve intersects the vertical axis, which signifies zero excitation frequency.

The influence of stiffener position on the frequency response characteristics is elaborated through Figure 5, where the abscissa represents forcing frequency in dimensional form (Hz.). The figure shows the response curves for different stiffener positions for excitation amplitude $\bar{p}$ = 100 kPa along with the backbone curves. It is seen from Figure 5 that as the stiffener shifts towards the plate boundary the response curves shift towards lower frequency values for a given excitation amplitude. Also it is noticed that for a particular value of exciting frequency the maximum response amplitude (w_{max} / t_p) is higher when the offset of the stiffener is more. The specific reason for this is that the system stiffness decreases due to the offset position of the stiffener. When a system becomes less stiff its natural frequency decreases while deflection of the system increases.

The plots of the deflected shape for the increasing branch of the response curves are presented in Figures 6(a) through 6(d) for different stiffener positions. In each plot both the surface and contour plots have been presented which corre-

Figure 7. A detailed study on changes in operational deflection shapes due to variation of stiffener position



spond to the made shapes of vibrating plate. It is also to be noted that the amplitude of vibration for all the surface plots is normalized by the corresponding maximum transverse displacement amplitude. It is observed from the operational deflection shape (ODS) plots presented in Figure 6 that for symmetric stiffener position the maximum amplitude is at the two central positions of the two equal sized panels, whereas for the offset stiffener position it occurs on the larger of the two panels. Hence, it should be noted that the location of maximum amplitude ($w_{\max}$) for the cases shown in Figure 4 and Figure 5 are different.

The effect of stiffener positions on the response of the system is studied in greater detail in Figure 7 where the same deflected shapes are presented in a different fashion. This figure is essentially a sectional view of the earlier ODS plots taken along the x-axis $\eta = 0.5$. The displacement amplitude presented in ordinate of the figure is normalised by plate thickness, whereas the abscissa represents normalized axial coordinate, ξ. This figure not only shows how the shift in stiffener position effects the operational deflection shape but also confirms that maximum stiffness corresponds to a central stiffener position.

DETAILED STUDY ON OPERATIONAL DEFLECTION SHAPE (ODS)

The effects of excitation frequency on the ODS is shown for a single stiffened rectangular plate with simply supported boundary conditions under UDL having $\bar{p} = 250$ kPa. The frequency response curve for the above mentioned plate is presented in Figure 8(a) with indications of five specific representative points (A-E). The deflection shapes along with the contour plots at those representative points on the response curve are furnished in Figures 8(b) through 8(f).

Figure 8. Operational deflection shape plots for a uni-axially single stiffened rectangular plate with simply supported boundary conditions under UDL having $\overline{p}$ *= 250 kPa: (a) Response curve showing representative points and (b-f) Operational deflection shapes corresponding to the representative points, A-E*

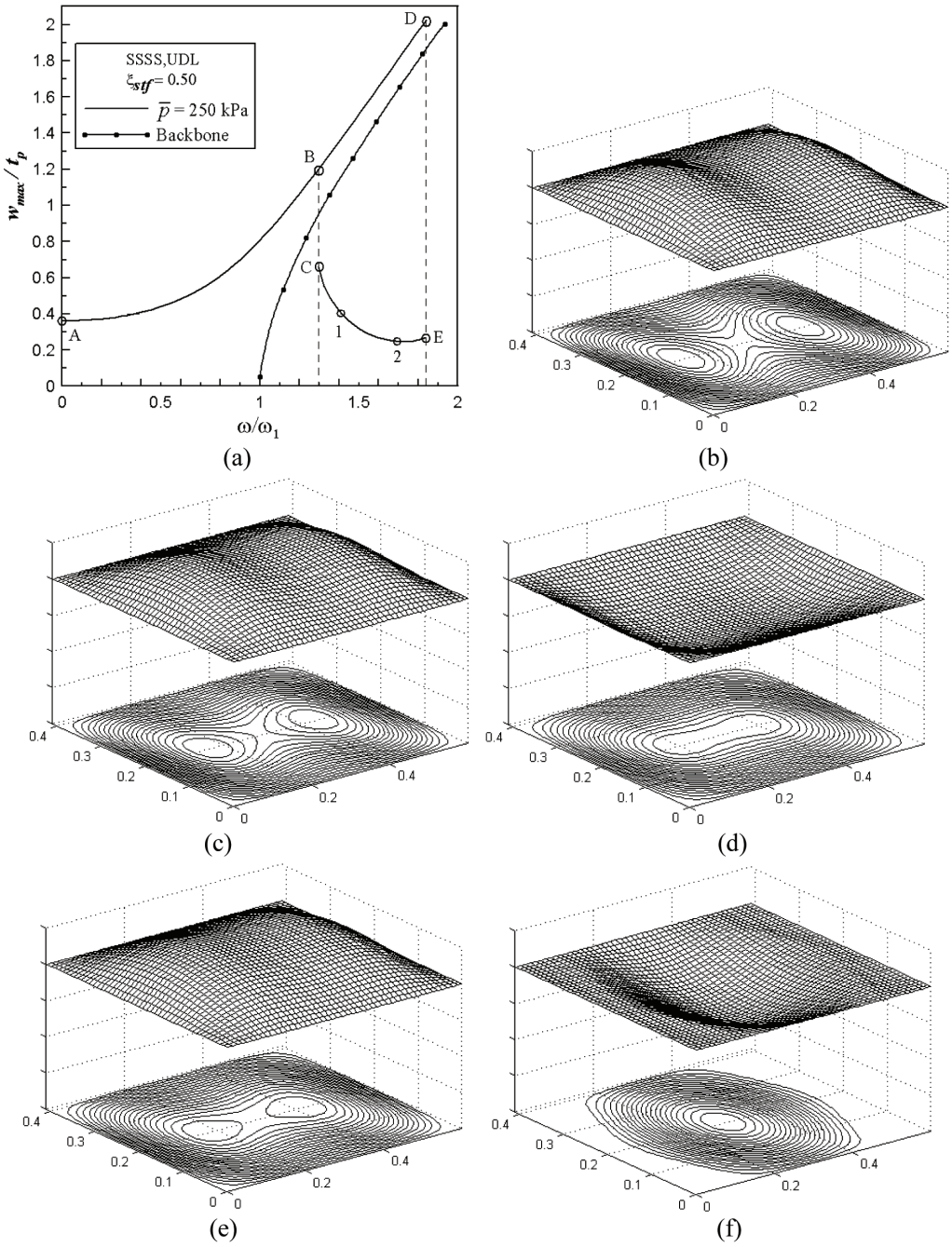
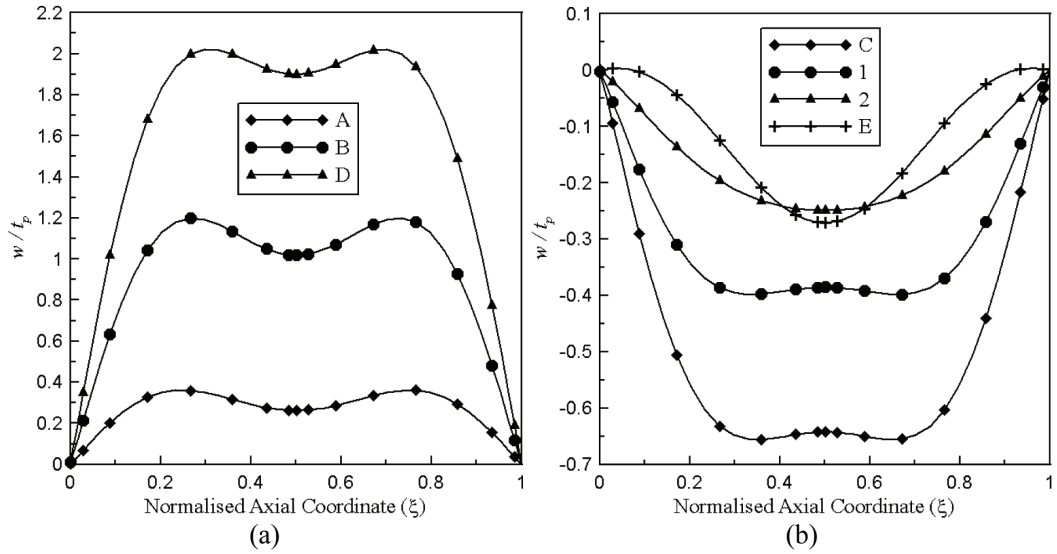


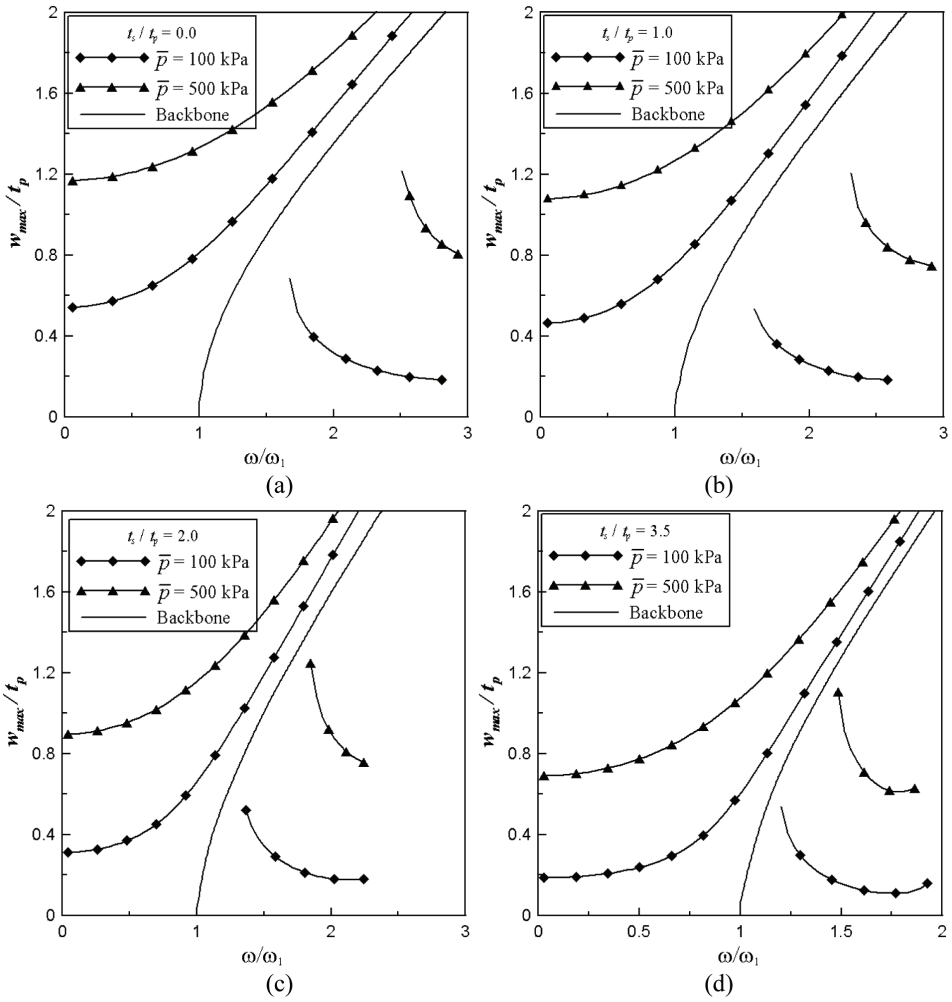
Figure 9. Changes in dynamic displacements along $\eta = 0.5$ line at various representative points on (a) increasing and (b) decreasing branch of the frequency response as shown in Figure 8(a)



The points on the response curve at which the ODS are shown correspond to different frequency-amplitude combinations. Point A represents the case where the external excitation frequency is zero, i.e., it is equivalent to static deflection of the stiffened plate under transverse loading. Point B on the higher branch of response represents the frequency at which the multi-valued response zone initiates and point C corresponds to the same frequency but on the lower branch of response. Point D represents the case when the system attains the maximum response amplitude (w_{max}/t_p = 2.0) and the point with the same frequency as point D but on the lower branch is represented by point E. It is seen that the ODS for point B is quite similar to that for point A, but ODS for point C is entirely different from the previous cases. In fact the response is out of phase when compared to the ODS of the poins on the higher branch. The ODS for point D is similar to other points on the higher branch of response, while the ODS for point E differs completely even from that of point C. In order to investigate this further, a detailed study similar to that discussed in the previous section has been carried out and the dynamic displacements along the line $\eta = 0.5$ are plotted for seven representative points in Figure 10 (A-E, 1 and 2).

Figure 9(a) corresponds to representative points A, B and D and indicates that the general nature of the operational deflection shapes remain almost same along the increasing branch of the response. The plots show that with increase in excitation frequency, the system response increases and they are always in phase. The figure also shows that maximum dynamic displacement is attained near the midpoint of the two symmetric panels. Similarly, Figure 9(b) presents the plot of dynamic displacements for the points on the lower branch of response. Here, apart from the two points C and E two other intermediate points 1 and 2 are considered and all the results show that the displacements are out of phase as expected. However, it is observed that the amplitude slightly increases from point 2 to E and the ODS is completely different from the previous points, as also noticed in Figure 8. A closer inspection of the response curve in Figure 8(a) reveals that near the end of the curve a reversal of trend takes place as the response amplitude starts to increase again.

Figure 10. Normalized frequency response plots for uni-axially single stiffened rectangular plate with simply supported boundary conditions under uniformly distributed loading for different thickness ratio: (a) t_s/t_p = 0.0, (b) t_s/t_p = 1.0, (c) t_s/t_p = 2.0 and (d) t_s/t_p =3.5



This probably happens as the excitation frequency nears a natural frequency of the system corresponding to a different vibration mode. The transition from one deflection shape to the other takes place in between points 2 and E and this explains the change in the nature of the response.

Effect of Thickness Ratio on Frequency Response

The dynamic response of the system for variation in thickness ratio (t_s/t_p) for uniformly distributed loading is presented in Figures 10(a) through 10(d). The variations in the system behaviour are shown for thickness ratios t_s/t_p = 0.0, 1.0, 2.0 and 3.5 with a fixed value of aspect ratio (a/b = 1.5) and position of the stiffener ($\xi_{stf} = 0.50$). The geometry with t_s/t_p = 0.0 actually represents an unstiffened plate. The details of the geometry of the stiffened plate are as follows: a = 0.60 m, b = 0.40 m, t_p = 0.006 m. The variation of the thickness ratio is effected by changing the stiffener thickness (t_s) keeping the plate thickness (t_p) fixed.

In each of the plots in Figure 10 frequency response curve is furnished for excitation amplitudes, $\bar{p}$ = 100 kPa and 500 kPa, along with the backbone curve. These frequency response curves depict similar characteristics as those discussed in relation to Figure 4. The system exhibits hardening type nonlinearity and the response curves envelop the backbone curve. As in the previous case, lowering the excitation amplitude tends to bring the frequency response closer to the backbone curve of the system, which is theoretically the zero load amplitude-excitation response of the system. The response curves for different thickness ratios corresponding to $\bar{p}$ = 100 kPa are shown in dimensional frequency axis in Figure 11.

From Figure 11 it is evident that increase in thickness ratio causes the response to shift towards higher frequency values. It is expected that with increase in stiffener thickness the overall stiffness of the system increases and hence the frequency response also moves towards higher values. For a particular value of exciting frequency the maximum response amplitude is lower for higher thickness ratios. Increased system stiffness is also directly responsible for this behaviour.

The effect of variation of thickness ratio on the system response is studied in greater detail through ODS plots and subsequent sectional plots of the vibrating system corresonding to the increasing branch of the response. The deflection shape and contour plots for the various cases shown in Figure 11 are presented in Figures 12(a) through 12(d) and the results for the sectional-study are furnished in Figure 13. The consequence of thickness ratio variation is evident in the difference of operational deflection shapes and contour plots for different thickness ratios. However, as each of the ODS plots are separately normalized in

Figure 11. Frequency response plots for uni-axially single stiffened rectangular plate with simply supported boundary conditions under UDL for different thickness ratios

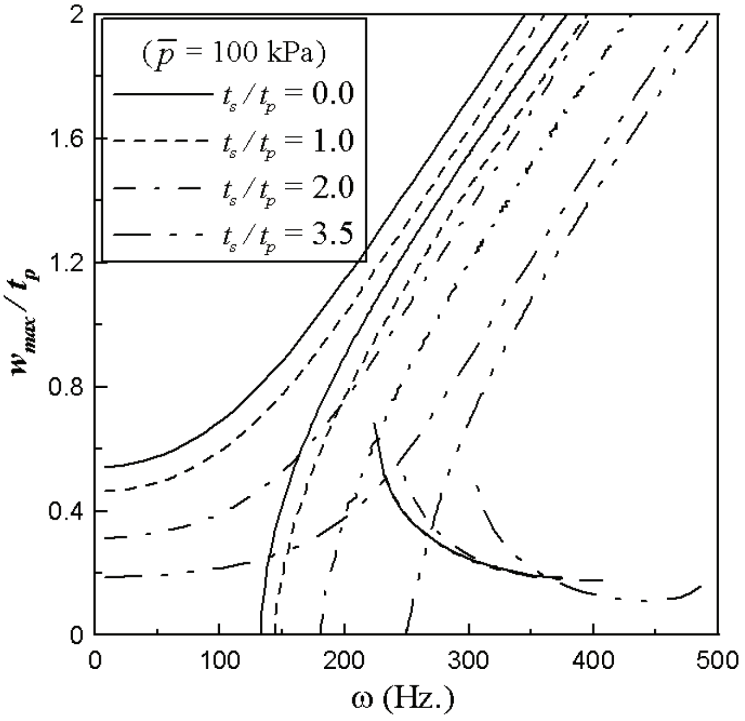
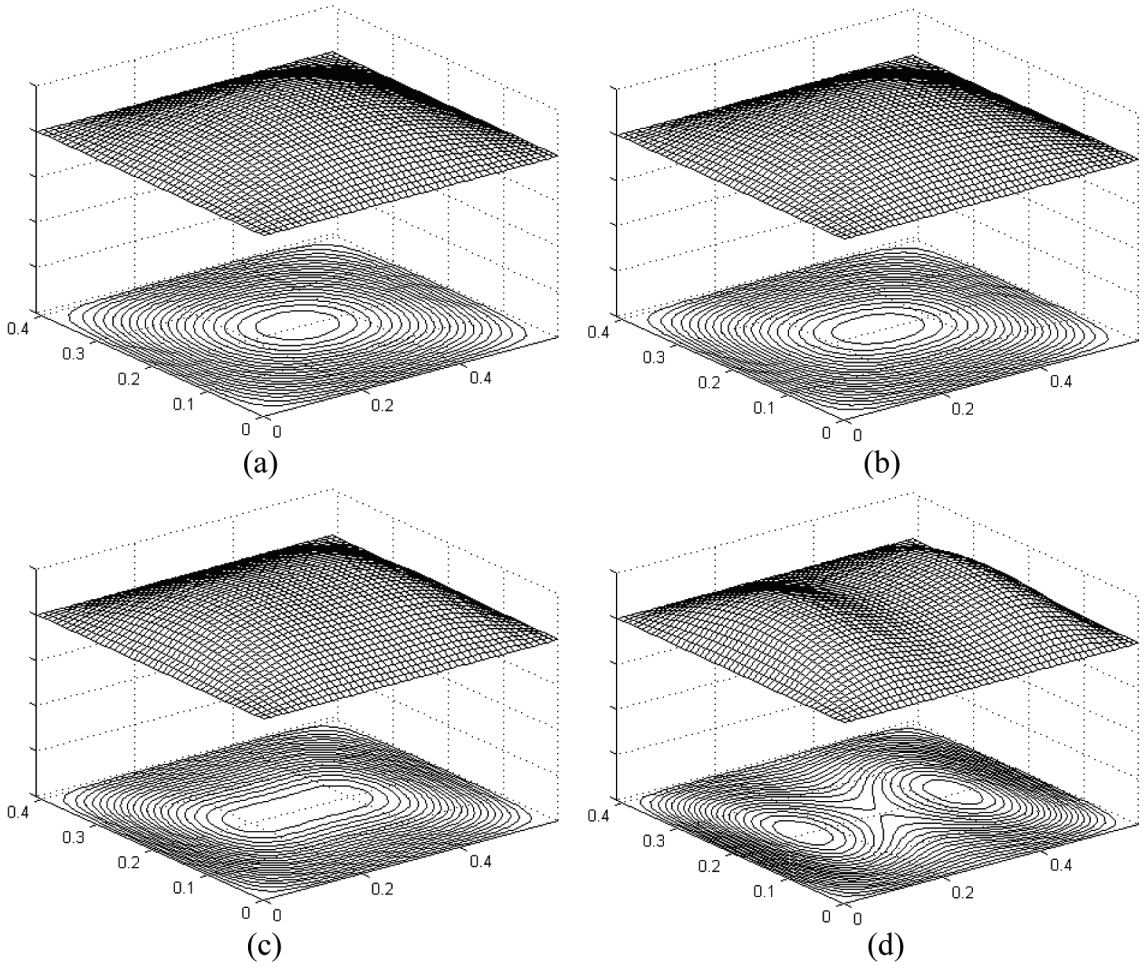
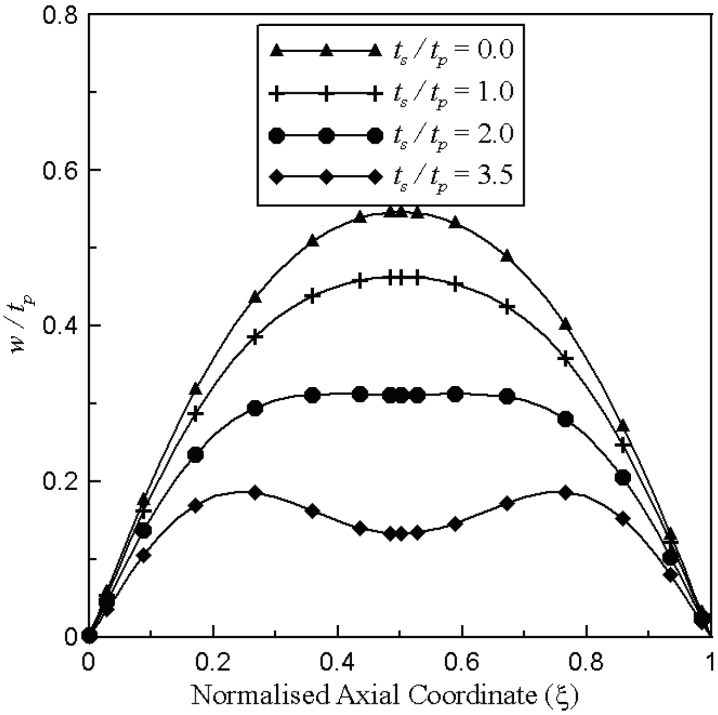


Figure 12. Operational deflection shape plots corresponding to increasing branches of response curves for different thickness ratio: (a) t_s/t_p = 0.0, (b) t_s/t_p = 1.0, (c) t_s/t_p = 2.0 and (d) t_s/t_p =3.5



terms of their respective maximum transverse displacement amplitude, these plots only provide a qualitative idea about the influence of thickness ratio on the response of the system. On the other hand, Figure 13 shows the dynamic displacements of the stiffened plates for a particular excitation frequency at a specific position for different values of the thickness ratio. Here the normalisation for all the four cases have been carried out with respect to the plate thickness. So, a quantitative idea about the effect of thickness ratio parameter on system response can be obtained. It is seen from the figure that maximum dynamic displacement decreases as thickness ratio increases. As expected the unstiffened plate (t_s/t_p = 0.0) shows least stiffness characteristics and a normalised maximum amplitude of 0.5467 at the mid point of the plate is obtained. Increse in stiffener thickness brings this maximum value down sharply and for t_s/t_p = 3.5 the corresponding value is 0.1867 obtained near the middle of the two sub-panels. This figure also demonstrates the gradual change in the ODS with the increase of thickness ratio and shifting of the point of maximum displacement away from the center.

Figure 13. A detailed study showing changes in dynamic displacements along $\eta = 0.5$ line for different thickness ratio

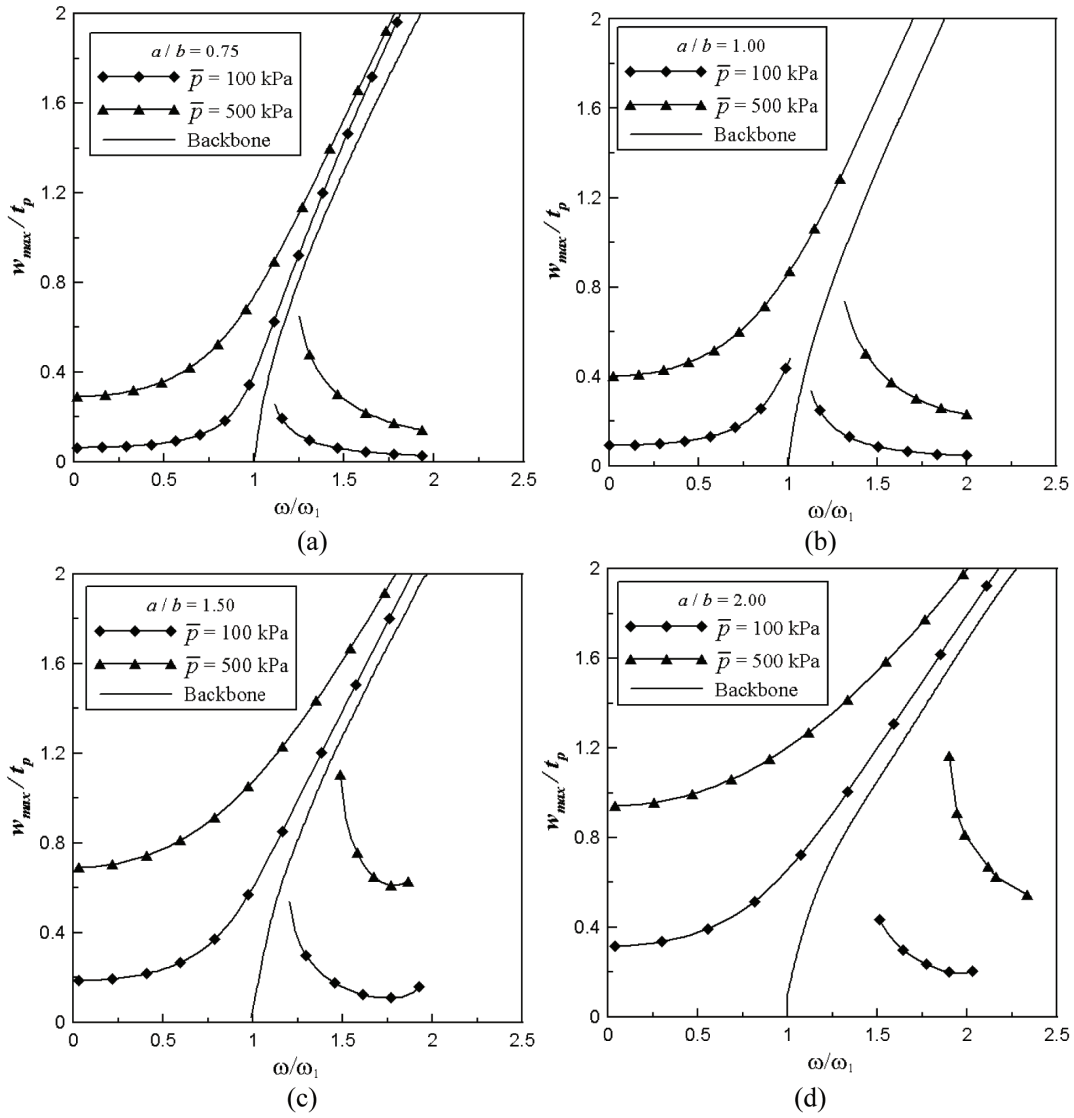


EFFECT OF ASPECT RATIO ON FREQUENCY RESPONSE

In this section the effect of variation of plate aspect ratio (*a/b*) on the forced vibration behaviour of stiffened plate under uniformly distributed loading is studied. The variations in the response behaviour is shown for aspect ratios *a/b* = 0.75, 1.0, 1.5 and 2.0 for a plate of thickness (t_p) of 0.006 m with a fixed value of stiffener to plate thickness ratio (t_s/t_p =3.5). In all the cases a centrally placed ($\xi_{stf} = 0.50$) eccentric stiffener parallel to *y*-axis is considered. It should be pointed out that the variation in aspect ratio can be achieved either by changing length (*a*) with width (*b*) constant or by varying width (*b*) while keeping length (*a*) fixed. However, in the first instance the length of the stiffener remains same in all the cases, whereas for the second case it changes with the lateral dimension. Figures 14(a) through 14(d) shows the frequency response curves for variation in plate aspect ratio *(a/b)* obtained by varying length (*a*) with constant width (*b*). These frequency response curves have similar characteristics as those discussed in relation to the previous cases. Hardening type nonlinearity is observed for the different aspect ratios and multi-valued response zone is present in all the cases. It is known that nonlinear systems may exhibit super-harmonic and sub-harmonic responses, however, for the given set of system parameters and loading condition these nonlinear characteristics are not manifested.

Figure 15(a) presents the response curves plotted on a dimensional *x*-axis representing forcing frequency along with the system backbone curves corresponding to various aspect ratios, which are obtained by changing the length (*a*). Figure 15(b) presents similar frequency response plots, but here the variation of aspect ratio is

Figure 14. Normalized frequency response plots for a uni-axially single stiffened rectangular plate with simply supported boundary conditions under uniformly distributed loading for different plate aspect ratio obtained by varying length (a) with constant width (b): (a) a/b = 0.75, (b) a/b = 1.00, (c) a/b = 1.50 and (d) a/b = 2.00



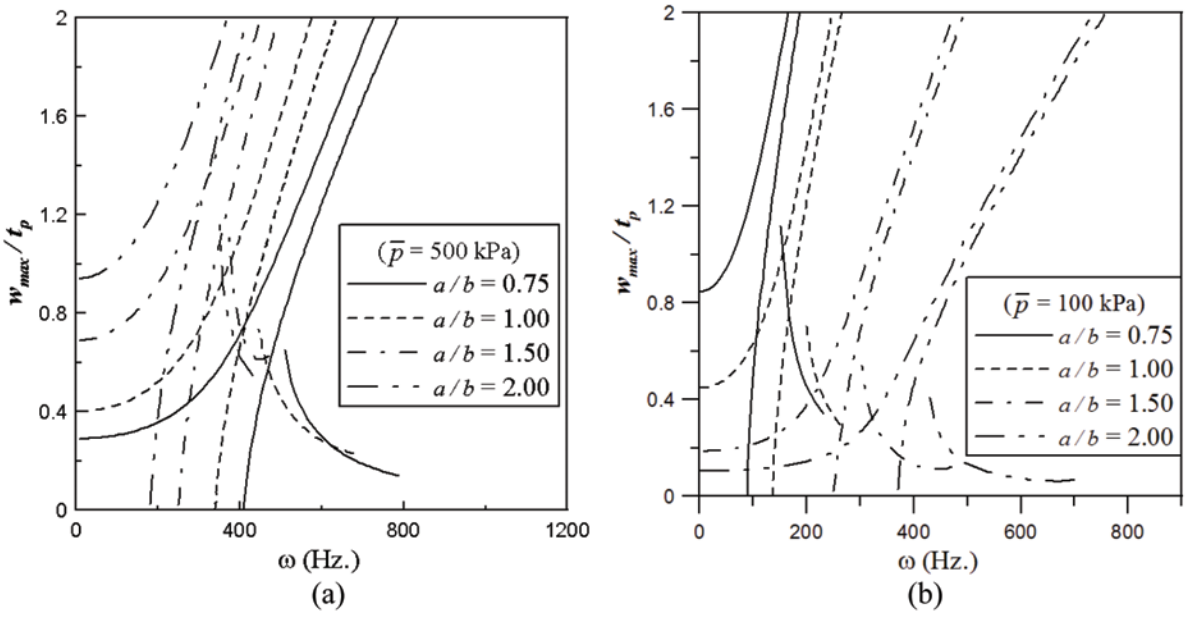
achieved by varying the width (*b*) of the plate. From Figure 15(a) it is clear that as the length increases the frequency response moves towards lower frequency values. The natural frequencies of the system at the base of the backbone curves for the aspect ratios 0.75, 1.0, 1.5 and 2.0 are 407.8143, 338.9342, 252.3573 and 184.6779 Hz. respectively. Also, for a particular value of excitation frequency the maximum response amplitude in the increasing branch of response is higher for higher aspect ratios. However, a completely opposite trend is observed in Figure 15(b), where, increase in width shifts the frequency response towards higher frequency values. Here the natu-

ral frequencies of the system at unloaded condition corresponding to aspect ratios 0.75, 1.0, 1.5 and 2.0 are given by 88.2052, 135.5836, 252.3573 and 329.3578 Hz. respectively. In this case the maximum response amplitude for a particular value of excitation frequency in the increasing branch of response is lower for higher aspect ratios. The ODS and contour plots for the different cases shown in Figure 15(a) are presented in Figures 16(a) through 16(d) and the effect of variation of aspect ratio on the system is quite apparent.

Effect of Boundary Condition on Frequency Response

The results that have been provided in the preceding sections are for simply supported stiffened rectangular plates and in this section the effect of change in boundary conditions is studied. For this purpose, frequency response curves for different combinations of clamped and simply supported edges (SCSS, CCSS, CSCS, and CCCS) for a uni-axially single stiffened plate under uniformly distributed harmonic excitation are presented in Figures 17(a) through 17(d). The forced vibration behaviours, as can be viewed from Figures 17(a) through 17(d), remain same as that discussed earlier for the SSSS stiffened plates. However, in case of CCCS (Figure 17(a)) and SCSS (Figure 17(d)) boundary conditions, backbone curves are presented for the first two vibration modes and they are represented by dotted (A1A2) and solid lines (B1B2) respectively. In these two cases the first two backbone curves intersect each other, giving rise to a phenomenon known as mode switching. In Figure 17(a) C denotes the point of intersection or mode switching between the two backbone curves and A1CB2 and B1CA2 denote the first and second mode of vibration respectively. The frequency response curves envelope the backbone curve of mode 1 and mode 2 for low amplitude of vibration, whereas for high vibration amplitude

Figure 15. Frequency response plots for uni-axially single stiffened rectangular plate with simply supported boundary conditions under UDL for different plate aspect ratios: (a) varying a with b constant, (b) varying b with a constant



they envelope backbone curve for the second mode of vibration.

ODS and contour plots for the vibrating system with CCCS boundary condition corresponding to the two extremities of the increasing branch i.e. at $\omega = 0$ Hz. and $w_{max} / t_p = 2.0$ for $\bar{p} = 100$ kPa are provided in Figure 18. A slight difference between the two deflection shapes is observed. In Figure 19(a) the linear (point A1 in Figure 17(a)) and nonlinear (point B2 in Figure 17(a)) mode shapes of the first vibration mode are furnished, whereas in Figure 19(b) the linear (point B1 in Figure 17(a)) and nonlinear (point A2 in Figure 17(a)) mode shapes are furnished for mode 2. These mode shapes are obtained from the large amplitude dynamic study for CCCS boundary condition. Interchange of linear and nonlinear mode shapes depicted in Figures 19(a) and 19(b) appropriately support the case of mode switching between the first and second mode. It is seen that the ODS obtained for the increasing branch of the frequency response closely resembles the mode shapes at point B1 and B2, as shown in Figure 19. This is the reason why the response curve is found to envelop the second backbone curve (B1CB2) through out the entire range of vibration.

Figure 16. Operational deflection shape plots corresponding to increasing branches of response curves for different plate aspect ratio obtained by varying length (a) with constant width (b): (a) a/b = 0.75, (b) a/b = 1.00, (c) a/b = 1.50 and (d) a/b = 2.00

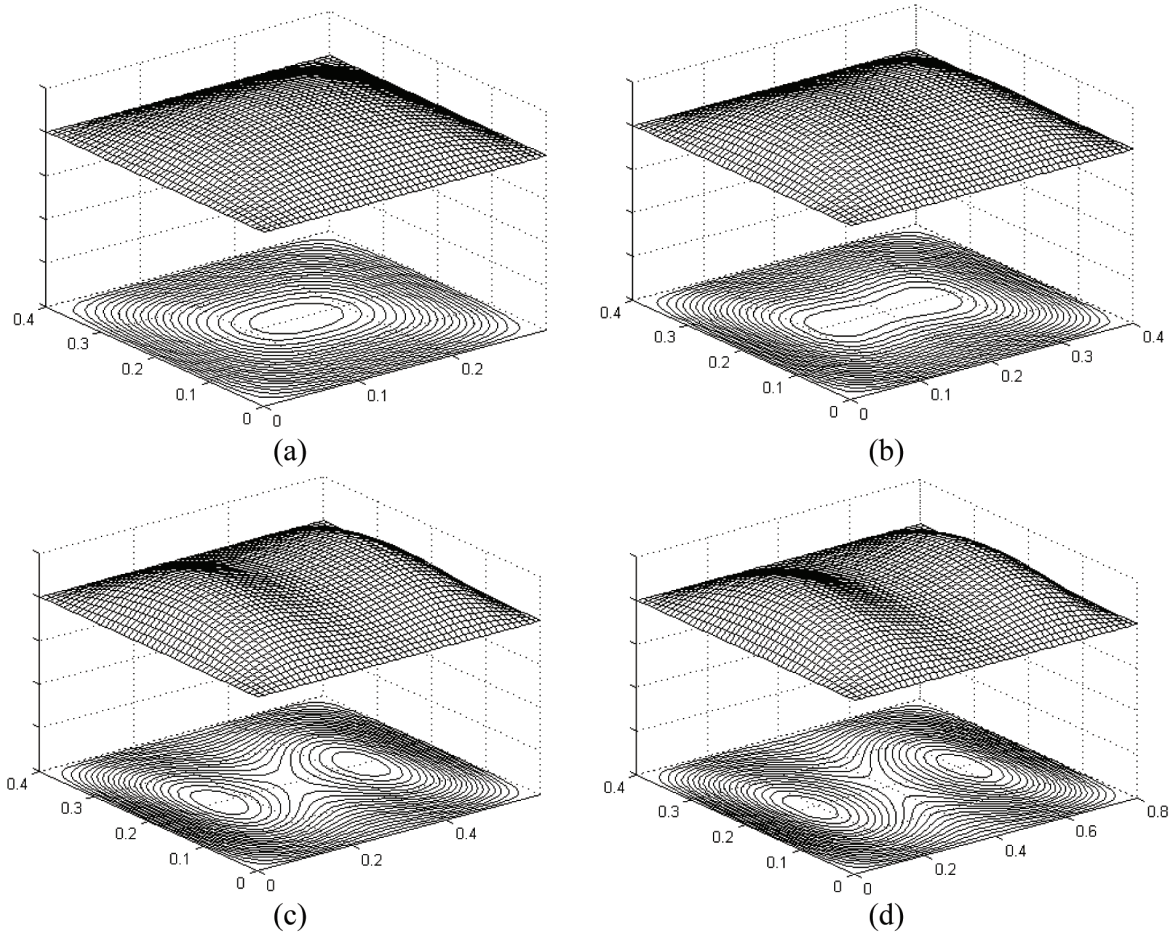
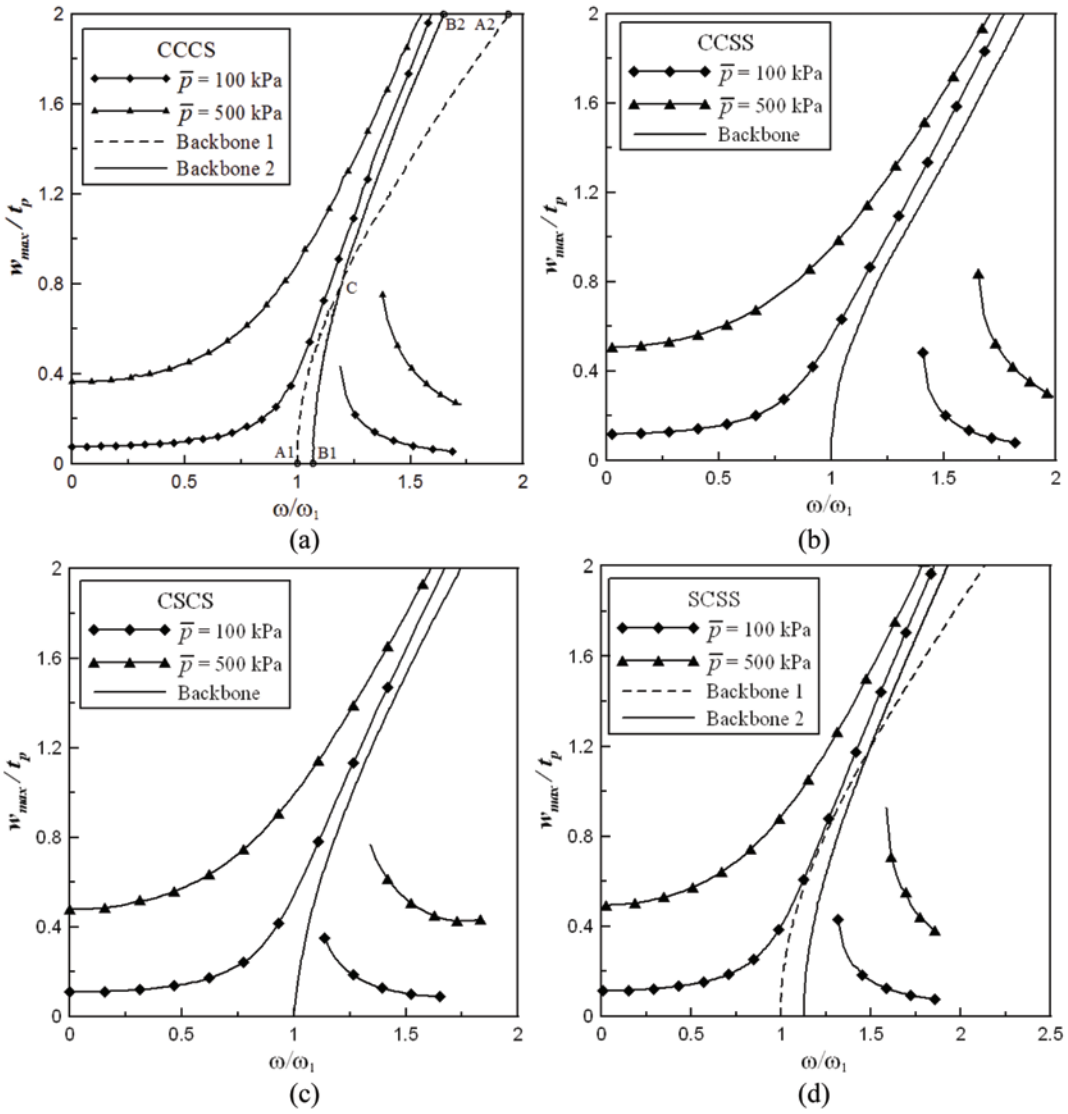


Figure 17. Normalized frequency response plots for uni-axially single stiffened rectangular plate under uniformly distributed loading for different boundary conditions: (a) CCCS, (b) CSCS (c) CCSS and (d) SCSS

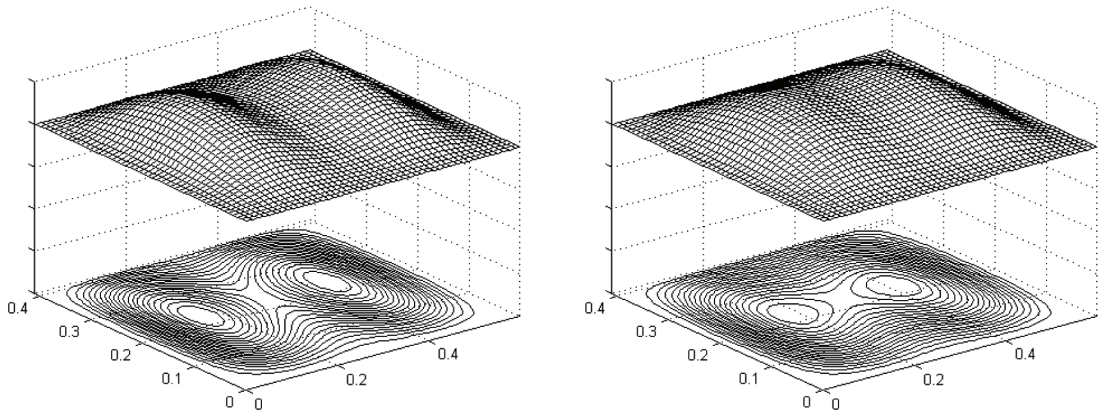


In fact, this exhibits true system behaviour because for the specific boundary conditions and transverse loading, the stiffened plate can only assume the configuration as shown in Figures 19(b) and 19(c), but cannot obtain the typical configuration of the modes shown in Figures 19(a) and 19(d).

CONCLUSION

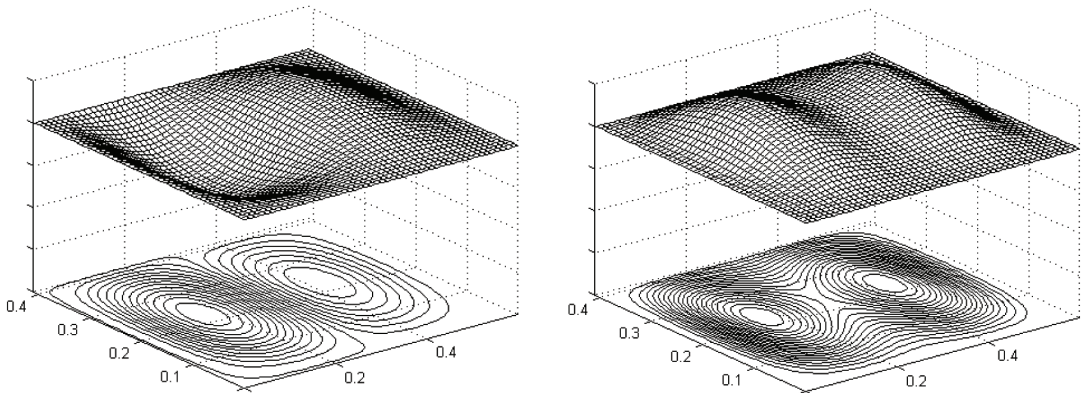
In the present paper large amplitude forced vibration analysis of stiffened plates subjected to transverse harmonic excitation is undertaken using variational formulation. The forced vibration analysis is carried out in an indirect manner reducing the problem to an equivalent static case.

Figure 18. Operational deflection shape plots corresponding to increasing branch of response curve for CCCS boundary condition at (a) $\omega = 0$ Hz and (b) $w_{max} / t_p = 2.0$

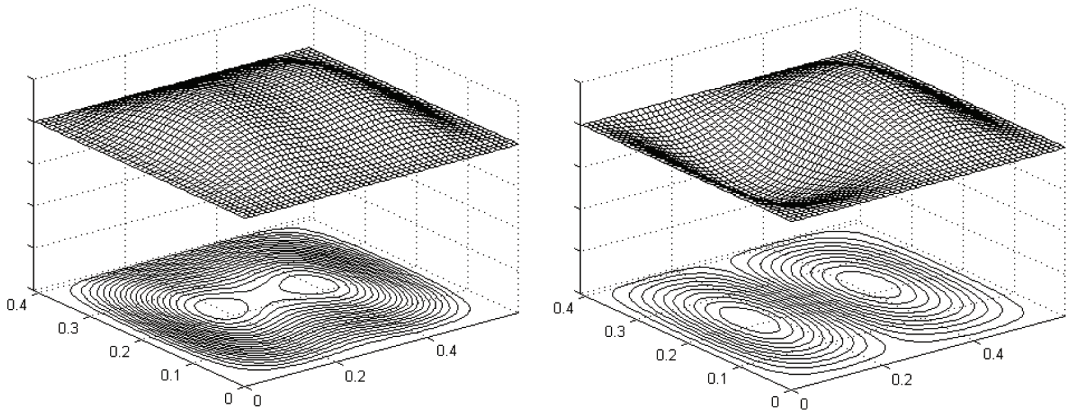


(a) (b)

Figure 19. Linear ($w_{max} / t_p = 0.0$) and nonlinear ($w_{max} / t_p = 2.0$) mode shape plots for uni-axially single stiffened rectangular plate with CCCS boundary condition corresponding to points (a) A1, (b) B2, (c) B1 and A2 on backbone curves of Figure 17(a)



(a) $w_{max} / t_p = 0.0$ (A1) (b) $w_{max} / t_p = 2.0$ (B2)



(c) $w_{max} / t_p = 0.0$ (B1) (d) $w_{max} / t_p = 2.0$ (A2)

A separate large amplitude free vibration study is also taken up to determine the backbone curves of the system. This analysis is carried out in two steps. The first step involves solving the static displacement of the stiffened plate and then the subsequent dynamic study is taken up on the basis of known static displacement field. The results of both forced and free vibration analyses are validated with the published results of other researchers and fairly good agreement is observed in almost all the cases. Results are presented as frequency response curves in non-dimensional frequency-amplitude plane and are accompanied by the backbone curves of the system. Influence of stiffener position, plate aspect ratio and stiffener to plate thickness ratio on the frequency response has been studied. The system responses indicate a hardening type nonlinearity and two stable zones of the response curve is obtained. It is observed that, as the amplitude of load reduces, the nonlinear response of the system tends to attain the shape of backbone curve. Although results are mainly generated for simply supported stiffened plates, effect of the other classical boundary conditions on the forced vibration behaviour is also analyzed. Three dimensional ODS plots along with contour plots are provided in a few cases.

ACKNOWLEDGMENT

The first author acknowledges the research support received from AICTE, India, vide File No.:1-10/ RID/NDF/PG/(17)2008-09 Dated: 13.03.2009.

REFERENCES

Aksu, G. (1982). Free vibration analysis of stiffened plates by including the effect of inplane inertia. *Journal of Applied Mechanics Transactions of ASME*, *49*(1), 206–212. doi:10.1115/1.3161972

Aksu, G., & Ali, R. (1976). Free vibration analysis of stiffened plates using finite difference method. *Journal of Sound and Vibration*, *48*(1), 15–25. doi:10.1016/0022-460X(76)90367-9

Amabili, M. (2006). Theory and experiments for large-amplitude vibrations of rectangular plates with geometric imperfections. *Journal of Sound and Vibration*, *291*(3-5), 539–565. doi:10.1016/j.jsv.2005.06.007

Bedair, O. K. (1997). Analysis of stiffened plates under lateral loading using sequential quadratic program. *Computers & Structures*, *62*(1), 63–80. doi:10.1016/S0045-7949(96)00281-7

Bedair, O. K. (1997). Fundamental frequency determination of stiffened plates using sequential quadratic programming. *Journal of Sound and Vibration*, *199*(1), 87–106. doi:10.1006/jsvi.1996.0606

Bedair, O. K. (1998). A contribution to the stability of stiffened plates under uniform compression. *Computers & Structures*, *66*(5), 535–570. doi:10.1016/S0045-7949(97)00102-8

Bedair, O. K., & Troitsky, M. (1997). A study of fundamental frequency characteristics of eccentrically and concentrically simply supported stiffened plates. *International Journal of Mechanical Sciences*, *39*(11), 1257–1272. doi:10.1016/S0020-7403(97)00016-7

Brubak, L., & Hellesland, J. (2008). Strength criteria in semi-analytical, large deflection analysis of stiffened plates in local and global bending. *Thin-walled Structures*, *46*, 1382–1390. doi:10.1016/j.tws.2008.03.013

Chen, C. J., Liu, W., & Chern, S. M. (1994). Vibration analysis of stiffened plates. *Computers & Structures*, *50*(4), 471–480. doi:10.1016/0045-7949(94)90017-5

Crandall, S. H. (1956). *Engineering analysis: A survey of numerical procedures*. New York, NY: McGraw-Hill.

Dozio, L., & Ricciardi, M. (2009). Free vibration analysis of ribbed plates by a combined analytical–numerical method. *Journal of Sound and Vibration*, *319*, 681–697. doi:10.1016/j.jsv.2008.06.024

Efimtsov, B. M., & Lazarev, L. A. (2009). Forced vibrations of plates and cylindrical shells with regular orthogonal system of stiffeners. *Journal of Sound and Vibration*, *327*(1-2), 41–54. doi:10.1016/j.jsv.2009.05.021

El Kadiri, M., & Benamar, R. (2003). Improvement of the semi-analytical method, based on Hamilton's principle and spectral analysis, for determination of the geometrically non-linear response of thin straight structures. Part III: Steady state periodic forced response of rectangular plates. *Journal of Sound and Vibration*, *264*(1), 1–35. doi:10.1016/S0022-460X(02)01162-8

Harik, I. E., & Guo, M. (1993). Finite element analysis of eccentrically stiffened plates in free vibration. *Computers & Structures*, *49*(6), 1007–1015. doi:10.1016/0045-7949(93)90012-3

Koko, T. S., & Olson, M. D. (1991). Non-linear analysis of stiffened plates using super elements. *International Journal for Numerical Methods in Engineering*, *31*(2), 319–343. doi:10.1002/nme.1620310208

Koko, T. S., & Olson, M. D. (1992). Vibration analysis of stiffened plates by super elements. *Journal of Sound and Vibration*, *158*(1), 149–167. doi:10.1016/0022-460X(92)90670-S

Leissa, A. W. (1989). Closed form exact solutions for the steady state vibrations of continuous systems subjected to distributed exciting forces. *Journal of Sound and Vibration*, *134*(3), 435–453. doi:10.1016/0022-460X(89)90568-3

Mukherjee, A., & Mukhopadhyay, M. (1986). A review of dynamic behavior of stiffened plates. *Shock Vibration Digest*, *18*(6), 3–8. doi:10.1177/058310248601800603

Mukherjee, A., & Mukhopadhyay, M. (1988). Finite element free vibration of eccentrically stiffened plates. *Computers & Structures*, *30*(6), 1303–1317. doi:10.1016/0045-7949(88)90195-2

Mukhopadhyay, M. (1994). Stiffened plates in bending. *Computers & Structures*, *50*(4), 541–548. doi:10.1016/0045-7949(94)90024-8

Ojeda, R., Prusty, B. G., Lawrence, N., & Thomas, G. (2007). A new approach for the large deflection finite element analysis of isotropic and composite plates with arbitrary orientated stiffeners. *Finite Elements in Analysis and Design*, *43*, 989–1002. doi:10.1016/j.finel.2007.06.007

Peng, L. X., Liew, K. M., & Kitipornchai, S. (2006). Buckling and free vibration analyses of stiffened plates using the FSDT mesh-free method. *Journal of Sound and Vibration*, *289*(3), 147–164. doi:10.1016/j.jsv.2005.02.023

Prathap, G., & Varadan, T. K. (1978). Large amplitude flexural vibration stiffened of plates. *Journal of Sound and Vibration*, *57*(4), 583–593. doi:10.1016/0022-460X(78)90547-3

Press, W. H., Teukolsky, S. A., Vetterling, W. T., & Flannery, B. P. (2005). *Numerical recipes in Fortran 77* (2nd ed.). Cambridge, MA: Press Syndicate.

Rao, D. V., Sheikh, A. H., & Mukhopadhyay, M. (1993). A finite element large displacement analysis of stiffened plates. *Computers & Structures*, *47*(6), 987–993. doi:10.1016/0045-7949(93)90303-U

Rao, S. R., Sheikh, A. H., & Mukhopadhyay, M. (1993). Large-amplitude finite element flexural vibration of plates/stiffened plates. *The Journal of the Acoustical Society of America*, *93*(6), 3250–3257. doi:10.1121/1.405710

Ribeiro, P. (2004). Non-linear forced vibrations of thin/thick beams and plates by the finite element and shooting methods. *Computers & Structures*, *82*, 1413–1423. doi:10.1016/j.compstruc.2004.03.037

Rossow, M. P., & Ibrahimkhail, A. K. (1978). Constraint method of analysis of stiffened plates. *Computers & Structures*, *8*, 51–60. doi:10.1016/0045-7949(78)90159-1

Saha, K. N., Misra, D., Pohit, G., & Ghosal, S. (2004). Large amplitude free vibration study of square plates under different boundary conditions through a static analysis. *Journal of Vibration and Control*, *10*, 1009–1028. doi:10.1177/1077546304038101

Sapountzakis, E. J., & Katsikadelis, J. T. (2000). Elastic deformation of ribbed plates under static, transverse and inplane loading. *Computers & Structures*, *74*, 571–581. doi:10.1016/S0045-7949(99)00066-8

Sapountzakis, E. J., & Mokos, V. G. (2008). An improved model for the dynamic analysis of plates stiffened by parallel beams. *Engineering Structures*, *30*(6), 1720–1733. doi:10.1016/j.engstruct.2007.11.016

Sheikh, A. H., & Mukhopadhyay, M. (2000). Geometric non-linear analysis of stiffened plates by spline finite strip method. *Computers & Structures*, *76*(3), 765–785. doi:10.1016/S0045-7949(99)00191-1

Varadan, T. K., & Pandalai, K. A. V. (1979). Large amplitude flexural vibration of eccentrically stiffened plates. *Journal of Sound and Vibration*, *67*(3), 329–340. doi:10.1016/0022-460X(79)90540-6

Voros, G. M. (2009). Buckling and free vibration analysis of stiffened panels. *Thin-walled Structures*, *47*, 382–390. doi:10.1016/j.tws.2008.09.002

Wutzow, W. W., & Paiva, J. B. (2008). Analysis of stiffened plates by the boundary element method. *Engineering Analysis with Boundary Elements*, *32*, 1–10. doi:10.1016/j.enganabound.2007.06.005

Xu, H., Du, J., & Li, W. L. (2010). Vibrations of rectangular plates reinforced by any number of beams of arbitrary lengths and placement angles. *Journal of Sound and Vibration*, *329*(18), 3759–3779. doi:10.1016/j.jsv.2010.03.023

APPENDIX

Details of Matrix Elements

The total stiffness matrix [K] is given by, $\left[K\right]=\left[K_b\right]+\left[K_m\right]+\sum_{p=1}^{ns_x}\left[K_{sx}\right]^p+\sum_{q=1}^{ns_y}\left[K_{sy}\right]^q$.

The form of $\left[K_b\right]$ is given by: $\left[K_b\right]=\begin{bmatrix}k_{11}^b & k_{12}^b & k_{13}^b\\ k_{21}^b & k_{22}^b & k_{23}^b\\ k_{31}^b & k_{32}^b & k_{33}^b\end{bmatrix}$, where,

$$[k_{11}^b]=D(ab)\sum_{j=1}^{nw}\sum_{i=1}^{nw}\int_0^1\int_0^1\left[\left\{\frac{1}{a^4}\left(\frac{\partial^2\varphi_i}{\partial\xi^2}\right)\left(\frac{\partial^2\varphi_j}{\partial\xi^2}\right)+\frac{1}{b^4}\left(\frac{\partial^2\varphi_i}{\partial\eta^2}\right)\left(\frac{\partial^2\varphi_j}{\partial\eta^2}\right)+\frac{1}{a^2b^2}\left(\frac{\partial^2\varphi_i}{\partial\xi^2}\right)\left(\frac{\partial^2\varphi_j}{\partial\eta^2}\right)\right.\right.$$
$$\left.+\frac{1}{a^2b^2}\left(\frac{\partial^2\varphi_i}{\partial\eta^2}\right)\left(\frac{\partial^2\varphi_j}{\partial\xi^2}\right)\right\}-\frac{(1-\upsilon)}{a^2b^2}\left\{\left(\frac{\partial^2\varphi_i}{\partial\xi^2}\right)\left(\frac{\partial^2\varphi_j}{\partial\eta^2}\right)+\left(\frac{\partial^2\varphi_i}{\partial\eta^2}\right)\left(\frac{\partial^2\varphi_j}{\partial\xi^2}\right)\right.$$
$$\left.\left.-2\left(\frac{\partial^2\varphi_i}{\partial\xi\,\partial\eta}\right)\left(\frac{\partial^2\varphi_j}{\partial\xi\,\partial\eta}\right)\right\}\right]d\xi\,d\eta$$

$$[k_{12}^b]=[k_{13}^b]=[k_{21}^b]=[k_{22}^b]=[k_{23}^b]=[k_{31}^b[=[k_{32}^b]=[k_{33}^b]=0$$

The form of $\left[K_m\right]$ is given by: $\left[K_m\right]=\begin{bmatrix}k_{11}^m & k_{12}^m & k_{13}^m\\ k_{21}^m & k_{22}^m & k_{23}^m\\ k_{31}^m & k_{32}^m & k_{33}^m\end{bmatrix}$, where,

$$[k_{11}^m]=\frac{E_p t_p}{2(1-\upsilon^2)}(ab)\sum_{j=1}^{nw}\sum_{i=1}^{nw}\int_0^1\int_0^1\left[\frac{1}{a^4}\left(\sum_{i=1}^{nw}d_i\frac{\partial\varphi_i}{\partial\xi}\right)^2\frac{\partial\varphi_i}{\partial\xi}\frac{\partial\varphi_j}{\partial\xi}+\frac{1}{b^4}\left(\sum_{i=1}^{nw}d_i\frac{\partial\varphi_i}{\partial\eta}\right)^2\frac{\partial\varphi_i}{\partial\eta}\frac{\partial\varphi_j}{\partial\eta}\right.$$
$$+\frac{1}{a^2b^2}\left(\sum_{i=1}^{nw}d_i\frac{\partial\varphi_i}{\partial\xi}\right)^2\frac{\partial\varphi_i}{\partial\eta}\frac{\partial\varphi_j}{\partial\eta}+\frac{1}{a^2b^2}\left(\sum_{i=1}^{nw}d_i\frac{\partial\varphi_i}{\partial\eta}\right)^2\frac{\partial\varphi_i}{\partial\xi}\frac{\partial\varphi_j}{\partial\xi}$$
$$+\frac{2}{a^3}\left(\sum_{i=nw+1}^{nw+nu}d_i\frac{\partial\alpha_{i-nw}}{\partial\xi}\right)\frac{\partial\varphi_i}{\partial\xi}\frac{\partial\varphi_j}{\partial\xi}+\frac{2}{b^3}\left(\sum_{i=nw+nu+1}^{nw+nu+nv}d_i\frac{\partial\beta_{i-nw-nu}}{\partial\eta}\right)\frac{\partial\varphi_i}{\partial\eta}\frac{\partial\varphi_j}{\partial\eta}$$
$$+\frac{2\upsilon}{a^2b}\left(\sum_{i=nw+nu+1}^{nw+nu+nv}d_i\frac{\partial\beta_{i-nw-nu}}{\partial\eta}\right)\frac{\partial\varphi_i}{\partial\xi}\frac{\partial\varphi_j}{\partial\xi}+\frac{2\upsilon}{ab^2}\left(\sum_{i=nw+1}^{nw+nu}d_i\frac{\partial\alpha_{i-nw}}{\partial\xi}\right)\frac{\partial\varphi_i}{\partial\eta}\frac{\partial\varphi_j}{\partial\eta}$$
$$+\frac{(1-\upsilon)}{ab^2}\left\{\left(\sum_{i=nw+1}^{nw+nu}d_i\frac{\partial\alpha_{i-nw}}{\partial\eta}\right)\frac{\partial\varphi_i}{\partial\xi}\frac{\partial\varphi_j}{\partial\eta}+\left(\sum_{i=nw+1}^{nw+nu}d_i\frac{\partial\alpha_{i-nw}}{\partial\eta}\right)\frac{\partial\varphi_i}{\partial\eta}\frac{\partial\varphi_j}{\partial\xi}\right\}$$
$$\left.+\frac{(1-\upsilon)}{a^2b}\left\{\left(\sum_{i=nw+nu+1}^{nw+nu+nv}d_i\frac{\partial\beta_{i-nw-nu}}{\partial\xi}\right)\frac{\partial\varphi_i}{\partial\xi}\frac{\partial\varphi_j}{\partial\eta}+\left(\sum_{i=nw+nu+1}^{nw+nu+nv}d_i\frac{\partial\beta_{i-nw-nu}}{\partial\xi}\right)\frac{\partial\varphi_i}{\partial\eta}\frac{\partial\varphi_j}{\partial\xi}\right\}\right]d\xi\,d\eta$$

$$[k_{12}^m] = [k_{13}^m] = 0$$

$$[k_{21}^m] = \frac{E_p t_p}{2(1-\upsilon^2)}(ab)\sum_{j=nw+1}^{nw+nu}\sum_{i=1}^{nw}\int_0^1\int_0^1 \left[\frac{1}{a^3}\left(\sum_{i=1}^{nw} d_i \frac{\partial \varphi_i}{\partial \xi}\right)\frac{\partial \varphi_i}{\partial \xi}\frac{\partial \alpha_{j-nw}}{\partial \xi} + \frac{\upsilon}{ab^2}\left(\sum_{i=1}^{nw} d_i \frac{\partial \varphi_i}{\partial \eta}\right)\frac{\partial \varphi_i}{\partial \eta}\frac{\partial \alpha_{j-nw}}{\partial \xi} + \frac{(1-\upsilon)}{ab^2}\left(\sum_{i=1}^{nw} d_i \frac{\partial \varphi_i}{\partial \xi}\right)\frac{\partial \varphi_i}{\partial \eta}\frac{\partial \alpha_{j-nw}}{\partial \eta}\right] d\xi\, d\eta$$

$$[k_{22}^m] = \frac{E_p t_p}{2(1-\upsilon^2)}(ab)\sum_{j=nw+1}^{nw+nu}\sum_{i=nw+1}^{nw+nu}\int_0^1\int_0^1 \left[\frac{2}{a^2}\frac{\partial \alpha_{i-nw}}{\partial \xi}\frac{\partial \alpha_{j-nw}}{\partial \xi} + \frac{(1-\upsilon)}{b^2}\frac{\partial \alpha_{i-nw}}{\partial \eta}\frac{\partial \alpha_{j-nw}}{\partial \eta}\right] d\xi\, d\eta$$

$$[k_{23}^m] = \frac{E_p t_p}{2(1-\upsilon^2)}\sum_{j=nw+1}^{nw+nu}\sum_{i=nw+nu+1}^{nw+nu+nv}\int_0^1\int_0^1 \left[2\upsilon\frac{\partial \beta_{i-nw-nu}}{\partial \eta}\frac{\partial \alpha_{j-nw}}{\partial \xi} + (1-\upsilon)\frac{\partial \beta_{i-nw-nu}}{\partial \xi}\frac{\partial \alpha_{j-nw}}{\partial \eta}\right] d\xi\, d\eta$$

$$[k_{31}^m] = \frac{E_p t_p}{2(1-\upsilon^2)}(ab)\sum_{j=nw+nu+1}^{nw+nu+nv}\sum_{i=1}^{nw}\int_0^1\int_0^1 \left[\frac{1}{b^3}\left(\sum_{i=1}^{nw} d_i \frac{\partial \varphi_i}{\partial \eta}\right)\frac{\partial \varphi_i}{\partial \eta}\frac{\partial \beta_{j-nw-nu}}{\partial \eta} + \frac{\upsilon}{a^2 b}\left(\sum_{i=1}^{nw} d_i \frac{\partial \varphi_i}{\partial \xi}\right)\frac{\partial \varphi_i}{\partial \xi}\frac{\partial \beta_{j-nw-nu}}{\partial \eta} + \frac{(1-\upsilon)}{a^2 b}\left(\sum_{i=1}^{nw} d_i \frac{\partial \varphi_i}{\partial \xi}\right)\frac{\partial \varphi_i}{\partial \eta}\frac{\partial \beta_{j-nw-nu}}{\partial \xi}\right] d\xi\, d\eta$$

$$[k_{32}^m] = \frac{E_p t_p}{2(1-\upsilon^2)}\sum_{j=nw+nu+1}^{nw+nu+nv}\sum_{i=nw+1}^{nw+nu}\int_0^1\int_0^1 \left[2\upsilon\frac{\partial \alpha_{i-nw}}{\partial \xi}\frac{\partial \beta_{j-nw-nu}}{\partial \eta} + (1-\upsilon)\frac{\partial \alpha_{i-nw}}{\partial \eta}\frac{\partial \beta_{j-nw-nu}}{\partial \xi}\right] d\xi\, d\eta$$

$$[k_{33}^m] = \frac{E_p t_p}{2(1-\upsilon^2)}(ab)\sum_{j=nw+nu+1}^{nw+nu+nv}\sum_{i=nw+nu+1}^{nw+nu+nv}\int_0^1\int_0^1 \left[\frac{2}{b^2}\frac{\partial \beta_{i-nw-nu}}{\partial \eta}\frac{\partial \beta_{i-nw-nu}}{\partial \eta} + \frac{(1-\upsilon)}{a^2}\frac{\partial \beta_{i-nw-nu}}{\partial \xi}\frac{\partial \beta_{i-nw-nu}}{\partial \xi}\right] d\xi\, d\eta$$

The form of $\left[K_{sx}\right]$ is given by: $\left[K_{sx}\right] = \begin{bmatrix} k_{11}^{sx} & k_{12}^{sx} & k_{13}^{sx} \\ k_{21}^{sx} & k_{22}^{sx} & k_{23}^{sx} \\ k_{31}^{sx} & k_{32}^{sx} & k_{33}^{sx} \end{bmatrix}$, where,

$$[k_{11}^{sx}]=\sum_{p=1}^{ns_x}\left[\frac{E_s a}{2}\sum_{j=1}^{nw}\sum_{i=1}^{nw}\int_0^1 \left\{I_y^p\frac{2}{a^4}\frac{\partial^2\varphi_i}{\partial\xi^2}\frac{\partial^2\varphi_j}{\partial\xi^2}-Q_y^p\frac{2}{a^4}\left(\sum_{i=1}^{nw}d_i\frac{\partial\varphi_i}{\partial\xi}\right)^2\frac{\partial^2\varphi_i}{\partial\xi^2}\frac{\partial\varphi_j}{\partial\xi}\right.\right.$$
$$-Q_y^p\frac{1}{a^4}\left(\sum_{i=1}^{nw}d_i\frac{\partial\varphi_i}{\partial\xi}\right)\frac{\partial\varphi_i}{\partial\xi}\frac{\partial^2\varphi_j}{\partial\xi^2}+A_y^p\frac{1}{a^4}\left(\sum_{i=1}^{nw}d_i\frac{\partial\varphi_i}{\partial\xi}\right)^2\frac{\partial\varphi_i}{\partial\xi}\frac{\partial\varphi_j}{\partial\xi}$$
$$\left.\left.+A_y^p\frac{2}{a^3}\left(\sum_{i=nw+1}^{nw+nu}d_i\frac{\partial\alpha_{i-nw}}{\partial\xi}\right)^2\frac{\partial\varphi_i}{\partial\xi}\frac{\partial\varphi_j}{\partial\xi}\right\}d\xi\right]$$

$$[k_{12}^{sx}]=\sum_{p=1}^{ns_x}\left[\frac{E_s a}{2}\sum_{j=1}^{nw}\sum_{i=nw+1}^{nw+nu}\int_0^1\left\{-Q_y^p\frac{2}{a^3}\frac{\partial\alpha_{i-nw}}{\partial\xi}\frac{\partial^2\varphi_j}{\partial\xi^2}\right\}d\xi\right]$$

$$[k_{21}^{sx}]=\sum_{p=1}^{ns_x}\left[\frac{E_s a}{2}\sum_{j=nw+1}^{nw+nu}\sum_{i=1}^{nw}\int_0^1\left\{-Q_y^p\frac{2}{a^3}\frac{\partial^2\varphi_i}{\partial\xi^2}\frac{\partial\alpha_{j-nw}}{\partial\xi}+A_y^p\frac{1}{a^3}\left(\sum_{i=1}^{nw}d_i\frac{\partial\varphi_i}{\partial\xi}\right)\frac{\partial\varphi_i}{\partial\xi}\frac{\partial\alpha_{j-nw}}{\partial\xi}\right\}d\xi\right]$$

$$[k_{22}^{sx}]=\sum_{p=1}^{ns_x}\left[\frac{E_s a}{2}\sum_{j=nw+1}^{nw+nu}\sum_{i=nw+1}^{nw+nu}\int_0^1\left\{A_y^p\frac{2}{a^2}\frac{\partial\alpha_{i-nw}}{\partial\xi}\frac{\partial\alpha_{j-nw}}{\partial\xi}\right\}d\xi\right]$$

$$[k_{33}^{sx}]=\sum_{p=1}^{ns_x}\left[\frac{E_s a}{2}\sum_{j=nw+nu+1}^{nw+nu+nv}\sum_{i=nw+nu+1}^{nw+nu+nv}\int_0^1\left\{I_{yz}^p\frac{2}{a^4}\frac{\partial^2\beta_{i-nw-nu}}{\partial\xi^2}\frac{\partial^2\beta_{i-nw-nu}}{\partial\xi^2}\right\}d\xi\right]$$

$$[k_{13}^{sx}]=[k_{23}^{sx}]=[k_{31}^{sx}]=[k_{32}^{sx}]=0$$

The form of $[K_{sy}]$ is given by: $\left[K_{sy}\right]=\begin{bmatrix}k_{11}^{sy} & k_{12}^{sy} & k_{13}^{sy}\\ k_{21}^{sy} & k_{22}^{sy} & k_{23}^{sy}\\ k_{31}^{sy} & k_{32}^{sy} & k_{33}^{sy}\end{bmatrix}$, where,

$$[k_{11}^{sy}]=\sum_{q=1}^{ns_y}\left[\frac{E_s b}{2}\sum_{j=1}^{nw}\sum_{i=1}^{nw}\int_0^1\left\{I_x^q\frac{2}{b^4}\frac{\partial^2\varphi_i}{\partial\eta^2}\frac{\partial^2\varphi_j}{\partial\eta^2}-Q_x^q\frac{2}{b^4}\left(\sum_{i=1}^{nw}d_i\frac{\partial\varphi_i}{\partial\eta}\right)^2\frac{\partial^2\varphi_i}{\partial\eta^2}\frac{\partial\varphi_j}{\partial\eta}\right.\right.$$
$$-Q_x^q\frac{1}{b^4}\left(\sum_{i=1}^{nw}d_i\frac{\partial\varphi_i}{\partial\eta}\right)\frac{\partial\varphi_i}{\partial\eta}\frac{\partial^2\varphi_j}{\partial\eta^2}+A_x^q\frac{1}{b^4}\left(\sum_{i=1}^{nw}d_i\frac{\partial\varphi_i}{\partial\eta}\right)^2\frac{\partial\varphi_i}{\partial\eta}\frac{\partial\varphi_j}{\partial\eta}$$
$$\left.\left.+A_x^q\frac{2}{b^3}\left(\sum_{i=nw+nu+1}^{nw+nu+nv}d_i\frac{\partial\beta_{i-nw-nu}}{\partial\eta}\right)^2\frac{\partial\varphi_i}{\partial\eta}\frac{\partial\varphi_j}{\partial\eta}\right\}d\eta\right]$$

$$[k_{22}^{sy}] = \sum_{q=1}^{ns_y}\left[\frac{E_s b}{2}\sum_{j=nw+1}^{nw+nu}\sum_{i=nw+1}^{nw+nu}\int_0^1 \left\{I_{xz}^q \frac{2}{b^4}\frac{\partial^2 \alpha_{i-nw}}{\partial\eta^2}\frac{\partial \alpha^2{}_{j-nw}}{\partial\eta^2}\right\}d\eta\right]$$

$$[k_{33}^{sy}] = \sum_{q=1}^{ns_y}\left[\frac{E_s b}{2}\sum_{j=nw+nu+1}^{nw+nu+nv}\sum_{i=nw+nu+1}^{nw+nu+nv}\int_0^1 \left\{A_x^q \frac{2}{b^2}\frac{\partial \beta_{i-nw-nu}}{\partial\eta}\frac{\partial \beta_{i-nw-nu}}{\partial\eta}\right\}d\eta\right]$$

$$[k_{31}^{sy}] = \sum_{q=1}^{ns_y}\left[\frac{E_s b}{2}\sum_{j=nw+nu+1}^{nw+nu+nv}\sum_{i=1}^{nw}\int_0^1 \left\{-Q_x^q \frac{2}{b^3}\frac{\partial^2\varphi_i}{\partial\eta^2}\frac{\partial \beta_{j-nw-nu}}{\partial\eta} + A_x^q \frac{1}{b^3}\left(\sum_{i=1}^{nw} d_i \frac{\partial\varphi_i}{\partial\eta}\right)\frac{\partial\varphi_i}{\partial\eta}\frac{\partial \beta_{j-nw-nu}}{\partial\eta}\right\}d\eta\right]$$

$$[k_{13}^{sy}] = \sum_{q=1}^{ns_y}\left[\frac{E_s b}{2}\sum_{j=1}^{nw}\sum_{i=nw+nu+1}^{nw+nu+nv}\int_0^1 \left\{-Q_x^q \frac{2}{b^3}\frac{\partial \beta_{i-nw-nu}}{\partial\eta}\frac{\partial^2\varphi_j}{\partial\eta^2}\right\}d\eta\right]$$

$$[k_{12}^{sy}] = [k_{21}^{sy}] = [k_{23}^{sy}] = [k_{32}^{sy}] = 0$$

The total mass matrix [M] is given by, $[M] = [M_p] + [M_{sx}] + [M_{sy}]$.

The form of plate mass matrix $[M_p]$ is given by: $\left[M_p\right] = \begin{bmatrix} M_{11}^p & 0 & 0 \\ 0 & M_{22}^p & 0 \\ 0 & 0 & M_{33}^p \end{bmatrix}$, where,

$$[M_{11}^p] = \rho_p t_p (ab)\sum_{j=1}^{nw}\sum_{i=1}^{nw}\int_0^1\int_0^1 \varphi_i\varphi_j \, d\xi \, d\eta$$

$$[M_{22}^p] = \rho_p t_p (ab)\sum_{j=nw+1}^{nw+nu}\sum_{i=nw+1}^{nw+nu}\int_0^1\int_0^1 \alpha_{i-nw}\alpha_{j-nw} \, d\xi \, d\eta$$

$$[M_{33}^p] = \rho_p t_p (ab)\sum_{j=nw++nu1}^{nw+nu+nv}\sum_{i=nw+nu+1}^{nw+nu+nv}\int_0^1\int_0^1 \beta_{i-nw-nu}\beta_{j-nw-nu} \, d\xi \, d\eta$$

The form of $[M_{sx}]$ is given by: $\left[M_{sx}\right] = \begin{bmatrix} M_{11}^{sx} & 0 & 0 \\ 0 & M_{22}^{sx} & 0 \\ 0 & 0 & M_{33}^{sx} \end{bmatrix}$, where

$$[M_{11}^{sx}] = \sum_{p=1}^{ns_x}\left[\rho_s t_{sx}^p (ab_{sx}^p)\sum_{j=1}^{nw}\sum_{i=1}^{nw}\int_0^1 \varphi_i\varphi_j \, d\xi\right]$$

$$[M_{22}^{sx}] = \sum_{p=1}^{ns_x}\left[\rho_s t_{sx}^p (ab_{sx}^p) \sum_{j=nw+1}^{nw+nu} \sum_{i=nw+1}^{nw+nu} \int_0^1 \alpha_{i-nw}\alpha_{j-nw}\, d\xi\right]$$

$$[M_{33}^{sx}] = \sum_{p=1}^{ns_x}\left[\rho_s t_{sx}^p (ab_{sx}^p) \sum_{j=nw+nu+1}^{nw+nu+nv} \sum_{i=nw+nu+1}^{nw+nu+nv} \int_0^1 \beta_{i-nw-nu}\beta_{j-nw-nu}\, d\xi\right]$$

The form of $[M_{sy}]$ is given by: $\left[M_{sy}\right] = \begin{bmatrix} M_{11}^{sy} & 0 & 0 \\ 0 & M_{22}^{sy} & 0 \\ 0 & 0 & M_{33}^{sy} \end{bmatrix}$, where,

$$[M_{11}^{sy}] = \sum_{q=1}^{ns_y}\left[\rho_s t_{sy}^q (bb_{sy}^q) \sum_{j=1}^{nw} \sum_{i=1}^{nw} \int_0^1 \varphi_i \varphi_j\, d\eta\right]$$

$$[M_{22}^{sy}] = \sum_{q=1}^{ns_y}\left[\rho_s t_{sy}^q (bb_{sy}^q) \sum_{j=nw+1}^{nw+nu} \sum_{i=nw+1}^{nw+nu} \int_0^1 \alpha_{i-nw}\alpha_{j-nw}\, d\eta\right]$$

$$[M_{33}^{sy}] = \sum_{q=1}^{ns_y}\left[\rho_s t_{sy}^q (bb_{sy}^q) \sum_{j=nw+nu+1}^{nw+nu+nv} \sum_{i=nw+nu+1}^{nw+nu+nv} \int_0^1 \beta_{i-nw-nu}\beta_{j-nw-nu}\, d\eta\right]$$

The load vector $\left\{f\right\}$ is of the form $\left\{f\right\} = \left\{f_{11} \quad f_{12} \quad f_{13}\right\}^T$, where $\left\{f_{11}\right\} = \sum_{j=1}^{nw} P\varphi_j \big|_{\xi,\eta} + p(ab)\sum_{j=1}^{nw}\int_0^1\int_0^1 \varphi_j d\xi\, d\eta$ and $\left\{f_{12}\right\} = \left\{f_{13}\right\} = 0$.

This work was previously published in the International Journal of Manufacturing, Materials, and Mechanical Engineering, Volume 1, Issue 2, edited by J. Paulo Davim, pp. 62-98, copyright 2011 by IGI Publishing (an imprint of IGI Global).

Chapter 3
Design and Evaluation of Hydro-Pneumatic Friction Damper Suspension System

S.V. Gorabal
SKSVMA College of Engineering & Technology, India

S.N. Kurbet
Basaveshwar Engineering College, India

K.K. Appukuttan
National Institute of Technology Karnataka, India

ABSTRACT

Perceived comfort level and ride stability are the two most important factors in the evaluation of suspension system in a mobile vehicle. It is extremely difficult to simultaneously maintain a high standard of vehicle ride, handling and body control in the vehicle by using conventional passive suspension system. However, the use of active suspensions would result in better comforts than the passive ones. This paper presents the design and analysis of a pneumatic friction damper and hydro-pneumatic friction damper. A non-linear quarter car model is developed, which includes pneumatic actuation by pressure regulation. The performance of the proposed model was assessed in terms of level of vibration reduction. Simulations on a prototype model show that the proposed system has good performance and robustness.

1. INTRODUCTION

The main functions of a vehicle suspension system are to isolate the body from road unevenness disturbances and to maintain the contact between the road and the wheel. Therefore, the suspension system is responsible for the ride quality and driving stability. The design of a passive suspension system is a compromise between this conflict demands. However, the improvement in vertical vehicle dynamics is possible by developing active suspension system. In recent years, the development of pneumatics controlled suspension dampers and actuator has increased the research

DOI: 10.4018/978-1-4666-1867-1.ch003

Copyright © 2013, IGI Global. Copying or distributing in print or electronic forms without written permission of IGI Global is prohibited.

on vehicle safety versus ride comfort trade off. In order to maintain the level of comfort for passengers and drivers, and still maintain the high safety standards of automobiles, suspension designers have been forced to look beyond the conventional suspension systems.

Crosby and Karnopp (1974) originally proposed the basic concept of semi-active damping and then the use of semi-active dampers in automobiles has been studied extensively. The authors have contributed an excellent review of many of the past efforts in the area of semi-active suspension design and provided a background of the information that is required to understand semi-active suspension systems. A review of the state-of-the-art of controlled suspensions has been carried out by Hedrick and Wormely (1975) and by Goodall and Kortum (1983). In these investigations, semi-active control and linear optimal control with full state feedback along with simple on-off control strategies were employed to reduce both the tyre force and body acceleration of a heavy truck. However, it is worth mentioning here that the air springs for passenger cars are commercially available and there are not enough researches devoted on their performances. The work presented by Quaglia and Sorly (1996) discussed the vehicular air suspensions from design aspects, but not from control viewpoint. Considering the market requirement for passenger vehicles, it was found that integration of leveling, variable damper control technology and stiffness control are very beneficial. The new active friction damper provides a possible solution for the problem.

There are two basic types of suspension namely, the primary suspension used between the vehicle chassis and axle assembly and secondary suspension system mounted between the vehicle body and seat. Much work has-been reported (Reynolds, 1993; Rayliegh, 1945) regarding the primary and secondary suspension systems. The study carried out by Williams (1997) classified the active suspensions as the high-bandwidth (fast active) and low bandwidth (slow active). High bandwidth active hydraulic actuators control the body motion and wheel motion. On the other hand, low bandwidth suspensions employ pneumatic actuators to control the body motion while the wheel motion is controlled by conventional passive spring and damper. Over the past three decades, many control methods for active suspension have been studied. Review studies by Clarr and Vogel (1989) and Sharp and Corolla (1987) summarized the various commonly used control techniques. More recently, controls based on different approaches have been employed in active suspension system. These include approaches based on linear and non-linear control (Gao et al., 2006; Hong et al., 2002; Elimadany & Abdlizabbar, 1999), optimal control (Elbheiry & Karnoop, 1996) and modern robust control such as H-infinity (Palmeri et al., 1995; Stribrsky et al., 2002; Wang et al., 2001). In the past, Fuzzy logic based active and semi-active suspension system (Kashani & Strelow, 1999) was also being employed for the control purpose. Among them, skyhook control (Hong et al., 2002) is the most important concept considered for active suspensions.

The main aim of this paper is to discuss the investigations carried on the pneumatic friction and hydro-pneumatic friction dampers. In this approach, laboratory prototype models of the aforementioned friction dampers have been developed. In order to study the complete system behavior, the developed prototype models have been interfaced to Lab VIEW software module with laser displacement pickup. The details of the key design features and test results were presented. The pressure control regulator controls the friction load coming to the damper is considered in the present model. The non-linearity behavior of the friction pads and pressure developed at the axial hole on the piston for different loads are investigated.

2. DRY FRICTION DAMPING

Coulomb or dry friction damping results when sliding contact exists between two dry surfaces. The damping force is equal to the product of the normal force and the coefficient of dry friction. The friction force is always opposite to the direction of motion. The friction force is given by

$$F = \mu N \tag{1}$$

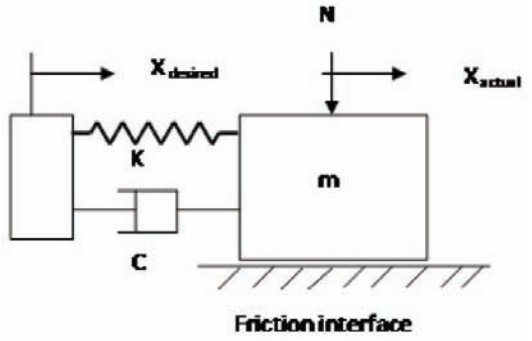
where μ is coefficient of friction, F is frictional force, and N is normal reaction. Frictional force divided by the velocity of the piston gives frictional damping.

The friction model is shown in the Figure 1. Friction has often been modeled by an algebraic equation relating velocity and normal force to friction. It is well known however that friction possesses dynamics associated with varying velocity. A rather complete description of friction modeling and its impact on control is well documented in the literature (Armstrong et al., 1994). However, it was recognized that dynamics associated with varying normal force play an important role in the system response. Friction dynamics associated with variations in normal force are fast in comparison to those due to velocity fluctuations (Dupont, 1993; Guglielmino & Edge, 1980). It is observed that pure dry friction characteristics' are of no practical use because of their non-linearity, but a controlled friction damper can be made to behave in a variety of ways emulating spring-like pseudo, viscous characteristics. The external force (F_{ext}) required by an active friction damper is generally defined as,

$$F_{ext} = M\ddot{x} + C\dot{x} + Kx + \sum_{i=1}^{m} \mu N_i \tag{2}$$

where M is the mass in Kg, C is the damping coefficient, K is the spring stiffness, N_i is the normal force of ith friction damper and μ is the

Figure 1. Friction model



friction coefficient. When C = 0, the system work as pure friction damper

In this work, the controlled damping element is modeled as a frictional damper. This device, which conceptually is composed of a plate fixed to a moving mass and a pad against it. An external normal force is applied to a mass by the pad and consequently, in the presence of relative motion between the pad and the plate, a frictional damping force is produced.

The pneumatic friction model is depicted in Figure 2. The model mainly consists of a conventional spring and piston-cylinder assembly system. A friction damper was constructed in the piston such a manner it enable to work as pure friction damper and friction damper with a conventional viscous damper used in a vehicle. In the piston two shoes are provided which activated by the compressed air. When the pressure acts on the shoe cylinder, shoe displace towards the cylinder surface with force is equal to shoe cylinder area multiplied by supply pressure. The friction force acting on the surface of the cylinder is μ times the applied force on the shoe. Compressed air is supplied through the centre of the piston rod and pressure is controlled by the pressure regulator. On the axial direction on the piston two 2 mm holes are provided for Hydraulic damping purpose. The damper can be used as pure friction damper without filling the oil and Hydro-friction damper with filling the oil inside the cylinder. External

energy supplied by the air compressor regulates the pressure; which actuates the friction pad, according to variable static and dynamic load of the system. The friction pads undergo dry friction damping. In the present investigation, coulomb damping is considered. When the vehicle is in static state i.e., the vehicle with dead weight, a radial pressure is imparted on the friction pads, which sustain the sudden shock when the rider sits on it. This causes friction pads to expand and recoil slowly. On the other hand, when the vehicle is in motion, the suspension system is active type, i.e., both linear and radial pressures are acting on it.

Figure 3 shows the photograph of the fabricated damper with spring assembly. A 5 kg weight is added on the top of the platform and it is displaced to 5 mm step input and the response curves were obtained. Vibration levels are measured using laser pickup and Lab VIEW software and analyzed through the origin software. Laser pick up is mounted on the top of the damper to measure the displacement. Figure 4 shows the 2D drawing of the friction damper model and Figure 5 shows the experimental setup of the friction damper.

3. RESULTS AND DISCUSSIONS

Friction in the actuator was represented by coulomb friction and velocity-dependent terms obtained from previous study (Gao et al., 2006). Experiments were performed with different pressures supplied to the friction pad for step input and results were obtained using the Lab VIEW software. The damper is actuated without lubricant oil inside the cylinder. The dynamic response in terms of the variation of displacement with respect to time obtained is illustrated in the Figure 6. X axis the time is in mille seconds and Y axis is the displacement in mm.

Figure 2. Pneumatic/hyrdo-pneumatic damper

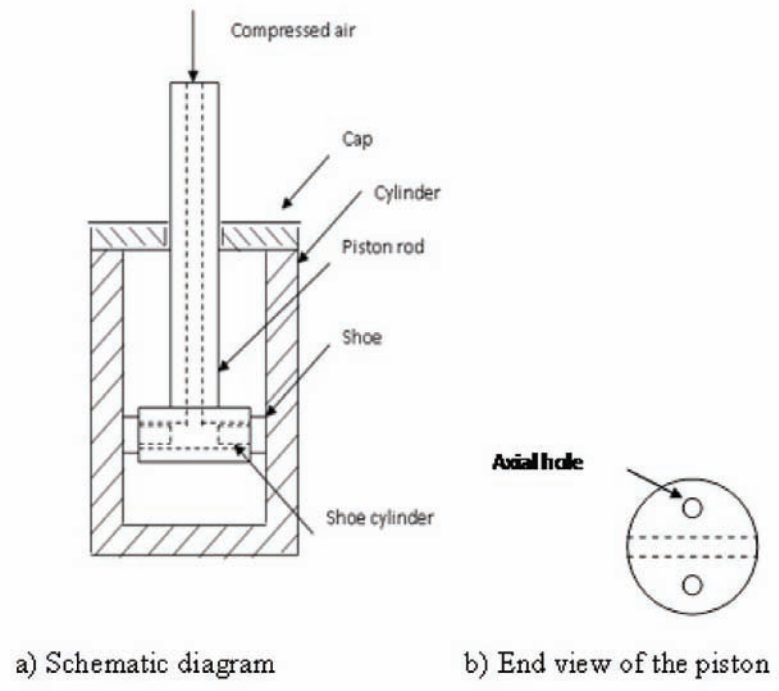


Figure 3. Photograph of the fabricated hydraulic –pneumatic damper

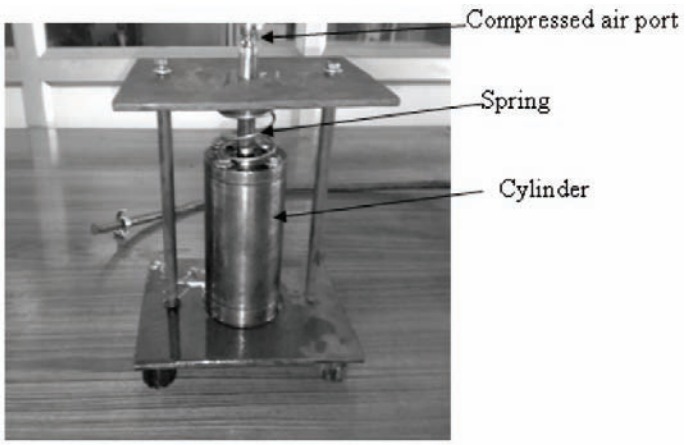


Figure 4. 2D drawing of the friction damper model

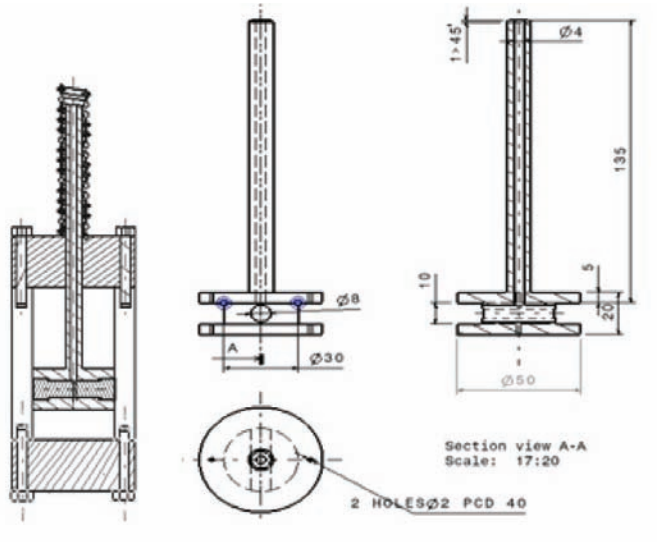


Figure 5. Experimental model of friction damper

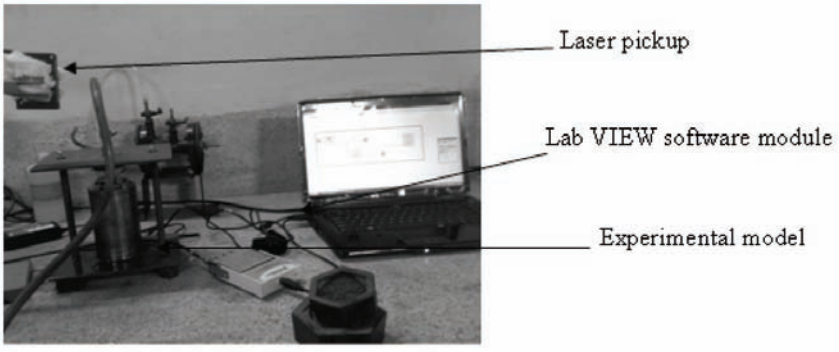
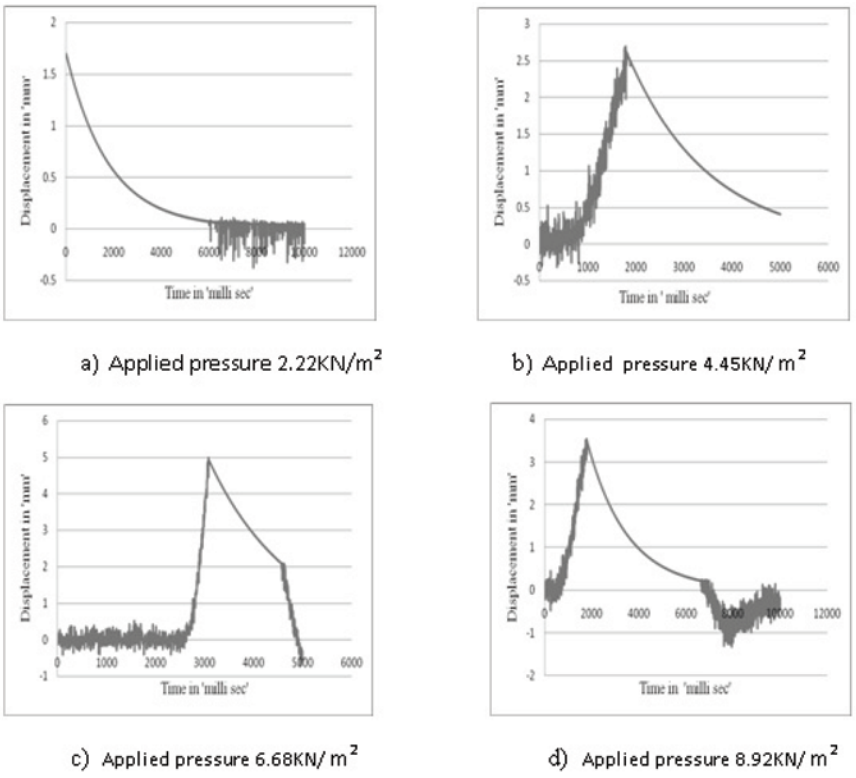


Figure 6. Dynamic response of the pneumatic friction damper



It is observed from Figure 6 that the behavior of system is highly non-linear. Moreover, when the applied pressure is low (2.22KN/m^2), due to harshness of the friction pad, the system can exert the damping effect. Hence, it is observed that the displacement sharply decreases with time (Figure 6a). On the other hand, for increased applied pressure, the friction pad initially exerts large friction and hence the system exhibits an increased displacement with time. However, as time progressed, the damping effect improves which turn reduces the displacement as depicted in Figure 6(b-d).

The hydro pneumatic friction model analysed in the study is similar to pneumatic friction model. However, in the hydro pneumatic friction model, oil is employed in the cylinder and two axial holes are provided in the piston. Thus, there are two dampers provided in the system, one is the pneumatic friction damper provided by friction pad and the other is the hydraulic damper due to oil flow in the cylinder through the hole provided in the piston. When the piston is in compression, part of the oil flow from cylinder bottom chamber to the upper chamber through the orifice.

For analytical modeling of the hydraulic damper, consider piston area A_p and area of opening of the axial hole A_0, when piston displaced by the action of dynamic force, the quantity of fluid displaced is:

$$Q_p = A_P \frac{dy}{dt} = A_p V_p \tag{3}$$

where y is the displacement of the piston and V_p is the velocity of the piston moment.

The fluid flow rate, Q_0 through the axial hole can be obtained using continuity equation and momentum equation as:

Table 1. Damping factor for different orifice diameter

Applied pressure P_1 K N/m²	Orifice diameter, d_o=1mm, calculated Damping factor	Orifice diameter, d_o=2mm, calculated Damping factor	Orifice diameter, d_o=3mm, calculated Damping factor
2.229	0.358	0.357	0.358
4.459	0.359	0.358	0.358
6.688	0.359	0.359	0.359
8.198	0.359	0.359	0.359

$$Q_0 = A_0\sqrt{2g\frac{(p_1 - p_2)}{\rho}} = A_P V_P \qquad (4)$$

where p_1 and p_2 are upstream and downstream pressure ρ is the specific weight of the fluid and g is the gravitational constant.

The force carried by the piston is equal to area of piston multiplied by difference in pressure and fixed hydraulic damping coefficient is equal to force acting on the piston divided by velocity of the piston. By manipulating Equations (3) and (4) the damping coefficient, $C = \frac{F_P}{V_P} = \frac{A_P(p_1 - p_2)}{V_P}$ can be obtained as:

$$C = \frac{A_P{}^3 V_P \rho}{A_0{}^2 2g} \qquad (5)$$

where FP is the viscous force which can be obtained from the force acting on the piston and $V_P = \frac{F_P}{A_P}$. Using the Equation (1) and (5) theoretical damping factor due to friction and hydraulic damping can be determined. The damping factor of the orifice is determined from

$$\zeta = \frac{C}{C_c} \qquad (6)$$

where, C is the actual damping factor and C_c is the critical damping factor. Table 1 gives the damping factor for different axial hole diameter on the piston for different pressures.

The theoretical damping factor values were determined as a function of applied pressure for different orifice diameters is depicted in Figure 7. It is observed from Figure 7 that the system

Figure 7. Plot of pressure Vs damping ration for different diameters

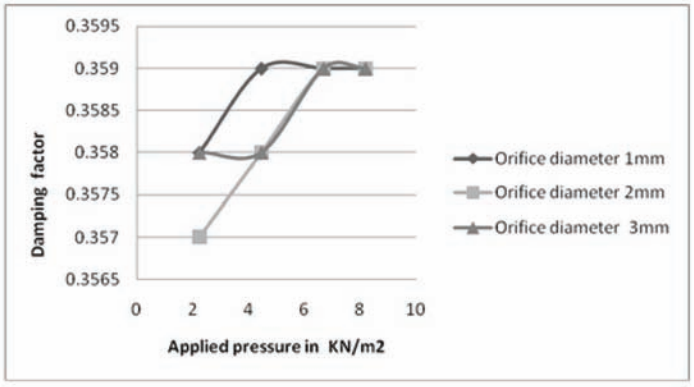
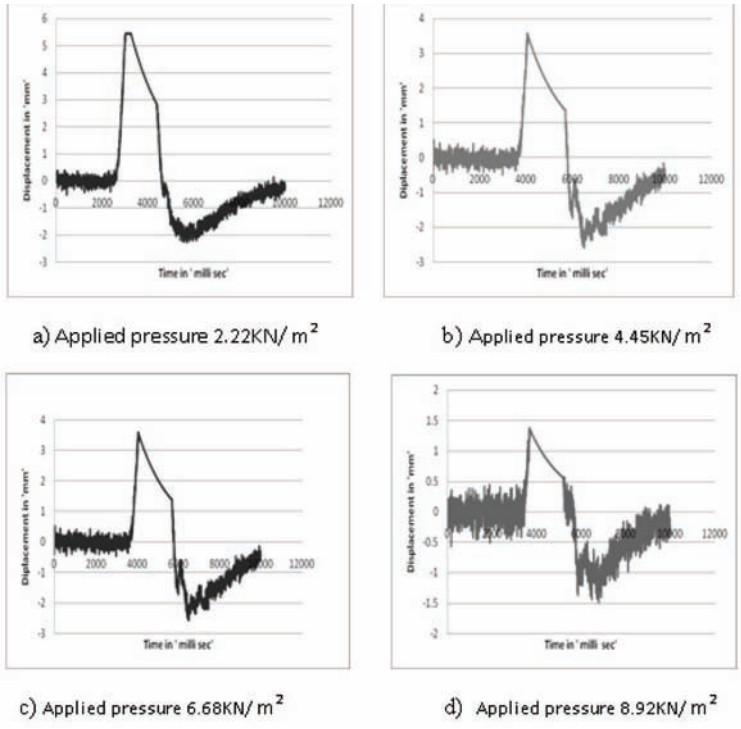


Figure 8. Dynamic response of the hydro-pneumatic system for different loads



exhibits linear responses for different applied pressure for 2mm orifice diameter. Hence, 2 mm orifice diameter was considered in the prototype design.

model, dynamic response of the system is obtained and is shown in Figure 6 and Figure 8. Two important observations can be drawn from the dynamic response shown in Figure 6 and Figure 8. It is observed that the system exhibits similar responses for different applied pressure. Also, the hydro pneumatic friction model takes more time with reduced displacement as compared to pneumatic friction model. Therefore hydro pneumatic friction model provide larger damping effect with reduced vibrations and better riding comfort as compared with pneumatic friction model.

From the above discussions, it is seen that the experimentation on the pneumatic friction damper system showed an unexpected behaviour at low supply pressure, dynamic performance was extremely poor. The first hypothesis made was that at low pressure an air pocket could have been trapped inside the valve: at low pressures, a small quantity of air enormously reduces bulk modulus, which adversely affects the dynamical response of the system. Hence it can be that the pure pneumatic friction damper is not suitable for better rider comfort.

CONCLUSION

The details of the investigations carried out on pneumatically activated friction damper and hydro pneumatic friction damper models are presented in this paper. Laboratory prototype models were developed and dynamic testing performance was carried out by means of Lab-VIEW software module with laser pick up. The details of the key design were provided. The dynamic test results illustrated that the hydro-pneumatic friction damper model

exhibits better damping performance as compared to pneumatically activated friction damper.

REFERENCES

Armstrong-Hélouvry, B., Dupont, P., & Canudas de Wit, C. (1994). A survey of models, analysis tools and compensation methods for the control of machines with friction. *Automatica*, *30*, 1083–1138. doi:10.1016/0005-1098(94)90209-7

Clarr, P. W., & Vogel, J. M. (1989). *Review of active suspension control for on and off highway vehicles*. Retrieved from http://papers.sae.org/892482/

Dupont, P. (1993). The effect of friction on the forward dynamics problem. *The International Journal of Robotics Research*, *12*, 164–179. doi:10.1177/027836499301200205

Eimadany, M. M., & Abdlizabbar, Z. S. (1999). Linear quadratic Gausssian control of a quarter-car suspension. *Vehicle System Dynamics*, *32*, 479–497. doi:10.1076/vesd.32.6.479.4224

Elbheiry, E. M., & Karnoop, D. C. (1996). Optimal control of vehicle random vibration with constrained suspension deflection. *Journal of Sound and Vibration*, *189*, 547–564. doi:10.1006/jsvi.1996.0036

Gao, B., Darling, J., Tilley, D. G., Williams, D. G., & Donahue, J. (2006). Control of a hydropneaumatic active suspension based on a non-linear quarter car model. *Journal of Systems and Control Engineering*, *220*(1), 15–31.

Goodall, R. M., & Kortum, W. (1983). Active control in ground transportation-a review of the state-of-art and future potential. *Vehicle System Dynamics*, *12*, 225–257. doi:10.1080/00423118308968755

Guglielmino, E., & Edge, K. A. (1980). *A controlled friction damper for vehicle applications*. Bath, UK: University of Bath.

Hedrick, J. K., & Wormely, D. N. (1975). Active suspension for ground support vehicles - a state-of-the-art review. *ASME Applied Mechanics Division Journal*, *15*, 21–40.

Hong, K. S., Sohn, H. C., & Hedrick, J. K. (2002). Modified skyhook control of semi-active suspensions-A new model, gain scheduling and hardware-in-the loop tuning. *Journal of Dynamics. Measurements and Control*, *124*, 158–167. doi:10.1115/1.1434265

Karnoop, R. M., Crosby, R. A., & Harwood, R. A. (1974). Vibration control using semi–active force generators. *ASME Journal of Engineering for Industry*, *96*, 619–626. doi:10.1115/1.3438373

Kashani, R., & Strelow, J. E. (1999). Fuzzy logic active and semi active control of road-vehicle suspensions. *Vehicle System Dynamics*, *32*, 409–420. doi:10.1076/vesd.32.4.409.2075

Lord Rayliegh. (1945). *Controlled suspensions. Theory of sound* (*Vol. 1-2*). New York, NY: Dover Publications.

Palmeri, P. S., Moschetti, A., & Gortan, L. H. (1995). *Infinity control for active suspension system*. Retrieved from http://www.papers.sae.org/950583

Quaglia, G., & Sorli, M. (1996). Analysis of vehicular air suspensions. In *Proceedings of the Fourth JHPS International Symposium on Fluid Power*, Tokyo, Japan (pp. 389-384).

Reynolds, H. M. (1993). *Automotive ergonomics* (pp. 99–116). London, UK: Taylor and Francis.

Sharp, R. S., & Corolla, D. A. (1987). Road vehicle suspension design–A review. *Vehicle System Dynamics*, *16*, 169–192. doi:10.1080/00423118708968877

Stribrsky, A., Honcu, J., Hyniova, K., & Kruczek, A. (2002). H-infinity control of active suspension systems. In *Proceedings of the Conference on Process Control*, Pardubice, Czech Republic (Vol. 35).

Wang, J., Wilson, D. A., & Halikias, G. D. H. (2001). Robust-performance control of decoupled active suspension system based on LMI method. In *Proceedings of the American Control Conference*, *4*, 2658–2663.

Williams, R. A. (1997). Automotive active suspensions. *Automobile Engineering*, *211*, 415–426. doi:10.1243/0954407971526551

This work was previously published in the International Journal of Manufacturing, Materials, and Mechanical Engineering, Volume 1, Issue 4, edited by J. Paulo Davim, pp. 65-74, copyright 2011 by IGI Publishing (an imprint of IGI Global).

Section 2
Manufacturing

Chapter 4
An Investigation into the Environmental Impact of Product Recovery Methods to Support Sustainable Manufacturing within Small and Medium-Sized Enterprises (SMEs)

Michaela R. Appleby
Lancaster University, UK

Chris G. Lambert
Lancaster University, UK

Allan E. W. Rennie
Lancaster University, UK

Adam B. Buckley
The Manufacturing Institute, UK

ABSTRACT

The effects of climate change and government legislation has changed the way in which manufacturers can dispose of their waste, encouraging SMEs to source alternative disposal methods such as those indicated in the waste hierarchy. It is economically and environmentally beneficial to use product recovery methods to divert waste from landfill. The environmental impact of two product recovery methods, remanufacturing and repairing, has been compared via a carbon footprint calculation for a UK-based SME. The calculation has identified that repairing has a lower carbon footprint than remanufacturing, however this only extends the original life-cycle of the product, whereas remanufacturing provides a new life-cycle and warranty, and therefore seen as the most preferable method of product recovery to support sustainable manufacturing.

DOI: 10.4018/978-1-4666-1867-1.ch004

Copyright © 2013, IGI Global. Copying or distributing in print or electronic forms without written permission of IGI Global is prohibited.

INTRODUCTION

Global concerns of rising Greenhouse Gas (GHG) emissions and human induced climate change has led to the development of an internationally recognised agreement between European Nations (EU) and 37 industrialised countries, known as The Kyoto Protocol (Korhonen & Savolainen, 1999). The Kyoto Protocol agreement has been extended further, through the development of the Copenhagen Accord, as a result of the Copenhagen Summit in Denmark, December 2009. The combination of these political agreements aims to reduce GHG emissions and stabilise the rate at which climate change is occurring through meeting social, economical and technological criteria, and has led to the development of international and national legislation to support this motive. Legislation targets both the domestic sector and the industrial sector, with the principal purpose of encouraging individuals to lower their GHG emissions through human activities.

Increased GHG emissions in the atmosphere change the radiation balance of the earth and can lead to a rise in global temperatures and climate change. The six principal gases, recognised by the Kyoto Protocol, as being the most harmful to the environment are: Methane (CH_4), Nitrous Oxide (N_2O), Sulphur Hexafluoride (SF_6), Hydro-Fluorocarbons (HFC's), Per-Fluorocarbons (PFC's) and Carbon Dioxide (CO_2), which is believed to be the most harmful to the environment, accounting for approximately 60% of enhanced global warming (Argüelles, Benavides, & Junquera, 2006). Within the industrial sector, manufacturing accounts for a significant proportion of GHG emissions (Sutherland, Adler, Haapala, & Kumar, 2008), as manufacturing processes are often highly energy intensive, consuming vast amounts of fossil fuels and natural resources, and generate large volumes of waste. For this reason, the attention of policy makers has become increasingly focused on environmental concerns (Cole, Elliott, & Shimamoto, 2005), such as pollution control, resource efficiency and waste management, in order to curb the amount of GHG emissions associated with the manufacturing industry.

THE UK MANUFACTURING INDUSTRY

The UK manufacturing industry remains the sixth largest manufacturing nation worldwide, contributing £150 billion annually to the economy, despite recent diversion from traditional operations to technology driven high-value operations, such as aerospace and nano-technology (Gregory, Prisk, Lucas, & Thurso, 2009). However, the industry is under intense pressure to reduce its environmental impact from increasing government legislation, environmental demands from market force and customer preference, and economic factors related to rising energy prices, diminishing natural resources and growing demand for raw materials. Therefore, manufacturers are being encouraged to implement sustainable manufacturing techniques (Patton & Worthington, 2003) and manage sustainable solutions to face the challenges posed by climate change.

The key objective behind sustainable manufacturing techniques is to ensure processes and products associated with the industry are more environmentally friendly by reducing energy and material consumption during manufacture, decreasing the use of natural resources, eliminating waste wherever possible, and simplifying product design for efficient manufacture, use and disposal. Allwood (2005) defines sustainable manufacturing as "developing technologies to transform materials without emissions of greenhouse gases, use of non-renewable or toxic materials or generation of waste." However, there needs to be continuous management of the whole life-cycle of a product, from the initial extraction of raw materials, manufacturing processes, transport, usage and end-of-life (EOL) disposal, to ensure the success of sustainable manufacturing (Hu &

Bidanda, 2009). This article investigates waste management within a small to medium-sized enterprise (SME) in the manufacturing sector, focusing on EOL product recovery methods and the related environmental impacts, in order to support sustainable manufacturing.

SUSTAINABLE MANUFACTURING THROUGH WASTE MANAGEMENT IN SMEs

The UK still produces more waste per head of population, between 500kg and 600kg per person, than many of its European neighbours (Monk, 2010), however, the movement towards a more sustainable waste management system has been identified by international strategies. Government legislation and environmental pressure has changed the way in which manufacturing SMEs can dispose of their waste. Manufacturing companies are now legally obliged to comply with EU policies and UK regulations aimed at curbing GHG emissions from waste in this sector by minimising waste wherever possible, finding substitutes to harmful and toxic materials, and to recycle or recover any unavoidable waste (Cohen, 2007).

Melton (2005) identifies seven different forms of waste which can be described as:

- **Over production:** when a product is made but never used;
- **Defects:** errors which occur in the product or materials during the manufacturing stage;
- **Inventory:** unnecessary storage of inventory for a long period of time;
- **Waiting:** time wasted during development, manufacture and delivery. Money, resources and knowledge can also be wasted through waiting;
- **Transport:** vehicle emissions and distances between supply and demand create waste along with unnecessary transit packaging;
- **Energy:** inefficient, old machinery and unnecessary use of electrical equipment when not required;
- **Natural resources:** water, raw materials and fossil fuels are expensive and valuable.

It is vital to the success of sustainable manufacturing that SMEs implement waste management strategies within their business, in order to minimise the overall environmental impact while maximising economic profits.

Diverting Waste from Landfill

Diverting waste from landfill is particularly important to aiding the reduction of GHG emissions associated with the manufacturing industry, as degrading waste emits large amounts of CH_4, resulting in soil and air pollution, and pollution of surface and ground water channels (Burnley, 2001).

Since the introduction of the UK Landfill Tax in 1996, (Morris, Phillips, & Read, 1998) producers of waste have been taxed on the volume of waste they generate, currently standing at £48 per tonne of waste, and is set to rise by £8 per year until 2014. This has driven SMEs to source different routes of waste disposal, diverting waste from landfill and applying waste management strategies into their daily production and operations. Sustainable waste management encourages a reduction in the amount of waste material which is sent to landfill throughout all stages of a products life-cycle (Gungor & Gupta, 1999), promoting alternative methods of disposal such as recycling, reusing and ultimately waste minimisation.

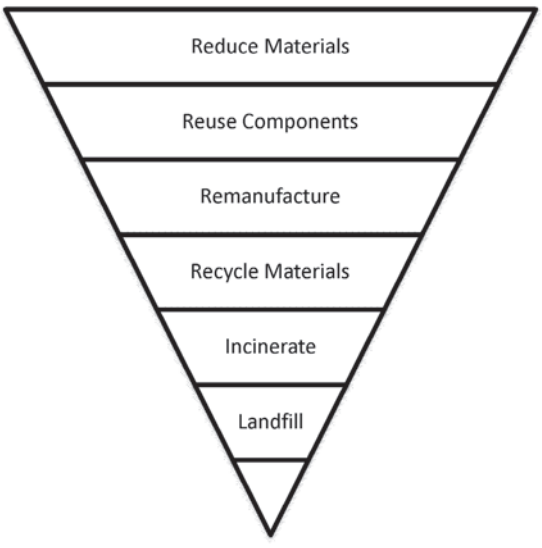
The Waste Hierarchy and Product Recovery Methods for EOL Products

The waste hierarchy, as shown in Figure 1, demonstrates methods of waste disposal, with the most

preferable method being to reduce the amount of material integrated within the product at the design stage, so that there is less waste material to dispose of at the EOL stage. The hierarchy then demonstrates three product recovery methods, which are to reuse components, remanufacture and recycle waste materials. All of these recovery methods add value to the discarded waste material, diverting waste away from landfill and avoiding the use of virgin raw materials by using the existing material incorporated in the EOL products (Steinhilper, 1998). Incinerating and sending waste to landfill are seen as the most environmentally damaging and the hierarchy encourages original equipment manufacturers (OEMs) to diversify from these traditional methods and move up the waste hierarchy in terms of the practised methods of waste management.

Product recovery methods are often referred to as the 3R's, (reduce, reuse and recycle), and are considered to be the least harmful method of waste management to the environment when compared with depositing of waste on landfill (Östlin, Sundin, & Björkman, 2009). EOL products which may be obsolete, broken or simply out-of-date with technology, are processed, adding value to the material and energy captured in the original manufacturing of the product and either returned back to the raw material value through recycling, or restored to an original specification or 'like-new' condition, through repairing and remanufacturing.

Figure 1. Waste hierarchy demonstrating the most preferable methods of waste disposal



This paper compares the product recovery method of remanufacturing EOL products with the repairing of EOL products, by investigating the impact that each product recovery method has on the environment. This is carried out by calculating the carbon footprint of each method to distinguish the least environmentally harmful method of product recovery.

REMANUFACTURING VS REPAIRING

Remanufacturing and repairing are similar with respect to the end result as both processes take an EOL or broken product and return it to a fully functional product. However, remanufacturing adds value to the waste product by providing a full disassembly, inspection, cleaning of components, replacing of worn components, and reassembly process (Brown, 2010). This gives the remanufactured product a new life-cycle with product quality and a warranty equal to, and in some cases better than, the OEM specification. Repairing concentrates on the failed section of the product by replacing any worn components, without total disassembly of the product, resulting in a warranty and quality lower than that of the original specification.

Benefits of Remanufacturing and Repairing

Both remanufacturing and repairing are preferable to recycling, as they transform EOL products in to functional products, where as recycling simply returns the product to a raw material value (Ijomah, 2007). The benefits of the remanufacturing and

repairing product recovery methods are summarised below.

Remanufactured and repaired products are typically sold at 30-40% lower cost than new identical products, however, cost 40-65% less than new products to produce (Mitra, 2007), resulting in a low-cost, high-profit business. In 2007, the remanufacturing and repairing market was worth £5 billion, however, due to the global recession this figure is expected to grow as the market has seen an increase from the economic crisis as businesses become aware of the alternative options and explore new methods of waste disposal (Reidy, 2010). Remanufacturing and repairing EOL products saves large quantities of raw materials and natural resources, with total savings attributed to the industry of 10 million tonnes CO_2 (Chapman, Bartlett, McGill, Parker, & Walsh, 2009) and consuming 15% of the energy required in original product manufacture (Gray & Charter, 2006).

Barriers of Remanufacturing and Repairing

Although remanufacturing and repairing offer benefits over other methods of waste disposal and product recovery, there are also barriers which hinder the processes.

The remanufacturing process is only profitable for high-value goods such as automotive and aerospace components, and some domestic appliances, as the processes require a skilled workforce and can often be time consuming. Both remanufacturing and repairing lack sufficient tools to efficiently automate the product recovery process, therefore resulting in manual operations which are highly labour intensive (Guide, 2000). Consumers are regularly tempted to purchase a brand-new product as opposed to a remanufactured or repaired product, as they often perceive remanufactured and repaired products to be of a lower quality and value than new alternatives (Seitz, 2006). Like any manufacturing system, the remanufacturing and repairing of EOL products will generate some form of waste during the processes which are carried out, as worn casings, fastenings and seals all have to be disposed of and are often contaminated with dirt and oil (Steinhilper, 1998). The processes can also consume vast amounts of energy due to machining and use of electrical equipment.

To investigate further the benefits and barriers of remanufacturing and repairing, the two methods of product recovery have been compared via a carbon footprint calculation. This shows the environmental impact of each product recovery method, in terms of the amount of GHG emissions released during the processes carried out, and can be used to show which method of waste disposal is most sustainable.

CALCULATING THE ENVIRONMENTAL IMPACT OF PRODUCT RECOVERY METHODS

As climate change is becoming more apparent in all sectors, monitoring the environmental impact which processes and products have is becoming increasingly expected. One method of measuring the environmental impact of any process is by calculating the carbon footprint of that given process. A carbon footprint quantifies the GHG emissions, in terms of CO_2 equivalent (CO_2e), associated with the whole life-cycle of a product or process, and is crucial to supporting environmental impacts in the manufacturing industry.

There are several methods of calculating a carbon footprint, and for the purpose of this study, the carbon footprint has been calculated using PAS 2050 (Publically Available Specification 2050) methodology.

A Carbon Footprint Calculation using PAS 2050

In 2008, the first British Standard (BSI) for calculating a carbon footprint, PAS 2050, was published

which combines previous international standards, ISO 14040 (Life Cycle Assessment Principles and Framework) and ISO 14044 (Life Cycle Assessment Requirements and Guidelines) for analysing the environmental impact of a product or process. PAS 2050 is supported by The Carbon Trust, UK industry experts and international stakeholders and provides a recognised accurate method of calculating a carbon footprint (Carbon Trust, 2008) in terms of the amount of GHGs released throughout the whole life-cycle of a product.

The PAS 2050 methodology has been used to calculate the environmental impact of the remanufacturing process and repairing process of EOL products at a Northwest UK SME, that carry out product recovery methods on EOL automotive components.

Data Confidentiality

Due to a commercial confidentiality agreement between Lancaster University and the SME, specific data relating to the operations carried out cannot be accessed by third parties. Therefore for the purpose of this paper only the results of the calculation have been shown and analysed.

Stages of PAS 2050 Methodology

Several stages had to be carried out to calculate the carbon footprint of remanufacturing and repairing, using PAS 2050 methodology, which comprise of:

1. Building a process map;
2. Develop boundaries and prioritisation;
3. Data collection;
4. Perform calculation;
5. Evaluate results.

Before the data could be collected, a functional unit had to be developed to allow for a fair comparison to be made between the two methods of product recovery, and to indicate the most sustainable method of EOL product recovery. The functional unit for the comparison of EOL product recovery by remanufacturing and repairing is:

'The total amount of carbon emissions released during the product recovery processes for a single EOL automotive component to a fully functional product.'

The functional unit determines the level of the calculation and for the purpose of this paper; the business-to-business (B2B) methodology has been used. B2B ensures the carbon footprint calculation ends once the recovered product reaches the end user and does not take into account the usage stage of the component by the user. If this was to be taken into account then the business-to-consumer (B2C) method would have been used, however the B2C level calculation can be very complex and time consuming requiring vast amounts of data which was not feasible within the timeframe of the study.

PROCESS MAP DEVELOPMENT

By analysing the procedures and daily operations that are carried out by the SME, a process map was developed for each product recovery method, which displays all inputs, functions and outputs carried out during the process.

Figure 2 illustrates the process map for the remanufacturing process of an automotive component at the SME studied. The process begins when the used or broken component (core) is delivered to the SMEs manufacturing site and then various procedures are carried out until the core is returned to the OEMs specification, when it is then returned back to the consumer. Similarly, Figure 3 illustrates the process map for the repairing process of the same automotive component at the SME. The procedures which are carried out have been broken down into five stages, which has allowed for a comparison of each stage of the product recovery methods. These stages are:

- **Inspection:** Visual checks for obvious defaults and wearing of components. Broken or worn casings, seals and fasteners are discarded into waste.
- **Disassembly:** For the remanufacturing process, the core is stripped down into individual components, which are cleaned to remove any dirt. In the repairing process, only the defective part is disassembled.
- **Recovery:** Cores are re-engineered, such as re-boring, in the remanufacturing process to return the core to its original specification. In the repairing process the defective part is replaced or fixed.
- **Assembly:** Cores are reassembled, with the remanufacturing process using new seals and fastenings, whereas in repairing, the original fastenings are used. Remanufactured cores are painted so that they appear identical to the original.
- **Distribution:** Cores are packaged and orders processed, which are then distributed either back to the original supplier of the used core or to a new customer.

BOUNDARIES AND PRIORITISATION

The process maps (Figure 2 and Figure 3) distinguish the boundary of the study, and only those processes demonstrated in the process maps are accounted for in the carbon footprint calculation. According to PAS 2050 (Carbon Trust, 2008), "any one source resulting in more than 1% of the total anticipated life-cycle emissions of the product" has to be accounted for in the calculation. Therefore, those processes illustrated in Figure 2 and Figure

Figure 2. A process map for the remanufacturing of an EOL automotive component

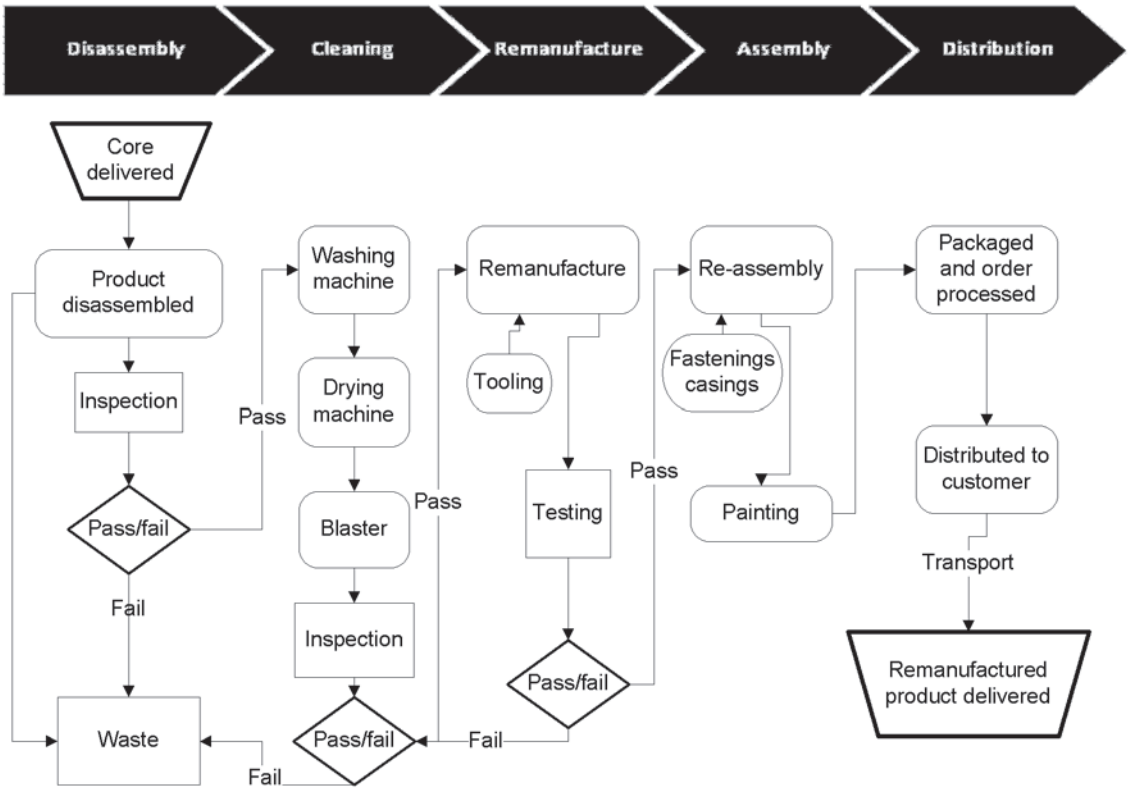
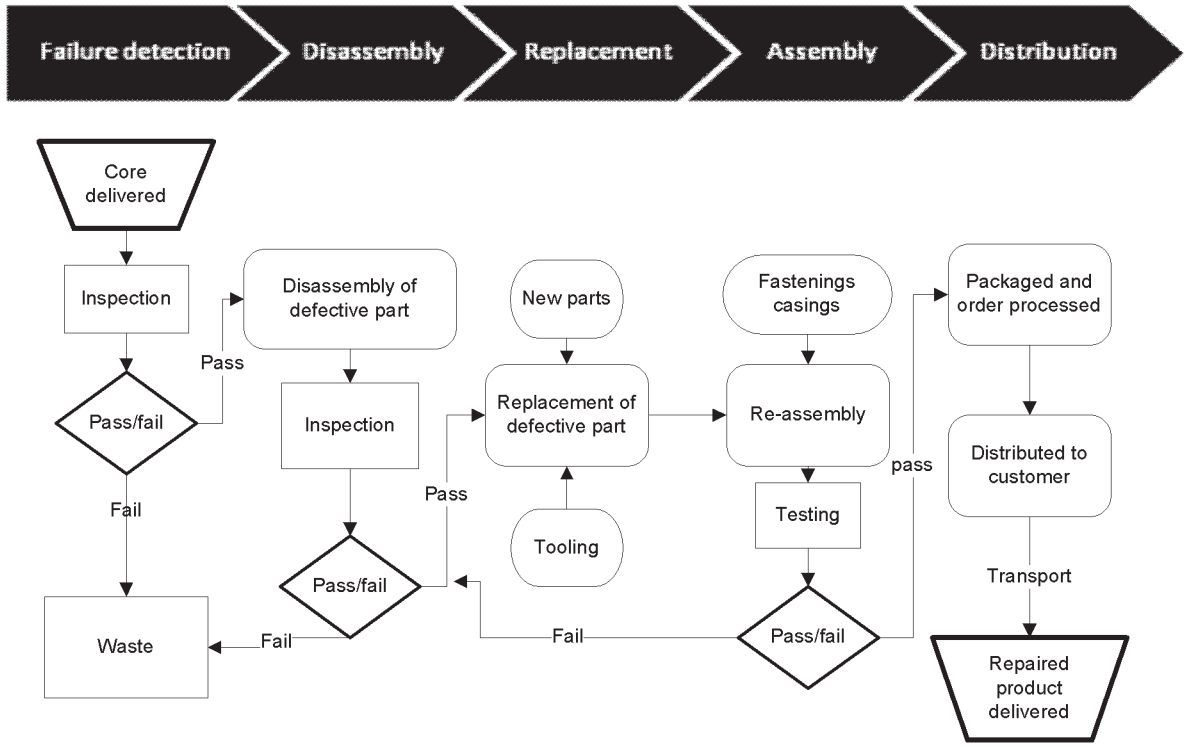


Figure 3. A process map for the repairing of an EOL automotive component



3, account for over 1% of the life-cycle emissions and are seen as a priority within the boundary of the study. However, there are several assumptions which have been made, to ensure a fair comparison between the two product recovery methods. It has been assumed that the used core, which is being recovered, is the same automotive component for remanufacturing and repairing. It has also been assumed that waste values, energy inputs and tooling techniques will be a constant regardless of the time taken to do so. This has allowed for a fair comparison to be made of each product recovery method to distinguish which is the most suitable to support the sustainable manufacturing of EOL products.

Limitations

This study is only valid for the SME participant and their operating process of remanufacturing and repairing. The carbon footprint is relative to automotive components repaired and remanufactured at the SME, based on their weekly and annual production rates, and may differ if another automotive component was studied.

DATA COLLECTION

To accurately calculate the carbon footprint of remanufacturing and repairing, extensive data had to be obtained which was within the B2B methodology. This meant that certain values could be eliminated from the study, as only data which accounts for 1% of the total emissions is defined within the boundary of the study. This included the movement of products from one stage to another and products which are held in inventory.

Two sets of data were required for the carbon footprint calculation, as defined in PAS 2050 methodology, these being:

- Primary activity data from the SME which includes all inputs and outputs, such as masses of waste material, energy consumption, fuel consumption, cleaning processes and packaging;
- Secondary emission data from the official government database published by the Department of Environment, Food, and Rural Affairs (DEFRA), which is a set value for the amount of GHG emissions released during a certain process.

To calculate the carbon footprints in accordance with the functional unit, two sets of data were used, as in Equation 1, for the particular process being calculated for each stage of the recovery method, from the initial inspection to the final distribution of the product.

Equation 1. A carbon footprint calculation:

Carbon Footprint (kg CO_2e per unit) =

Activity Data (unit) X Emission Data (kg CO_2e)

The carbon footprint calculation which has been carried out gives a value for the specific stage of the process, which was then summed together to give the total carbon footprint value of each product recovery method in terms of the amount of GHG emissions (kg CO_2e per unit) released and the related environmental impact.

Primary Activity Data

Primary activity data was collected from the SME through several site visits over a six-month period, in which time was spent monitoring and recording sources of emissions, such as the generation of waste, and water and energy consumption. At the beginning of the data collection stage, staff members were briefed on the research being carried out, to ensure that accurate and precise data could be collected within the timeframe of the study. Key contact people at the SME were identified and advised to keep weekly records of all waste streams, which were segregated into material types for ferrous waste and non-ferrous waste, so that this could be analysed for the final calculation.

Research was carried out by the lead-author, alongside experienced team leaders and senior management within the SME, who provided existing data from company records on the percentage of failed components and material types sent to waste. The downtime and the efficiency rates of each machine had to be calculated depending on the productivity rates of the SME. It was estimated that the average working day lasts seven hours; this was divided by the number of components in each product-cycle and therefore gave the energy consumption of the machine for each product which was to be recovered.

The accuracy of the data was discussed with the senior management and team leaders and the importance of this issue was emphasized during the briefing of the research project. All data collected had to be either from existing company records, such as the annual utility bills, machine technical specifications, productivity rates and waste collection records, or from physical measurements and calculations on the factory floor. This data was confirmed by senior management who agreed that the data was accurate and that it gave a reliable representation of the company's activity. A resource efficiency scheme was already in place at the SME, to measure the weekly energy consumption of machines and to monitor productivity and failures rates on the factory floor, and therefore the company already has generated some experience in this field.

As described in the data confidentiality section, specific activity data related to the operations and

Table 1. Emission data for the processes carried out during product recovery methods (adapted from Defra, 2009)

Source of Emissions	Description of emission source	Emission value in kg CO_2e
Treatment of waste materials	Disposal of ferrous waste per kg	-1.30
	Disposal of non-ferrous waste per kg	0.40
Energy consumption	Consumption of grid electricity per kWh	0.547
Water consumption	Consumption of water per litre	0.267
Chemical consumption	Chemical solution per kg	4.77
	Chemical paints per litre	4.13
Manufactured fastening, casings, fixings for assembly	Ferrous material used per kg	3.10
	Non-ferrous material used per kg	11.0
Cardboard packaging	Cardboard packaging used for transit of product per kg	0.95
Transport	Distribution using 3.5 tonne diesel van with 40% load per km	0.339

functions carried out at the SME cannot be disclosed to third parties. Therefore detailed results showing the actual values of the primary activity data have not been published in this paper.

Secondary Emission Data

Emission data identifies the amount of harmful GHGs released during the given activity. An example is the use of transport to distribute the final product, as the emission data gives the amount of GHGs released depending on the vehicle type, the load and the distance travelled. Table 1 summarises the emission data for each activity associated with the remanufacturing and the repairing of an EOL component.

Emissions data has been sourced from Defra guidelines (2009), which are the UK government department responsible for policy and regulations relating to the environment, food and rural affairs. This set of guidelines has been derived as part of the government's implementation of the Climate Change Act 2008 (Defra, 2009) and are the official set of government guidelines used in policy. The aim of the guidelines is to help businesses and individuals report on their company's carbon emissions, by using existing data such as utility bills, refrigeration consumption, fuels consumption and mileage. The SME agreed with the author that this was a reliable source to use secondary data emissions, as it is approved by government officials and is publically available for the purpose of this research. However, despite the reliability of the source, there were several minor issues concerned with the accuracy of the emissions. Due to the vast amount of data and sources of emissions, it was not always possible to find the exact value for the given process in the recovery method. This occurred when calculating the emissions for paint used in the assembly stage of the recovery process. The paint used in the recovery method was corrosive-resistant metal paint, however the value for paint within the Defra database was for general household paint, and therefore the actual emission value for metal paint was not known. It was assumed for the purpose of the research that the two-types of paint had the same emission value, as it was not known whether it would be higher or lower than the recorded emission data for paint. This assumption may have affected the results, but it is not known whether an over estimation or an under estimation will have occurred for this specific value.

Negative emission values occur (Table 1) for the treatment of ferrous waste per kg, and is due to the waste being recycled by a local recycling company who collect and recover the energy and return the waste material to a raw material. GHG emissions are prevented from being emitted into the atmosphere as although the recycling process itself uses energy and generates GHG emissions, this value is less than the disposal of waste by sending it to landfill. Therefore it creates a negative emission value as emissions are being prevented from entering the atmosphere by diverting waste from landfill, minimising the need for virgin raw materials and the use of highly energy intensive manufacturing processes (Ayres, 1997). In general, the larger the numerical value, the larger the amount of GHGs released into the atmosphere and therefore the more environmentally damaging the process is.

RESULTS

The results of the carbon footprint calculation for the product recovery method of remanufacturing and repairing are shown in Table 2. The results have been calculated for each individual product which is recovered, and also the annual GHG emission associated with the SME based on productivity rates. The total amount of GHG emissions released during each product recovery method, from the inspection of the core through to the distribution, is shown in kg CO_2e, which accounts for the six most harmful GHGs released during all processes carried out. Remanufacturing emits 23.76 kg CO_2e for every automotive component remanufactured, whereas repairing the same automotive component emits only 0.783 kg CO_2e. The annual GHG emissions released during the operations carried out at the SME are also illustrated, with remanufacturing emitting 834 tonnes of GHGs into the atmosphere annually and repairing emitting 8.1 tonnes of GHGs.

The total carbon footprint, in terms of GHG emissions released, of a remanufactured product is significantly higher than that of a repaired product as shown in Table 2. The reason for this is the difference in the processes which are carried out during each product recovery method. The remanufacturing process, as shown in Figure 2, is much more intensive than that of the repairing process (Figure 3). Remanufacturing involves additional processes at each stage, which require a higher energy input and use of natural resources such as water for cleaning. Therefore, it can be stated that the higher the number of inputs and processes, the larger the impact on the environment and hence the higher the carbon footprint will be. This indicates a positive relationship between the use of resources, such as energy and raw materials, and the environmental impact of the function. The annual carbon footprint of repairing an EOL product is significantly lower than that of remanufacturing an EOL product, however, this does not take into account the production rates at the SME. Remanufacturing accounts for 80% of the annual product recovery carried out by the SME and therefore contributes a larger proportion of GHGs as the process is more frequent.

Table 2. Total GHG emissions released for each product recovery stage, per unit and per annum

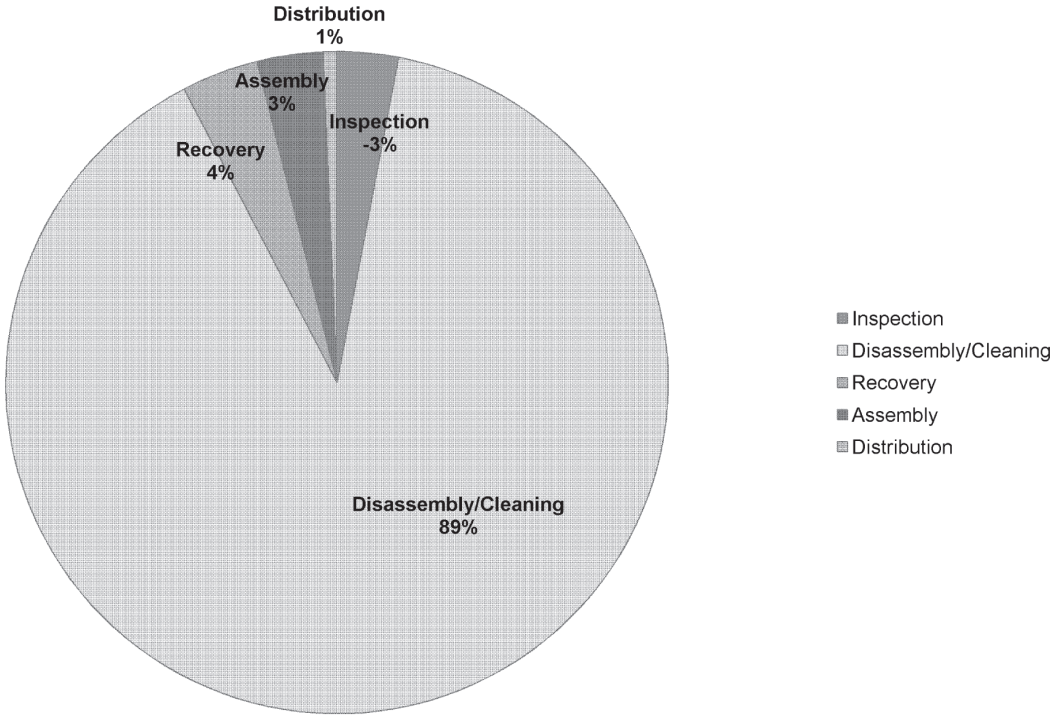
Product recovery method and stages	Total carbon footprint of GHG emissions released in kg CO_2e	
	Remanufacturing	Repairing
Inspection	-0.752	-0.756
Disassembly/ Cleaning	22.58	-0.101
Recovery	0.95	0.88
Assembly	0.81	0.64
Distribution	0.17	0.12
Per product recovered	**23.76**	**0.783**
Per annum	**834,000**	**8,100**

Analysis of Results

It is important to analyse the emissions released during each stage of the processes carried out during the remanufacturing and repairing, to identify which stages are the most harmful on the environment and which could be altered to reduce the carbon footprint of the SME. For this reason, the emissions released during each stage have been illustrated in Figure 4 and Figure 5, which has allowed for interpretation of each stage to be carried out.

The GHG emissions produced at each stage of the remanufacturing process are illustrated in Figure 4. It can clearly be seen that the greatest source of emissions is generated during the disassembly stage, which accounts for 89% of the total emissions during remanufacturing. This is due to the intensive cleaning phases which occur at this stage, as components are washed, dried and then blasted with iron shot, all of which are performed in large industrial machines which consume vast amounts of energy. The washing process also requires large volumes of water and chemical detergents, which have an emission value of 0.267 kg CO_2e and 4.77 kg CO_2e respectively, to remove the oil and dirt contaminants on the components before they can be remanufactured. This can be compared with the disassembly process in repairing (Figure 5) which accounts for -4% of the total GHG emissions, as during the disassembly stage in repairing the defective component is discarded to waste, which is recycled and therefore prevents harmful GHG emissions being emitted. However, the disassembly process for repairing does not include any washing, drying or blasting processes, which is why the value of disassembly for repairing is much lower than that of remanufacturing.

Figure 4. Graphical breakdown of emissions released at each stage of the remanufacture of an EOL product



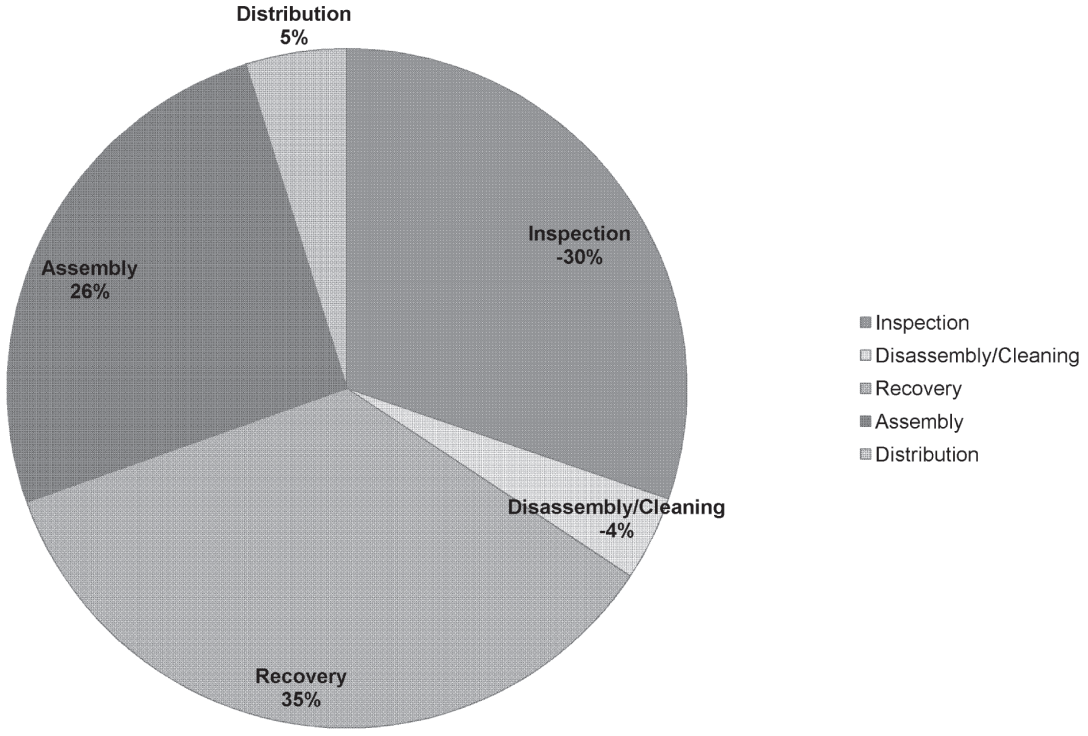
The inspection stage of each product recovery method produces negative emission values, with -0.752 kg CO_2e for remanufacturing and -0.756 kg CO_2e for repairing, which indicates that no emissions are released during this stage. However, the negative emission value is not because the process does not generate any emissions, as this is not possible, it is due to the process generating fewer emissions than the alternative process. If the material was sent to landfill it would generate a greater proportion of emissions than recycling the material. Therefore by recycling the material, a negative value occurs as emissions are prevented from entering the atmosphere as the original material value of the waste is recovered, decreasing the need for virgin raw materials and disposing of waste to landfill.

During the remanufacturing process, tooling is required to disassemble the product which requires energy. A larger mass of ferrous material is sent for recycling than in repairing, such as grey-iron component cases, therefore this counteracts the energy required in tooling.

The recovery processes carried out during the remanufacturing of a component are very specific to the industry and often require specialist knowledge and expertise (Steinhilper, 1998). Components have to be machined back to their original specification, which may involve several specialised techniques, whereas in repairing, the defective component is fixed or replaced without rework of the material. This leads to the recovery during the remanufacturing process to have a higher value than that of the repairing processes as shown in Table 2.

The main contributor to the total amount of GHG emissions released during the assembly stage is the use of new seals, fastenings and casings as these contain large amounts of non-ferrous materials. During the manufacture of non-ferrous

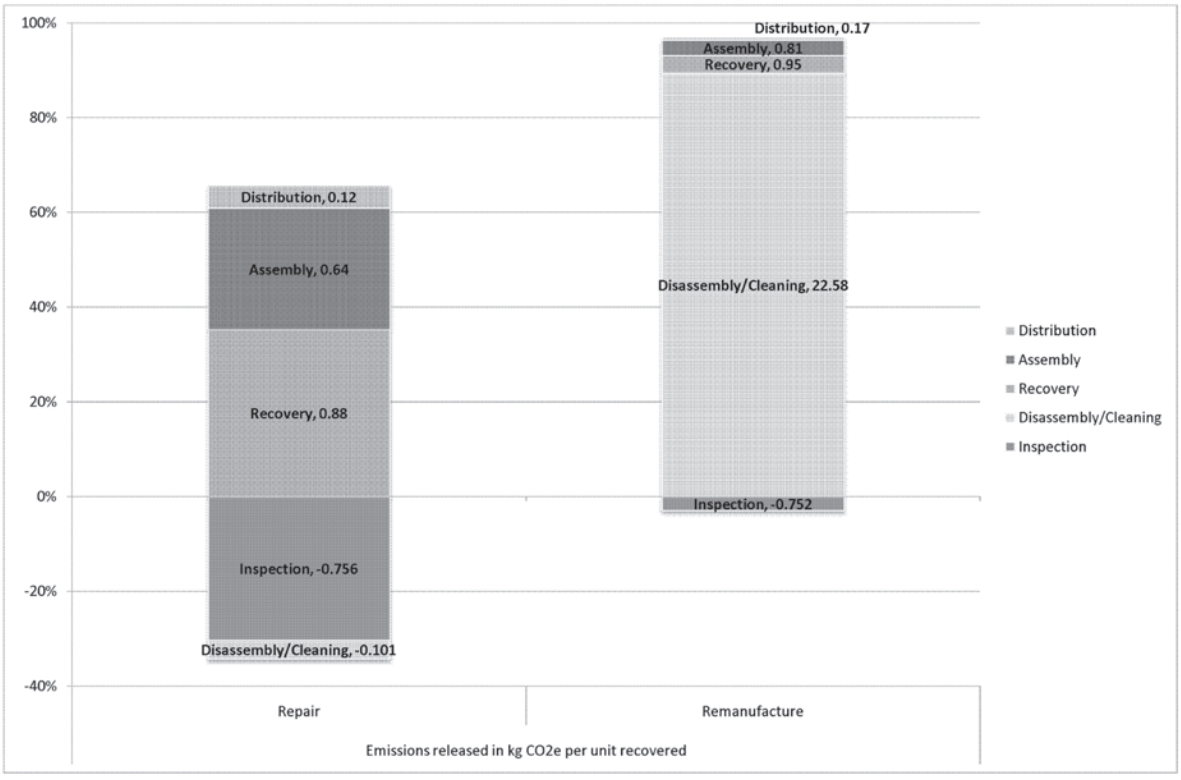
Figure 5. Graphical breakdown of emissions released at each stage of the repairing of an EOL product



materials, harmful GHGs are emitted (11.0 kg CO_2e per kg of material produced) using high energy intensive processes and virgin raw materials. In the remanufacturing process all worn seals fastenings and casings are disposed of at the disassembly stage and therefore have to be replaced at the assembly stage, whereas during the repairing of an EOL component, only the defective part of the product is discarded which results fewer seals and fastenings needing to be replaced. Also during the assembly of the remanufactured product, chemical paint is used to return the product to a like-new condition, which has an emission value of 4.13 kg CO_2e per litre used. This leads to the assembly stage accounting for 26% of the total carbon footprint during remanufacturing, compared to only 3% in repairing.

Once the EOL products have been recovered, either by remanufacturing or repairing, the products go through the same distribution process. Recovered products are packaged and processed and then delivered using a diesel fuelled 3.5 tonne van. Although the distribution process is the same for each method, remanufacturing has a higher carbon footprint value than that of repairing accounting for 5% of the total emissions, whereas repairing accounts for only 1%. This is due to remanufacturing being a specialised form of product recovery and therefore there are fewer companies which perform the operation locally. This leads to the average distance from the SME to the customer being greater, and therefore the transport stage has to cover a larger number of kilometres resulting in a larger proportion of GHG

Figure 6. A graphical comparison of the emissions released during the remanufacturing and repairing of an EOL product



emissions being released due to burning of fossil fuels in diesel.

The variation in the carbon footprint results for remanufacturing and repairing is illustrated in Figure 6, and the greatest difference between the two product recovery methods is the cleaning which occurs during the remanufacturing process. The chemical cleaning detergents used in the process contain high levels of PFC's and are used during each cycle of the washing machine. High volumes of water are also consumed to remove contaminants from the products before they can be recovered which has a negative impact on the environment and causes an increase in the total value of the carbon footprint.

Consumption of grid electricity emits 0.547 kg CO_2e per kWh consumed, and as the remanufacturing process is heavily reliant on energy to power specialist tools and large industrial cleaning machines, the proportion of electricity is significantly higher than that of repairing. Tooling processes occur at four out of the five stages during remanufacturing, which has a substantial effect on the energy consumption of the process, whereas minimal tooling is required during repairing as defective components are manually removed reducing the electricity consumption of this process.

From carrying out the carbon footprint calculations, it can be seen that not all stages produce a negative impact on the environment, as shown on Figure 6 as the inspection stage produces negative emission values for each product recovery method. Initially it was assumed that any waste generated would create a negative impact and therefore increase the amount of GHG emissions in the total footprint. However, due to the large volume of ferrous waste generated, it has a positive effect, as the waste is sent to be recycled and therefore is returned to its raw material value, which prevents harmful GHG emissions being released during the manufacture of virgin ferrous raw materials which would have otherwise had to be used. Non-ferrous waste generated by the SME is not currently recycled and is sent to landfill which has a negative impact on the environment as upon degrading emits 0.40 kg CO_2e per kg of waste material.

Great care was taken during the data collection to ensure that all results were constituent and within the boundary of the study. The use of an official government database, for the secondary emission data values, also supports the accuracy of the study, as they have been derived in accordance with accepted guidelines (Defra, 2009) and therefore are considered to be the most accurate source of data available for the study. Only one assumption was made regarding the emission value for paint used in the assembly stage of the process, however it is not possible to justify if this will have given an over estimation or an under estimation on the results of the study.

Benefits of Remanufacturing Over Repairing

Although the carbon footprint of repairing is significantly lower than that of remanufacturing there are several benefits of remanufacturing an EOL product over repairing it, which gives justification for the additional GHG emissions released. For the SME studied, remanufacturing of an individual automotive component is carried out up to three times, which results in the carbon footprint value being displaced over three life-cycles of the product. This prevents emissions from the OEM being generated, which consumes vast amounts of raw materials and energy, as the original product can be remanufactured instead of being discarded and replaced by a new product. This minimises the environmental impact of remanufacturing throughout the supply chain and often influences the use of remanufactured products over alternatives. If products are designed for remanufacture during the product development stage, economic benefits can be achieved by decreasing waste management costs throughout the life-cycle of the product and decreasing disas-

sembly times, increasing remanufacturing yield for products re-entering the life-cycle use phase (Sundin, 2004). Whereas repairing EOL products can often be difficult and costly.

During the recovery process remanufacturing fully disassembles, cleans and recovers all individual components in the EOL product whereas repairing only recovers the defective component. For this reason remanufacturing a used or broken product generates a full new life-cycle, with a specification and warranty matching that of the OEM, which is appealing to consumers as remanufactured products are often sold at a slightly lower cost than that of a brand-new identical product (Gray & Charter, 2006). The warranty for a repaired product only covers the part which has been repaired extending the original life-cycle, however this does not provide the same quality or guarantee as a remanufactured product and could be prone to further defects from general wear and tear.

CONCLUSION AND FUTURE RESEARCH

Product recovery methods of remanufacturing and repairing support the waste hierarchy within sustainable manufacturing. Remanufacturing an EOL product emits a larger volume of GHG emissions into the atmosphere than repairing a product, however in theory there is no limit to the number of times an individual product can be remanufactured (Reidy, 2010), resulting in fewer natural resources, energy and raw materials being consumed than in the initial manufacture of a new product (Japke, 2009). Remanufacturing not only promotes the multiple recovery of materials and components but it also allows for the steady upgrading of quality and functions of products, without the need to manufacture completely new products and dispose of used products (Sundin, 2004).

A remanufactured product provides a new life-cycle, warranty and specification identical to that of the OEM, whereas repairing only fixes the defect component extending the original life-cycle of the product with a quality lower than that of the OEM. Therefore, out of the two investigated product recovery methods, remanufacturing can be considered as the most sustainable option to support waste management, as repairing occurs during the usage stage in the life-cycle of the product where as remanufacturing occurs during the disposal stage, when the product reaches its EOL and therefore diverts large volumes of waste away from landfill.

As the carbon footprint has been calculated for the SME, it would be possible to investigate further methods of reducing the amount of GHG emissions associated and hence lower the carbon footprint of the company. One method of doing this would be to implement resource efficiency measures into the SME manufacturing system, which would focus on reducing the amount of natural resources that the processes consume. This may require investing in new efficient machinery to minimise the amount of energy and water wasted during the present processes which are undertaken. Alongside implementing resource efficiency, which focuses on environmental issues, it may be viable to adopt lean manufacturing techniques, which focus on economical factors within the company. Lean manufacturing is a multi-dimensional approach, which produces finished products with little or no waste, by reducing work-in-progress, minimising stock held in inventory and using management strategies such as just-in-time and quality management (Rubio & Corominas, 2008). Once such methods have been incorporated in the SME manufacturing system, the carbon footprint of the company could then be calculated again to analyse the GHG savings.

ACKNOWLEDGMENT

The authors would like to acknowledge the North-west Regional Development Agency, European Regional Development Fund, and the Higher Education Innovation Fund for supporting this research activity.

REFERENCES

Allwood, J. (2005). *What is sustainable manufacturing?* Paper presented at the Sustainable Manufacturing Seminar Series. Retrived from www.ifm.eng.cam.ac.uk/sustainability/seminar/documents/050216lo.pdf

Argüelles, M., Benavides, C., & Junquera, B. (2006). The impact of economic activity in Asturias on greenhouse gas emissions: Consequences for environmental policy within the Kyoto Protocol framework. *Journal of Environmental Management*, *81*(3), 249–264.

Ayres, R. U. (1997). Metals recycling: Economic and environmental implications. *Resources, Conservation and Recycling*, *21*(3), 145–173. doi:10.1016/S0921-3449(97)00033-5

Brown, T. (2010). Sustainable manufacturing: Regeneration through remanufacture. *The Manufacturer, 13*.

Burnley, S. (2001). The impact of the European landfill directive on waste management in the United Kingdom. *Resources, Conservation and Recycling*, *32*(3-4), 349–358. doi:10.1016/S0921-3449(01)00074-X

Carbon Trust. (2008). *Publically Avaliable Specification 2050 Briefing Document, BSI British Standards*. London, UK: The Carbon Trust.

Chapman, A., Bartlett, C., McGill, I., Parker, D., & Walsh, B. (2009). *Remanufacturing in the UK: A snapshot of the remanufacturing industry in the UK in 2009*. Retrieved from: http://www.remanufacturing.org.uk/free-reuse-publication.lasso?report=342.

Cohen, D. (2007). Earth's natural wealth: An audit. *The New Scientist Magazine*, *2605*, 34–41.

Cole, M. A., Elliott, R. J. R., & Shimamoto, K. (2005). Industrial characteristics, environmental regulations and air pollution: An analysis of the UK manufacturing sector. *Journal of Environmental Economics and Management*, *50*(1), 121–143. doi:10.1016/j.jeem.2004.08.001

Defra. (2009). *2009 Guidelines to Defra / DECC's GHG conversion factors for company reporting* (Version 2.0). London, UK: AEA.

Gray, C., & Charter, M. (2006). *Remanufacturing and product design, designing for the 7th generation*. Retrieved from www.cfsd.org.uk/Remanufacturing%20and%20Product%20Design.pdf

Gregory, M., Prisk, M., Lucas, I., & Thurso, J. (2009). *The annual manufacturing report* (pp. 3-60). London, UK: SayOne Media. Retrieved from http://www.themanufacturer.com/uk/reports.html

Guide, V. D. R. (2000). Production planning and control for remanufacturing: Industry practice and research needs. *Journal of Operations Management*, *18*(4), 467–483. doi:10.1016/S0272-6963(00)00034-6

Gungor, A., & Gupta, S. M. (1999). Issues in environmentally conscious manufacturing and product recovery: A survey. *Computers & Industrial Engineering*, *36*(4), 811–853. doi:10.1016/S0360-8352(99)00167-9

Hu, G., & Bidanda, B. (2009). Modeling sustainable product lifecycle decision support systems. *International Journal of Production Economics*, *122*(1), 366–375. doi:10.1016/j.ijpe.2009.06.011

Ijomah, W. L., McMahon, C. A., Hammond, G. P., & Newman, S. T. (2007). Development of design for remanufacturing guidelines to support sustainable manufacturing. *Robotics and Computer-integrated Manufacturing*, *23*(6), 712–719. doi:10.1016/j.rcim.2007.02.017

Japke, O. E. (2009). *Practical guideline: Development of a framework for assessing the economic benefits of remanufacturing*. Bedfordshire, UK: Cranfield University.

Korhonen, R., & Savolainen, I. (1999). Contribution of industrial and developing countries to the atmospheric CO_2 concentrations: Impact of the Kyoto protocol. *Environmental Science & Policy*, *2*(4-5), 381–388. doi:10.1016/S1462-9011(99)00035-0

Melton, T. (2005). The benefits of lean manufacturing: What lean thinking has to offer the process industries. *Chemical Engineering Research & Design*, *83*(6), 662–673. doi:10.1205/cherd.04351

Mitra, S. (2007). Revenue management for remanufactured products. *Omega*, *35*(5), 553–562. doi:10.1016/j.omega.2005.10.003

Monk, D. (2010). Europe goes down under. *The Journal for Waste and Resource Management Professionals*, 42-43.

Morris, J. R., Phillips, P. S., & Read, A. D. (1998). The UK landfill tax: An analysis of its contribution to sustainable waste management. *Resources, Conservation and Recycling*, *23*(4), 259–270. doi:10.1016/S0921-3449(98)00037-8

Östlin, J., Sundin, E., & Björkman, M. (2009). Product life-cycle implications for remanufacturing strategies. *Journal of Cleaner Production*, *17*(11), 999–1009. doi:10.1016/j.jclepro.2009.02.021

Patton, D., & Worthington, I. (2003). SMEs and environmental regulations: A study of the UK screen-printing sector. *Environment and Planning. C, Government & Policy*, *21*(4), 549–566. doi:10.1068/c0321

Reidy, H. (2010). As good as new. *Professional Engineering and Manufacturing*, 23-24.

Rubio, S., & Corominas, A. (2008). Optimal manufacturing-remanufacturing policies in a lean production environment. *Computers & Industrial Engineering*, *55*(1), 234–242. doi:10.1016/j.cie.2007.12.009

Seitz, M. A. (2006). A critical assessment of motives for product recovery: The case of engine remanufacturing. *Journal of Cleaner Production*, *15*, 1147–1157. doi:10.1016/j.jclepro.2006.05.029

Steinhilper, R. (1998). *Remanufacturing the ultimate form of recycling*. Stuttgart, Germany: Fraunhofer IRB Verlag.

Sundin, E. (2004). *Product and process design for successful remanufacturing*. Unpublished doctoral dissertation, Linkopings University, Sweden.

Sutherland, J. W., Adler, D. P., Haapala, K. R., & Kumar, V. (2008). A comparison of manufacturing and remanufacturing energy intensities with application to diesel engine production. *CIRP Annals:Manufacturing Technology*, *57*(1), 5–8. doi:10.1016/j.cirp.2008.03.004

This work was previously published in the International Journal of Manufacturing, Materials, and Mechanical Engineering, Volume 1, Issue 2, edited by J. Paulo Davim, pp. 1-18, copyright 2011 by IGI Publishing (an imprint of IGI Global).

Chapter 5
Recycling of Waste Epoxy-Polyester Powders for Foam Production

Carmine Lucignano
University of Rome "Tor Vergata," Italy

Erica Anna Squeo
University of Rome "Tor Vergata," Italy

Alessandro Guglielmotti
University of Rome "Tor Vergata," Italy

Fabrizio Quadrini
University of Rome "Tor Vergata," Italy

ABSTRACT

This paper proposes a new foaming technology (solid-state foaming) to produce structural foams from waste thermosetting resins. The proposed technology is easy and does not require specific and expensive equipments. Solid tablets are produced by cold compaction of resin powder, and foam by heating in an oven. Composite foams can be produced by mixing fillers and resin powder before the cold compaction. In the experiment, an epoxy-polyester (EP-PE) resin powder, deriving from the waste of a manufacturer of domestic appliances, was used with montmorillonite (MMT) particles. Resulting foams with a filler content ranging from 0 to 10 wt% were characterized in terms of physical and mechanical properties (by compression tests). Although the effect of the MMT content seems to be negative for the adopted resin, the feasibility of producing composite foams by recycling waste industrial powders is shown. The properties of the unfilled foams are sufficient for many industrial applications.

DOI: 10.4018/978-1-4666-1867-1.ch005

Copyright © 2013, IGI Global. Copying or distributing in print or electronic forms without written permission of IGI Global is prohibited.

INTRODUCTION

The modern industrial development must take under consideration the enormous waste of materials and energy in these last years. Even if people have been made aware of the environmental risk connected with the industrial production, there are only few initiatives which allow to reduce the related energy consumption or to extract raw materials from waste. Nowadays the social and political attention on these themes is very strong but the Government agencies do not operate efficiently, and the scientific research is often inadequate. A typical example is given by the management of waste thermosetting resin powders used for coatings as the amount of this waste is considerable. In fact, powder coating is a settled technology thanks to its flexibility and to aesthetics and performances of final coatings. A large waste is generated in the coating chamber due to over-spray: actually the powder should be collected and re-used but, in such applications, the need of producing parts with zero defects makes it impossible, and manufacturers prefer to discard collected powders rather than coated parts. Moreover, large amounts of powders often remain on the chamber walls and are removed only during the ordinary maintenance operations or for color change. In conclusion, the amount of waste thermosetting powders is increasing every year and new technological solutions are necessary to overcome this problem.

The scientific community has proposed several technical solutions to recycle thermosets but generally only structural parts are considered rather than powders. Dealing with bulk thermosets, recycling operations can be divided in two categories: processes that involve mechanical comminution to reduce the size of the scraps; and thermal processes to produce materials and energy from scraps (Pickering, 2006). However, discarded thermosetting powders generally exhibit characteristics similar to fresh powders, and should be recycled exploiting their properties. A recent study has compared the properties of re-used and recycled polyester resins with fresh and as-received resins in terms of shape, size, particle size distribution, moisture content, density, flowability, fluidity and chargeability (Lothongkum, 2007). The effect of the weight ratio of fresh and re-used polyester resins was analyzed in the case of electrostatic powder coating by measuring the film thickness. It was found that the optimal weight ratio of fresh and re-used polyester resin was 3:1. In order to prevent loss of powder particles in automatic electrostatic coating due to over-spraying, a simulation was proposed to define the relation between the movement of the spray gun and the distance from the conveyor.

Latest studies only deal with the use of waste powders from recycling of fiber reinforced plastics for the production of bulk molding compounds (Hwang & Jeon., 2010), filled concrete (Asokan et al., 2010), cement composites (Asokan et al., 2009), and natural rubber compounds (Ansarifar et al., 2009). Instead, apart from re-using, there is no way to recycle thermosetting resins in spite of their residual properties. In the present study, the authors propose to recycle waste epoxy-polyester (EP-PE) powders by a new foaming technology called "solid-state foaming" (Quadrini & Squeo, 2008), which has been recently developed to foam thermoset materials without using any external agent. The term "solid state foaming" comes from an analogy with some metal foams. In fact, titanium foams can be produced by the expansion of pressurized argon-filled pores within titanium at elevated temperature (Murray et al., 2003). The analogy depends on the fact that a solid tablet foams by heating but the involved physical mechanisms are very different. In particular, for thermosetting powders, this foaming technology is very promising because of its easiness and the absence of special equipments.

Even if porosity in dense engineering materials is often undesirable for load-bearing applications, it is highly beneficial for weight and cost reduction, damping, thermal insulation and specific strength.

Structural foams are extensively used in several industrial applications (automotive, aerospace, naval) as they combine good mechanical properties with low weight, and, in the last years, several efforts were made to produce and characterize new foams. There are two main foaming techniques for plastic foams: soluble foaming (or physical foaming) and reactive foaming (or chemical foaming). The former is generally applied to thermoplastics and involves the mixture of a polymer melt and a blowing agent. The latter is typical for thermosets and involves the addition of reactants for the gas evolution. In both cases, the same three steps are necessary: gas implementation, gas expansion and foam stabilization. A blowing agent is always present: different organic solvents can also be used as physical blowing agents, as well as a chemical foaming agent can be adopted so that a gas is released during the cross-linking reaction. Moreover, the polymer matrix is always processed in a liquid state by means of plasticators (for thermoplastics) or mixers (for thermosets). As a consequence, conventional foaming technologies are generally complex and expensive, and the presence of organic solvents or chemical agents for the gas implementation and release often produce high environmental impacts. On the contrary, the proposed foaming technology presents a lot of advantages: the absence of a blowing agent, the low cost of equipments, the easiness of the application, the possibility of using waste powders. It is possible to produce structural foams with good mechanical performances by exploiting the residual properties of the collected powders and with low energy requirement and emissions (Guglielmotti et al., 2007).

In previous studies, the solid state foaming process was applied only to virgin materials, in one case for epoxy resins (Quadrini & Squeo, 2008), in another case also for epoxy-polyester resins but with very poor results (Guglielmotti et al., 2007). In the current study, for the first time, a waste epoxy-polyester resin has been used with very good results thanks to a different setting of the process variables. Moreover, the effect of the addition of nano-fillers has been also evaluated. The waste powders were provided by a manufacturer of domestic appliances and used to produce solid tablets by room temperature compression. Before compaction, montmorillonite (MMT) nano-particles were mixed with the resin powder at different weight contents so as to evaluate the effect of nano-clay on foaming process and foam performances. After compaction, the tablets foamed in a metallic mold by addition of heat. The foaming efficiency was evaluated in terms of foaming ratio and foam structure whereas foam structural performances were evaluated by means of compression tests.

Materials and Methods

Waste epoxy-polyester powders for coating applications were used in the experimentation: they were provided by a manufacturer of domestic appliances (such as washing machines) which collected the powders after cleaning some coating chambers. The fresh resin was generally used by the manufacturer to coat sheet metals by electrostatic spraying: it consisted of an uncured gray powder but it is reasonable that the purity of the waste powder would be affected by the cleaning procedure. Composite foams were synthesized using a nanoclay (Laviosa Dellite 43B) deriving from a naturally occurring montmorillonite (MMT) especially purified and modified with a quaternary ammonium salt (dimethyl benzyl-hydrogenated tallow ammonium).

The EP-PE powder was used “as received” and no blowing agent was mixed together; only MMT particles were added by hand mixing. A cylindrical stainless steel mold was used for compacting the powder mixtures in tablets with an external diameter of 20 mm. The compaction was performed by means of a universal testing machine to control the compaction rate and pressure, which were 5 mm/min and 125 MPa, respectively. The tablets were fabricated with the

same total weight (4 g) but different MMT content (0, 1, 3, 5, 10 wt%); 3 tablets were produced for each percentage of MMT. The tablets foamed by means of the insertion in a muffle at 250 °C for 10 min. The foaming process was performed in air, placing the tablets in cylindrical stainless steel molds. After foaming, the molds were left to cool in air, and the specimens were extracted from the molds.

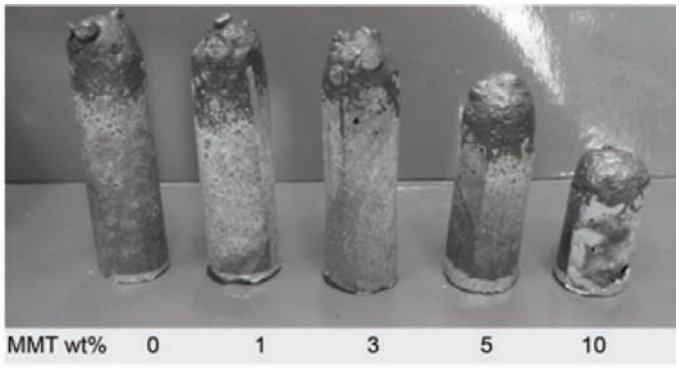
Foam samples and powders were analyzed by X-ray diffractometry (XRD) using a Philips X'Pert PRO Diffractometer with Cu radiation. The scanning speed and the step size were 0.6 deg/min and 0.02 deg, respectively. XRD analyses were carried out on MMT particles, epoxy-polyester powders, and composite foams with different MMT content (after grinding).

The efficiency of the foaming process was evaluated by means of the density ratio, which is the ratio between the initial tablet density and the foam density. The foam tip was cut to have a cylindrical shape before extracting the foam density. For this reason, the density ratio was also expressed as the ratio between the foam and the tablet height. In both cases, the higher is the density ratio, the higher is the foaming efficiency. In order to evaluate the mechanical performances of the foams, compression tests were performed on 20 mm long cylindrical specimens at 5 mm/min (according to ASTM D1621). Generally compression tests are used to qualify foam samples as compressive properties are strongly dependent by the foam structure and morphology. Two specimens were extracted from each foam, one from the bottom and the other from the top: this way, it was possible to evaluate the effect of the foam structure on the properties of two adjacent zones of each sample. Only one sample was extracted from the 5% and 10% MMT filled foams because of their low height.

Results and Discussion

Thanks to solid-state foaming, thermosetting tablets rapidly foam by means of heat addition only. No blowing agent is necessary as the foaming mechanism depends on the intrinsic resin boiling point. During boiling, the resin polymerizes and the bubbles inside the foam become stable: even if higher temperatures lead to more efficient boiling phenomena, the foaming temperature has to be limited to avoid resin burning. In the proposed foaming process, the compacted tablets are inserted into a muffle at a very high temperature (higher than the degradation temperature) and during the thermal transition from the initial tablet temperature to the muffle temperature, the resin boils and hardens. Boiling is fast whereas the polymerization needs more time and during this time the bubbles can expand. The use of metallic molds, as well as the increase of the tablet density,

Figure 1. Foam samples



is very important factors to rapidly spread the heat inside the tablet.

Figure 1 shows some foams with different content of MMT. It is clearly visible that the foam height decreases by increasing the MMT content. All the foams have a similar surface aspect: the white color of the surfaces in contact with the mold walls depends on the presence of a mold release agent which is absent on the foam tip. However, no porosity is present on the external surfaces and the foam structure is visible only after sectioning (Figure 2). Foam sections show the effect of the MMT content on the foam structure as bubble coalescence can occur at low filler contents and irregular structures are visible at high contents. A homogeneous structure was obtained for 3 wt% MMT filled tablets without affecting the foam height. However, it is not excluded that different foaming conditions (in terms of foaming time and temperature or tablet size) would produce more regular structures also in absence of MMT filler.

Figure 3 reports the density values of the tablets as a function of the MMT content: as expected, an almost linear increase of the density is observed with increasing filler content because of the higher density of the MMT particles in comparison with the resin powder particles. As a consequence, also the foam density increases by increasing the filler content (Figure 4). Two samples were extracted from each foam for compression tests; therefore the density ratio was calculated separately for the top and the bottom of each foam. In the case of foams with higher filler contents, because of the small height, only one sample was extracted and referred as "bottom". Also the foam density is linearly dependent on the MMT content, but only for low MMT contents. Data scattering is observed for the 5% and 10% MMT filled samples as it was not possible to separate the two different contributions of the foam top (in contact with the air during foaming) and the foam bottom (in contact with the mold). However, the slope and the relative position of the foam density trends in the 0-3 wt% range show that a stronger effect of the MMT content is measured at the top of the foams despite the direct contact of the bottom with the metallic mold. Probably, if boiling starts at the bottom of the foams where material heating is more rapid, larger bubbles are present, and the bubble formation may push away the MMT particles.

In Figure 5, the foaming efficiency is evaluated by means of the foaming ratio, both in terms of density ratio and height ratio. Errors in evaluating the height of the foam (which is not regular on the top, as Figure 1 shows) led to a slight difference in the foaming ratio evaluated by means of the two ways. The foaming ratio always decreases by increasing the MMT content: in accordance with Figures 3 and 4, also the height ratio is almost linear as a function of the filler content as well as the density ratios from 0 to 3

Figure 2. Section of the foams

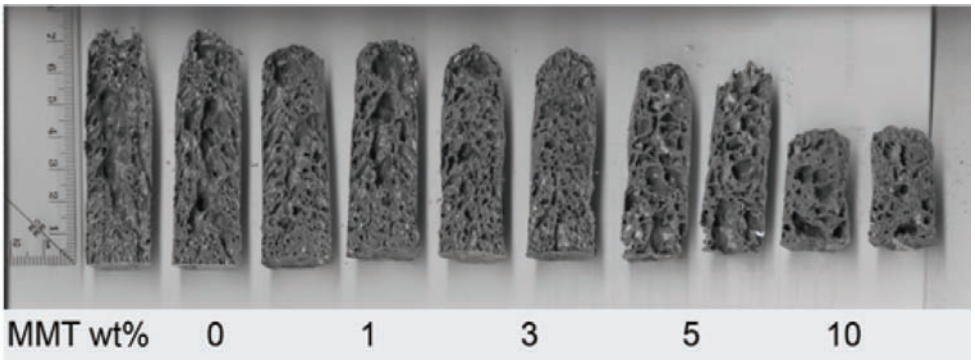


Figure 3. Tablet density as a function of the MMT content

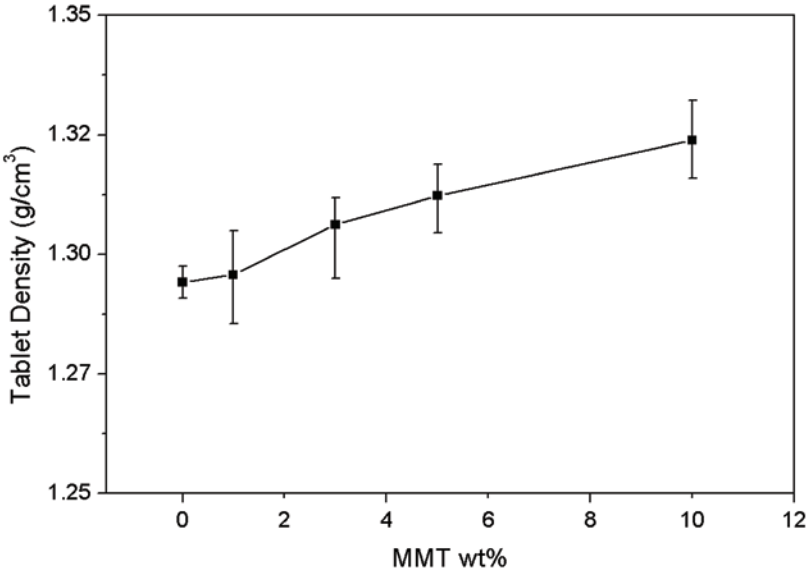
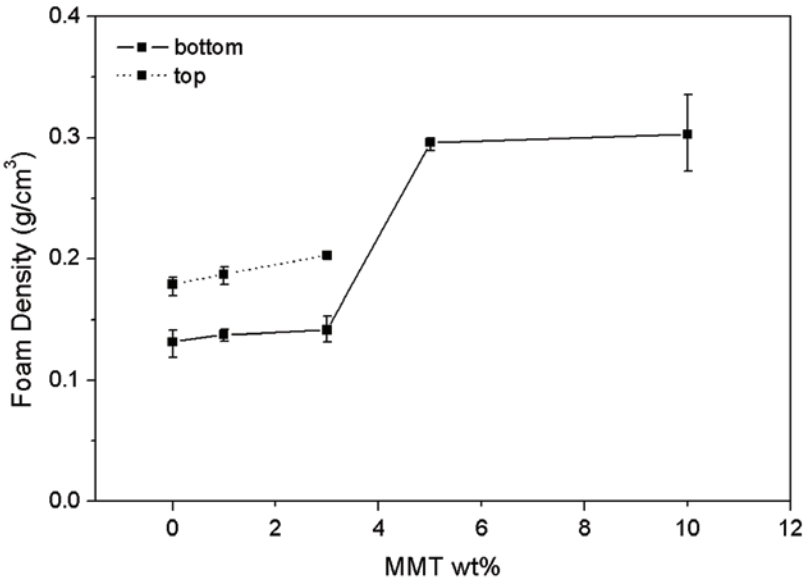


Figure 4. Foam density as a function of the MMT content



wt%. Figure 5 shows that the height ratio is placed between the density ratios, being an average of the values of the two different foam parts. However, higher foaming ratios were measured for the specimens extracted from the bottom of the foams because of the size distribution of the bubbles and the MMT distribution. As previously reported, the direct contact between the tablet and the mold could exalt the resin foamability and the particle segregation during heating.

In order to give a first attempt to evaluate the effect of the foaming process on the MMT distri-

Figure 5. Foaming ratio as a function of the MMT content

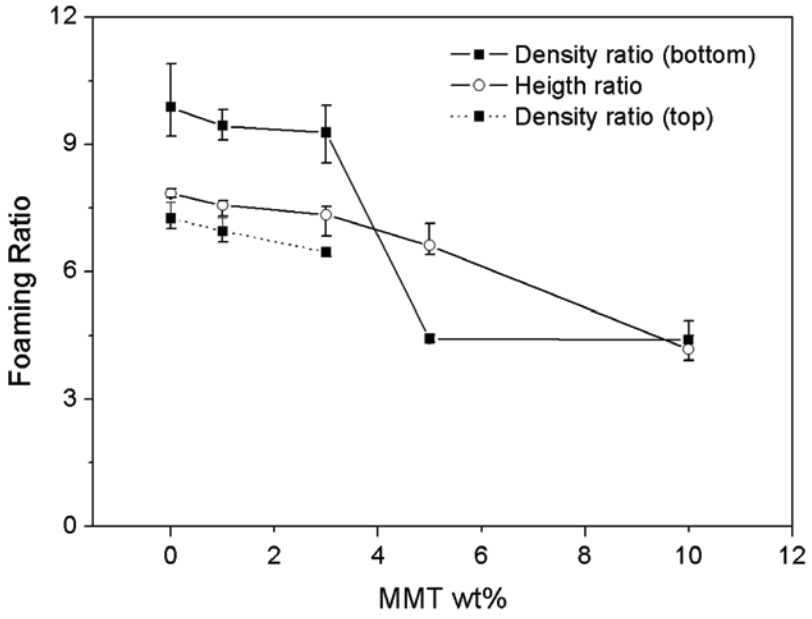
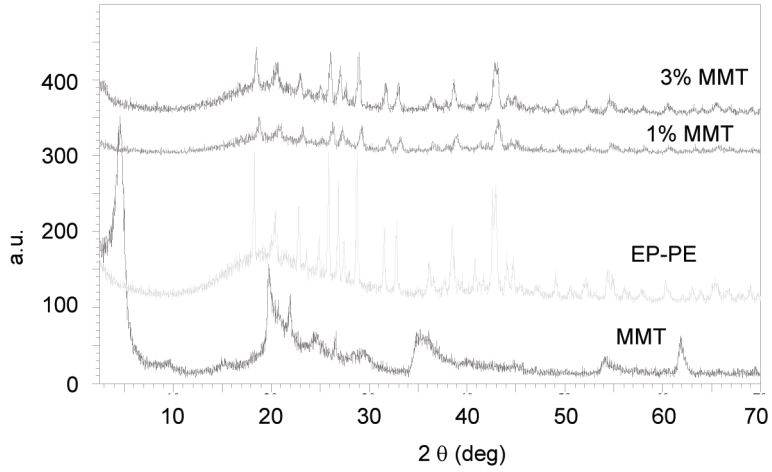


Figure 6. XRD results



bution, XRD analyses were carried out on "as received" powders and foams. Figure 6 shows the XRD spectra of MMT and epoxy powders together with spectra of 1 and 3 wt% MMT filled foams. It is known that the nano-particle exfoliation cannot be evaluated by means of XRD only, however reported results do not exclude that the adopted mixing strategy and the subsequent foaming step is able to eliminate at least macro-aggregates of MMT. Particularly, the (001) plane peak ($2\theta = 4.57$ deg), which is related to the interlamellar spacing of the clay (19.3Å), is not visible in the MMT filled foams as well as in the EP-PE powder. The peaks visible in the EP-PE spectrum,

which are also transferred to the foam spectra, are due to the presence of other silicates or aluminosilicates in the coating powder but it was not possible to identify all the components.

Results from compression tests are reported in Figures 7 through 9. Figure 7 shows some typical compression curves in the case of unfilled, 1 and 3 wt% MMT filled foams. The effect of the foam density is evident as samples extracted from the top (with higher density) show higher compression stresses independently from the filler content. All the tested specimens exhibited the typical compression behavior of foams, and all the stress-strain curves can be divided into three typical parts. In the first part, at low strains, the stress increases almost linearly as the foam mainly behaves in a rigid way. Subsequently, the bubbles start to collapse and a plateau is reached. This plateau is kept for a wide range of the strain, in which the foam dissipates the energy provided by the compression by means of the bubble rupture. In the last part of the curve, a slight increase of the stress is observed because of the material densification and its inability to dissipate more energy.

From compression tests, both the plateau stress (i.e. the mean value of the compression stress in the 10-60% strain range) and the compressive toughness (i.e. the area under the stress-strain curve in the same strain range) were extracted and are reported in Figures 8 and 9, respectively. Despite the MMT content induces an increase in foam density, it does not seem to have an appreciable effect on mechanical properties as a clear trend is not visible. Moreover, if an effect is present, it is not positive as plateau stress decreases in the 0-3 wt% MMT content range. An increase at higher filler contents for the samples extracted from the bottom depend on the already discussed impossibility of extracting samples from the top. Moreover, samples with high filler contents showed a poor foamability and behaved in a rigid way over a wide strain range: densification occurred beforehand. It was not possible to extract

Figure 7. Typical compression curves

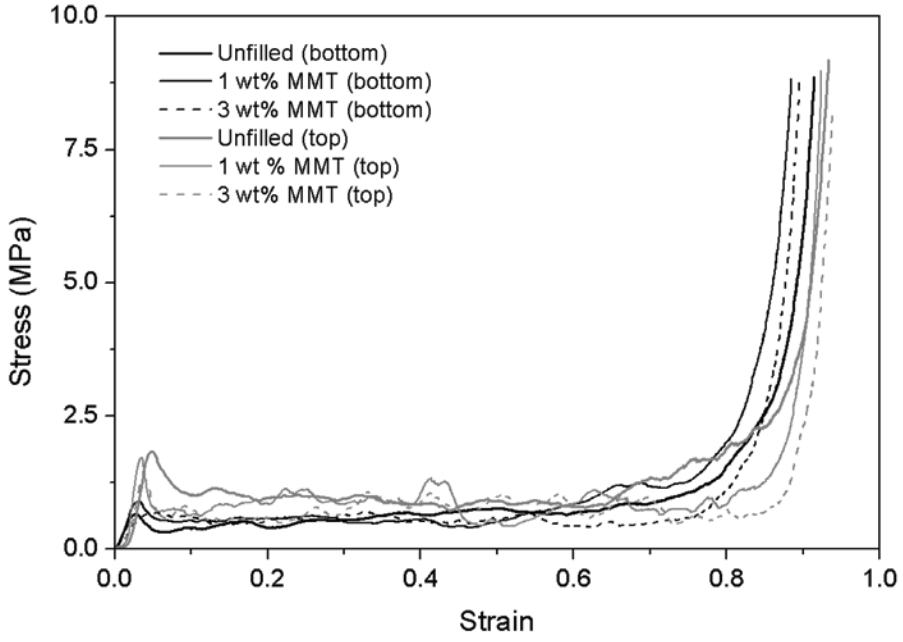


Figure 8. Plateau stress of the compression curves

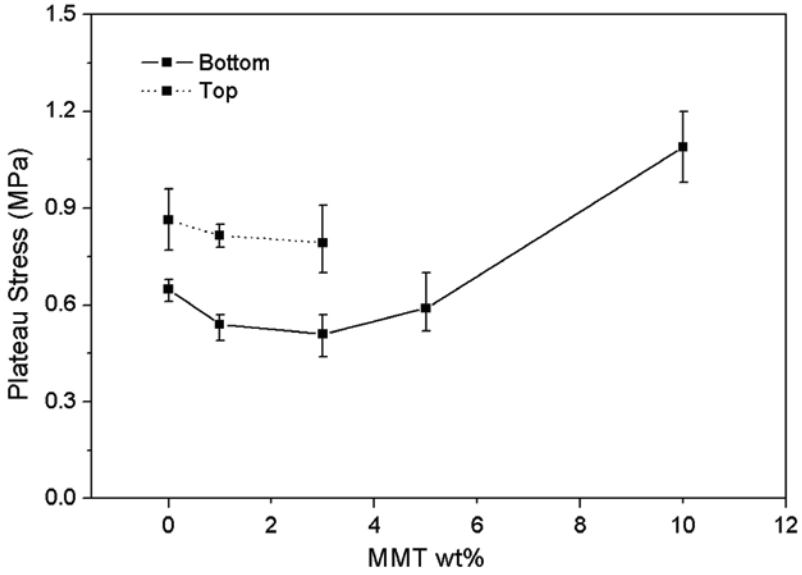
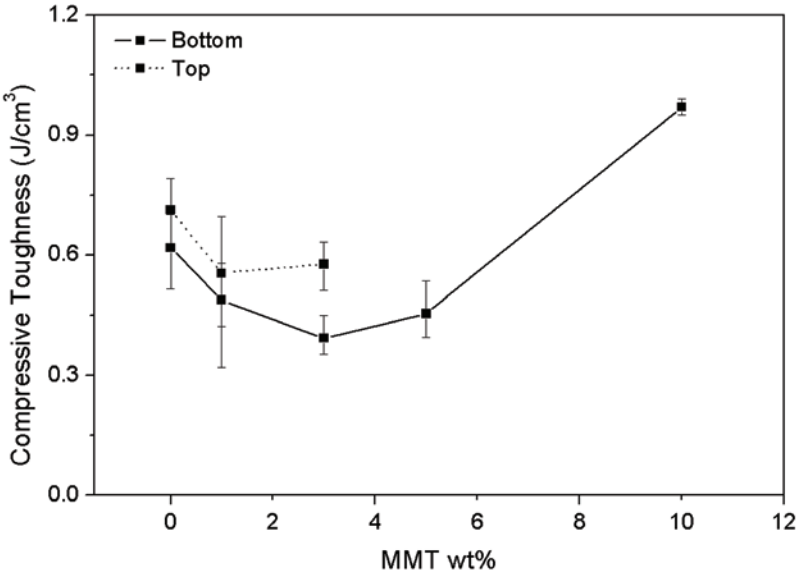
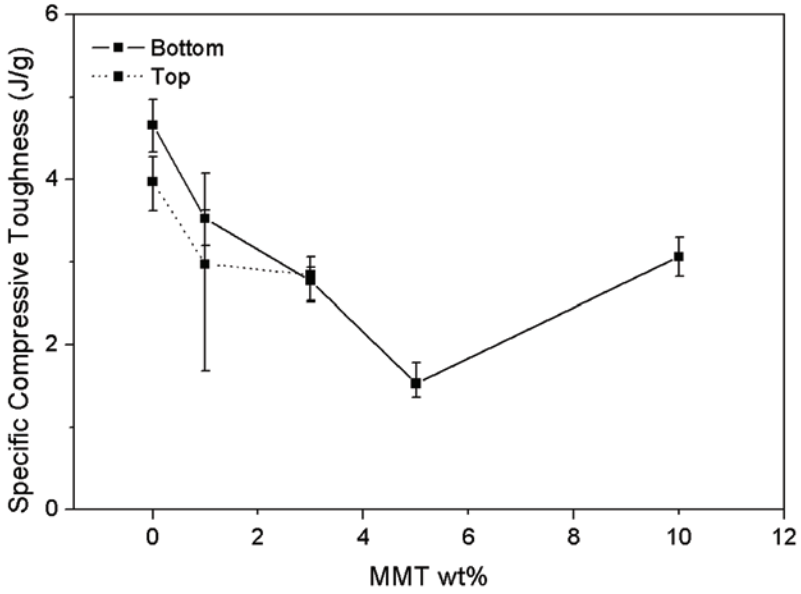


Figure 9. Compressive toughness of the foams



a plateau value for all the samples and elastic stresses were always important. The performance decrease with MMT content seems to be higher for the compressive toughness (Figure 9) but data scattering was very high in this case because of the non homogeneity. However, at least for the comparison between the unfilled foam and the foams filled with low MMT contents, it is visible that both plateau stress and compressive toughness got worse by adding MMT particles. It is reasonable that MMT particles can affect the resin polymerization (Harsch et al., 2007). Another ap-

Figure 10. Specific compressive toughness of the foams



preciable effect is linked to the bubble and density distribution as the compression curves of the top specimens are shifted towards higher values of stress in comparison with bottom specimens.

Apart from data scattering, data of Figures 8 and 9 are very similar: that is due to the fact that plateau stress and compressive toughness are both referred to mechanical properties per volume unit. In order to make a further comparison, the compressive toughness of each sample was divided by the related sample density: resulting specific compressive toughness is reported in Figure 10. The negative effect of the filler content on the ability of the foams to absorb energy is more evident, and the differences between the top and the bottom samples are reduced. If a difference is present, it is visible only up to 1 wt% of filler and is opposite to the case of Figures 8 and 9 as bottom samples show higher specific compressive toughness.

CONCLUSION

Recycling of thermosetting resin powders coming from over-spray of coating processes is a serious problem: even if powders could be collected to be re-used, the presence of polluting particles (such as different particles from previous operations) can spoil the coated surface in terms of aesthetics and performances. As a consequence, a large waste of powders has to be managed, generating expenses and environmental disturbances due to non-biodegradable nature of the powders and dangerous situations as the risk of fire. The first aim of this study was to show that thermosetting resins powders can be re-used to produce structural foams for several applications if a solid-state technology is used: it is very easy to produce and foam tablets, and special equipments are not necessary. Rigid polyester foams are typically used as safety foams in automotive or for heat and noise insulation in construction. Moreover, foam panels could be used as core of sandwich structures or in other applications where rigid polyurethanes are generally used.

Unfilled and composite foams may be produced as well: in fact, before compaction, the resin powder may be mixed with several filler materials such as ceramic or metallic micro and nano-particles. In the reported study, the case of MMT filler was studied but the final results were not very satisfactory. By adding MMT particles, the foams become more and more rigid and brittle, losing the typical performances of foams. However, as the effect of the MMT content on the foam properties is evident in terms of density and mechanical data, the feasibility of the production of composite foams by solid-state foaming was shown; further improvements are necessary to find the best combination of resin powders and fillers to enhance final properties of foams.

REFERENCES

Ansarifar, A., Wang, L., Osmani, M., & Pappu, A. (2009). Assessing effects of thermoset polyester resin waste powder on the processing and mechanical properties of natural rubber. *Journal of Rubber Research*, *12*(1), 12–26.

Asokan, P., Osmani, M., & Price, A. (2009). Assessing the recycling potential of glass fibre reinforced waste in concrete and cement composites. *Journal of Cleaner Production*, *17*(9), 821–829. doi:10.1016/j.jclepro.2008.12.004

Asokan, P., Osmani, M., & Price, A. (2010). Improvement of the mechanical properties of glass fibre reinforced plastic waste powder filled concrete. *Construction & Building Materials*, *24*(4), 448–460. doi:10.1016/j.conbuildmat.2009.10.017

Guglielmotti, A., Quadrini, F., Squeo, E. A., & Tagliaferri, V. (2007, October 2-3). Solid-state foaming of thermosets. In *Proceedings of the Polymer Foam Conference*, Newark, NJ.

Harsch, M., Karger-Kocsis, J., & Holst, M. (2007). Influence of fillers and additives on the cure kinetics of an epoxy/anhydride resin. *European Polymer Journal*, *42*(4), 1168–1178. doi:10.1016/j.eurpolymj.2007.01.025

Hwang, E.-H., & Jeon, J.-K. (2010). Preparation and mechanical properties of bulk molding compound composite prepared using recycled FRP waste powder. *Journal of the Korean Industrial and Engineering Chemistry*, *21*(2), 217–223.

Lothongkum, A. W., Nonthapone, R., Seangkiatiyuth, K., & Tanthapanichkoon, W. (2007). Powder characteristics and coating conditions of fresh and re-used polyester resins for electrostatic powder coating: powder recycling and loss prevention. *Advanced Powder Technology*, *18*(2), 175–186. doi:10.1163/156855207780208664

Murray, N. G. D., Schuh, C. A., & Dunand, D. C. (2003). Solid-state foaming of titanium by hydrogen-induced internal stress superplasticity. *Scripta Materialia*, *49*, 879–883. doi:10.1016/S1359-6462(03)00438-X

Pickering, S. J. (2006). Recycling technologies for thermoset composite materials—current status. *Composites: Part A*, *37*, 1206–1215. doi:10.1016/j.compositesa.2005.05.030

Quadrini, F., & Squeo, E. A. (2008). Solid-state foaming of epoxy resin. *Journal of Cellular Plastics*, *44*, 161–173. doi:10.1177/0021955X07082486

This work was previously published in the International Journal of Manufacturing, Materials, and Mechanical Engineering, Volume 1, Issue 3, edited by J. Paulo Davim, pp. 10-20, copyright 2011 by IGI Publishing (an imprint of IGI Global).

Chapter 6
Feature Recognition and Datum Extraction for Setup Planning and Operation Sequencing for Prismatic Parts

T. Srikanth Reddy
Indian Institute of Technology Madras, India

M. S. Shunmugam
Indian Institute of Technology Madras, India

ABSTRACT

An automated planning system extracts data from design models and processes it efficiently for transfer to manufacturing activity. Researchers have used face adjacency graphs and volume decomposition approaches which make the feature recognition complex and give rise to multiple interpretations. The present work recognizes the features in prismatic parts considering Attributed Adjacency Matrix (AAM) for the faces of delta volume that lie on rawstock faces. Conceptually, intermediate shape of the work-piece is treated as rawstock for the next stage and tool approach direction is used to recognize minimum, yet practically feasible, set of feature interpretations. Edge-features like fillets/undercuts and rounded/chamfer edges are also recognized using a new concept of Attributed Connectivity Matrix (ACM). In the first module, STEP AP-203 format of a model is taken as the geometric data input. Datum information is extracted from Geometric Dimension and Tolerance (GD&T) data. The second module uses features and datum information to arrive at setup planning and operation sequencing on the basis of different criteria and priority rules.

1. INTRODUCTION

In a Computer Integrated Manufacturing system (CIM), Computer Aided Process Planning (CAPP) plays a major role in bridging the gap between Computer Aided Design (CAD) and Computer Aided Manufacturing (CAM) systems. If CAD addresses 'what to build', a planning system addresses the most critical issue of 'how to build'. However, the geometric model of a part designed in a conventional CAD system is not adequate for an automated planning system. First basic requirement in any automated planning system is to obtain the feature data from geometric data. This

DOI: 10.4018/978-1-4666-1867-1.ch006

Copyright © 2013, IGI Global. Copying or distributing in print or electronic forms without written permission of IGI Global is prohibited.

feature data has to be effectively be transferred in an explicit form to the planning modules. Problems still exists in the existing feature extraction systems particularly while dealing with the interacting features because of the feature representations and methodologies adopted.

A survey of literature shows that various methodologies like object oriented models, feature-based models, feature recognition methods have been proposed earlier. In object oriented models (Beg & Shunmugam, 2002; Bhaskara Reddy et al., 1999), feature data is entered interactively for inspection planning and operation sequencing respectively. Though the data entry can be made error-free, it requires high-level intelligence and takes considerable time. Feature based modeling systems (Lin et al., 1997; Harun & Case, 2000; Kim et al., 2001; Patil & Pande, 2002; Faraj, 2003; Liu & Wang, 2007) require the part model in terms of manufacturing features rather than design features so that the feature data can directly be used in the downstream applications. They are limited by the number of manufacturing features one can include in a predefined library and it is essential that the designer should also have a thorough knowledge of manufacturing features, in order to use them effectively.

Feature recognition overcomes the above mentioned limitations of interactive data entry and feature-based design approaches. It deals with interpretation of given geometric data by implementing specific algorithms. In other words, it can be considered as a 'virtual eye' that looks at the model and recognizes the manufacturing features present in it. Of various methodologies reported for its development, prominent ones are graph based methods and volume decomposition methods.

In Graph based methods (Joshi & Chang, 1988; Gavankar & Henderson, 1995), boundary model of a part is represented as a graph-based structure such as face-adjacency graph. This graph is then searched for sub-graphs or feature-graphs where each sub-graph represents a feature. Concepts of sub-graph isomorphism are used in these approaches. These graph-based representations become very complex for parts with complex geometry and topology due to the complex feature representation adopted.

Volume decomposition approaches (Tseng & Joshi, 1994; Sakurai, 1995; Woo & Sakurai, 2002) have been proposed to deal with interacting features, where volume to be removed from the rawstock to produce the part, referred to as delta volume, is decomposed into small blocks. They are then combined in such a way that the recognizable features are reconstructed. They require a large number of Boolean operations. However, these approaches give large number of interpretations, sometimes ambiguous ones, to which machining heuristics are applied subsequently to arrive at those interpretations that give the machining sequence. Most of the researchers dealing with prismatic parts have considered initial rawstock to be a rectangular block, but the initial shape cannot be ignored, as the amount of material to be removed and the production time are dependent on it (Khailash et al., 2001).

Edge-features like fillets, undercuts, rounded and chamfered edges may also be present in the part. Rahmani and Arezoo (2006) and Zhu and Menq (2002) have proposed the suppression of fillets to convert them into sharp edges to reduce the complexity during feature recognition. The sharp edges, fillets, rounded edges etc, specifically introduced by the designer cannot be neglected and additional operations may be required to get those features which will lead to a considerable change in the process plan.

Literature study on feature recognition reveals that (1) complex methodologies have been followed to obtain interacting features (e.g. volume decomposition methods); (2) a large number of interpretations of features are obtained initially without considering practical aspects of machining and additional heuristics are used later to arrive at proper interpretations, thus making the systems cumbersome; (3) feature representations adopted

are not simple which lead to complex feature recognition methodologies; (4) initial rawstock shape is assumed to be a rectangular block; and (5) the part model is assumed to have all sharp edges and recognition of additional features like fillets/ undercuts, rounds/chamfers is not dealt with.

There is a need for development of a feature recognition system that considers rawstock shape, uses simpler feature representation, and identifies the interacting features explicitly in a better way to give minimum and practical feature interpretations and also deals with recognition edge-features.

3D CAD model data input for the feature recognition system can be in native or neutral formats. The neutral exchange formats such as IGES (Liu & Hui 2000; Nasr & Kamrani, 2006), DXF (Gibson et al., 1999) and STEP (Bhandarkar & Nagi, 2000; Kang et al., 2003; Rameshbabu & Shunmugam, 2008; Kannan & Shunmugam, 2009) widen the scope of application. STEP, standing for Standard for the Exchange of Product Model Data, an ISO standard provides an effective neutral data exchange format with a wide range of application protocols. AP-203 (Configuration Controlled 3D Designs of Mechanical Parts and Assemblies) protocol deals with the geometric data representation in B-rep format. Use of STEP AP-203 in setup planning for prismatic parts (Rameshbabu & Shunmugam, 2008) and planning for sheet metal parts (Kannan & Shunmugam, 2009) can be found in the literature. AP-224 (Mechanical product definition for process planning using machining features) is being developed with feature recognition from AP 203. Therefore, in the present work, AP-203 is considered more appropriate for use in feature recognition.

A meaningful plan can be obtained, only when geometric dimensions and tolerance (GD&T) data are extracted automatically from the CAD model (Chiabert et al., 1998, Zhang et al., 2001). Second edition of AP-203 is expected to provide GD &T data, but available commercial CAD software have not yet adapted this. Therefore, in the present work the GD &T data is extracted from native files. When commercial CAD software adapting the second edition of AP-203 becomes available, the approach presented in this paper can take directly this input data.

Considering the above issues, an automated planning system for prismatic parts is developed in the current work for setup planning and operation sequencing. The feature recognition system takes STEP AP-203 as geometric data input format and it also considers the initial shape of the rawstock. A simplified approach is presented for feature recognition of interacting features that gives minimum and more practical sets of machining features. Fillets, rounded edges etc. are also recognized and a new concept of Attributed Connectivity Matrix (ACM) for features is proposed to represent the type of feature and its direction, and this data is effectively transferred to planning module to account for their presence. The datum information is also extracted automatically from GD&T data in the native format and is associated with the recognized features. On the basis of different criteria and priority rules, final setup plan and operation sequence for the features is arrived at.

2. PROPOSED FEATURE RECOGNITION APPROACH

For sake of understanding, the basic concepts involved in the proposed recognition approach are explained in this section. Details are presented later in relevant sections.

2.1. Feature Definition

In the context of setup planning, Rameshbabu and Shunmugam (2008) have defined a manufacturing feature as unified chunk of total delta volume that can be machined in a single setup. Feature recognition is then carried out with the aid of the faces of the delta volume that lie on the faces of the assumed rectangular block for the raw-

stock model. This method simplifies the feature recognition as less number of faces is used for representing a feature. However, for sequencing applications, all the features in a delta volume are to be recognized explicitly. Also, the system must be able to recognize the features from part given in Figure 1(a), if the raw stock shape is given as Figure 1(b). For this, the feature definition has to be made more precise. Researchers have recognized interacting features in terms of basic recognizable features called 'feature blocks' (Tseng & Joshi, 1994) and 'maximal features' (Woo & Sakurai, 2002) etc. In a similar way, in the current work, a basic recognizable feature termed as a 'primitive feature' is introduced and it is defined as largest possible volume of uniform rectangular or circular cross section in a delta volume that can be machined in a single stage. In this paper, the symbol F^p_i is used to represent a ith primitive feature along a pth projection direction (details given in section 3.3). Delta volume-1 shown in Figure 1(c) consists of two primitive features (F^1_1 and F^1_2) of rectangular cross section as shown in Figure 2(a). Using approach proposed in the present work, manufacturing features are identified as blind-pockets (details given in section 3.4). A typical manufacturing feature classification considered in the present work is shown in Figure 3.

2.2. Tool Approach Direction

Tool Approach Direction (TAD), an important consideration in machining, is an unobstructed direction from which a cutting tool can access

Figure 1. An example part: (a) part model; (b) initial rawstock; and (c) delta volumes

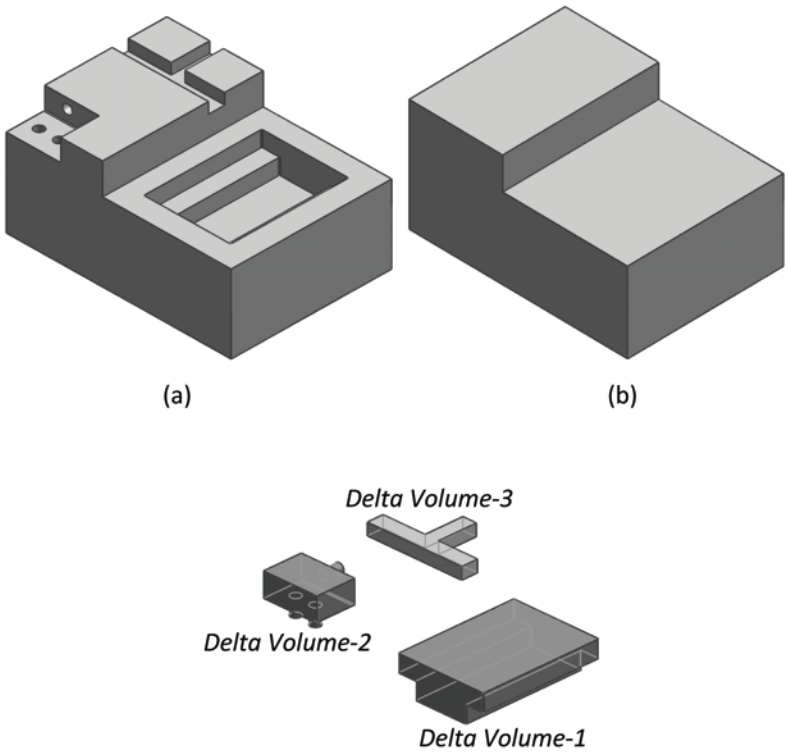
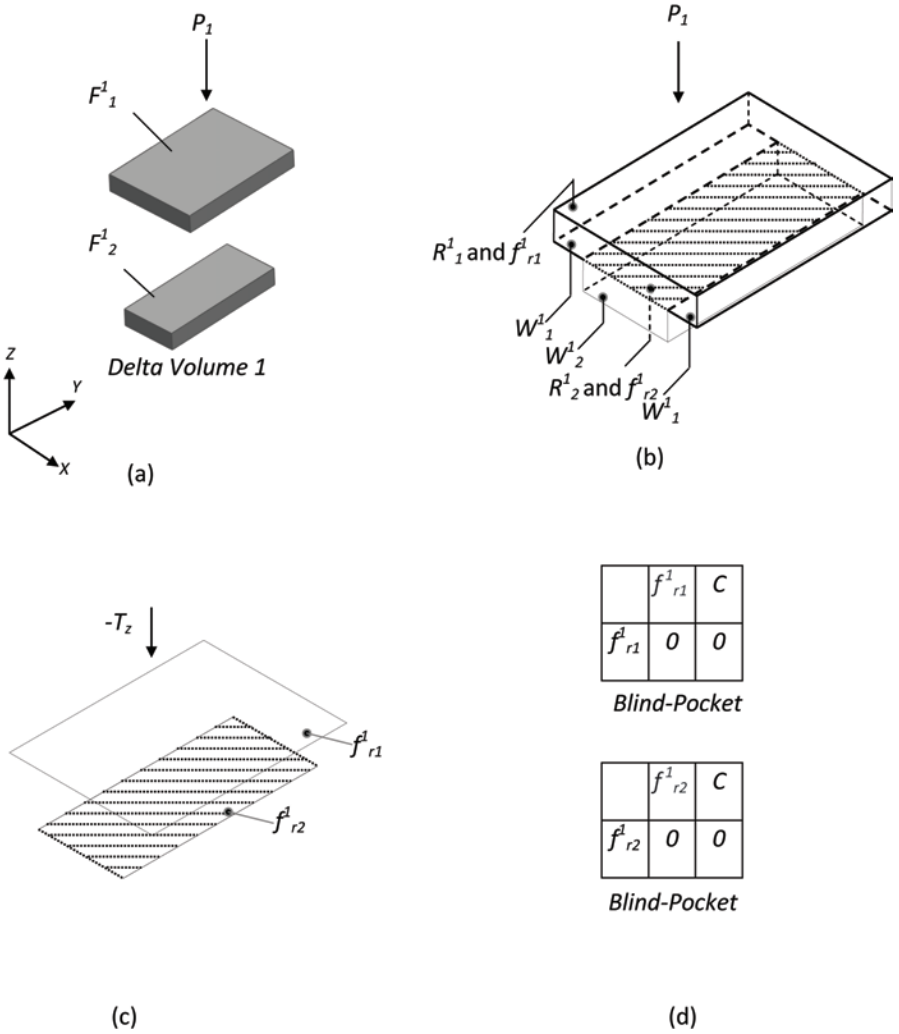
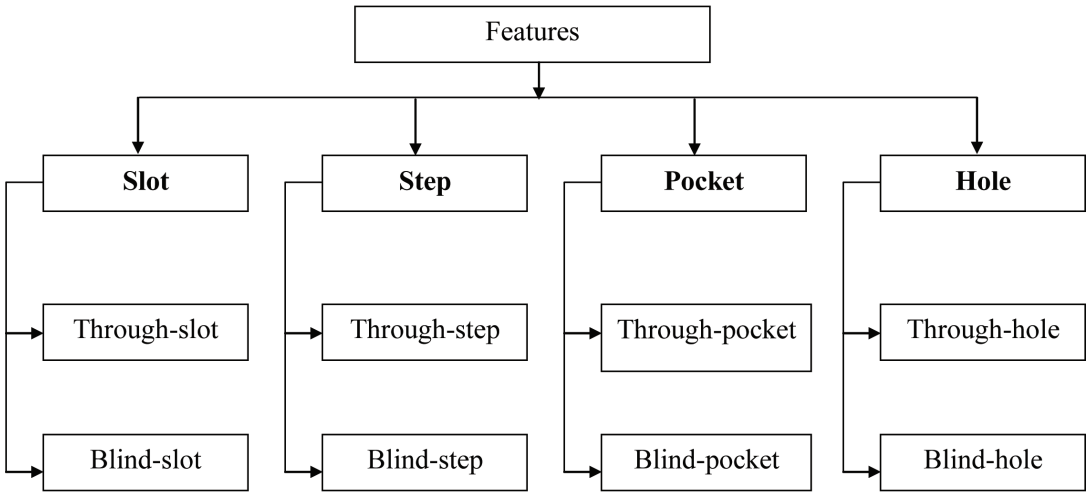


Figure 2. Recognizing manufacturing features: (a) Possible primitives for delta volume-1 of example part model in Figure 1. An example part: (a) part model; (b) initial rawstock; and (c) delta volumes 1; (b) Faceprocessing along projection direction P1;(c)



the workpiece for material removal (Khailash et al., 2001; Gaoling et al., 2005). For the delta volume-1, TAD for the primitive features is shown in Figure 2(c). Along this direction the material is removed in terms of definite primitive feature volumes in a given sequence. For a delta volume, if such volumes are considered along all TADs, more practical sets of machinable features are obtained. Each of these sets is an interpretation of features in the delta volume. The number of interpretations obtained this way will only be equal to the number of TADs along which the part can be accessed. Thus, problem of handling large number of interpretations can be avoided. As TAD is used for obtaining features, it can help setup planning where features needing a similar TAD can be grouped into one setup.

Figure 3. Typical classification of manufacturing features

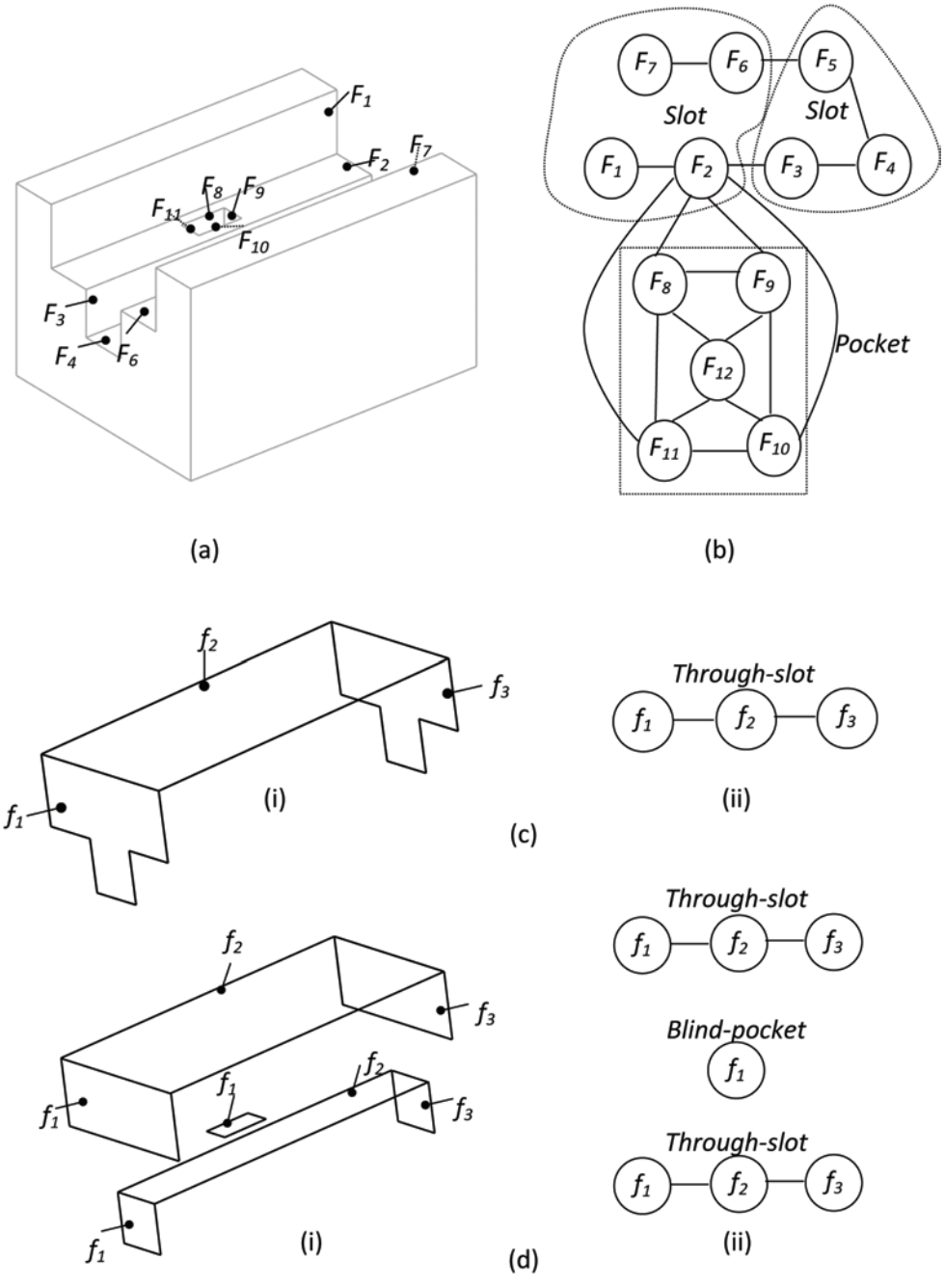


2.3. Feature Representation

Joshi and Chang (1988) have used Attributed Adjacency Graph (AAG) for representing a given part model and recognized the features from its AAG. The adjacency information can also be expressed in a matrix form, referred to as Attributed Adjacency Matrix (AAM). For an example model shown in Figure 4(a), AAG obtained by them is shown in Figure 4(b) and three features (two slots and a pocket) are identified. However, this AAG is very complex graph having twelve nodes for each of the twelve faces used for feature representation. In a different attempt, Rameshbabu and Shunmugam (2008) have used a 'hybrid approach' in which faces of a delta volume lying on the rectangular rawstock are referred to as processed faces and AAG/AAM for these processed faces is used to recognize the feature. For the same model in Figure 4(a), three processed faces and their AAG are shown in Figure 4(c) (i) and (ii) respectively. The AAG identifies the feature as a through-slot. This hybrid approach for feature recognition is useful only from the point of view of setup planning.

In the proposed approach, faces of the delta volumes that lie on the initial rawstock as well as intermediate workpiece shapes and TADs are considered to arrive at the processed faces. This is conveniently done by taking intermediate workpiece shape, obtained after each stage of removal in terms of primitive feature, as the rawstock for the next stage. From Figure 4(d)(i), it can be seen that seven processed faces are obtained and AAGs of processed faces are used to recognize two through-slots and one blind-pocket (Figure 4(d)(ii)), thereby reducing the feature representation complexity. With the use of TAD, number of feature interpretations obtained here is also a minimum and the features are recognized in the same sequence as the machining sequence. No additional heuristics are necessary to recognize the features as required in earlier approaches. The present system gives feature sequence which can be used for operation sequencing as well. Also, presence of additional features like fillets, rounded edges etc. can be addressed by the proposed system, whereas the earlier approaches may become much more complex.

Figure 4. Comparison of different approaches: (a) 3D part model with interacting features; (b) AAG from Joshi and Chang (1988) approach; (c) Approach of Rameshbabu and Shunmugam (2008): (i) feature representation (ii) AAG and feature recognized; and (d) Present approach: (i) feature representation (ii) AAG and features recognized



3. FEATURE RECOGNITION AND DATUM EXTRACTION

First module includes various steps involved in the feature recognition method and datum information extraction from GD&T data. The outline of this module is shown in Figure 5. The details are given in the following subsections.

3.1. Extraction of Geometric Data

The 3D CAD model when exported into STEP AP 203 neutral exchange format, the data is embedded in it in B-rep format. This file format stores complete geometrical data of the solid part model. Each of an unconnected solid volume in the model is defined as *closed shell*, which is surrounded by faces defined as *advanced face*. These faces are represented as *face outer bound* or *face bound* based on their nature whether it is an outer loop or an inner loop respectively. Apart from the nature of the advanced face, the type of the face is also defined as *plane*, *cylindrical surface*, *toroidal surface* and *spherical surface*. Each of the faces contains the edge loop bounding the face and these are defined as *edge loop*. Each edge loop further has *oriented edges* in it and each oriented edge constitutes *vertex points*.

Boolean subtraction of 3D part model from the given rawstock results in a set of unconnected delta volumes. The proposed algorithm takes STEP-AP 203 files of the delta volumes and initial rawstock. The STEP file of delta volumes will have one or more number closed shells where each closed shell represents one delta volume. The data is extracted from STEP files of delta volumes and initial rawstock model separately and faces lying on the rawstock are obtained for use in the next stage of 'face processing' as explained in section 3.3.

3.2. Extracting Tolerance (GD&T) Data

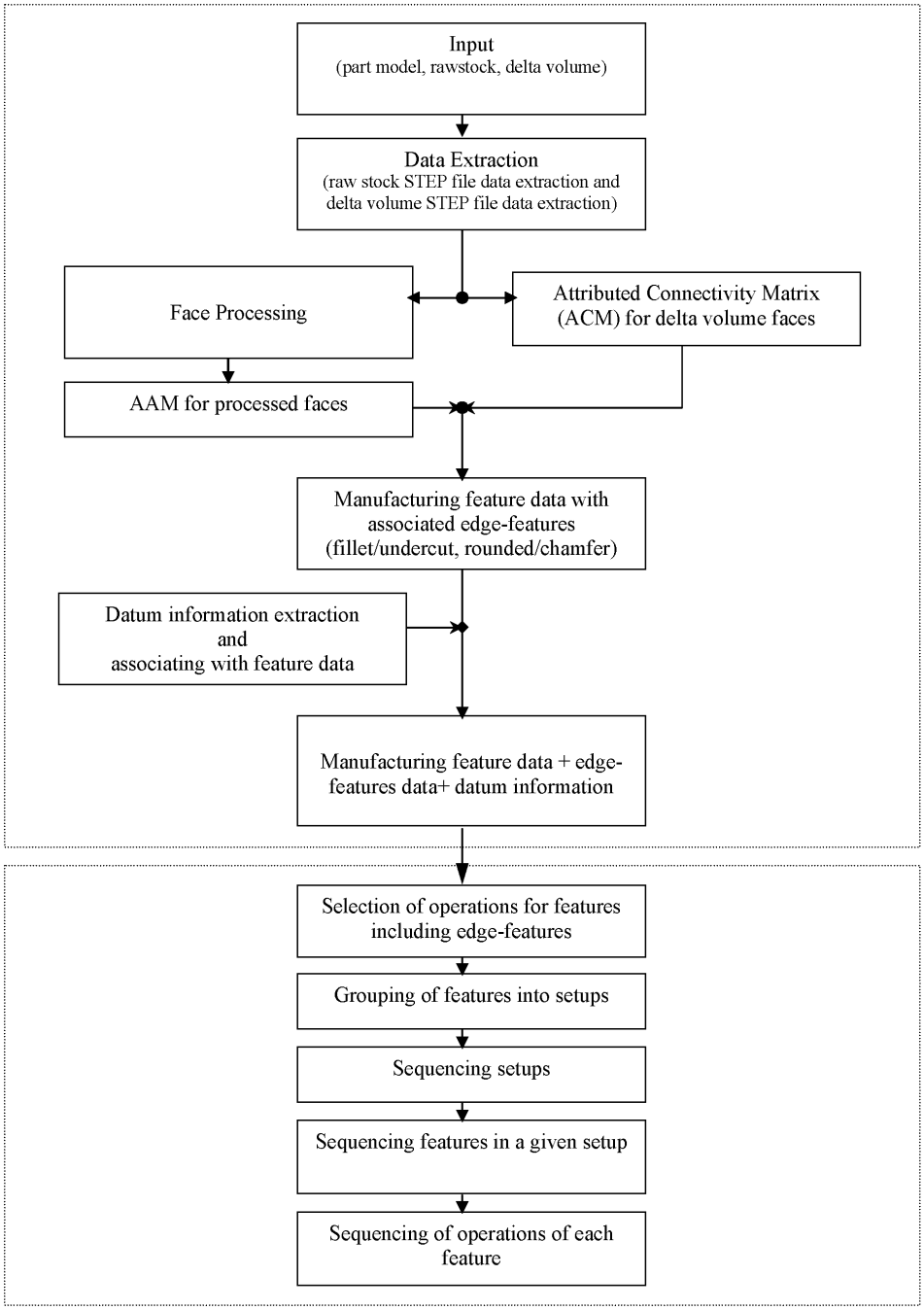
The GD&T data in any CAD model package is entered as annotations that have leaders pointing to the model. Here, in the present work, the modeling is done by using UG NX3® package and the GD&T data is fed to the 3D model. An 'information file' is then generated by selecting 'sort by face index' option provided in UG NX3, that gives the GD&T data (annotation data). This file contains the listing of tolerance features in terms of faces to which each of those tolerance features are associated. An excerpt of the file is shown in Figure 6.

Each of the face in that file is associated with the following information

- Type of the surface of that face (planar, cylindrical etc,).
- Dimensional tolerance, if any, associated with it along with the nominal size, plus or minus tolerance values.
- Type of tolerance feature associated with it.
    - If it is a datum face, it also gives the tolerance feature to which it is associated.
    - If it has a geometric tolerance, then it gives the type of the geometric tolerance, nominal size, material conditional modifier, if any, the datums associated to it.
    - The coordinate data is given for the location of leader line of tolerance feature control pointing to that face.

Datum information extracted from the above file is used suitably for setup planning and operation sequencing applications. Associating this information to the respective features is explained in section 3.8.

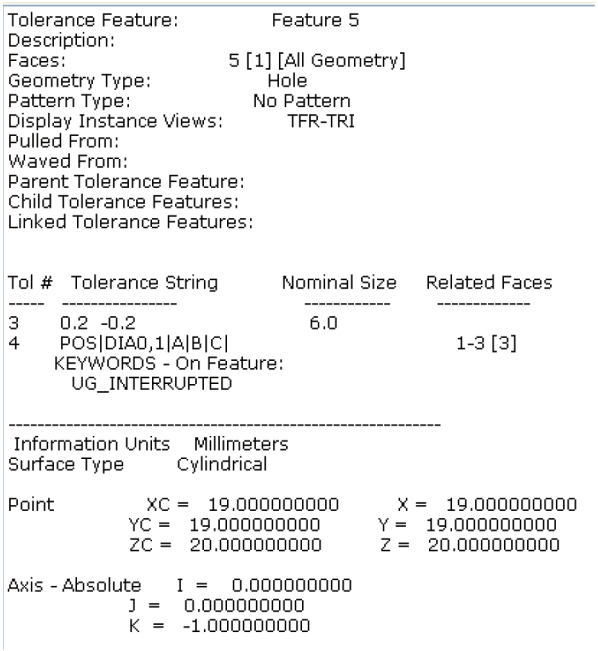
Figure 5. Outline of the proposed system



3.3. Face Processing

Face processing of delta volume is to be done for obtaining the faces to represent a feature and thus aid in feature recognition. The delta volume faces that lie on the rawstock are found (explained in Appendix-A1). Such faces can be called as *external faces*. Each of the normals of these faces is a probable TAD and is chosen as a *projecting direction.* For the delta volume-1

Figure 6. An excerpt from 'information file' showing GD&T data



```
Tolerance Feature:            Feature 5
Description:
Faces:                  5 [1] [All Geometry]
Geometry Type:               Hole
Pattern Type:             No Pattern
Display Instance Views:      TFR-TRI
Pulled From:
Waved From:
Parent Tolerance Feature:
Child Tolerance Features:
Linked Tolerance Features:


Tol #  Tolerance String        Nominal Size    Related Faces
-----  ----------------          ------------     -------------
3      0.2  -0.2                  6.0
4      POS|DIA0,1|A|B|C|                          1-3 [3]
     KEYWORDS - On Feature:
       UG_INTERRUPTED

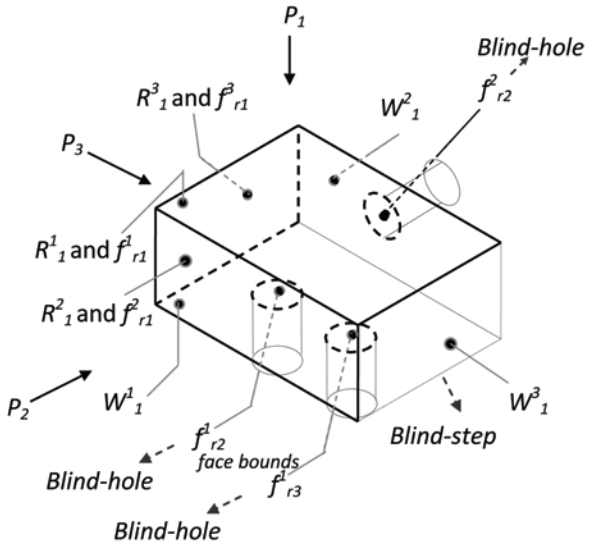
-------------------------------------------------------------
 Information Units   Millimeters
Surface Type       Cylindrical

Point          XC =  19.000000000      X =  19.000000000
               YC =  19.000000000      Y =  19.000000000
               ZC =  20.000000000      Z =  20.000000000

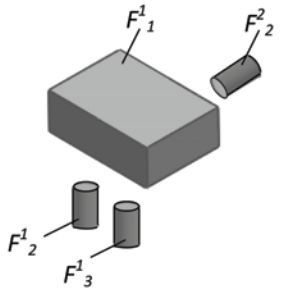
Axis - Absolute    I =   0.000000000
               J =   0.000000000
               K =  -1.000000000
```

shown in Figure 1(c), material removal starts at an *external face* and this face is termed as a *reference face* R^1_1 (Here, R^p_i is used to represent an ith reference face along p^{th} projecting direction). As it is assumed that material is removed in terms of primitive features, *reference face* can be only of rectangular or circular shape. The *reference face* R^1_1 is projected along the *projection direction* P_1 as shown in Figure 2(b) onto the nearest parallel face(s). As the material removal ends here for that stage, the resulting area(s) is marked as a *working face* W^1_1. In general, for a primitive feature, a reference face, all external faces connected to the reference face and working face (only if the working face is an external face of delta volume) are taken as processed faces. In the present case, primitive feature F^1_1 has only a reference face and hence the *reference face* R^1_1 is the processed face f^1_{r1}. An ith processed face along a pth projection direction is represented by notation f^p_i and if such face is also a reference face, it is represented by f^p_{ri}. Since the working face W^1_1 is not the last plane of the delta volume in that direction, overlap between *reference face* and *working face* areas is checked. The shaded area now represents a new face (f^1_{r2} in Figure 2(b)) on the intermediate workpiece shape at which the material removal for the next stage starts. Conceptually, this face is taken to lie on the intermediate workpiece shape and hence it also serves as a *reference face* R^1_2 for primitive feature F^1_2. Again, the process is repeated till the last plane along that direction in the delta volume is reached. As the *working face* W^1_2 corresponding to *reference face* R^1_2 is the last plane in the delta volume, the primitive feature F^1_2 is the last feature in that projection direction. The reference face R^1_2 is the processed face (f^1_{r2} in Figure 2(b)) for representing the feature F^1_2. The projection direction P_1 is taken as probable TAD for the features recognized along that direction. However, after all the features are recognized, all these probable TADs are evaluated and only those that are feasible are considered (explained in section 3.4). Details of obtaining working face and finding the plane equation of new face after projection are given in Appendix-A2 and A3.

Figure 7. Recognizing face-bounds and multiple face-bounds: (a) Face processing for delta volume-2 of example part model in Figure 1. An example part: (a) part model; (b) initial rawstock; and (c) delta volumes 1(a) by projecting along P_1, P_2, P_3 and combining features; and (b) Manufacturing features recognized – a blind-slot [F^1_1]and three blind-holes [F^1_2, F^1_3, F^2_2]



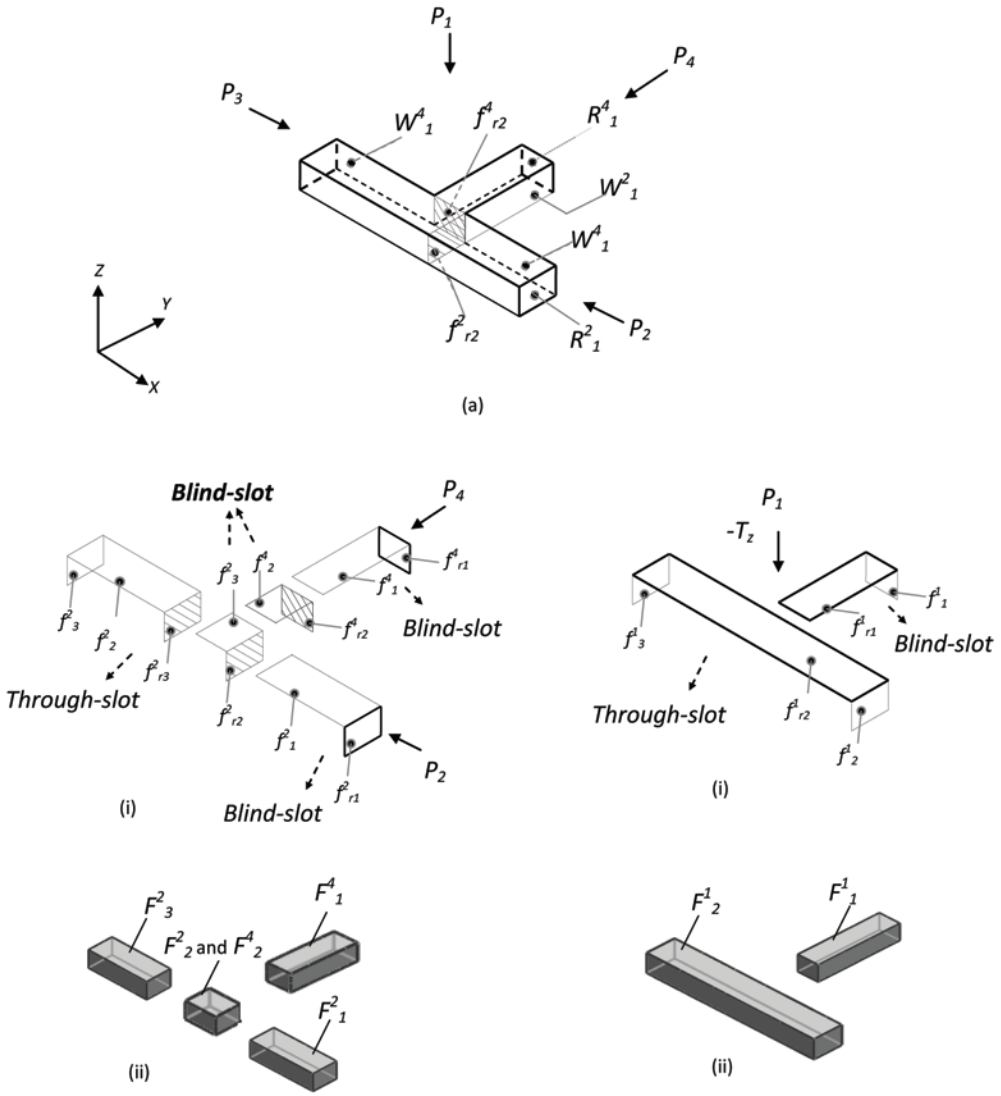
(a)



(b)

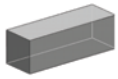
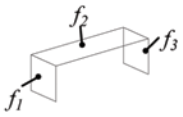
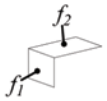
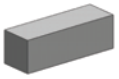
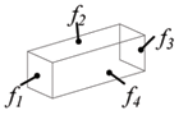
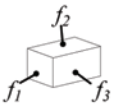
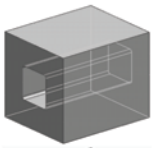
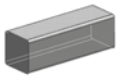
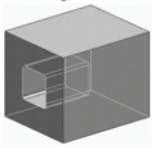
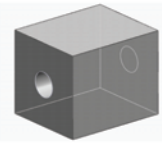
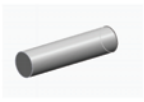
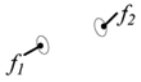
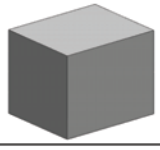
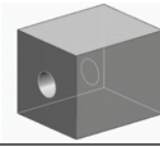
While considering delta volume-2, it may be noted from Figure 7(b) that two 'face bounds' are obtained on working face along the projection direction P_1 and one face bound is present on the working face along P_2. The 'face-bounds' encountered along a projecting direction in a delta volume are directly taken as processed faces (e.g. f^1_{r2},f^1_{r3} and f^2_{r2} in Figure 7(b)). Figure 8(a) shows

Figure 8. Splitting faces and avoiding feature repetitions: (a) Possible projections for delta volume-3 of example part model in Figure 1(a); (b) (i) Considering features from two projecting directions P2 and P4 (ii) identifying repeated recognition of blind-slot [F^2_2 and F^4_2]; and (c) Projection along P1: (i) splitting the external face into two faces [f^1r1 and f^1r2] (ii) obtained manufacturing features, a blind-slot [F11] and a through-slot [F^1_2]



the delta volume-3 (Figure 1(c)) with different projection directions, namely P_1, P_2, P_3 and P_4. The projection directions P_2 and P_3 result in same set of processed faces and hence projection is carried out only along one of these directions, namely P_2, to arrive at seven processed faces as shown in Figure 8(b). Similarly, 4 processed faces are obtained along P_4. If the external face is not of rectangular shape in any projection direction, then it must be split into least possible number of

Figure 9. Feature shapes and their Attributed Adjacency Matrices

Manufacturing feature	Rawstock	3D model of the feature	Delta Volume	Faces of delta volume lying on rawstock	Attributed Adjacency Matrix
Through-Slot					f_1 f_2 f_3 C f_1 0 1 0 1 f_2 1 0 1 2 f_3 0 1 0 1
Blind-Slot					f_1 f_2 C f_1 0 1 1 f_2 1 0 1
Through-Step					f_1 f_2 f_3 f_4 C f_1 0 1 0 1 2 f_2 1 1 0 1 3 f_3 0 1 0 1 2 f_4 1 1 1 0 3
Blind-Step					f_1 f_2 f_3 C f_1 0 1 1 2 f_2 1 0 1 2 f_3 1 1 0 2
Through-Pocket					f_1 f_2 C f_1 0 0 0 f_2 0 0 0
Blind-Pocket					f_1 C f_1 0 0
Through-Hole					f_1 f_2 C f_1 0 0 0 f_2 0 0 0
Blind-Hole					f_1 C f_1 0 0

rectangular faces. Along the projection direction P_1, two rectangular faces are obtained and the projection is carried out for each of these faces which result in five processed faces as shown in Figure 8(c).

3.4. Feature Recognition

The attributed adjacency matrix of the processed faces is used for feature recognition. If two faces have a common edge then the adjacency count

*Table 1. Feature recognition criteria *Rameshbabu and Shunmugam (2008)*

Manufacturing feature	Number of faces	Recognition criterion
Through-Slot	3	*C(1)=2* and *C(2)=1**
Blind-Slot	2	*C(1)=2**
Through-Step	4	*C(2)=2* and *C(3)=2**
Blind-Step	3	*C(2)=3**
Through-Pocket	2	*C(0)=2**
Blind-Pocket	1	*C(0)=1**
Through-Hole	2	*C(0)=2* and edges are circular
Blind-Hole	1	*C(0)=1* and edge is circular

C(x) = n; where *x* = adjacency count-value *n*= number of faces with adjacency count-value as *x*

between them is given as '1' else it is given as '0' based on which the total adjacency count '*C*' of each face is obtained. As the manufacturing features considered here in terms of primitive features, rules are formed for recognizing them based on the number of processed faces and their respective adjacency counts. For example, from the adjacency matrix shown in first row of Figure 9, it can be inferred that if the number of the faces are '3' and two of the faces have an adjacency count of '1' i.e. *C(1)=2* and one face has an adjacency count of '2' i.e. *C(2)=1*, then it can be recognized as a through-slot. A set of typical manufacturing features along with adjacency matrix of the processed faces and recognition criteria are given in Figure 9 and Table 1 respectively.

Considering delta volume-1 of example part shown in Figure 1(a), two processed faces, f^1_{r1} and f^1_{r2}, are formed (Figure 2(c)) and corresponding AAMs obtained are shown in Figure 2(d). From the recognition criterion *C(0) =1* given in Table 2, these are recognized as blind-pockets and corresponding manufacturing features in terms of primitive features are marked as F^1_1 and F^1_2 for easy identification. For delta volume-3, along the projection direction P_2, two blind-slots F^2_1 and F^2_2 with processed faces as (f^2_{r1}, f^1_1) and (f^2_{r2}, f^2_3) respectively are recognized as shown in Figure 8(b). Also the processed faces f^2_{r3}, f^2_2 and f^2_3 lead to recognition of feature F^2_3 as a through-slot. Only two blind-slots (F^4_1, F^4_2) are recognized along P_4 and the features F^2_1 and F^2_3 are not recognized. Since the external faces from where the projections start are mutually perpendicular and non-adjacent, all the features in the delta volume-3 could be taken together. However, a blind-slot will be recognized twice (F^2_2 and F^4_2) as shown in Figure 8(b). Since the processed faces f^2_{r2} and f^4_{r2} are mutually perpendicular and adjacent to each other, any one of the features F^2_2 and F^4_2 can be omitted. Figure 8(c) shows blind- slot F^1_1 and through-slot F^1_2, along projection direction P_1. Similarly, in delta volume-2, the features recognized along P_1, P_2 and P_3 are considered together and the features, including those from all the face-bounds f^1_{r2}, f^2_{r3} and f^2_{r2}, in delta volume are recognized as a blind-step F^1_1 and three blind-holes, F^1_2, F^1_3 and F^2_2 as shown in Figure 7(b).

For interacting features in a delta volume, different projecting directions may result in different set of features, leading to multiple interpretations, all of which are equally valid (Tseng & Joshi, 1994). However, an interpretation may exist which can optimize an objective function like 'less machining time'. Arriving at this optimal interpretation is possible by taking other inputs such as machine tools used, machining practice adopted, fixture plan, available tools etc. (Woo & Sakurai, 2002). In the present work, for sake of simplicity, an interpretation with minimum

Table 2. Case Study-Hand Spike (Figure 12 (a))

(a) List of features recognized with datum information and necessary operations						
Raw face/ feature (id)	**TAD**	**Geometrical Tolerance** type, value (in mm)	**Datum face/ feature id**	**Operations required**	**Fillet/Round edges' attributes from ACM**	**Additional operations required for fillets/ rounded/sharp edges**
Raw face (A)(*1*)						
Through-hole (B)(*2*)	$-T_z$, T_z	Perpendicularity, 0.05	A(*1*)	Drilling, Reaming	S	-
					S	-
Blind-hole(*3*)	$-T_z$	Positional, 0.05	B(*2*)	Drilling, Reaming	S	-
					S	-
Blind-hole(*4*)	$-T_z$	Positional, 0.05	B(*2*)	Drilling, Reaming	S	-
					S	-
Blind-hole(*5*)	$-T_z$	Positional, 0.05	B(*2*)	Drilling, Reaming	S	-
					S	-
Through-hole(*6*)	$-T_z$, T_z	-	-	Drilling Reaming	S	-
					S	-
Through-Pocket (*7*)	$-T_z$, T_z	-	-	Pocket milling	S,(1,0,0)	-
					S,(0,1,0)	-
					S,(1,0,0)	-
					S,(0,1,0)	-
					F,(0,0,1)	End milling
					F,(0,0,1)	End milling
					F,(0,0,1)	End milling
					F,(0,0,1)	End milling
					S,(1,0,0)	-
					S,(0,1,0)	-
					S,(1,0,0)	-
					S,(0,1,0)	-

(b) Grouping of features based on priority rule 2		
Datum and its TAD	Features associated with this datum	Features with this TAD (with no other constraints)
A, $-T_z$	*2*	
2, $-T_z$	*3,4,5*	*6,7*

(c) Setup and operations sequence plan			
Setup no.	TAD	Datum	Sequence of Operations (Feature no.-operation)
Setup 1	$-T_z$	A*(1)*	*2*-Drilling, *2*-Reaming
		B(*2*)	*3*-Drilling, *3*-Reaming, *4*-Drilling, *4*-Reaming, *5*-Drilling, *5*-Reaming
			6-Drilling, *6*-Reaming, *7*-Pocket milling, *7* F(0,0,1)-End milling, *7* F(0,0,1)- End milling, *7* F(0,0,1)- End milling, *7* F(0,0,1)- End milling

number of features for the delta volume-3 (Figure 8(c)) is adopted. In case of interpretations having equal number of features, any one of them can be chosen.

For each recognized feature, along with the projection direction, all the normals of its processed faces are taken as additional probable TADs. These are evaluated for 'feasible TADs' by checking if each or a combination of them can give all desired edges in the feature. For example, if P_4 is taken as a TAD for the blind-slot feature recognized along the same direction in Figure 8(b), then fillets are bound to form due to tool radius. However, the sharp edges desired here can be obtained in the next step by using its additional TAD along the direction P_1. If there is no such additional TAD that can give these sharp edges, then P_4 is considered as an infeasible TAD. The identified feasible TADs are then carried along with the features to the next module. If none of the probable TADs are feasible, the feature is recognized as invalid feature that cannot be machined.

3.5. Face Processing in Presence of Edge-Features

Face processing explained in the earlier section is suitable for delta volumes having all faces with sharp edges. However, presence of features such as fillets, undercuts, chamfers, rounded edges or corners, will result in cylindrical or toroidal or spherical or conical surfaces connected to planar faces. Face processing of such delta volumes will be very complex. To simplify, all the edge-features in the delta volume are recognized first and then the faces are modified appropriately so that the surfaces corresponding to edge-features are eliminated and all edges are made sharp. This delta volume with sharp edges is now taken up for face processing followed by feature recognition.

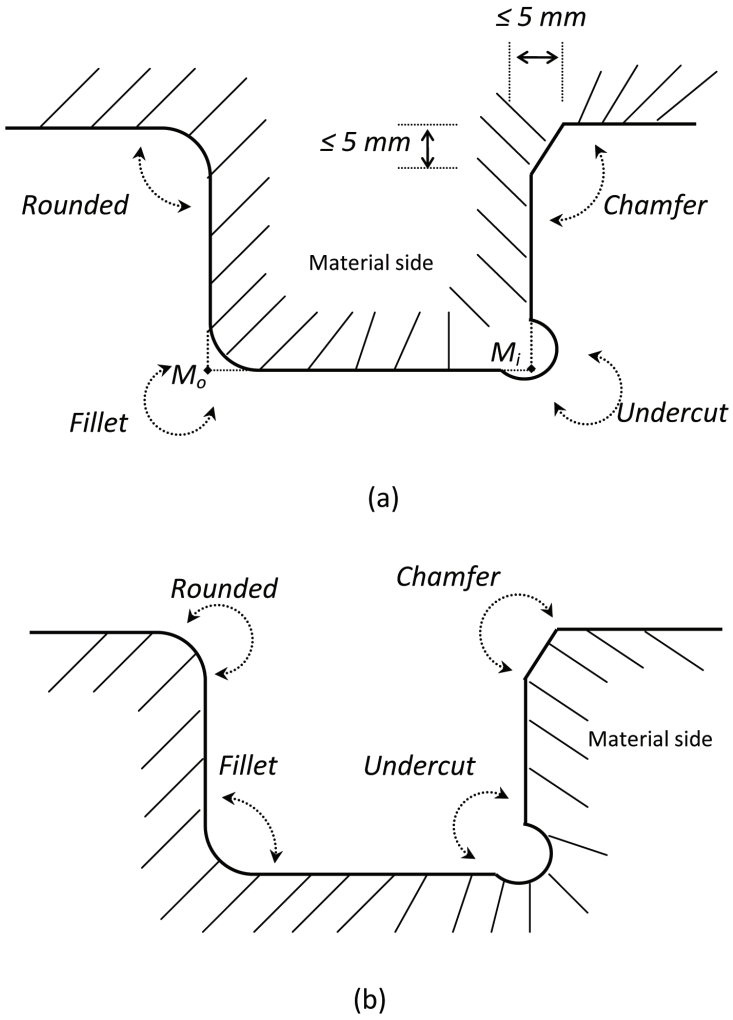
The information about the recognized edge-features is retained till the manufacturing features are found. It is then used for developing an Attributed Connectivity Matrix (ACM) for each manufacturing feature. Recognizing the edge-features in delta volume and development of ACM is explained in the following section.

3.6. Attributed Connectivity Matrix for Features

Apart from the usual attributed adjacency matrix, an attributed connectivity matrix is developed for each recognized feature to represent the fillet/undercut, rounded/chamfered or sharp edge between the faces. Information from ACM is used during planning stage to determine the additional operations, setups that may be required to get such edge-features. Building an ACM needs recognition of edge-features from the delta volume along with their absolute directions. Figure 10(a) and Figure 10(b) give an illustration of edge-features in the delta volume and the original part model respectively. Assuming that the example part model shown in Figure 1(a) is filleted, rounded and chamfered edges, a delta volume-2 shown in Figure 11(a) is obtained. Edge-features, including sharp edges, between two planar faces in a delta volume are recognized by following criteria.

- A sharp edge *(S)*; if faces share a common edge.
- A filleted edge *(F)*; if faces are convex with a common cylindrical surface and edges of the faces meet at an imaginary point 'M_o' falling outside the delta volume as shown in Figure 10(a) (details given in Appendix A4). These faces actually represent a filleted edge in the original model as shown in Figure 10(b). Figure 11(a) shows a filleted edge between faces fd_3 and fd_4 in the delta volume.
- An undercut edge *(U)*; if faces are convex with a common cylindrical surface and edges of the faces meet at an imaginary point 'M_i' falling inside the delta volume as shown in Figure 10(a).

Figure 10. Illustration of fillet/undercut and rounded/chamfer edges: (a) in delta volume; and (b) in original 3D model



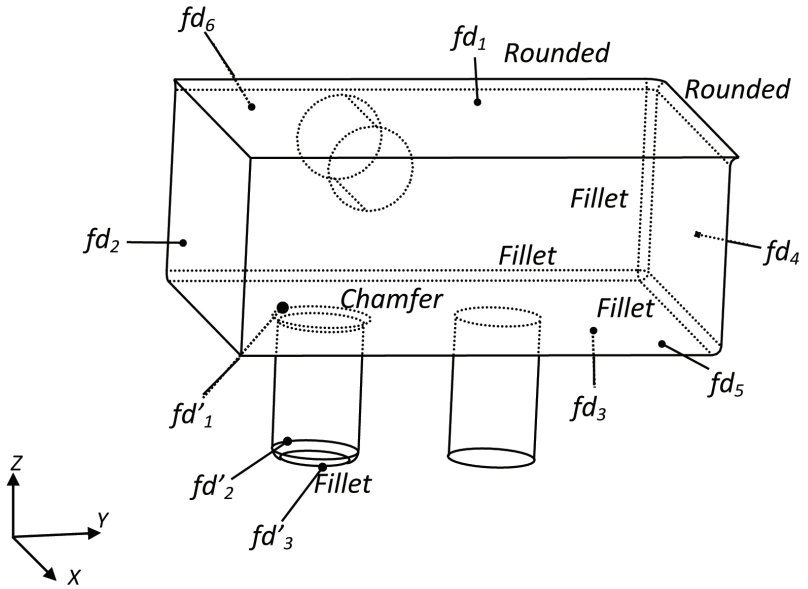
- A rounded edge *(R)*; if faces are concave with a common cylindrical surface. These faces represent a rounded edge in the original model as in Figure 10(b). A rounded edge between faces fd_1 and fd_6 in the delta volume is shown in Figure 11 (a).
- A chamfered edge *(C)*; if faces are concave and share an inclined planar face whose horizontal and vertical projection lengths are not greater than 5 mm. (Here, chamfers are assumed to have a maximum width of 5 mm)

There is no need to recognize corners at which three planar faces meet, as edge-features determine whether a sharp, toroidal or spherical corner is obtained.

For features with circular cross-section, the delta volume will have two circular planar faces with a cylindrical surface in between. For such volumes the edge-features, including sharp edge, are recognized by following criteria.

- A sharp edge *(S)*; if radii of cylindrical surface and circular face are equal.

Figure 11. Attributed Connectivity Matrix (ACM): (a) delta volume-2 of example part shown in Figure1 [assuming that the model has filleted, rounded and chamfered edges for illustration purpose]; (b) ACM for the filleted and rounded blind-step; and (c) ACM for the filleted and chamfered blind-hole



(a)

	fd_1	fd_2	fd_3	fd_4	fd_5	fd_6
fd_1	-	S, (1,0,0)	-	R, (1,0,0)	S, (0,1,0)	R, (0,1,0)
fd_2	S, (1,0,0)	-	S, (1,0,0)	-	S, (0,0,1)	S, (0,0,1)
fd_3	-	S, (1,0,0)	-	F, (1,0,0)	S, (0,1,0)	F, (0,1,0)
fd_4	R, (1,0,0)	-	F, (1,0,0)	-	S, (0,0,1)	F, (0,0,1)
fd_5	S, (0,1,0)	S, (0,0,1)	S, (0,1,0)	S, (0,0,1)	-	-
fd_6	R, (0,1,0)	S, (0,0,1)	F, (0,1,0)	F, (0,0,1)	-	-

(b)

	fd'_1	fd'_2	fd'_3
fd'_1	-	C	-
fd'_2	C	-	F
fd'_3	-	F	-

(c)

- A fillet edge *(F)*; if radius of cylindrical surface is greater than that of the circular face with a toroidal surface in between. As an example, a filleted edge between cylindrical surface fd'_2 and circular face fd'_3 in the delta volume is shown in Figure 11(a).
- A rounded edge *(R)*; if radius of cylindrical surface is less than that of the circular face with a toroidal surface in between.
- A chamfered edge *(C)*; if radius of cylindrical surface is less than that of the circular face with a conical surface in between. Figure 11(a). shows a chamfered edge be-

tween cylindrical surface fd'_2 and circular face fd'_1 in the delta volume.

In addition to the type of the additional feature, its absolute direction is also determined. For example, in Figure 11(a), faces fd_4 and fd_6 are connected with a filleted edge along the Z-axis and the direction is identified as (0,0,1). No such direction is determined if the edges are circular.

After the manufacturing features are obtained, the information about the type of edge-feature and its direction found from the pairs of faces in delta volume is assigned to respective faces of the manufacturing features. Such an assignment gives a matrix called Attributed Connectivity Matrix (ACM) for each manufacturing feature with a cell for each pair of faces. The order of this matrix is the total number of faces of that feature and cells are filled only if two faces are adjacent to each other. Each cell holds two attributes representing the type of edge-feature and its direction. However, a cell in ACM of circular cross section manufacturing features holds only one attribute, namely edge-feature type. Figure 11(b) and 11(c) show the ACMs developed for blind-step and blind-hole features respectively obtained from delta volume shown in Figure 11(a).

3.7. Associating GD&T Data to the Features

As GD&T data is being extracted separately (explained in section 3.2), it is associated with the manufacturing features recognized earlier for effective use. This is done by matching the coordinate data of the placement of the leader line of each tolerance feature control frame on to faces of features or on to rawstock model faces that represent datums.

The final output from the first module will be

- Manufacturing features with direction of each edge
- Tool approach direction(s) for each feature
- Edge-features for manufacturing feature, if any
- Datum information from GD&T data, if any

4. SETUP PLANNING AND OPERATION SEQUENCING

All the recognized manufacturing features and datums extracted in the previous module are used here to arrive at the setup and sequence plan. Utmost priority has to be given to the datums, as setup plan and operation sequence are dependent on it (Zhang et al., 2001). Setup planning and operation sequencing is carried out in various stages as shown in Figure 5, following different criteria and priority rules which is explained in the following subsections.

4.1. Determining the Set of Operations Required for Each Feature

For sequencing, the set of operations required to machine each manufacturing feature are to be determined. Here a 3-axis vertical machining center is assumed as the machine tool used. The operations such as slot-milling, step-milling, pocket-milling and drilling and reaming are selected based on the type of the manufacturing feature (Patil & Pande, 2002). Additional operations are to be chosen for machining of edge-features. It is discussed in the following section.

4.2. Effect of Presence of Edge-Features

Typical industrial parts will have edge-features to strengthen the part, to avoid sharp edges or to reduce stress concentration in the part. If these features are present in the part model, they can be termed as intended edge-features. Edge-features may also arise due to tool radius, though not in-

tended. Such features can be termed as unintended edge-features. Appropriate machining operations have to be carried out to get the intended edge-features and avoid unintended ones.

The direction of the edge-feature obtained from ACM is compared with tool approach direction to arrive at the additional machining operations needed for edge-features as explained in the following sub-sections. In case of circular cross-section feature, its axis direction is used.

4.2.1. Case I: Tool Approach Direction is Parallel to Edge-Feature Direction

a. **Fillet/undercut edge-feature:** A fillet with direction parallel to TAD may be machined with appropriate tool-radius or by an additional end milling operation using an appropriate ball-nosed tool. The undercuts also require additional end-milling operations with special undercut tools.
b. **Round/chamfer edge-feature:** These edge-features require an additional operation to smoothen/chamfer the edges by appropriate tools like peripheral milling cutter and c-shaped cutter.
c. **Sharp edge:** These can be obtained only if such an edge is between two convex faces of the part model; else fillets are bound to form due to the tool radius and need an additional operation to remove them. Removal of such unintended fillets also needs a change in the setup along other feasible TAD(s) of that manufacturing feature.

4.2.2 Case II: Tool Approach Direction is Perpendicular to the Edge-Feature Direction

a. **Fillet/undercut edge-feature:** For obtaining these kinds of fillets, initially material is to be removed till the start of the fillet. The remaining material can be removed with an appropriate tool that can give desired fillet. For undercuts, additional operations with special undercut tools have to be carried out.
b. **Round/chamfer edge-feature:** These edge-features need an additional operation to smoothen/chamfer the sharp edge by an appropriate tool like ball-nose end mill and c- shaped cutter.
c. **Sharp edge:** These sharp edges can be obtained without any additional operations.

4.3. Criteria for Grouping Features into Setups

The manufacturing features, including edge-features, which are recognized and associated with datum, are grouped for different setups. Only the geometric tolerances associated with two or more features like parallelism, perpendicularity, positional, coaxiality, symmetry, circular runout, total runout and profile tolerances with a datum (profile of a line and profile of a surface) are considered for setup planning, as these are influenced by the setup plans (Rong et al., 2005). Grouping of manufacturing features into a setup is done based on the criteria like features having a common datum reference frame or a common datum. If the features are not associated with any datum, grouping is done based on a common TAD. Following the above criteria, the features are grouped into setups with the following priority rules.

1. Features are grouped first such that each group has a common datum.
2. Other features having any one or more of the grouped features as datum and having same TAD are also added to the respective groups.
3. If TAD of remaining features coincides with TAD of any groups, the features are added to the respective group.
4. If the features are not grouped even after the third step, all the remaining features are grouped only on the basis of TAD.

Application of priority rules for grouping of features is explained with reference to a case study considered in section 5.

4.4. Criteria for Sequencing the Setups

After grouping the features, setups are sequenced. Highest priority is given to setups containing manufacturing features with tolerance relationships. The sequencing of setups is also followed in the same order as the priority rules listed in the previous section. Considering the fourth priority rule (of section 4.3), if different setup groups are present with different TADs, then they are sequenced in ascending order of number of manufacturing features present in each setup to avoid instability problems (Gaoling et al., 2005).

4.5. Criteria for Sequencing the Features in a Given Setup

After sequencing the setups, the manufacturing features, including edge-features, in each setup are sequenced. All the manufacturing features that are associated with geometric tolerances are to be machined first. This allows the immediate inspection against the specified tolerance, if desired, before going for the next operation. If manufacturing features in a setup are associated with a geometric tolerance with a datum, then datum feature is machined first. Based on the above criteria the features in a given setup are sequenced with following priority order:

1. Datum feature followed by its associated feature
2. Interacting features in the same order as obtained during feature recognition along a projection direction
3. Features that require similar machining operations

4.6. Criteria for Sequencing the Operations of a Feature or Features of the Same Setup

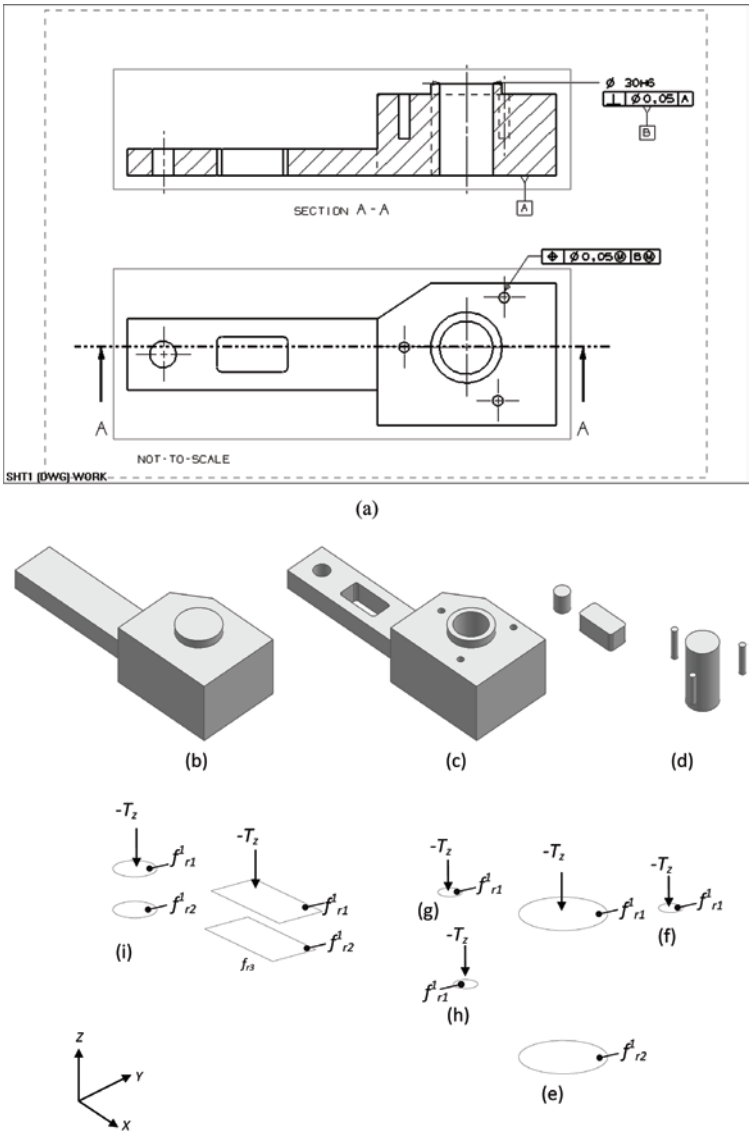
In this stage of sequencing, the operations of single feature or set of features in a given setup are sequenced. For a given feature roughing operations (e.g. drilling) are carried out first, followed by finishing operations (e.g. reaming). If a set of similar features in a feature sequence do not have any geometric tolerance constraints, then their operations can be combined so that all of their roughing operations are carried out together followed by their finishing operations. The machining of intended edge-feature is taken as final operation.

5. RESULTS AND DISCUSSION

A hand-spike part (Irani et al., 1995; Bhaskar Reddy et al., 1999) is modified as shown in Figure 12(a) and this example part is taken as a case-study to explain the implementation and results of the proposed system. The figure also includes the GD&T information of the part. Figure 12(b) and Figure 12(c) show the pre-shaped body of the rawstock that is taken for machining and the final shape of the hand spike respectively. The resultant delta volume obtained is shown in Figure 12 (d) and processed faces are shown in Figure 12(e)-(j). Fragment of STEP AP-203 file of the delta volume is shown in Appendix B.

a. gives the details of the recognized manufacturing features along with datum information (labeled from *1-7* for explanation), the edge-features obtained from attributed connectivity matrices and the operations required along with the additional operations for obtaining edge-features. The symbol T_z indicates a possible tool approach direction along the positive Z-direction. Since, model

Figure 12. Case study-Modified Hand spike: (a) part drawing; (b) initial rawstock; (c) final 3D model; (d) delta volumes; [(e)-(j)] processed faces(enlarged views) considered for feature recognition; (e) Through-hole[2]; (f) Blind-hole[3]; (g) Blind-hole[4]; (h) Blind-hole[5]; (i) Through-hole [6]; and (j) Through-pocket[7]



entities numbered as 2 and 6 are through-holes and 7 is a through-pocket, they have two possible tool approach directions – one along positive Z-direction (T_z) and another along negative Z-direction ($-T_z$). Hence, these entities are given two symbols as tool approach directions. The edge-features of each manufacturing-feature are registered according to the order in which they are read from the data structure. In Table 2(a), the lines of filleted edges correspond to the feature through-pocket (7) which does not

have any geometric tolerances or a datum associated with it. For sake of clarity, all the empty fields in the table are filled with a hyphen mark.

The priority rules applied for grouping features into a setup, results in grouping as given in Table 2(b). Using rule-1 and 2, the manufacturing feature through-hole *2*, has a datum of face 'A'(*1*) and this through-hole itself is a datum (B) for other three blind-holes *3, 4, 5*. As both these datums have same TAD, these features are grouped into a setup. The remaining features, through–hole *6*, and through-pocket *7*, also have same TAD as that of the previous features without any datum constraints. Hence, these features are also grouped in the same setup, using rule-3. The order, in which edge-features are read, does not have any effect, as these features are grouped appropriately during grouping of features into setups as given in section 4.3.

While sequencing features, the through-hole *2*, is sequenced first as it serves as datum for the other three blind-holes, *3, 4* and *5*. The feature through-hole *6*, follows next as it requires similar machining operation. The remaining feature through-pocket *7*, and its edge-features follow next. Final feature sequence is given as *2*, *3, 4, 5, 6* and *7*.

During operation sequencing, operations (drilling and reaming) for through-hole *2*, are sequenced first as it has tolerance constraint and also that it serves as datum. The operations for blind-holes *3, 4, 5,* which also have tolerance constraints, follow next. This is followed by operations for through-hole *6*, and through-pocket *7* (pocket-milling followed by end-milling for edge-features), as per the respective occurrence in feature sequence. Table 2(c) gives the sequence of operations for all the manufacturing features including edge-features of the example part considered.

6. CONCLUSION

A feature recognition and datum extraction system for setup planning and operation sequencing has been developed, taking STEP AP-203 format for geometric CAD model data and native file for tolerance data as input. The manufacturing features are recognized explicitly by the feature recognition system which also considers the initial rawstock. As the features are being recognized from the delta volume faces that lie on the initial workpiece, the complexity is reduced and lesser number of faces are finally considered for recognition. The present feature recognition system is found to be efficient over the previous approaches that use graph-based methodology. The datum information, a major player in deciding a process plan, is also extracted automatically and associated with the respective features. Fillets/undercuts, rounded/chamfered edges and sharp edges that have a significant impact on setup plan and operations sequencing are also recognized explicitly in a simple way. The information obtained from current feature recognition system and the datum extraction module like the feature data, datum information, tool approach directions, the nature and direction of the edges, is being carried over efficiently to aid in the downstream application modules, namely setup planning and operation sequencing. Hence, the real intent of the feature recognition system developed is met which is vital in realizing any CAPP system. Finally the setup planning and operation sequence are carried out based on criteria and priority rules framed.

The present system was developed in PERL programming language on a Windows XP platform. The STEP files and GD&T data files were obtained from UG NX3® solid modeling package. STEP AP-203 data format was used in the current system. With the availability of AP-203 ed2 format that claims to give GD&T data, as may be the case in near future, the tolerance data extraction module can be avoided. It can be directly associated with the feature list with minor modifications in the

program. The current feature recognition system is limited to the features that can be represented in terms of the feature shapes shown in Table 1.

REFERENCES

Beg, J., & Shunmugam, M. S. (2002). An object oriented planner for inspection of prismatic parts-OOPIPP. *International Journal of Advanced Manufacturing Technology*, *19*, 905–916. doi:10.1007/s001700200103

Bhandarkar, M. P., & Nagi, R. (2000). STEP-based feature extraction from STEP geometry for agile manufacturing. *Computers in Industry*, *41*, 3–24. doi:10.1016/S0166-3615(99)00040-8

Bhaskara Reddy, S. V., Shunmugam, M. S., & Narendran, T. T. (1999). Operation sequencing using genetic algorithms. *International Journal of Production Research*, *37*(5), 1063–1074. doi:10.1080/002075499191409

Chiabert, P., Lombardi, F., & Orlando, M. (1998). Benefits of geometric dimensioning and tolerancing. *Journal of Materials Processing Technology*, *78*, 29–35. doi:10.1016/S0924-0136(97)00459-7

Faraj, I. (2003). Manufacturing features: Verification interaction accessibility and machinability. *International Journal of Production Research*, *41*(10), 2249–2272. doi:10.1080/0020754031000090630

Gaoling, P., Wenjian, L., & Xutang, Z. (2005). An Internet-based system for setup planning in machining operations. In *Proceedings of the 10th IEEE International Conference on Engineering of Complex Computer Systems* (pp. 245-251).

Gaoling, P., Wenjian, L., & Yuru, Z. (2005). Intelligent setup planning in manufacturing by fuzzy set theory based approach. In *Proceedings of the IEEE International Conference on Automation Science and Engineering* (pp. 130-135).

Gavankar, S. P., & Henderson, R. M. (1995). Graph based extraction of two morphological features from boundary representation. *Journal of Intelligent Manufacturing*, *6*, 401–413. doi:10.1007/BF00124066

Gibson, P., Ismail, H. S., & Sabin, M. A. (1999). Optimisation approaches in feature recognition. *International Journal of Machine Tools & Manufacture*, *39*, 805–821. doi:10.1016/S0890-6955(98)00068-6

Harun, W. A., & Case, K. (2000). Feature-based representation for manufacturing planning. *International Journal of Production Research*, *38*(17), 4285–4300. doi:10.1080/00207540050205091

Hoffman, M. C., & Joan-Arinyo, R. (1998). CAD and the product master model. *Computer Aided Design*, *30*(11), 905–918. doi:10.1016/S0010-4485(98)00047-5

Irani, S. A., Koo, H. Y., & Raman, S. (1995). Feature-based operation sequence generation in CAPP. *International Journal of Production Research*, *33*, 17–39. doi:10.1080/00207549508930135

Joshi, S., & Chang, T. C. (1988). Graph-based heuristics for recognitions of machined features from a 3D Solid model. *Computer Aided Design*, *20*(2), 58–66. doi:10.1016/0010-4485(88)90050-4

Kang, M., Han, J., & Moon, J. C. (2003). An approach for interlinking design and process planning. *Journal of Materials Processing Technology*, *139*, 589–595. doi:10.1016/S0924-0136(03)00516-8

Kannan, T. R., & Shunmugam, M. S. (2009). Processing of 3D sheet metal components in STEP AP-203 format. Part I: Feature recognition system. *International Journal of Production Research*, *47*(4), 941–964. doi:10.1080/00207540701510055

Khailash, S. B., Zhang, Y. F., & Fuh, J. Y. H. (2001). A volume decomposition approach to machining feature extraction of casting and forging components. *Computer Aided Design*, *33*, 605–617. doi:10.1016/S0010-4485(00)00107-X

Kim, Y. S., Wang, E., & Rho, H. M. (2001). Geometry-based machining precedence reasoning for feature-based process planning. *International Journal of Production Research*, *39*, 2077–2103. doi:10.1080/00207540110038513

Li, C. L., & Hui, K. C. (2000). Feature recognition by template matching. *Computers & Graphics*, *24*, 569–582. doi:10.1016/S0097-8493(00)00059-5

Lin, A. C., Lin, S. Y., & Cheng, S. B. (1997). Extraction of manufacturing features from a feature-based design model. *International Journal of Production Research*, *35*(12), 3249–3288. doi:10.1080/002075497194066

Liu, Z., & Wang, L. (2007). Sequencing of interacting prismatic machining features for process planning. *Computers in Industry*, *58*, 295–303. doi:10.1016/j.compind.2006.07.003

Nasr, E. S. A., & Kamrani, A. K. (2006). A new methodology for extracting manufacturing features from CAD system. *Computers & Industrial Engineering*, *51*, 389–415. doi:10.1016/j.cie.2006.08.004

Patil, L., & Pande, S. S. (2002). An intelligent feature-based process planning system for prismatic parts. *International Journal of Production Research*, *40*, 4431–4447. doi:10.1080/00207540210155855

Rahmani, K., & Arezoo, B. (2006). Boundary analysis and geometric completion for recognition of interacting machining features. *Computer Aided Design*, *38*, 845–856. doi:10.1016/j.cad.2006.04.015

Rameshbabu, V., & Shunmugam, M. S. (2008). Hybrid feature recognition method for setup planning from STEP AP-203. *Robotics and Computer-integrated Manufacturing*, *25*(2), 393–408. doi:10.1016/j.rcim.2007.09.014

Rong, Y., Huang, S. H., & Hou, Z. (2005). *Advanced computer-aided fixture design*. London, UK: Elsevier Academic Press.

Sakurai, H. (1995). Volume decomposition and feature recognition: Part 1-polyhedral objects. *Computer Aided Design*, *27*(11), 833–843. doi:10.1016/0010-4485(95)00007-0

Shah, J. J., & Mantyla, M. (1995). *Parametric and feature-based CAD/CAM*. New York, NY: John Wiley & Sons.

Tseng, Y., & Joshi, S. (1994). Recognizing multiple interpretations of interacting machining features. *Computer Aided Design*, *26*(9), 667–688. doi:10.1016/0010-4485(94)90018-3

Woo, Y., & Sakurai, H. (2002). Recognition of maximal features by volume decomposition. *Computer Aided Design*, *34*, 195–207. doi:10.1016/S0010-4485(01)00080-X

Zhang, C., Chan, K. W., & Chen, Y. H. (1998). A hybrid method for recognizing feature interactions. *Integrated Manufacturing Systems*, *9*(2), 120–128. doi:10.1108/09576069810202078

Zhang, Y. F., Hu, W., Rong, Y., & Yen, D. W. (2001). Graph-based set-up planning and tolerance decomposition for computer aided fixture design. *International Journal of Production Research*, *39*(14), 3109–3126. doi:10.1080/00207540110056171

Zhu, H., & Menq, C. H. (2002). B-rep model simplification by automatic fillet/round suppression for efficient automatic feature recognition. *Computer Aided Design*, *34*, 109–123. doi:10.1016/S0010-4485(01)00056-2

APPENDIX A

Mathematical Expressions Used in the Present Work

A1. Finding external faces on delta volume:

For any given face, the normal vector $\overline{N}$ is found by the cross product of its two edge vectors $\bar{i}$ and $\bar{j}$ as $\overline{N} = \bar{i} \times \bar{j}$. If a, b and c are the coefficients of the normal vector $\overline{N}$, the equation of the plane is obtained as $ax + by + cz + d = 0$. Here, d is found as $d = -(ax_0 + by_0 + cz_0)$, where (x_0, y_0, z_0) is a point on the face.

The external faces on delta volume are now found by checking the coplanarity of delta volume face with rawstock model face and checking for the existence of all the points of a face of delta volume on the rawstock model face.

A2. Finding working face from a reference face:

The distance between two parallel planes $ax + by + cz + d_1 = 0$ and $ax + by + cz + d_2 = 0$ is given by $|d_1 - d_2|$. During projection along a projecting direction, by getting the least distance, the nearest parallel face (working face) is found from a reference face.

A3. Finding plane equation of the new face:

When a new face is formed after projection, its plane equation is found by three-point plane equation form $\begin{vmatrix} x - x_1 & y - y_1 & z - z_1 \\ x_2 - x_1 & y_2 - y_1 & z_2 - z_1 \\ x_3 - x_1 & y_3 - y_1 & z_3 - z_1 \end{vmatrix} = 0$, where (x_1, y_1, z_1), (x_2, y_2, z_2) and (x_3, y_3, z_3) are three points on the face.

A4. Finding whether a point is inside or outside a circle

While finding whether imaginary point M_o falls inside or outside the delta volume, it is checked if it lies inside or outside of circular arc Figure 9(a). For this 'Power of point (P_p)' is found as $P_p = \overline{M_o O}^2 - r^2$ where, O is the center and r is the radius of the circle. If $P_p > 0$, then A lies outside the circle; If $P_p < 0$, then A lies inside the circle; If $P_p = 0$, then A lies on the circle.

APPENDIX B

Figure 13. Fragment of STEP AP 203 file of the delta volume of Case study part (Ssec.5)

```
ISO-10303-21;
HEADER;
FILE_DESCRIPTION();
FILE_NAME(..);
FILE_SCHEMA (('CONFIG_CONTROL_DESIGN'));
ENDSEC;
DATA;
...
#11=ADVANCED_BREP_SHAPE_REPRESENTATION('PAPER DV-NONE',(#127,#128,#129,#130,#131,#132),#629);
...
#127=MANIFOLD_SOLID_BREP('',#133);
#128=MANIFOLD_SOLID_BREP('',#134);
...
#133=CLOSED_SHELL('',(#158,#159,#160));
#134=CLOSED_SHELL('',(#161,#162,#163));
#135=CLOSED_SHELL('',(#164,#165,#166));
#136=CLOSED_SHELL('',(#167,#168,#169));
#137=CLOSED_SHELL('',(#170,#171,#172));
#138=CLOSED_SHELL('',(#173,#174,#175,#176,#177,#178,#179,#180,#181,#182));
...
#158=ADVANCED_FACE('',(#199),#183,.T.);
#159=ADVANCED_FACE('',(#200),#184,.F.);
#199=FACE_OUTER_BOUND('',#219,.T.);
#183=PLANE('',#397);
#219=EDGE_LOOP('',(#249));
#397=AXIS2_PLACEMENT_3D('',#546,#443,#444);
#443=DIRECTION('',(0.,0.,1.));
#444=DIRECTION('',(1.,0.,0.));
#249=ORIENTED_EDGE('',*,*,#343,.T.);
#343=EDGE_CURVE('',#317,#317,#377,.T.);
#377=CIRCLE('',#396,3.);
#317=VERTEX_POINT('',#545);
#545=CARTESIAN_POINT('',(67.4432974320939,16.9154773493539,46.));
...
GEOMETRIC_REPRESENTATION_CONTEXT(3)
...
ENDSEC;
END-ISO-10303-21;
```

APPENDIX C

Abbreviations

AAM – Attributed Adjacency Matrix
AAG – Attributed Adjacency Graph
ACM – Attributed Connectivity Matrix
TAD – Tool Approach Direction
GD&T – Geometric Dimensioning and Tolerancing

Nomenclature

$\mathbf{P}_p$ - p^{th} projection direction; p varies from 1 to maximum number of external faces
$\mathbf{R}^p_i$ - i^{th} reference face along p^{th} projection direction
$\mathbf{W}^p_i$ - i^{th} working face along p^{th} projection direction
$\mathbf{f}^p_i$ - i^{th} processed face along p^{th} projection direction – used for AAM
$\mathbf{f}^p_{ri}$ - i^{th} processed face, which is also a reference face, along p^{th} projection direction – used for AAM
$\mathbf{F}^p_i$ - i^{th} primitive feature along p^{th} projection direction
C(x) = n; C(x) - adjacency count-value; n - number of faces with adjacency count-value x
$\pm\mathbf{T}_i$ - tool approach direction along i ; i holds a value of x, y, z for X, Y, Z axes directions respectively
$\mathbf{fd}_i$ - i^{th} face of delta volume with cuboidal crossection - used for ACM
$\mathbf{fd'}_i$ - i^{th} face of delta volume with circular crossection - used for ACM

This work was previously published in the International Journal of Manufacturing, Materials, and Mechanical Engineering, Volume 1, Issue 2, edited by J. Paulo Davim, pp. 19-45, copyright 2011 by IGI Publishing (an imprint of IGI Global).

Chapter 7
Laser Sub-Micron Patterning of Rough Surfaces by Micro-Particle Lens Arrays

Ashfaq Khan
University of Manchester, UK

Zengbo Wang
University of Manchester, UK

Mohammad A Sheikh
University of Manchester, UK

Lin Li
University of Manchester, UK

ABSTRACT

Laser surface patterning by Contact Particles Lens Arrays (CPLA) has been widely utilized for patterning of smooth surfaces but there is no technique developed by which CPLA can be deposited on a rough surface. For deposition of CPLA, conventional techniques require the surface to be flat, smooth and hydrophilic. In this study, a new method for the deposition of CPLA on a rough surface is proposed and utilized for patterning. In this method, a hexagonal closed pack monolayer of SiO_2 spheres was first formed by self-assembly on a flat glass surface. The formed monolayer of particles was picked up by a flexible sticky surface and then placed on the rough surface to be patterned. A Nd:YVO_4 laser was used to irradiate the substrate with the laser passing through the sticky plastic and the particles. Experimental investigations have been carried out to determine the properties of the patterns.

INTRODUCTION

Within the last two decades research in novel manufacturing techniques on sub-micron, nano and even atomic scales has been accelerated by the increasing demand for miniaturized devices. Ever smaller devices can only be realized with modern precision manufacturing techniques which are also economical. With the reducing size of these devices surface patterning is also gaining more importance. Lasers have been extensively used for surface patterning at micron scale (Bäuerle, 2000; Hon et al., 2008; Pena et al., 2009). Laser is a tool which is widely utilized for manufacturing because

DOI: 10.4018/978-1-4666-1867-1.ch007

Copyright © 2013, IGI Global. Copying or distributing in print or electronic forms without written permission of IGI Global is prohibited.

of the advantages of being a non contact process, capable of generating complicated structures without the need of photomask and able to work in air, vacuum or water. These advantages have earned lasers a reputable position in the manufacturing industry. Moreover the laser can easily be focused down to a micrometer scale which makes it a tool of choice in the micro device fabrication.

Laser assisted Lithography is one of the commonly used industrial technique for submicron and nano production. However, lithography is also reaching its limit. Although smaller features can be generated by using F_2 157 nm and Extreme Ultra Violet lithography (EUV) but high resolution comes with the drawback of high cost, low output and unstable light intensity. Also these lasers need to carry the process in vacuum or high purity dry nitrogen because of the high absorption of the laser in air. Moreover there is a need of special reflective mirrors, and need very high power to achieve intensities suitable for lithography (Bjorkholm et al., 1990; Ito et al., 2000; Chong et al., 2009). These limitations have thus restricted the use of EUV for industrial production. Lithography techniques and their limitation have summarized by Ito et al. (Ito et al., 2000). The direct use of laser in sub-micron patterning is limited because of the fact that light cannot be confined to a lateral dimension smaller than half its wavelength called the diffraction limit of light (Abbe, 1873). However, this limitation can be overcome by utilizing near-field enhancement. Laser processing in the near-field has been successfully utilized to generate features with sizes smaller than 100 nm (Chong et al., 2009). Several techniques for utilizing the advantages of near-field have been developed including Near-field Scanning Optical Microscope (NSOM) patterning (Betzig et al., 1992; Chong et al., 2009), Plasmonic Lithography (Srituravanich et al., 2004; Liu et al., 2005; Chong et al., 2009) and Laser in combination with Scanning Probe Microscopy (SPM) for tip patterning (Chimmalgi et al., 2003; Chong et al., 2009; Miyashita et al., 2009), Microlens array (MLA) nanolithography.

In laser assisted NSOM method an optical fibre cone with a nano scaled output aperture diameter is used to transmit laser for surface processing in the near field region. The tip surface is coated with metal thin film for improved transmission of the fibre. The fibre tip can have output aperture diameter of about 50 nm. The process was utilized by Korte et al. (1999) to generate 200 nm wide and 100 nm deep groves on a Cr thin film by using a frequency tripled Femtosecond laser ($\lambda \sim 260$ nm) with an aperture size of 100 nm (Korte et al., 1999). The technique was used by Lieberman et al. to remove the manufacturing defects from a Cr thin film mask (Lieberman et al., 1999). Laser in combination with Scanning Probe Microscopy (SPM) is a modification of Scanning probe microscopy. In SPM a fine tip is scanned over the sample to be characterized and the morphology of the surface is recorded by the movement of the tip. In this method a laser is focused on a SPM tip. During laser irradiation the SPM tip acts as a source of near field enhancement. The high electric field in the near field region causes the material removal and generates nano features on the substrate surface. Grigoropoulos et al. use the technique with a femto-second laser to achieve spatial resolution down to 10 nm (Chimmalgi et al., 2003). The technique has the advantage/capability to fabricate complicated designs. Alphabets "DSI" abbreviation for Data Storage Institute were written by this technique in a space of 400 nm x 400 nm (Hong et al., 2003)

Micro Lens Array (MLA) patterning is a near field patterning technique which could be used to generate patterns over large area efficiently. The technique consists of micro lenses with same size and focal length fixed on a substrate. The lenses are arranged in a square or hexagonally packed structure. These micro lens arrays focus the laser into a series of parallel light spots. Each of the spots generates features on the substrate in the near field. The technique was used by Kato et al.

(2005) using a Femtosecond laser to generate arrays of 1600 "N" microletters with a thickness of 300 nm. By proper control of parameters and stage movement in 3D they also generated a self standing micro spring. However, these techniques share some common disadvantages. These techniques need to accurately control distances between the sample and the components in the range of zero to several hundred nanometres and thus require expensive and sophisticated equipment. In addition, they have a very low throughput because of their serial nature. Moreover, they require a smooth polished surface to start with. Thus, there is a need for a simple, high speed and economical patterning method to satisfy the industrial demands.

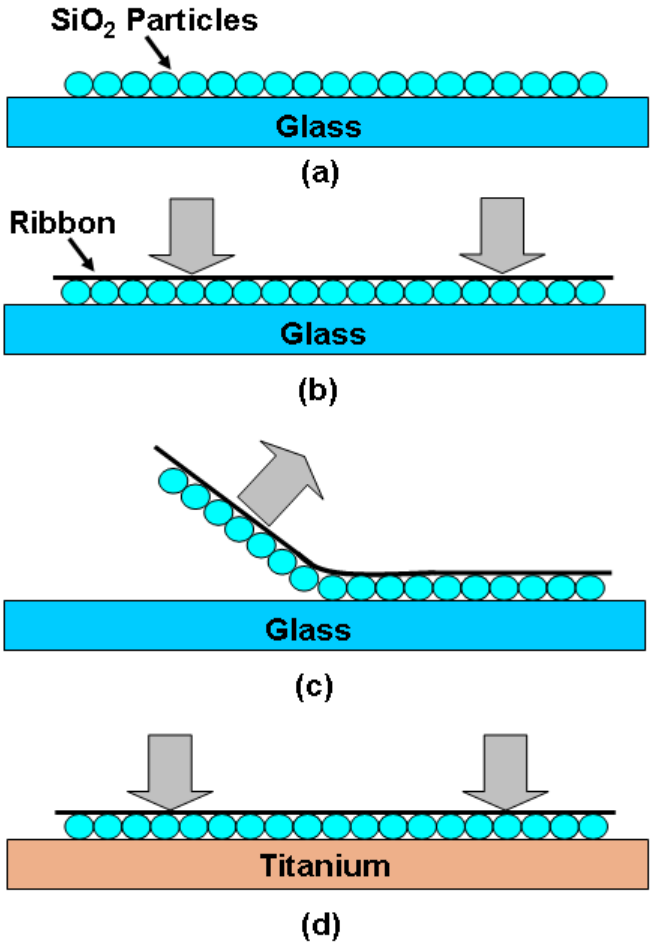
Laser assisted CPLA is a near-field technique which was introduced recently. The technique could generate features over large areas at a very high speed. The greatest advantage of the CPLA technique is that microns sized particles could be used to generate sub-micron and nano features. In this technique, a monolayer is formed on the surface of the substrate by drying an aqueous solution of the particles. During drying the particles arrange themselves into a hexagonal closed pack monolayer array under the self assembly (Denkov et al., 1992). The substrate with the monolayer CPLA is then scanned by a laser beam of a suitable wavelength. During laser irradiation laser interacts with the particles and generates high intensity evanescent waves in the near-field. The laser is thus effectively split into hundreds of high intensity spots with sub-micron or even nano-sized diameters, each generating a feature on the surface of the substrate. Several million similar patterns can be generated in a few seconds by this method (Guo et al., 2007).

Laser assisted CPLA patterning has got immense advantages but its applications are limited because the process can only be applied to ideal surfaces (i.e. flat, smooth and hydrophilic) (Burmeister et al., 1997, 1998). For patterning of a surface by micro particles, the surface needs to be perfectly polished so that the particles could form a monolayer array on it. To the best of authors' knowledge, there is no known method by which a monolayer array can be deposited on a rough surface. Polishing itself is an expensive and tedious job. In this work, the possibility of a rough surface for patterning with CPLA is demonstrated.

This paper reports a technique for generating a monolayer on a smooth surface and then transporting it to a rough surface by using a flexible, transparent sticky surface (referred to as the 'Ribbon'). Although attempts have been made nearly a decade earlier by Burmiester et al. (1997, 1998) to transport CPLA monolayer but the process required sophisticated equipment, was applicable only to polystyrene particles and patterning was not demonstrated. Recently a method for transporting monolayer was demonstrated and used for patterning but the process was only applicable to smooth and flat surface (O'Connell et al., 2010). In our earlier work, the proposed method was used to pattern curved surface (Khan et al., 2010).

For accurate modelling in the near field Particle on Surface (POS) model is used instead of Mie theory. Mie theory is the exact solution for the Maxwell equation for the excitation of arbitrary sphere under plan wave. Mie theory was developed independently by German Physicist Gustav Mie and Danish Physicist Ludwig Valetine Lorenz. However, the Mie theory is limited because it deals with the interaction of only single particle and does not take into account the electromagnetic interactions of the substrate with the particle. The POS theory was developed to describe the propagation of dipole interaction along a flat surface (Bobbert et al., 1986). The field distribution by the POS is quiet different because of the reflection and secondary scattering of the reflected radiations from the substrate. Simply put the substrate acts as a mirror which is coupled with and spherical resonator which results in an increase in the optical enhancement and decrease in the area of the field.

Figure 1. Schematic representation of the transfer of the particles (a) Monolayer on the surface of the glass (b) monolayer secured by the ribbon (c) monolayer is lifted by the ribbon (d) particles transferred to the rough surface



EQUIPMENT AND EXPERIMENTAL PROCEDURE

Materials and Equipment

A high purity titanium substrate was used as the rough surface (Ra~ 0.23 µm) to be patterned. Pure titanium has a melting point of ~1870 °C (Park et al., 2009) which is 480°C greater than one of the commonly used Stainless steel (Melting point of 316L ~1387 °C) (Wang et al., 2007).

The surface of titanium was too rough for the particles to form a monolayer array of particles by self-assembly. Silica Spheres (Bangs Laboratories, diameter $2a = 4.74$ µm, refractive index $\eta = 1.51$) are used for patterning. A Glass slide (Agar Scientific, soda lime microscope glass slide) was used as the smooth surface for the preparation of a monolayer array of particles.

A Diode pumped Nd:YVO_4 (Laserline - Laserval Violino, wavelength λ =532 nm, pulse duration τ =7 ns and repetition rate from 1 to 30 kHz, S-polarized) laser was used as the irradiation source.

The ribbon used for the transportation of particles array monolayer is a carefully chosen

flexible thin, transparent (to the laser at 532 nm) plastic (Biaxial oriented polypropylene, thickness 45 µm) with an adhesive resin (polyolefin) for firmly securing the particles monolayer array. The ribbon material was chosen to have maximum transmission at the laser wavelength and flexibility to conform to rough surface. The transmission spectrum of light for the transparent plastic was measured by a Spectrophotometer (Analytik Jena - Specord 250, 200-1100 nm).

A Scanning Electron Microscope (Hitachi High Technologies - S-3400N) was used for imaging the surface of the sample. A 3D optical Microscope (Alicona Infinite Focus) was used for measuring the depth of the patterns.

Glass Cleaning and Monolayer Preparation

The glass slides were first cleaned by soapy water and then sonicated in warm acetone and methanol for 10 minutes each, respectively. The samples were rinsed and treated by 30% Nitric Acid solution for 24 hours for making them hydrophilic. A solution of the particles diluted to an appropriate concentration was applied to the cleaned glass slide. The samples were finally rinsed with DI water and dried by flow of N_2 gas (Wang et al., 2008). A hexagonal closed pack monolayer of silica spheres was formed on the cleaned surface of a glass slide by self-assembly under room conditions. The glass slides were dried overnight which formed a perfect monolayer array of the particles.

Monolayer Transportation

The complete monolayer was picked up by the ribbon. The ribbon was placed perpendicularly from the top over the monolayer to secure the particles firmly at its positions and was then peeled off. Although the monolayer adhered strongly to the glass (Guo et al., 2008), the adhesion of the resin was sufficient to peel off the particles as a monolayer array. The flexible surface along with the particles was then carefully placed on the titanium rough surface to be patterned. Since the ribbon was flex-

Figure 2. Transmission spectrum of light for the ribbon

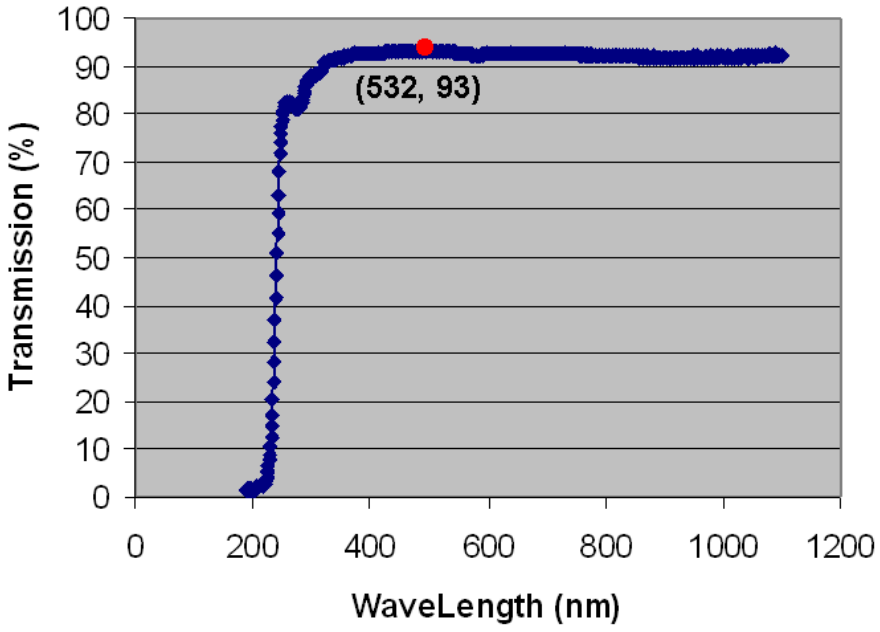
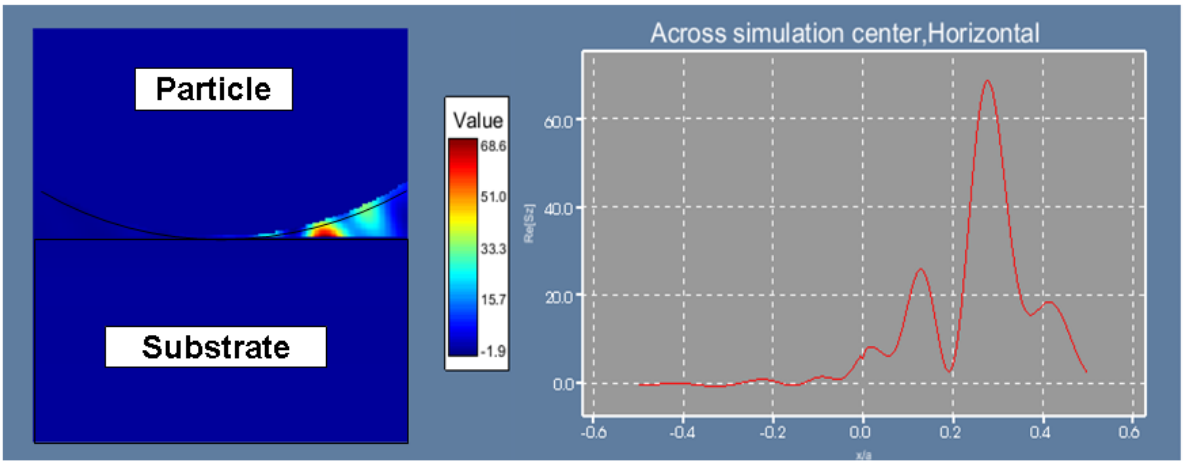


Figure 3. Calculated Poynting intensity distribution Sz for λ = 532 nm radiation under a SiO_2 sphere (n = 1.51) on a Ti substrate. The maximum field enhancement is about 68 times



ible, it followed the contours of the rough surface and the whole surface was covered by particles array. Schematic representation of the procedures developed for transfer of the particles from the smooth to rough surface is shown in Figure 1. The sample was then irradiated by the laser such that the laser passed through the flexible surface and was then focused by the particles monolayer array. The transmission spectrum of light for the ribbon, as measured by the Spectrophotometer, is shown in Figure 2.

RESULTS AND DISCUSSION

Particle on surface model (Extended Mie Theory) was used to calculate the optical near-field around the particle (Bobbert et al., 1986). FDTD (Finite Difference Time Domain) simulation was used to simulate the electromagnetic modes and evanescent modes; shown in Figure 3. A detailed explanation of the theoretical formulation can be found in work done earlier (Wang et al., 2004). It can be seen that the maximum field intensity is just outside the particle and decays rapidly along the incident path.

The roughness of the unprocessed surface of titanium is clearly visible in the SEM images shown in Figure 4a and 4b. At laser fluence higher than 0.379 J/cm^2 the ribbon was ablated by the laser and the melted plastic was deposited on the surface of titanium as shown in Figure 5a. However, at fluence below 0.379 J/cm^2 an optimum processing window was investigated. Under the reduced laser fluence, the ribbon was not damaged. The laser passed through the ribbon and was focused by the Contact particles. The intensity enhancement by the particles was found to be sufficient to pattern the titanium surface. Figure 5b to 5f shows the patterns generated on the rough surface of titanium by laser incident at 15 Degrees. An area of 1 cm^2 was scanned by the laser and good quality patterns were generated on the scanned area. Figure 5f shows the diameter of the features to be between 500 to 700 nm. Since a material with very high melting point has been patterned, the technique can be expected to work for materials with a wide range of melting points.

The depth of generated patterns was measured by a 3D optical imaging Microscope. In addition, to the depth, the true colour and the roughness of

Figure 4. SEM Images of Surface of Titanium before patterning

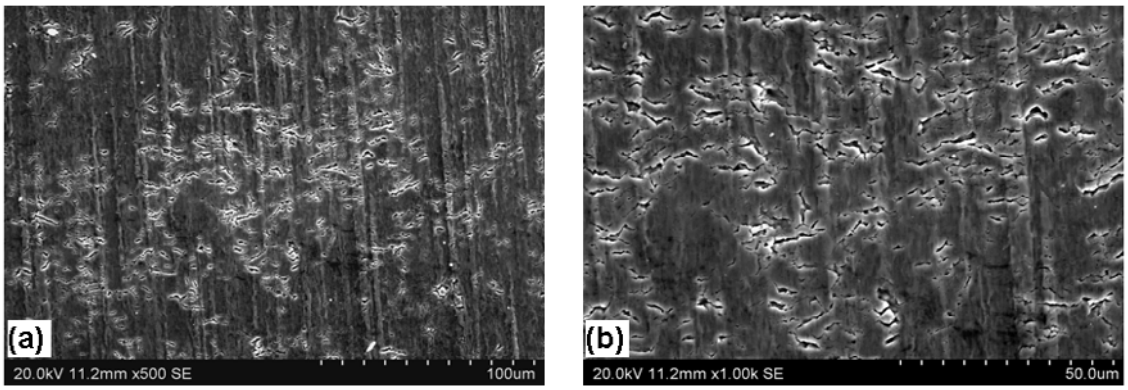


Figure 5. (a) SEM Images of debris from the ribbon on the surface of titanium. (b-f) SEM Images of patterns generated on the surface of Titanium

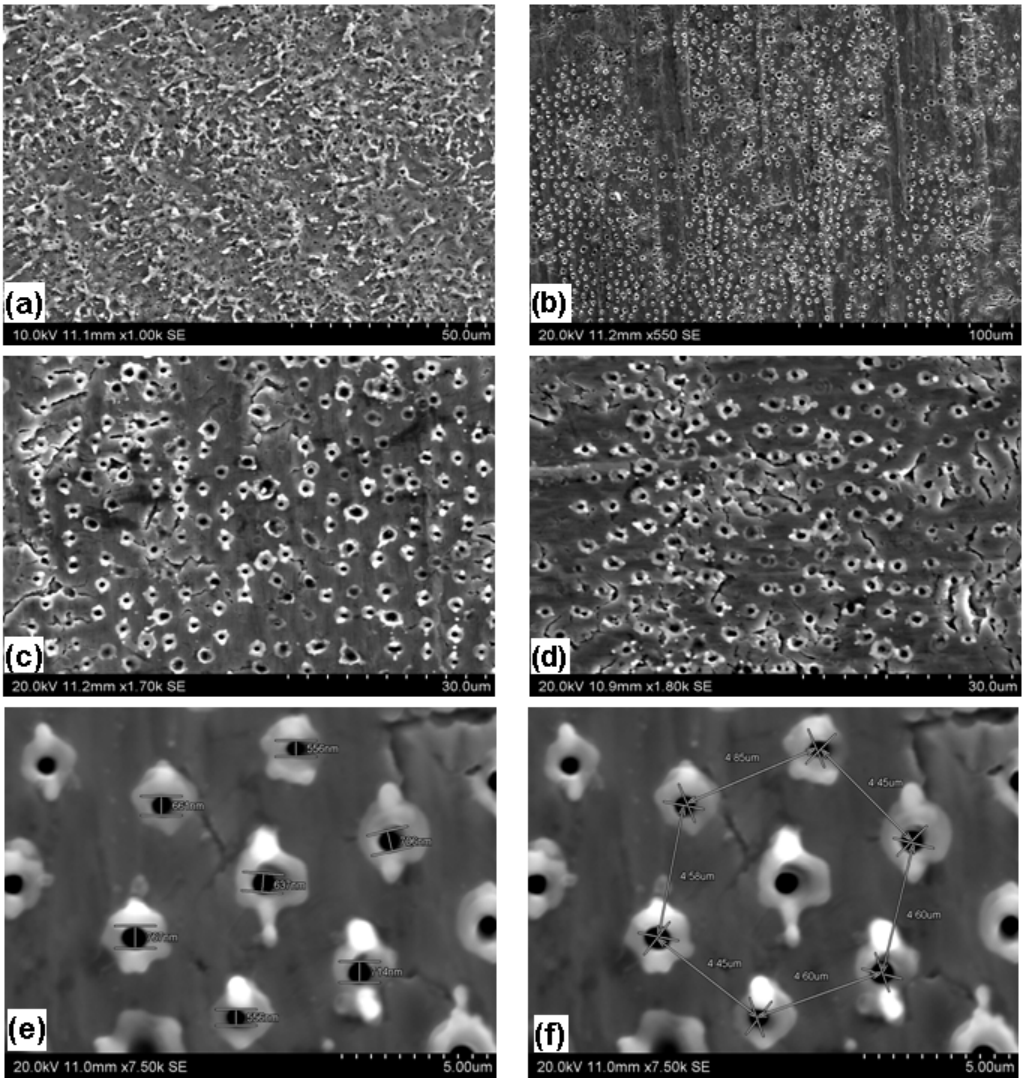
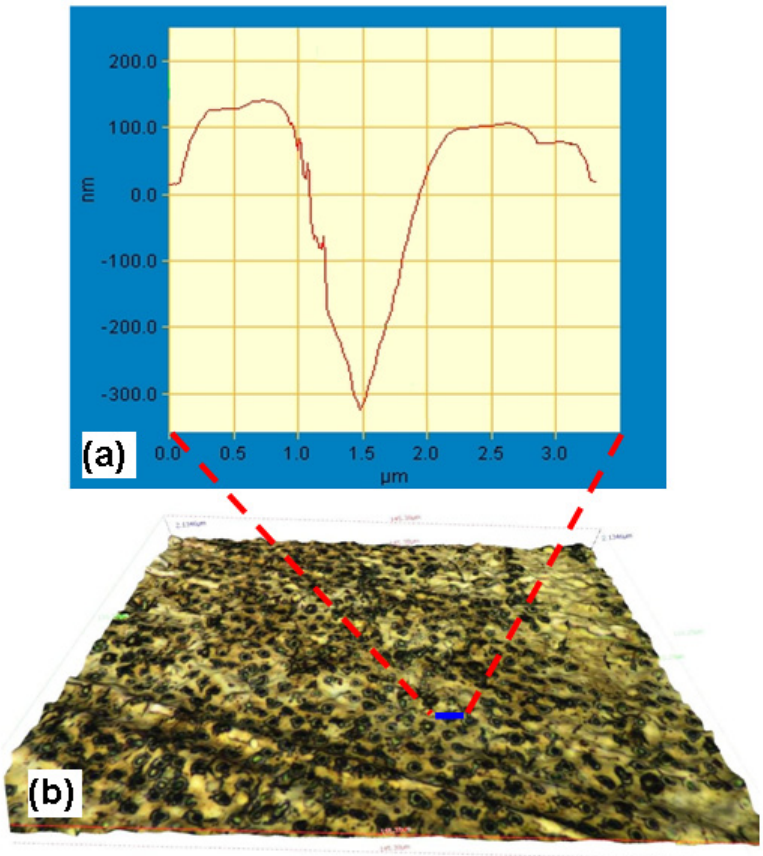


Figure 6. (a) Depth of the generated feature (b) Patterned surface



the sample are also visible in Figure 6. The depth of the features generated was in the range of 300 nm to 400 nm

CONCLUSION

A technique for patterning of rough surfaces using particles lens array has been demonstrated which was previously not possible. It is shown that selection of a suitable flexible plastic and optimized fluence range can lead to the successful patterning of rough surfaces. Features with high spatial density were generated over large areas on a rough surface of titanium. The high melting point of titanium suggests that the technique could be applied to materials with a wide range of melting points.

ACKNOWLEDGMENT

One of the authors (A.Khan) gratefully acknowledges the support from the NWFP University of Engineering and Technology (UET), Pakistan. The authors want to thank the faculty and technical staff of the Laser Processing Research Centre (LPRC), University of Manchester, UK for their valuable support.

REFERENCES

Abbe, B. Z. E. (1873). Theorie des Mikroskops und der mikroskopischen Wahrnehmung. *Archiv Microskop Anatomy*, *9*, 413. doi:10.1007/BF02956173

Bäuerle, D. (2000). *Laser processing and chemistry*. Berlin, Germany: Springer-Verlag.

Betzig, E., Trautman, J. K., Wolfe, R., Gyorgy, E. M., Finn, P. L., & Kryder, M. H. (1992). Near-field magneto-optics and high density data storage. *Applied Physics Letters*, *61*(2), 142–144. doi:10.1063/1.108198

Bjorkholm, J. E., Bokor, J., Eichner, L., Freeman, R. R., Gregus, J., & Jewell, T. E. (1990). Reduction imaging at 14 nm using multilayer coated optics: Printing of features smaller than 0.1 μm. *Journal of Vacuum Science and Technology*, *8*(6), 1509. doi:10.1116/1.585106

Bobbert, P. A., & Vlieger, J. (1986). Light scattering by a sphere on a substrate. *Physica A. Statistical and Theoretical Physics*, *137*(1-2), 209–242. doi:10.1016/0378-4371(86)90072-5

Burmeister, F., Schafle, C., Keilhofer, B., Bechinger, C., Boneberg, J., & Leiderer, P. (1998). From mesoscopic to nanoscopic surface structures: Lithography with colloid monolayers. *Advanced Materials (Deerfield Beach, Fla.)*, *10*(6), 495–497. doi:10.1002/(SICI)1521-4095(199804)10:6<495::AID-ADMA495>3.0.CO;2-A

Burmeister, F., Schafle, C., Matthes, T., Bohmisch, M., Boneberg, J., & Leiderer, P. (1997). Colloid monolayers as versatile lithographic masks. *Langmuir*, *13*(11), 2983–2987. doi:10.1021/la9621123

Chimmalgi, A., Choi, T. Y., Grigoropoulos, C. P., & Komvopoulos, K. (2003). Femtosecond laser aperturless near-field nanomachining of metals assisted by scanning probe microscopy. *Applied Physics Letters*, *82*(8), 1146–1148. doi:10.1063/1.1555693

Chong, T. C., Hong, M. H., & Shi, L. P. (2009). Laser precision engineering: From microfabrication to nanoprocessing. *Laser and Photonics Reviews*, *4*(1), 123–143. doi:10.1002/lpor.200810057

Denkov, N., Velev, O., Kralchevski, P., Ivanov, I., Yoshimura, H., & Nagayama, K. (1992). Mechanism of formation of two-dimensional crystals from latex particles on substrates. *Langmuir*, *8*(12), 3183–3190. doi:10.1021/la00048a054

Guo, W., Wang, Z. B., Li, L., Whitehead, D. J., Luk'yanchuk, B. S., & Liu, Z. (2007). Near-field laser parallel nanofabrication of arbitrary-shaped patterns. *Applied Physics Letters*, *90*(24), 3. doi:10.1063/1.2748035

Guo, W., Wang, Z. B., Luk'yanchuk, B. S., Whitehead, D. J., Li, L., & Liu, Z. (2008). Generation of nano-bumps on transparent quartz glass surface under femtosecond laser irradiation. In *Proceedings of the 27th International Congress on Applications of Lasers and Electro-Optics*, Temecula, CA

Hon, K. K. B., Li, L., & Hutchings, I. M. (2008). Direct writing technology-advances and developments. *CIRP Annals-Manufacturing Technology*, *57*(2), 601–620. doi:10.1016/j.cirp.2008.09.006

Hong, M. H., Huang, S. M., Luk'yanchuk, B. S., & Chong, T. C. (2003). Laser assisted surface nanopatterning. *Sensors and Actuators. A, Physical*, *108*(1-3), 69–74. doi:10.1016/S0924-4247(03)00364-9

Ito, T., & Okazaki, S. (2000). Pushing the limits of lithography. *Nature*, *406*(6799), 1027–1031. doi:10.1038/35023233

Kato, J., Takeyasu, N., Adachi, Y., Sun, H.-B., & Kawati, S. (2005). Multiple-spot parallel processing for laser micronanofabrication. *Applied Physics Letters*, *86*(4), 3. doi:10.1063/1.1855404

Khan, A., Wang, Z., Sheikh, M. A., Whitehead, D. J., & Li, L. (2010). Parallel near-field optical micro/nanopatterning on curved surfaces by transported micro-particle lens arrays. *Journal of Physics. D, Applied Physics*, *43*(30), 305302. doi:10.1088/0022-3727/43/30/305302

Korte, F., Nolte, S., Chichkov, B. N., Bauer, T., Kamlage, G., & Wagner, T. (1999). Far-field and near-field material processing with femtosecond laser pulses. *Applied Physics. A, Materials Science & Processing*, *69*, 7–11.

Lieberman, K., Shani, Y., Melnik, I., Yoffe, S., & Sharon, Y. (1999). Near-field optical photomask repair with a femtosecond laser. *Journal of Microscopy-Oxford*, *194*, 537–541. doi:10.1046/j.1365-2818.1999.00547.x

Liu, Z., Wei, Q., & Zhang, X. (2005). Surface plasmon interference nanolithography. *Nano Letters*, *5*(5), 957–961. doi:10.1021/nl0506094

Miyashita, K., Nishimura, S., Toyofuku, T., & Shirakashi, J.-I. (2009). Nanoscale patterning of NiFe surface by scanning probe microscopy scratch nanolithography. *Journal of Vacuum Science & Technology B Microelectronics and Nanometer Structures*, *27*(2), 953–957. doi:10.1116/1.3077488

O'Connell, C., Sherlock, R., & Glynn, T. J. (2010). Fabrication of a reusable microlens array for laser-based structuring. *Optical Engineering (Redondo Beach, Calif.)*, *49*(1), 4.

Park, J., Ryu, Y., Kim, H., & Yu, C. (2009). Simple and fast annealing synthesis of titanium dioxide nanostructures and morphology transformation during annealing processes. *Nanotechnology*, *20*(10), 105608. doi:10.1088/0957-4484/20/10/105608

Pena, A., Wang, Z. B., Whitehead, D. J., & Li, L. (2009). High speed laser micro-texturing of Si wafer for improved light trapping for photovoltaic application. In *Proceedings of the 28th International Congress on Applications of Lasers & Electro-Optics*, Orlando, FL.

Srituravanich, W., Fang, N., Sun, C., Luo, Q., & Zhang, X. (2004). Plasmonic nanolithography. *Nano Letters*, *4*(6), 1085–1088. doi:10.1021/nl049573q

Wang, X., Lei, M. K., & Zhang, J. S. (2007). Surface modification of 316L stainless steel with high-intensity pulsed ion beams. *Surface and Coatings Technology*, *201*(12), 5884–5890. doi:10.1016/j.surfcoat.2006.10.040

Wang, Z. B., Guo, W., Pena, A., Whitehead, D. J., Luk'yanchuk, B. S., & Li, L. (2008). Laser micro/nano fabrication in glass with tunable-focus particle lens array. *Optics Express*, *16*(24), 19706–19711. doi:10.1364/OE.16.019706

Wang, Z. B., Hong, M. H., Luk'yanchuk, B. S., Lin, Y., Wang, Q. F., & Chong, T. C. (2004). Angle effect in laser nanopatterning with particle-mask. *Journal of Applied Physics*, *96*(11), 6845–6850. doi:10.1063/1.1786652

This work was previously published in the International Journal of Manufacturing, Materials, and Mechanical Engineering, Volume 1, Issue 3, edited by J. Paulo Davim, pp. 1-9, copyright 2011 by IGI Publishing (an imprint of IGI Global).

Chapter 8
A Finite Element Study of Buckling and Upsetting Mechanisms in Laser Forming of Plates and Tubes

M. S. Che Jamil
The University of Manchester, UK

M. A. Sheikh
The University of Manchester, UK

L. Li
The University of Manchester, UK

ABSTRACT

Laser beam forming has emerged as a viable technique to form sheet metal by thermal residual stresses. Although it has been a subject of many studies, its full industrial application is not yet established. This article aims to complement the existing research in the area of laser forming in order to gain a better understanding of the process. A numerical investigation of laser forming of stainless steel sheets has been carried out and validated experimentally using a High Power Diode Laser (HPDL). Three processing parameters are tested; laser power, beam diameter and plate thickness. Also, laser bending of stainless steel tube is simulated and compared against the published experimental data. The main underlying mechanisms of laser forming are demonstrated through the simulations.

INTRODUCTION

Conventional mechanical bending process for sheet material involves a set of bending die and punch with a sheet material placed in between. During bending, the sheet material is plastically deformed into the desired shape by the application of forces. This process is generally suitable for mass production. However, for production of rapid prototyping of a few parts, the conventional sheet metal forming processes are often uneconomical due to high cost of dies and the possibility of redesign of the dies in case of design error.

DOI: 10.4018/978-1-4666-1867-1.ch008

Copyright © 2013, IGI Global. Copying or distributing in print or electronic forms without written permission of IGI Global is prohibited.

In recent years laser forming has emerged as a viable technique to form sheet metal by thermal residual stress. The important element in laser forming process is the material which is scanned with a defocused laser beam such that laser-material interaction causes localized heating of the surface without melting. Laser forming idea was first discovered by Kitamura (1983) who successfully bent a 22mm thick steel plates using a 15kW CO_2 laser. Since then many research works have been carried out in this area for applications in aerospace, automotive, shipbuilding, and electronic industries.

There are many advantages of laser forming compared to conventional sheet bending. Among these are design flexibility, production of complex shapes (which is not achievable by conventional methods), forming of thick plates and the possibility of rapid prototyping. Dearden and Edwardson (2003) in their review, described recent developments and techniques of laser forming for both micro and macro scale applications. Recently, Shen and Vollertsen (2009), in their review on laser forming, described many recent developments and new techniques in modelling of laser forming, including analytical models, numerical simulations and empirical models.

High Power Diode Laser (HPDL) has been used widely in laser processing including laser forming. The wide usage of HPDL is generally attributed to its high efficiency, long life and competitive capital and operating costs (Lawrence, Schmidt, & Li, 2001; Pinkerton, 2004). This laser normally produces a rectangular or an elliptical beam shape with various sizes and geometries. The first attempt to use a 2.5kW HPDL to bend mild steel plate was conducted by Lawrence, Schmidt, and Li (2001). Later, Lawrence (2002) compared laser forming using CO_2 laser and HPDL. Casamichele, Quadrini, and Tagliaferri (2007) investigated laser forming of stainless steel and aluminum alloy sheets using a 1.5kW diode laser. Chen, Jeswiet, Bates, and Zak (2008) used a medium power diode laser to bend thinner metal sheets. Guglielmotti, Quadrini, Santo, and Squeo (2009) performed a mechanical performance test on stainless steel sheets bent by a 1.5kW diode laser.

Modelling of laser beam forming is a complex and demanding task due to its highly non-linear and transient nature. Ju and Wu (1998) have done a comparison between Finite Element Method (FEM) and Finite Difference Method (FDM) simulations on laser forming of sheet metal and studied the temperature fields during the process. Kyrsanidi, Kermanidis, and Pantelakis (1999) have numerically investigated laser forming by Temperature Gradient Mechanism (TGM) with the results validated by a series of experiments. These results were then used by Zhang and Michaleris (2004) in their investigations using Lagrangian and Eulerian formations of the FEM for modelling laser forming process.

Sichun and Zhong (2002) and Yongjun Shi et al. (2007) have numerically investigated temperature gradient mechanism of thin plates irradiated with a straight line laser beam. Chen, Wu, and Li (2004) and Zhang, Guo, Shan, and Ji (2007) have also numerically investigated the deformation behaviour of laser path which is along a curve rather than in a straight line on sheet metal. Hu et al. (2002) investigated the buckling instability of laser sheet forming and concluded that buckling mechanism is activated when there is an insignificant temperature gradient through the thickness.

Tube bending has many applications in many industries for products such as air conditioners, boilers, heat exchangers, tubes, and pipes. Conventional mechanical tube bending has a limitation on minimal bending radius due to material thinning at the extrados (outside arc of the bent tube) (Zhang et al., 2006). To reduce thinning, pressure bending may be adopted. At the intrados, there is a tendency for buckling and wrinkling to occur as a result of the compressive stresses. Mandrels can be used to prevent these defects but this will increase the complexity of the process.

A great advantage of tube laser bending compared to mechanical bending is less ovalization

and wall thickness reduction. Normally laser tube bending is achieved by laser heating the outer circumference of the tube, typically 180°. Li and Yao (2001) studied the laser bending mechanism for mild steel of circular cross section. The deformation characteristics were compared with mechanical bending. They concluded that bending is primarily achieved through the thickening of the scanned region instead of the thinning of the unscanned region, which counters the limitation of mechanical bending.

Zhang et al. (2006) have numerically investigated various schemes of axial scanning using a line source laser beam and comparing with the circumferential scanning scheme using a point source. They concluded that the line source axial scanning is better than the point source circumferential scanning in terms of energy consumption and processing time. This finding was then supported by Safdar et al. (2006) when they numerically compared the two scanning schemes using the same laser source geometry. They found that the axial scanning scheme gives twice the bending angle compared to the circumferential scanning scheme.

Silve (1998) discussed procedures for laser bending of square cross-section tubes. An analytical model for laser tube bending was proposed by Hao and Li (2003). Hsieh and Lin (2005) conducted a numerical study of buckling mechanism in laser tube forming. Zhang et al. (2006) investigated various scanning schemes and cooling effect on a low carbon steel tube. Safdar, Li, and Sheikh (2007) investigated the effect of non-conventional beam geometries on the deformation of laser bend tube. Guglielmotti, Quadrini, Squeo, and Tagliaferri (2008) conducted a numerical and experimental study on laser bending of stainless steel tubes using a high power diode laser.

Although there has been an increase in the scientific interest of the laser forming process in recent times, the full industrial application is still far from being realized. This could be due to the complexity of the process design and the equipment cost. Therefore, for industrial applications of the process more research effort is still needed. This article aims to complement the existing research available in the area of laser forming in order to gain a better understanding of the process. A numerical investigation of laser bending of stainless steel sheet has been carried out and experimental validation has been conducted using a High Power Diode Laser (HPDL). Three processing parameters are tested; laser power, beam diameter and plate thickness. Also, laser bending of stainless steel tube is simulated and compared against the published experimental data by Safdar et al. (2006). The results from the simulations are then used to assess and explains the mechanisms involved in laser forming.

Laser Forming Mechanisms

To date, a number of laser forming mechanisms have been suggested (Arnet & Vollertsen, 1995; Geiger & Vollertsen, 1993, 2005; Hu et al., 2002; Shi et al., 2007; Vollertsen, Komel, & Kals, 1995; Vollertsen, 1994). The most extensively studied and reported in literature are Temperature Gradient Mechanism (TGM), Buckling Mechanism (BM) and Upsetting Mechanism (UM). In particular, TGM has been extensively studied and reported in literature. When the material surface is irradiated with a laser beam, a fraction of the laser energy is absorbed into the material. Hence the laser energy is deposited on a very thin layer of material. The layers of the material close to the irradiated surface are at higher temperature than those away from the surface, thus creating a steep temperature gradient within the thickness of the material. Hence the material layers close to the surface expand more. This differential thermal expansion produces thermal stresses in the material leading to counter-bending of the sheet away from the laser beam. The yield strength and the flow stress of the material decreases with increasing temperature. When the generated thermal stress exceeds the yield stress of the material, further

expansion of the heated region results in compressive plastic deformation. After the laser scan, the surface is rapidly cooled which causes thermal contraction. The thermal contraction results in local shortening of the surface layers thus causing the sheet to bend towards the laser beam.

On the other hand, Buckling Mechanism (BM) dominates when there is small or almost no temperature gradient across the thickness. When the diameter of the laser beam is significantly larger than the thickness of the sheet (i.e., for thin sheets) and when the ratio of thermal conductivity to the thickness of the material is large, very small temperature gradients are developed in the thickness direction. These negligibly small temperature gradients cause a uniform thermal strain throughout the thickness. The free expansion of the sheet is restricted by the surrounding material resulting in compressive stresses in the laser heated region. These compressive stresses in the sheet result in elastic strain in the surrounding material. The compressive stress region tends to buckle when the stresses exceed a certain value. Further increase in temperature results in plastic strains to develop in the buckled region. The tendency to buckle is enhanced when the sheet is thin and the temperature dependent flow stress is not too low. Once buckling is initiated, the buckle is extended along the laser scanning path due to thermal expansion of the subsequent material. The temperature-dependent flow stress in the top irradiated region is low due to higher temperature, thus causing the deformation at the top irradiated surface to be nearly plastic, whereas the surrounding region remains nearly purely elastic. When the laser beam leaves the scanning path, the sheet develops a bending angle which is primarily determined by the plastic region in the bend of the sheet.

Similar to the Buckling Mechanism, the Upsetting Mechanism (UM) occurs when the temperature gradient across the thickness is insignificant. However, the thickness of the sheet for UM is much larger than the heated region of the sheet. The localized heating of the sheet causes uniform thermal expansion of the material throughout the thickness of the laser-heated region. Resistance from surrounding material will create compressive strain in the sheet. Local shortening of the sheet in the laser-heated region will take place resulting in the increase of thickness on the heated region.

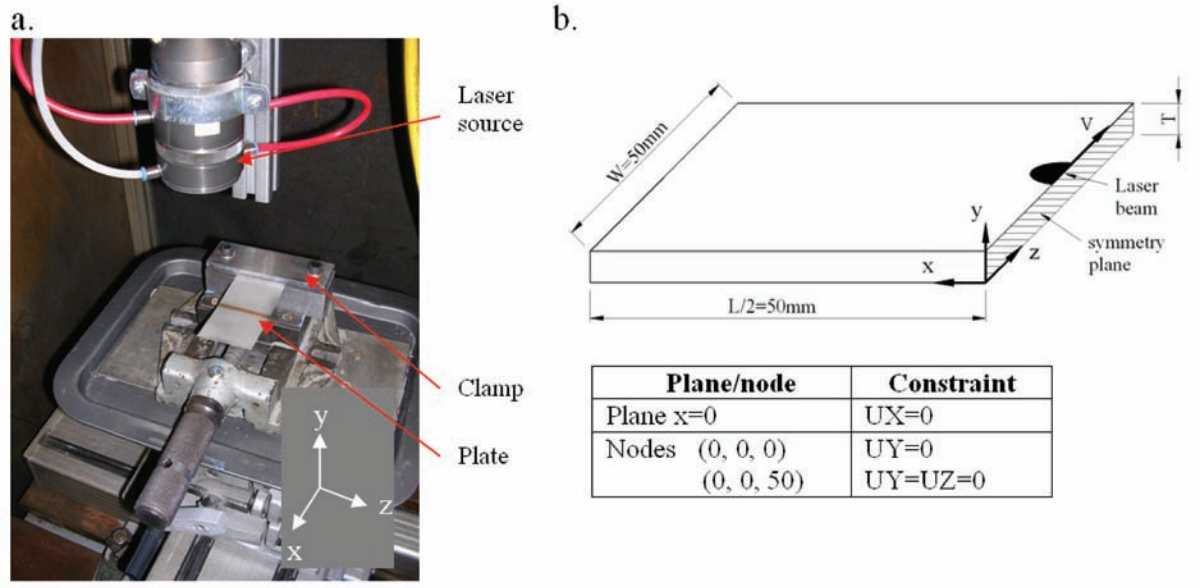
EXPERIMENTAL SET-UP FOR PLATE BENDING

Equipment

Laser used in these experiments is HPDL, Laserline LDL 160-1500 diode laser with a maximum power of 1.5kW. The raw laser beam has a rectangular beam profile with a Gaussian intensity distribution. Additionally it is coupled with a 1mm diameter, 5m long optical fibre cable and a 1:1 optical imaging system with a focal length of 85mm. The output of the fibre coupled diode laser is a circular beam with a 'top-hat' intensity distribution, which was used for this work. The 'top hat' intensity distribution is approximately uniform. The validity of this assumption has been proved by a close temperature matching between the model and the experiments. The delivered power loss using the fibre coupling was around 28%.

A series of tests were conducted to measure the beam size of the circular laser beams. The vertical displacement along y-axis, as shown in Figure 1(a), on the CNC machine can be adjusted manually to get the desired distance from the optical lens and hence the beam diameter. Two methods were used here to measure the circular beam diameter. The first one was by exposing the infra-red detector card, with a sensitivity of 1.75×10^{-9} W/mm, to a 20mW pilot beam of the diode laser and then using a vernier calliper to measure the size. The limitation of this method is that over a certain distance away from the focal position, the pilot beam intensity reduces and become invisible on

Figure 1. (a) Experimental setup of plate bending (b) Boundary condition of the half plate modelled in the simulations



Plane/node	Constraint
Plane x=0	UX=0
Nodes (0, 0, 0)	UY=0
(0, 0, 50)	UY=UZ=0

the detector card. Therefore, another technique was used by firing a set of 40ms pulse lasers on a graphite coated brick. The burn marks were then measured using a vernier calliper.

Specimens

The plate material used was AISI 304 stainless steel (composition in Table 1) which is an austenitic low carbon steel. The plates were cut into 110mm length x 50mm width. The plate was clamped 10mm at one end, giving an overhang length of 100mm (Figure 1). The clamp was mounted on a CNC table, controlled by a CNC Automation Controller C116-4 isel.

The optical reflectivity of the plate was measured using an SD 2000 fibre optic spectrometer manufactured by Ocean Optics Inc., USA. For the diode laser wavelength, the reflectivity of the investigated material was found to be 40% given at room temperature without any surface processing (Table 1).

Test Parameters and Procedure

The plates were used as received and no surface processing or graphite coating was applied. Methanol liquid was used to clean the surface from any grease or dirt. Methanol was applied on a clean cloth and the cloth was then used to wipe the plate. Laser was fired at 50mm from the free end along z-axis (Figure 1). Laser path length was 80mm, starting and ending 15mm off

Table 1. Material composition of AISI 304 stainless steel (Oberg, Jones, Horton, & Ryffel, 2008)

Material composition of AISI 304 stainless steel							
Cr	**Ni**	**C**	**Mn**	**Si**	**P**	**S**	**N**
18-20	10.5	0.08	2	0.75	0.045	0.03	0.1

the plate edges. The movement of the CNC table was set at a speed of 10mm/s.

Laser Power

Laser power values of 400, 600, 800 and 1000W were used with a constant beam diameter of 16mm. The tests were conducted on 0.9mm plates. Each test was repeated five times. For each test, the magnitude of the plate bending and its direction, either concave or convex, was obtained.

Beam Size

Laser beams of diameter 10, 13, 16 and 19mm were used, with a constant power of 800W. The beam size was controlled by changing the distance from the end of the nozzle to the plate. The tests were conducted on 0.9mm plates. Each test was repeated twice.

Plate Thickness

Four different thicknesses were used, 0.5, 0.9, 1.5 and 2.0mm, with a constant power of 800W and beam of 16mm diameter. The bending angles for 0.5mm and 0.9mm sheets were measured using a protractor with a resolution of $1/12^{o}$ (5'). Due to small range of bending angle ($< 1^{o}$) for the 1.5mm and 2.0mm thick plates, the displacements were measured using a laser surface profiling system, Keyence LK-031, with measuring range of ±5mm and a resolution of 1μm. All displacements and bending angles were measured along the centre line of the plates.

NUMERICAL MODELING

A commercial finite element package (ANSYS) has been used in this study to simulate the laser forming process of tube and plates. The temperature field caused by a moving laser beam is transient in nature. If the energy dissipation due to plastic deformation is neglected, when compared with the energy involved in the thermal process, the analysis can be uncoupled into sequential thermal and stress analyses. This model has also been used previously by other researchers (Chen et al., 2004; Shi et al., 2007; Shichun & Zhong, 2002). The thermal problem is solved first to obtain the temperature field, which is then used as thermal loading for the structural problem. The same mesh is used for both thermal and mechanical calculations.

The finite element equation for transient heat transfer analysis can be expressed as follows:

$$\left[C\right]\left[\dot{T}\right]+\left[K\right]\left\{T\right\}=\left\{Q\left(t\right)\right\} \tag{1}$$

Where

$\left[C\right]$ *Specific heat matrix*
$\left[\dot{T}\right]$ Time derivative *of temperature*
$\left[K\right]$ Heat conduc*tivity matrix*
$\left\{T\right\}$ *Temperature*
$\left\{Q\left(t\right)\right\}$ *Heat flux column*

The nonlinear transient dynamic structural equation based on FEM can be written in the matrix form as follows:

$$[M(T)]\{u''(t)\}+[D(T)]\{u'(t)\}+[S(T)]\{u(t)\}+\{F(t)\}+\{F^{th}(t)\}=0 \tag{2}$$

where

$[M(T)]$ = temperature dependent mass matrix
$[D(T)]$ = temperature dependent damping matrix
$[S(T)]$ = temperature dependent stiffness matrix
$\{F(t)\}$ = external load vector
$\{F^{th}(t)\}$ = thermal load vector
$\{u''(t)\}$ = acceleration vector
$\{u'(t)\}$ = velocity vector
$\{u(t)\}$ = nodal displacement vector

For the case of transient thermal stresses generated due to laser scanning with no damping or external forces/loadings Equation (2) can be reduced to

$$[S(T)]\{u(t)\} = \{F^{th}(t)\} \tag{3}$$

Thermal load vector $\left\{F^{th}\left(t\right)\right\}$ can be evaluated by using,

$$\{F^{th}\} = \int_{vol} [B]^T \frac{E\bar{\alpha}(T)\Delta T}{1-2v} \delta dV \tag{4}$$

Where

[B] = strain displacement matrix
$\delta = [1\ 1\ 1\ 0\ 0\ 0]^T$
E = elastic modulus
v = Poisson's ratio
ΔT = temperature difference

Total strains can be evaluated from nodal displacements by using,

$$\left\{\varepsilon\right\} = \left[B\right]\left\{u\right\} \tag{5}$$

where $\left\{u\right\}$ is the nodal displacement vector.

The difference between total strain and thermal strain gives mechanical strain which consist of plastic and elastic strain components as expressed below:

$$\left\{\varepsilon\right\} - \left\{\varepsilon^{th}\right\} = \left\{\varepsilon^{pl}\right\} + \left\{\varepsilon^{el}\right\} \tag{6}$$

where

$\left\{\varepsilon\right\}$ = Total strain vector
$\left\{\varepsilon^{el}\right\}$ = Elastic strain vector
$\left\{\varepsilon^{pl}\right\}$ = Plastic strain vector
$\left\{\varepsilon^{th}\right\}$ = Thermal strain vector

Laser heating is modelled as moving heat flux with ANSYS APDL language used to incorporate the laser beam motion. The laser beam intensity had a top-hat distribution and thus assumed to be constant over the beam area. All exposed surfaces were subjected to convection. Heat losses due to radiation were not considered as they were very small.

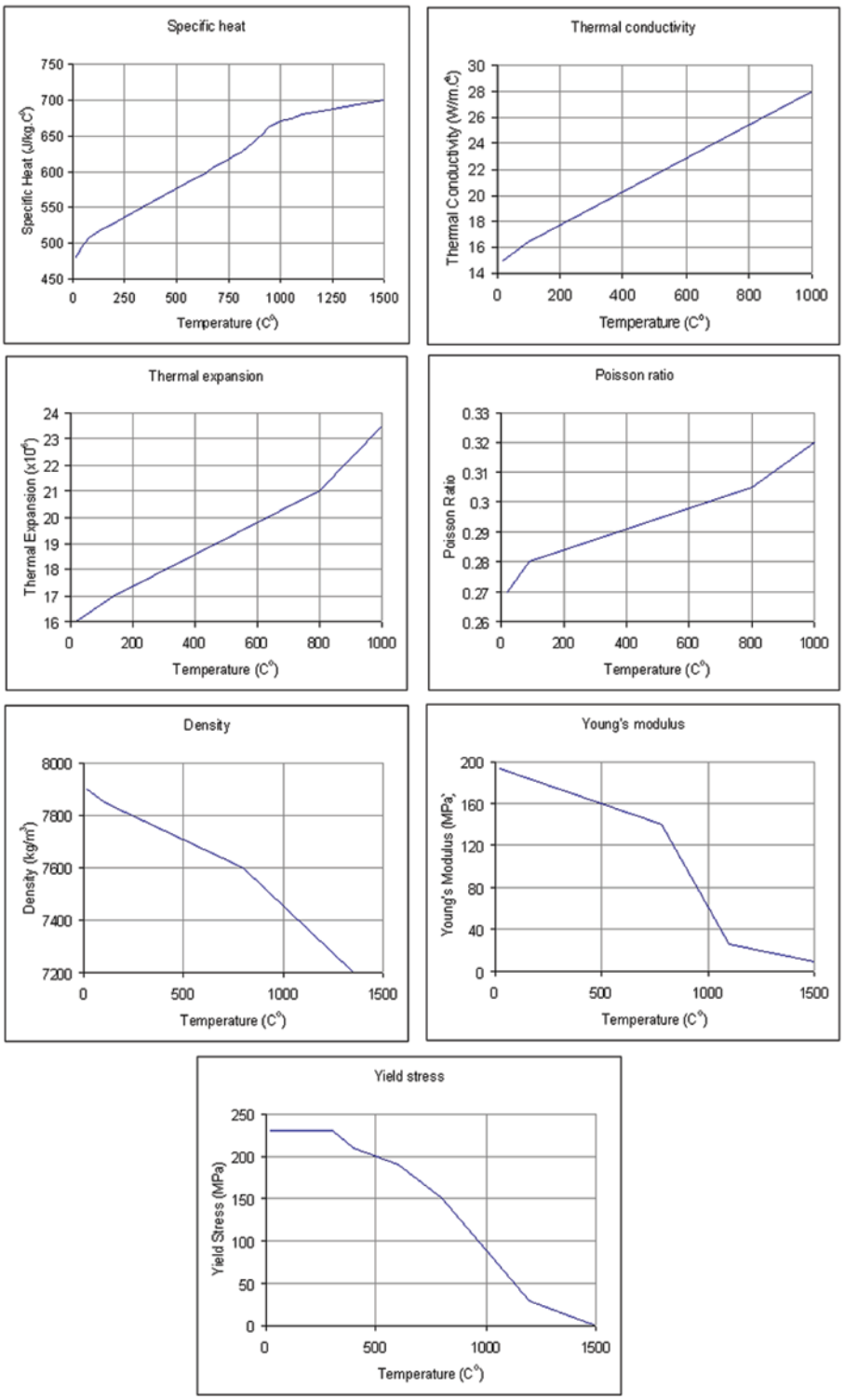
The basic assumptions for the model are as follows:-

- Material is isotropic.
- Laser intensity distribution is assumed to be uniform.
- Bauschinger's effect is neglected.
- Von-Misses criterion has been used for plastic yielding.
- Energy dissipation due to plastic deformation is neglected when compared with the energy involved in the thermal process.

Plate Bending Simulation

Laser forming of plate was modeled using similar parameters as used in the experiments. Three variables were tested; laser power, beam diameter and plate thickness. One scan along the z-axis, as shown in Figure 1(b), was simulated for a beam velocity of 10 mm/s. The coefficient of absorption of the material was assumed to be 0.6. The power loss of 28% through the fibre coupling of the diode laser was also considered. The scanning track started and ended 15mm off the entry and the exit sides so that the total scanning length was 80mm, and thus the scanning duration was 8s. The temperature-dependant material properties of AISI 304 stainless steel are considered including thermal conductivity, specific heat, thermal expansion coefficient, Poisson's ratio, elastic modulus, yield stress and density, as shown in Figure 2.

Figure 2. Temperature dependent thermal and mechanical properties of AISI 304 stainless steel plate (Hsieh-Shen Hsieh & Lin, 2004)



The problem is symmetric and therefore only half of the plate is modelled with a symmetric boundary condition, as shown in Figure 1(b). Eight noded 3D brick element (ANSYS: SOLID70) with thermal conduction capability is used for the thermal analysis. For structural analysis ANSYS: SOLID185 type element is used which is defined by eight nodes having three degrees of freedom (u_x, u_y, u_z) at each node. The element has plasticity, large deflection, and large strain capabilities (ANSYS, 2007). The laser beam intensity (I) on the workpiece was obtained from the following equation;

$$I = \frac{\eta \times \mu \times P}{A} \tag{7}$$

where

I = Laser beam intensity
η = Absorption coefficient
μ = Fibre cable efficiency
P = Power applied
A = Laser beam area.

Tube Bending Simulation

A tube bending simulation was performed to replicate the experimental work conducted by Safdar et al. (2006). There are two type of laser scanning schemes for tube bending; along the circumference of the tube and along the axial direction of the tube. Only axial scanning scheme was considered for this work. The tube was an AISI 304L stainless steel tube with dimension of 100mm length x 14mm diameter x 1mm wall thickness. The temperature dependant material properties of the tubes are shown in Table 2.

A total of four axial scans with track length of 20mm were simulated and the beam velocity was 10 mm/s (Figure 3). The time interval between successive scans was kept at 10s. The beam diameter of 3.56mm was used. The power density was initially set up at 2.0 kW/cm^2. As the tubes became oxidized during the first scan at higher temperatures, material absorptivity increased. To avoid melting of tubes, subsequent scans were carried out with power density reductions of 0.2 kW/cm^2, i.e., with 1.8, 1.6 1.4 kW/cm^2 for second, third and fourth scans respectively. Absorption

Figure 3. Schematic of the laser tube bending (Ø14mm x 100mm length x 1mm thick)

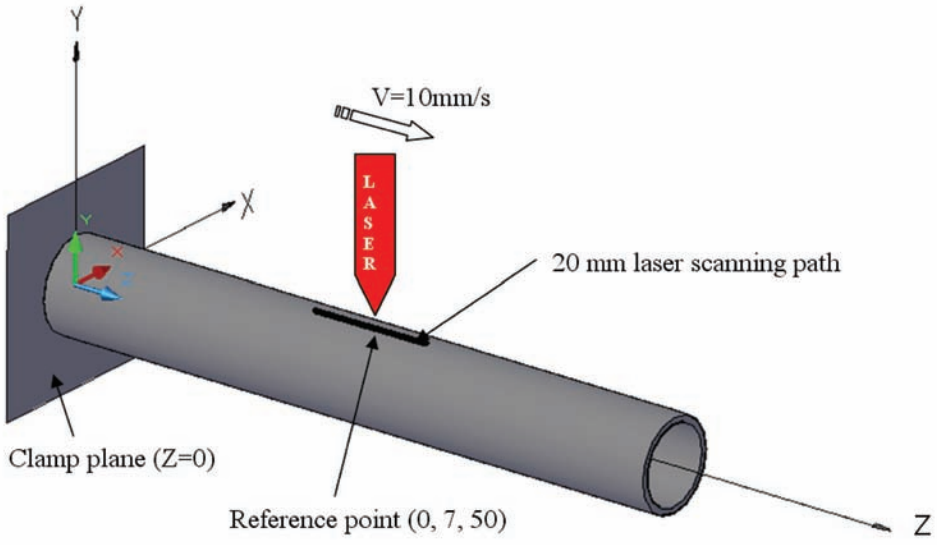


Table 2. Material Properties of AISI 304L tube (Safdar et al., 2006)

Temperature (K)	200	300	400	600	800	1000	1200	1500
Thermal conductivity, K (W/m·K)	12.6	14.9	16.6	19.8	22.6	25.4	28	31.7
Specific heat, Cp (J/kg·K)	402	477	515	557	582	611	640	682
Convection coefficient, h (W/m^2)	20							
Density, ρ (kg/m^3)	7854							
Coefficient of thermal expansion, α (10^{-5} K^{-1})	1.7 (293)	1.7 (473)	1.8 (673)	1.9 (873)	1.95 (1073)	2.00 (1273)	-	-
Poisson's ratio, *v*	0.29	0.29	0.2925	0.296	0.308	0.33	0.36	0.39
Elastic modulus, E (GPa)	193 (293)	191 (373)	183 (473)	168 (673)	148 (873)	128 (1073)	110 (1273)	-
Yield Stress (MPa)	410 (293)	331 (478)	265 (813)	214 (923)	112 (1143)	66 (1253)	-	-
Tangent modulus (MPa)	29370	27791	23435	21761	18413	16739	-	-

coefficient was not considered in the tube bending simulation as the value provided is the final intensity absorbed by the material.

In the experiment (Safdar et al., 2006), an Impac Pyrometer was used for temperature measurement. The temperature range of this pyrometer was from 250°C to 2000°C. The temperature sensitivity at the lower limit was poor. The bending angle for the scanned tube was assessed by measuring the y-direction displacement along a straight line on top of the tube by laser optical scanning system. Due to the limitation of displacement range of the CNC table, only half of the length of the tube was scanned (approximately 55mm).

RESULTS AND DISCUSSION

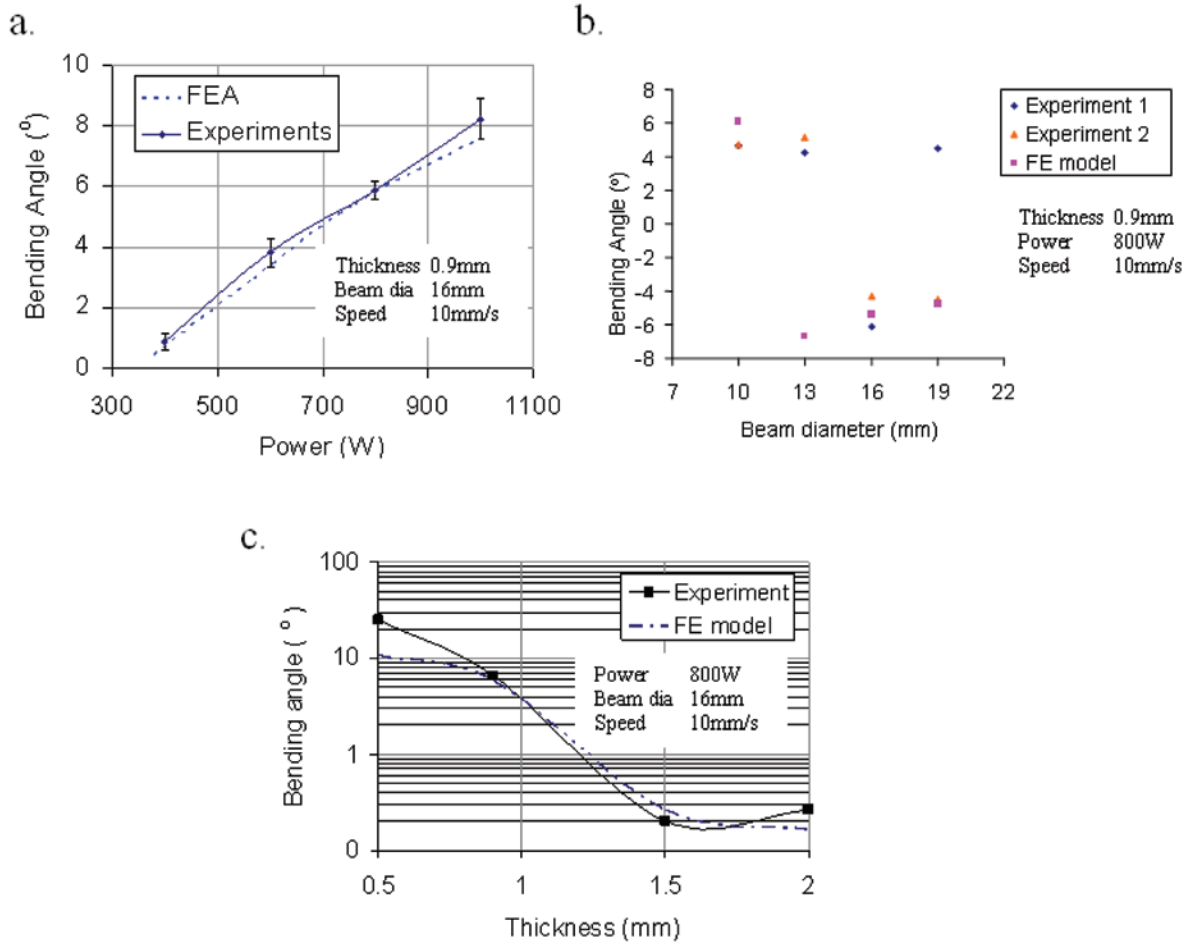
Plate Bending

Figure 4(a) shows the magnitude of the plate bending angle from the experiments and the numerical study. The bending angle shown is the average of five tests, and the error bars represent the standard deviation. The results show that the numerical results are generally in good agreement with experimental results. As expected, buckling mechanism dominates the process due to high beam size to plate thickness ratio (>10). From the experiments, the bending directions obtained are mixture of concave and convex bending. This variation is possibly caused by the experimental uncertainty due to the internal residual stresses and the plate geometrical imperfections that could trigger bending in either direction for the buckling mechanism.

For the range of laser power used in the experiments, the bending angle is almost proportional with the laser power, as shown in Figure 4(a). This is expected as higher power means more energy is supplied and hence higher temperature is developed in the material. A linear relationship is obtained until the melting temperature is reached where the bending efficiency starts to drop.

Figure 4(b) shows the results for the bending angle with four different beam diameters. FE model results produced convex bending for beam diameter 13, 16 and 19mm while experimental results produced convex bending for beam diameter 16and 19mm and concave for the others. The discrepancies between the simulations and

Figure 4. Results of bending angle vs (a) laser power, (b) beam diameter, (c) plate thickness for plate bending

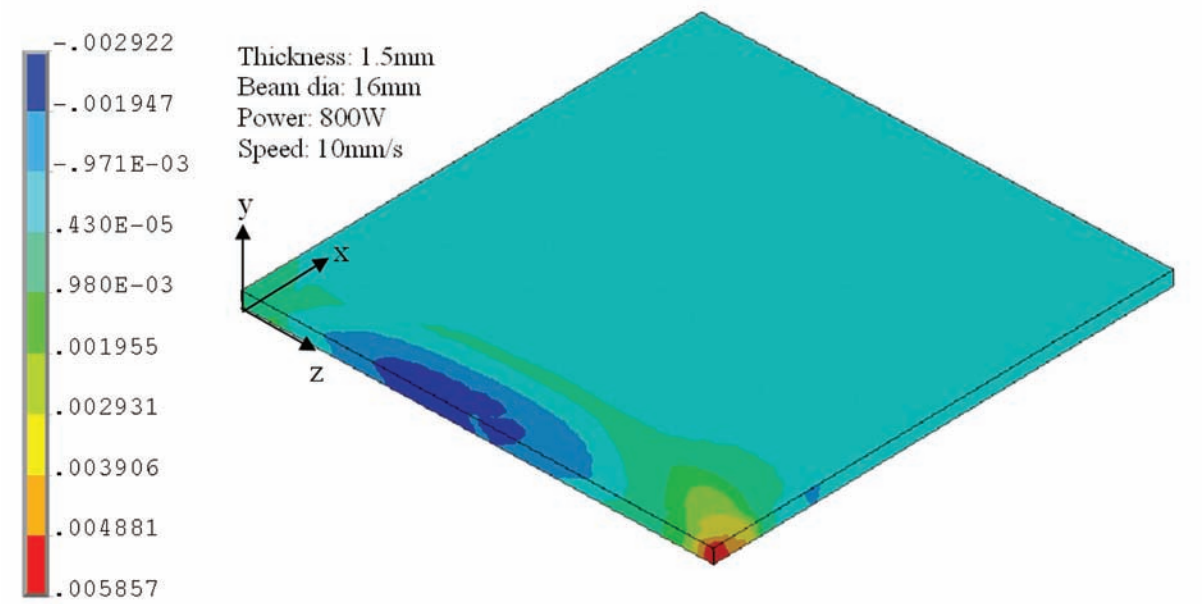


experiments are presumably caused by the internal residual stresses in the plate which are unknown and assumed to be zero in the simulations.

From the FE models, it is observed that the main mechanism for all the four beam sizes investigated (10, 13, 16 and 19mm) is BM. However, the bending direction is concave for the case of 10mm beam diameter, and convex for the rest. As the FE model does not consider any geometrical imperfection or residual stress, the bending direction is solely triggered by the slight of unbalance in the in-plane thermal loading. Therefore, based on the temperature distribution, beam of size 13mm and above could trigger convex bending. As expected, for the experimental results, the bending direction is unpredictable due to uncertainty factors such as plate internal residual stresses and geometry imperfections. From the two tests conducted with 10mm and 13mm beam size, both produced concave bending. For the 16mm beam, both tests produced convex bending.

Figure 4(c) shows the relationship between the bending angle and the plate thickness. The relation between bending angle and plate thickness is not linear due to the variation of forming mechanisms for different thickness. The bending angle drops rapidly with increase in plate thickness before it flattens out at thickness of 1.5mm and 2.0mm.

Figure 5. Distribution of plastic strain in x-direction, ε_x, for plate bending



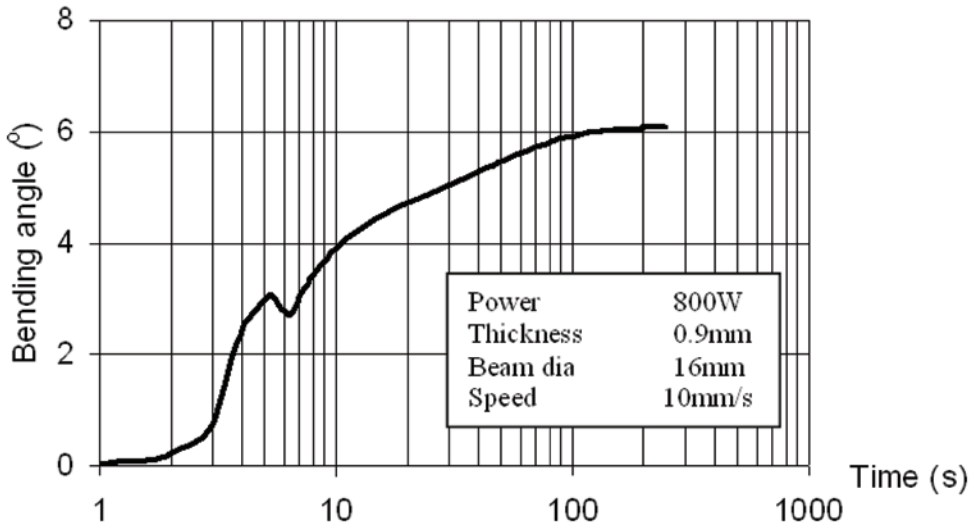
For 0.5mm thick plate, the bending angle from the experiment is much higher in magnitude than predicted by the simulation. This is due to the fact that the thin sheet is fired with a relatively large beam size, which causes a highly unstable buckling process. Slight geometric imperfection and variation of internal residual stress in the test work piece could contribute to a large distortion in the final deformation.

The bending angle for the 1.5mm and 2.0mm plates is small ranging from only 0.1^o to 0.3^o. This is caused by a combination of Temperature Gradient Mechanism (TGM) and Upsetting Mechanism (UM). The presence of UM can be seen in Figure 5, where compressive plastic strains (ε_x) occur in the middle of the scan on both the top and the bottom surfaces. This is expected since the beam size (16mm diameter) is relatively large compared to the thickness of the plate (1.5mm). The stiffness of the plate prevents buckling from occurring. Instead, the material is plastically compressed in plane to form UM. Due to the small temperature gradients which exist between the top and bottom surfaces, a slight out-of-plane deformation is developed thereby forming a small bending angle.

On the other hand, a large angle for 0.5mm and 0.9mm plate is caused by Buckling Mechanism (BM). Figure 6 shows the bending angle of the plate measured at the beam entrance side ($z = 0$). The bending angle at the beginning of the scan until about a third of the scanning time (total scanning time is 8s) is very small. After about 3s the bending angle develops rapidly. This is caused by buckling triggered by out-of-plane instability of the expanding heated material. The bending angle increases until it reaches its peak position at about 5.2s. Then it reduces slightly when the beam reaches the end of the scan, before it increases again during the cooling periods. During the cooling period, as the temperature drops to the ambient temperature, the thermal strains decrease to zero and leave the residual elastic and plastic strains. The final deformation depends on the amount of plastic strain developed during the heating cycle.

In general, the FE model developed here could quite accurately predict the deformation of the

Figure 6. Bending angle vs time for plate bending from FE model (measured at the beam entrance side (z=0))



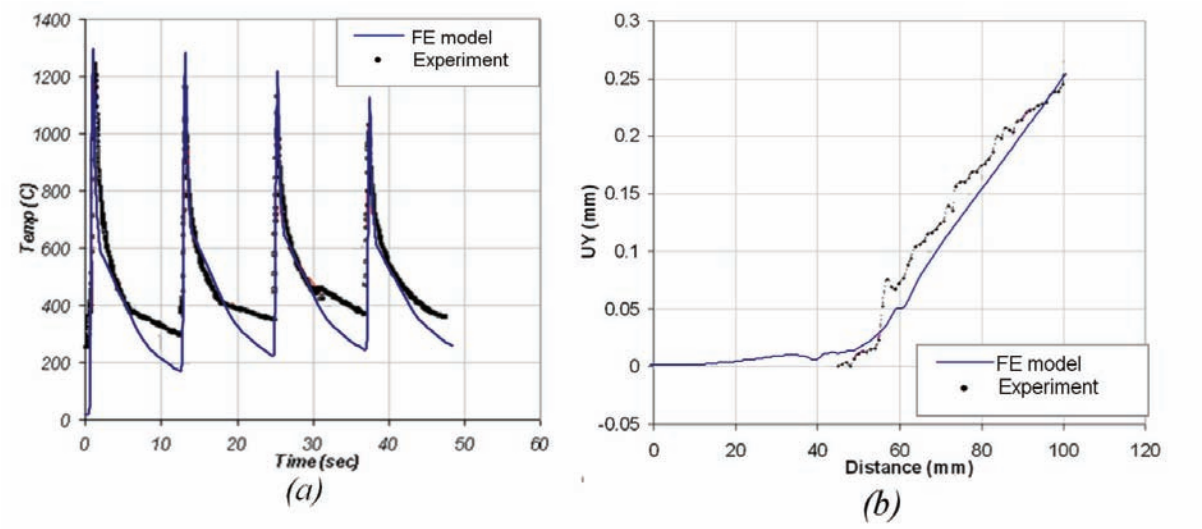
plates for various forming mechanisms. However, for Buckling Mechanism, the discrepancies exist in term of bending directions (concave or convex bending). This is possibly due to the fact that the FE model does not consider any geometrical imperfection or residual stress. Thus, the bending direction is solely triggered by the slightest of unbalance in the in-plane thermal loading during buckling. The observed thermal and mechanical behavior of the plate under a single straight line scan clearly shows the complexity of the laser forming process.

As discussed above, there are a few sources of possible error in the experiments that could lead to discrepancies between the experiments and the simulation results. One explanation for these discrepancies is that these are mainly due to geometrical imperfections and/or residual stresses. However, without measuring the geometrical imperfections and estimating the residual stresses, it is difficult to draw any definitive conclusions for the causes of these discrepancies. There is also a possibility that the proposed model is not able to represent the full experimental window thereby resulting in large discrepancies between the experimental and numerical results such as shown for a certain plate thicknesses value in Figure 4c. To reduce the experimental error, plates may be annealed to minimize the residual stresses in the material. Also, the initial flatness of the plate needs to be checked before the start of the bending process, especially for thin plates. In this way, the effect of the plate's initial geometrical condition on the bending direction could be identified.

Tube Bending

A reference point on the tube is chosen at the middle of the 20mm scanning track with coordinates (0, 7, 50), as shown in Figure 2. The origin (0, 0, 0) is set up at the circular centre of one end of the tube where it is clamped or constrained. Figure 7(a) shows the temperature at the reference point for the four scans from the simulation. Experimental result from the work conducted by Safdar et al. (2006) is also plotted for comparison. It can be seen that in general, the FE model agrees with the experiment. There are some discrepancies during the cooling period where the FE model temperature drops at a higher rate compared to

Figure 7(a). Temperature vs time for tube bending at reference point (0, 7, 50), (b): Displacement in Y-direction along the top path



the test result. This is due to low sensitivity of the pyrometer at low temperatures resulting in temperature measurement error during the test (Safdar et al., 2006).

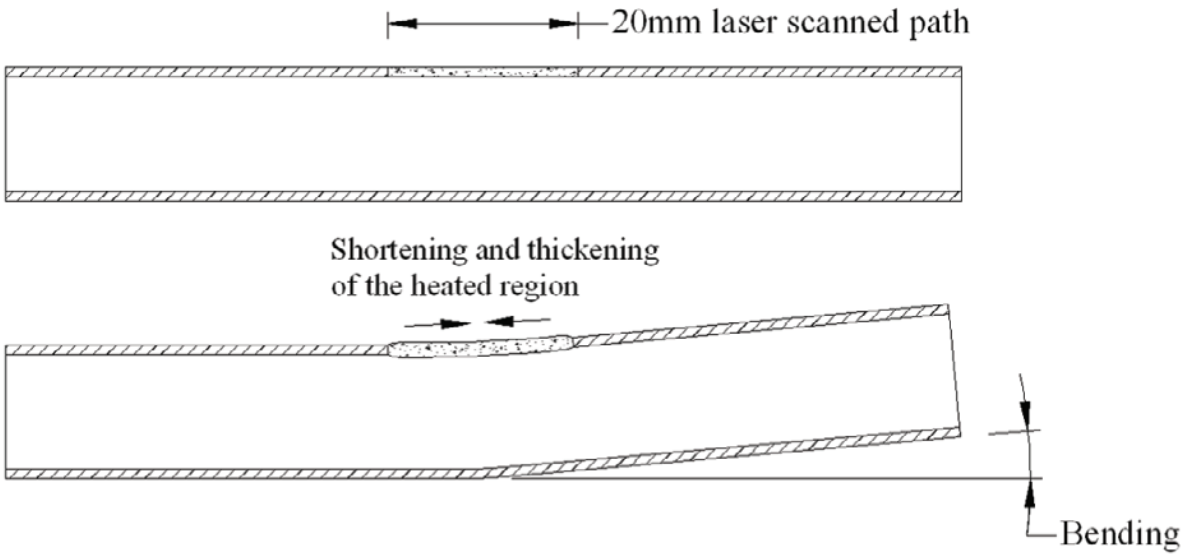
Figure 7(b) shows a comparison of displacement in y-direction for the FE model and the experimental results, measured on the top path [(0, 7, 0) to (0, 7, 100)]. It can be seen that the simulation result is in good agreement with the experiment. Observation on the FE model results shows that the bending of the tube is mainly achieved by the shortening of the heated region in the axial direction. Most researchers agree that the primary mechanism in tube bending is a combination of upsetting; that is the thickening of the scanned region, and buckling (Hom-Shen Hsieh & Lin, 2005). The upsetting mechanism is especially valid for tube bending with scans along the axial direction of the tube, where the shortening and thickening in the axial direction of the heated region caused the tube to bend upwards as schematically illustrated in Figure 8.

CONCLUSION

3D FEM models for laser forming process of plates and tubes have been developed. The simulations involve a nonlinear, transient and sequential thermo-mechanical analysis, also accounting for the temperature dependant thermal and physical material properties. The plate forming simulation results have been validated experimentally. The tube simulation results are compared against published experimental data conducted at the Laser Processing Research Centre of the University of Manchester (Safdar et al., 2006).

The simulations give an insight to the mechanisms active in the laser forming process which is difficult to be examined through experiments. From the variation of the processing parameters (laser power, beam diameter and plate thickness), the presence of the main mechanisms in laser forming are clearly shown through the simulations. For the first time, the formation of Buckling Mechanism (BM) on 0.5 and 0.9mm thick plates is demonstrated through the abrupt bending angle formation when the laser is about a third of the distance of the scanning track. This is caused by

Figure 8. Schematic of Upsetting Mechanism for axial scan tube bending



out-of-plane instability of the expanding heated material as the plate's stiffness is reduces with the laser scanning. Even though FE model can predict the bending angle quite accurately, discrepancies exist in term of bending directions (concave or convex bending), due to geometrical imperfections or residual stress on the actual workpiece.

The presence of Upsetting Mechanism (UM) on the 1.5 and 2.0mm thick plate is demonstrated by the distribution of compressive transverse plastic strain, ε_x, in the middle of the scanning line, both on top and bottom surfaces (Figure 5). Due to the small temperature gradients which exist between the top and bottom surfaces, a slight out-of-plane deformation is developed thereby forming a small bending angle.

Simulation results of laser tube bending show that the bending of the tube is mainly achieved by the shortening and thickening of the heated region in the axial direction. The proposed FE models serve as an efficient tool towards the understanding of various aspects of a complex laser forming process.

REFERENCES

Ansys, I. (2007). *Release 11.0 Documentation for ANSYS*.

Arnet, H., & Vollertsen, F. (1995). Extending laser bending for the generation of convex shapes. *Proceedings of the Institution of Mechanical Engineers. Part B, Journal of Engineering Manufacture*, *209*(No. B6), 433–442. doi:10.1243/PIME_PROC_1995_209_107_02

Casamichele, L., Quadrini, F., & Tagliaferri, V. (2007). Process-efficiency prediction in high power diode laser forming. *Transactions of the ASME*, *129*, 868–873.

Chen, D., Wu, S., & Li, M. (2004). Deformation behaviours of laser curve bending of sheet metals. *Journal of Materials Processing Technology*, *148*(1), 30–34. doi:10.1016/j.jmatprotec.2003.12.024

Chen, M. L., Jeswiet, J., Bates, P. J., & Zak, G. (2008). Experimental study on sheet metal bending with medium-power diode laser. *Journal of Engineering Manufacture*, *222*, 381–389. doi:10.1243/09544054JEM951

Dearden, G., & Edwardson, S. P. (2003). Some recent developments in two and three-dimensional laser forming for 'macro' and 'micro' applications. *Journal of Optics. A, Pure and Applied Optics*, *5*, S8–S15. doi:10.1088/1464-4258/5/4/352

Geiger, M., & Vollertsen, F. (1993). The mechanism of laser forming. *CIRP*, *42*, 301–304. doi:10.1016/S0007-8506(07)62448-2

Guglielmotti, A., Quadrini, F., Santo, L., & Squeo, E. A. (2009). Double indentation of laser bended stainless steel sheets. *International Journal of Material Forming*, *2*, 665–668. doi:10.1007/s12289-009-0465-1

Guglielmotti, A., Quadrini, F., Squeo, E. A., & Tagliaferri, V. (2008). Diode laser forming of stainless steel tubes. *International Journal of Material Forming*, *1*, 1343–1346. doi:10.1007/s12289-008-0112-2

Hao, N., & Li, L. (2003). An analytical model for laser tube bending. *Applied Surface Science*, *208-209*, 432–436. doi:10.1016/S0169-4332(02)01428-9

Hsieh, H.-S., & Lin, J. (2004). Laser-induced vibration during pulsed laser forming. *Optics & Laser Technology*, *36*, 431–439. doi:10.1016/j.optlastec.2003.11.005

Hsieh, H.-S., & Lin, J. (2005). Study of the buckling mechanism in laser tube forming. *Optics & Laser Technology*, *37*(5), 402–409. doi:10.1016/j.optlastec.2004.06.004

Hu, Z., Kovacevic, R., & Labudovic, M. (2002). Experimental and numerical modeling of buckling instability of laser sheet forming. *International Journal of Machine Tools & Manufacture*, *42*(13), 1427–1439. doi:10.1016/S0890-6955(02)00075-5

Ji, Z., & Wu, S. (1998). FEM simulation of the temperature field during the laser forming of sheet metal. *Journal of Materials Processing Technology*, *74*(1-3), 89–95. doi:10.1016/S0924-0136(97)00254-9

Kitamura, N. (1983). Tecnical report of joint project on material processing by high power laser. *JWES-TP*, *8302*, 359–371.

Kyrsanidi, A. K., Kermanidis, T. B., & Pantelakis, S. G. (1999). Numerical and experimental investigation of the laser forming process. *Journal of Materials Processing Technology*, *87*, 281–290. doi:10.1016/S0924-0136(98)00367-7

Lawrence, J. (2002). A comparative investigation of the efficacy of CO_2 and high-power diode lasers for the forming of EN3 mild steel sheets. *Journal of Engineering Manufacture*, *216*, 1481–1491. doi:10.1243/095440502320783521

Lawrence, J., Schmidt, M. J., & Li, L. (2001). The forming of mild steel plates with a 2.5 kW high power diode laser. *International Journal of Machine Tools & Manufacture*, *41*, 967–977. doi:10.1016/S0890-6955(00)00117-6

Li, W., & Yao, Y. L. (2001). Laser bending of tubes: Mechanism, analysis, and prediction. *Journal of Manufacturing Science and Engineering. Transactions of the ASME*, *123*(4), 674–681.

Oberg, E., Jones, D. F., Horton, H. L., & Ryffel, H. H. (2008). *Machinery's Handbook*. Industrial Press.

Pinkerton, A. J. (2004). *A mathematical and experimental investigation of thin wall laser direct metal deposition*. Manchester, UK: UMIST.

Safdar, S., Li, L., & Sheikh, M. A. (2007). The effect of non-conventional laser beam geometries on stress distribution and distortions in laser bending of tubes. *Journal of Manufacturing Science and Engineering*, *129*, 592–600. doi:10.1115/1.2716715

Safdar, S., Li, L., Sheikh, M. A., & Zhu, L. (2006). Finite element simulation of laser tube bending: Effect of scanning schemes on bending angle, distortions and stress distribution. *Optics & Laser Technology*, *39*(6), 1101–1110. doi:10.1016/j.optlastec.2006.09.014

Shen, H., & Vollertsen, F. (2009). Modelling of laser forming - An review. *Computational Materials Science*, *46*, 834–840. doi:10.1016/j.commatsci.2009.04.022

Shi, Y., Shen, H., Yao, Z., & Hu, J. (2007). Temperature gradient mechanism in laser forming of thin plates. *Optics & Laser Technology*, *39*(4), 858–863. doi:10.1016/j.optlastec.2005.12.006

Shichun, W., & Zhong, J. (2002). FEM simulation of the deformation field during the laser forming of sheet metal. *Journal of Materials Processing Technology*, *121*(2-3), 269–272. doi:10.1016/S0924-0136(01)01241-9

Vollertsen, F., Komel, I., & Kals, R. (1995). The laser bending of steel foils for microparts by the buckling mechanism-a model. *Modelling and Simulation in Materials Science and Engineering*, *3*(1), 107–119. doi:10.1088/0965-0393/3/1/009

Vollertsen, F. F. (1994). An analytical model for laser bending. *Lasers in engineering, 2*, 261-276.

Zhang, J., Cheng, P., Zhang, W., Graham, M., Jones, J., & Jones, M. (2006). Effects of scanning schemes on laser tube bending. *Transactions of the ASME*, *128*, 20–33.

Zhang, L., Reutzel, E. W., & Michaleris, P. (2004). Finite element modeling discretization requirements for the laser forming process. *International Journal of Mechanical Sciences*, *46*(4), 623–637. doi:10.1016/j.ijmecsci.2004.04.001

Zhang, P., Guo, B., Shan, D., & Ji, Z. (2007). FE simulation of laser curve bending of sheet metals. *Journal of Materials Processing Technology*, *184*(1-3), 157–162. doi:10.1016/j.jmatprotec.2006.11.017

This work was previously published in the International Journal of Manufacturing, Materials, and Mechanical Engineering, Volume 1, Issue 1, edited by J. Paulo Davim, pp. 1-17, copyright 2011 by IGI Publishing (an imprint of IGI Global).

Chapter 9
The Impact of FEM Modeling Parameters on the Computed Thermo-Mechanical Behavior of SLA Copper Shelled Electrodes

Vassilios Iakovakis
Technological Educational Institute of Larissa, Greece

John Kechagias
Technological Educational Institute of Larissa, Greece

George Petropoulos
University of Thessaly, Greece

Stergios Maropoulos
Technological Educational Institute of West Macedonia, Greece

ABSTRACT

In this study, the authors use the finite element method to model and analyse a cylindrical copper shelled SLA electrode for EDM operations, which is investigated experimentally in literature. A uniform silver paint thickness and copper shell thickness is assumed around the SLA epoxy core. In the experiment, 2-D analysis was used due to the axissymmetric shape, and steady state and transient die sink EDMing simulations were followed. Modelling parameters are varied and their impact on the resulting temperature and stress fields is evaluated. The intermittent nature of the electrode thermal loading is also simulated with FEM transient analysis. It is shown that, using the finite element method, the influence of the copper shelled SLA electrode manufacturing and EDM-process parameters can be studied.

DOI: 10.4018/978-1-4666-1867-1.ch009

Copyright © 2013, IGI Global. Copying or distributing in print or electronic forms without written permission of IGI Global is prohibited.

INTRODUCTION

Electro-Discharge Machining (EDM), one of the most extensively used non-conventional material removal processes, has been studied extensively by a number of researchers (Ho & Newman, 2003; Kechagias et al., 2008). In addition, EDM electrode fabrication attempts, using Stereo-Lithography Apparatus (SLA) prototypes or patterns, were made (Jacobs, 1996; Björke, 1992; Arthur et al., 1996), in parallel to RP development. It was proposed that an investigation of the electro-deposition of metal coatings, especially if it is applied on a complex geometry, is required.

An investigation of heat distribution and the associated failure modes of the above electrodes was conducted (Arthur & Dickens, 1998). It was concluded that the electrode failure occurs through a combination of thermal effects which lead to several failure modes. Moreover, attempts to improve electroplated electrode efficiency were made using copper pyrophosphate electrolyte instead of acid copper in the stage of secondary metallization of the electrode (Bocking et al., 1997). Although good pore closure properties were achieved in this way, the shear stresses between the epoxy core and the copper increased due to the operating temperature (55 ^{o}C) resulting in distortions of the electrode shell.

A finite elements analysis was performed in an electrode with simple cylindrical form (Mathew, 2005) in order to identify the failure mechanism of electroformed stereo-lithography electrodes using LSDYNA-970. The FEM model is validated by comparing calculated temperatures to measured ones. It was concluded that the temperature distribution and coefficient of thermal expansion mismatches are the main reasons for high stresses, which in turn could cause the premature failures experienced in these types of electrodes. Some design modifications including heat conduction channels and stress relaxation notches did notably alter the temperature and stress distribution in the electrode (Iakovakis et al., 2009), that was modeled using ANSYS. Mesh refinement, which was done in the latter work, has some significant influence on the calculated stresses but not on the temperature distribution.

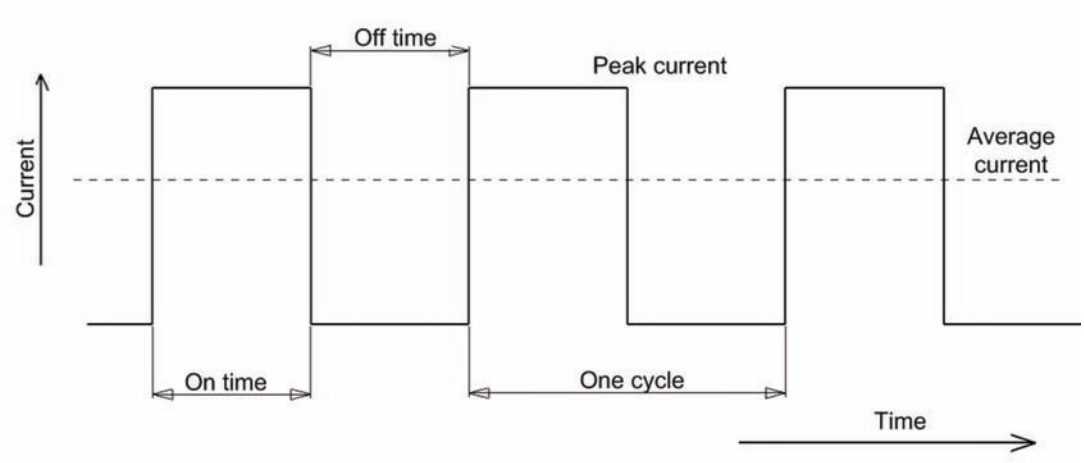
In the present work thermo-mechanical simulations were applied in the same cylindrical copper shelled SLA electrode using again the ANSYS FEM commercial code. The electrode consists of an SLA epoxy core surrounded by a copper shell. A thin layer of silver paint is inserted between them. The thicknesses of the silver paint and the copper shell are assumed as uniform and constant around the SLA epoxy core. Due to the axis-symmetric shape, a 2-D analysis was used, and simulations mainly in steady state die sink EDMing conditions were followed. Emphasis was given this time on the dominant simulation parameters such as the value of the thermal load, the influence of the ambient and the dielectric fluid temperature and the need of the incorporation of the silver paint layer in the FE model. The ability of the used software to handle the intermittent loading of the electrode during real EDMing was also tested.

It is clearly stated, that the scope of this work is the investigation of the impact of the modelling parameters on the computed temperature and stress distribution. Accompanying the simulation with some evidence of its validity, the FE analysis could be a powerful tool not only for the prediction of the premature failure of the copper shelled SLA electrodes but also for the improvement of their performance.

THERMOMECHANICAL SIMULATIONS

As aforementioned, the thermal load generated during EDM (Figure 1) causes failure of the SLA electrodes. The very unlike response to heat of the resin core and the copper shell is the main reason for most failure modes (Arthur & Dickens, 1998). This is justified as it is well known that heat affects distortions, which depend on the physical

Figure 1. Periodic discharges



properties of the structure subjected to the thermal load. The knowledge of the influence of the various parameters on the electrode behaviour can help in the development of SLA electrodes, which show acceptable wear when loaded with higher currents. Since experimental research is difficult, the Finite Element Method (FEM) can be used to approach the temperature and stress distributions in the electrode.

A coupled field analysis is required when the coupled interaction of thermal and mechanical phenomena is significant. The matrix equation, which is used, has the general form:

$$\begin{bmatrix} \underline{\underline{M}} & \underline{\underline{0}} \\ \underline{\underline{0}} & \underline{\underline{0}} \end{bmatrix} \cdot \begin{bmatrix} \ddot{\underline{u}} \\ \ddot{\underline{T}} \end{bmatrix} + \begin{bmatrix} \underline{\underline{C}} & \underline{\underline{0}} \\ \underline{\underline{0}} & \underline{\underline{C^t}} \end{bmatrix} \cdot \begin{bmatrix} \dot{\underline{u}} \\ \dot{\underline{T}} \end{bmatrix} + \begin{bmatrix} \underline{\underline{K}} & \underline{\underline{0}} \\ \underline{\underline{0}} & \underline{\underline{K^t}} \end{bmatrix} \cdot \begin{bmatrix} \underline{u} \\ \underline{T} \end{bmatrix} = \begin{bmatrix} \underline{F} & \underline{F^{th}} \\ \underline{Q} & \underline{Q^{ted}} \end{bmatrix} \tag{1}$$

where

$\underline{\underline{M}}$, $\underline{\underline{C}}$, $\underline{\underline{K}}$ are the structural mass, damping and stiffness matrices respectively,

$\underline{\underline{C^t}}$, $\underline{\underline{K^t}}$ are the thermal specific heat and conductivity matrices respectively,

$\underline{u}$, $\dot{\underline{u}}$, $\ddot{\underline{u}}$ is the displacement vector and its time derivatives,

$\underline{T}$, $\dot{\underline{T}}$, $\ddot{\underline{T}}$ is the temperature vector and its time derivatives,

$\underline{F}$, $\underline{Q}$ are the mechanical (e.g. forces) and thermal loads (e.g. heat flows) respectively,

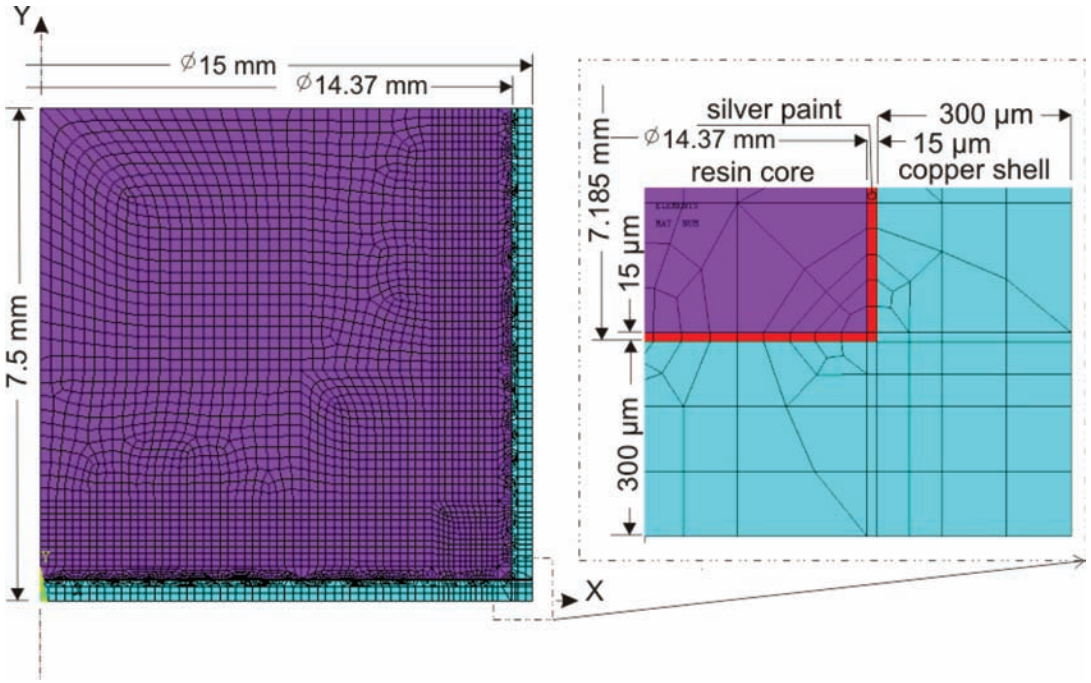
$\underline{F^{th}}$ is the thermal strain force vector and

$\underline{Q^{ted}}$ is the heat generation rate vector for thermoelastic damping

The SLA-electrode, which is investigated, was presented in (Mathew, 2005) and has a simple cylindrical form with 15 mm in diameter and 7.5 mm in height. The selection of this simple form facilitates the interpretation of the results, which are caused by variations in the physical parameters (material properties, thermal loads etc.). The electrode consists of a resin core, a conductive silver paint of 15 µm and the copper layer of 300 µm thickness. Temperatures were recorded in the electrode during EDM, which was conducted with a current of 2 A, pulse on time of 30 ms, 10 ms pulse off time and a gap voltage of 65 V. These measures are used for the validation of the simulation.

A FEM analysis is carried out using the commercial software ANSYS R7.1, which has advanced capabilities regarding coupled field analysis. The axis-symmetry form of the elec-

Figure 2. FEM Model of the SLA-Electrode (Colours indicate regions with the same properties)



trode is turned to advantage and a corresponding axisymmetric model can be implemented using the PLANE-13 ANSYS-Element, which has three degrees of freedom (DOF) in every node, translations to X- and Y-direction and the node temperature. The most essential requirement of the mesh in FEM-Analysis is that the exact form of the object has to be reproduced in the model, which in this particular case taking into account the very thin layer of the silver paint together with the requirement of uniform elements having no extreme oblique angles or very unequal sides, leads to a very fine mesh (Figure 2) incorporating about 4,500 elements. This is adequate for the scope of this investigation, since a model with about 15,000 elements (Iakovakis et al., 2009) shows a noticeable change only on the calculated stresses.

The material properties shown in Table 1 are considered constant during processing. This is valid for the resin too, as long as its temperature remains well below its glass transition temperature.

The applied boundary conditions are based on the following assumptions. Considering that the ambient temperature remains constant during

Table 1. Material properties (Mathew, 2005)

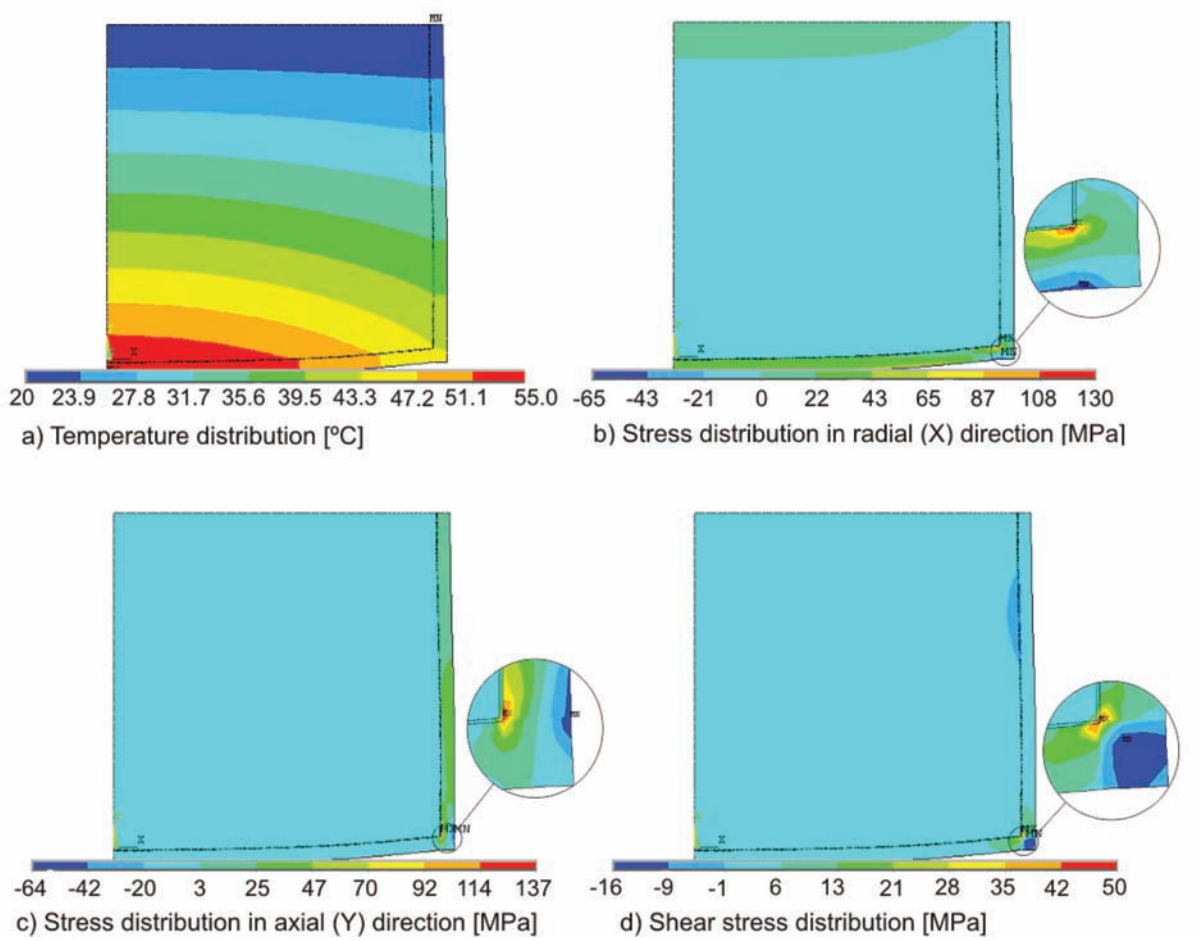
Property	Units	Resin	Silver paint	Copper
Density	Kg/m^3	1,100	10,500	8,960
Modulus of Elasticity	N/m^2	0.3117x1010	4.0 x1010	11.0 x1010
Poisson's Ratio	-	0.3	0.35	0.343
Coefficient of Thermal Expansion	m/(m.K)	$0.79x10^{-4}$	$0.30x10^{-4}$	$0.164x10^{-4}$
Thermal Conductivity	W/(m.K)	0.17	0.04	385
Specific Heat Capacity	J/(Kg.K)	50	300	385

EDM, the temperature on the top side of the model can also take the same value. Heat is transferred by convection from the outer (right) side of the electrode to the dielectric fluid, which has a constant temperature. The thermal-energy plasma, which loads the electrode during EDM, is simulated by heat flux on the model's bottom, which is assumed to be uniform over the entire surface. Y-translations at the model's top side are not allowed. Although the validity of these assumptions is not secured, their impact on the results is shown in this article.

RESULTS AND DISCUSSION

A reference model is intended to provide a basis for the calculations. The parameter values for these initial steady state analysis are: The ambient and the dielectric fluid temperature is 20°C, the heat transfer coefficient to the dielectric fluid is 100 W/(m^{2}K) and the heat flux is 100,000 W/m^2. The resulting temperature and stress distribution is shown in Figure 3. It is obvious that the highest temperature appears at the centre of the model. High stresses are located along the circumference of the bottom face. They reach extreme values

Figure 3. Temperature and stress distribution in the model – Steady state analysis



near the resin-copper interface. This result could be an explanation for the edge failures of SLA electrodes appearing during EDM (Arthur & Dickens, 1998).

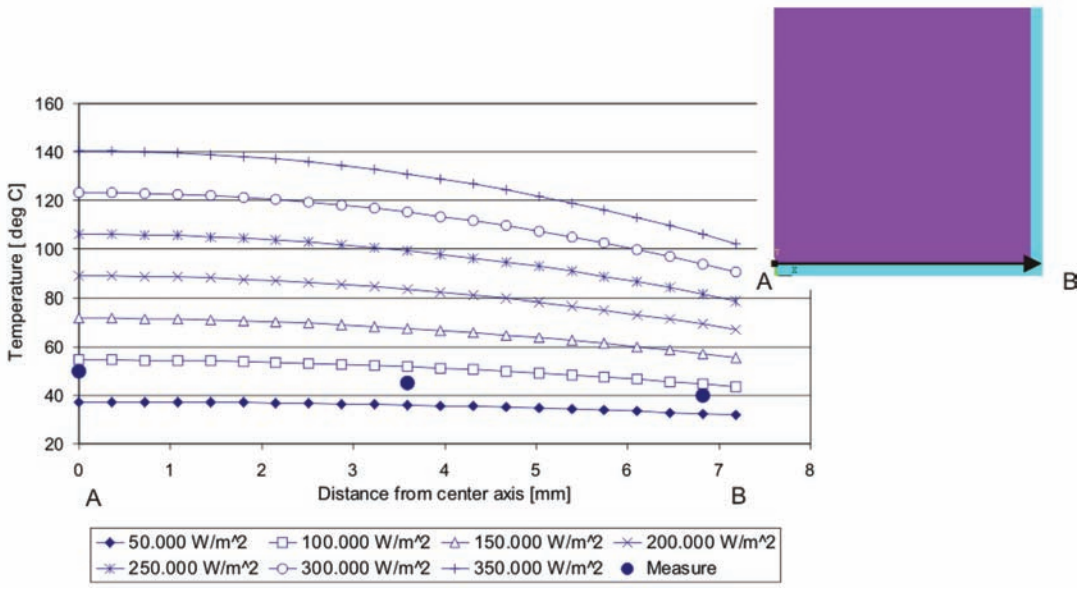
The heat flux on the bottom face has a weighty influence on the results. Various theories have been proposed to quantify the heat transferred to the electrodes during EDM. According to these theories the power of the heat source could be estimated as half of the electric power dissipated during the pulse (Arthur & Dickens, 1998). Considering that the electric power results from the product of the gap voltage and the current, which in this particular case is 130 W, the heat which is directed to the electrode is computed to be 65 W. The theoretical value of the heat flux, according to the above mentioned article, is about 367,824 W/m^2 (after dividing with the face area).

The diagram in Figure 4 shows how the temperature is changing along the radial direction at the resin – silver paint interface, when the given heat flux is varying between 50,000 and 350,000 W/m^2. The temperatures measured (Mathew, 2005) are lower than, but close to, those calculated with the heat flux being 100,000 W/m^2. Any evaluation of these results should take into account the possibility, that the data recorded using thermocouples may be lower than the actual temperatures since thermocouples act as a heat-sink, providing a more rapid dissipation of heat from the coating (Arthur & Dickens, 1998). The assumption, however, that half of the electric power is dissipated in the electrode has to be reconsidered.

The impact of other modelling parameters on the results can be studied, if the appropriate heat flux in this particular case, is accepted to be 100,000 W/m^2. The diagram in Figure 5 shows that if the ambient and dielectric fluid temperature is varying, the temperatures in the model have to be changed proportionally to this variation.

Another interesting aspect is the function of the silver paint. It has already been mentioned that the existence of the very thin layer of the silver paint leads to a very fine mesh. It could be assumed that the accuracy is not affected by the modelling of the silver paint. Assuming that the silver paint has similar properties to the copper and excluding it from the model, the resulting

Figure 4. Temperature distribution along the line AB – Variation of the heat flux



FEM-Model can have about 2,200 elements (Figure 6a), which are about half of the original model (Figure 2). The resulting temperature distribution (Figure 6b) is almost the same with that resulting from the reference model (Figure 3a). The stresses, however, are very different. The maximum stress in the radial (X) direction (Figure 6c) is about 30% lower than that in the reference model (Figure 3b). The maximum shear stress (Figure 6c) is less than half the value of the reference model (Figure 3d). It is concluded that exclusion of the silver paint from the modelling has a significant impact on the results.

The presented results were obtained from steady state calculations. To take into account the intermittent character of the thermal loading, which occurs during EDM, a transient analysis is carried out. The Newmark method, which is applied, uses finite difference expansions in the time interval $\Delta t = t_{n+1} - t_n$, in which it is assumed that

$$\underline{\dot{u}}_{n+1} = \underline{\dot{u}}_n + \{(1-\delta)\cdot \underline{\ddot{u}}_n + \delta \cdot \underline{\ddot{u}}_{n+1}\}\cdot \Delta t \qquad (2)$$

$$\underline{u}_{n+1} = \underline{u}_n + \underline{\dot{u}}_n \cdot \Delta t + \left\{\left(\frac{1}{2} - a\right)\underline{\ddot{u}}_n + a \cdot \underline{\ddot{u}}_{n+1}\right\}\cdot (\Delta t)^2 \qquad (3)$$

$$\underline{T}_{n+1} = \underline{T}_n + (1-\theta)\cdot \Delta t \cdot \underline{\dot{T}}_n + \theta \cdot \Delta t \cdot \underline{\dot{T}}_{n+1} \qquad (4)$$

where, δ, α and θ are integration constants.

Using ANSYS, a transient analysis can be conducted either by defining multiple load steps or by using a single load step and tabular boundary conditions with an array parameter to define the time points. The second method was preferred in this work because of its simplicity. The bottom face of the reference model is step-loaded with the appropriate thermal loads at the corresponding time intervals (Figure 7). During pulse on time heat flux 100,000 W/m^2 loads the bottom face. In the following pulse off period heat is transferred from the model to the surrounding dielectric fluid with the same parameters as for the outer (right) surface of the model. The results (temperature, deformations and stresses) of every time interval

Figure 5. Temperature distribution along the line AB – Variation of the ambient and dielectric fluid temperature

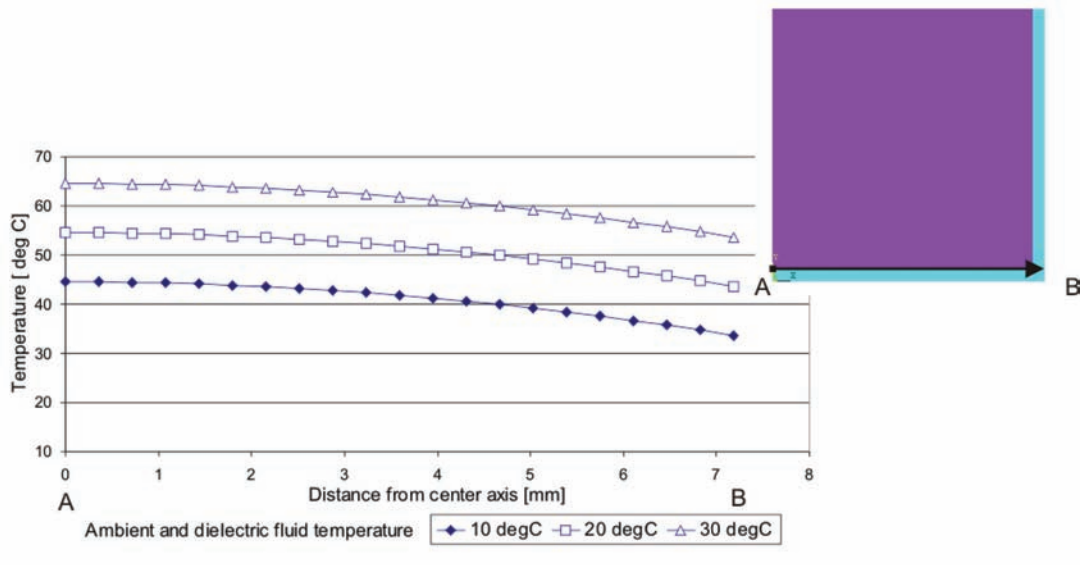
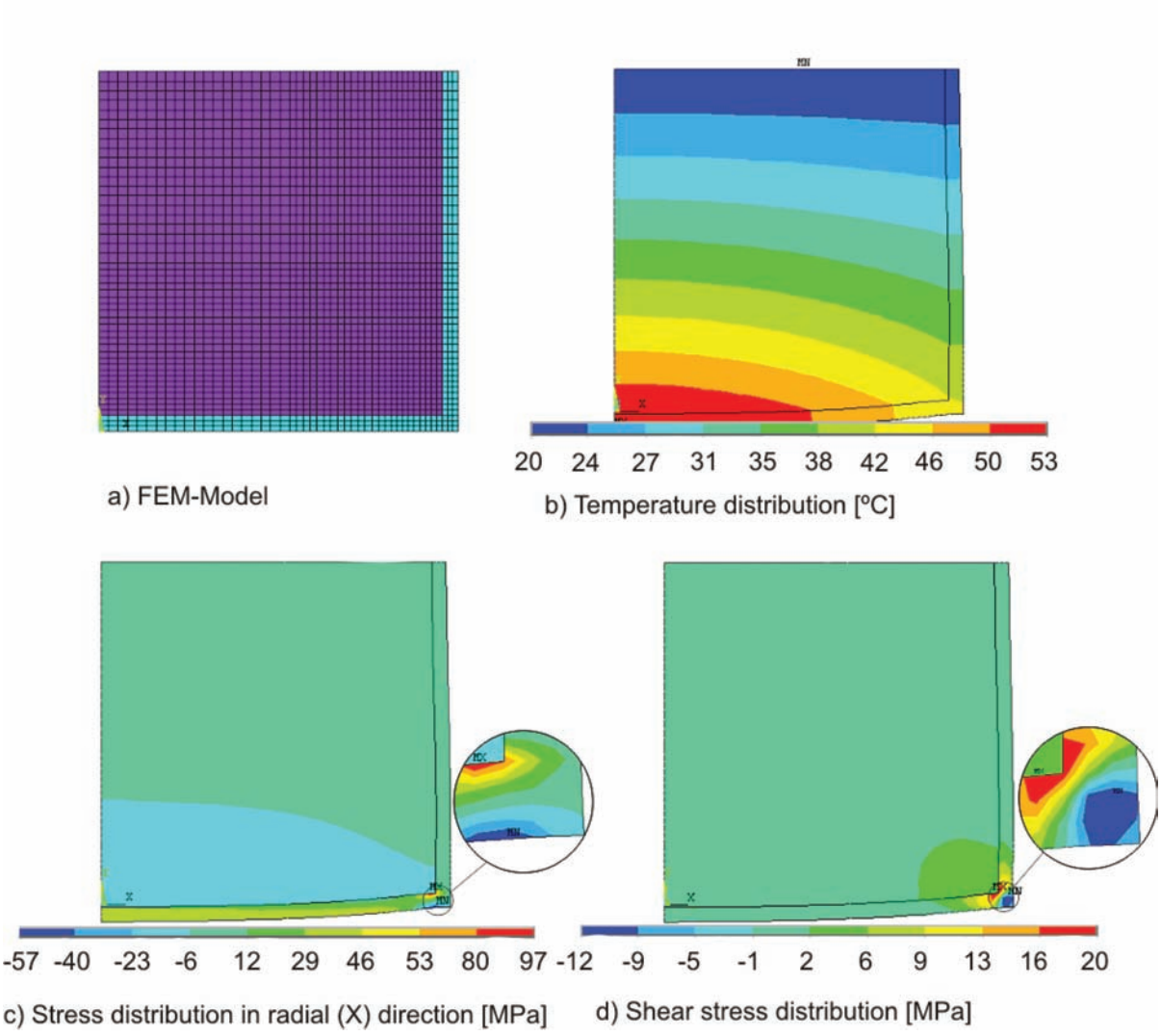


Figure 6. Temperature and stress distribution in the model – Steady state analysis



are comprised in the initial conditions of the next time interval.

This simulation ran up to 1.6 s and was interrupted because of the large amount of data produced, which includes the resulting temperatures, deformations and stresses in every node for every time point. The temperature growth for three selected points, which are located in the interface between the resin core and the silver paint, is shown in Figure 8. Point A lies on the central axis. The distances AB and BC are 3.4 mm. It is obvious that temperature increases rapidly in the first second and reaches approximately 65% of its final value, which according to the steady state analysis is 54°C.

Using FEM and the disciplines, which were presented in this paper, it could be possible to investigate the impact of various EDM process parameters, in addition to the SLA electrode configuration, on crucial quantities such as the temperatures and the stresses appearing in the electrodes. Indisputable is the dominating role of the given thermal load. Experimental work is required in order to estimate the relationship

Figure 7. Heat flux on the bottom face

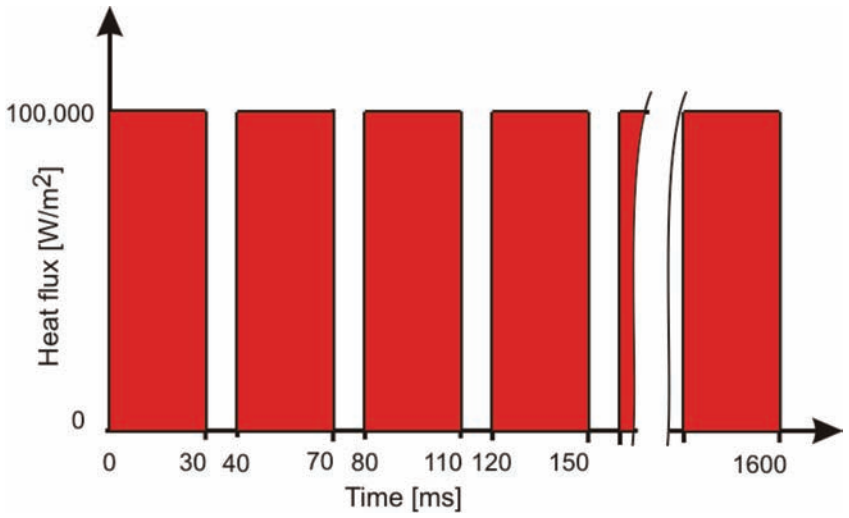
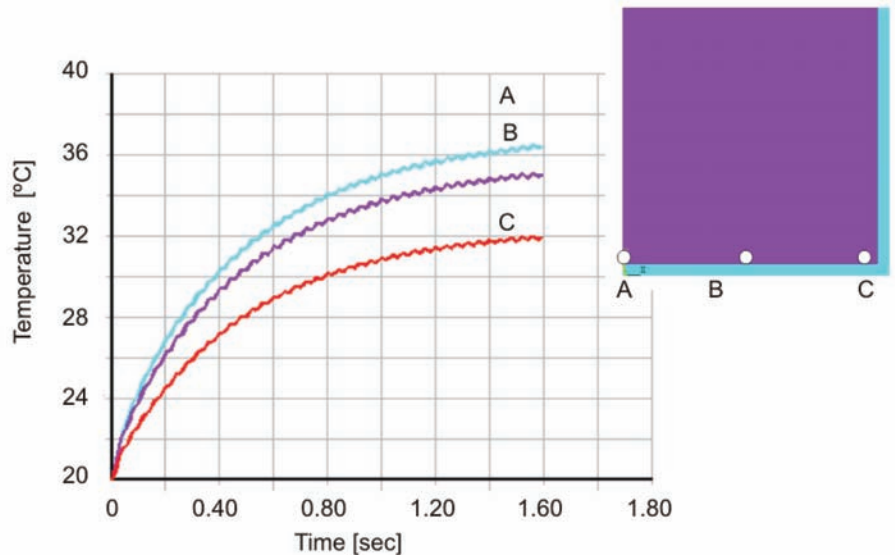


Figure 8. Temperature at the locations A, B, C after a transient analysis



between EDM process parameters and the corresponding heat flux.

CONCLUSION AND FURTHER RESEARCH

The proposed FEM-model facilitates the investigation of the effects of the physical parameters on the resulting temperatures and stresses. The calculated temperatures are close to experimentally obtained data in view of the literature. However it is shown that the results depend on the boundary conditions applied. Temperatures and stresses in the model alter proportionally to the applied heat flux. Also the change of the temperature of the dielectric fluid has a significant impact on the results. Sinking of the electrode temperature could be achieved

by cooling the dielectric fluid, which could lead to a better performance of the SLA electrodes. Modelling of the silver paint layer is inevitable, otherwise reduced stresses are calculated. However, this effect could be turned to advantage for SLA electrodes, if the mechanical properties of the conductive metal paints could approach those of copper. In all cases high stresses appear in areas, where the literature reports SLA electrode failures. Transient analysis was used to simulate the intermittent thermal load on the electrode. It is shown, that the temperatures in the electrode rise very fast reaching in a few seconds their steady state value. Different combinations of pulse- on and pulse- off times can be easily studied.

The above analysis assumed a constant copper shell as well as silver paint thickness. In practice both are variable and strongly dependent on electroplating parameters as well as on the electrode shape. Another witness of the presented model is the assumption of the uniformly distributed thermal load. Subject of future work could be the determination of an appropriate load algorithm, which could simulate the non-uniformly distributed spark discharges over the electrode surface in an actual EDM process

If the above mentioned problems find adequate solutions, then the FEM-simulation could be easily applied on different materials, EDMing initial conditions and other variation of rapid tooling electrodes and predict their thermo-mechanical behaviour.

REFERENCES

Arthur, A., & Dickens, P. M. (1998). The measurement of heat distribution in stereolithography electrodes during electro-discharge machining. *International Journal of Production Research*, *36*(9), 2451–2461. doi:10.1080/002075498192625

Arthur, A., Dickens, P. M., & Cobb, R. (1996). Using rapid prototyping to produce electrical discharge machining electrodes. *Rapid Prototyping Journal*, *2*(1), 4–12. doi:10.1108/13552549610109036

Björke, O. (1992). *Layer manufacturing – a challenge of the future*. Trondheim, Norway: Tapir Academic Press.

Bocking, C. E., Bennett, G. R., Dover, S. J., Arthur, A., Cobb, R. C., & Dickens, P. M. (1997). Electrochemical routes for engineering tool production. *The GEC Journal of Technology*, *14*(2), 66–74.

Ho, K. H., & Newman, S. T. (2003). State of the art electrical discharge machining (EDM). *International Journal of Machine Tools & Manufacture*, *43*, 1287–1300. doi:10.1016/S0890-6955(03)00162-7

Iakovakis, V., Kechagias, J., Petropoulos, G., & Maropoulos, S. (2009). Finite elements analysis of cylindrical copper shelled SLA electrodes. In da Silva Bartolo, P. J., Jorge, M. A., da Conceicao Batista, F., Almeida, H. A., Matias, J. M., & Vasco, J. C., (Eds.), *Innovative development in design and manufacturing* (pp. 651–656). Boca Raton, FL: CRC Press.

Jacobs, P. F. (1996). *Stereolithography and other RP&M techniques: From rapid prototyping to rapid tooling*. New York, NY: ASME Press.

Kechagias, J., Iakovakis, V., Katsanos, K., & Maropoulos, S. (2008). EDM electrode manufacture using rapid tooling: A review. *Journal of Materials Science*, *43*, 2522–2535. doi:10.1007/s10853-008-2453-0

Mathew, J. (2005). *Thermo-mechanical analysis of metallized stereolithography EDM electrodes*. Retrieved from http://hdl.handle.net/10057/572

This work was previously published in the International Journal of Manufacturing, Materials, and Mechanical Engineering, Volume 1, Issue 3, edited by J. Paulo Davim, pp. 21-30, copyright 2011 by IGI Publishing (an imprint of IGI Global).

Chapter 10
Micro Machining of Nonconductive Al_2O_3 Ceramic on Developed TW-ECSM Setup

Alakesh Manna
PEC University of Technology, India

Amandeep Kundal
PEC University of Technology, India

ABSTRACT

Advanced ceramic materials are gradually becoming very important for their superior properties such as high hardness, wear resistance, chemical resistance, and high strength to weight ratio. But machining of advanced ceramic like Al_2O_3 ceramics is very difficult by any well known and common machining processes. Normally, cleavages and triangular fractures generate when machining of these materials is done by traditional machining methods. It is essential to develop an efficient and accurate machining method for processing advanced ceramic materials. For effective machining of Al_2O_3 ceramics, a traveling wire electrochemical spark machining (TW-ECSM) setup has been developed. The developed TW-ECSM setup has been utilized to machine Al_2O_3 ceramic materials and subsequently test results are utilized to analyze the machining performance characteristic. Different SEM photographs show the actual condition of the micro machined surfaces. The practical research analysis and test results on the machining of Al_2O_3 ceramics by developed TWECSM setup will provide a new guideline to the researchers and manufacturing engineers.

INTRODUCTION

Advancement in today's materials technology need appropriate processes for machining of low machinability materials. Advanced machining processes are being successfully used in industries for production of components made of low machinability but electrically conducting materials. With the rapid technological development of engineering ceramic materials, the machining of the ceramics is an imperative for manufacturing engineers and applied researchers. But it becomes more difficult to machine non conductive ceramic materials once they are highly sintered. Hence, it is essential for developing an efficient and accurate machining method for processing advanced

DOI: 10.4018/978-1-4666-1867-1.ch010

Copyright © 2013, IGI Global. Copying or distributing in print or electronic forms without written permission of IGI Global is prohibited.

ceramic materials. For effective machining of non conductive ceramic materials e.g. Al_2O_3-ceramic, Traveling Wire Electro-chemical Spark Machining (TW-ECSM) setup has been developed. The developed setup has been utilized to machine Al_2O_3 ceramic materials and subsequently **analyze** the machining performance characteristics with respect to various parameters of TW-ECSM.

Traveling Wire Electro-chemical Spark Machining (TW-ECSM) is a hybrid non-conventional machining process. The TW-ECSM setup **is** made based on the combine phenomena of electrochemical machining (ECM) and the wire electro discharge machining (WEDM) processes. TW-ECSM has combined characteristics of ECM and WEDM, can **be** effectively used for machining of high strength electrically non-conductive materials e.g. Al_2O_3-ceramic. In the TW-ECSM process, the material removal takes place due to the combined effects of electrochemical (EC) reaction and electrical spark discharge (ESD) action. It has two electrodes dipped in an electrolyte which may be acidic or alkaline. The material to be machined is dipped in the electrolyte and placed very near to the cathode (tool). A constant DC voltage is applied between the machining-tool or tool-electrode (cathode) and the counter electrode (anode). The counter electrode is a flat plate with a much larger surface than the tool surface (about a factor 100). When the applied voltage is below a critical voltage of about 25 V, electrolysis occurs. Hydrogen gas bubbles are formed at the tool electrode (cathode) and oxygen bubbles at the counter electrode (anode). It has been observed that if the two electrodes are of different sizes then beyond a certain value of applied voltage, electric sparks appear at the electrode-electrolyte interface on the smaller electrode and the cell current drops. As voltage is increased, current density rapidly increases too. The density and the mean radius of the bubbles increase and bubbles finally coalesce into a gas film around the tool-electrode.

However, from the past literature survey, it is evident that some research on electrochemical discharge machining have been carried out by the previous researchers but still a lot of applied research in the above fields are required so as to explore the successful utilizations of the process in the area of machining of non conductive ceramics. Singh et al. (1996) studied on electrochemical spark machining (ECSM) process and concluded that material removal rate is found to increase with increase in supply voltage. Peng and Liao (2004) studied on electrochemical discharge machining for slicing non-conductive brittle materials and concluded that the pulsed DC power proves better spark stability and more spark energy release proportion than constant DC power. Bhattacharyya et al. (1999) studied on electrochemical discharge machining (ECDM) of non conductive ceramic materials and suggested a range of parametric combinations for enhancing the machining rate and accuracy. Kulkarni et al. (2002) conducted an experimental study on electrochemical discharge machining and discussed the basic mechanism of material removal. Jain et al. (2002) studied on electrochemically spark abrasive drilling (ECSAD) and concluded that abrasive cutting tools gave the improved performance related to machining of electrically non conducting materials. Chak and Rao (2007) investigated on the electro-chemical discharge machining (ECDM) process and concluded that machining performance gradually deteriorates with increase in tool depth. Masuzawa et al. (1985) studied on wire electro-discharge grinding for micro-hole ED drilling and analyzed machining characteristics including accuracy and repeatability. Lin et al. (2007) studied on micro-slit EDM machining and observed that pure water could obtain high material removal rate (MRR). Jain et al. (1999) performed the analysis of the electrochemical spark machining process and explained various experimental results, on the basis of circuit and arc discharge valve characteristics. Basak and Ghosh (1997) studied on the mechanism of spark generating during electrochemical discharge machining. Authors developed a theoretical model of the

discharge phenomenon and estimated the critical voltage and current required to initiate discharge between the electrode and the electrolyte.

DESIGN AND DEVELOPMENT OF TRAVELING-WIRE ECSM SETUP

Figure 1 shows line diagram of the designed and fabricated traveling-wire ECSM setup utilized for machining of electrically non-conductive alumina (Al_2O_3) ceramic material.

The main supply 220 volt A.C. is utilized for operating an A.C motor which rolls the wire around a pulley fixed on it. A step down transformer is used for stepping down the main supply 220 volt AC to 18 volt. The stepped down 18 volts AC is used to run a stepper motor which gives feed motion to the work-piece fixture. A jig and fixture is **designed** and fabricated to hold the work-piece and locate the tool. A printed circuit board is deigned and fabricated, and used to give automatic feed motion to the stepper motor. A scale is fixed along the side of the electrolyte tank to measure the gap between micro tool i.e. cutting wire and copper anode. The gap between cutting wire and anode can be increased or decreased by moving the anode towards travel wire i.e. cathode. A D.C generator is used to convert the AC voltage into D.C voltage and its output terminals are connected to anode and cathode. A potentiometer is used in the circuit to vary the output voltage. The output negative terminal of the D.C generator is connected to the tool i.e. wire electrode. The output positive terminal of the D.C generator is connected to a copper strip of 1 mm thickness

Figure 1. Line diagram of TW-ECSM set up

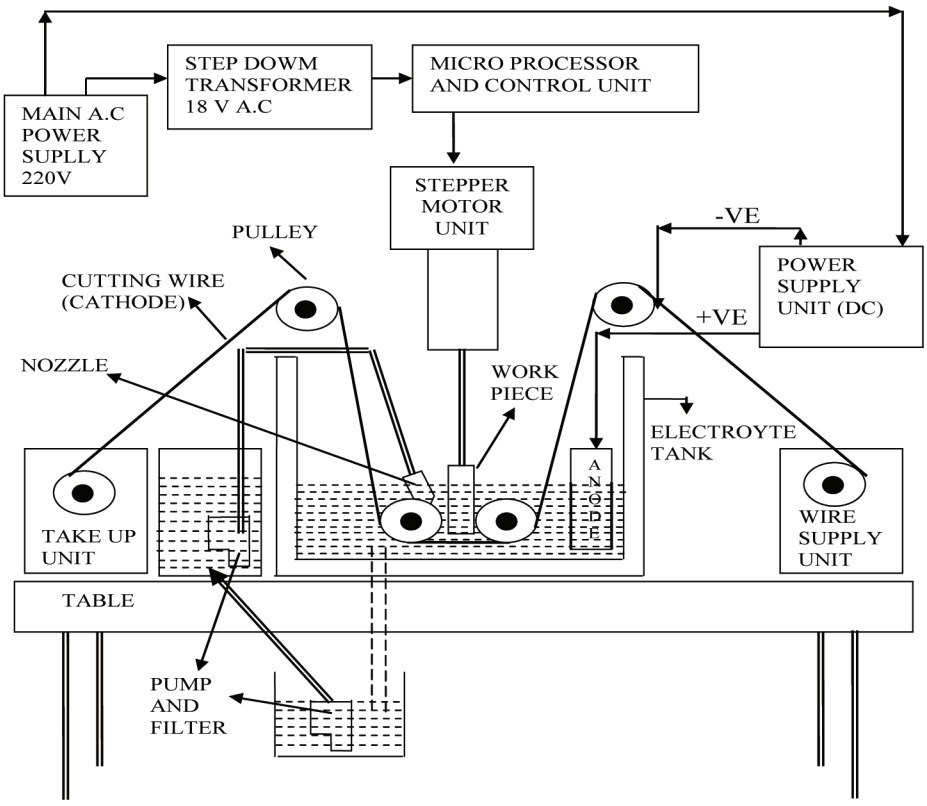


Table 1. Details of experimental conditions

Machine tool	Developed Micro TW-ECSM setup
Electrolyte used	Sodium Hydroxide (NaOH),96% Assay,2% Na_2CO_3
Electrolyte concentration: ratio of NaOH and Dematerialized deionised water	(i) 50 g: 1 Litre
	(ii)70 g:1 Litre
	(iii) 90 g: 1 Litre
	(iv)110 g:1 Litre
Work-piece material	Electrically non-conductive high strength-high-temperature-resistant aluminium oxide (Al_2O_3) ceramics
Work-piece thickness	2.8 mm
Tool i.e. wire electrode	(i) IS- 3748/ T35Cr5Mo1V30/ 70 µm and 90 µm diameter
	(ii) Brass /200 µm and 250 µm diameter

and 50 mm wide. About 90% of the copper plate (i.e. anode) is dipped in the electrolyte. The copper anode plate is fixed on an insulated square rod and hanged from the top of the electrolyte tank. The concentration of the electrolyte is controlled initially by mixing the proper ratios of NaOH pellets and demineralised water. The ratio of NaOH and demineralised water was varied from 30 g: 1 liter to 110 g: 1 liter during conducting the experiments.

PLANNING FOR EXPERIMENTATION

A traveling-wire electrochemical spark machining setup has been developed and fabricated for conducting the experiments. Different micro cutting tests were performed on electrically non-conductive high strength-high-temperature-resistant aluminium oxide (Al_2O_3) ceramics using developed TW-ECSM setup. Table 1 shows the details of the developed TW-ECSM setup, tool i.e. wire electrode, work-piece and electrolyte used for experimentation. Table 2 shows the different parameters and their levels considered for the experimental investigation. The material removal is determined by difference of weight of work-pieces before and after each micro cutting. Contech (Instrument) Electronic Balance of resolution 0.001g is used to weight the work-pieces before and after each run. The depth of cut of micro cutting was measured by a digital depth gauge of resolution **0.001mm.** Scanning Electro Micrograph (SEM) photographs are taken to analyze the surface texture of the machined surface. The micro cutting time is recorded by utilizing a decimal-minute stop watch of accuracy 0.1s. The cutting time for a complete micro cut is estimated by difference between the starting time and finishing time of each micro machining operation.

RESULTS AND DISCUSSIONS

A series of experiments have been carried out keeping constant current supply i.e. 0.5A with variation of different parametric setting value as mentioned in Table 2 and the results are presented for discussion. Different graphs have been plotted to analyze the effect of various parameters of traveling-wire electrochemical spark machining (TW-ECSM) setup on the machining characteristics e.g. material removal, spark gap width. Different scanning electron micrographs (SEM) show the characteristics of the generated spark gap width during TW-ECSM operation.

Figure 2 represents different curves showing the investigated results obtained during machining

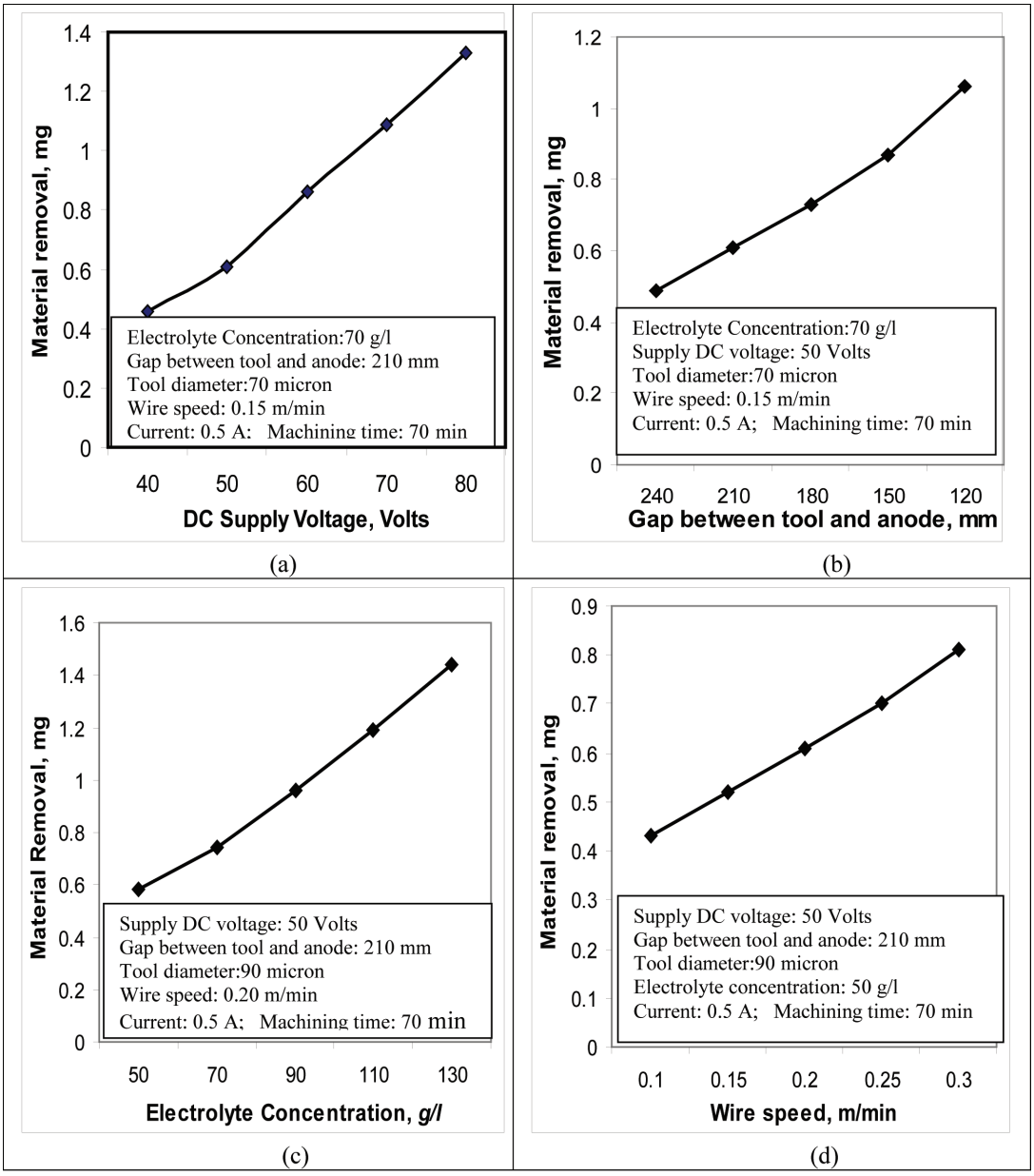
Table 2. Developed TW-ECSM parameters and their levels

Parameters, their symbols and units	Parametric Levels				
	1	2	3	4	5
A: DC supply voltage (X_1, Volt)	40	50	60	70	**80**
B: Electrolyte concentration X_2, (g/*l*)	50	70	90	110	**130**
C: Gap between tool and anode (X_3, mm)	240	210	180	150	**120**
D: Wire Speed (X4, m/min)	0.10	0.15	0.20	0.25	**0.3**

of electrically non-conductive high strength-high-temperature-resistant aluminium oxide (Al_2O_3) ceramics material by developed TW-ECSM setup. Figure 2 shows the variation in material removal with that of DC supply voltage, gap between tool and anode, electrolyte concentration and wire speed in TW-ECSM by IS-3748/T35 Cr5Mo1V30/ 70 µm and 90 µm diameter steel wire electrode. From Figure 2(a), it is clear that initially there is slight increase in MR with increase in supply DC voltage thereafter MR increases sharply with increase in supply DC voltage. Maximum material removals 1.33 mg is observed after 70 min continuous machining and at 80 volts of DC supply voltage with at constant 210 *mm* gap between tool and anode, 70 *g/l* electrolyte concentration, 0.5A current supply. Figure 2(b) shows the effect of gap between electrodes on MR during slicing of Al_2O_3 ceramics by developed TW-ECSM setup. From Figure 2(b), it is clear that initially there is regular increase in MR with decrease in gap between electrodes. Maximum material removal 1.06mg is observed after 70 *min* continuous machining and at 120 *mm* of gap between electrodes. Figure 2(c) represents a curve showing the effect of electrolyte concentration on material removal. From Figure 2(c), it is clear that there is increase in MR with increase in concentration of electrolyte. Maximum material removal 1.44 (mg) is observed at 130 *g/l* of electrolyte concentration. This curve is plotted utilizing the results obtained after 70 *min* continuous machining and at 50 *volts* DC supply voltage, 210 *mm* gap between electrodes, 90 µm steel wire diameter, 0.2 m/min wire speed, 0.5 A current supply. Figure 2(d) shows the effect of tool i.e. wire electrode speed on material removal. From Figure 2(d), it is clear that there is increase in MR with the increase in wire speed. Maximum material removal 0.81mg is observed after 70 *min* continuous machining and at 0.30 *m/min* of wire speed.

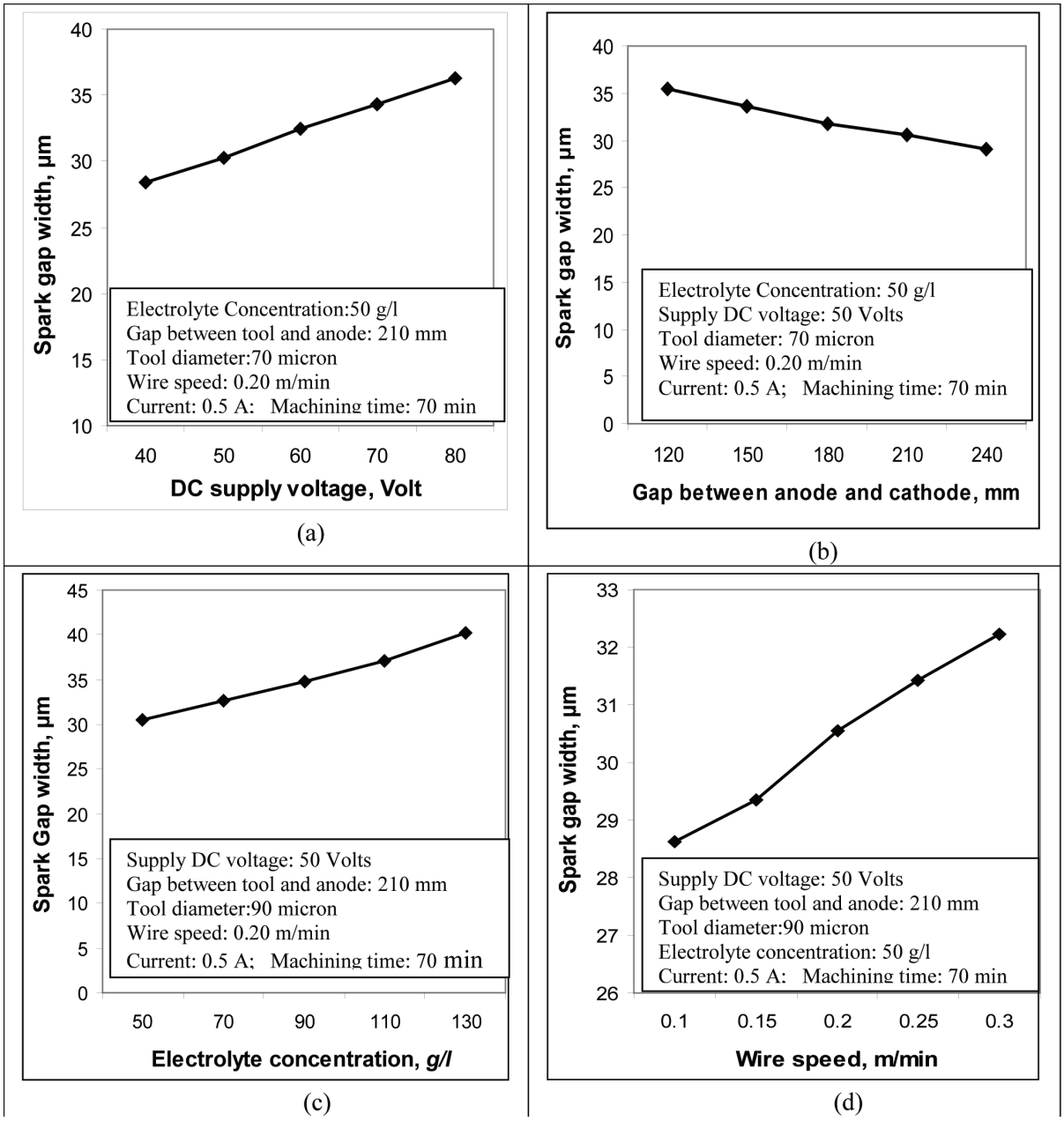
Figure 3 represents the different curves showing the variation in spark gap width with that of DC supply voltage, gap between tool and anode, electrolyte concentration and wire speed in TW-ECSM of electrically non-conductive Al_2O_3-ceramics by IS- 3748/ T35Cr5Mo1V30/ 70 µm and 90 µm diameter steel wire electrodes. From Figure 3(a), it is observed that there is regular increase in the spark gap width with increase of supply DC voltage. Maximum spark gap width 36.32 µm is observed at 80 *volts* of DC supply voltage. Figure 3(b) shows the effect of gap between cathode and anode on spark gap width. From Figure 3(b), it is clear that there is sharply decrease in spark gap width with increase in gap between electrodes. Maximum spark gap width 35.5 µm is observed at 120 *mm* gap between electrodes and at 0.20 m/min wire electrode speed. Figure 3(c) represents a curve showing the effect of electrolyte concentration on spark gap width. From Figure 3(c), it is observed that there is increase in spark gap width with increase in concentration of electrolyte. Maximum spark gap width 40.24 µm is observed at 130 *g/l* of electrolyte concentration. This curve is plotted utilizing the results obtained after 70 *min* continuous machining and at 50 *volts* DC supply voltage, 210

Figure 2. Variation in material removal with that of DC supply voltage, gap between tool and anode, electrolyte concentration and wire speed in TW-ECSM of electrically non-conductive high strength-high-temperature-resistant aluminium oxide (Al_2O_3) ceramics material by IS- 3748/ T35Cr5Mo1V30/ 70 µm and 90 µm diameter steel wire electrode.



mm gap between electrodes, 90 µm steel wire diameter, 0.2 m/min wire speed, 0.5A current supply. Figure 3(d) shows the effect of wire speed on spark gap width. From Figure 3(d), it is clear that spark gap width increases with increase in wire speed. Maximum spark gap width 32.22 µm is observed at 0.30 *m/min* of wire speed.

Figure 3. Variation in spark gap width with that of DC supply voltage, gap between tool and anode, electrolyte concentration and wire speed in TW-ECSM of electrically non-conductive high strength-high-temperature-resistant aluminium oxide (Al_2O_3) ceramics material by IS- 3748/ T35Cr5Mo1V30/ 70 µm and 90 µm diameter steel wire electrode.



SEM GRAPHS

Figure 4 shows the SEM photographs of different micro slice section on aluminum oxide (Al_2O_3) ceramics work-piece by traveling wire electro-chemical spark machining (TW-ECSM) setup. The SEM graph shows the actual condition of the micro machined surface. The micro slicing

shown in Figure 4(a) is the result of continuous 20 minutes machining with 90 μm diameter wire electrode at 0.10 m/min cutting speed. From the SEM graph, it is observed that micro slicing proceeds in the conical manner. From Figure 4(a), it is also observed that the surface of the micro slicing is irregular and poor surface finish. Some fins and burs are also observed during cutting in either sides of the sliced surface. During experiments it is observed that the particles from the surface of the work-piece material are scattered along the depth due to electrical sparking and generates irregular cutting surface throughout the depth of cut. Figure 4(b) represents a SEM micrograph obtained during micro slice on Al_2O_3 ceramics work-piece by developed TW-ECSM setup at parametric setting value 70 volts D.C supply, 240 mm gap between anode and cathode, and 110 g/*l* electrolyte concentration. The micro slice shown in Figure 4(b) is the result of continuous 70 minutes machining with 200 μm diameter brass wire electrode at 0.20 m/min cutting speed. From Figure 4(b), it is observed that the particles of the material are scattered along the depth due to electrical sparking and the generated cutting surface become irregular throughout the depth of cut. Figure 4(c) and Figure 4(d) show a picture of a micro slice section on Al_2O_3-ceramic work-piece taken by Coherence Correlation Interferometer Machine. The view shows the actual shape and spark gap width of the micro machined surface. This micro slice was machined at parametric setting value 40 volts D.C supply, 210 mm gap between anode and cathode and 70 g/*l* electrolyte concentration. The micro slicing shown in Figures 4(c) and 4(d) is the result of continuous 10 minutes machining with IS- 3748/ T35Cr5Mo1V30/ 70 μm diameter steel wire electrode at 0.15 m/ min cutting speed.

Figure 4(e) represents a SEM micrograph obtained during micro slice on Al_2O_3 ceramics material by utilizing developed TW-ECSM setup at 60 volts D.C supply voltage, 240 mm gap between anode and cathode, and 90 g/*l* electrolyte concentration. The micro slicing shown in Figure 4(e) is the result of continuous 70 minutes machining with 200 μm diameter wire electrode at 0.15 m/min cutting speed. At the beginning the width of the micro slice is slightly more than the wire diameter but after few minutes of cutting the width of the micro slice increases along the depth of cut. From the Figure 4(e), it is also observed that the surface of the micro slicing is irregular and generated circular shape of large gap at the end of cutting (i.e. at the end of 70 min of continuous cutting).

The micro slicing shown in Figure 4(f) is the result of continuous 70 minutes machining with 250 μm diameter wire electrode at 0.20 m/min cutting speed. At the beginning the width of the micro slice is more than the wire diameter but after few minutes of cutting the width decreases along the depth of cut. From the Figure 4(f), it is also observed that the surface of the micro slicing is irregular and poor surface finish. Burrs are noticed on the surface of the work-piece.

During traveling wire electrochemical spark machining process it is observed that machining performance gradually deteriorates with increase in tool depth and finally cause micro cracks on the machined surface due to thermal shocks at high voltage. Three most influential parameters are identified such as DC supply voltage, gap between cathode and anode and electrolyte concentration. Results revealed that moderate DC supply voltage has reduced the tendency of cracking; and at lower gap between cathode and anode generated debris during micro slicing of Al_2O_3 ceramics. It also observed that the sparking is started when the cutting wire touches the work-piece dipped under the electrolyte. Fins and scattered along the cutting surfaces are observed that may be due to the adhering of small particles scattered from the work surface during cutting and are not flash out by the die-electric fluid flow. It is may be due to low flashing pressure of electrolyte; again high flashing pressure of electrolyte may vibrate the wire during traveling and generates poor surface

Figure 4. Different SEM photographs shows the actual condition of the micro machined surface

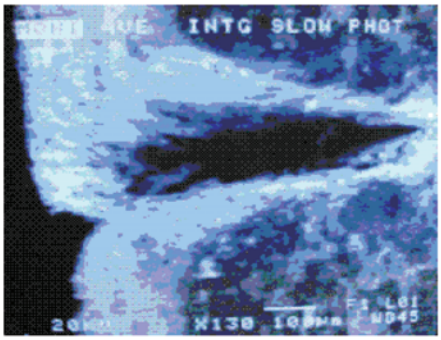


Figure 4(a). SEM of a micro slice work-piece produced at 40 volts D.C supply, 240 mm gap between electrodes, 50 g/*l* electrolyte concentration and 0.10 m/min cutting speed by 70 µm diameter steel wire.

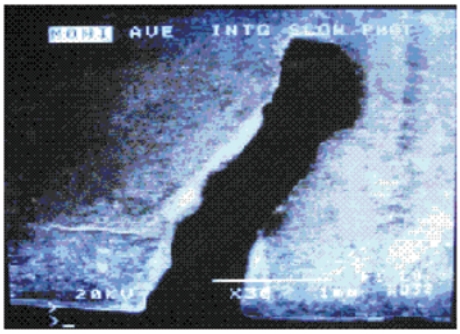


Figure 4(b). SEM of a micro slice work-piece produced at 70 volts D.C supply, 240 mm gap between electrodes, 110 g/*l* electrolyte concentration and 0.20 m/min cutting speed by 90 µm diameter brass wire.

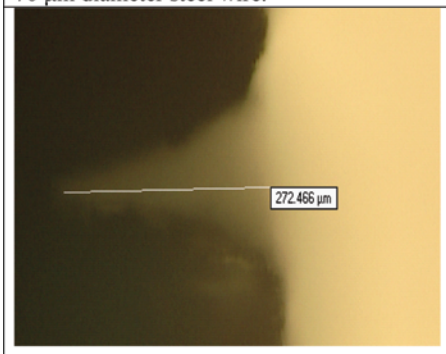


Figure 4(c). shows observed value of total depth of cut on Al_2O_3 ceramics by 70 µm diameter steel wire after continuous 10 minutes machining with parameter setting value 40 volts DC supply, 210 mm gap between anode and cathode, and 70 g/l electrolyte concentration.

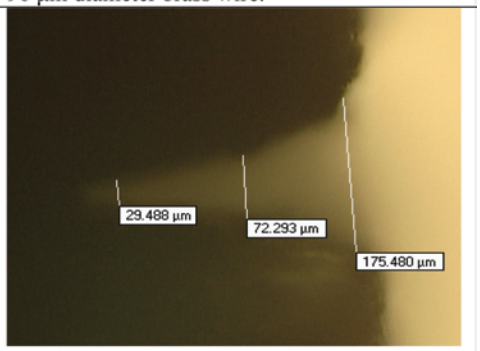


Figure 4(d). shows observed value of spark gap width on Al_2O_3 ceramics by 70 µm diameter steel wire after continuous 10 minutes machining with parameter setting value 50 volts DC supply, 240 mm gap between anode and cathode, and 70 g/*l* electrolyte concentration.

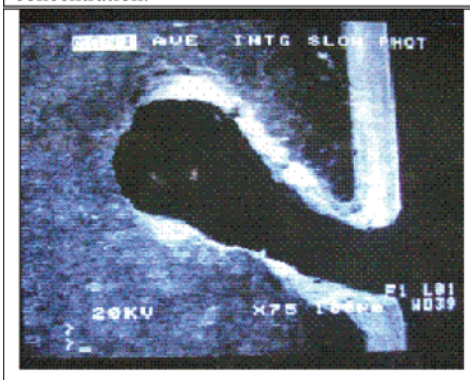


Figure 4(e). SEM of a micro slice work-piece produced at 60 volts D.C supply, 240 mm gap between electrodes, 90 g/*l* electrolyte concentration and 0.15 m/min cutting speed with 200 µm diameter steel wire.

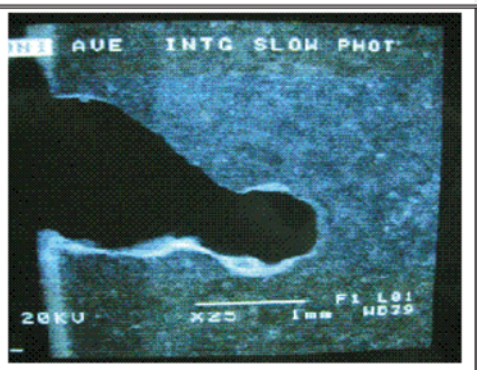


Figure 4(f). SEM of a micro slice work-piece produced at 70 volts D.C supply, 240 mm gap between electrodes, 110 g/*l* electrolyte concentration and 0.20 m/min cutting speed by 250 µm diameter brass wire.

finish. It is also observed that after few minutes of cutting the width of the micro slice increases along the depth of cut it may be due to improper tension and vibration of the travel wire. The burrs are also noticed along the surface of micro cutting, it may be due to the generation of debris during micro slicing and after certain time debris in the hydrogen bubbles turns into fins and burs. From the above discussion, it is clear that very fine micro cutting on electrically non-conducting ceramic material is a typical exercise. However, micro cutting on alumina ceramic is possible.

CONCLUSION

On the basis of the experimental results during machining of electrically non-conductive high strength-high-temperature-resistant aluminium oxide (Al_2O_3) ceramics by developed traveling wire electrochemical spark machining (TW-ECSM) setup and thereafter discussion on the investigated results the following conclusions are drawn as listed below.

1. Machining of electrically non-conductive Al_2O_3 ceramics is possible by non-conventional hybrid traveling wire electrochemical spark machining method.
2. At the beginning of micro cutting the width of the micro slice is slightly more than the wire diameter but after few minutes of cutting the width of the micro slice increases along the depth of cut. It is also concluded that the surface of the micro slicing is irregular and generated circular shape of large gap at the end of cutting.
3. Fins and scattered along the cutting surfaces are observed that may be due to the adhering of small particles scattered from the work surface during cutting and are not flash out by the die-electric fluid flow. The burrs are also noticed along the surface of micro cutting. Very fine micro cutting is a typical exercise on highly sintered electrically non-conducting ceramic material.

However, micro cutting on alumina ceramic is possible but compromise with the accuracy i.e. close tolerance and surface quality.

REFERENCES

Basak, I., & Ghosh, A. (1997). Mechanism of material removal in electrochemical discharge machining: A theoretical model and experimental verification. *Journal of Materials Processing Technology*, *71*, 350–359. doi:10.1016/S0924-0136(97)00097-6

Bhattacharyya, B., Doloi, B. N., & Sorkhel, S. K. (1999). Experimental investigations into electrochemical discharge machining (ECDM) of non-conductive ceramic materials. *Journal of Materials Processing Technology*, *95*, 145–154. doi:10.1016/S0924-0136(99)00318-0

Chak, S. K., & Rao, P. V. (2007). Trepanning of Al_2O_3 by electro-chemical discharge machining (ECDM) process using abrasive electrode with pulsed DC supply. *International Journal of Machine Tools & Manufacture*, *47*, 2061–2070. doi:10.1016/j.ijmachtools.2007.05.009

Jain, V. K., Choudhury, S. K., & Ramesh, K. M. (2002). On the machining of alumina and glass. *International Journal of Machine Tools & Manufacture*, *42*, 1269–1276. doi:10.1016/S0032-3861(02)00241-0

Jain, V. K., Dixit, P. M., & Pandey, P. M. (1999). On the analysis of the electrochemical spark machining process. *International Journal of Machine Tools & Manufacture*, *39*, 165–186. doi:10.1016/S0890-6955(98)00010-8

Kulkarni, A., Sharan, R., & Lal, G. K. (2002). An experimental study of discharge mechanism in electrochemical discharge machining. *International Journal of Machine Tools & Manufacture*, *42*, 1121–1127. doi:10.1016/S0890-6955(02)00058-5

Lin, C.-T., Chow, H.-A., Yang, L.-D., & Chen, Y.-F. (2007). Feasibility study of micro-slit EDM machining using pure water. *International Journal of Advanced Manufacturing Technology*, *34*, 104–110. doi:10.1007/s00170-006-0570-y

Masuzawa, T., Fujino, M., Kobayashi, K., Suzuki, T., & Kinoshita, N. (1985). Wire electro-discharge grinding for micro-machining. *CIRP Annals: Manufacturing Technology*, *34*(1), 431–434. doi:10.1016/S0007-8506(07)61805-8

Peng, W. Y., & Liao, Y. S. (2004). Study of electrochemical discharge machining technology for slicing non-conductive brittle materials. *Journal of Materials Processing Technology*, *149*, 363–369. doi:10.1016/j.jmatprotec.2003.11.054

Singh, Y. P., Jain, V. K., Kumar, P., & Agrawal, D. C. (1996). Machining piezoelectric (PZT) ceramics using an electrochemical spark machining (ECSM) process. *Journal of Materials Processing Technology*, *58*, 24–31. doi:10.1016/0924-0136(95)02102-7

This work was previously published in the International Journal of Manufacturing, Materials, and Mechanical Engineering, Volume 1, Issue 1, edited by J. Paulo Davim, pp. 46-55, copyright 2011 by IGI Publishing (an imprint of IGI Global).

Chapter 11
3D Finite Element Modeling of High Speed Machining

A.P. Markopoulos
National Technical University of Athens, Greece

K. Kantzavelos
National Technical University of Athens, Greece

N.I. Galanis
National Technical University of Athens, Greece

D.E. Manolakos
National Technical University of Athens, Greece

ABSTRACT

This paper presents simulation of High Speed Machining of steel with coated carbide tools. More specifically, Third Wave Systems AdvantEdge commercial Finite Element Method code is employed in order to present turning models, under various machining conditions. As a novelty, the proposed models for High Speed Machining of steel are three-dimensional and are able to provide predictions on cutting forces, tool and workpiece temperatures, chip formation, and chip morphology. Model validation is achieved through experimental work carried out under the same conditions as the ones used in modeling. For the experimental work, the principles for design of experiment were used in order to minimize the required amount of experiments and obtain useful results at the same time. Furthermore, a Taguchi analysis is carried out based on the results. The analysis indicates that there is a good agreement between experiment and modeling, and the proposed models can be further employed for the prediction of a range of machining parameters, under similar conditions.

DOI: 10.4018/978-1-4666-1867-1.ch011

Copyright © 2013, IGI Global. Copying or distributing in print or electronic forms without written permission of IGI Global is prohibited.

INTRODUCTION

High Speed Machining (HSM) is of special interest to the industry and the academia in the last few years due to the advantages it exhibits in comparison to conventional machining. The boundary between conventional machining and HSM depends on factors such as the workpiece material and the process. Most commonly, definitions of HSM make use of cutting speeds pertaining to turning, separately for ferrous and non-ferrous materials; the limit above which an operation is characterized as HSM for some non-ferrous materials can be higher at about one order of magnitude to that of alloyed steel. However, the highest cutting speeds can be achieved for non-ferrous materials that exhibit good machinability, such as aluminum, but they are limited by the attained cutting speeds of the machine tools. On the other hand, machining speeds of materials with poor machinability, such as titanium, are limited by the available cutting tools. Furthermore, operations such as turning, milling and grinding are more suitable for performing HSM than other operations, based on the achievable cutting speeds of each type of machining operation (Byrne, Dornfeld, & Denkena, 2003). Thus, definitions that account only for cutting speed or only one cutting operation or wide material groups tend to have a lot of exceptions and to soon be outdated due to the ongoing research regarding machine tools and cutting tools for HSM.

Considering the above, a global definition of HSM operations is rather difficult to be provided since a number of factors need to be accounted for; cutting speed, spindle speed, feed, the cutting operation, workpiece material, cutting tool and cutting forces are the features included in some definitions (Byrne, Dornfeld, & Denkena, 2003; Erdel, 2003; Grzesik, 2008), while a definition including the cutting tool and spindle dynamics has been proposed (Smith & Tlusty, 1997). A definition by Tlusty (1993) states that HSM refers to processes with cutting speed or spindle rotational speed substantially higher than some years before or also than the still common and general practice. The definition, even though is very general, avoids to give a spectrum of speeds or a lower value above which a machining process is characterized as HSM and can be applied to various materials and processes.

Although the rate of tool wear increases at high speeds (List, Sutter, & Bi, 2009), thus reducing tool life, several features of HSM can be considered as advantageous. A very important advantage of HSM is the high material removal rate achieved, which is a function of the cutting speed as well as the undeformed chip cross-section, and leads to higher productivity, especially in the case of light metal alloys.

Besides the increase in the material removal rate an increase in surface quality is achieved with HSM, thus making these processes suitable for precision machining and micromachining; high speed milling is used for the fabrication of tools e.g., EDM electrodes and dies, while high speed drilling is used for micro-drills on printed circuits. The excellent surface finish reported in HSM operations, further reduces machining time and cost as it makes subsequent finishing operations, such as grinding, redundant.

It is understood that when cutting speed is increased, a subsequent increase in cutting temperatures takes place and no decrease is observed with further increase in speed, despite the predictions of the opposite phenomenon by some researchers. On the other hand with increased speed, a decrease in cutting forces is observed (Schulz & Moriwaki, 1992). As experimental work has shown, cutting forces tend to reduce, in some cases by 10-15%, as the speed is increased to high values (Trent & Wright, 2000; Schulz, 2001; Grzesik, 2002; Erdel, 2003). This force reduction may be attributed to the reduced strength of the workpiece material due to the elevated temperatures of the process (Trent & Wright, 2000). High temperatures in HSM may be observed when cutting fluids are reduced or even omitted and so is their cooling

effect. Additionally, it could be stated that cutting fluids in HSM contribute little to the quality of the process and their cost, impact on the environment and inability to cool and lubricate in limited time contact needs to be taken under consideration (Nouari & Ginting, 2004; Mamalis, Kundrák, Markopoulos, & Manolakos, 2008). It is evident that dry machining would be preferable but tool wear does not allow this in the modern production environment.

Other explanations for the force reduction are either a decrease in friction or the tendency of many materials to produce segmented chip at high cutting speeds; this saw-toothed chip also referred as "shear localized" is considered by some researchers to be energetically favorable and thus resulting in lower cutting forces (Bäker, 2006; Tang et al., 2009). In any case, lower loads simplify part fixture design and allow for the machining of thin-walled sections, a common geometry of workpieces in the aerospace industry.

Nevertheless, the phenomena taking place and the complexity of chip formation at high speeds call for the application of sophisticated methods for the analysis of HSM. The use of modeling and especially the Finite Element Method (FEM) is very common for machining simulation and has also been used for the case of HSM. In the next paragraph an account on previous work of FEM simulation and especially on 3D modeling and HSM will be given. Then the experimental work and the proposed 3D models for the simulation of machining of C45 steel workpieces with coated carbide tools will be described and the results will be discussed.

Finite Element Modeling of Metal Machining

Numerical modeling and especially FEM is widely used for the analysis and the prediction of the cutting performance in machining operations. The advantage of the method is that it can provide several difficult-to-measure data on variables such as temperatures, plastic strains, strain rates, and stresses. Simulations of metal machining using the finite element method have a background of about three decades; worth mentioning is an early pioneering work of Shirakashi and Usui (1974). The first models that appeared on the simulation of metal machining, and the majority of the work performed so far, pertain to two dimensional orthogonal cutting plain strain models. So far three types of analysis have been proposed, namely Eulerian, Lagrangian and the newer Arbitrary Lagrangian-Eulerian (ALE) analysis. In the Eulerian approach the finite element mesh is spatially fixed and the material flows through it in order to simulate the chip formation. The computational time in such models is reduced due to the few elements required for modeling the workpiece and the chip and is mainly used for simulating the steady state condition of the cutting process with continuous chip (Strenkowski & Carroll, 1986; Strenkowski & Moon, 1990; Childs & Maekawa, 1990; Dirikolu, Childs, & Maekawa, 2001). The elements do not undergo severe distortion since the mesh is a priori known but this formulation requires complex programming. Furthermore, experimental data must be known prior to the construction of the model in order to determine the chip geometry.

Although the Eulerian formulation is still utilized by some researchers, the Lagrangian formulation has been proposed. In this approach the elements are attached to the material and the undeformed tool is advanced towards the workpiece. For the analysis two techniques may be employed, i.e., the implicit and the explicit time integration technique, allowing for non steady state problems to be faced. A disadvantage of the method is connected to the large mesh deformation observed during the simulation. Due to the attachment of the mesh on the workpiece material, the mesh is distorted because of the plastic deformation in the cutting zone. For the formation of the chip, a chip separation criterion in front of the tool edge is applied. There are a lot of criteria proposed so

far; Black and Huang (1996) have performed an evaluation on some of them in their work. The proposed chip separation criteria are geometric or physical, involving critical distance between the tool and the workpiece, critical values of e.g., stress or strain, or even crack propagation criteria. A lot of Lagrangian formulation non steady state plain stress analysis models have enriched the relative literature (Strenkowski & Carroll, 1985; Komvopoulos & Erpenbeck, 1991; Lin & Lin, 1992; Zhang & Bagchi, 1994; Shih, 1995). The latest development in the Lagrangian formulation, the updated Lagrangian analysis, has overcome the disadvantage of the mesh distortion by continuous re-meshing and adaptive meshing. This method is more widely used today for simulating continuous and segmented chips (Marusich & Ortiz, 1995; Ceretti, Lucchi, & Altan, 1999; Özel & Altan, 2000; Klocke, Raedt, & Hoppe, 2001; Bäker, Rösler, & Siemers, 2002; Özel, 2006; Maranhão & Davim, 2010). Although this technique adds considerably to the required calculation time, the advances in computers have made it possible to reduce the time needed for such an analysis to acceptable levels.

Note that, an arbitrary Lagrangian-Eulerian formulation (ALE) has also been proposed with the aim to combine the advantages of the two methods (Olovsson, Nilsson, & Simonsson, 1999; Movahhedy, Altintas, & Gadala, 2002; Özel & Zeren, 2007; Arrazola & Özel, 2010).

Models of the early publications were constructed by FEM codes made by the researchers. For the past twenty years a wide range of commercial FEM packages became available, some of them being exclusively dedicated to machining such as the AdvantEdge from Third Wave Systems. The available FEM codes that have been used for the simulation of machining include: ABAQUS (Ng & Aspinwall, 2002; Mabrouki & Rigal, 2006; Bäker, 2006), FORGE 2 (Ng et al., 1999), NIKE-2D (Strenkowski & Carroll, 1985), DEFORM 2D (Ceretti et al., 1996; Özel, 2006; Umbrello et al., 2007), MARC (Mamalis et al., 2001) and AvantEdge (Özel, 2003; Grzesik, 2006; Mamalis et al., 2008, Davim et al., 2009; Maranhão & Davim, 2010); Bil, Kılıç, and Tekkaya (2004) have compared models from three different commercial software, namely, MARC, DEFORM 2D and AdvantEdge.

All the proposed models in the relevant literature deal mainly with features such as chip morphology, cutting forces, temperatures, surface integrity, residual stresses and tool wear for the machining of steels and other metals such as aluminum and titanium. Most of the relative work examines turning but milling is considered as well.

Of special interest and crucial to the success of the simulation are the material modeling and the friction scheme used in the analysis. Several plasticity models have been proposed and used so far in the simulation of metal machining. The models of Usui and Shirakashi (1982), Johnson and Cook (1983) and Zerilli and Armstrong, (1987) are some to be found in the relative literature, with Johnson-Cook model being the most popular (Ng & Aspinwall, 2002; Umbrello, M'Saoubi, & Outeiro, 2007).

Coulomb's friction law is the simplest method for modeling friction in metal machining and is widely used. Zorev's model (1963) is also very popular. It is a temperature independent stick-slip friction model that implies the existence of two different regions of contact between tool and chip, where shear and normal stresses are considered. Several other friction models or modifications of them have been proposed (Obikawa et al., 1997; Dirikolu, Childs, & Maekawa, 2001); a collection of papers and discussion on the results can be found in the works by Childs (2006) and Vaz et al (2007). In recent works, Özel (2006), compared experimental results with friction models and came to the conclusion that predictions were more accurate with models included measured frictional and normal stresses on the tool rake face, which were implemented as variable friction models of the tool-chip contact in the simulations. Arrazola, Ugarte, & Domínguez (2008) proposed

the identification of friction during machining with the use of finite element models.

In the FEM modeling literature regarding HSM, Marusich and Ortiz (1995) were among the first to provide models of HSM and simulate the segmented chip formation. Bäker (2006) proposed an orthogonal machining model that implements a generic flow stress law in order to simulate the cutting force reduction and the chip formation. Hortig and Svendsen (2007) investigated the dependence of element size and orientation on chip formation, also using adaptive mesh refinement. Machining of aluminium alloys under high speeds is the main objective of a work presented by Davim et al. (2008). Iqbal, Mativenga, and Sheikh (2008) provide FEM models based on variable Coulomb and hybrid sticking-sliding friction models. Finally, Duan et al. (2009) as well as Tang et al. (2009) utilize the Johnson-Cook material model and fracture criterion for modeling the HSM of hardened steel.

However, models and simulations of 3D nature are not so common and 3D models of HSM are quite rarer. The reasons behind this are that for 3D modeling and simulation degree of complexity and computational power required are increased. 3D FEM modeling was used by Cerreti et al. (2000) in order to simulate orthogonal and oblique cutting conditions in turning of aluminum and steel. Hard tuning was modeled with the aid of 3D models by Guo and Liu (2002), Klocke and Kratz (2005) and Arrazola and Özel (2008). Aurich and Bil (2006) presented a 3D model that produced serrated chip, while Attanasio et al. (2008) and Özel (2009) dealt with tool wear.

A literature review on FEM modeling of machining operations can never be complete and such a task is out of the scope of this paper; in Refs (Ehmann et al., 1997; van Luttervelt et al., 1998; Mackerle, 1999; Mackerle 2003; Davim, 2008; Dixit & Dixit, 2008) a wide collection of papers for further reading on this topic can be found.

Experiments and Modeling

High speed turning experiments were carried out first in order to determine the cutting conditions to be simulated with FEM. Four cutting parameters were taken into account i.e., tool type, depth of cut, feed and cutting speed. Next, the obtained results were used for the simulation of HSM. The provided models are 3D turning models developed with Third Wave AdvantEdge software, which integrates special features appropriate for machining simulation. In the following paragraphs the experimental and the relative modeling procedure will be described.

Experimental Procedure

For efficiency in the design of experiments, orthogonal arrays were employed. This way a full factorial analysis, which is rather laborious, is avoided; instead a fractional factorial analysis was used. The value of fractional factorial experiments in general lies in the fact that higher order interactions are usually negligible. This leads to a notable reduction in the number of parameters that need to be considered in the analysis of the data from such experiments. This, in turn, also leads to a reduction in the number of treatment combinations to be used in an experiment and hence to a reduction in the number of observations to be taken. Orthogonal arrays are the foundation for design of experiments in Taguchi methodology and are capable of providing useful data for a small amount of experiments (Peace, 1992; Hinkelman & Kempthorne; 2008).

Four control factors, i.e., the four cutting parameters mentioned, with three levels each were used. A three level design parameter counts for two degrees of freedom while the interaction between the cutting parameters is neglected. Therefore, there are eight degrees of freedom owing to the four cutting parameters selected. The L_9 orthogonal array with four columns and nine rows can be used, as it can adequately handle the on hand problem

Table 1. Experimental layout using an L_9 orthogonal array

L_9 (3^4)				
Factor / Experiment	A	B	C	D
1	I	I	I	I
2	I	II	II	II
3	I	III	III	III
4	II	I	II	III
5	II	II	III	I
6	II	III	I	II
7	III	I	III	II
8	III	II	I	III
9	III	III	II	I

Table 2. Turning parameters and their levels

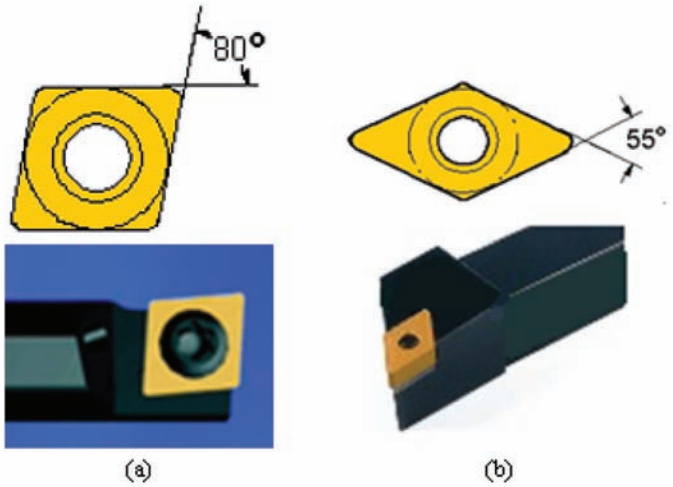
Symbol	Factor	Level 1	Level 2	Level 3
A	Tool type	Turning I	Turning II	Turning III
B	Depth of cut (mm)	0.2	0.6	0.4
C	Feed (mm/rev)	0.1	0.2	0.3
D	Cutting speed (m/min)	300	450	600

(Yang & Tarng, 1998; Kirby, Zhang, Chen, & Chen, 2006; Nalbant, Gökkaya, & Sur, 2007). With L_9 orthogonal array only 9 experiments need to be carried out instead of the 3^4=81 that the full factorial analysis would require. The orthogonal array used can be seen in Table 1, while factors and levels for turning experiments are tabulated in Table 2. Finally, the cutting conditions of the 9 experiments, as the data are combined from Tables 1 and 2, are shown in Table 3. In Tables 2 and 3, tool types Turning I, II and III refer to the cutting tools' characteristics, which are thoroughly

Table 3. Cutting conditions of the experiments

Number of experiment	Cutting tool	Depth of cut (mm)	Feed (mm/rev)	Cutting Speed (m/min)
1	Turning I	0.2	0.1	300
2		0.6	0.2	450
3		0.4	0.3	600
4	Turning II	0.2	0.2	600
5		0.6	0.3	300
6		0.4	0.1	450
7	Turning III	0.2	0.3	450
8		0.6	0.1	600
9		0.4	0.2	300

Figure 1. Tools used in the experimental procedure (a) CDCB and (b) DNMG



described later on. Figure 1 shows the tools used in the experimental procedure CDCB and DNMG.

In all the experiments that were carried out, the processes took place in an OKUMA LB10ii CNC revolver turning machine with a maximum spindle speed of 10,000 rpm and a 10 HP drive motor. The workpiece was a bar of C45 cold drawn, a common steel used in industry, with dimensions of 300 mm in length and 50 mm in diameter. The properties of the workpiece material are tabulated in Table 4. The cutting tools employed were common cutting tools from SECO. The specifications for Turning I are CCMT 060204-F1 with CP500 coated grade. This cutting tool is rhombic shaped with cutting edge angle 80°, and it is intended for general turning on superalloys, as it is coated with two layers of (Ti, Al) N + TiN. The rake angle mounted in the toolholder is γ=-6° and inclination angle is λ_s=−6°. The tool cutting edge angle is κ=95°. The specifications for Turning II and III were the same, namely, DNMG 110402-M3 with TP 2000 coated grade. This cutting tool has rhombic shape with cutting edge angle 55°, and it is intended for general turning on steels and alloyed steels, as it is coated with four layers of Ti (C, N) + Al2O3 + Ti (C, N) + TiN. The rake angle mounted in the toolholder is γ=−5° and inclination angle is λ_s=−9.5°. The tool cutting edge angle is κ=93°.

Cutting forces were measured through analog data measurement equipment and a dynamometer was adjusted on the tool. In order to avoid false measurements during the experimental procedure due to abnormal local conditions, two tests for each experiment were held and an average value was adopted. The cutting forces were measured in all the three directions, the x, y and z axis, with a Kistler dynamometer 9257A. This is a three-component piezoelectric dynamometer platform. The force data were recorded by a specifically designed, very compact multi-channel micropro-

Table 4. Material properties of the workpiece

Material Properties	AISI 1045, DIN 1654 C45 cold drawn
Density	7.85 g/cm^3
Hardness, Rockwell B	88
Tensile strength, ultimate	625 MPa
Tensile strength, yield	530 MPa
Elongation of break	12%
Modulus of elasticity	205 GPa
Poisson's ratio	0.29

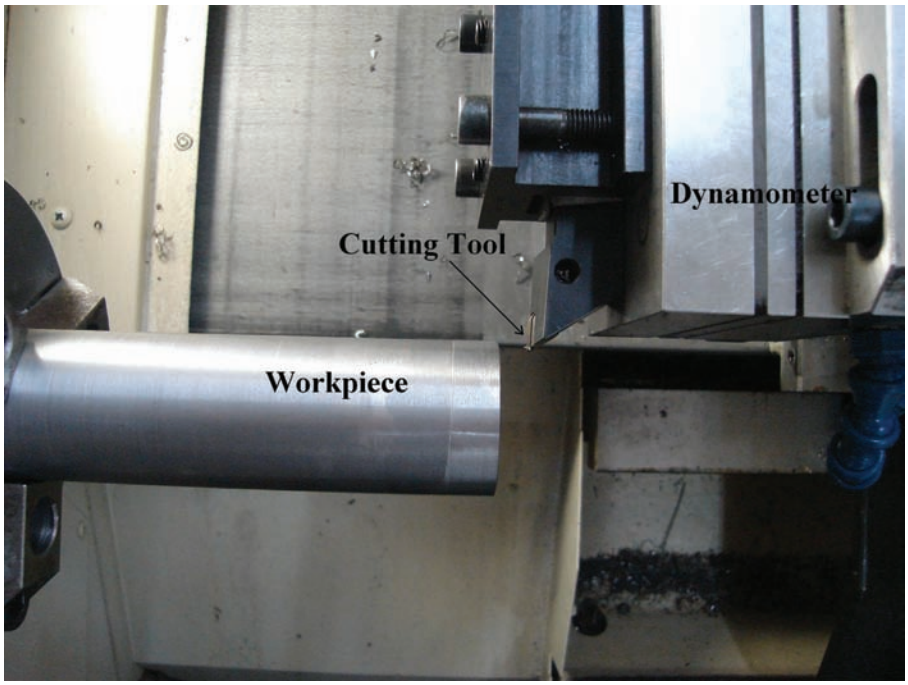
cessor controlled data acquisition system with a single A/D converter preceded by a multiplexer. Workpieces were cut for an adequate length, of about 100mm, in order to obtain clear results on the dynamometer. In Figure 2 the experimental setup can be observed. Furthermore, the chips were gathered at the end of each experiment so that they may be compared to the chips from the simulation.

Modeling Procedure

The finite element software used in a machining analysis is of great significance, regarding the success of the simulation. In order to increase as possible the reliability of the analysis a commercial software package that was built from the start with metal cutting operations in mind would be preferable. Third Wave AdvantEdge software integrates special features appropriate for machining simulation and was finally chosen for the analysis. It allows the simulation of various manufacturing processes such as turning, drilling, milling and micromachining among others, in either two or three dimensions. AdvantEdge is a Lagrangian, explicit, dynamic code which can perform coupled thermo-mechanical transient analysis. The program applies adaptive meshing and continuous remeshing for chip and workpiece, allowing for accurate results. The program menus are properly designed so that model preparation time is minimized. Furthermore, it possesses a wide database of workpiece and tool materials commonly used in cutting operations, offering all the required data for effective material modeling. The commercial FEM code employed makes the implementation of the latest developments very easy, reduces the model construction time and enhances the reliability of the models.

The models provided in the following paragraphs are 3D high speed turning models. They were chosen to be so in order to have the ability to make a more accurate comparison between the experimental and the numerical results, especially

Figure 2. Experimental setup



for the chip morphology. The cutting conditions used in the experimental work, as tabulated in Table 3, were also used as input to the FEM models, for the purpose of comparison of results. In Figure 3 the simulation setup of the finite element model can be observed.

Workpiece material, cutting tools and the processes' setup were modelled from the software menus and data library, with minimum intervention from the user for better results. The intervention of the user in the control of the simulation is limited, which may be considered as a drawback in some cases. Nevertheless, in most cases the defaults of the program can handle the machining operation simulation adequately.

The used constitutive model of the workpiece material is governed by the Power Law described by the following equation:

$$\sigma(\varepsilon^p, \dot{\varepsilon}, T) = g(\varepsilon^p) \cdot \Gamma(\dot{\varepsilon}) \cdot \Theta(T)$$

where $g(\varepsilon^p)$ is strain hardening, $\Gamma(\dot{\varepsilon})$ is strain rate sensitivity and $\Theta(T)$ is thermal softening.

The strain hardening function $g(\varepsilon^p)$ is defined as:

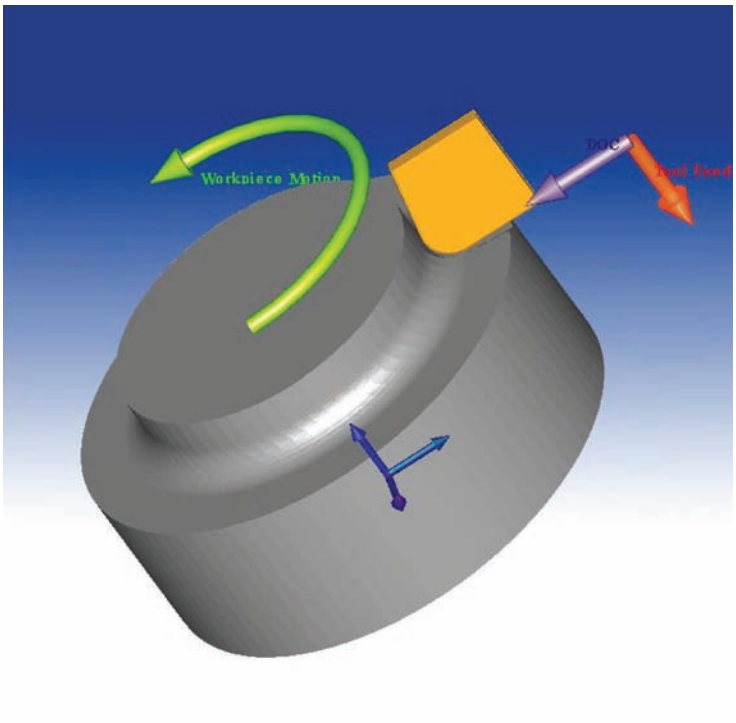
$$g(\varepsilon^p) = \sigma_0 \left[1 + \frac{\varepsilon^p}{\varepsilon_0^p}\right]^{1/n} \quad , \; if \;\; \varepsilon^p < \varepsilon_{cut}^p$$

$$g(\varepsilon^p) = \sigma_0 \left[1 + \frac{\varepsilon_{cut}^p}{\varepsilon_0^p}\right]^{1/n} \quad , \; if \;\; \varepsilon^p \geq \varepsilon_{cut}^p$$

where σ_0 is the initial yield stress, ε^p is the plastic strain, ε_0^p is the reference plastic strain, ε_{cut}^p is the cutoff strain and n is the strain hardening exponent.

The rate sensitivity function $\Gamma(\dot{\varepsilon})$ is provided as:

Figure 3. Setup of the FEM model



$$\Gamma(\dot{\varepsilon}) = \left(1 + \frac{\dot{\varepsilon}}{\dot{\varepsilon}_0}\right)^{\frac{1}{m_1}}, \text{ if } \dot{\varepsilon} \le \dot{\varepsilon}_t$$

$$\Gamma(\dot{\varepsilon}) = \left(1 + \frac{\dot{\varepsilon}}{\dot{\varepsilon}_0}\right)^{\frac{1}{m_2}} \left(1 + \frac{\dot{\varepsilon}_t}{\dot{\varepsilon}_0}\right)^{\left(\frac{1}{m_1} - \frac{1}{m_2}\right)}, \text{ if } \dot{\varepsilon} > \dot{\varepsilon}_t$$

where $\dot{\varepsilon}$ is strain rate, $\dot{\varepsilon}_0$ is reference plastic strain rate, $\dot{\varepsilon}_t$ is strain rate where the transition between low and high strain rate sensitivity occurs, m_1 is the low strain rate sensitivity coefficient, m_2 is the high strain rate sensitivity coefficient.

The thermal softening function $\Theta(T)$ is defined as:

$$\Theta(T) = c_0 + c_1 T + c_2 T^2 + c_3 T^3 + c_4 T^4 + c_5 T^5, \text{ if } T < T_{cut}$$

$$\Theta(T) = \Theta(T_{cut}) - \frac{T - T_{cut}}{T_{melt} - T_{cut}}, \text{ if } T \ge T_{cut}$$

where c_0 through c_5 are coefficients for the polynomial fit, T is the temperature, T_{cut} is the linear cutoff temperature and T_{melt} is the melting temperature.

All the required data for the workpiece material used for the analysis where taken from the material database of the software.

The cutting tool is modelled as rigid body with the geometrical characteristics laid out in Table 4. AdvantEdge allows for up to three coating layers for the cutting tools. For CDCB, two layers, a TiN and a TiAlN, were taken into account while for DNMG, three layers, TiN, Al_2O_3 and TiC were considered. The coating layers are important for the thermal analysis that is also of interest in the present study, besides the cutting forces. The predicted cutting forces from the FEM model are compared with the measured ones, while a comparison of the chips produced in each case is also provided. Additionally, the simulations can provide more results such as the temperature fields on the cutting tool and within the workpiece, which are essential in order to understand the physical phenomena taking place during the process (Sutter et al., 2008). The initial temperature was set at 20° C. Finally, the employed software incorporates Coulomb friction across the rake face in order to model the friction at the tool-chip interface.

Simulation time varied at about 3-4 days for each model, by using an Intel Core2 Duo processor (2.66GHz). The length of the simulations was held on more than a full rotation, namely 400°, in order to obtain steady state force conditions.

Results and Discussion

The proposed 3D FEM models can predict cutting forces. In Table 5 experimental and numerical results are shown. A comparison between the values indicates that in general the results are in good agreement. More specifically, for certain experiments, e.g., experiment 1, the disagreement between the values is rather high. Although this high difference is present only in exceptional cases, inadequate modeling for this case may be concluded. In turn it may be attributed to inadequate workpiece material or contact conditions modeling. In most cases of FE metal cutting simulations the simple Coulomb friction condition is adopted. Furthermore, the friction coefficient is assumed to be constant. Astakhov and Outeiro (2008) state that according to calculations there is a limiting value for the coefficient of friction above which no relative motion can occur at the tool-chip interface. Experimental data are in direct contradiction with this value but on the other hand FEM models always use a friction coefficient below the limiting value to suit the sliding condition at the interface. Still experiments and FEM models are in good agreement in the results they provide. It seems that there is an inherent difficulty in applying a suitable friction model, especially

Table 5. Experimental and numerical results for the cutting forces

Number of experiment	Cutting Forces (N)					
	Experimental	Numerical	Experimental	Numerical	Experimental	Numerical
	F_x	F_x	F_y	F_y	F_z	F_z
1	150	15	230	15	175	15
2	290	300	300	300	350	60
3	210	300	240	100	195	90
4	35	30	17,5	50	15	10
5	210	200	25	50	55	50
6	145	130	35	40	45	200
7	300	250	50	10	50	50
8	90	40	40	25	35	30
9	310	250	80	30	60	90

in the case of high speed machining where more complicated phenomena occur.

Apart from experiment number 1, it seems that experimental and numerical results present better correlation for F_x, while a poorer correlation for F_y and F_z is observed. For F_x, the widest discrepancy is for experiment number 8, where the experimental value is more than double that of the numerical results. In the other cases, the discrepancies are lower, with lowest being the one for experiment 5; experimental value is only 4.8% higher than the calculated one.

The Taguchi method offers also the ability to determine the effect of each factor, i.e., cutting condition, in the final result of the experiment, i.e., the cutting forces. The effect is defined from the SN value, which depends on the average value (y_i) and the variance (s_i), is extracted from the form:

$$SN_i = 10 \log \frac{\overline{y}_i^{-2}}{s_i^2}$$

Where

$$\overline{y}_i = \frac{1}{N_i} \sum_{u=1}^{N_i} y_{i,u}$$

and

$$s_i^2 = \frac{1}{N_i - 1} \sum_{u=1}^{N_i} \left(y_{i,u} - \overline{y}_i \right)$$

After estimating SN for each experiment separately, the average SN value is calculated from each factor and level as shown in Table 6, from the forms below:

$$SN_{P3,1} = \frac{S_{N1} + S_{N6} + S_{N8}}{3},$$

$$SN_{P3,2} = \frac{S_{N2} + S_{N4} + S_{N9}}{3} \text{ and}$$

$$SN_{P3,3} = \frac{S_{N3} + S_{N5} + S_{N7}}{3}$$

At the end of the Taguchi method's analysis, the R value is estimated for each factor as:

R = Max SN – Min SN.

The higher the R value is, the greater the effect of the factor in the final result is. As mentioned in the experimental procedure section, two values of the cutting force for each experiment were extracted from the dynamometer (N=2). That way the SN value could be estimated for each cutting force (Fx, Fy, Fz) and by using the Taguchi method analysis, the table that determines the rank of each factor and cutting force was extracted, in Table 7.

Table 6. The selection of the factors' values to determine the average SN value

Factor / Experiment	A Tool Type	B Depth of Cut	C Feed	D Cutting Speed	SN
1	I	I	I	I	SN1
2	I	II	II	II	SN2
3	I	III	III	III	SN3
4	II	I	II	III	SN4
5	II	II	III	I	SN5
6	II	III	I	II	SN6
7	III	I	III	II	SN7
8	III	II	I	III	SN8
9	III	III	II	I	SN9

Table 7. Rank of each factor at the cutting forces

Factor / Force	Tool Type	Depth of Cut	Feed	Cutting Speed
Fx	1	3	4	2
Fy	1	3	2	4
Fz	1	2	3	4

As it can be seen from the analysis, the tool type is the most important factor for the cutting force during a turning experiment, while the cutting speed determines mostly the main cutting force and leaves nearly unaffected the forces in y and z axis.

Figures 4, 5 and 6 show the chip as it is formed for three different experiments, namely experiments 2, 3 and 5. In all figures, the temperatures on the workpiece, as well as on the tool, can be seen. Temperatures are important for tool life and the estimation of areas where wear is more possible to show up. It can be seen that at the area close to the tip of the cutting tool, temperatures up to 1400° C may appear. In all the cases considered the maximum temperatures on the cutting tool have the same magnitude and appear in the same areas.

In Figure 7, a comparison of the chips between the experimental and the numerical results is made. More specifically, the chips for the same experiments shown in Figures 4 through 6 are depicted. The pictures of the actual chips collected from the experiments indicate that in all three cases the chips are strips with side curling, typical for the process examined. Chip in experiment 3 is longer than that of experiment 2. This can be explained by the fact that the chip of experiment 2 is thinner because of the smaller depth of cut used from experiment 3 and with more thermal load and because of that also more distorted; the chip breaks easier and forms shorter strips than the chip from experiment 3.

CONCLUSION

The models of High Speed Machining of steel with coated carbide tools presented in this paper are able to predict cutting forces and chip morphology. In order to present more realistic results, the

Figure 4. High speed turning experiment 2 with CDCB tool, depth of cut 0.6 mm, feed 0.2 mm/rev and cutting speed 450 m/min

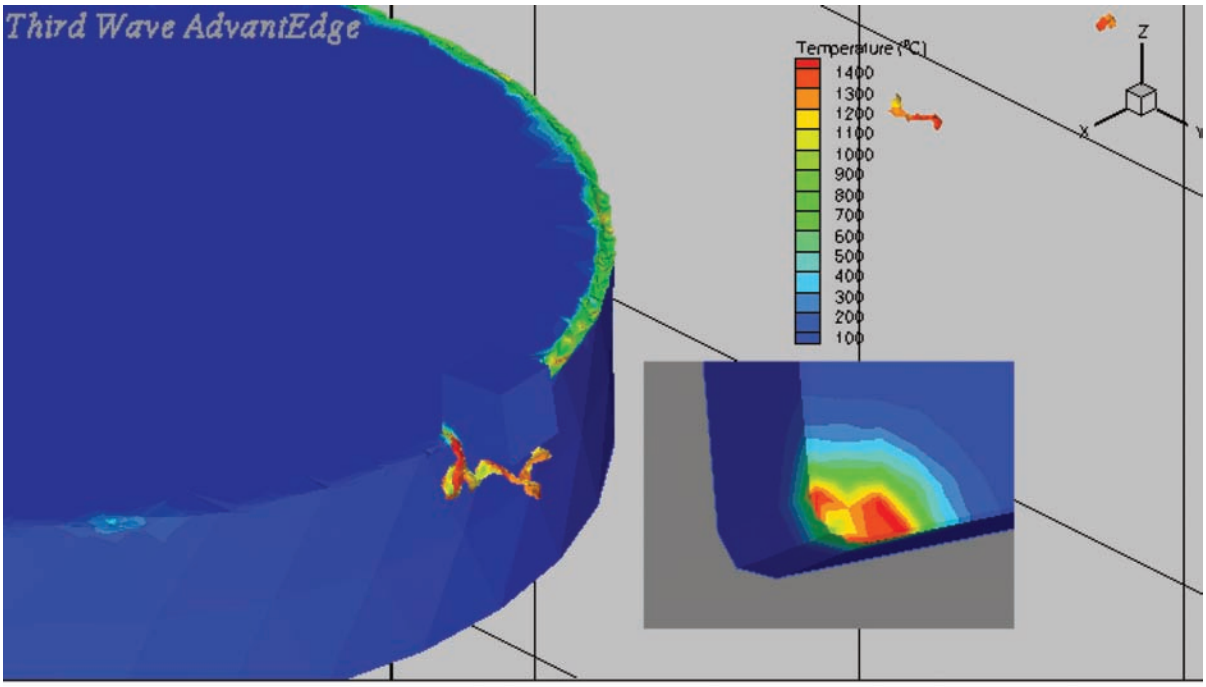
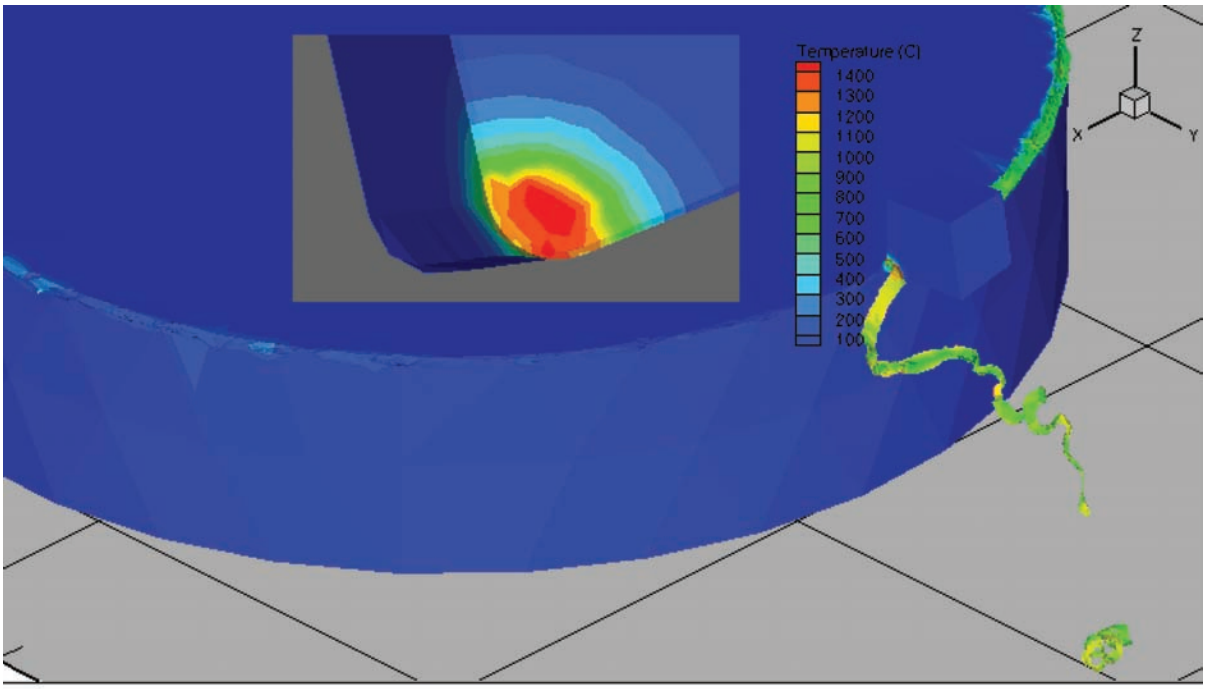


Figure 5. High speed turning experiment 3 with CDCB tool, depth of cut 0.4 mm, feed 0.3 mm/rev and cutting speed 600 m/min



simulation was performed with three dimensional models. These models require more computer power and take more time to run but on the other hand can provide more results.

Furthermore, nine experiments with various characteristics concerning cutting conditions and cutting tool type were carried out. The characteristics of each experiment were determined based on orthogonal arrays theory. Additionally, nine simulations were performed under the same conditions for comparison reasons.

From the comparison it may be concluded that the proposed models can adequately predict the chip shape and estimate the cutting forces. Furthermore, FEM models can provide extra data such as the temperatures on the workpiece, the chip and the cutting tool that are very important for the outcome of the process.

From the analysis it is also concluded that in future works a more adequate friction model needs to be incorporated to the analysis to provide more reliable results. Nevertheless, the proposed models offer a useful and reliable tool for the analysis of high speed machining.

Figure 6. High speed turning experiment 5 with DNMG tool, depth of cut 0.6 mm, feed 0.3 mm/rev and cutting speed 300 m/min

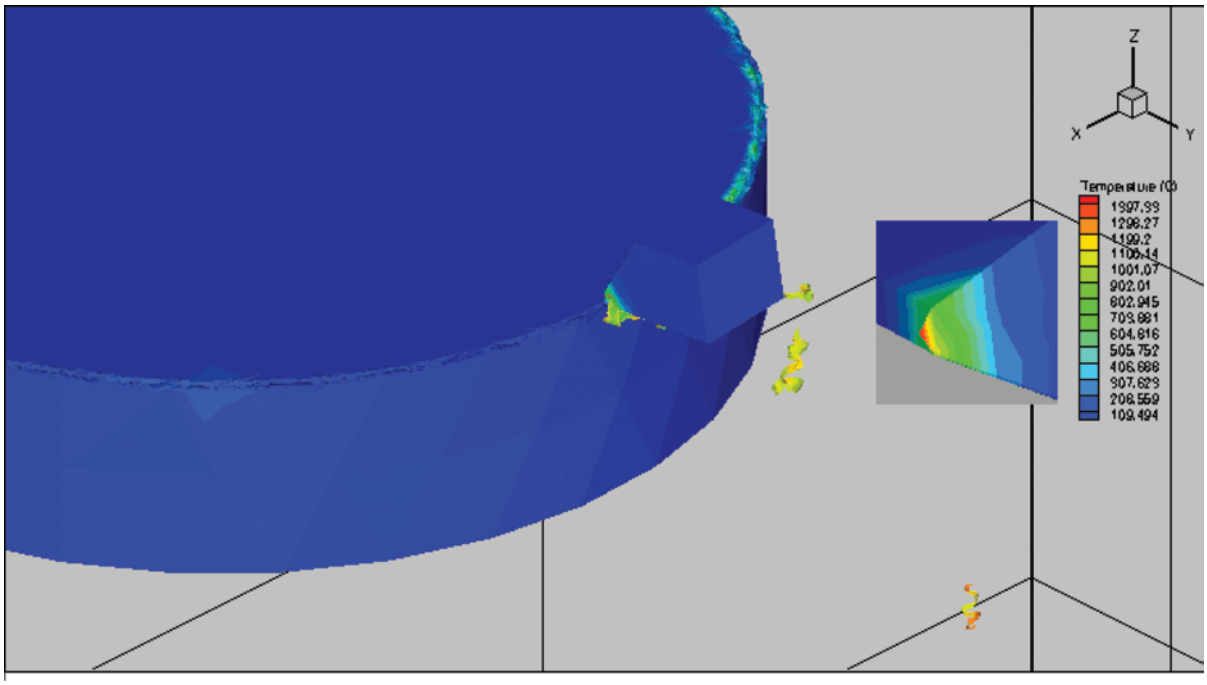
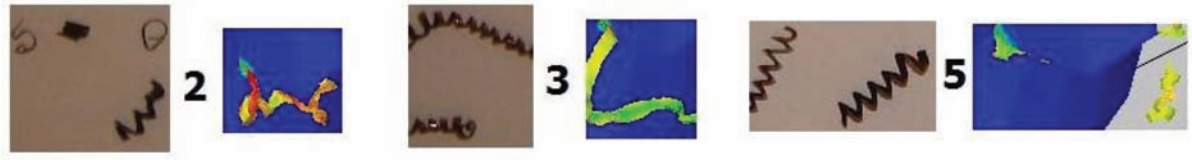


Figure 7. Chips as collected from the experiments and as predicted by the models for high speed turning experiments 2, 3 and 5



REFERENCES

Arrazola, P. J., & Özel, T. (2008). Numerical modelling of 3-D hard turning using arbitrary Eulerian Lagrangian finite element method. *International Journal of Machining and Machinability of Materials*, *3*, 238–249.

Arrazola, P. J., & Özel, T. (2010). Investigations on the effects of friction modeling in finite element simulation of machining. *International Journal of Mechanical Sciences*, *52*, 31–42. doi:10.1016/j.ijmecsci.2009.10.001

Arrazola, P. J., Ugarte, D., & Domínguez, X. (2008). A new approach for friction identification during machining through the use of finite element modelling. *International Journal of Machine Tools & Manufacture*, *48*, 173–183. doi:10.1016/j.ijmachtools.2007.08.022

Astakhov, V. P., & Outeiro, J. C. (2008). Metal cutting mechanics, finite element modelling. In Davim, J. P. (Ed.), *Machining: Fundamentals and recent advances*. Berlin, Germany: Springer-Verlag.

Attanasio, A., Ceretti, E., Rizzuti, S., Umbrello, D., & Micari, F. (2008). 3D finite element analysis of tool wear in machining. *Annals of the CIRP*, *57*(1), 61–64. doi:10.1016/j.cirp.2008.03.123

Aurich, J. C., & Bil, H. (2006). 3D finite element modelling of segmented chip formation. *Annals of the CIRP*, *55*(1), 47–50. doi:10.1016/S0007-8506(07)60363-1

Bäker, M. (2006). Finite element simulation of high-speed cutting forces. *Journal of Materials Processing Technology*, *176*, 117–126. doi:10.1016/j.jmatprotec.2006.02.019

Bäker, M., Rösler, J., & Siemers, C. (2002). A finite element model of high speed metal cutting with adiabatic shearing. *Computers & Structures*, *80*, 495–513. doi:10.1016/S0045-7949(02)00023-8

Bil, H., Kılıç, S. E., & Tekkaya, A. E. (2004). A comparison of orthogonal cutting data from experiments with three different finite element models. *International Journal of Machine Tools & Manufacture*, *44*, 933–944. doi:10.1016/j.ijmachtools.2004.01.016

Black, J. T., & Huang, J. M. (1996). An evaluation of chip separation criteria for the FEM simulation of machining. *Journal of Manufacturing Science and Engineering*, *118*, 545–553. doi:10.1115/1.2831066

Byrne, G., Dornfeld, D., & Denkena, B. (2003). Advancing cutting technology. *Annals of the CIRP*, *52*(2), 483–507. doi:10.1016/S0007-8506(07)60200-5

Ceretti, E., Fallböhmer, P., Wu, W. T., & Altan, T. (1996). Application of 2D FEM to chip formation in orthogonal cutting. *Journal of Materials Processing Technology*, *59*, 169–180. doi:10.1016/0924-0136(96)02296-0

Ceretti, E., Lazzaroni, C., Menegardo, L., & Altan, T. (2000). Turning simulations using a three-dimentional FEM code. *Journal of Materials Processing Technology*, *98*, 99–103. doi:10.1016/S0924-0136(99)00310-6

Ceretti, E., Lucchi, M., & Altan, T. (1999). FEM simulation orthogonal cutting: Serrated chip formation. *Journal of Materials Processing Technology*, *95*, 17–26. doi:10.1016/S0924-0136(99)00261-7

Childs, T. H. C. (2006). Friction modelling in metal cutting. *Wear*, *260*, 310–318. doi:10.1016/j.wear.2005.01.052

Childs, T. H. C., & Maekawa, K. (1990). Computer-aided simulation and experimental studies of chip flow and tool wear in the turning of low alloy steels by cemented carbide tools. *Wear*, *139*, 235–250. doi:10.1016/0043-1648(90)90048-F

Davim, J. P. (2008). *Machining: Fundamentals and recent advances*. Berlin, Germany: Springer-Verlag.

Davim, J. P., Maranhão, C., Faria, P., Abrão, A., Rubio, J. C., & Silva, L. R. (2009). Precision radial turning of AISI D2 steel. *International Journal of Advanced Manufacturing Technology*, *42*, 842–849. doi:10.1007/s00170-008-1644-9

Davim, J. P., Maranhão, C., Jackson, M. J., Cabral, G., & Grácio, J. (2008). FEM analysis in high speed machining of aluminum alloy (Al7075-0) using polycrystalline diamond (PCD) and cemented carbide (K10) cutting tools. *International Journal of Advanced Manufacturing Technology*, *39*, 1093–1100. doi:10.1007/s00170-007-1299-y

Dirikolu, M. H., Childs, T. H. C., & Maekawa, K. (2001). Finite element simulation of chip flow in metal machining. *International Journal of Mechanical Sciences*, *43*, 2699–2713. doi:10.1016/S0020-7403(01)00047-9

Dixit, P. M., & Dixit, U. S. (2008). *Modeling of metal forming and machining processes: By finite element and soft computing methods*. London, UK: Springer.

Duan, C. Z., Dou, T., Cai, Y. J., & Li, Y. Y. (2009). Finite element simulation and experiment of chip formation process during high speed machining of AISI 1045 hardened steel. *International Journal of Recent Trends in Engineering*, *1*(5), 46–50.

Ehmann, K. F., Kpoor, S. G., DeVor, R. E., & Lazoglu, I. (1997). Machining processes modeling: A review. *ASME Journal of Manufacturing Science and Engineering*, *119*, 655–663. doi:10.1115/1.2836805

Erdel, B. P. (2003). *High-speed machining*. Toronto, ON, Canada: Society of Manufacturing Engineers.

Grzesik, W. (2002). Developments in metal removal processes. In *Proceedings of the 4th International Scientific Conference on Development of Metal Cutting*, Kosice, Slovakia (pp. 103-110).

Grzesik, W. (2006). Determination of temperature distribution in the cutting zone using hybrid analytical-FEM technique. *International Journal of Machine Tools & Manufacture*, *46*, 651–658. doi:10.1016/j.ijmachtools.2005.07.009

Grzesik, W. (2008). *Advanced machining processes of metallic materials: Theory, modelling and applications*. Oxford, UK: Elsevier.

Guo, Y. B., & Liu, C. R. (2002). 3D FEA modeling of hard turning. *ASME Journal of Manufacturing Science and Engineering*, *124*, 189–199. doi:10.1115/1.1430678

Hinkelmann, K., & Kempthorne, O. (2008). Design and analysis of experiments: *Vol. 1. Introduction to experimental design*. Hoboken, NJ: John Wiley & Sons.

Hortig, C., & Svendsen, B. (2007). Simulation of chip formation during high-speed cutting. *Journal of Materials Processing Technology*, *186*, 66–76. doi:10.1016/j.jmatprotec.2006.12.018

Iqbal, S. A., Mativenga, P. T., & Sheikh, M. A. (2008). Contact length prediction: Mathematical models and effect of friction schemes on FEM simulation for conventional to HSM of AISI 1045 steel. *International Journal of Machining and Machinability of Materials*, *3*(1-2), 18–32. doi:10.1504/IJMMM.2008.017622

Johnson, G. R., & Cook, W. H. (1983). A constitutive model and data for metals subjected to large strains, high strain rates and high temperatures. In *Proceedings of the 7th International Symposium on Ballistics*, The Hague, The Netherlands (pp. 541-547).

Kirby, E. D., Zhang, Z., Chen, J. C., & Chen, J. (2006). Optimizing surface finish in a turning operation using the Taguchi parameter design method. *International Journal of Advanced Manufacturing Technology*, *30*, 1021–1029. doi:10.1007/s00170-005-0156-0

Klocke, F., & Kratz, H. (2005). Advanced tool edge geometry for high precision hard turning. *Annals of the CIRP*, *54*(1), 47–50. doi:10.1016/S0007-8506(07)60046-8

Klocke, F., Raedt, H.-W., & Hoppe, S. (2001). 2D-FEM simulation of the orthogonal high speed cutting process. *Mining Science and Technology*, *5*, 323–340.

Komvopoulos, K., & Erpenbeck, S. A. (1991). Finite element modeling of orthogonal metal cutting. *ASME Journal of Engineering for Industry*, *113*, 253–267.

Lin, Z. C., & Lin, S. Y. (1992). A couple finite element model of thermo-elastic-plastic large deformation for orthogonal cutting. *ASME Journal of Engineering for Industry*, *114*, 218–226.

List, G., Sutter, G., & Bi, X. F. (2009). Investigation of tool wear in high speed machining by using a ballistic set-up. *Wear*, *267*, 1673–1679. doi:10.1016/j.wear.2009.06.018

Mabrouki, T., & Rigal, J.-F. (2006). A contribution to a qualitative understanding of thermo-mechanical effects during chip formation in hard turning. *Journal of Materials Processing Technology*, *176*, 214–221. doi:10.1016/j.jmatprotec.2006.03.159

Mackerle, J. (1999). Finite-element analysis and simulation of machining: A bibliography (1976-1996). *Journal of Materials Processing Technology*, *86*, 17–44. doi:10.1016/S0924-0136(98)00227-1

Mackerle, J. (2003). Finite element analysis and simulation of machining: An addendum a bibliography (1996-2002). *International Journal of Machine Tools & Manufacture*, *43*, 103–114. doi:10.1016/S0890-6955(02)00162-1

Mamalis, A. G., Horvath, M., Branis, A. S., & Manolakos, D. E. (2001). Finite element simulation of chip formation in orthogonal metal cutting. *Journal of Materials Processing Technology*, *110*, 19–27. doi:10.1016/S0924-0136(00)00861-X

Mamalis, A. G., Kundrák, J., Markopoulos, A., & Manolakos, D. E. (2008). On the finite element modeling of high speed hard turning. *International Journal of Advanced Manufacturing Technology*, *38*(5-6), 441–446. doi:10.1007/s00170-007-1114-9

Maranhão, C., & Davim, J. P. (2010). Finite element modelling of machining of AISI 316 steel: Numerical simulation and experimental validation. *Simulation Modelling Practice and Theory*, *18*, 139–156. doi:10.1016/j.simpat.2009.10.001

Marusich, T. D., & Ortiz, M. (1995). Modelling and simulation of high-speed machining. *International Journal for Numerical Methods in Engineering*, *38*, 3675–3694. doi:10.1002/nme.1620382108

Movahhedy, M. R., Altintas, Y., & Gadala, M. S. (2002). Numerical analysis of metal cutting with chamfered and blunt tools. *ASME Journal of Manufacturing Science and Engineering*, *124*, 178–188. doi:10.1115/1.1445147

Nalbant, M., Gökkaya, H., & Sur, G. (2007). Application of Taguchi method in the optimization of cutting parameters for surface roughness in turning. *Materials & Design*, *28*, 1379–1385. doi:10.1016/j.matdes.2006.01.008

Ng, E. G., & Aspinwall, D. K. (2002). Modeling of hard part machining. *Journal of Materials Processing Technology*, *127*, 222–229. doi:10.1016/S0924-0136(02)00146-2

Ng, E. G., Aspinwall, D. K., Brazil, D., & Monaghan, J. (1999). Modelling of temperature and forces when orthogonally machining hardened steel. *International Journal of Machine Tools & Manufacture*, *39*, 885–903. doi:10.1016/S0890-6955(98)00077-7

Nouari, M., & Ginting, A. (2004). Wear characteristics and performance of multi-layer CVD-coated alloyed carbide tool in dry end milling of titanium alloy. *Surface and Coatings Technology*, *200*(18-19), 5663–5676. doi:10.1016/j.surfcoat.2005.07.063

Obikawa, T., Sasahara, H., Shirakashi, T., & Usui, E. (1997). Application of computational machining method to discontinuous chip formation. *ASME Journal of Manufacturing Science and Engineering*, *119*, 667–674. doi:10.1115/1.2836807

Olovsson, L., Nilsson, L., & Simonsson, K. (1999). An ALE formulation for the solution of two-dimensional metal cutting problems. *Computers & Structures*, *72*, 497–507. doi:10.1016/S0045-7949(98)00332-0

Özel, T. (2003). Modeling of hard part machining: Effect of insert edge preparation in CBN cutting tools. *Journal of Materials Processing Technology*, *141*, 284–293. doi:10.1016/S0924-0136(03)00278-4

Özel, T. (2006). The influence of friction models on finite element simulations of machining. *International Journal of Machine Tools & Manufacture*, *46*, 518–530. doi:10.1016/j.ijmachtools.2005.07.001

Özel, T. (2009). Computational modeling of 3D turning: Influence of edge micro-geometry on forces, stresses, friction and tool wear in PcBN tooling. *Journal of Materials Processing Technology*, *209*, 5167–5177. doi:10.1016/j.jmatprotec.2009.03.002

Özel, T., & Altan, T. (2000). Process simulation using finite element method – prediction of cutting forces, tool stresses and temperatures in high-speed flat end milling process. *International Journal of Machine Tools & Manufacture*, *40*, 713–738. doi:10.1016/S0890-6955(99)00080-2

Özel, T., & Zeren, E. (2007). Finite element modeling the influence of edge roundness on the stress and temperature fields induced by high-speed machining. *International Journal of Advanced Manufacturing Technology*, *35*, 255–267. doi:10.1007/s00170-006-0720-2

Peace, G. S. (1993). *Taguchi methods: A hands-on approach*. Reading, MA: Addison-Wesley.

Schulz, H. (2001). *Scientific fundamentals of HSC*. Munich, Germany: Carl Hanser Verlag.

Schulz, H., & Moriwaki, T. (1992). High-speed machining. *Annals of the CIRP*, *41*(2), 637–643. doi:10.1016/S0007-8506(07)63250-8

Shih, A. J. (1995). Finite element simulation of orthogonal metal cutting. *ASME Journal of Engineering for Industry*, *117*, 84–93. doi:10.1115/1.2803283

Shirakashi, T., & Usui, E. (1974). Simulation analysis of orthogonal metal cutting mechanism. In *Proceedings of the First International Conference on Production Engineering, Part I* (pp. 535-540).

Smith, S., & Tlusty, J. (1997). Current trends in high-speed machining. *ASME Journal of Manufacturing Science and Engineering*, *119*, 664–666. doi:10.1115/1.2836806

Strenkowski, J. S., & Carroll, J. T. (1985). A finite element model of orthogonal metal cutting. *ASME Journal of Engineering for Industry*, *107*, 346–354. doi:10.1115/1.3186008

Strenkowski, J. S., & Carroll, J. T. (1986). Finite element models of orthogonal cutting with application to single point diamond turning. *International Journal of Mechanical Sciences*, *30*, 899–920.

Strenkowski, J. S., & Moon, K. J. (1990). Finite element prediction of chip geometry and tool/workpiece temperature distributions in orthogonal metal cutting. *ASME Journal of Engineering for Industry*, *112*, 313–318. doi:10.1115/1.2899593

Sutter, G., Ranc, N., Molinari, A., & Pina, V. (2008). Experimental measurement of temperature distribution in the chip generated during high speed orthogonal cutting process. *International Journal of Machining and Machinability of Materials*, *3*(1-2), 52–61. doi:10.1504/IJMMM.2008.017624

Tang, D. W., Wang, C. Y., Hu, Y. N., & Song, Y. X. (2009). Finite-element simulation of conventional and high-speed peripheral milling of hardened mold steel. *Metallurgical and Materials Transactions A*, *40*, 3245–3257. doi:10.1007/s11661-009-9983-1

Tlusty, J. (1993). High-speed machining. *Annals of the CIRP*, *42*(2), 733–738. doi:10.1016/S0007-8506(07)62536-0

Trent, E. M., & Wright, P. K. (2000). *Metal cutting*. Woburn, MA: Butterworth-Heinemann.

Umbrello, D., Filice, L., Rizzuti, S., Micari, F., & Settineri, L. (2007). On the effectiveness of finite element simulation of orthogonal cutting with particular reference to temperature prediction. *Journal of Materials Processing Technology*, *189*, 284–291. doi:10.1016/j.jmatprotec.2007.01.038

Umbrello, D., M'Saoubi, R., & Outeiro, J. C. (2007). The influence of Johnson-Cook material constants on finite element simulation of machining of AISI 316L steel. *International Journal of Machine Tools & Manufacture*, *47*, 462–470. doi:10.1016/j.ijmachtools.2006.06.006

Usui, E., & Shirakashi, T. (1982). Mechanics of machining – from "descriptive" to "predictive" theory. In Kops, L., & Ramalingam, S. (Eds.), *On the art of cutting metals – 75 years later: A tribute to F. W. Taylor* (*Vol. 7*, pp. 13–35). New York, NY: ASME.

van Luttervelt, C. A., Childs, T. H. C., Jawahir, I. S., Klocke, F., & Venuvinod, P. K. (1998). Present situation and future trends in modelling of machining operations. *Annals of the CIRP*, *47*(2), 587–626. doi:10.1016/S0007-8506(07)63244-2

Vaz, M. Jr, Owen, D. R. J., Kalhori, V., Lundblad, M., & Lindgren, L.-E. (2007). Modelling and simulation of machining processes. *Archives of Computational Methods in Engineering*, *14*, 173–204. doi:10.1007/s11831-007-9005-7

Yang, W. H., & Tarng, Y. S. (1998). Design optimization of cutting parameters for turning operations based on the Taguchi method. *Journal of Materials Processing Technology*, *84*, 122–129. doi:10.1016/S0924-0136(98)00079-X

Zerilli, F. J., & Armstrong, R. W. (1987). Dislocation-mechanics-based constitutive relations for material dynamics calculations. *Journal of Applied Physics*, *61*, 1816–1825. doi:10.1063/1.338024

Zhang, B., & Bagchi, A. (1994). Finite element formation of chip formation and comparison with machining experiment. *ASME Journal of Engineering for Industry*, *116*, 289–297. doi:10.1115/1.2901944

Zorev, N. N. (1963). Inter-relationship between shear processes occurring along tool face and shear plane in metal cutting. In *Proceedings of the International Research in Production Engineering Conference* (pp. 42-49).

This work was previously published in the International Journal of Manufacturing, Materials, and Mechanical Engineering, Volume 1, Issue 4, edited by J. Paulo Davim, pp. 1-18, copyright 2011 by IGI Publishing (an imprint of IGI Global).

Chapter 12
A Finite Element Study of Chip Formation Process in Orthogonal Machining

Amrita Priyadarshini
Indian Institute of Technology, Kharagpur, India

Surjya K. Pal
Indian Institute of Technology, Kharagpur, India

Arun K. Samantaray
Indian Institute of Technology, Kharagpur, India

ABSTRACT

This paper examines the plane strain 2D Finite Element (FE) modeling of segmented, as well as continuous chip formation while machining AISI 4340 with a negative rake carbide tool. The main objective is to simulate both the continuous and segmented chips from the same FE model based on FE code ABAQUS/ Explicit. Both the adiabatic and coupled temperature displacement analysis has been performed to simulate the right kind of chip formation. It is observed that adiabatic hypothesis plays a critical role in the simulation of segmented chip formation based on adiabatic shearing. The numerical results dealing with distribution of stress, strain and temperature for segmented and continuous chip formations were compared and found to vary considerably from each other. The simulation results were also compared with other published results; thus validating the developed model.

INTRODUCTION

Machining is a term that covers a large collection of manufacturing processes designed to remove material from a workpiece. This is one of the most important mechanical processes in industry because almost all the products get their final shape and size by material removal either directly or indirectly. Although metal cutting process is commonplace, the underlying physical phenomena are highly complex. Therefore, this area has always been of great interest to the researchers. During the cutting process, the unwanted material is removed from the workpiece with the aid of a

DOI: 10.4018/978-1-4666-1867-1.ch012

Copyright © 2013, IGI Global. Copying or distributing in print or electronic forms without written permission of IGI Global is prohibited.

machine tool and a cutting tool by straining a local region of the workpiece by the relative motion of the tool and the workpiece. As the tool advances, the material ahead of it is sheared continuously along a narrow zone called the shear plane; thus, removing the excess material in the form of chip that flows along the rake surface of the tool.

Chip formation and its morphology are the key areas in the study of machining process that provide significant information on the cutting process itself. The chip morphology depends upon the workpiece material properties and the cutting conditions. The main chip morphologies observed in cutting process are the continuous and the cyclic or serrated chips. Many parameters, namely, cutting force, temperature, tool wear, machining power, friction between tool-chip interface and surface finish are affected by the chip formation process and chip morphology. Thus, for determining the optimum cutting conditions, it is very essential to simulate the real machining operation by using various analytical and numerical models. Availability of an accurate model aids in the selection of optimal process parameters so that the metal removal process can be carried out more efficiently and economically.

With the advent of powerful computers and efficient commercial software packages, Finite Element Method (FEM) has become one of the most powerful tools for the simulation and analysis of cutting process. This not only allows studying the cutting process in greater detail than possible in experiments, but also takes into account the material properties and non-linearity better than analytical models.

Pioneering work in the analysis of metal cutting by using FEM has been carried out by Klamecki (1973) and Tay et al. (1974). Generally, application of finite element modeling to cutting process involves Eulerian, Lagarangian or Arbitary Lagrangian Eulerian (ALE) formulations. Tay et al. (1974) used the Eulerian formulation technique that is often being used till date. In Eulerian approach, the reference frame is fixed in space that allows for the material to flow through the grid (Raczy et al., 2004). As the mesh is fixed in space, the numerical difficulties associated with the distortion of elements are eliminated. In one of the recent works, an Eulerian finite element model has been applied to the simulation of machining which showed good overall correlation with the experimental results (Akarca et al., 2008). This approach permits simulation of machining process without the use of any mesh separation criterion. The main drawback of Eulerian formulation is that it is unable to model the unconstrained flow of material or free boundaries and may only be used when boundaries of the deformed material are known a priori. Hence, in this case, dimension of the chip must be specified in advance to produce a predictive model for chip formation (Mackerle, 1962). While in Lagrangian approach, no a priori assumption is needed about the shape of the chip. In Lagrangian approach, the reference frame is set by fixing the grid to the material of interest such that as the material deforms the grid also deforms. Lagrangian formulation is easy to implement and is computationally efficient. Difficulties arise when elements get highly distorted during the deformation of the material in front of the tool tip.

Therefore, many chip separation criteria have been used in the literature to simulate the cutting action at the cutting zone (Strenkowski & Moon, 1990). These criteria are grouped as geometrical and physical types. A geometrical criterion is based on a specified small distance from the tool tip, beyond which the separation of nodes is allowed along the predefined parting line. Komvopoulos and Erpenbeck (1991) used a distance tolerance of half of the length of the side length of the element in front of the tool tip. According to the physical criteria, the nodes get separated when the value of a predefined physical parameter, such as stress, strain or strain energy density, at nodes reaches a critical value that has been selected depending upon the work material properties and the cutting condition (Iwata et al., 1984). Strenkowski and

Carrol (1985) introduced the chip separation criterion based on the effective plastic strain at the node nearest to the cutting edge, the typical limit ranging from 0.25 to 1.00. Many researchers have used this criterion to model the cutting process by considering various limit values. Even if the criterion is chosen properly, there is no physical indication as to what limit value should be used; thus making the chip separation model more of arbitrary nature. Consequently, this limits the application of Lagrangian formulation in modeling the metal cutting process.

Both the approaches, Eulerian and Lagrangian, have their own advantages and disadvantages. The strong point of one is the weakness of the other. Keeping this in view, a more general approach, Arbitrary Lagrangian Eulerian (ALE) approach was introduced by the end of the last decade which takes the best part of both the formulations and combines them in one (Obikawa et al., 1997). ALE reduces to a Lagrangian form on free boundaries while maintains an Eulerian form at locations where significant deformations occur, as found during the deformation of material in front of the tool tip; thus avoiding the need of remeshing (Rakotomalala et al., 1993). Olovsson et al. (1999) stated that implementation of ALE into the special purpose computer code Exhale2D allowed flow boundary conditions whereby a small part of the workpiece in the vicinity of the tool tip needs to be modeled. Movaheddy et al. (Movahhedy et al., 2008) presented the ALE model for continuous chip to study the effect of tool edge preparation. Attanasio et al. (2008) predicted flank wear and crater wear evolution by utilizing a diffusion wear model implemented in an ALE numerical simulation of turning operation on AISI 1045 by uncoated WC tool.

Ng and Aspinwall (1999) pointed out in a review that majority of the works concerned with the numerical modeling deals with the 2D FEM of continuous chip formation. The continuous chip is an ideal type of chip for analysis because the shear deformation imposed by the cutting tool on the workpiece is uniformly distributed throughout the chip which makes it stable. Shi and Liu (2004) performed a fully coupled thermal stress analysis using ABAQUS/Explicit v6.2 to compare the results obtained from four different material models for simulating the formation of continuous chips. Li et al. (2002) employed Johnson–Cook's model as constitutive equation of the workpiece material for qualitative understanding of crater-wear from the calculated temperature distribution by using Abaqus and other commercially available FE codes. Ozel (2006) has simulated continuous chip formation process by using DEFORM-2D software to study the effect of tool-chip interfacial friction models on the FE simulations.

But in actual practice, transition from continuous to segmented chip formation occurs at higher cutting speeds, especially in case of tools with negative rake angles while machining numerous metals such as, titanium, hardened steel and nickel iron super alloys. In segmented chips, however, deformation is not uniform where the shear zones appear periodically and the chip thickness varies with time. This non-uniformity may result from the dynamic response of the machine-tool structures at certain cutting speeds that may lead to rapid tool wear and poor surface finish (Elbastwani et al., 1996). But, it is also reported that machining under such conditions produces the chips that are easier to break as compared to the long continuous chips; thus saving the additional requirements for cleaning and chip disposal (Konig et al., 1990). Moreover, it is also found that continuous chips formed under identical conditions would need a larger cutting force than the segmented chips (Baker, 2005).

Although predicting the cutting conditions that lead to serrated chips is important, not much work is found in the literature till the year 1999. Recently, there are many significant papers that explain the segmented chip formation by considering negative rake angle (Ohbuchi & Obikawa, 2005). Basically, two different mechanisms are proposed, namely adiabatic shear banding and

propagation of cracks for the chip segmentation. Baker et al. (2002) studied the chip segmentation in detail based on adiabatic shearing while machining Ti6Al4V by using ABAQUS/Standard by considering simple isotropic plastic flow law as the material model. Similarly, Mabrouki et al. (2006) focused on adiabatic shearing using Johnson cook material model for AISI 4340 steel and compared the results obtained from ABAQUS/Explicit and Thirdwave Systems' AdvantEdge with those obtained experimentally. Calamaz et al. (2008) proposed a new material model that takes into account not only the strain hardening and the thermal softening phenomenon, as in case of Johnson-Cook model, but also strain softening phenomenon by using the finite element solver FORGE 2005. Vyas and Shaw (1999) have argued that the root cause of saw tooth chip formation is cyclic cracking. Baker et al. (2002) focused on the effects that a growing crack has on the plastic deformation of the material. In one of the recent papers (Lorentzon & Jarvstrat, 2009), the effect of different fracture criteria on the segmented chip formation has been investigated for the alloy 718. A conclusion from that study is that both thermal softening and material damage cause the transition from continuous chip to segmented chip formation.

The importance of predicting the right kind of chip accurately under various cutting conditions motivates the authors to develop finite element models that should have the capability to satisfactorily analyze both the continuous and the segmented chip formation. Several efforts are being constantly made by the researchers worldwide to come up with significant results in this area. The main objective of this work is to simulate the chip formation process by incorporating ALE along with appropriate material and damage model by following both the adiabatic and coupled temperature displacement analysis. This work mainly focuses on the segmentation of chip due to adiabatic shearing while hard turning with a cutting tool having negative rake angle. Both continuous and segmented chip formation processes are simulated by using the same FE model under same cutting conditions and the variation in stress, strain, temperature distribution and forces for both the cases are analyzed in details.

FINITE ELEMENT METHOD

A finite element model of the machining process was developed from two-dimensional orthogonal analysis. Although two-dimensional analysis is a restrictive approach from practical point of view, it reduces the computational time considerably and provides satisfactory results regarding the details of the chip formation. A commercially available general purpose finite element package, ABAQUS/Explicit version 6.7-4 along with ALE technique was employed to conduct the simulation.

In the cutting operation, heat transfer largely depends on the cutting velocity. It is often assumed that at high cutting speeds, there is nearly no time for conduction to occur and adiabatic conditions may exist with high local temperatures in the chip. In the present work, firstly an adiabatic analysis was performed to obtain much clear shear bands on the chip surface. This helps in explaining the phenomena that leads to the formation of the saw-teeth chips. However, in real machining, ignoring the heat transfer is unacceptable and also it is not possible to determine the temperature field over the tool surface with adiabatic analysis module. This motivated us to exploit the fully coupled temperature-displacement module of the Abaqus/Explicit. A very simple approach was followed to demonstrate the formation of both the continuous and segmented chip, namely in one case thermal conductivity of the workpiece was considered while in the other, it was neglected. Although neglecting the thermal conductivity makes the approach hypothetical to some extent, it aids in proper understanding of the chip segmentation process as seen in the case of adiabatic analysis as well as to understand the temperature field over the tool surface.

Geometrical Details of the Model and Modeling Assumptions

The 2 D FE model for the analysis of chip formation consists of a portion of the cutting tool and a block representing the workpiece. Since the cutting width is much larger than the undeformed chip thickness, plane strain condition was assumed. The cutting tool was assumed to be perfectly sharp. Both the cutting tool and the workpiece were considered as the deformable bodies. A chamfer (gap DFL) was incorporated in the workpiece to form the initial chip without termination of program that may occur due to heavy distortion of elements at the starting part of the workpiece due to the negative rake of the cutting tool. Though in actual practice chamfer does not exist, it hardly matters in the simulation because the study is based on the steady state machining conditions. An intermediate layer of elements known as damage zone has been considered in the workpiece block that defines the path of separation of chip from the workpiece material which is going to take place as the tool progresses. It is noted that width of the chip surface is the thickness of the material to be cut or the undeformed chip thickness which is actually equal to the feed in the orthogonal cutting conditions. Details of the geometric model and the working parameters have been shown in Figure 1 and Table 1, respectively.

The Figure 1 shows the desired chip separation surface and desired machined surface separated by a narrow line of sacrificial layer of elements called damage zone, width of which has been mentioned as ε. It is noted that in reality these two surfaces should be same but such assumption has been taken only for the modeling purpose as a chip separation criterion where in $\varepsilon \to 0$. Consequently, a very small value of ε (0.04 mm) which is computationally acceptable has been taken as the width of the damage zone. The choice of the height of the designated damage zone is purely based on computational efficiency. It could be reduced further if faster computing facilities are available. The material model is defined for the entire workpiece while the damage model is

Figure 1. Geometric details and initial mesh configuration

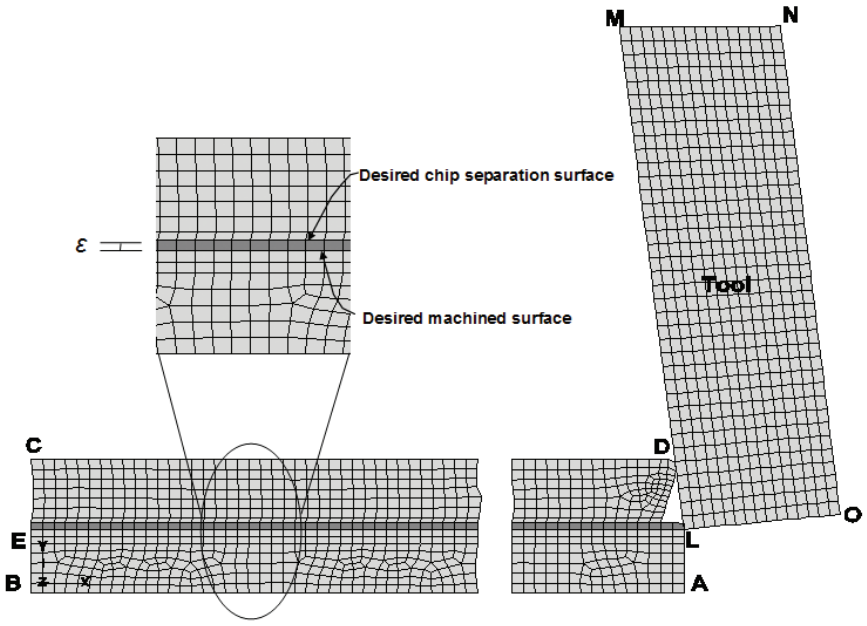


Table 1. Details of the geometric model and cutting parameters

Description	Parameter	Value
Cutting tool	Rake angle, γ	-6°
	Clearance angle, α	5°
Workpiece model geometry	Length (mm)	8
	Width (mm)	0.4
	Damage zone width (mm)	0.04
Cutting parameters	Feed, *f* (mm)	0.2
	Cutting Velocity, V_c (m/min)	100

defined specifically in the damage zone such that when the accumulated damage in an element in the sacrificial layer immediately ahead of the tool exceeds one, the element is supposed to fail. It is then removed from the mesh and consequently the tool moves further into the workpiece. Note that the fracture as such is not modeled.

Element Formulation

Four-node plane strain bilinear quadrilateral (CPE4RT) elements with reduced integration scheme and hourglass control are used for the discretization for both the workpiece and the cutting tool. The workpiece is meshed with 2331 CPE4RT type elements by unstructured grid generation which utilizes advancing front algorithm in ABAQUS/Explicit. Since the elements produced by this method follow the boundary nodes, the resulting mesh may involve some skew in the element as observed in certain regions. Finite element formulation of this type of element is based on the isoparametric procedure i.e., the element geometry and the displacements are interpolated in the same way. The nodal degrees of freedom (DOF) of the quadrilateral element are shown in Figure 2.

The element geometry and displacement field are defined in terms of nodal coordinates and DOFs by the following functions:

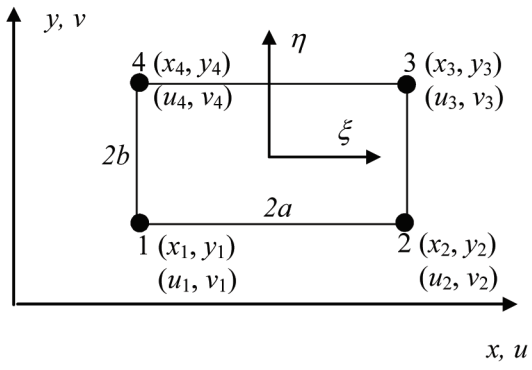
$$\begin{cases} x = \sum_{i=1}^{4} N_i(\xi,\eta)\, x_i \\ y = \sum_{i=1}^{4} N_i(\xi,\eta)\, y_i \end{cases} \quad \begin{cases} u = \sum_{i=1}^{4} N_i(\xi,\eta)\, u_i \\ v = \sum_{i=1}^{4} N_i(\xi,\eta)\, v_i \end{cases} \Rightarrow \mathbf{u}=\mathbf{Nq} \tag{1}$$

where

x_i, y_i = global x-y coordinates at *i*-th node

u_i, v_i = displacements at *i*-th node along global X, Y axes, respectively

Figure 2. Description of 2D quadrilateral element



$N_i(\xi,\eta)$ = interpolation or shape function for *i*-th node defined in the natural coordinates

ξ_i, η_i = natural coordinates of the *i*-th element node

The nodal interpolation function $N_i(\xi,\eta)$ for quadrilateral elements is of the form (Liu & Quek, 2003):

$$N_i(\xi,\eta) = \frac{1}{4}(1+\xi_i\xi)(1+\eta_i\eta) \text{ for } i = 1,2,3,4 \tag{2}$$

The strains at any point within element can be expressed as follows:

$$\begin{bmatrix}\varepsilon_x\\ \varepsilon_y\\ \gamma_{xy}\end{bmatrix} = \begin{bmatrix}\frac{\partial u}{\partial x}\\ \frac{\partial v}{\partial y}\\ \frac{\partial v}{\partial y}+\frac{\partial u}{\partial x}\end{bmatrix} = \begin{bmatrix}\frac{\partial}{\partial x} & 0\\ 0 & \frac{\partial v}{\partial y}\\ \frac{\partial}{\partial y} & \frac{\partial}{\partial x}\end{bmatrix}\begin{bmatrix}u\\ v\end{bmatrix}$$
$$= \begin{bmatrix}\frac{\partial}{\partial x} & 0\\ 0 & \frac{\partial v}{\partial y}\\ \frac{\partial}{\partial y} & \frac{\partial}{\partial x}\end{bmatrix}\begin{bmatrix}N_1 & 0 & N_2 & 0 & N_3 & 0\\ 0 & N_1 & 0 & N_2 & 0 & N_4\end{bmatrix}\begin{bmatrix}u_1\\ v_1\\ \vdots\\ u_2\\ v_3\end{bmatrix} \tag{3}$$

$$\therefore \varepsilon = \mathbf{du} = \mathbf{dNq} = \mathbf{Bq} \tag{4}$$

where $\mathbf{B}$ = strain-displacement matrix and $\mathbf{q}$ =vector of nodal displacements.

Finally the stress- strain relationship becomes

$$\sigma = \mathbf{D}\varepsilon = \mathbf{DBq} \tag{5}$$

where **D** is the elasticity matrix defining the mechanical properties of the material in terms of the Young's modulus and the Poisson's ratio.

Boundary Conditions

For the simulation of cutting operation, proper type of boundary conditions should be imposed. The kinematic boundary conditions are as follows:

For the workpiece:

$$u_y = 0 \text{ on AB, } u_x = 0 \text{ on BC, } v_x = V_c \text{ on ABEF} \tag{6}$$

where v_x is the velocity in X-direction, V_c is the cutting velocity, and AB, BC and ABEF refer to edges in Figure1.

For the cutting tool, boundary conditions on sides ON and MN in Figure1 are:

$$u_x = 0 \text{ on ON, } u_y = 0 \text{ on MN} \tag{7}$$

The thermal boundary conditions are as follows:

In case of adiabatic analysis, no heat transfer is allowed from the top surface of the workpiece, exposed surface of the chip and the machined surface to the cutting tool and to the atmosphere, i.e., $\frac{\partial T}{\partial n} = 0$. While for the coupled temperature displacement analysis, boundaries CDF and LM in Figure1 have convective heat transfer boundary conditions, with the overall heat transfer coefficient (h), thermal conductivity (k) and ambient temperature (T_o) given as input:

$$-k\frac{\partial T}{\partial n} = h(T_o - T) \tag{8}$$

Rest of the surfaces for both tool and work piece were initially kept at (T_o). It is noted that the heat transfer coefficient h, being the ratio of average heat flow across the interface to the temperature drop, is a function of several variables such as, contact pressure, temperature, contacting materials, etc. Due to difficulties in measuring

temperatures at tool-chip interface, there is hardly any data available for heat transfer coefficient for chip formation process. In the present work, simulations at a particular speed-feed combination were done for h varying within a range of 100-1000 kW/m^{2}K. Since the difference in temperature was found to be very less with the change in heat transfer coefficient, h = 500 kW/m^{2}K was considered as a fair compromise. Moreover, this value has also been used by Coelho (2006) for machining aisi 4340 and thus, taken as the reference value for the entire set of simulations.

Governing Equations

The governing equations of a body undergoing deformation consists of two sets of equations, namely, the conservations laws of physics and the constitutive equations. The conservation laws can be applied to body of any material. But to distinguish between different materials undergoing deformation of varied degrees, one needs the constitutive equations.

Conservation Laws

Proper implementation of kinematics is important while developing a FE model for chip formation process. These kinematics refer to the mass, momentum and energy equations governing the continuum, which are given as follows:

$$\dot{\rho} + \rho \operatorname{div} \vec{v} = 0 \tag{9}$$

$$\rho \dot{\vec{v}} = \vec{f} + \operatorname{div} \sigma \tag{10}$$

$\rho \dot{e} = \sigma : \mathbf{D} - \operatorname{div} \vec{q} + r$ where ρ is the mass density, $\vec{v}$ material velocity, $\vec{f}$ body forces, σ Cauchy stress tensor, *e* specific internal energy, D strain rate tensor, $\vec{q}$ heat flux vector and *r* is body heat generation rate. The superposed '$\bullet$' denotes material derivative in a Lagrangian description and ':' denotes contraction of a pair of repeated indices which appear in the same order such as,

$$\mathrm{A{:}B} = A_{ij} B_{ij} . \tag{11}$$

The basic idea of using FEM is to discretize the above equations and then to seek a solution to the momentum equation.

Work Piece Material Constitutive Equations

Constitutive equations are a set of equations which describe the thermo-mechanical properties of a material undergoing deformation. Based on the simplicity or complexity of the material behaviour, there could be one constitutive equation or a set of constitutive equations that relate the deformation in the body to the stresses.

It is assumed that elastic and inelastic responses are separable based on the fact that there is an additive relationship between the strain rates such that:

$$\dot{\varepsilon} = \dot{\varepsilon}^{\mathrm{e}} + \dot{\varepsilon}^{\mathrm{pl}} \tag{12}$$

where $\dot{\varepsilon}$ is the total strain rate, $\dot{\varepsilon}^{\mathrm{e}}$ the rate of change of elastic strain and $\dot{\varepsilon}^{\mathrm{pl}}$ rate of change of plastic strain. This indicates initially the material responds elastically (recoverable) and when the stress is beyond the elastic limit, plastic deformation (non-recoverable) takes place.

The elastic response can be described by simple linear elastic relationship given by:

$$\sigma = \mathbf{D}^{\mathrm{el}} : \varepsilon^{\mathrm{el}} \tag{13}$$

where D^{el} is the elasticity stress tensor and $\varepsilon^{\mathrm{el}}$ is the elastic strain.

The constitutive equations of plasticity usually contain yield criterion, flow rule and strain hardening rule. The yield criterion describes the stress state when yielding occurs, the flow rule

defines increment of plastic strain when yielding occurs, and the hardening rule describes how the material is strain hardened as the plastic strain increases. For large deformation problems, as in case of machining, plasticity models based on von Mises yield criterion and Prandtl–Reuss flow rule are generally used to define the isotropic yielding and hardening (Wu, 2004).

In case of machining process, isotropic yielding occurs when plastic deformation or straining occurs. The energy consumed here because of plastic deformation and tool-chip friction is converted largely into heat which raises the temperature in the cutting zone. Hence, realistic constitutive equations of plasticity (plasticity models) are an indispensable input in any FE simulations that are efficient enough to describe stress-strain response as well as its dependence on strain rate, temperature and work hardening.

The Johnson–Cook constitutive equation is one such model that is widely used to characterize the material behaviour of the workpiece satisfactorily (Johnson & Cook, 1983). This has been developed with data obtained from a series of Hopkinson bar tests at high strain rates and temperatures. The SHPB method enables to perform material tests at strain rates up to 10^4 s^{-1} by exposing the sample to stress waves. Furthermore, it can be used up to reasonable strains and can be tailored for tests at an elevated temperature (Jaspers & Dautzenberg, 2002). So far, this method has been found to be the most suitable one for the determination of mechanical behaviour of materials under conditions similar to those found in machining and thus, widely used in modeling of machining process (Shi & Liu, 2004; Umbrello et al., 2007; Davim & Maranhao, 2009; Vaziri et al., 2010). This model is also considered numerically robust as most of the variables are readily acceptable to the computer codes. The formulation of Johnson–Cook constitutive equation is based upon second deviatoric stress invariant flow theory with isotropic hardening which is defined as follows (Johnson & Cook, 1983, 1985):

$$\sigma' = 2\mathrm{G}(\dot{\varepsilon}' - \dot{\varepsilon}^{\mathrm{p}}) \tag{14}$$

$$\bar{\varepsilon}^{\mathrm{p}} = \int \sqrt{\frac{2}{3}\dot{\varepsilon}^{\mathrm{p}} : \dot{\varepsilon}^{\mathrm{p}}}\,\mathrm{d}t \tag{15}$$

$$\bar{\sigma} = \sqrt{\frac{3}{2}\sigma' : \sigma'} \tag{16}$$

where σ' is the deviatoric Cauchy stress, $\dot{\varepsilon}'$ is the deviatoric strain rate, $\dot{\varepsilon}^{\mathrm{p}}$ is the plastic strain rate, $\bar{\varepsilon}^{\mathrm{p}}$ is the equivalent plastic strain, $\bar{\sigma}$ is the equivalent flow stress and G is the shear modulus.

In this work, the following equivalent flow stress formulation has been used:

$$\bar{\sigma} = \left(A + B\left(\bar{\varepsilon}^{\mathrm{p}}\right)^{n}\right)\left(1 + C\,\ln\dot{\bar{\varepsilon}}^{\mathrm{p}*}\right)\left(1 - \left(\frac{T - T_{\mathrm{room}}}{T_{\mathrm{m}} - T_{\mathrm{room}}}\right)^{m}\right) \tag{17}$$

$$\dot{\bar{\varepsilon}}^{*} = \frac{\dot{\bar{\varepsilon}}^{\mathrm{p}}}{\dot{\bar{\varepsilon}}_{0}^{\mathrm{p}}} \text{ for } \dot{\bar{\varepsilon}}_{0}^{\mathrm{p}} = 1\ \mathrm{s}^{-1} \tag{18}$$

where T_{room} is the room temperature taken as 25ºC, T_{melt} is the melting temperature of the workpiece taken as 1520 ºC, A is the initial yield stress (MPa), B the hardening modulus, n the work-hardening exponent, C the strain rate dependency coefficient (MPa), and m the thermal softening coefficient. These material parameters are fitted to the data obtained from a series of Hopkinson bar tests at high strain rates and temperatures.

A ductile failure model is also incorporated, as a chip separation criterion, along with the material model in the damage zone in order to simulate the movement of the cutting tool into workpiece without any mesh distortion near the tool tip. Material failure refers to the complete loss of load carrying capacity which results from progressive degradation of material stiffness. Specification of damage model includes a material response (undamaged), damage initiation

criterion, damage evolution and choice of element deletion. Damage initiation criterion is referred to as the material state at the onset of damage. In the present case, the damage model or failure model is based on Johnson-Cook damage initiation criterion. This model makes use of the damage parameter ω_D defined as the sum of the ratio of the increments in the equivalent plastic strain $\Delta\bar{\varepsilon}^{\mathrm{p}}$ to the fracture strain ε^{f} (ABAQUS Theory manual), given as follows.

$$\omega_{\mathrm{D}}=\sum\frac{\Delta\bar{\varepsilon}^{\mathrm{p}}}{\varepsilon^{\mathrm{f}}} \tag{19}$$

The fracture strain ε^{f} is of the form as follows:

$$\bar{\varepsilon}_f=\left[D_1+D_2\exp\left(D_3\sigma^*\right)\right]\times\left[1+D_4\ln\dot{\bar{\varepsilon}}^{\mathrm{p}*}\right]\times\left[1+D_5\left(\frac{T-T_{\mathrm{room}}}{T_{\mathrm{melt}}-T_{\mathrm{room}}}\right)\right] \tag{20}$$

$$\sigma^*=\frac{-\mathrm{P}}{\bar{\sigma}} \tag{21}$$

where P is the hydrostatic pressure and D_1 to D_5 are failure parameters determined experimentally. The expression in the first set of brackets of Equation (20) indicates the decrease in fracture strain as the hydrostatic pressure increases and the yield stress decreases. The damage initiation criterion is met when ω_D reaches one.

In machining, it is known that the maximum stress and strain occur in front of the cutting tool. With the advancement of tool the plastic strain increases within the workpiece material near the tool tip. Since damage model is defined, particularly, in the damage zone, as the plastic strain increases ω_D of the elements in damage zone gradually reaches a value of one indicating that damage initiation criterion is met. Once the element satisfies the damage initiation criterion, Abaqus/Explicit assumes that progressive degradation of the material stiffness occurs, leading to material failure based on the damage evolution. At any given time during the analysis, the stress tensor in the material is given by:

$$\sigma=\left(1-D\right)\bar{\sigma} \tag{22}$$

where $\bar{\sigma}$ is the effective (undamaged) stress tensor computed in the current increment. When D reaches a value 1, it indicates that the material has lost its load carrying capacity completely. At this point, failure occurs and the concerned elements are removed from the computation. The ELEMENT DELETION = YES module along with the Johnson Cook damage model of the software enables to delete the elements that fail. This produces the chip separation and allows the cutting tool to penetrate further into the workpiece through a predefined path (damage zone). The Johnson–Cook material and damage constants for AISI 4340 standard alloy steel are given in Table 2 (Johnson & Cook, 1983; Johnson & Cook, 1985).

Thermo-Mechanical Properties of Workpiece and Cutting Tool

The physical properties of the AISI 4340 workpiece and the tungsten carbide cutting tool such as, density (ρ), Elastic modulus (E), Poisson's ratio (ν), specific heat (C_p), thermal conductiv-

Table 2. Johnson-Cook parameters for AISI 4340

A (MPa)	B (MPa)	n	C	m	D_1	D_2	D_3	D_4	D_5
792	510	0.26	0.014	1.03	0.05	3.44	−2.12	0.002	0.61

Table 3. Workpiece and cutting tool properties

Material	ρ (kg/m^3)	E (GPa)	ν	C_p (J kg^{-1} K^{-1})	k (W m^{-1} K^{-1})	α (µm m^{-1}K^{-1})
AISI 4340	7850	205	0.30	475	44.5	13.7
Carbide tool	11900	534	0.22	400	50	-

ity (k) and thermal expansion coefficient (α) are mentioned in Table 3 (Ozel & Zeren, 2006).

Interfacial Contact and Heat Generation

A kinematic contact algorithm has been used to enforce contact constraints in master-slave contact pair, where rake surface of the cutting tool is defined as the master surface and chip as the slave (node based) surface. This method conserves momentum between the contacting bodies. The kinematic contact algorithm works in two steps. Firstly, it determines which slave nodes in the predicted configuration penetrate in the surface and then calculates the resisting force required to oppose the penetration based on depth of each slave node's penetration, mass associated with it and the time increment. Secondly, the contact algorithm determines the total internal mass of the contacting interfaces and calculates the acceleration correction for the master surface nodes. Acceleration correction for the slave nodes are then determined using the predicted penetration of each node, the time increment and the acceleration correction for the master surface nodes. This is required to obtain a corrected configuration in which the contact constraints are enforced. Both the frictional forces and the friction-generated heat are included in the kinematic contact algorithm through tangential behaviour and gap heat generation modules of the software.

In actual practice, the stress distribution is not uniform over the rake face of the cutting tool, as shown in the Figure 3 (Zorev, 1963). It is assumed that no relative motion occurs between the tool and the chip when the normal stress is very large and the frictional stress is equal to the equivalent shear stress $\bar{\tau}_{\max}$. This region is called sticking zone (L_{stick}). On the contrary, in the sliding zone (L_{slip}), normal stress is small and frictional stress is proportional to the normal pressure, σ_n, through a constant coefficient of friction, μ. Relative sliding of chip on the rake surface occurs and thus, Coulomb's law holds good for this phenomenon (Ng, 2002) (see Box 1).

During the machining process, heat is generated in the primary shear deformation zone due to severe plastic deformation and in the secondary deformation zone due to both plastic deformation and the friction in the tool-chip interface. The

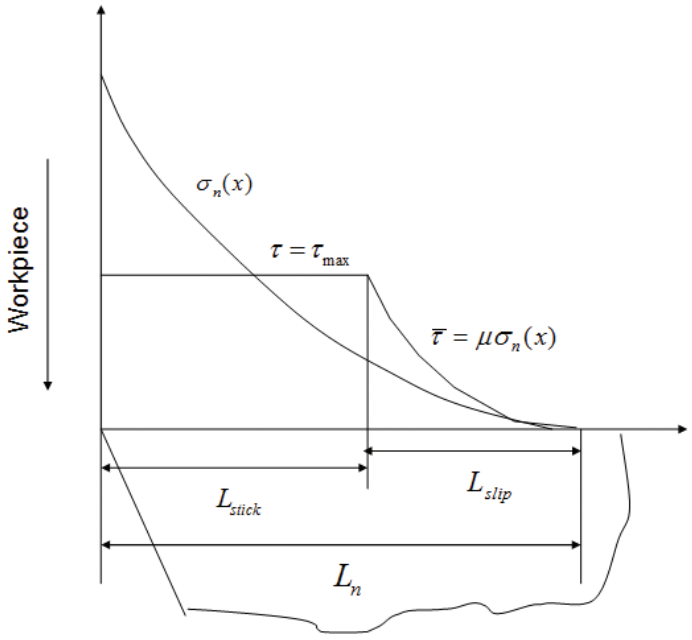
Box 1.

Mathematically, frictional stress $\bar{\tau}$ is given by :

$$\bar{\tau}(x) = \begin{cases} \tau_{\max}, \text{ when } \mu\sigma_n(x) \geq \bar{\tau}_{\max} & 0 < x \leq L_{stick} \quad \text{(sticking zone)} \\ \mu\sigma_n(x), \text{ for } \mu\sigma_n(x) \leq \bar{\tau}_{\max} & L_{stick} < x \leq L_n \quad \text{(slipping zone)} \end{cases} \tag{23}$$

where $\tau_{\max} = \dfrac{A}{\sqrt{3}}$ and A is the yield stress (MPa).

Figure 3. Stress distributions over the rake surface of the tool



steady state two dimensional form of the energy equation governing the orthogonal machining process is given as:

$$k\left(\frac{\partial^2 T}{\partial x^2}+\frac{\partial^2 T}{\partial y^2}\right)T-\rho C_{\mathrm{p}}\left(u_x\frac{\partial^2 T}{\partial x^2}+v_y\frac{\partial^2 T}{\partial y^2}\right)+\dot{q}=0 \tag{24}$$

$$\dot{q}=\dot{q}_{\mathrm{p}}+\dot{q}_{\mathrm{f}} \tag{25}$$

$$\dot{q}_{\mathrm{p}}=\eta_{\mathrm{p}}\overline{\sigma}\dot{\overline{\varepsilon}}^{\mathrm{p}} \tag{26}$$

$$\dot{q}_{\mathrm{f}}=\eta_{\mathrm{f}}J\overline{\tau}\dot{\gamma} \tag{27}$$

where $\dot{q}_p$ is the heat generation rate due to plastic deformation, η_{p} the fraction of the inelastic heat, $\dot{q}_{\mathrm{f}}$ is the volumetric heat flux due to frictional work, $\dot{\gamma}$ the slip rate, η_{f} the frictional work conversion factor considered as 1.0, J the fraction of the thermal energy conducted into the chip, and $\bar{\tau}$ is defined in Equation (21). The value of J may vary within a range, say, 0.35-1 for carbide cutting tool and AISI 4340 workpiece material (Mabrouki & Rigal, 2006). In the present work, 0.5 (default value in ABAQUS) has been taken. The fraction of the heat generated due to plastic deformation remaining in the chip, η_{p}, is taken to be 0.9 (Mabrouki et al., 2004). Thus, partition of heat that actually goes to the chip is taken care by the software during simulation by combining both the heat fractions i.e., J and η_{p} giving an average value within a range of 70-80% of the total heat.

Solution Procedure

An ALE approach is incorporated to conduct the FEM simulation. As mentioned earlier, ALE technique combines the features of pure Lagrangian and Eulerian analysis. The adaptive meshing technique in ABAQUS/Explicit implements ALE approach that allows flow boundary technique

without altering elements and connectivity of the mesh. The idea is generally to apply features of Eulerian approach for modeling the area around the tool tip, while Lagrangian form can be applied to the free surface of the chip. This avoids severe element distortion and entanglement in the cutting zone without the use of remeshing criterion.

ALE Formulation

In the ALE approach, the grid points are not constrained to remain fixed in space (as in Eulerian description) or to move with the material points (as in Lagarangian description) and hence have their own motion governing equations. Hence, the Equations (9) to (11) can be rewritten according to the ALE description such that:

$$\tilde{(\ )} = \dot{(\ )} + \vec{c}\nabla(\ ) \tag{28}$$

$$\vec{c} = \vec{v} - \vec{\hat{v}} \tag{29}$$

where superposed '$\sim$' is defined in the ALE description, $\vec{c}$ is the convective velocity, $\vec{v}$ is the material velocity, $\vec{\hat{v}}$ is the grid velocity and ∇ is the gradient operator. Consequently, the conservation laws are as follows:

$$\tilde{\rho} + \vec{c}\nabla\rho + \rho \operatorname{div}\vec{v} = 0 \tag{30}$$

$$\rho\tilde{\vec{v}} + \rho\vec{c}\nabla\vec{v} = \vec{f} + \operatorname{div}\sigma \tag{31}$$

$$\rho\tilde{e} + \rho\vec{c}\nabla e = \sigma : \mathrm{D} - \operatorname{div}\vec{q} + r \tag{32}$$

FEM is basically used for discretizing the domain of interest into finite number of elements. The corresponding discretized equations of the above equations are obtained by employing the divergence theorem, the variational forms associated with these equations and finally using the Galerkin approach (Hutton, 2004). As a consequence, this leads to the metrical form of the conservative equations given as follows:

$$M^{\rho}\tilde{\rho} + L^{\rho}\rho + K^{\rho}\rho = 0 \tag{33}$$

$$M^{v}\tilde{v} + L^{v}v + f^{\text{int}} = f^{ext} \tag{34}$$

$$M^{e}\tilde{e} + L^{e}e = r \tag{35}$$

where M^{ρ}, M^{v}, M^{e} are the generalized mass matrices for the corresponding variables, L^{ρ}, L^{v}, L^{e} are the generalized convective matrices, K^{ρ} is the stiffness matrix for density, f^{int} is the internal energy force vector, f^{ext} is the external load vector and r is the generalized energy source vector. These matrices are defined in terms of shape functions of the elements and force vectors are defined in terms of shape functions, body force as well as traction acting on the surface (including contact forces).

Explicit Dynamic Analysis

The explicit dynamic ALE formulation is primarily used to solve highly non-linear problems involving large deformations and changing contact, as observed in the case of machining. The explicit dynamic procedure in Abaqus/Explicit is based upon the implementation of an explicit integration scheme for time dicretization of Equations (33) to (35). This analysis calculates the state of a system at a later time from the state of system at the current time. The explicit formulation advances the solution in time with the central difference method:

$$\dot{v}^{i} = M^{-1}\left(f^{ext^{(i)}} - f^{\text{int}^{(i)}}\right) \tag{36}$$

$$v^{(i+1/2)} = v^{(i-1/2)} + \frac{\Delta t^{(i+1)} - \Delta t^{i}}{2}\dot{v}^{i} \tag{37}$$

$$x^{(i+1)} = x^i + \frac{\Delta t^{(i+1)} - \Delta t^i}{2} v^{(i+1/2)} \quad (38)$$

where v is the velocity and $\dot{v}$ is the acceleration, M is the lumped mass matrix, f^{ext} is the external force vector and f^{int} is the internal force. The subscript (i) refers to the increment number (i–1/2) and (i+1/2) and refer to mid-increment values. Since the kinematic state can be obtained using known values of and from the previous increment, the central difference integration operator is said to be explicit.

The explicit procedure integrates through time by using many small time increments. The central difference operator is conditionally stable and the stability limit for the operator is based upon a critical time step. The critical time step for a mesh is considered to be the minimum taken over all the elements which is given by:

$$\Delta t_{\text{crit}} \leq \min\left(L_e / c_e\right) \quad (39)$$

where L_e is the characteristic length of the element and c_e is the current wave speed of an element.

When explicit dynamic ALE formulation is used, it introduces advective terms into the conservation equations to account for independent mesh motion as well as material motion. Advection refers to the process of mapping solution variables from an old mesh to a new mesh. In ALE approach, the solution for a time step advances step-wise. First part is a Lagrangian step which calculates the incremental motion of the material where the displacements are computed using the explicit integration rule and then all the internal variables are updated. Second part is referred to as an Eulerian or advection step where a mesh motion is performed to relocate the nodes such that the element distortion becomes minimum and the grid nodes can be moved according to any one or combination of the three algorithms namely, volumetric, Laplacian and equipotential smoothing. Then the element and the material variables are transferred from the old mesh to the new mesh in each advection step. In the present work, second order momentum advection (ABAQUS Theory manual) is carried out for the ALE mesh domains.

RESULTS AND DISCUSSION

The type of chip formed affects the stress field generated in the workpiece which determines the residual stresses, cutting temperatures and cutting forces. Therefore, simulating the right kind of chip is essential for the proper analysis of the metal cutting process. This necessitates that FE simulations have the capability to develop both continuous and segmented chips. The present work considers the machining of AISI 4340 with a negative rake carbide tool. Experimental studies available in the literature show that segmented chips are produced for such type of tool-workpiece combination, specifically at higher cutting speeds. Thus, the goal of this work is to develop a finite element model that not only simulates the saw-tooth chips but also explains the mechanism governing it.

In this section, results dealing with von Mises equivalent stresses, equivalent strains, temperatures and machining forces during adiabatic analysis are presented showing the efficiency of this module to explain the chip formation phenomenon. But, in order to obtain more realistic results, fully coupled temperature displacement analysis was performed by considering the thermal conductivity of the workpiece in one case while neglecting it in the other case. Incorporating such variation in the given module shows the strong dependence of the chip morphology on thermal conductivity. Numerical results dealing with both the cases are presented and compared. The cutting force, thrust force and other related parameters were determined at different cutting speeds for each of the cases in coupled analysis. Feed values and cutting speeds are also varied for the chip formation in adiabatic analysis. Simulated results

are then compared with each other as well as with the results available in the literature; thus, proving the validity of the developed FE model. The comparative study of the continuous and the segmented chips developed demonstrates the critical importance of modeling the correct type of chip.

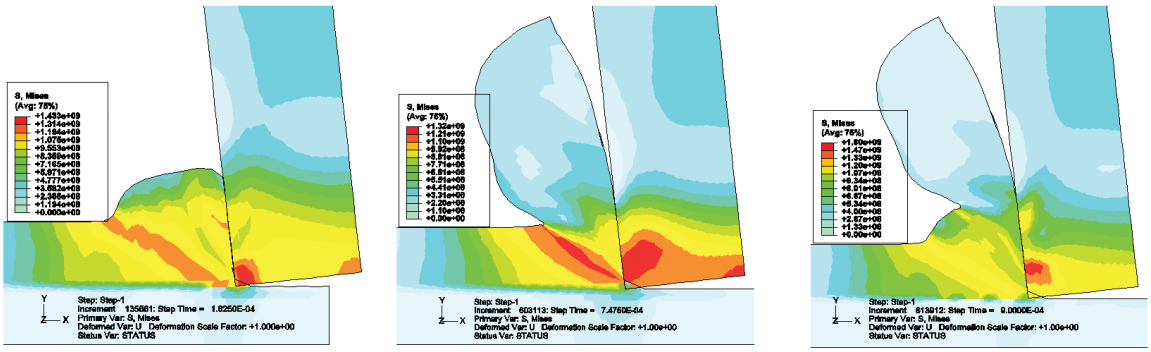
Finite Element Modeling Based on Adiabatic Analysis

As already mentioned, there is very less time for the heat conduction to occur at higher cutting speeds during machining and thus adiabatic hypothesis can possibly be imposed for the modeling of the chip formation process.

Chip Morphology and its Mechanism

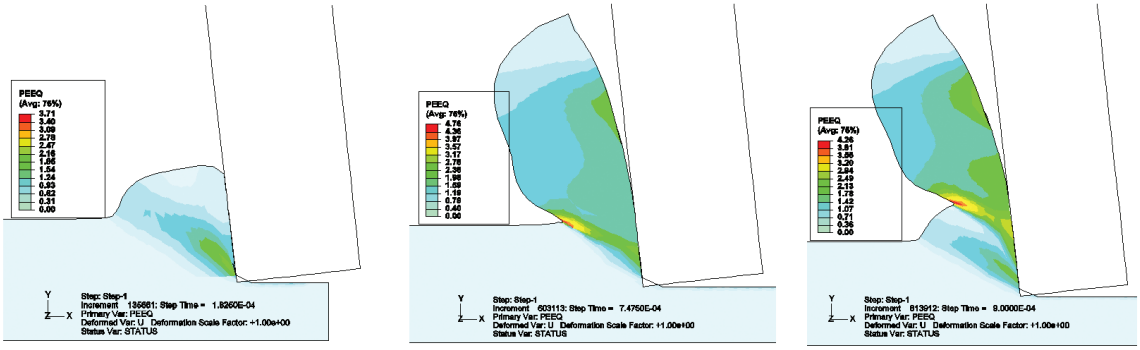
Saw teeth or segmented chips are produced under adiabatic conditions with cutting parameters set at $V_c = 100$ m/min and $f = 0.2$ mm. The chip segmentation is the result of a softening state at elevated temperatures during tool-workpiece interaction. Figures 4 (a–c), 5 (a–c) and 6 (a–b) are presented that help in explaining the mentioned phenomenon elaborately, by focusing on the formation of one chip segment only (onset at about

Figure 4. von Mises equivalent stresses (Pa) at (a) 0.182 ms, (b) 0.747 ms and (c) 0.9 ms



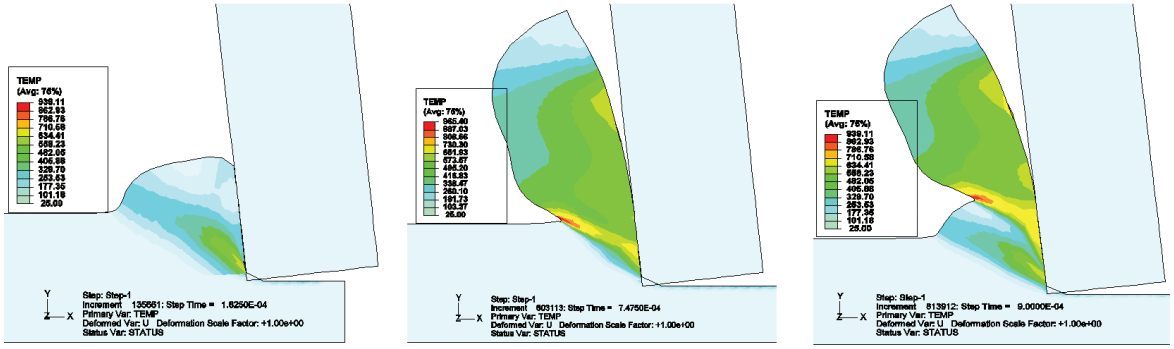
(a) (b) (c)

Figure 5. von Mises equivalent strains at (a) 0.182 ms, (b) 0.747 ms and (c) 0.9 ms



(a) (b) (c)

Figure 6. Temperature distribution (°C) at (a) 0.182 ms, (b) 0.747 ms and (c) 0.9 ms



(a) (b) (c)

0.182 ms, segmentation at about 0.747 ms and final state at 0.9 ms).

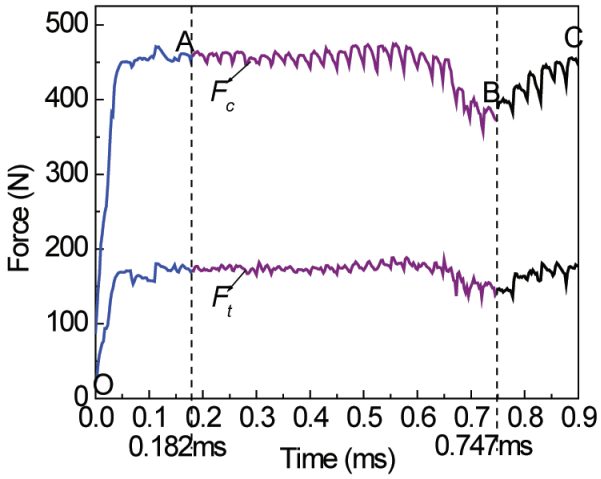
Figure 7 shows the cutting force (F_c) and thrust force (F_t) developed during the process

Chip formation begins with the bulging of the workpiece material in front of the tool as shown in the Figure 3(a). It can be seen that the stresses with the higher values are mainly distributed in the primary shear deformation zone, values ranging between 1.19–1.31 GPa, followed by the secondary shear deformation zone. At a particular instant, the stress along the primary shear zone becomes so high that it causes higher strains, ranging from 2–2.5 as shown in Figure 5 (a), and results in material damage. This causes a plastic deformation and localized heating. Consequently, rapid increase in temperature occurs near the tool tip that extends towards the chip free side causing the shear bands, known as the adiabatic shear bandings, to form. From the Figures 6 (b–c), it is noted that the temperature in the primary shear deformation zone becomes as high as 600–700°C which continues to increase as we move towards the chip free side. The maximum temperature is observed at a highly localized region at the chip free side with a value reaching up to 800–950°C. This induces thermal softening on the back of the chip and decreases the chip thickness. Such high temperatures in the valleys of the saw tooth profile were also reported by Ng and Aspinwall (Ng et al., 1999). Then the repeated occurrence of bulging and the shear banding results in waved irregularities on the chip back in the form of saw-teeth.

Temperature rises gradually at the time of bulging of the chip but increases rapidly once the shear banding begins to form. Accordingly, regions of low and high temperatures occur alternately thus, giving a stripped pattern of temperature distribution as illustrated in Figure 8. As the cutting continues, because of the bulging of the chip the chip thickness gradually increases and so also the cutting forces. But the chip thickness decreases suddenly due to rapid increase of temperature and subsequent thermal softening. As a consequence, cutting force reduces sharply at point B as shown in Figure 7 and then increases as the next bulge starts to build up.

The segmented chip produced in the present case closely matches with the experimental results of Belhadi et al. (2005) found under equivalent cutting conditions i.e., $V_c = 100$ m/min and $f = 0.2$ mm. The interval between teeth on the simulated chip is 0.292 mm (Figure 8) as compared to the value of 0.28 mm obtained by Belhadi et al. (2005). However, the predicted cutting forces are found to be underestimated when compared with the experimental values of Belhadi et al.

Figure 7. Variation of the F_c and F_t at 0.182ms, 0.747 ms and 0.9 ms



(2005) and Lima et al. (2005), with the former the deviation being 30% and with later 10%.

Variation of Feed and Cutting Speed

In order to validate the developed model, feed (uncut chip thickness) is varied over a range of 0.1–0.4 mm and its effect on the cutting and thrust forces are studied and compared with the existing results. Figure 9 (a) shows the effect of feed rate on the turning forces F_c and F_t when cutting AISI 4340 steel at $V_c = 100$ m/min. The cutting force and thrust force, as expected, increase almost linearly with increasing feed rate (Lima et al., 2005); thus confirming the results obtained by the present model.

Figure 8. Temperature distribution (°C) for segmented chip at 2 ms during adiabatic analysis

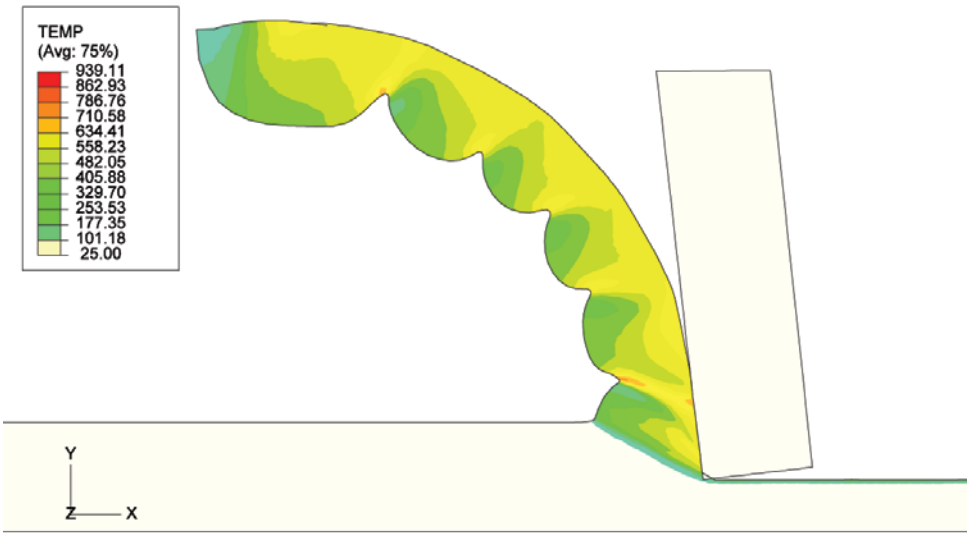
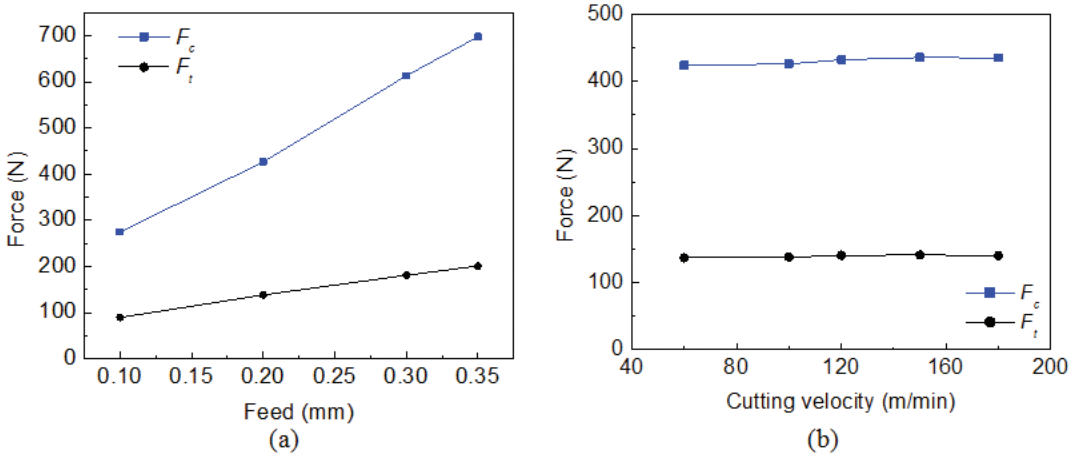


Figure 9. Effect of the (a) feed and (b) cutting speed on F_c and F_t in adiabatic analysis



Similarly, cutting speed was varied over a range of 60–180 m/min during the formation of the segmented chip by using adiabatic analysis and its effect on the cutting force and thrust force is shown in the Figure 9 (b).

It is observed that cutting force and thrust force remained almost constant over the varying cutting speeds. Similar observations were reported by Mabrouki et al. (2008) while simulating the segmented chips, considering adiabatic hypothesis, for machining of aluminum alloy. This is, however, not the case for experimental results as found by Lima et al. (2005), where in decrease of about 22% in the cutting force and 30% in the thrust force has been observed as the cutting velocity increases from 60 to 180 m/min for machining AISI 4340 using a carbide tool.

Finite Element Modeling Based on Fully Coupled Temperature-Displacement Analysis

Adiabatic conditions in metal cutting, no doubt, make the study of chip formation simpler but are not completely acceptable as far as real machining conditions are considered. Thus, coupled temperature displacement analysis is considered that not only provides a more practical approach for the simulation of chip formation but also determines the temperature field on the tool surface. This information is very useful in the study of tool wear progress.

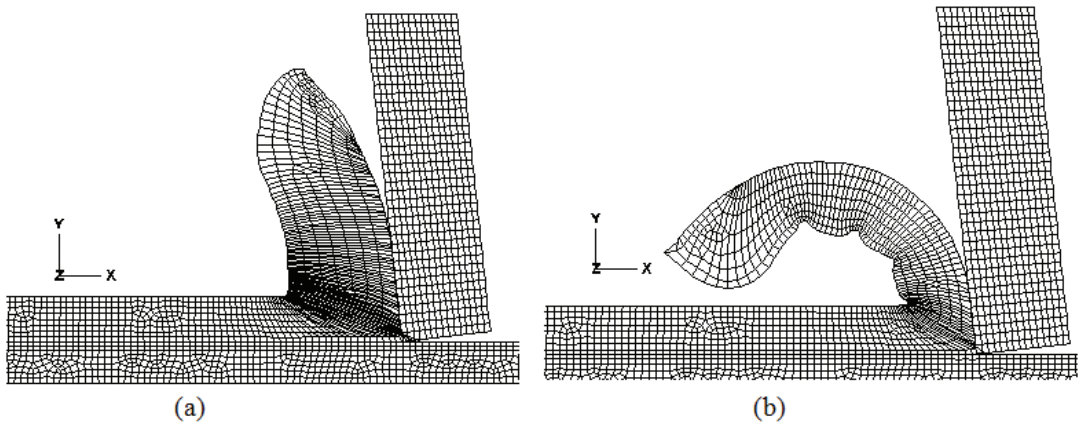
To demonstrate the ability of the model to simulate both continuous and segmented chips, thermal conductivity of the workpiece is considered in one case while neglected in the other case. The cutting speed was varied in both the cases and its effect on the cutting force was studied. This parametric study, in one way, helps in validating the developed models.

Chip Morphology

When the thermal conductivity of the workpiece material was considered in the coupled temperature displacement analysis, continuous chips were obtained in contrast to the previous section where segmented chips, as found experimentally (Belhadi et al., 2005), were produced under the same cutting conditions. Figure 10 (a) shows the deformed finite element mesh for the continuous chip formation.

Since adiabatic conditions allow maximum amount of heat to be retained on the chip surface,

Figure 10. Deformed FE mesh for (a) continuous chip formation and (b) segmented chip formation



adiabatic shearing was very prominent; thus reproducing saw-teeth due to thermal softening on the back of the chip. While, in the case of coupled temperature analysis with thermal conductivity of the workpiece defined, heat conduction occurred and the heat generated due to plastic deformation was not confined to the primary shear deformation zone only. This produced uniform and continuous chips which in the present case is not the desired type of chip. On one hand, adiabatic hypothesis plays a vital role in simulating the segmented chips while on the other hand, these are unacceptable in real machining. Therefore, to simulate the correct type of chip in a more realistic manner, the simplest way is to combine the relevant features of both the approaches, i.e., to incorporate the adiabatic boundary conditions in the coupled temperature displacement analysis. It is possible by neglecting the thermal conductivity of the workpiece that allows the localized heating due to plastic deformation to extend from the tool tip towards the chip free side. This induces thermal softening and consequently, the saw tooth profile on the back of the chip. Figure 10 (b) shows the deformed finite element mesh for the segmented chip formation by neglecting the thermal conductivity of the workpiece.

Figures 11 (a–c) and 12 (a–c) clearly depict the variation in distribution of equivalent von Mises stresses, equivalent strain and the temperature

Figure 11. (a) von Mises equivalent stresses, (b) von Mises equivalent strains and (c) Temperature distribution (°C) for continuous chip formation

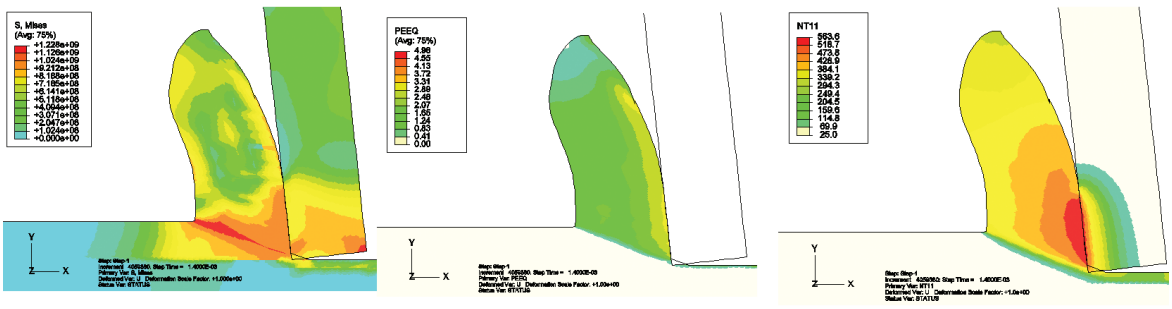
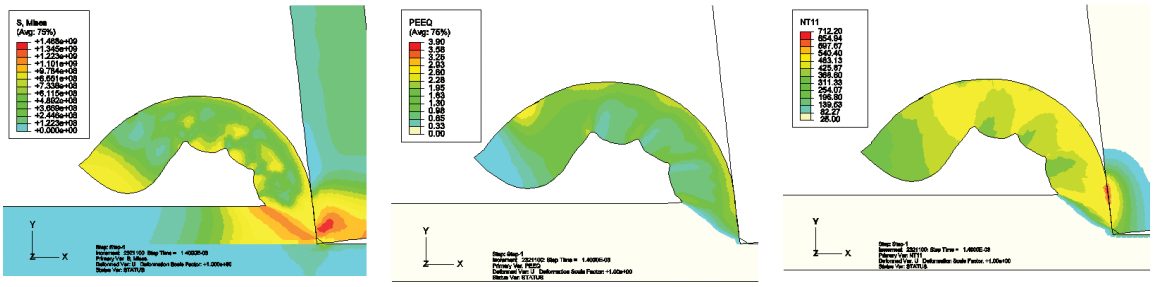


Figure 12. (a) von Mises equivalent stresses (Pa), (b) von Mises equivalent strains and (c) Temperature distribution (°C) for segmented chip formation



(a) (b) (c)

over the chip surface when the chip morphology changes.

From Figures 11 (a) and 12 (a), it is observed that the levels of stresses for both the cases were similar but the distribution pattern of the stresses varied significantly for continuous and segmented chips. In the segmented chips highly localized stresses were found in the shear zone with values in the range of 1.19–1.24 GPa; same as those found in the case of adiabatic analysis. While in continuous chips the stresses are distributed over a wider region over the chip surface. Similar comparisons were reported by Ng and Aspinwall (1999) and Wu and Matsumoto (1990), thus confirming the results obtained.

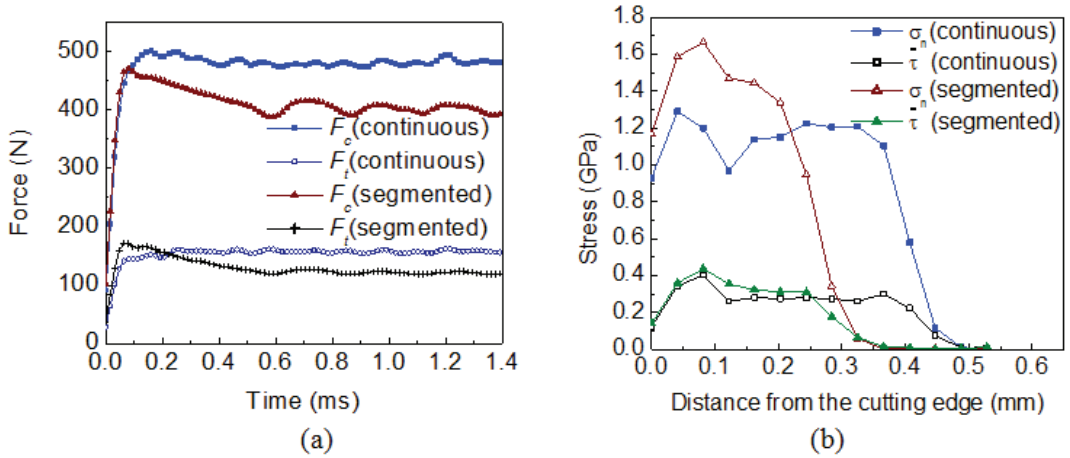
Figures 11 (c) and 12 (c) show that the distribution of temperature over the chip surface, again, differs considerably in both the cases. The shear zone temperature for continuous chip was found to be lower, in the range of 250–300°C as compared to the segmented chips. During the formation of segmented chips, shear zone temperature initially falls in this range but then gradually attains a higher value of 430–460°C. This increased temperature in the shear zone of segmented chips is attributed to highly localized stresses and strains as shown in Figures 12 (a–b), respectively. Highest temperatures were observed along the tool-chip interface for the continuous chips, specifically in the sliding zone of the rake surface, the value corresponding to 550–566°C. As one moves from the tool tip towards the chip free surface, temperature decreases to 400°C. Shih (1996) found the location of maximum temperature in the same region while simulating the continuous chip formation. With segmented chips, higher temperatures are observed in the valleys of the saw tooth along with the tool chip interface region. The temperature at these valleys was found to be around 500°C. The temperature profile obtained in this case is similar with the one obtained in the previous section by adiabatic analysis (Figure 8) with the difference that higher values of temperatures were obtained in the shear banding region for adiabatic analysis. Besides, the bending of the chip is also highly prominent in the latter case.

Cutting Forces

Figures 13 (a) and (b) show the evolution of the forces F_c and F_t over time and distribution of the normal stress σ_n and frictional stress $\bar{\tau}$ on the rake surface for both continuous and segmented chip formation, respectively.

The force signature shows that the cutting force corresponds to the type of chip produced in the cutting process. During continuous chip formation, the cutting force did not show much fluctuation. Whereas, in the case of segmented chip formation,

Figure 13. (a) Evolution of F_c and F_t over time and (b) Distribution of σ_n and $\bar{\tau}$ on the rake surface for continuous and segmented chip formation



cutting force fluctuates due to change in the deformed chip thickness and thus, shows prominent depletion and accumulation of stresses.

It is also noted that the formation of continuous chips exhibited higher value of cutting force. Since the thermal conductivity of the workpiece material was negligible in the case of segmented chips, the material deformed more easily leading to lower value of cutting force. Baker (2003) also found that cutting force is the largest for the case of no segmentation and degree of segmentation decreases as the conductivity is increased.

As already mentioned, bending of the chip was also highly prominent when the thermal conductivity of the workpiece was neglected. As a consequence, the tool chip contact length decreased. This is much clear in the Figure 13 (b) which shows the normal stress and frictional stress distribution on the rake surface for continuous as well as segmented chip formation.

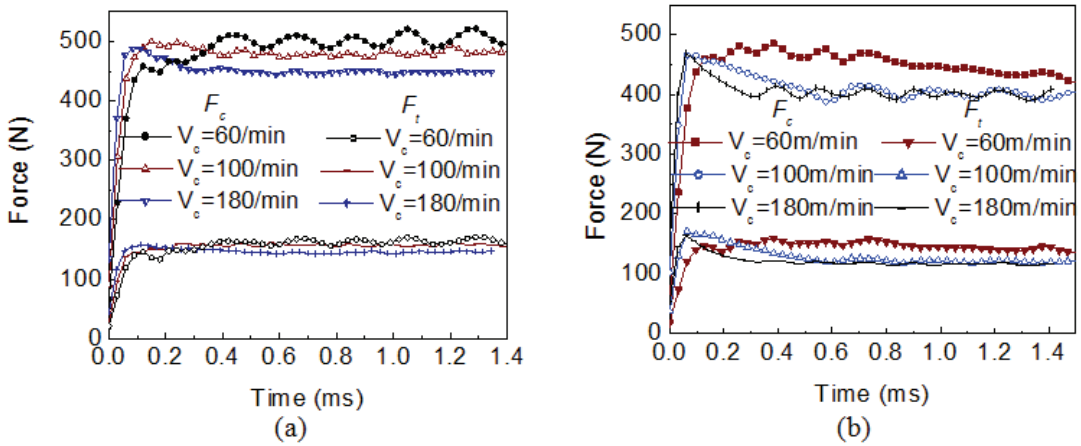
It is observed that the normal stress reaches its maximum value at a short distance away from the tool tip because no load acts at this location as the element gets deleted. Then gradually the normal stress decreases to zero at the point where the chip leaves the rake surface; thus indicating the tool-chip contact length (Shi et al., 2002). Since tool chip contact length is smaller for segmented chips, cutting force is lower. Besides, cutting forces are also known to vary with the deformed chip thickness. Thus, this can be attributed to the higher value of cutting force in continuous chip formation because a larger deformed chip thickness was observed with continuous chips.

Variation of Cutting Speed

The cutting speed was varied over a range of 60–180 m/min at a feed of 0.2 mm for both continuous and segmented chip formation. Figures 14 (a) and (b) show the variation of F_c and the F_t at different cutting velocities for continuous chips and segmented chips, respectively. It is known that as the cutting velocity increases the cutting force and thrust force decrease. The reason for this can be explained from the expressions of the cutting force and thrust forces which are given as follows:

Cutting force, $F_c = ts\tau_s\left(\zeta - \tan\gamma + 1\right)$ (40)

Figure 14. Variation of F_c and F_t for (a) continuous chip and (b) segmented chip at different cutting velocities



Thrust force, $F_t = ts\tau_s\left(\zeta - \tan\gamma - 1\right)$, (41)

where, t is the depth of cut (mm), s is the feed rate (mm/rev), τ_s is the dynamic shear strength of the workpiece, γ is the rake angle and ζ is the chip reduction coefficient, i.e., the ratio of deformed chip thickness to undeformed chip thickness.

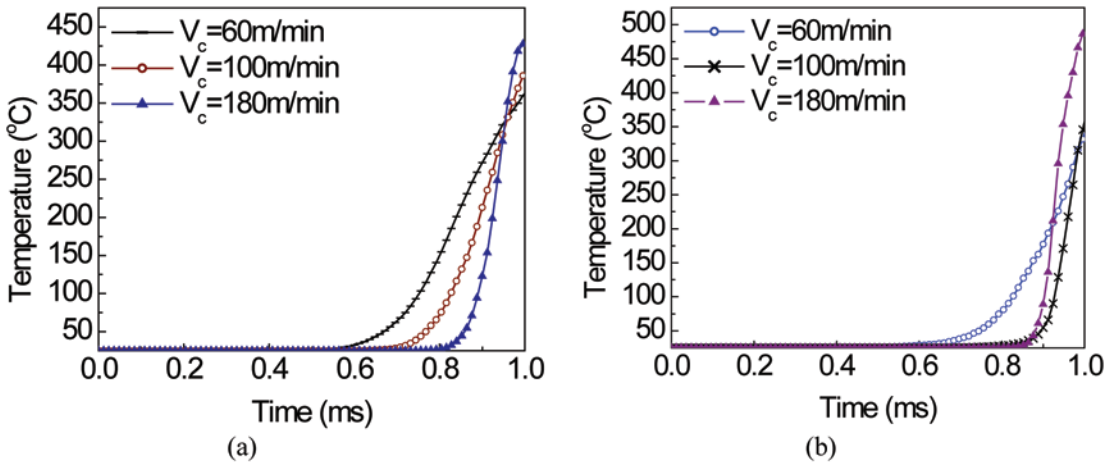
As the cutting velocity increases, temperature of the shear zone increases. This causes softening of the work piece, which means the value of τ_s decreases and thereby reduces the value of cutting and thrust force as shown in Figures 15 (a) and (b). In Figure 14 (a), it is observed that cutting force reduced by 11% as the cutting velocity is varied from 60 m/min to 180 m/min. However, not much reduction is observed in the thrust forces. Figure 14(a) shows the corresponding increase of mean temperature in the primary shear deformation zone with cutting velocity, during continuous chip formation for a simulation time of 1 ms.

From Figure 14 (b), it is observed that the cutting force reduced by 10% as the cutting velocity increased from 60 m/min to 100 m/min but remained almost constant even when the cutting velocity was increased to 180 m/min. Such an unexpected behavior can be attributed to the adiabatic hypothesis considered by neglecting the thermal conductivity of the workpiece. When the thermal conductivity is neglected, it possibly does not take into account the softening of the workpiece material which actually occurs near the tool tip due to increased temperature at high cutting speeds; thus showing fairly constant value at higher cutting speeds. The variation of mean shear zone temperature at variable cutting speeds for a simulation time of 1ms, presented in Figure 15 (b), explains this phenomenon fairly well. Although the temperature in the primary shear deformation zone has increased when cutting speed increased from 100 m/min to 180 m/min, there is no change in the corresponding forces. One more reason for the decrease of these forces is that the value of chip reduction ratio ζ decreases by a small amount as the cutting velocity, shown in Figure 16 (a), increases.

The reason for such variation can be explained from the expression of ζ which is given as follows (Bhattacharyya, 2006):

$$\zeta = \cot\beta\cos\gamma + \sin\gamma \quad (42)$$

Figure 15. Temperature history of nodes in primary shear deformation zone at V_c = 60, 100 and 180m/min for (a) continuous chip and (b) segmented chip



As the cutting velocity increases, the shear zone shrinks and results in the increase of shear angle β which in turn decreases the chip reduction ratio, ζ. Consequently the deformed chip thickness decreases as shown in Figure 16 (b).

The tool-chip contact length (L_n) which in turn affects the cutting force considerably, also changes with variable cutting speed. Figure 16 (c) shows effect of cutting velocity on tool-chip contact length for both continuous and segmented chip formation.

Chip reduction coefficient, deformed chip thickness and tool-chip contact length showed fairly constant value at higher cutting speeds during the formation of segmented chip formation as observed in the case of forces.

Verification of Simulated Results

Verification of FE model is the final and mandatory stage of the FEM authentication in metal cutting. As far as the authenticity of the present model is concerned, predicted results are compared

Figure 16. Variation of (a) chip reduction ratio (b) deformed chip thickness and (c) tool-chip contact length with cutting velocity for continuous and segmented chip formation

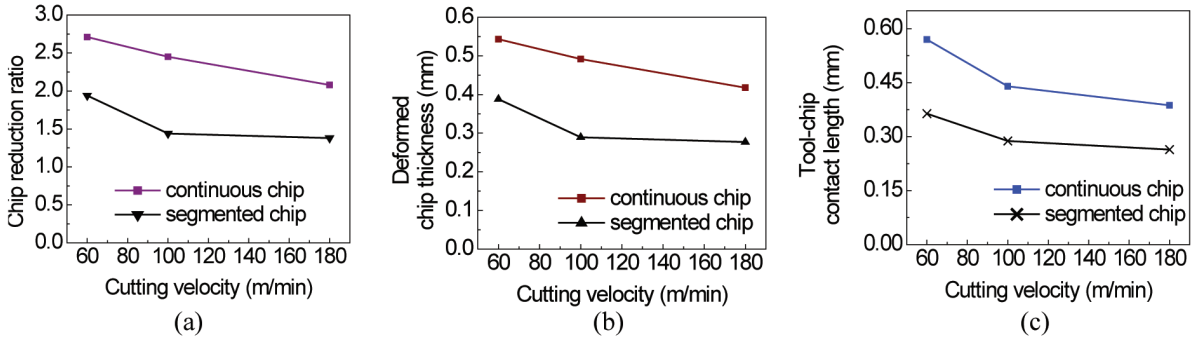
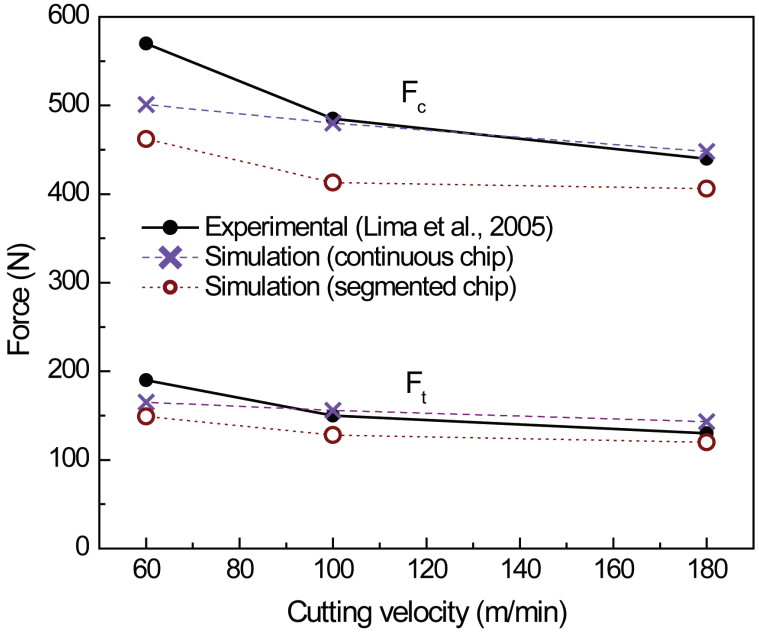


Figure 17. Comparison of predicted forces during simulation of continuous and segmented chip formation with experimental forces



with the experimental results presented by Lima et al. (2005) for machining AISI 4340 using carbide cutting tool ($\gamma = -6^{o}$) under similar cutting conditions. Figure 17 shows the deviation between experimental values (Lima et al., 2005) of cutting force and the thrust force with that of the predicted values, as deduced from the simulation of continuous and segmented chip formation. It is found that the simulated results lie well within the acceptable range. In case of continuous chip formation, the cutting force and thrust values closely match with that of the experimental ones, with largest deviation not more than 12-13% observed for low cutting speed (60 m/min). In case of segmented chip formation, both the forces show underestimated values over the considered cutting speed range with maximum deviation not exceeding 20%. It is interesting to note that predicted results, for both continuous and segmented chip formation, showed maximum deviation at the lowest cutting speed, while in higher cutting speeds the values are closer to the experimental ones.

Discussion

The present work shows that stress, strain and temperature fields are greatly affected by the chip formation process. Since the goal is to focus on the segmented chip formation, adiabatic analysis module of Abaqus/Explicit was used at the beginning. Well-defined adiabatic shear bandings are observed in this case as no heat conduction is allowed during the machining process. When feed rate was varied, the cutting force and thrust force increased, as expected. On the other hand, when the cutting speed was varied, the forces remained almost constant. This emphasizes that ignoring the heat conduction completely is impractical, though it produces prominent saw tooth chips based on adiabatic shearing. Hence, coupled temperature displacement analysis was employed to make the study more realistic. In this study, an attempt was

made to simulate both continuous and segmented chip formation.

Continuous chips were produced when thermal conductivity of the workpiece was defined in the coupled temperature displacement analysis as compared to the segmented chips produced in the experimental findings of Belhadi et al. (2005) under similar cutting conditions. During continuous chip formation, stress fields are not as localized in primary shear zone as observed in the case of segmented chip. As a consequence, highest equivalent strains and temperature levels are not found in this region, but in the secondary shear deformation zone. The chip which is entering into the secondary shear deformation zone already possesses accumulated plastic strain and heat. The instant it begins to flow over the rake surface, further plastic straining and local heating occurs because of severe contact and friction in the contact zone (Shi et al., 2002). Therefore, the maximum equivalent plastic strain and temperature are found along the tool-chip interface, specifically in the sliding region in contrast to segmented chip formation during adiabatic analysis where maximum temperature is shown at the back of the chip as no heat conduction exists between rake surface and the chip surface. Though the desired chip morphology could not be predicted with this module, the cutting forces were found to match closely with the experimental ones. This motivated to combine the adiabatic hypothesis, as considered in adiabatic analysis (predicting desired chip morphology) with the coupled temperature-displacement analysis (predicting forces satisfactorily). Hence, the thermal conductivity of the workpiece was simply neglected in the coupled analysis to cater to the present need of generating segmented chips. In this case, maximum values of temperature are observed in the secondary shear zone due to high straining along the tool-chip interface as well as at the back of the chip in a highly localized region that induces thermal softening causing the desired saw tooth profile.

The present work focuses on predicting the right kind of chip morphology. It is known that type of chip produced depend upon the type of cutting tool and workpiece materials, cutting conditions and so on. Chip morphology is an important index in the study of machining because it affects the stress field generated in the workpiece which determines the residual stresses, the cutting temperatures and the cutting force.

Determination of the cutting forces facilitate estimation of power consumption which is required for the design of machine-fixture-tool system, evaluation of role of various machining conditions and condition monitoring of the cutting tools. The variation in the cutting force has been shown to be related to the chip morphology. A smoother time signature of the cutting force indicates continuous chip formation with good surface finish whereas wavy time signature of the cutting force indicates segmented chip formation. Obviously, magnitude of the waviness (difference between the peak and lower values) relates to surface finish quality. It is also important to consider the regularity of the waviness which indicates the intervals (time interval correlates to space interval at known cutting conditions) at which residual stresses are released. The developed model beautifully exposes these physical understandings.

Moreover, the knowledge of the cutting temperature gives idea about the tool wear progress, residual stresses and the surface finish of the machined surface. It is, thus, clear that controlling these variables can lead to higher productivity and accuracy which in case of metal cutting leads to higher tool life and better surface finish. The stresses, strains, temperatures and many other outputs that are obtained from FE simulations greatly help in understanding the basic mechanism of chip formation under different cutting conditions. Note that various aspects of metal cutting like, cutting tool design, optimization of cutting parameters for higher tool life and good surface finish, prediction of tool wear growth, etc. are achievable only when we are able to comprehend the underlying

physics of the chip formation process correctly by simulating right kind of chip morphology under different cutting conditions.

CONCLUSION

A 2D plane strain FE model has been developed by using simulation software ABAQUS/Explicit with appropriate material and damage models. Numerical results showed that adiabatic hypothesis plays a crucial role in the formation of segmented chips due to adiabatic shearing. Adiabatic analysis module proved useful in explaining formation of adiabatic shear banding that consequently lead to thermal softening and thus the formation of saw-tooth chips during machining of AISI 4340 steel. However, this module was unable to satisfactorily show the effect of the cutting speed on the turning forces.

In coupled temperature displacement analysis, simulation of continuous and segmented chip formation was demonstrated successfully. Thermal conductivity of the workpiece was neglected to satisfy the adiabatic hypothesis for simulating the formation of segmented chip. Highest temperature levels were observed only along the tool-chip interface during continuous chip formation. But during the formation of segmented chip formation, temperatures closer to tool-chip interface temperature were found in highly localized regions at the back of the chip. Such variations in temperatures are attributed to the corresponding variation in the stress and strain fields. Prediction of right kind of chip morphology is important as it affects the stress field generated in the workpiece which determines the residual stresses, the cutting temperatures and the cutting force. It has been shown that there exists a correlation between the type of chip produced and the time signature of the cutting force. Knowledge of the cutting forces are useful in estimation of power consumption which is required for the design of machine-fixture-tool system, evaluation of role of various machining conditions and condition monitoring of the cutting tools.

It is found that the predicted forces for segmented chips by neglecting the thermal conductivity are underestimated when compared with the experimental values (Lima et al., 2005) and the simulated values for continuous chip formation. This approach can still be considered as a fair compromise because it not only simulates the desired segmented chips and but also, predicts the cutting force and thrust values with maximum deviation not exceeding 20%. Moreover, the difference between the predicted and the experimental values are prominent in low cutting speed. It is observed that as the cutting speed increases the deviation in the predicted values gradually decrease. This can be attributed to the fact that at higher cutting speeds adiabatic hypothesis satisfies well whereas at lower cutting speeds the assumption shows inadequacy.

REFERENCES

Akarca, S. S., Song, X., Altenhof, W. J., & Alpas, A. T. (2008). Deformation behaviour of aluminum during machining: Modelling by Eulerian and smoothed-particle hydrodynamics methods. *Proceedings of the Institute of Mechanical Engineers –Journal of Materials: Design and Applications, 222*, 209-219.

Attanasio, A., Cerretti, E., Rizzuti, S., Umbrello, D., & Micari, F. (2008). 3D finite element analysis of tool wear in machining. *CIRP Annals - Manufacturing Technology, 57*(1), 61-64.

Baker, M. (2003). An investigation of the chip segmentation process using finite elements. *Technische Mechanik*, *23*, 1–9.

Baker, M. (2005). Does chip formation minimize energy. *Computational Materials Science*, *33*, 407–418. doi:10.1016/j.commatsci.2004.08.007

Baker, M., Rosler, J., & Seimers, C. (2002). A finite element model of high speed metal cutting with adiabatic shearing. *Computers & Structures*, *80*, 495–513. doi:10.1016/S0045-7949(02)00023-8

Baker, M., Rosler, J., & Seimers, C. (2002). Finite element simulation of segmented chip formation of Ti6Al4V. *Journal of Manufacturing Science and Engineering*, *124*, 485–488. doi:10.1115/1.1459469

Bhattacharyya, A. (2006). *Metal cutting theory and practice*. Calcutta, India: Central Book Publishers.

Calamaz, M., Coupard, D., & Girot, F. (2008). A new material model for 2D numerical simulation of serrated chip formation when machining titanium alloy. *International Journal of Machine Tools & Manufacture*, *48*, 275–288. doi:10.1016/j.ijmachtools.2007.10.014

Coelho, R. T., Ng, E.-G., & Elbestawi, M. A. (2006). Tool wear when turning AISI 4340 with coated PCBN tools using finishing cutting conditions. *Journal of Machine Tools & Manufacture*, *47*(1-2), 263–272.

Davim, J. P., & Maranhao, C. (2009). A study of plastic strain and plastic strain rate in machining of steel AISI 1045 using FEM analysis. *Materials & Design*, *30*, 160–165. doi:10.1016/j.matdes.2008.04.029

Elbastwani, M. A., Srivatava, A. K., & Wardany, E.-L. (1996). A model for chip formation during machining of hardened steel. *Annals of CIRP*, *45*, 71–76. doi:10.1016/S0007-8506(07)63019-4

Hibbit, Karlsson and Sorens Inc. (2011). *HKS ABAQUS Theory manual* (version 6.7). Pawtucket, RI: Hibbit, Karlsson and Sorens Inc.

Hutton, D. V. (2004). *Fundamentals of finite element analysis*. New York, NY: McGraw-Hill.

Iwata, K., Osakada, K., & Terasaka, Y. (1984). Process modeling of orthogonal cutting by the rigid-plastic finite element method. *ASME Journal of Engineering Materials and Technology*, *106*, 132–138. doi:10.1115/1.3225687

Jaspers, S. P. F. C., & Dautzenberg, J. H. (2002). Material behavior in conditions similar to metal cutting: Flow stress in the primary shear zone. *Journal of Materials Processing Technology*, *122*, 322–330. doi:10.1016/S0924-0136(01)01228-6

Johnson, G. R., & Cook, W. H. (1983). A constitutive model and data for metals subjected to large strains, high strain rates and high temperatures. In *Proceedings of the 7th International Symposium on Ballistics*, The Hague, The Netherlands (pp. 541-547).

Johnson, G. R., & Cook, W. H. (1985). Fracture characteristics of three metals subjected to various strains, strains rates, temperatures and pressures. *Engineering Fracture Mechanics*, *21*(1), 31–48. doi:10.1016/0013-7944(85)90052-9

Klamecki, B. E. (1973). *Incipient chip formation in metal cutting- A three dimensional finite element analysis*. Unpublished doctoral dissertation, University of Illinois, Urbana, IL.

Komvopoulous, K., & Erpenbeck, S. A. (1991). Finite element modeling of orthogonal metal cutting. *ASME Journal of Engineering for Industry*, *113*, 253–267.

Konig, W., Jinge, M. K., & Link, R. (1990). Machining with hardened steels with geometrically defined cutting edges. *Annals of CIRP*, *39*, 61–64. doi:10.1016/S0007-8506(07)61003-8

Li, K., Gao, X.-L., & Sutherland, J. W. (2002). Finite element simulation of the orthogonal metal cutting process for qualitative understanding of the effects of crater wear on the chip formation. *Journal of Materials Processing Technology*, *127*, 309–324. doi:10.1016/S0924-0136(02)00281-9

Lima, J. G., Avila, R. F., Abrao, A. M., Faustino, M., & Davim, J. P. (2005). Hard turning: AISI 4340 high strength alloy steel and AISI D2 cold work tool steel. *Journal of Materials Processing Technology*, *169*, 388–395. doi:10.1016/j.jmatprotec.2005.04.082

Liu, G. R., & Quek, S. S. (2003). *The finite element method: A practical course*. Oxford, UK: Butterworth Heinemann.

Lorentzon, J., & Jarvstrat, N. (2009). Modelling chip formation of alloy 718. *Journal of Materials Processing Technology*, *209*, 4645–4653. doi:10.1016/j.jmatprotec.2008.11.029

Mabrouki, T., Deshayes, L., Ivester, R., Regal, J.-F., & Jurrens, K. (2004, April 4-5). Material modeling and experimental study of serrated chip morphology. In *Proceedings of the 7th CIRP International Workshop on Modeling of Machining Operations* (pp. 53-66).

Mabrouki, T., Girardin, F., Asad, M., & Regal, J.-F. (2008). Numerical and experimental study of dry cutting for an aeronautic aluminum alloy. *International Journal of Machine Tools & Manufacture*, *48*, 1187–1197. doi:10.1016/j.ijmachtools.2008.03.013

Mabrouki, T., & Rigal, J.-F. (2006). A contribution to a qualitative understanding of thermo-mechanical effects during chip formation in hard turning. *Journal of Materials Processing Technology*, *176*, 214–221. doi:10.1016/j.jmatprotec.2006.03.159

Mackerle, J. (1962). Finite element methods and material processing technology, an addendum (1994–1996). *Engineering Computations*, *15*, 616–690. doi:10.1108/02644409810225788

Movahhedy, M., Gadala, M. S., & Atlantis, Y. (2000). Simulation of the orthogonal metal cutting process using an arbitrary Lagrangian Eulerian finite element method. *Journal of Materials Processing Technology*, *103*, 267–275. doi:10.1016/S0924-0136(00)00480-5

Ng, E. G., Aspinwall, D. K., & Monaghan, D. (1999). Modeling of temperature and forces when orthogonally machining hardened steel. *International Journal of Machine Tools & Manufacture*, *39*, 885–903. doi:10.1016/S0890-6955(98)00077-7

Ng, E. G., Tahany, I., Wardany, E.-L., Dumitrescu, M., & Elbestawi, M. A. (2002). Physics based simulation of high speed machining. *Mining Science and Technology*, *6*, 301–329.

Obikawa, T., Sasahara, H., Shirakashi, T., & Usui, E. (1997). Application of computational machining method to discontinuous chip formation. *Journal of Manufacturing Science and Engineering*, *119*, 667–674. doi:10.1115/1.2836807

Ohbuchi, Y., & Obikawa, T. (2005). Adiabatic shear in chip formation with negative rake angle. *International Journal of Mechanical Sciences*, *47*, 1377–1392. doi:10.1016/j.ijmecsci.2005.05.003

Olovsson, L., Nilsson, L., & Simonsson, K. (1999). An ALE formulation for the solution of two-dimensional metal cutting problems. *Computers & Structures*, *72*, 497–507. doi:10.1016/S0045-7949(98)00332-0

Ozel, T. (2006). The influence of friction models on finite element simulations of machining. *International Journal of Machine Tools & Manufacture*, *46*, 518–530. doi:10.1016/j.ijmachtools.2005.07.001

Ozel, T., & Zeren, E. (2006). A methodology to determine work material flow stress and tool-chip interfacial friction properties by using anaysis of machining. *ASME Journal of Manufacturing Science and Engineering*, *128*, 119–129. doi:10.1115/1.2118767

Raczy, A., Elmadagli, M., Altenhof, W. J., & Alpas, A. T. (2004). An Eulerian finite-element model for determination of deformation state of a copper subjected to orthogonal cutting. *Metallurgical and Materials Transactions*, *35A*, 2393–2400. doi:10.1007/s11661-006-0219-3

Rakotomalala, R., Joyot, P., & Touratier, M. (1993). Arbitrary Lagrangian-Eulerian thermomechanical finite element model of material cutting. *Communications in Numerical Methods in Engineering*, *9*, 975–987. doi:10.1002/cnm.1640091205

Shi, G., Deng, X., & Shet, C. (2002). A finite element study of the effect of friction in orthogonal metal cutting. *Finite Elements in Analysis and Design*, *38*, 863–883. doi:10.1016/S0168-874X(01)00110-X

Shi, J., & Liu, C. R. (2004). The influence of material models on finite element simulation of machining. *ASME Journal of Manufacturing Science and Engineering*, *126*, 849–857. doi:10.1115/1.1813473

Shih, A. J. (1996). Finite element analysis of orthogonal metal cutting mechanics. *Journal of Machine Tools & Manufacture*, *36*, 255–273. doi:10.1016/0890-6955(95)98765-Y

Strenkowski, J. S., & Carroll, J. T. III. (1985). A finite element model of orthogonal metal cutting. *ASME Journal of Engineering for Industry*, *107*, 349–354. doi:10.1115/1.3186008

Strenkowski, J. S., & Moon, K.-J. (1990). Finite element prediction of chip geometry and tool/workpiece temperature distributions in orthogonal metal cutting. *ASME Journal of Engineering for Industry*, *112*, 313–318. doi:10.1115/1.2899593

Tay, A. O., Stevenson, M. G., & de Vahl Davis, G. (1974). Using the finite element method to determine temperature distribution in orthogonal machining. *Proceedings - Institution of Mechanical Engineers*, *188*(55), 627–638. doi:10.1243/PIME_PROC_1974_188_074_02

Umbrello, D., M'Saoubi, R., & Outeiro, J. C. (2007). The influence of Johnson–Cook material constants on finite element simulation of machining of AISI 316L steel. *International Journal of Machine Tools & Manufacture*, *47*, 462–470. doi:10.1016/j.ijmachtools.2006.06.006

Vaziri, M. R., Salimi, M., & Mashayekhi, M. (2010). A new calibration method for ductile fracture models as chip separation criteria in machining. *Simulation Modelling Practice and Theory*, *18*, 1286–1296. doi:10.1016/j.simpat.2010.05.003

Vyas, A., & Shaw, M. C. (1999). Mechanics of saw tooth chip formation in metal cutting. *Journal of Manufacturing Science and Engineering*, *121*, 163–173. doi:10.1115/1.2831200

Wu, D. W., & Matsumoto, Y. (1990). The effect of hardness on residual stresses in orthogonal machining of AISI 4340 steel. *Journal of Engineering for Industry*, *112*, 245–252. doi:10.1115/1.2899582

Wu, H.-C. (2004). *Continuum mechanics and plasticity*. Boca Raton, FL: Chapman and Hall/CRC.

Zorev, N. N. (1963). Inter-relationship between shear processes occurring along tool face and shear plane in metal cutting. *International Research in Production Engineering*, 42-49.

This work was previously published in the International Journal of Manufacturing, Materials, and Mechanical Engineering, Volume 1, Issue 4, edited by J. Paulo Davim, pp. 19-45, copyright 2011 by IGI Publishing (an imprint of IGI Global).

Chapter 13
Cold End Forming of Welded Steel Tubes

L. M. Alves
Instituto Superior Tecnico, Portugal

J. G. Medeiros
MC Graça, Portugal

P. A. F. Martins
Instituto Superior Tecnico, Portugal

ABSTRACT

The production of custom and specific tube end shapes by cold end forming using a die is generally limited to seamless tubular parts. Current research work in the field follows the same trend as that of industry and, therefore, there is no accumulated experience, no practical design rules, and no information available in the specialized literature concerning the utilization of tube end forming for shaping the end of thin-walled welded tubes. This paper is concerned with the lack of knowledge and is a contribution towards the understanding of the mechanics of deformation of tube end forming applied to welded tubes. The presentation addresses the influence of major operating parameters on the formability limits of the process with the purpose of understanding feasibility and establishing design rules for the benefit of those who design tubular parts in daily practice. The authors effectively contribute to transferable technological knowledge opening new market opportunities that stimulate innovations among carbon and stainless steel tubular products.

INTRODUCTION

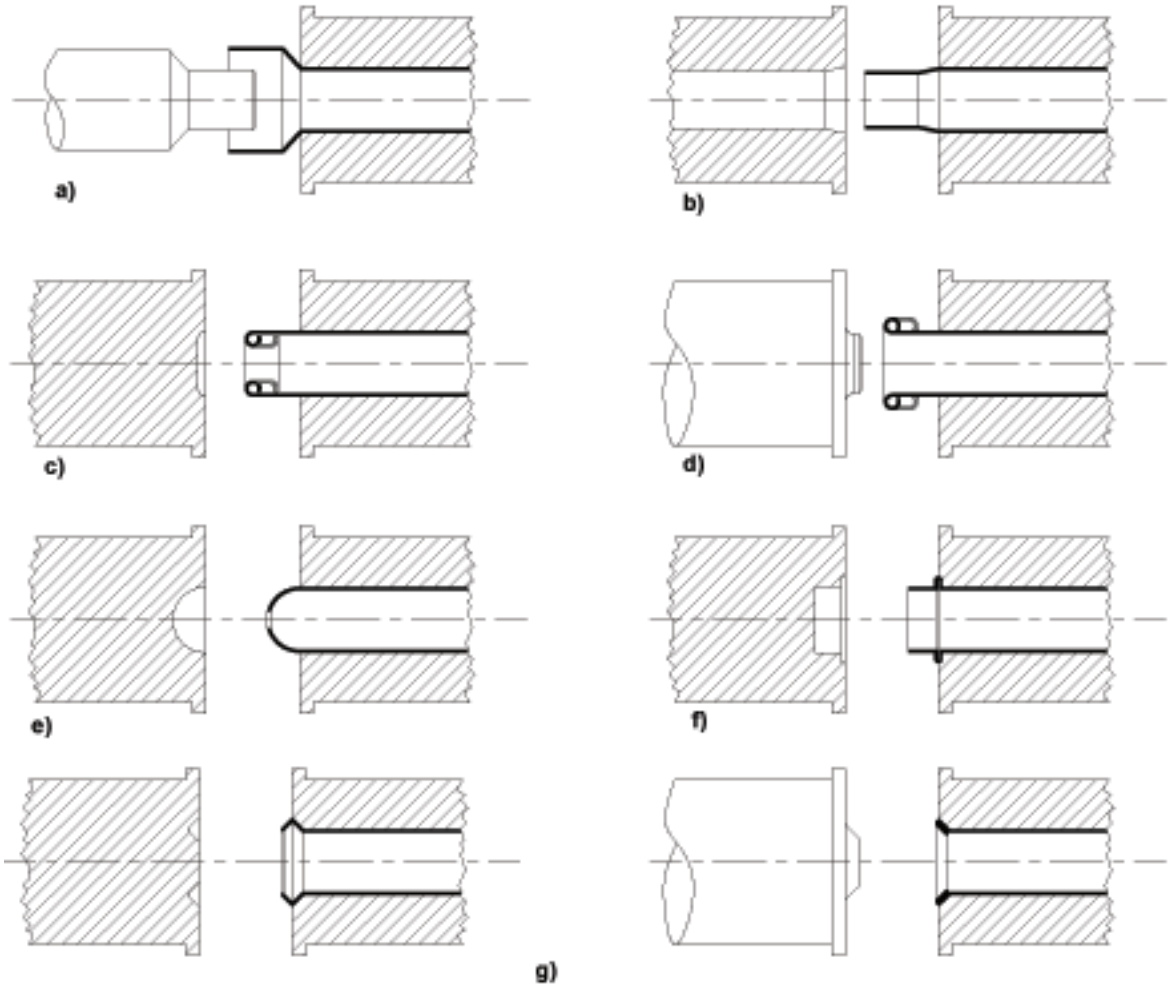
Tube end forming processes are commonly utilized for producing of a wide variety of shapes and profiles such as inversions, flares, expansions, reductions, beads and noses by means of single or multiple forming operations (Figure 1).

DOI: 10.4018/978-1-4666-1867-1.ch013

The historical review of research on tube end forming can be organized in three different periods. The first period (1960-1990) draws from pioneer studies on axial loading (Alexander, 1960; Allan, 1968) to the external and internal inversion (Guist & Marble, 1966; Al-Hassani et al., 1972; Al-Qureshi & Morais, 1976; Reddy, 1989). In this period most attention was given to the identifica-

Copyright © 2013, IGI Global. Copying or distributing in print or electronic forms without written permission of IGI Global is prohibited.

Figure 1. Tube end forming processes. a) Expansion, b) Reduction, c) Internal inversion, d) External inversion, e) Nosing, f) Compression beading and g) Flaring



tion of the main operative parameters, development of theoretical models to explain the mechanics of the processes (Avitzur, 1980) and correlation between theory and experimentation (Kinkead, 1983).

The second period (1990-2000) kept research focus on tube inversion and refined existing knowledge on the mechanics of deformation. The investigation on forming load and formability limits by means of analytical methods (Reddy, 1992; Tomesani, 1997; El-Domiaty, 1997) was progressively replaced by numerical simulation based on the finite element method (Yang, 1995) in an effort to better understand the typical modes of deformation. In contrast to tube inversion, published research work in other tube end forming processes during this period, was practically inexistent. At the end of the second period basic design rules were mainly derived from the accumulated experience of both manufacturers of tubular parts and suppliers of machine tools (Miller, 2003).

The third period (2000-until now) has been the most active in research and is being driven by

the objective of consolidating existing knowledge and extending research for other tube end forming processes and materials. Recent published work provides a better insight into the deformation mechanics and formability limits of tube end forming (Yang, 2001; Sun & Yang, 2002; Sekhon et al., 2003; Rosa et al., 2003; Rosa et al., 2004) and extends investigation to nosing (Lu, 2005), reduction, expansion and flaring (Almeida et al., 2006) and compression beading (Gouveia et al., 2006). The utilization of tubes other than seamless metal tubes was only recently accomplished by Alves and Martins (2009a, 2009b) who successfully shaped the end of thin-walled polymer tubes.

From an industrial point of view there is a contribution to knowledge need to be given on the feasibility of applying conventional tube end forming processes to welded tubes made from carbon and stainless steel. This is important because the prospect of extending the actual offer of custom and specific end shapes to welded tubes will open new market opportunities and stimulate innovations among tubular based products. Under these circumstances, the main objective of this paper is to present recent developments in the experimental and numerical modelling of tube end forming applied to carbon and stainless steel welded thin-walled tubes.

EXPERIMENTAL BACKGROUND

Commercial S460MC (carbon steel) and AISI 304 (stainless steel) welded tubes in the form of 32 mm diameter and 1.5 mm thickness were utilized in the 'as-received' condition. The mechanical characterization tests and the tube end forming experiments were performed at room temperature on a universal testing machine with a cross-head speed equal to 100 mm/min (1.7 mm/s).

Stress-Strain Curve

Tensile and compression tests were performed in order to obtain the true stress-strain behaviour of S460MC and AISI 304. The specimens utilized in the tensile tests were machined from the supplied tube stock while the specimens utilized in the compression tests were assembled by pilling up circular discs cut from the tube stock by a hole saw. The stress-strain curves of both materials are given below,

$$\sigma = 1265.7\,\varepsilon^{0.34} \text{ (AISI 304)}$$

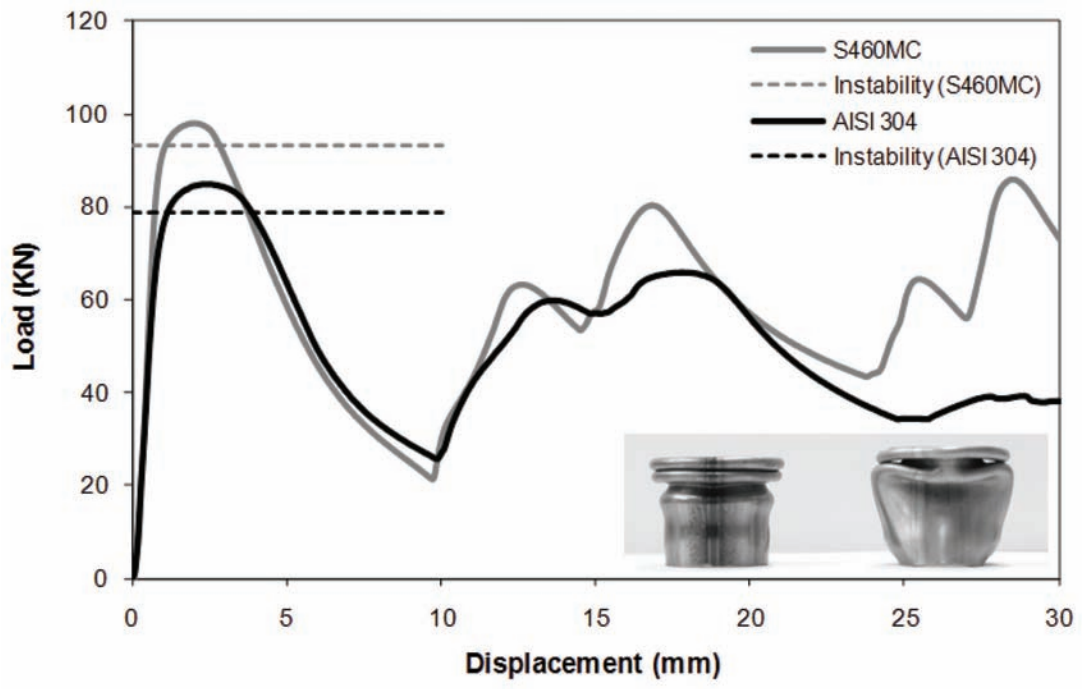
$$\sigma = 616.4\,\varepsilon^{0.06} \text{ (S460MC)} \quad (1)$$

Critical Instability Load

The critical instability load P_{cr} for the occurrence of local buckling in S460MC and AISI 304 welded tubes subjected to axial loading was experimentally determined by compressing tubular specimens with $l_0 = 65$ mm initial length, between flat dies. Figure 2 shows the load recorded during the experiments as a function of the displacement of the upper flat die for the two types of tubes.

As seen, the load increases sharply from zero and local buckling occurs upon reaching a critical experimental value $P_{cr} \cong 93.5$ kN in case of S460MC tubes and $P_{cr} \cong 79$ kN in case of AISI 304 tubes. Subsequent deformation of the tubular specimens results in additional folds (additional instability waves with circular shape in case of S460MC tubes and polygonal shape in case of AISI 304 tubes) and to the development of a cyclic peak-to-peak load-displacement evolution.

Figure 2. Load-displacement curve for the axial compression of S460MC and AISI 304 welded tubes



Tube End Forming

The experiments on tube end forming comprised expansion, reduction, external and internal inversion of commercial S460MC and AISI 304 welded tubes. The work on expansion and reduction was accomplished by forcing a tapered, dedicated punch (or die) into the tube end, and then retracting the punch (or die) back off after achieving the desired shape (Figure 3). The expansion punch is dedicated to an outside radius r_p and a required length of expansion while the reduction die is dedicated to an inside radius r_d and a required length of reduction. The lengths of expansion and reduction are a function of the angle of inclination α.

The work on external and internal inversion was accomplished by compressing the tube against a die in order to undergo inside-out inversion or vice-versa and to form a double-walled part (Figure 3). The external and internal inversion dies are dedicated to an outside and inside die corner radius r_d respectively.

The experiments made use of dies with different geometries and fillet radii and were designed in order to cope with the expansion r_p / r_0, reduction r_d / r_0 and invert-curling r_d / r_0 ratios of the processes as well as the angle α of the conical surfaces of the expansion punches and reduction dies. The aspect ratio t_0 / r_0 of the tubes was kept constant during the tests and lubrication was performed with a Polytetrafluoroethylene (PTFE) based oil. The influence of anisotropy was not taken into account.

The experimental work plan is listed in Table 1 and at least two replicates were produced for each test case conditions in order to provide statistical meaning.

Figure 3. Schematic representation of the tube end forming processes that were utilized in the investigation. a) Expansion, b) Reduction, c) External inversion and d) Internal inversion. Photographs in e) show details of active tool components.

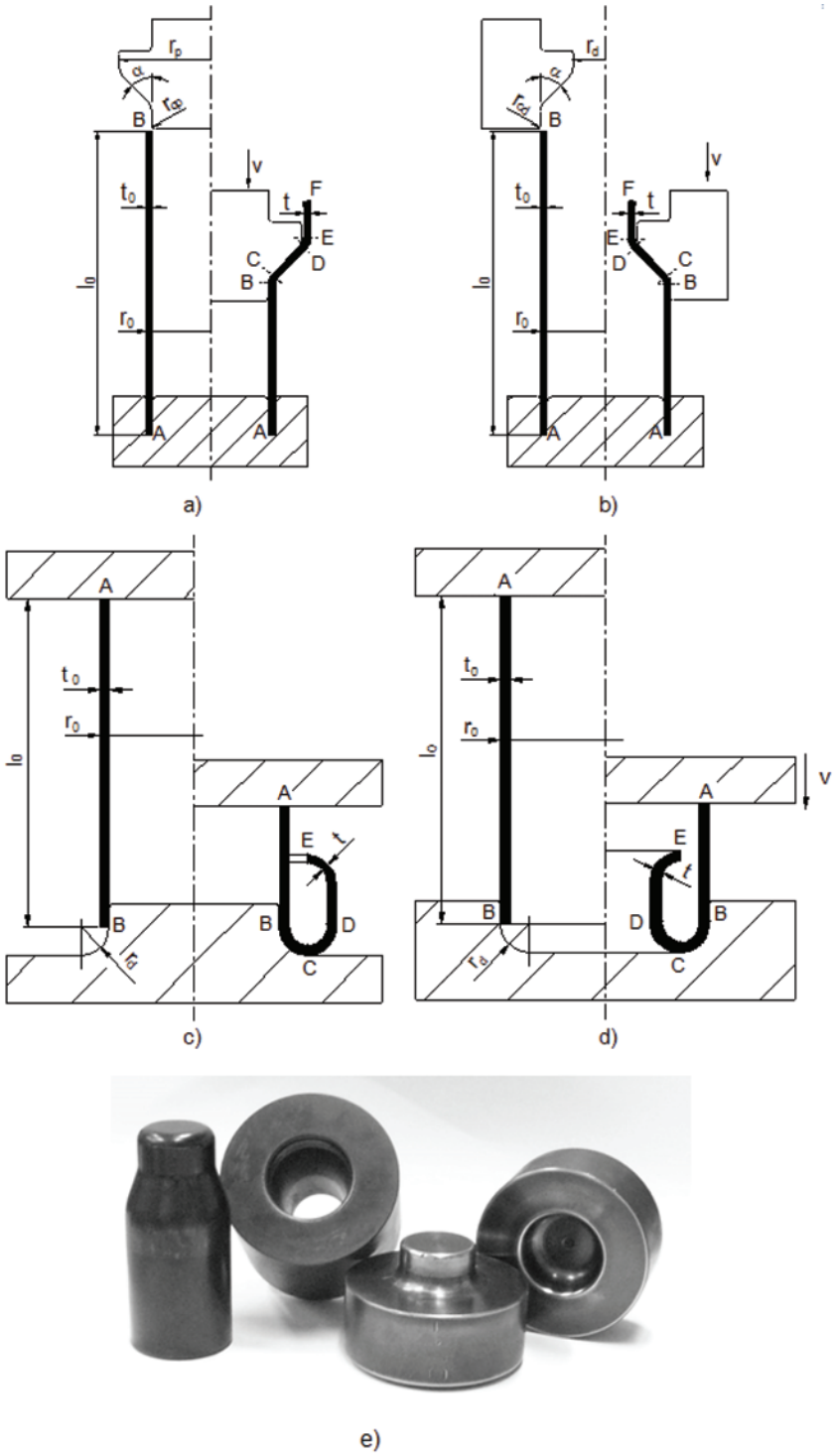


Table 1. The plan of experiments

Type	r_0 (mm)	t_0 (mm)	l_0 (mm)	α (°)	r_p/r_0	r_d/r_0	r_d/r_0	Material
Compression between flat parallel platens	16	1.5	65	-	-	-	0	S460MCAISI304
Expansion	16	1.5	65	20-40	1.3-1.9	-	-	S460MCAISI304
Reduction	16	1.5	65	20-40	-	0.5-0.72	-	S460MCAISI304
External inversion	16	1.5	65	-	-	-	0.125-0.5	S460MCAISI304
Internal inversion	16	1.5	65	-	-	-	0.125-0.5	S460MCAISI304

Note: Experiments were performed with lubrication (PTFE) and without lubrication (dry conditions).

FINITE ELEMENT MODELLING

Because the experiments in cold end forming of welded steel tubes were performed under a quasi-static constant displacement rate of the upper-table of the press, no inertial effects on forming mechanisms are likely to occur and therefore no dynamic effects in deformation mechanics are needed to be taken into account. These operating conditions allowed numerical modelling of the process to be performed with the finite element flow formulation and enabled the authors to utilize the in-house computer program I-Form2 that has been extensively validated against experimental measurements of metal forming processes since the end of the 80's (Alves et al., 2003).

The finite element flow formulation giving support to the computer program I-Form2 is built upon the following variational statement,

$$\Pi = \int_V \bar{\sigma}\,\dot{\bar{\varepsilon}}\,dV + \tfrac{1}{2}K\int_V \dot{\varepsilon}_v^2\,dV - \int_{S_T} T_i u_i\,dS + \int_{S_f}\left(\int_0^{|u_r|}\tau_f\,du_r\right)dS \tag{2}$$

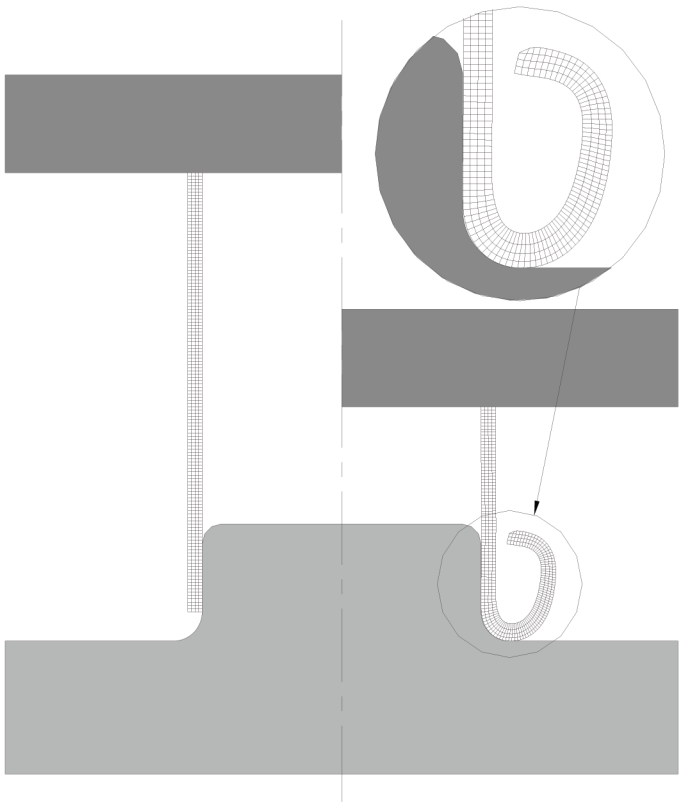
where, K is a large positive constant enforcing the incompressibility constraint and V is the control volume limited by the surfaces S_U and S_T, where velocity and traction are prescribed, respectively. Friction at the contact interface S_f between workpiece and tooling is assumed to be a traction boundary condition and the additional power consumption term is modelled through the utilization of the law of constant friction $\tau_f = mk$. The friction factor m was set to vary in the range 0.02 to 0.1 by checking the predicted tube end forming loads that best matched the experimental results.

The numerical evaluation of the volume integrals included in equation (2) is performed by means of a standard discretization procedure that, on account of the rotational symmetry of the forming process and because no anisotropy effects due to material or welding seam were taken into consideration, consisted on the discretization of the initial cross section of the tubular preforms by means of four-node axisymmetric quadrilateral elements (Figure 4).

Convergence studies with varying arrangements of quadrilateral elements in the thickness direction showed that the utilization of four elements was adequate for modelling the distribution of the major field variables and for getting a proper evolution of the load-displacement curve. The contours of the dies were discretized by means of contact-friction linear elements. No intermediate remeshing operations were utilized and, therefore, no influence of field variable recovery techniques on the final results needed to be taken into account.

The numerical simulation of the process was accomplished through a succession of displacement increments each of one modelling approximately

Figure 4. Finite element modelling of the external inversion of a thin-walled S460MC tube. Discretization of the preform and computed predicted geometry at the end of the process ($(r_d/r_0 = 0.19$in Table 1)



0.1% of the initial tube length. The convergence of the computational procedure was very stable and the overall CPU time for a typical analysis containing a total number of 700 elements was below 3 min. on a standard laptop computer.

RESULTS AND DISCUSSION

Finite element modelling supported by experimentation under laboratory controlled conditions was utilized for understanding the influence of major operative parameters, predicting the forming loads, identifying the modes of deformation and understanding the formability limits of tube end forming of carbon and stainless steel welded tubes.

Modes of Deformation

Expansion and reduction of tubes is the result of three different mechanisms (Figure 3); bending/unbending, stretching/compression along the circumferential direction θ (for expansion/reduction of tubes) and friction. Bending takes place at point B, where the tube first contacts the punch (or die), while unbending takes place at point D, where the tube leaves contact with the punch (or die). Point E fixes the beginning of free deformed region of the tube that spans from E to the leading edge F. The free deformed region of the tube undergoes near-rigid body motion. Stretching/compression develops while the tube gradually deforms over the punch (or against the die) – refer to CD in Figure 3. The influence of friction predominantly occurs between points B and D although, some

minor restraint, is also likely to take place at the entrance of the punch (or die) – refer to the cylindrical surface adjacent to point B.

The experimental work on tube expansion confirmed the existence of three different modes of deformation. For large ratios of r_p/r_0 and high values of the angle α, formability is limited by the occurrence of plastic instability while for larger lengths of expansion (α <<) restrictions are set by ductile damage (fracture) in the regions that are highly stretched in case of S460MC tubes and by plastic instability in case of AISI 304 tubes. This difference in behaviour is due to the fact that the instability load P_{cr} of AISI 304 tubes is 15.5% smaller than that of S460MC tubes (Figure 2) and also because strain-hardening of AISI 304 is much higher than that of S460MC (refer to Equation (1)). The combination of both phenomena justifies the reason why it is energetically more favourable to develop plastic instability than to start a crack at the upper tube end. Figure 5a) and Figure 5c) show photographs of successful and unsuccessful modes of deformation.

The experimental work on tube reduction also revealed the existence of three different modes of deformation. For small values of r_d/r_0 and small lengths of reduction formability is mainly limited by the development of plastic instability modes whilst for larger lengths of reduction restrictions are normally set by excessive thickening of the tube wall and by the occurrence of wrinkling at the conical wall of the tubes. Figure 5b) and Figure 5d) show photographs of successful and unsuccessful modes of deformation.

The role of friction in the expected mode of deformation was analysed by performing reduction of S460MC tubes without lubrication (dry lubrication regime). As a result of such severe

Figure 5. Photographs showing samples of successful and unsuccessful expanded and reduced tubular parts made from a-b) S460MC and c-d) AISI 304 welded tubes



Figure 6. Experimental and finite element predicted cross section of tubular reduced specimens (S460MC) performed a) with and b) without lubrication (r_d / r_0 = 0.5 in Table 1)

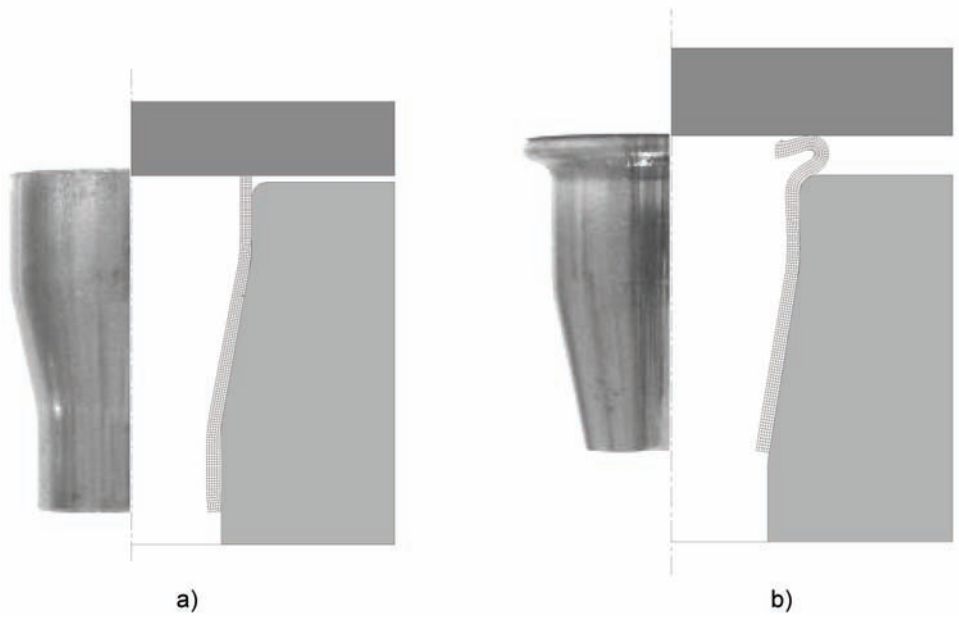


Figure 7. Photographs showing samples of successful and unsuccessful invert-formed tubular parts made from a-b) S460MC and c-d) AISI 304 welded tubes



frictional conditions, undesirable local buckling takes the place of the successful reduction mode previously obtained under lubricated forming conditions (Figure 6).

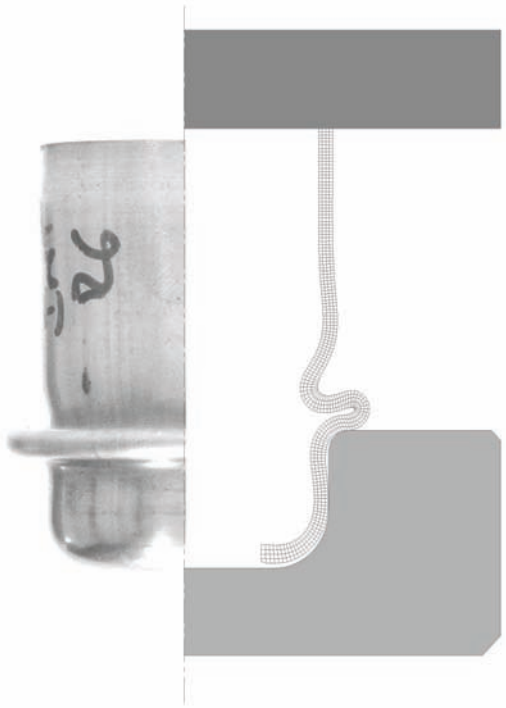
The estimate of the predicted cross section of the tubular specimens provided by finite element modelling compare well with the experimentally observed and allow us to conclude that unacceptable local buckling can easily take the place of a successful mode of deformation whenever the lubrication conditions become inadequate.

Invert-forming of tubes is the result of three different mechanisms; bending, stretching (external inversion)/compression (internal inversion) and friction. Bending takes place at point B, where the tube contacts the die, and at point D (unbending) placed at the free region facing point B (Figure 3). Stretching/compression along the circumferential direction θ progresses while the tube turns around the corner of the die (BD). The influence of interface friction occurs between points B and C.

The experiments on tube invert-forming disclosed two different behaviours. In case of S460MC tubes, experiments revealed the existence of three different modes of deformation both in external and internal inversion (Figure 7a and Figure 7b)) whereas in case of AISI 304 tubes, experiments pointed out the impossibility of producing sound tubular parts (Figure 7c and Figure 7d)). This difference in behaviour is again attributed to the higher strain hardening and smaller critical instability load of the AISI 304 welded tubes.

The three different modes of deformation that are observed in invert-forming of S460MC tubes can be explained as follows: for small values of the die radius formability is limited by the development of plastic instability modes (local buckling) whilst for larger values restrictions are normally set by excessive thickening of the tube wall and occurrence of local buckling (in case of internal inversion) or excessive thinning of the tube wall and occurrence of fracture (in case of external inversion) at the unsupported curved wall

Figure 8. Experimental and finite element predicted shape of an unsuccessful mode of deformation during the internal inversion of an AISI 304 welded tube (r_d/r_0 = 0.375 in Table 1)



of the tubes. As a consequence, material flow leading to successful inwardly inverted modes of deformation can only be achieved within a compact range of process parameters.

Figure 8 shows the development of an unsuccessful mode of deformation when performing internal inversion with AISI 304 tubes. The failure is caused by high values of the tangential compressive stresses σ_θ acting at the unsupported curved wall of the tube that lead to excessive thickening and to the occurrence of local buckling (Figure 8).

Forming Load

The observation of the predicted and experimental load–displacement curves for tube expansion in Figure 9 allows the identification of three dif-

Figure 9. Theoretical and experimental load-displacement curve for the expansion of S460MC and AISI 304 welded tubes (r_d / r_0 = 0.5 in Table 1)

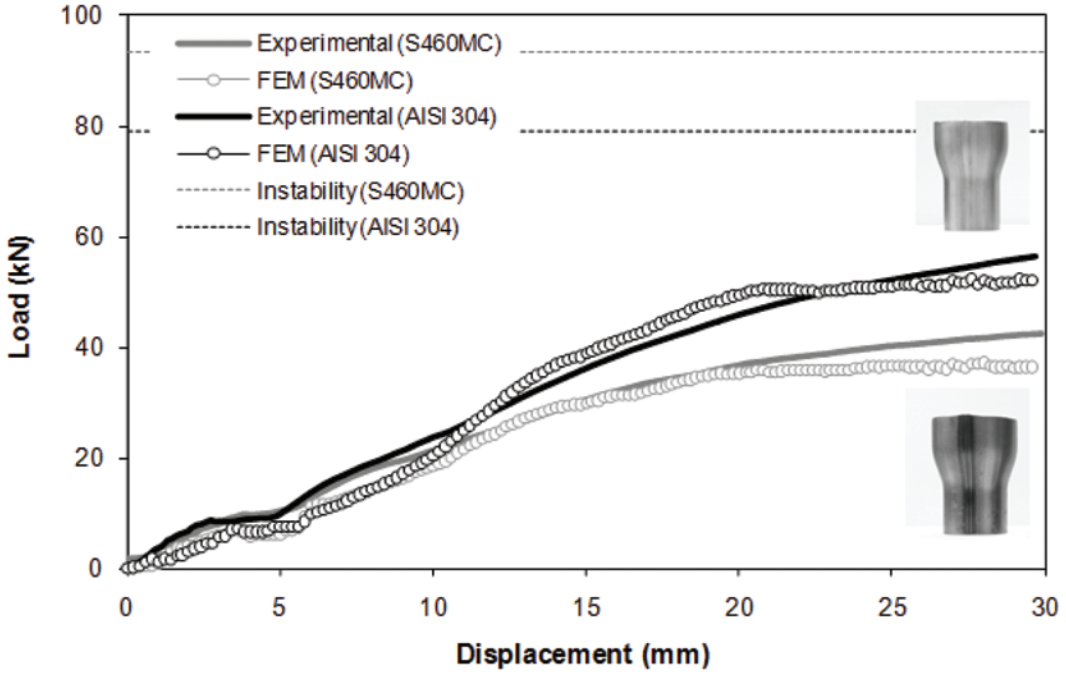
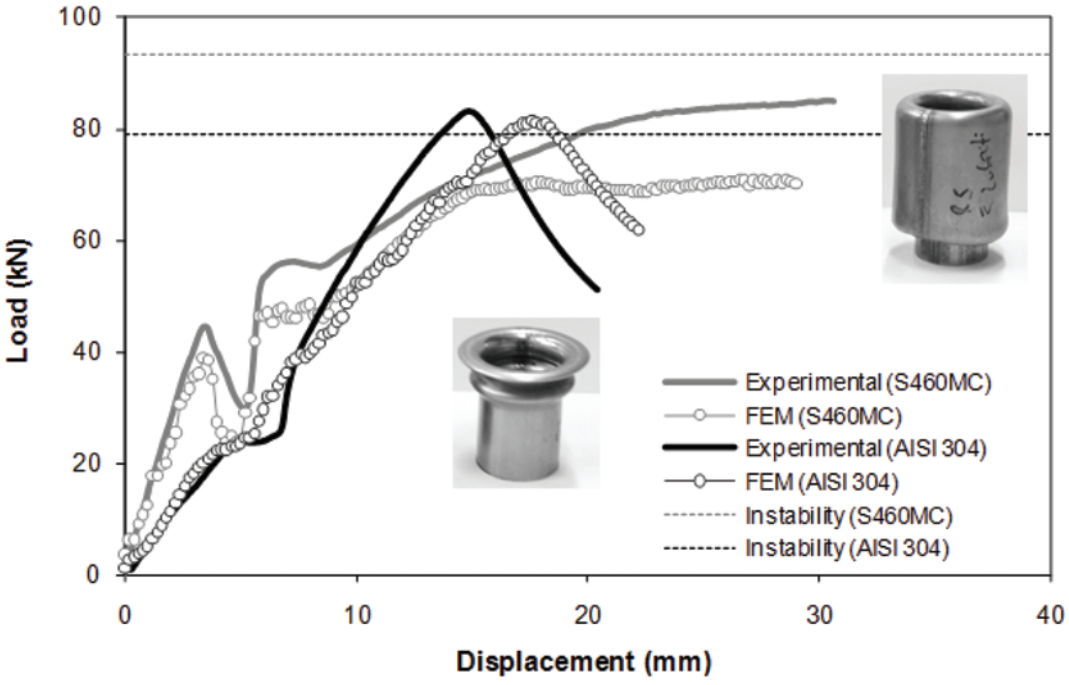


Figure 10. Theoretical and experimental load-displacement curve for the external inversion of S460MC and AISI 304 welded tubes (r_d / r_0 = 0.31 in Table 1)



ferent forming phases: (i) the axial compression stage, (ii) the transient expansion stage and (iii) the steady-state expansion stages. In the first stage, the load increases as the punch is forced into the tube end. Peak loads within the range 8 to 9 kN are obtained for both S460MC and AISI 304 tubes after which the tube bends axially in order to match the conical surface of the punch. Subsequently (second stage), the leading edge of the tube starts to flow along the conical surface of the punch and as a consequence of progressive circumferential stretching, the load grows moderately from a lowered level. The rate of load growth during the second forming stage is different for both types of tubes due to differences in strain hardening. AISI 304 experiences higher levels of strain hardening than S460MC and, because of this, the corresponding tubes present a much higher rate of load growth than those made from carbon steel. The forming load in steady-state conditions is 25% higher in case of AISI 304 tubes.

Figure 10 presents the theoretical and experimental load-displacement curve for test cases in which inversion was successfully (S460MC) and unsuccessfully (AISI304) accomplished.

In case of S460MC tubes, three phases may be distinguished; the axial compression, the transient invert-forming and the steady-state invert-forming stages. In the first stage the load increases steeply as the tube is axially compressed against the surface of the die. A peak load of 42 kN is obtained after which the tube starts to bend axially in order to match the contour of the die. Subsequently (second stage), the leading edge of the tube starts to turn around the die corner and, as a consequence of progressive circumferential stretching, the load grows moderately from a lowered level. After the leading edge of the tube completes a 270º rotation the invert-forming process reaches steady-state conditions and, therefore, the value of the forming load becomes constant. Numerical and experimental load-displacement curves compare well.

The higher rate of load growth of AISI 304 tubes due to strain hardening in conjunction with the smaller value of the critical instability load P_{cr} explains the reason why AISI 304 tubes are not adequate for external inversion.

CONCLUSION

This paper evaluates the possibility of employing conventional tube end forming processes to the low cost, small-batch, production of custom and specific shapes at the ends of thin-walled carbon and stainless steel welded tubes.

As in the case with seamless tubes, free expansion, reduction and invert-forming of thin-walled welded tubes using a die are only achievable within a compact range of operating parameters. Formability limits are associated with the development of non-admissible modes of deformation related to local buckling and fracture. Process parameters related to the aspect ratio t_0 / r_0 of the tubular preforms and to the expansion r_p / r_0, reduction r_d / r_0 and invert-curling r_d / r_0 ratios as well as the angle α of the conical surfaces of the expansion punches and reduction dies must be properly chosen so that material deformation does not approach any of the above mentioned formability limits.

The range of formability is strongly influenced by frictional boundary conditions and lubrication plays an important role on the overall success of tube end forming processes.

The high level of strain hardening combined with the small value of the critical instability load explains the difficulties in producing tube end formed parts from AISI 304 welded tubes.

ACKNOWLEDGMENT

Luis Alves and Paulo Martins would like to acknowledge the support of MCG – Mind for Metal during this investigation. The work of MSc. Eduardo Dias is greatly acknowledged.

REFERENCES

Al-Hassani, S., Johnson, W., & Lowe, W. T. (1972). Characterization of inversion tubes under axial loading. *Journal of Mechanical Engineering Science*, *14*, 370–381. doi:10.1243/JMES_JOUR_1972_014_046_02

Al-Qureshi, H. A., & Morais, G. A. (1976). Analytical investigation of thin wall tube expansion by the inversion process. In *Proceedings of the Design Engineering Conference* (ASME paper No. 76-DE-9).

Alexander, J. M. (1960). An approximate analysis of the collapse of thin cylindrical shells under axial loading. *The Quarterly Journal of Mechanics and Applied Mathematics*, *13*, 10–15. doi:10.1093/qjmam/13.1.10

Allan, T. (1968). Investigation of the behaviour of cylindrical tubes subject to axial compressive forces. *Journal of Mechanical Engineering Science*, *10*, 182–197. doi:10.1243/JMES_JOUR_1968_010_026_02

Almeida, B. P. P., Alves, M. L., Rosa, P. A. R., Brito, A. G., & Martins, P. A. F. (2006). Expansion and reduction of thin-walled tubes using a die: experimental and theoretical investigation. *International Journal of Machine Tools & Manufacture*, *46*, 1643–1652. doi:10.1016/j.ijmachtools.2005.08.018

Alves, L. M., & Martins, P. A. F. (2009a). Cold expansion and reduction of thin-walled PVC tubes using a die. *Journal of Materials Processing Technology*, *209*, 4229–4236. doi:10.1016/j.jmatprotec.2008.11.015

Alves, L. M., & Martins, P. A. F. (2009b). Understanding invert forming of thin-walled polyvinyl chloride tubes using a die based on a mechanical flow formulation. *Materials and Manufacturing Processes*, *24*, 1398–1404. doi:10.1080/10426910902997530

Alves, L. M., Rodrigues, J. M. C., & Martins, P. A. F. (2003). Simulation of three-dimensional bulk forming processes by the finite element flow formulation. *Modelling and Simulation in Materials Science and Engineering – Institute of Physics, 11*, 803-821.

Avitzur, B. (1980). *Metal Forming: the Application of Limit Analysis*. New York: Marcel Dekker, and Basel.

El-Domiaty, A. (1997). Curling of thin tubes: analytical and experimental study. *Journal of Materials Engineering and Performance*, *6*, 481–495. doi:10.1007/s11665-997-0120-2

Gouveia, B. P. P., Alves, M. L., Rosa, P. A. R., & Martins, P. A. F. (2006). Compression beading and nosing of thin-walled tubes using a die: experimental and theoretical investigation. *International Journal of Mechanics and Materials in Design*, *3*, 7–16. doi:10.1007/s10999-006-9009-8

Guist, L. R., & Marble, D. P. (1966). Prediction of the inversion load of a circular tube. In *TND 3622, NASA*.

Kinkead, A. N. (1983). Analysis for inversion load and energy absorption of a circular tube. *Journal of Strain Analysis*, *18*, 177–188. doi:10.1243/03093247V183177

Lu, Y. H. (2005). Study of perform and loading rate in the tube nosing process by spherical die. *Computer Methods in Applied Mechanics and Engineering*, *194*, 2839–2858. doi:10.1016/j.cma.2004.07.032

Miller, G. (2003). *Tube forming processes: A comprehensive guide*. Dearborn, MI: SME-Society of manufacturing Engineers.

Reddy, T. Y. (1989). Tube inversion – an experiment in plasticity. *International Journal of Mechanical Engineering Education*, *17*, 277–291.

Reddy, T. Y. (1992). Guist and Marble revisited – on the natural knuckle radius in tube inversion. *International Journal of Mechanical Sciences*, *34*, 761–768. doi:10.1016/0020-7403(92)90040-N

Rosa, P. A. R., Rodrigues, J. M. C., & Martins, P. A. F. (2003). External inversion of thin-walled tubes using a die: experimental and theoretical investigation. *International Journal of Machine Tools & Manufacture*, *43*, 787–796. doi:10.1016/S0890-6955(03)00062-2

Rosa, P. A. R., Rodrigues, J. M. C., & Martins, P. A. F. (2004). Internal inversion of thin-walled tubes using a die: experimental and theoretical investigation. *International Journal of Machine Tools & Manufacture*, *44*, 775–784. doi:10.1016/j.ijmachtools.2004.01.013

Sekhon, G. S., Gupta, N. K., & Gupta, P. K. (2003). An analysis of external inversion of round tubes. *Journal of Materials Processing Technology*, *133*, 243–256. doi:10.1016/S0924-0136(02)00438-7

Sun, Z., & Yang, H. (2002). Development of a finite element simulation system for the tube axial compressive precision forming process. *International Journal of Machine Tools & Manufacture*, *42*, 15–20. doi:10.1016/S0890-6955(01)00100-6

Tomesani, L. (1997). Analysis of a tension-driven outside-in tube inversion. *Journal of Materials Processing Technology*, *64*, 379–386. doi:10.1016/S0924-0136(96)02589-7

Yang, H., & Li, S. (1995). Process optimization of the inverting-forming of thin-walled tubes with radiused dies. *Journal of Materials Processing Technology*, *52*, 489–495. doi:10.1016/0924-0136(94)01621-7

Yang, H., Zhichao, S., & Yingjun, J. (2001). FEM analysis of mechanism of free deformation under dieless constraint in axial compressive forming process of tube. *Journal of Materials Processing Technology*, *115*, 367–372. doi:10.1016/S0924-0136(01)01018-4

This work was previously published in the International Journal of Manufacturing, Materials, and Mechanical Engineering, Volume 1, Issue 1, edited by J. Paulo Davim, pp. 31-42, copyright 2011 by IGI Publishing (an imprint of IGI Global).

Chapter 14
Study on Oxidation of Stainless Steels During Hot Rolling

Z. Y. Jiang
University of Wollongong, Australia

J. X. Huang
Baoshan Iron & Steel Co., Ltd., China

D. B. Wei
University of Wollongong, Australia

A. W. Zhang
Baoshan Iron & Steel Co., Ltd., China

K. Tieu
University of Wollongong, Australia

X. Shi
Baoshan Iron & Steel Co., Ltd., China

S. H. Jiao
Baoshan Iron & Steel Co., Ltd., China

ABSTRACT

The oxidation of stainless steels 304 and 304L during hot rolling is studied in this paper. Results show the oxide scale thickness decreases significantly with an increase of reduction, and the oxide scales of both 304 and 304L stainless steels were found more deformable than the steel substrate. Surface roughness shows a complicated transfer during the hot rolling process due to the complexity of oxide scale characteristics. Also, surface roughness decreases with an increase of reduction. The friction coefficient increases with reduction in all cases, and the increase is more significant in the case of the 304 stainless steel than that of 304L stainless steel.

INTRODUCTION

The finishing temperature of hot strip rolling of stainless steels is in a range of 850 - 1100°C, where there is a significant oxidation process, in which oxide scale layers are inevitably formed on the stainless steel surface. In a rolling pass, the oxide scale encounters a complicated stress state which includes: i) normal compressive pressure from the work roll; ii) shearing stress due to the relative speed between the oxide scale and the roll surface, and relative sliding between the oxide scale and the deforming bulk steel; iii) tension in the rolling direction due to the product elongation; and iv) bending stress when the oxide scale and the strip is deformed (Yu & Lenard, 2002).

The deformation of oxide scale plays a key role with regard to the strip surface roughness which has an important influence on the downstream metal forming and its surface quality,

DOI: 10.4018/978-1-4666-1867-1.ch014

Copyright © 2013, IGI Global. Copying or distributing in print or electronic forms without written permission of IGI Global is prohibited.

especially for stainless steels. The surface of the oxide scale is made up of asperities, and when two surfaces are placed in contact, only the tips of the asperities touch. Forces normal to the surface make the asperities deform, and they can weld together at points of contact. Forces parallel to the surfaces are resisted by the shearing strength of these junctions. The oxide scale particles are deeply depressed into the strip surface, and the hot metal is extruded outward to fill the void between the oxide scale particles, thus generate a rougher surface (Jiang et al., 2006). At present, an increasing interest has been shown on the deformation of oxide scale during hot strip rolling (Yu & Lenard, 2002; Munther & Lenard, 1999; Iordanova et al., 2000; Krzyzanowski & Beynon, 1999; Krzyzanowski et al., 2000; Krzyzanowski & Beynon, 2002; Sun et al., 2003; Sun et al., 2004). Li et al. (2000) conducted hot "sandwich" rolling of plain carbon steel, and found that the oxide scale was strongly sensitive to the rolling temperature and reduction, and finite element modelling has been carried out to evaluate the hot ductility of the oxide scale. Suarez et al. (2009) combined previous investigations with their results, and concluded that the thin oxide scale exhibits a plastic behavior at temperatures above 900°C, and a brittle behavior when deformed at temperatures below 700°C, and mixed behavior was observed within this temperature range, as the oxide scale was found to resist limited amounts of deformation.

However, investigation on the deformation and surface roughness behavior of oxide scales during hot strip rolling of stainless steels is limited. Most studies on oxide scale deformation were based on carbon steel which is consisted of wustite, magnetite and hematite. While the two major potential components of a stainless steel oxide scale are the M_2O_3 rhombohedral phase and the M_3O_4 spinel phase (Mark, 2001). In this paper, the oxide scale deformation and the surface roughness transfer of 304 and 304L stainless steels are investigated. The deformation features of the stainless steel surface roughness are also discussed.

EXPERIMENTAL

An electrical furnace was adopted for reheating. Hot rolling tests were carried out on a Hille 100 Experimental Rolling Mill. A computer was used for data collection using Lab Window Software. The rolls are 225mm diameter by 254mm wide, induction hardened to 65 - 70RC up to 2.5mm deep with an initial surface roughness of 0.4μm (R_a) (Sun, 2005). The samples after rolling were put into a cooling box connecting with nitrogen to prevent further oxidation. The surface roughness was measured by the Hommel Tester T1000, the detailed procedures can be found in (Wei et al., 2009a).

RESULTS AND DISCUSSION

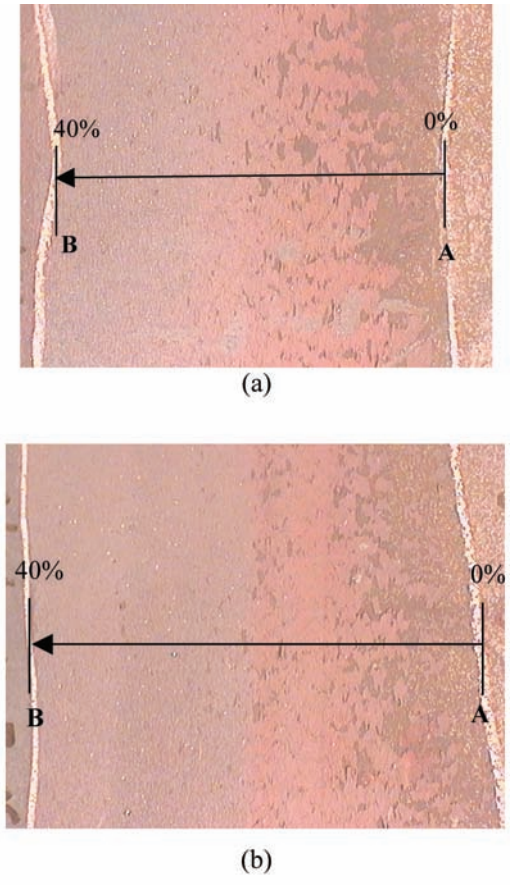
Deformation of Oxide Scale Under Various Reductions

The surface morphologies of oxide scale at the lead when the reduction is from 0 to 40% were photographed, as shown in Figure 1. It can be seen that the integrality of oxide scales and the surface finish after cooling increase with an increase of reduction. When the reduction is low, the hot rolled oxide scales were inclined to break after cooling. The bonding between the remained oxide scales and steel substrate is low, and there are a lot of macro cracks. This situation is improved with an increase of reduction. When the reduction is larger than about 20%, there are few macro cracks in the oxide scale, and the oxide scale is intact.

Stainless Steel 304

Figure 2 shows the microstructure of oxide scale of the 304 stainless steel under various reductions

Figure 1. Surface morphologies of oxide scale at the lead under reduction of 0 - 40% (a) 304 and (b) 304L



when the reheating time is 30min. The thickness of the oxide scale after rolling mainly depends on the reduction rather than the original thickness when the reduction is 20%. The relationship between the oxide scale thickness and reduction can be found from the conducted tests. It can be seen that there are still many cracks and splits on the oxide scale at 10% reduction (Figure 2a), while it decreases as the reduction increases. In Figure 2b and c, there are 20 and 30% reductions, and the oxide scales are more integrated than that of Figure 2a, and it shows highly integrality when the reduction reaches 40% (Figure 2d). Figure 2c and d also show that the boundary between the inner and outer layers is not clear once the reduction reaches 30%. These two layers are crushed together.

Stainless Steel 304L

Figure 3 shows the microstructures of the 304L stainless steel oxide scale under various reductions when the reheating time is 30 min, and an obvious decrease of oxide scale thickness is obtained as the reduction increases from 10 to 40%. A similar regularity can be illustrated as the stainless steel 304 that less cracks of oxide scale can be found when the reduction is higher. The bonding between the remained oxide scales and steel substrate of 304L stainless steel is higher than that of the 304 stainless steel.

Discussion

Figure 4 shows that the effect of reduction on oxide scale thickness for both 304 and 304L stainless steels. It can be seen that the oxide scale thickness decreases with an increase of reduction. The 304L stainless steel produces thinner oxide scale before rolling than that of the 304 stainless steel because of its higher oxidation resistance. The measured reductions of the oxide scales and the whole samples were also compared. The reductions of oxide scales are higher than that of the whole samples. This indicates that the oxide scales of 304 or 304L stainless steel are more deformable than the steel substrate, and they have good plasticity at the rolling temperature of 1050 °C, which is similar to the results obtained in Sun's work (Sun, 2005).

Surface Roughness Transfer After Hot Rolling

Surface roughness is an important index for hot rolled steel strip. There is always a layer of oxide scale on the surface of the workpiece in hot rolling, and the surface roughness is significantly affected by the oxide scale. An understanding of

Figure 2. Morpholgy of oxide scale of 304 steel under various reductions after hot rolling, reheating time: 30min

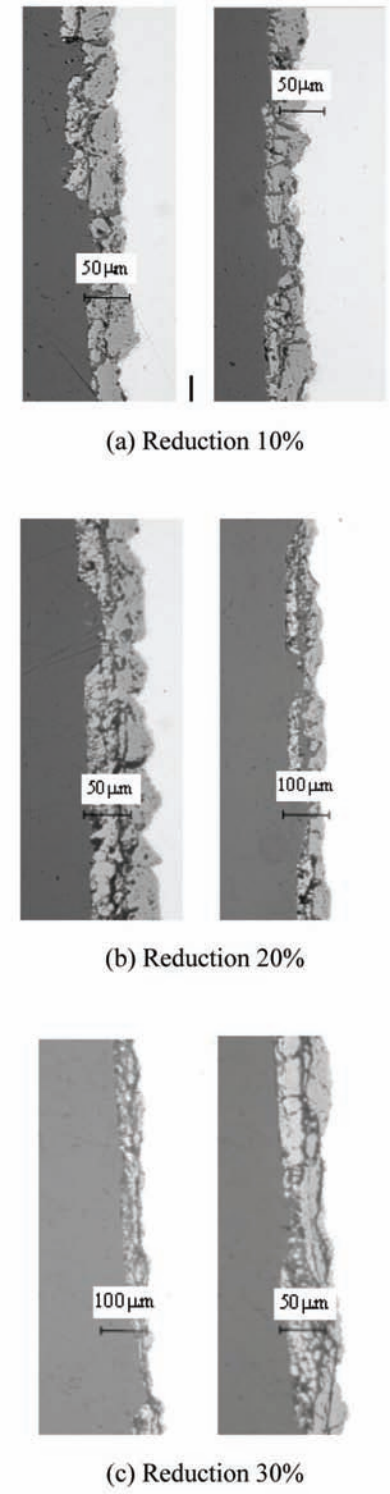


Figure 3. Morpholgy of oxide scale of 304L steel under various reductions after hot rolling, reheating time: 30min

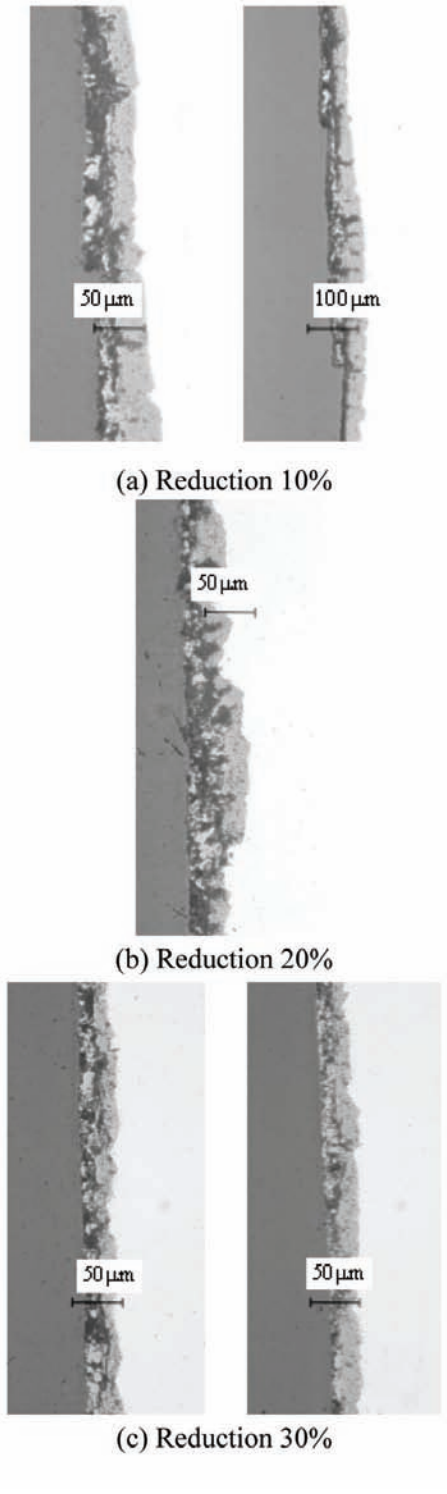
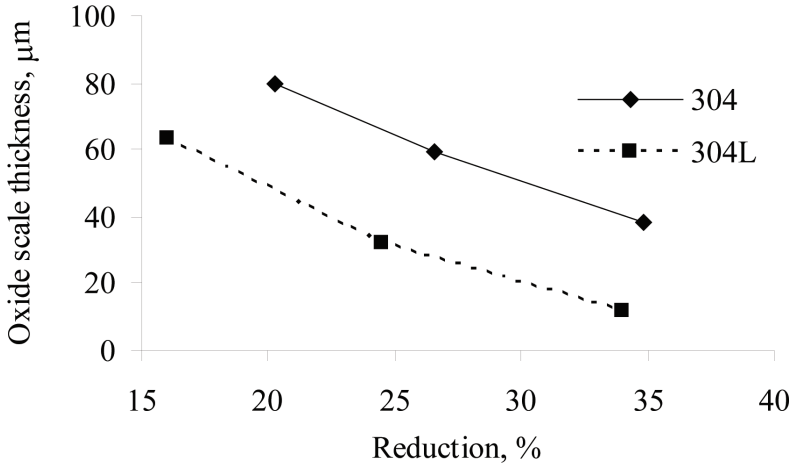


Figure 4. Relationship between the oxide scale thickness and reduction



the surface roughness transfer is needed to produce an accurate and reliable controlling model for hot rolling process.

Due to the possibilities of cracks and/or ploughing marks caused by rolling, it is important to select a representative value to assess the surface profile. Sun (Sun, 2005) confirms the values of surface roughness of both top and bottom surfaces and parallel and transverse rolling directions on one sample are close to each other. Therefore, it is reasonable to employ the surface roughness values parallel to the rolling direction on the top surface to indicate the surface roughness of a sample. Figure 5 shows the transfer of roughness average (R_a) after hot rolling under various reductions. When the reduction is 10%, the increase of R_a after rolling for the 304 stainless steel is nearly 7.0μm, while 304L stainless steel is only 0.3μm. There is a trend for the 304 stainless steel that as the reduction increases R_a decreases after rolling. However, for the 304L stainless steel, no such trend can be found in the graph, and most of the increase of R_a is similar to each other.

Figure 6 and Figure 7 show the surface profiles of 304 and 304L stainless steels respectively after rolling. The regularity of roughness transfer af-

Figure 5. R_a transfer after rolling, reheating time 30min

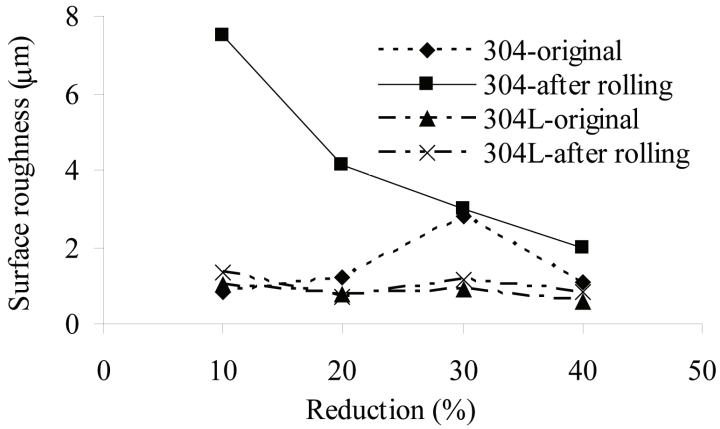
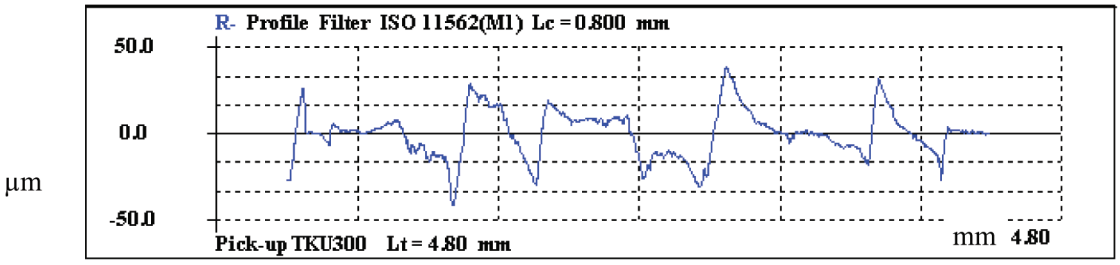
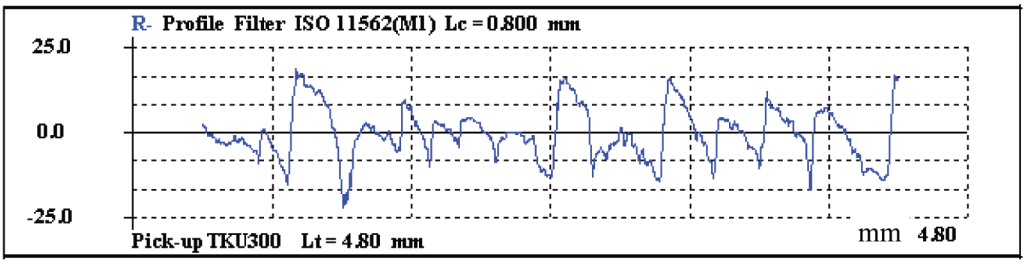


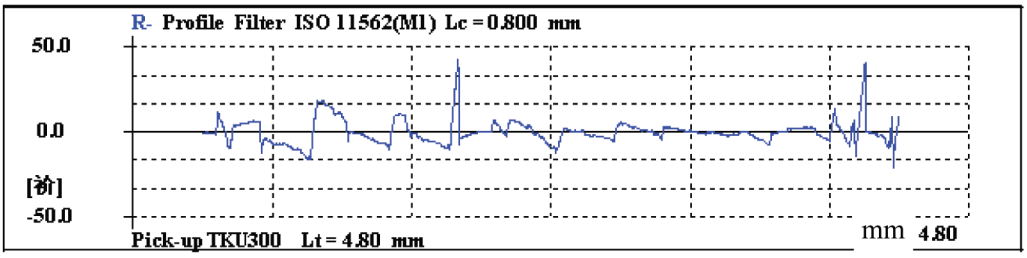
Figure 6. Surface profiles of 304 stainless samples after rolling, reheating time 30min



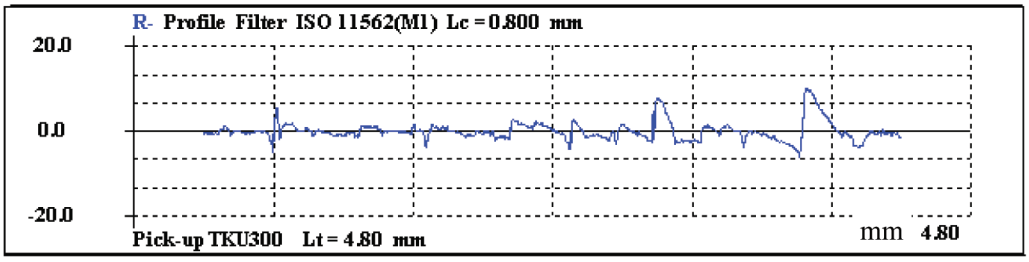
(a) Reduction 10%



(b) Reduction 20%

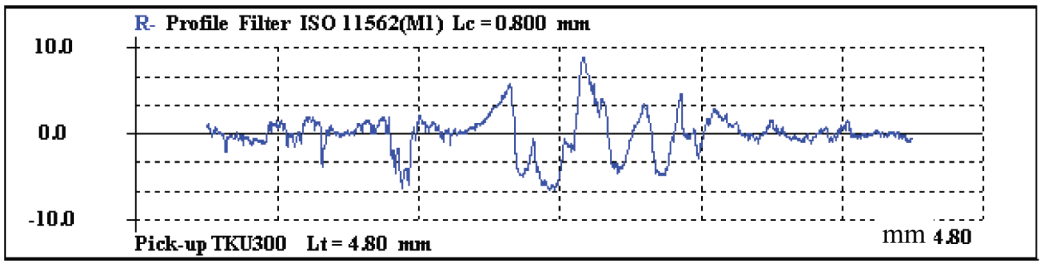


(c) Reduction 30%

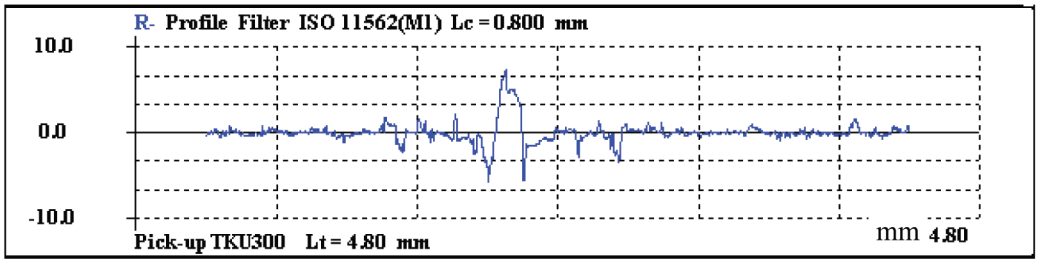


(d) Reduction 40%

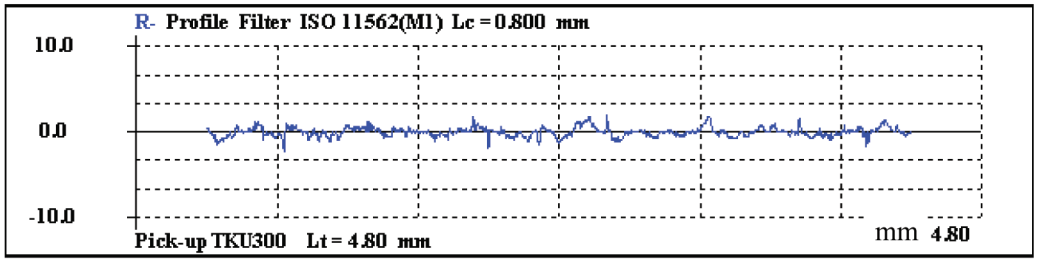
Figure 7. Surface profiles of 304L stainless samples after rolling, reheating time 30min



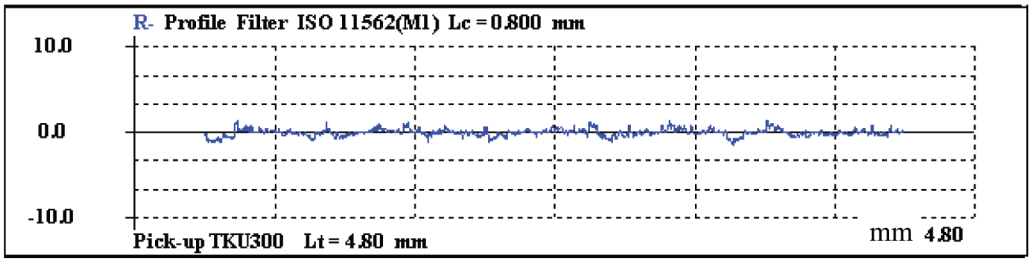
(a) Reduction 10%



(b) Reduction 20%

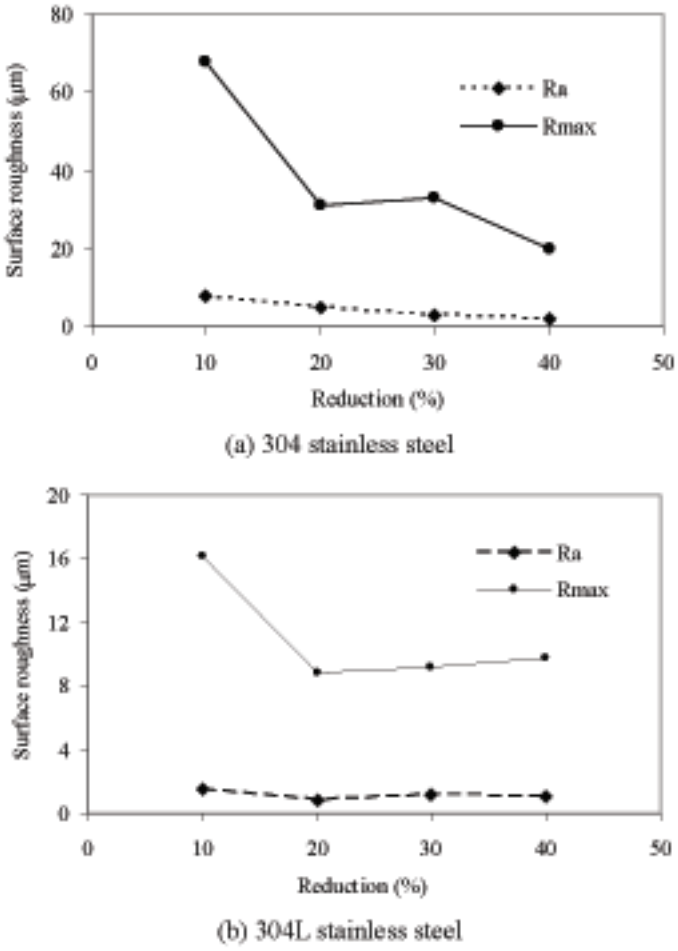


(c) Reduction 30%



(d) Reduction 40%

Figure 8. R_a and R_{max} transfer after rolling

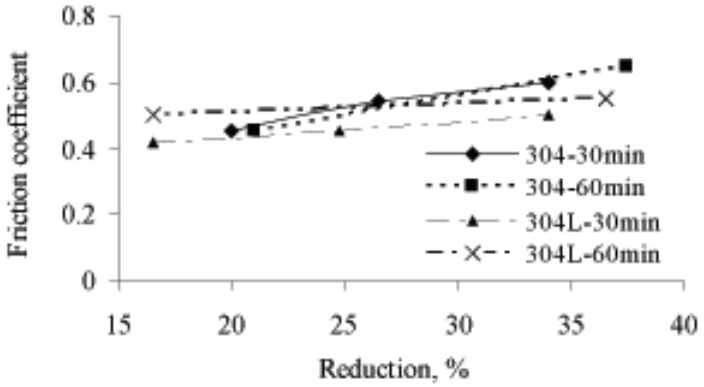


fected by reduction can be illustrated from the figures. The swing of the curves indicates a decreasing trend while increasing reductions. These two figures also indicate that the 304 stainless steel has higher surface roughness than that of 304L stainless steel. Figure 8 shows the transfer of R_a and R_{max} after rolling when the original stainless steel surface roughness R_a is 1.4 μm. For reheating time 30min of the 304 stainless steel, the R_{max} of 304 is 68 - 20.5μm from 10 to 40% reduction, which is larger than that of 304L, which is 16.5 - 9.7μm. It can also be seen that a large decrease from 10 to 20% reduction can be observed for both 304 and 304L stainless steels. However, there is not much change of the surface profile from 20 to 40% reduction for 304L, but for 304, a decrease of 10μm is found from 30 to 40% reduction.

Friction Coefficient During Hot Strip Rolling of Stainless Steel

A program (Alexander et al., 1987) developed on the basis of Orowan's model has been adopted for inversely determining the friction coefficient in the processes of hot rolling. It is capable of handling

Figure 9. Effect of reduction on friction coefficient



the mixed boundary condition at the roll-materials interface. The friction coefficients were changed until the calculated rolling force is less than 1% error with the measured data in each case (Wei et al., 2009b). The friction coefficient was also affected by oxide scale thickness, so both 30 and 60 min reheating cases were considered.

The results of friction coefficient derived by the reverse calculation are shown in Figure 9. As discussed the friction coefficient is affected by reduction and oxide scale thickness, therefore, both 30min and 60min reheating cases were considered under various reductions.

The friction coefficient increases with reduction in all cases, and the increase is more significant in the case of the 304 stainless steel than that of 304L stainless steel. For stainless steel 304L, friction coefficient decreases with an increase of oxide scale thickness, this is because the thick oxide scale performs as a lubricant during rolling process. The situation is more complicated for the 304 stainless steel. When the reduction is around 10%, the oxide scale thickness does not affect the friction coefficient significantly, and when the reduction is over 20%, the fiction coefficient increases significantly with a thicker oxide scale.

CONCLUSION

The results of hot rolling tests on both stainless steels 304 and 304L were analysed. The results show that the oxide scale thickness decreases significantly with an increase of reduction, and the oxide scales of both 304 and 304L stainless steels are more deformable than the steel substrate. Surface roughness has a complicated transfer during the hot rolling due to the complexity of the oxide scale characteristics. The surface roughness decreases with an increase of reduction. However, the decrease of the surface roughness for 340L stainless steel is less than that of the 304 stainless steel.

Friction coefficient is calculated by an inverse calculation and is found that it increases with reduction. In most cases, friction coefficient trends smaller with the thick oxide scale because the thick oxide scale can be as a lubricant during rolling process.

ACKNOWLEDGMENT

The authors appreciate the financial support from Baosteel for the current project. The authors also

appreciate Mr Joe Abbott assistance in conducting rolling tests.

REFERENCES

Alexander, J. M., Brewer, R. C., & Rowe, G. W. (1987). Manufacturing Technology: *Vol. 2. Engineering Process*. London: Ellis Horwood Limited, England.

Iordanova, I., Surtchev, M., Forcey, K. S., & Krastev, V. (2000). High-temperature surface oxidation of low-carbon rimming steel. *Surface and Interface Analysis*, *30*, 158–160. doi:10.1002/1096-9918(200008)30:1<158::AID-SIA744>3.0.CO;2-6

Jiang, Z. Y., Tieu, A. K., Sun, W. H., Tang, J., & Wei, D. B. (2006). Characterisation of thin oxide scale and its surface roughness in hot metal rolling. *Materials Science and Engineering A*, *435-436*, 434–438. doi:10.1016/j.msea.2006.07.070

Krzyzanowski, M., & Beynon, J. H. (1999). The tensile failure of mild steel oxides under hot rolling conditions. *Steel Research*, *70*, 22–27.

Krzyzanowski, M., & Beynon, J. H. (2002). Measurement of oxide properties for numerical evaluation of their failure under hot rolling conditions. *Journal of Materials Processing Technology*, *125-126*, 398–404. doi:10.1016/S0924-0136(02)00290-X

Krzyzanowski, M., Beynon, J. H., & Sellars, C. M. (2000). Analysis of secondary oxide scale failure at entry into the roll gap. *Metallurgical and Materials Transactions. B, Process Metallurgy and Materials Processing Science*, *31*(6), 1483–1490. doi:10.1007/s11663-000-0033-z

Li, Y. H., Krzyzanowski, M., Beynon, J. H., & Sellars, C. M. (2000). Physical simulation of interfacial conditions in hot forming of steels. *Acta Metallurgica Sinica*, *13*, 359–368.

Mark, R. (2001). Surface oxide formation and acid-descaling for stainless steel: Part 1. *Wire Industry*, *68*, 503.

Munther, P. A., & Lenard, J. G. (1999). The effects of scaling on interfacial friction of hot rolling of steels. *Journal of Materials Processing Technology*, *88*, 105–113. doi:10.1016/S0924-0136(98)00392-6

Suarez, L., Houbaert, Y., Vanden, X., & Colás, R. (2009). High temperature deformation of oxide scale. *Corrosion Science*, *51*, 309–315. doi:10.1016/j.corsci.2008.10.027

Sun, W. H. (2005). *A study on the characteristics of oxide scale in hot rolling of steel*. Unpublished doctoral dissertation, University of Wollongong, Australia.

Sun, W. H., Tieu, A. K., & Jiang, Z. Y. (2004). Effect of rolling condition on mill load and oxide scale deformation in hot rolling of low carbon steel. *Steel GRIPS Journal of Steel Related Materials*, *2*, 579–583.

Sun, W. H., Tieu, A. K., Jiang, Z. Y., Lu, C., & Zhu, H. T. (2003). Surface characteristics of oxide scale in hot strip rolling. *Journal of Materials Processing Technology*, *140*(1-3), 77–84. doi:10.1016/S0924-0136(03)00823-9

Wei, D. B., Huang, J. X., Zhang, A. W., Jiang, Z. Y., Tieu, A. K., & Wu, F. (2009a). Deformation of oxide scale and surface roughness transfer during hot rolling of stainless steel 304L. *International Journal of Surface Science and Engineering*, *3*, 459–470. doi:10.1504/IJSURFSE.2009.029141

Wei, D. B., Jiang, Z. Y., & Tieu, A. K. (2009b). *Study on friction in hot rolling of stainless steels, a progress report*. Gwynneville, Australia: University of Wollongong.

Yu, Y., & Lenard, J. G. (2002). Estimating the resistance to deformation of the layer of scale during hot rolling of carbon steel strips. *Journal of Materials Processing Technology*, *121*, 60–68. doi:10.1016/S0924-0136(01)01176-1

This work was previously published in the International Journal of Manufacturing, Materials, and Mechanical Engineering, Volume 1, Issue 1, edited by J. Paulo Davim, pp. 31-42, copyright 2011 by IGI Publishing (an imprint of IGI Global).

Section 3

Material Science and Engineering

Chapter 15
Material Selection Using a Novel Multiple Attribute Decision Making Method

R. V. Rao
S. V. National Institute of Technology, India

B. K. Patel
S. V. National Institute of Technology, India

ABSTRACT

Selection of a most appropriate material is a very important task in design process of every product. There is a need for simple, systematic, and logical methods or mathematical tools to guide decision makers in considering a number of selection attributes and their interrelations and in making right decisions. This paper proposes a novel multiple attribute decision making (MADM) method for solving the material selection problem. The method considers the objective weights of importance of the attributes as well as the subjective preferences of the decision maker to decide the integrated weights of importance of the attributes. Furthermore, the method uses fuzzy logic to convert the qualitative attributes into the quantitative attributes. Two examples are presented to illustrate the potential of the proposed method.

INTRODUCTION

An ever increasing variety of materials is available today, with each having its own characteristics, applications, advantages, and limitations. When selecting materials for engineering designs, a clear understanding of the functional requirements for each individual component is required and various important criteria or attributes need to be considered. Material selection attribute is defined as an attribute that influences the selection of a material for a given application. These attributes include: physical properties, electrical properties, magnetic properties, mechanical properties, chemical properties, manufacturing properties, material cost, product shape, material impact

DOI: 10.4018/978-1-4666-1867-1.ch015

Copyright © 2013, IGI Global. Copying or distributing in print or electronic forms without written permission of IGI Global is prohibited.

on environment, availability, fashion, market trends, cultural aspects, aesthetics, recycling, target group, etc.

The selection of an optimal material for an engineering design from among two or more alternative materials on the basis of two or more attributes is a multiple attribute decision making (MADM) problem. The selection decisions are complex, as material selection is more challenging today. There is a need for simple, systematic, and logical methods or mathematical tools to guide decision makers in considering a number of selection attributes and their interrelations. The objective of any material selection procedure is to identify appropriate selection attributes, and obtain the most appropriate combination of attributes in conjunction with the real requirement. Thus, efforts need to be extended to identify those attributes that influence material selection for a given engineering design to eliminate unsuitable alternatives, and to select the most appropriate alternative using simple and logical methods.

Various approaches had been proposed to help address the issue of material selection (Ashby, 2004; Edwards, 2005; Sapuan, 2001; Zha, 2005; Jalham, 2006). However, these systems and methods are complex and knowledge intensive. Jee and Kang (2000) proposed TOPSIS method for material selection. Shanian and Savadogo (2006a, 2006b) presented material selection models using a multiple attribute decision making (MADM) method known as ELECTRE. However, ELECTRE method uses the concept of outranking relationship and the procedure is rather lengthy. Only a partial prioritization of alternative materials is computed in ELECTRE models. Shanian and Savadogo (2006c) proposed TOPSIS method for material selection of metallic bipolar plates for polymer electrolyte fuel cell. However, the TOPSIS method proposed by them does not take into account the qualitative nature of the material selection attributes. Further, the 'entropy' concept used by the authors for deciding the relative importance of attributes does not give scope to designer's preferences and it involves more computation.

Rao (2006) presented a material selection model using graph theory and matrix approach. However, the method does not have a provision for checking the consistency made in the judgments of relative importance of the attributes. Rao and Davim (2006) proposed TOPSIS method combined with AHP for material selection. Manshadi et al. (2007) proposed a numerical method for materials selection combining non-linear normalization with a modified digital logic method. However, the method does not make a provision for considering the qualitative material selection attributes. Chan and Tong (2007) proposed weighted average method using grey relational analysis to rank the materials with respect to certain quantitative attributes. Rao (2008) proposed a compromise ranking method known as VIKOR and Chatterjee et al. (2009) proposed VIKOR and ELECTRE methods for material selection.

Fayazbakhsh et al. (2009) used Z-transformation in statistics for normalization of material properties for materials selection in mechanical design using. Khabbaz et al. (2009) proposed a fuzzy logic approach for material selection. However, the procedure needs many fuzzy IF-THEN rules and the quantitative values of the attributes are to be converted to fuzzy descriptions to fit into the fuzzy rules. Maniya and Bhatt (2010) proposed preference selection index (PSI) method for material selection. The method uses only the objective weights of the attributes and doesn't take into consideration the decision maker's expertise and judgment. Furthermore, the method doesn't have enough mathematically validity and no separate steps were suggested for conversion of a qualitative attribute into a quantitative one. Jahan et al. (2010) proposed a linear assignment technique for material selection. However, the linear assignment technique may not be as precise as other MADM methods when the material selection is based on quantitative material properties.

Keeping in view of the above research works on material selection, a novel decision making method is proposed in this paper for material selection for a given engineering design. The aim of the present paper is to propose a novel MADM method to deal with the material selection problems considering both qualitative and quantitative attributes. A ranked value judgment on a fuzzy conversion scale for the qualitative attributes is introduced. The proposed method helps the decision maker to arrive at a decision based on either the objective weights of importance of the attributes or his/her subjective preferences or considering both the objective weights and the subjective preferences. An example is included to illustrate the proposed method.

NOVEL DECISION MAKING METHODOLOGY

Multiple attribute decision making (MADM) is employed to solve problems involving selection from among a finite number of alternatives. Each decision table in MADM methods has four main parts, namely: (a) alternatives, (b) attributes, (c) weight or relative importance of each attribute, and (d) measures of performance of alternatives with respect to the attributes. The decision table, given in Table 1, shows alternatives, A_i (for i = 1, 2,….., n), attributes, B_j (for j = 1, 2,….., m), weights of attributes, w_j (for j=1, 2,….., m) and the measures of performance of alternatives, m_{ij} (for i= 1, 2,….., n; j=1, 2,….., m). Given the decision table information and a decision making method, the task of the decision maker is to find the best alternative and/or to rank the entire set of alternatives. It may be added here that all the elements in the decision table must be normalized to the same units.

The methodology presented in this paper for material selection is described below:

Step 1: preparation of the decision table

Identify the selection attributes for the considered material selection problem and short-list the materials on the basis of the identified attributes satisfying the requirements. The attributes are of two types, beneficial (i.e., higher values are desired) and non-beneficial (i.e., lower values are desired). A quantitative or qualitative value or its range may be assigned to each identified attribute as a limiting value or threshold value for its acceptance for the considered problem. An alternative with each of its attribute, meeting the acceptance value, may be short-listed. After short-listing the alternatives and determining the values associated with the attributes (x_{ij}), a decision table including the measures or values of all attributes for the short-listed alternative materials can be prepared and the values of attributes can be normalized for different alternatives using Equation (1).

Table 1. Decision table

Alternatives	Attributes					
	$B_1(w_1)$	$B_2(w_2)$	$B_3(w_3)$	--(--)	--(--)	$B_m(w_m)$
A_1	x_{11}	x_{12}	x_{13}	--	--	x_{1m}
A_2	x_{21}	x_{22}	x_{23}	--	--	x_{2m}
A_3	x_{31}	x_{32}	x_{33}	--	--	x_{3m}
--	--	--	--	--	--	--
--	--	--	--	--	--	--
A_n	x_{n1}	x_{n2}	x_{n3}	--	--	x_{nm}

Table 2. Fuzzy conversion scale for the qualitative attribute

Qualitative measures of attribute	Fuzzy number	Assigned total crisp score
Exceptionally low	M_1	0.0455
Extremely low	M_2	0.1364
Very low	M_3	0.2273
Low	M_4	0.3182
Below average	M_5	0.4091
Average	M_6	0.5000
Above average	M_7	0.5909
High	M_8	0.6818
Very high	M_9	0.7727
Extremely high	M_{10}	0.8636
Exceptionally high	M_{11}	0.9545

$$x_{ij}^{*} = x_{ij} / \sum_{i=1}^{n} X_{ij} \quad (1)$$

Where, x_{ij}* is the normalized value of x_{ij}.

It may be added here that the above Equation(1) can deal with quantitative attributes. However, there exists some difficulty in the case of qualitative attributes (i.e. quantitative value is not available). A ranked value judgment on a fuzzy conversion scale is proposed in this paper by using fuzzy set theory. This approach is based on the work of Chen and Hwang (1992). The presented numerical approximation system systematically converts linguistic terms to their corresponding fuzzy numbers. An eleven-point scale is proposed in this paper for better understanding and representation of the qualitative attribute. Table 2 is suggested which represents the attribute on a qualitative scale using fuzzy logic, corresponding to the fuzzy conversion scale shown in Figure 1 and helps the users in assigning the quantitative values. The details of conversion are given in the Appendix. Once a qualitative attribute is represented on a scale then the alternatives can be compared with each other on this attribute in the same manner as that for quantitative attributes.

Step 1: determination of weights of importance of the attributes

The weights of relative importance of the attributes may be decided by the decision maker for the considered application either, (a) based on the data of the attributes for various alternatives given in the decision table and normalized subsequently or (b) based on his/her subjective preferences on the attributes or (c) based on a combination of objective weights and the subjective preferences. These three cases are explained below (Table 1).

Step 2: determination of weights of importance of the attributes

The weights of relative importance of the attributes may be decided by the decision maker for the considered application either, (a) based on the data of the attributes for various alternatives given in the decision table and normalized subsequently or (b) based on his/her subjective preferences on the attributes or (c) based on a combination of objective weights and the subjective preferences.

Step 2.1: objective weights of importance of the attributes

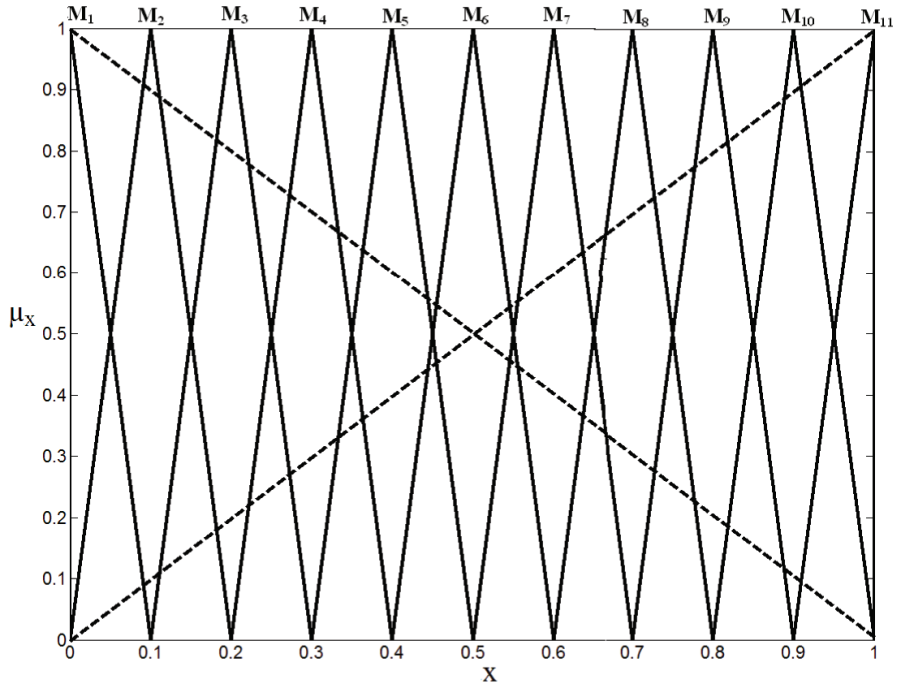
The statistical variance is proposed in this paper for determining the objective weights of importance of the attributes using Equation (2).

$$V_j = \left(1/n\right)\sum_{i=1}^{n}(X_{ij}^{*} - (X_{ij}^{*})mean)^2 \quad (2)$$

where, V_j is the variance of the data corresponding to the jth attribute. $(x_{ij}*)_{mean}$ is the mean or average value of x_{ij}*. The objective weight of the jth attribute (w_j^{o}) can be computed using Equation (3).

$$w_j^{o} = V_j / \sum_{j=1}^{m} V_j \quad (3)$$

Figure 1. Linguistic terms to fuzzy numbers conversion (11-point scale)



The statistical variance concept of determining the objective weights of the attributes is comparatively simpler than the entropy method suggested by Jee and Kang (2000) and Shanian and Savadogo (2006c).

Step 2.2: subjective weights of importance of the attributes

The weights of relative importance of the attributes may be assigned based on the decision maker's preferences over the attributes for the considered application. He/She may assign the weights of importance arbitrarily as per his/her preferences or may use any of the systematic methods of assigning relative importance such as analytic hierarchy process (AHP) method (Saaty, 2000), points method (Edwards and Newman, 1986), digital logic method (Manshadi et al., 2007), etc. For details, one may refer to Triantaphyllou (2000) and Rao (2007).

Step 2.3: integrated weights of importance of the attributes

If the decision maker wishes to utilize both the objective and subjective weights of the attributes as described in steps 2.1 and 2.2, then he/she may use the integrated weights described by Equation (4).

$$w_j^i = (w_j^o * w_j^s) \Big/ \sum_{j=1}^{m} (w_j^o * w_j^s) \qquad (4)$$

where, w_j^i is the integrated weight of jth attribute.

Step 3: computation of preference index

The preference index for each alternative indicates the score or merit of the alternative with respect to the other alternatives. The preference index (P_i) can be calculated using the following Equations (5) to (7).

$$P_i^o = \sum_{j=1}^{m} w_j^o \cdot x_{ij}^{**} \quad (5)$$

$$P_i^s = \sum_{j=1}^{m} w_j^s \cdot x_{ij}^{**} \quad (6)$$

$$P_i^i = \sum_{j=1}^{m} w_j^i \cdot x_{ij}^{**} \quad (7)$$

where, $x_{ij}^{**}=[x_{ij}^{*b}/(x_{ij}^{*b})_{max}]$ for beneficial attributes and $[(x_{ij}^{*nb})_{min}/x_{ij}^{*nb}]$ for non-beneficial attributes. x_{ij}^{*b} and x_{ij}^{*nb} indicate the normalized values of the beneficial and non-beneficial attributes, respectively. $(x_{ij}^{*b})_{max}$ indicates the maximum value of the jth beneficial attribute and $(x_{ij}^{*nb})_{min}$ indicates the minimum value of the jth non-beneficial attribute. Equation (5) can be used when the decision maker wishes to use the objective weights of the attributes; Equation (6) can be used if he/she wishes to use the subjective weights of the attributes; and Equation (7) can be used if he/she wishes to use the integrated weights of the attributes.

The alternatives may be arranged in the descending order of the preference index values. The alternative for which the value of preference index is highest is the best choice for the considered decision making problem.

Step 4: final selection

A final decision may be taken keeping in view the practical considerations. All possible constraints likely to be experienced by the user are looked in during this stage. These include constraints such as management constraints, social constraints, political constraints, etc. However, compromise may be made in favor of an alternative with a higher value of preference index.

EXAMPLES

Two examples are considered to demonstrate and validate the application of the proposed methodology of material selection for a given engineering design.

Example 1

Fayazbakhsh et al. (2009) proposed a material selection method and used *Z*-transformation statistics for scaling the material properties. The authors had presented an example problem of material selection which was solved previously by

Table 3. Material selection attributes of example 1 (Fayazbakhsh et al., 2009)

M	YS	YM	FR	RY	RC	FC	R	D	WS
1	234.4	204.1	H	VH	L	A	L	7800	Nil
2	137.9	67	L	H	H	L	A	2700	H
3	268.9	67	A	A	H	A	A	1800	VH
4	379.2	204.1	H	A	H	VH	H	5200	H
5	1496.2	227.5	L	A	VH	VH	A	1800	VH
6	220.6	53.9	VH	VH	VH	L	VH	2500	H

YS: Yield strength (MPa); *YM*: Young's modulus (GPa); *FR*: Fire resistance; *RY*: Repairability; *RC*: Resistance to corrosion; *FC*: Fabrication cost; *R*: Risk; *D*: Density(kg/m3); and *WS*: Overall potential for weight saving

M: Materials: 1. Grade A Steel; 2. Single Skin Aluminum (A5086-H34);

3. Aluminum Sandwich (honeycomb core); 4. LASCOR Steel; 5. Composite (CFRP) Carbon w/Vinyl Ester Resin; and 6. DUCTAL (UHP2C)

L: Low; A: Average; H: High; VH: Very high

Torrez (2007) using modified digital logic method. The material selection problem was related with a light-weight high-speed naval craft. The materials selection was sought for the structural components of the ship such as hull plating, superstructure panels, decks, and beams. The material selection problem considered 6 alternative materials and 9 attributes and the data is shown in Table 3. Now, various steps of the methodology are carried out.

Step 1: In the present work, the alternatives and the attributes considered are same as of Fayazbakhsh et al. (2009).

The attributes are: yield strength (YS), Young's modulus (YM), fire resistance (FR), repairability (RY), resistance to corrosion (RC), fabrication cost (FC), risk (R), density (D), and overall potential for weight savings (WS). YS, YM, FR, RY, RC, and WS are considered as the beneficial attributes and FC, R, and D are considered as the non-beneficial attributes for the considered application. The attributes YS, YM, and D are the quantitative attributes and the remaining are qualitative attributes. The qualitative attributes are converted to quantitative attributes using the fuzzy conversion scale proposed in Table 2. Table 4 presents the data of all 9 attributes after this conversion. The values of the attributes for the short-listed alternatives, given in Table 4, are normalized for different alternatives using Equation (1) and are given in Table 5.

Step 2.1: The statistical variance proposed in this paper (i.e., Equation (2)) is used for determining the objective weights of importance of the attributes. The variance values of the 9 attributes are computed as given below.

V_{YS} = 0.02966; V_{YM} = 0.00833; V_{FR} = 0.00303; V_{RY} = 0.00112; V_{RC} = 0.00156; V_{FC} = 0.00345; V_{R} = 0.00199, V_{D} = 0.01006; and V_{WS} = 0.00488.

Objective weights of the attributes are computed using Equation (3).

w_{YS}^{o} = 0.46201; w_{YM}^{o} = 0.13021; w_{FR}^{o} = 0.04723; w_{RY}^{o} = 0.01756; w_{RC}^{o} = 0.02442; w_{FC}^{o} = 0.05378; w_{R}^{o} = 0.03115; w_{D}^{o} = 0.15730; and w_{WS}^{o} = 0.07625.

Step 2.2: Fayazbakhsh et al. (2009) used modified digital logic method for assigning the subjective weights. To make a comparison of the results of the proposed method with that proposed by Fayazbakhsh et al. (2009), the same subjective weights are considered in this paper and these are: w_{YS}^{s} = 0.132; w_{YM}^{s} = 0.118; w_{FR}^{s} = 0.0833; w_{RY}^{s} = 0.0763; w_{RC}^{s} = 0.0694; w_{FC}^{s} = 0.125; w_{R}^{s} = 0.0763; w_{D}^{s} = 0.153; and w_{WS}^{s}=0.167.

Step 2.3: The integrated weights of importance of the attributes are computed using Equation (4). The integrated weights are computed

Table 4. Quantitative data of the material selection attributes of example 1

M	YS	YM	FR	RY	RC	FC	R	D	WS
1	234.4	204.1	0.6818	0.7727	0.3182	0.5000	0.3182	7800	0
2	137.9	67	0.3182	0.6818	0.6818	0.3182	0.5000	2700	0.6818
3	268.9	67	0.5000	0.5000	0.6818	0.5000	0.5000	1800	0.7727
4	379.2	204.1	0.6818	0.5000	0.6818	0.7727	0.6818	5200	0.6818
5	1496.2	227.5	0.3182	0.5000	0.7727	0.7727	0.5000	1800	0.7727
6	220.6	53.9	0.7727	0.7727	0.7727	0.3182	0.7727	2500	0.6818

Table 5. Normalized data for calculating the weights of attributes of example 1

M	YS	YM	FR	RY	RC	FC	R	D	WS
1	0.0856	0.248	0.2083	0.2073	0.0814	0.1571	0.0972	0.3578	0
2	0.0504	0.081	0.0972	0.1829	0.1744	0.1000	0.1528	0.1239	0.19
3	0.0982	0.081	0.1528	0.1341	0.1744	0.1571	0.1528	0.0826	0.21
4	0.1385	0.248	0.2083	0.1341	0.1744	0.2428	0.2083	0.2385	0.19
5	0.5466	0.276	0.0972	0.1341	0.1977	0.2428	0.1528	0.0826	0.21
6	0.0806	0.065	0.2361	0.2073	0.1977	0.1000	0.2361	0.1147	0.19

w_{FR}^{i} = 0.03045; w_{RY}^{i} = 0.01037; w_{RC}^{i} = 0.01311; w_{FC}^{i} = 0.05211; w_{R}^{i} = 0.01839; w_{D}^{i} = 0.18623; and w_{WS}^{i} = 0.09853.

as, w_{YS}^{i} = 0.47191; w_{YM}^{i} = 0.11889; w_{YS}^{i} = 0.47191; w_{YM}^{i} = 0.11889;

Step 3: The preference index values are computed for different alternatives using Equations (5) to (7). For example, using objective weights of importance of the attributes, the preference index of alternative materials 1 (i.e., Grade A steel) and 2 (i.e., A5086-H34Al 5052-O) are computed using Equation (5) as given below.

P_1=0.46201*(234.4/1496.2)+0.13021*(204.1/227.5)+0.04723*(0.6818/0.7727)+0.01756*(0.7727/0.7727)+0.02442*(0.3182/0.7727)+0.05378*(0.3182/0.5)+0.03115*(0.3182/0.3182)+0.15730*(1800/7800)+0.07625*(0/0.7727) = 0.3647.

P_2=0.46201*(137.9/1496.2)+0.13021*(67/227.5)+0.04723*(0.3182/0.7727)+0.01756*(0.6818/0.7727)+0.02442*(0.6818/0.7727)+0.05378*(0.3182/0.3182)+0.03115*(0.3182/0.5)+0.15730*(1800/2700)+0.07625*(0.6818/0.7727)= 0.3833.

The computed values of the preference index and the ranks are given in Table 6. The 6 alternative materials are then ranked based on the computed values of the preference index, which is also shown in Table 5.

From the results given in Table 6, it can be understood that usage of only subjective weights of the attributes leads to materials ranking of 5-6-3-2-4-1 and suggests material 5 as the first choice. This ranking exactly matches with that given by Torrez (2007). Usage of only objective weights of the attributes leads to 5-3-4-6-2-1 and suggests material 5 as the first choice. Usage of integrated weights also suggests material 5 as the first choice. It may be observed that Fayazbakhsh et al. (2009) used only the subjective weights obtained by modified digital logic method and the ranking order of alternative materials obtained by them was: 5-6-2-3-1-4, suggesting material 5 as the first choice. For the same subjective weights, the first two ranks obtained by the proposed novel method in this paper match with the ranks proposed by Fayazbakhsh et al. (2009). However, a close look at the values of the attributes for the materials 2 and 3 reveal that material 3 is comparatively better than material 2 in the case of four attributes (i.e., YS, SR, D, and WS), equal in the case of three attributes (i.e., YM, RC, and R) and comparatively worse in the case of two attributes (i.e., RY and FC). Thus, proposing material 3 as the third choice and material 2 as the fourth choice which is given by the proposed method seems more genuine than that proposed by Fayazbakhsh et al. (2009). Following the similar logic and keeping in view of the subjective weights of the attributes, proposing material 1 as the last choice by the present method is more genuine than proposing material 4 as the last choice by Fayazbakhsh et al. (2009). Thus, the proposed method is more

Table 6. Rankings of alternative materials of example 1

Material	Proposed decision making method w^s w^o w^i P^s Rank P^o Rank P^i Rank						*Fayazbakhsh et al. (2009)* Rank
1	0.5059	6	0.3647	6	0.3236	6	5
2	0.6327	4	0.3833	5	0.3867	5	3
3	0.6711	3	0.4725	2	0.4874	2	4
4	0.6108	5	0.4669	3	0.4529	3	6
5	0.8231	1	0.9230	1	0.9411	1	1
6	0.6904	2	0.4354	4	0.4324	4	2

logical and has ranked the alternative materials in few steps with simple calculations. Furthermore, the proposed method gives an option to the decision maker either to use only subjective weights, or objective weights, or integrated weights of importance of the attributes. The proposed method makes a provision to quantify the qualitative attributes using fuzzy logic, if such attributes are present in the problem.

Example 2

Now, another example is considered to further demonstrate and validate the proposed novel decision making method for evaluation of materials for a given engineering application. This example problem is related with selection of a suitable work material for a product which needs to be designed for operating in a high-temperature environment. The material selection problem considers four alternative materials and four attributes and the data is shown in Table 7.

Now, various steps of the methodology are carried out.

Step 1: In the present work, the attributes are: tensile strength (TS), Young's modulus (YM), density (D), and corrosion resistance (CR). TS, YM, and CR are considered as the beneficial attributes and D is considered as the non-beneficial attribute for the considered application. The attributes TS, YM, and D are the quantitative attributes and CR is qualitative attribute. The qualitative attribute is converted to quantitative attribute using the fuzzy conversion scale proposed in Table 2 and the corresponding values are given in parentheses in the last column of Table 7. The values of the attributes for the short-listed alternatives are normalized for different alternatives using Equation (1) but not shown here for space reasons.

Step 2.1: The statistical variance proposed in this paper (i.e., Equation (2)) is used for determining the objective weights of importance of the attributes. The variance values of the 4 attributes are computed as given below.

$V_{TS} = 0.01235$; $V_{YM} = 0.00685$; $V_D = 0.00074$; and $V_{CR} = 0.00240$

Objective weights of the attributes are computed using Equation (3).

$w_{TS}^o = 0.55278$; $w_{YM}^o = 0.30665$; $w_D^o = 0.03320$; and $w_{CR}^o = 0.10738$.

Step 2.2: AHP method proposed by Saaty (2000) is used for assigning the subjective weights. An attribute compared with self is always assigned the value 1 so the main diagonal entries of the pair-wise comparison matrix are all 1. The numbers 3, 5, 7, and 9 correspond to the verbal judgments 'moderate im-

Table 7. Material selection attributes of example 2

Material	Material selection attributes			
	Tensile strength (MPa)	Young's modulus (GPa)	Density (gm/ cm^3)	Corrosion resistance
1	1650	58.5	2.3	Average (0.5)
2	1000	45.4	2.1	Low (0.3182)
3	350	21.7	2.6	Low (0.3182)
4	2150	64.3	2.4	Average (0.5)
5	700	23	1.71	Above average (0.5909)

portance', 'strong importance', 'very strong importance', and 'absolute importance' (with 2, 4, 6, and 8 for compromise between the previous values). Let the decision maker assigns the following relative importance relations to the attributes:

$$\begin{array}{c} \\ TS \\ YS \\ D \\ CR \end{array} \begin{array}{c} \begin{array}{cccc} TS & YS & D & CR \end{array} \\ \begin{bmatrix} 1 & 1/3 & 1/4 & 3 \\ 3 & 1 & 1/3 & 4 \\ 4 & 3 & 1 & 5 \\ 1/3 & 1/4 & 1/5 & 1 \end{bmatrix} \end{array}$$

Following the AHP procedure, the weights of the attributes are calculated and these are: w_{TS}^{s}=0.1343; w_{YM}^{s}=0.2687; W_{D}^{s}= 0.5287; and w_{CR}^{s}=0.0683.

Step 2.3: The integrated weights of importance of the attributes are computed using Equation (4) for different objective and subjective weights of the attributes as shown below. The integrated weights are computed as, w_{TS}^{i} = 0.4090; w_{YM}^{i} = 0.4539; w_{D}^{i} = 0.0967; and w_{CR}^{i} = 0.0404.

Step 3: The preference index values are computed for different alternatives using Equations (5) to (7). The computed values of the preference index and the ranks are given in Table 8.

From the results given in Table 8, it can be understood that usage of only subjective weights of the attributes leads to materials ranking of 4-1-5-2-3 and suggests material 4 as the first choice. Usage of only objective weights of the attributes leads to 4-1-2-5-3 and suggests material 4 as the first choice. Usage of integrated weights also suggests material 4 as the first choice.

Table 8. Rankings of alternative materials of example 2

Material	Proposed decision making method w^s w^o w^i P^s Rank P^o Rank P^i Rank					
1	0.7984	2	0.8188	2	0.2692	2
2	0.7195	4	0.5585	3	0.1907	3
3	0.4970	5	0.2731	5	0.0991	5
4	0.8375	1	0.9739	1	0.3173	1
5	0.7368	3	0.4302	4	0.1235	4

CONCLUSION

A novel multiple attribute decision making method is proposed in this paper to deal with the problem of material selection for a given engineering design considering both qualitative and quantitative attributes. The proposed method helps the decision maker to arrive at a decision based on either the objective weights of importance of the attributes or subjective preferences or considering both the objective weights and the subjective preferences. If decision maker does not have adequate experience and knowledge to decide the subjective weights, the objective weights which are evaluated through the statistical variance procedure can be used as defaults. If decision maker possesses adequate experience and knowledge, then he or she can adjust the relative priority among design requirements using the subjective weights. If he or she wants to use both objective as well as subjective weights of the attributes, then the integrated weights can be used.

The methodology developed in this paper can simultaneously consider any number of quantitative and qualitative selection attributes and helps to obtain the preference index which evaluates and ranks alternative materials for a given selection problem. Furthermore, the paper suggests a ranked value judgment on a fuzzy conversion scale to represent the qualitative selection attribute (i.e. quantitative value is not available). The uniqueness of the proposed methodology is that it offers a general procedure that can be applicable to diverse selection problems encountered in design and manufacturing environment that incorporate vagueness and a number of selection attributes. The methodology is logical, simple and convenient to implement when compared with the other MADM methods.

ACKNOWLEDGMENT

The authors acknowledge the financial support of Council of Scientific and Industrial Research (CSIR), New Delhi, India to carry out this work.

REFERENCES

Ashby, M. F., Brechet, Y. J. M., Cebon, D., & Salvo, L. (2004). Selection strategies for materials and processes. *Materials & Design*, *25*, 51–67. doi:10.1016/S0261-3069(03)00159-6

Chan, J. W. K., & Tong, T. K. L. (2007). Multi-criteria material selections and end-of-life product strategy: a grey relational approach. *Materials & Design*, *28*, 1539–1546. doi:10.1016/j.matdes.2006.02.016

Chatterjee, P., Athawale, V. M., & Chakraborty, S. (2009). Selection of materials using compromise ranking and outranking methods. *Materials & Design*, *30*, 4043–4053. doi:10.1016/j.matdes.2009.05.016

Chen, S. J., & Hwang, C. L. (1992). *Fuzzy multiple attribute decision making-methods and applications (LNEMS)*. Berlin: Springer Verlag.

Edwards, K. L. (2005). Selecting materials for optimum use in engineering components. *Materials & Design*, *26*, 469–473. doi:10.1016/j.matdes.2004.07.004

Edwards, W., & Newman, J. R. (1986). *Multiattribute Evaluation*. Cambridge, UK: Cambridge University Press.

Fayazbakhsh, K., Abedian, A., Manshadi, B. D., & Khabbaz, R. S. (2009). Introducing a novel method for materials selection in mechanical design using Z-transformation in statistics for normalization of material properties. *Materials & Design*, *30*, 4396–4404. doi:10.1016/j.matdes.2009.04.004

Jahan, A., Ismail, M. Y., Mustapha, F., & Sapuan, S. M. (2010). Material selection based on ordinal data. *Materials & Design*. doi:10.1016/j.matdes.2010.02.024

Jalham, I. S. (2006). Decision-making integrated information technology (IIT) approach for material selection. *International Journal of Computer Applications and Technology*, *25*, 65–71. doi:10.1504/IJCAT.2006.008669

Jee, D. H., & Kang, K. J. (2000). A method for optimal material selection aided with decision making theory. *Materials & Design*, *21*(3), 199–206. doi:10.1016/S0261-3069(99)00066-7

Khabbaz, R. S., Manshadi, B. D., Abedian, A., & Mahmudi, R. (2009). A simplified fuzzy logic approach for materials selection in mechanical engineering design. *Materials & Design*, *30*, 687–697. doi:10.1016/j.matdes.2008.05.026

Maniya, K., & Bhatt, M. G. (2010). A selection of material using a novel type decision-making method: preference selection index method. *Materials & Design*, *31*, 1785–1789. doi:10.1016/j.matdes.2009.11.020

Manshadi, B. D., Mahmudi, H., Abedian, A., & Mahmudi, R. (2007). A novel method for materials selection in mechanical design: combination of non-linear normalization and a modified digital logic method. *Materials & Design*, *28*, 8–15. doi:10.1016/j.matdes.2005.06.023

Rao, R. V. (2006). A material selection model using graph theory and matrix approach. *Materials Science and Engineering A*, *431*, 248–255. doi:10.1016/j.msea.2006.06.006

Rao, R. V. (2007). *Decision making in the manufacturing environment using graph theory and fuzzy multiple attribute decision making methods*. London: Springer Verlag.

Rao, R. V. (2008). A decision making methodology for material selection using an improved compromise ranking method. *Materials & Design*, *29*, 1949–1954. doi:10.1016/j.matdes.2008.04.019

Rao, R. V., & Davim, J. P. (2006). A decision making methodology for material selection using a combined multiple attribute decision making method. *International Journal of Advanced Manufacturing Technology*, *35*, 751–760. doi:10.1007/s00170-006-0752-7

Saaty, T. L. (2000). *Fundamentals of decision making and priority theory with AHP*. Pittsburgh, PA: RWS Publications.

Sapuan, S. M. (2001). A knowledge-based system for materials selection in mechanical engineering design. *Materials & Design*, *22*, 687–695. doi:10.1016/S0261-3069(00)00108-4

Shanian, A., & Savadogo, O. (2006a). A material selection model based on the concept of multiple factor decision making. *Materials & Design*, *27*, 329–337. doi:10.1016/j.matdes.2004.10.027

Shanian, A., & Savadogo, O. (2006b). A non-compensatory compromised solution for material selection of bipolar plates for polymer electrolyte membrane fuel cell (PEMFC) using ELECTRE IV. *Electrochimica Acta*, *51*, 5307–5315. doi:10.1016/j.electacta.2006.01.055

Shanian, A., & Savadogo, O. (2006c). TOPSIS multiple-criteria decision support analysis for material selection of metallic bipolar plates for polymer electrolyte fuel cell. *Journal of Power Sources*, *159*, 1095–1104. doi:10.1016/j.jpowsour.2005.12.092

Torrez, J. B. (2007). *Light-weight materials selection for high-speed naval craft*. Unpublished doctoral dissertation, Massachusetts Institute of Technology, Cambridge, MA.

Triantaphyllou, E. (2000). *Multi-criteria decision making methods: a comparative study*. London: Springer Verlag.

Zha, X. F. (2005). A web-based advisory system for process and material selection in concurrent product design for a manufacturing environment. *International Journal of Advanced Manufacturing Technology*, *25*(3-4), 233–243. doi:10.1007/s00170-003-1838-0

APPENDIX

Converting Fuzzy Numbers to Crisp Scores

The method uses a fuzzy scoring approach. The crisp score of fuzzy number 'M' is obtained as follows:

$$\mu_{\max}(x) = \begin{cases} x, & 0 \le x \le 1 \\ 0, & \text{otherwise} \end{cases} \quad A \tag{1}$$

$$\mu_{\min}(x) = \begin{cases} 1 - x, & 0 \le x \le 1 \\ 0, & \text{otherwise} \end{cases} \quad A \tag{2}$$

The fuzzy-max and fuzzy-min of fuzzy numbers are defined in a manner such that absolute locations of fuzzy numbers can be automatically incorporated in the comparison cases.

The left score of each fuzzy number 'Mi' is defined as

$$\mu_L(M_i) = \text{Sup}_x[\mu_{\min}(x) \wedge \mu_{Mi}(x)] \; A \tag{3}$$

The $\mu_L(Mi)$ score is a unique, crisp, real number in (0,1). It is the maximum membership value of the intersection of fuzzy number M_i and the fuzzy min.

The right score may be obtained in a similar manner:

$$\mu_R(M_i) = \text{Sup}_x[\mu_{\max}(x) \wedge \mu_{Mi}(x)] \; A \tag{4}$$

Again, $\mu_R(M_i)$ is a crisp number [0,1].

Given the left and right scores, the total crisp score of a fuzzy number M_i is defined as:

$$\mu_T(M_i) = [\mu_R(M_i) + 1 - \mu_L(M_i)]/2 \; A \tag{5}$$

From Figure 1, membership functions of M_1, M_2, M_3, M_4, M_5, M_6, M_7, M_8, M_9, M_{10} and M_{11} are written as:

$$\mu M_1(x) == \begin{cases} 1, & x = 0 \\ (0.1 - x)/(0.1), & 0 \le x \le 0.1 \end{cases}$$

$$\mu M_2(x) = \begin{cases} (x - 0)/(0.1), & 0 \le x \le 0.1 \\ (0.2 - x)/(0.1), & 0.1 \le x \le 0.2 \end{cases}$$

$$\mu M_3(x) = \begin{cases} (x - 0.1)/(0.1), & 0.1 \le x \le 0.2 \\ (0.3 - x)/(0.1), & 0.2 \le x \le 0.3 \end{cases}$$

$$\mu M_4(x) = \begin{cases} (x-0.2)/(0.1), 0.2 \le x \le 0.3 \\ (0.4-x)/(0.1), 0.3 \le x \le 0.4 \end{cases}$$

$$\mu M_5(x) = \begin{cases} (x-0.3)/(0.1), 0.3 \le x \le 0.4 \\ (0.5-x)/(0.1), 0.4 \le x \le 0.5 \end{cases}$$

$$\mu M_6(x) = \begin{cases} (x-0.4)/(0.1), 0.4 \le x \le 0.5 \\ (0.6-x)/(0.1), \ 0.5 \le x \le 0.6 \end{cases}$$

$$\mu M_7(x) = \begin{cases} (x-0.5)/(0.1), \ 0.5 \le x \le 0.6 \\ (0.7-x)/(0.1), \ 0.6 \le x \le 0.7 \end{cases}$$

$$\mu M_8(x) = \begin{cases} (x-0.6)/(0.1), \ 0.6 \le x \le 0.7 \\ (0.8-x)/(0.1), \ 0.7 \le x \le 0.8 \end{cases}$$

$$\mu M_9(x) = \begin{cases} (x-0.7)/(0.1), \ 0.7 \le x \le 0.8 \\ (0.9-x)/(0.1), \ 0.8 \le x \le 0.9 \end{cases}$$

$$\mu M_{10}(x) = \begin{cases} (x-0.8)/(0.1), \ 0.8 \le x \le 0.9 \\ (1-x)/(0.1), \ 0.9 \le x \le \ 1 \end{cases}$$

$$\mu M_{11}(x) = \begin{cases} (x-0.9)/(0.1), \ 0.9 \le x \le 1 \\ 1, x \ = \ 1 \end{cases}$$

The right, left, and total scores are computed as follows for M_1:

$\mu_R(M_1)=\text{Sup}[\mu_{max}(x)\hat{}\mu_{Mi}(x)]=0.0909$ x

$\mu_L(M_1)=\text{Sup}[\mu_{min}(x)\hat{}\mu_{Mi}(x)]=1$ x

$\mu_T(M_i)=[\mu_R(M_i)+1-\mu_L(M_i)]/2=0.0455$

Similarly, the` right, left, and total scores are computed for the remaining ten fuzzy numbers and are tabulated as shown in Table 2.

This work was previously published in the International Journal of Manufacturing, Materials, and Mechanical Engineering, Volume 1, Issue 1, edited by J. Paulo Davim, pp. 43-56, copyright 2011 by IGI Publishing (an imprint of IGI Global).

Chapter 16
Attribute Based Selection of Thermoplastic Resin for Vacuum Infusion Process: A Decision Making Methodology

R. T. Durai Prabhakaran
Technical University of Denmark, Denmark

Aage Lystrup
Technical University of Denmark, Denmark

Tom Løgstrup Andersen
Technical University of Denmark, Denmark

ABSTRACT

The composite industry looks toward a new material system (resins) based on thermoplastic polymers for the vacuum infusion process, similar to the infusion process using thermosetting polymers. A large number of thermoplastics are available in the market with a variety of properties suitable for different engineering applications, and few of those are available in a not yet polymerised form suitable for resin infusion. The proper selection of a new resin system among these thermoplastic polymers is a concern for manufactures in the current scenario and a special mathematical tool would be beneficial. In this paper, the authors introduce a new decision making tool for resin selection based on significant attributes. This article provides a broad overview of suitable thermoplastic material systems for vacuum infusion process available in today's market. An illustrative example—resin selection for vacuum infused of a wind turbine blade—is shown to demonstrate the intricacies involved in the proposed methodology for resin selection.

DOI: 10.4018/978-1-4666-1867-1.ch016

Copyright © 2013, IGI Global. Copying or distributing in print or electronic forms without written permission of IGI Global is prohibited.

1. INTRODUCTION

Ever growing demand of composites for high productivity includes the use of thermoplastics resins for variety of engineering applications making it a vital business in the market. Industries are constantly developing new applications using thermoplastics technology to find solutions for high performance products by interacting with their customers, and business partners. Designing such a new material which can be processed similar to the processing of thermosetting polymers is a challenging and a critical task in the design and development of composite products for diverse engineering applications. Constituent materials play a crucial and important role during the entire design and manufacturing process of composites. Hence wrong selection of material often leads to huge cost involvement and ultimately drives towards premature component or product failure. So the designers need to identify and select proper materials, by defining proper functionalities satisfying attributes requirement and expecting the desired output with minimum cost involvement and specific applicability.

In spite of many advantages associated with processing of thermosetting composite, there is a recent industrial trend to choose high-performance thermoplastic resins due to its potential for recyclability, superior toughness, weldability, thermal processability and environmental friendly, but they require often high pressure and high temperature processing. This will end up with expensive processing techniques, especially for geometrically complex and larger products. Therefore, there is a wish to be able to use the versatile Vacuum Assisted Resin Infusion Method (VARIM), which is the preferred manufacturing process for complex and larger shaped geometrical products used in today's industrial environments for thermosetting composites. There is very few reports cited in the open literature about development and use of new kinds of thermoplastic polymers for the VARIM process (Brønsted et al., 2005; Van Rijswijk et al., 2006; Khattab & EI-Gizawy, 2008).

In general, liquid molding of thermoplastics has limitations because of high resin viscosity, high temperature processing requirements, and a narrow processing window (Ramesh & Jan-Anders,(2000; Rudd et al., 1997). The main obstacle to the economic manufacturing of a large thermoplastic composite like wind turbine blade is that the flow viscosity of most thermoplastic polymers is very high, in comparison to the viscosity of uncured thermosetting resins. Thermoplastic polymers with desirable mechanical properties such as polybutylene terephthalate (PBT), polyethylene terephthalate (PET), polyamide-6 (PA6), polyamide-12 (PA12), polyamide-6,6 (PA6,6) and also polyether ether ketone (PEEK), polyetherketoneketone (PEKK) and polyphenylene sulphide (PPS), have flow viscosities several orders of magnitude higher than uncured epoxy, polyester or vinyl ester resins. Few articles report how thermoplastic materials like casting grade PA6 - caprolactam with a sodium-based catalyst, and an initiator are used to study the intricacies involved in processing composites using VARIM (Van Rijswijk et al., 2005a, 2005b). This system allows the resin to maintain a very low viscosity (<1 Pa·s) for a reasonable period of time, at relatively low temperatures (1000C). Another resin called cyclic butylenes terephthalate (CBT®) resin, which is a solid material that melts to ultra-low viscosity and polymerizes into poly butylenes terephthalate (PBT). This resin is processed like a thermosetting and ends up like a thermoplastic (Mallon et al., 2003; Hakme et al., 2007) (http://www.eirecomposites.dom/wind_energy_composites.asp).

This paper attempts to solve the materials selection problem using the most potential multi-attribute decision-making (MADM) approach and compares their relative performance for a given resin selection to VARIM / (VARTM) process. The MADM approach used in this study is a combined TOPSIS (Technique for Order Prefer-

ence by Similarity to Ideal Solution) and Analytic Hierarchy Process (AHP) method, which is an entirely new ranking method (Rao, 2006; Chakladar & Chakraborty, 2008). The illustration shown in this article helps to demonstrate and validate the effectiveness and flexibility of this new MADM approach. In this illustration, a list of all the possible choices from the best to the worst suitable materials is obtained taking into account different material selection criteria. The proposed methodology is a general method and can consider any number of quantitative and qualitative resin selection attributes simultaneously and offers a more objective and rational resin selection approach.

2. LITERATURE OVERVIEW

Liquid Composite Moulding (LCM) becomes increasingly popular because of its low production cost, short cycle time, good quality control, ability to manufacture high performance composites with complicated geometry, and clean working environment. Processes in this category include resin transfer moulding (RTM), structural reaction injection moulding (SRIM), vacuum assisted resin transfer moulding (VARTM) / vacuum assisted resin infusion moulding (VARIM) etc (Ryan et al., 1995; Goren & Atas, 2008; Khattab, 2003). The present paper mainly focuses on VARIM process and its resin selection.

2.1. Vacuum Assisted Resin Infusion Molding Process

In the 1990s, Seeman patented his new methods for the manufacturing polymer composites (Williams et al., 1996). These methods are called "Seeman Composite Resin Infusion Moulding Process" (SCRIMP), in which a soft mould half (vacuum bag) and a rigid mould half were used and highly permeable medium and peel ply were employed. In fact, SCRIMP is a type of VARTM (also named as VARIM). Because external heating may not be necessary and soft vacuum bag can be used as a mould, the cost of VARIM is much lower than that of RTM. Moreover, VARIM is also a close-mould process, and volatile organic chemical (VOC) emissions are significantly reduced. Hence, this process has become a preferably used industrial process for large scale products with less emission. In general, the infusion process comprises from two basic steps. First, sufficient dry reinforcement is placed onto the surface of the substrate so to meet the structural requirements, and secondly a curable resin is introduced such that the reinforcement is impregnated and the resin is solidified. Figure 1 shows various materials used in the infusion process.

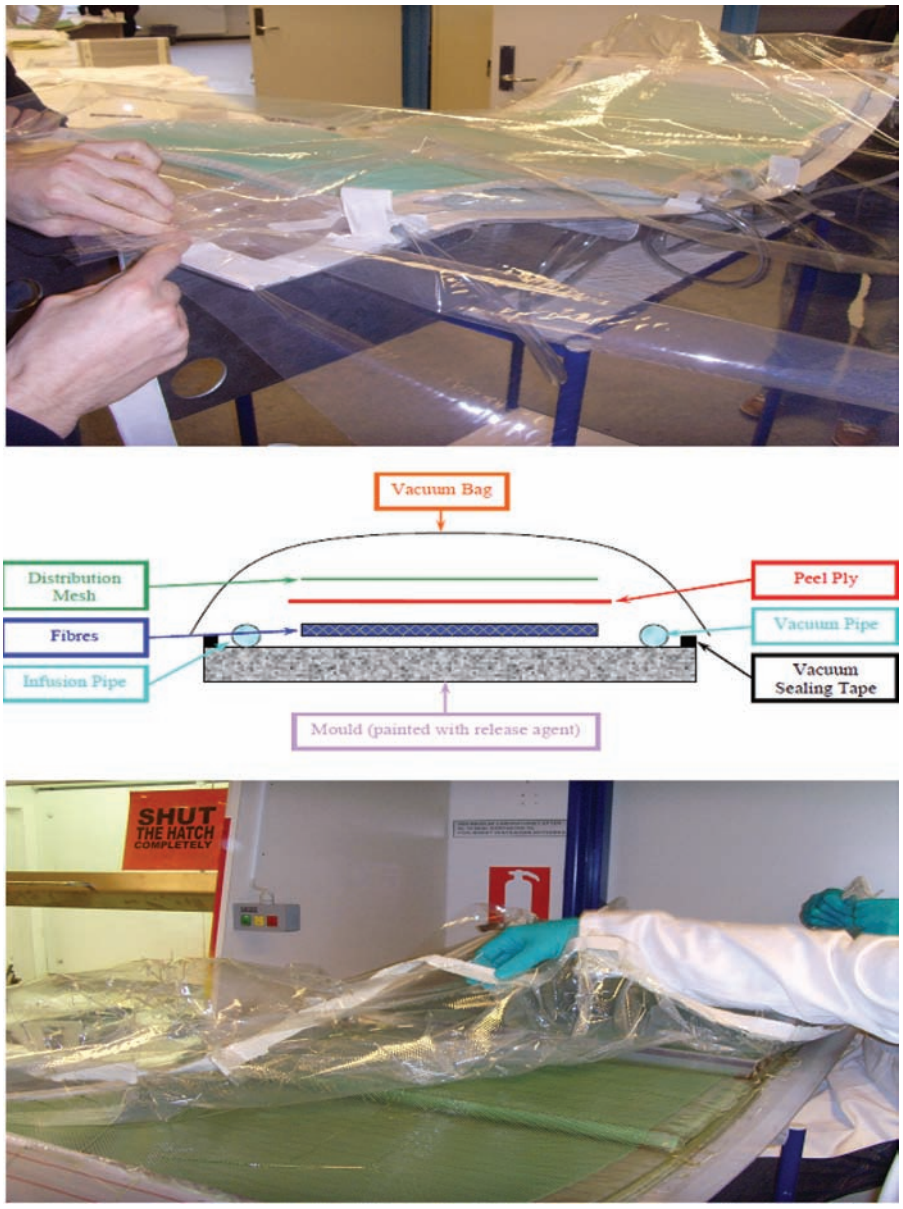
2.2. Thermoplastic Resins

Substantial work in liquid moulding of thermoplastic resin composites has recently been reported using thermoplastic resins like anionic polyamide 12 (APA12) (Zingraff et al., 2002; Luiser et al., 1999), cyclic polybutylene therephthalate (PBT) (Ciavacco& Winckler, 2000; Parton & Verpoest, 2003) and anionic polyamide 6 (APA6) (Vlasveld et al., 2003; Van Rijswijk et al., 2003).

2.2.1. Polyamide 6 (PA 6)

Anionic polymerization of lactams is the most developed way for reactive processing of thermoplastics through ring-opening polymerization (ROP). The anionic ROP of e-caprolactam (Tm = 69°C) into high molecular weight polyamide-6 (PA6), is a catalyzed reaction performed at 130–170°C. Final conversions of up to 99.3% can be obtained in 3–60 min, depending on the type and amount of activator and catalyst added. Since processing takes place below the polymer melting and crystallization point, the polymerization and crystallization take place simultaneously, resulting in solid highly crystalline PA6. Van Rijswijk et al. (2006b) and Joncas et al. (2006) are using an AP Nylon® casting resin with water-like viscosity

Figure 1. Schematic diagram and experimental set up for the VARIM process (Top: Sealing of the vacuum bag to the tool. Middle: Schematic diagram. Bottom: Removal of vacuum bag from cured part)



to impregnate a stack of 'dry' glass fibre fabrics, after which in situ polymerization of the semi-crystalline anionic polyamide-6 (APA6) matrix takes place within 30 minutes at temperatures around 180ºC. Using vacuum as driving force for infusion, impregnation and shaping allows manufacturing of composite parts of virtually infinite size and thickness. The Van Rijswijk et al. (2006b) conducted research in the following three inter-related steps: (1) polymerization of APA6, (2) processing of un-reinforced APA6 panels, and (3) vacuum infusion of APA6 composites. On a parallel track, the necessary processing equipment and tooling were developed by Delft University of Technology, Netherlands.

Composites with 25 mm thick and 50% glass fibres by volume were successfully infused with the technology described in a European patent ('EP1975 191 A1'). The formation of crystals related to the self-braking mechanism that is incorporated in the exothermic polymerization of APA6 has important consequences for manufacturing of thick composites as it will prevent the occurrence of excessive core temperatures and will allow the use of fast curing APA6 systems (Vaidya& Chawla, 2008). It is emphasized that the sensitivity of the polymerization reaction to moisture and oxidation requires a clean and controlled production process and a certain level of skill. Furthermore, the reacted PA6 resin is completely dry right after processing, but it may take up about 2-3% of moisture when exposed to standard environment; which is 23 °C and 50% relative humidity. For example, big structures like wind turbine blade (4 tons) with a fibre content of 65% (weight) may take up about 40 kg of moisture.

Selvum et al. (2005) presented a study on processing parameters, methodology, and limitations of using PA6 matrix materials for VARIM composites. They did microscopic studies, which evaluate wet-out of the fibres at both the tow and the filament levels. The effects of infusion (temperature, flow distance) on the fibre weight fraction and crystallinity of the PA6 resin are investigated. The increase in degradation temperature is attributed to the increase in crystallinity of the PA6 in the composite. The degree of conversion of monomer to polymer was studied as a function of processing conditions.

2.2.2. Poly-Butylene Terephthalate (PBT)

Parton and Verpoest (2005), reported an experimental study on production and mechanical properties of glass fibre reinforced polybutylene terephthalate (PBT) starting from cyclic butylenes terephthalate (CBT resin). They use a new processing sequence and a higher reactivity of the oligomer/catalyst mixture, leading to a more rapid increase in viscosity, limiting the time window for impregnation in a RTM process. The prepolymers used in their study were the cyclic butylene terephthalate oligomers (CBT resin), which are precursors for the semi-crystalline engineering thermoplastic polymer PBT. The number of butylgroups in the oligomer mixture varies from two to seven, resulting in a melting range from 130–160°C. Before processing, the oligomers were dried overnight at 110°C to remove residual moisture, which could interfere with the polymerization reaction. The production method described by the author is based on the RTM process, in general associated with manufacturing of thermosetting composites. Few research articles (Shahzad et al., 2010; Mohd Ishak et al., 2006) report that the CBT matrix material with high degree of crystallization results in a brittle matrix, which has low elongation at break and poor impact strength. To reduce the crystallinity during isothermal processing, few additions like polycaprolactone and Carbon NanoTubes (CNTs) can be added into the CBT oligomers in order to improve the fracture toughness of the thermoplastic composites (Baets et al., 2008).

Éire Composites Teo., Ireland, has participated in a project (Green Blade) on development of a larger wind turbine blade using vacuum infusion of liquid thermoplastics CBT resin as listed in Table 1, which has the following advantages:

- A two-thirds decrease in manufacturing time for large blades over existing thermosetting composites technology
- Significant reduction in cost of manufacturing blades
- A recyclable wind turbine blade at end of life
- Recycling possible of manufacturing waste / cut-offs
- Zero emissions of Volatile Organic Compounds into the workplace

Table 1. CBT® resin descriptions and properties: Typical values (http://www.cyclics.com/)

Property	Unit	CBT® 100	CBT® 160	CBT® 500	CBT® XL101
Product Description		**Cyclic polybutylene teraphthalate used as an additive**	**Cyclic polybutylene teraphthalate with polymerization catalyst for use with composites**	**Cyclic polybutylene teraphthalate used for casting and properties**	**Cyclic polybutylene teraphthalate containing polyester modifier, polymerization catalyst and processing stabilization package used for rotational molding**
Appearance		White pellets or powder	White pellets or powder	White pellets or powder	White pellets
Melting Range	^{0}C	120 - 200	120 - 200	120 - 200	120 - 200
Density 20^{0}C (Solid)	g/cm^3	1.3	1.3	1.3	1.3
Water content	ppm	<2000 target <1000 typical	<2000 target <1000 typical	<2000 target <1000 typical	<1000 <50 (dry bagged)
Typical processing Temperature	^{0}C	n/a	180 - 250	180 - 210	Similar to PE profile in rotomolding
Max Processing temperature	^{0}C	340	260	260	260
Polymerization Molecular Weight[1]	g/mol	n/a	>100,000	>100,000	>100,000
1 Gel permeation chromatography relative to polystyrene standards					

They developed a 12.6m long demonstration blade in thermoplastic composites. The 'Green Blade Project' consisted of design of the blade, development of tooling, characterization of materials, manufacturing and testing of the blade [http://www.eirecomposites.com/wind_energy_composites.asp] (However, it is unclear if the blade were manufactured by the above mentioned material and process).

2.2.3. Polyphthalamide (PPA)

Polyphthalamide ((PPA) - High Performance Polyamide) is a thermoplastic synthetic resin of the nylon family with semi-crystalline material, aromatic polyamide composed from a diacid and a diamine. However, the diacid portion contains at least 55% terephthalic acid (TPA) or isophthalic acid (IPA). TPA or IPA are aromatic components which serve to raise the melting point, glass transition temperature and generally improve chemical resistance vs. standard aliphatic nylon polymers. Compared to nylon 6/6, it is stronger, stiffer, less sensitive to moisture, and has higher thermal capabilities. It has significant chemical fatigue and creep resistance. It is used to replace metals in high temperature automotive applications, as the housing for high temperature electrical connectors and multiple other uses Niccolo et al. (2006).

Niccolo et al. (2006) presented perspectives for reactive molding of a high-temperature resistant polyphthalamide (PPA). Thermoanalytical, rheological, and optical tests were performed to assess the behavior of low-melting PA 6T/6I oligomers with increasing temperature and to monitor the polymerization and crystallization reactions. At higher temperatures, the viscosity of the oligomeric melt decreases further until a high temperature crystallization process occurs at about 180^{0}C. Polymerization starts at about 220^{0}C and ends at 290^{0}C. During the reaction the polymer crystallizes as soon as it is formed with an achievable degree of crystallinity considerably higher than that of melt-crystallized samples.

2.2.4. Polymethylmethacrylate (PMMA)

Poly(methyl methacrylate) (PMMA) is the synthetic polymer of methyl methacrylate; simply called Acrylic, which also refers to polymers or copolymers containing polyacrylonitrile. Methyl methacrylate is the basic molecule, or monomer, from which polymethyl methacrylate and many other acrylic plastic polymers are formed. The chemical notation for this material is CH2=C(CH3) COOCH3. Methyl methacrylate may be formed in several ways. One common way is to react acetone [CH3COCH3] with sodium cyanide [NaCN] to produce acetone cyanhydrin [(CH3)2C(OH)CN]. This in turn is reacted with methyl alcohol [CH3OH] to produce methyl methacrylate.

The density of this polymer is 1.15–1.19 g/cm^3. Control of temperature is especially critical to the polymerization process. Even the initial temperatures of the monomer and catalyst are controlled before they are introduced into the mold. During the entire process, the temperature of the reacting material is monitored and controlled to ensure the heating and cooling cycles have the proper temperature and duration (Subramaniyan & Sub, 2006).

2.2.5. Polyethylene Terephtalate (PET)

PET exists both as an amorphous (transparent) and as a semi-crystalline (opaque and white) thermoplastic material. Generally, it has good resistance to mineral oils, solvents and acids but not to bases. The semi-crystalline PET has good strength, ductility, stiffness and hardness. The amorphous PET has better ductility but less stiffness and hardness (Van Rijswijk & Bersee, 2007).

Macrocyclic oligomers can be obtained through cyclodepolymerization (CDP) of linear PET and subsequently repolymerized through ring-opening metathesis polymerization (ROMP) into high molecular weight (MW) PET with polymerization using a cyclic dimer (T_m = 250°C). Up to 100% conversion at 250–325°C are obtained in several hours without a catalyst, whereas addition of a catalyst reduces the reaction time to 3–15 min at 225°C. The initial melt viscosity of the cyclic precursors is 30 mPa·s.

3. IDENTIFICATION OF RESIN SYSTEM ATTRIBUTES

Composite processing involves a very careful review of the constituent properties mainly resin system properties. The intricacies of the interaction of the properties have to be understood clearly, in order to make a selection of resin (whether it is thermosetting or thermoplastic resins). The following are the attributes of typical resin system which have major influence in selection of process, selection of reinforcements, selection of tooling system, and selection of product design parameters (Durai Prabhakaran et al., 2006a).

General Resin Properties

1. Density
2. Colour of resin
3. Melting temperature
4. Molecular weight
5. Heat deflection temperature
6. Moisture content
7. Viscosity
8. Degree of crystallization
9. Percentage of conversion
10. Glass transition temperature
11. Processing temperature
12. Specific gravity

Mechanical Properties

13. Tensile strength
14. Elongation at break
15. Tensile modulus
16. Flexural strength
17. Flexural modulus

18. Izod impact strength
19. Compression strength
20. Hardness
21. Strain to failure
22. Permeability

Chemical Properties

23. Chemical resistivity
24. Corrosion resistance
25. Water absorption
26. UV stability

Other Properties

27. Cost/Price per kg
28. Availability
29. Recycling
30. Paint-ability
31. Weldability
32. Coefficient of thermal expansion
33. Thermal conductivity
34. Dielectric strength

4. DECISION MAKING METHODOLOGY

Materials selection is a technical activity that bridges a number of engineering areas, viz., design, cost, materials and processes, but can also be related to non-technical issues, such as marketing and techno-economic forecast. The systematic approach presented here is a mathematical tool, available to arrive at a decision under different criteria of material selection. One of these is TOPSIS (Technique for Order Preference by Similarity to Ideal Solution), based on the concept that the chosen alternative should have the shortest Euclidean distance from the ideal solution and the farthest from the negative ideal solution by Hwang and Yoon (1982). The TOPSIS is an MADM approach suitable for computer programming as observed by Ahluwalia et al. (1993). They presented a methodology for the evaluation and optimum selection of roller bearings on the basis of TOPSIS.

4.1. Attribute Based Selection Procedure

The objective of the paper is to describe a selection methodology to enable a user to first narrow down the list of (see Table 2 for general thermoplastic resins) alternative available materials to a manageable limit and then to devise a method of trade-off between alternatives to make it possible to rank them accordingly. The evaluation and selection procedure is described below under the algorithm section.

4.2. Algorithm - Combined MADM Method

The multiple attribute decision making procedure first proposed by Hwang and Yoon (1982) is discussed in details by Durai Prabhakaran et al. (2006b), Waigaonkar et al. (2008) and other researchers like (Rao & Davim, 2008). A brief step by step procedure is presented below:

Stage 1. Elimination search: From the available resin system attributes in the electronic database related to several design aspects, obtain pertinent resin attributes of threshold values with manageable number which may satisfy all the requirements and constraints of several design activities concurrently.

Stage 2. Evaluation and Ranking Procedure using combined TOPSIS and AHP **(**Combined MADM Method):

Step1. Prepare a design database matrix or decision matrix 'D', where row 'i' corresponds to ith alternative design system and column 'j' corresponds to the selected pertinent design attribute of the concurrent design system. The matrix $D_{mxn} = [d_{ij}]$ where i = 1,2,..,m; j = 1,2,…,n.

Table 2. List of thermoplastic resins available in the market

Material Type	Structure	T_g (^{0}C)	Service Temp Long Time (^{0}C)	T_m (^{0}C)	Density (g/cm^3)	Tensile Strength (MPa)	Tensile Modulus (GPa)	Elongation at Break (%)	Water absorption (%)
Polybutylene Terephtalate (PBT)	**SCr**	**(25-60)**	**60-120**	**225**	**1,31**	**85**	**1,8-2,7**	**30**	**0,09**
Polyethylene Naphtalate (PEN)	SCr	120	155	270	1,36		5,5	60	-
Polyethylene Terephtalate (PET)	**SCr**	**72**	**80-150**	**255**	**1,38**	**69**	**3**	**13**	**0,5**
Polypropylene (PP)	**SCr**	**-10**	**100-110**	**166**	**0,9**	**26**	**1,4**	**32**	**0,03**
Polyphenyle sulfide (PPS)	SCr	90	240	280	1,35	90	3,8-4,2	3	-
Polyamide 6 (PA 6)	**SCr**	**40-60**	**90-150**	**219-230**	**1,13**	**85**	**2-3,8**	**19**	**6-11**
Polyamide 66 (PA 66)	**SCr**	**78**	**90-160**	**263**	**1,14**	**70**	**1,5-3**	**>50**	**8,5**
Polyamide 11 (PA 11)	SCr	(115-170)	90-140	181-183	1,03-1,05	25	0,2-2,1	>50	1,1-2,0
Polyamide 12 (PA 12)	SCr	(115-170)	60-150	171-178	1,01-1,06	45	1,1	-	1,1-1,8
Polyamide 4,6 (PA 46)	SCr	75	160	295	1,17-1,18	50	1-1,4	-	3,7
Polyethylene -High Density (HDPE)	**SCr**	**-**	**60-100**	**127**	**0,95**	**30**	**1,2**	**>200**	**0,01**
PolyetherimidE (PEI)	A	220	150-180	370-410	1,27	105	3,2	>50	1,25
Polyimide (PI)	SCr	250-300	250-320	>400	1,42	124	6,9	3,3	0,2-2,9
PolyethersulfonE (PES)	A	230	180	340-390	1,37	90	2,7	40	2,1
Polymethylmethacrylate (Akryl) (PMMA)	A	-	50-90	-	1,18	68	3,2	4	1,7-2,5
Polyoxymethylene (Acetal) (POM)	SCr	-30	90-110	166-178	1,39-1,42	64	2,6	30	0,6-1,9
Polyphenylsulfone (PPSU)	A	220	150-220	360-390	1,28-1,3	76	2,3	>5	0,6
Polycarbonate (PC)	A	150	100-130	300	1,20	60	2,2	>100	0,16
Polysulfone (PSU)	A	187-190	100-150	343	1,24-1,25	70	2,4	75	0,8
Polyvinyliden Flouride (PVDF)	SCr	-40	50-150	175	1,77	57	2,4	23	0,02-0,15
Polyphthalamide (PPA)	-	-	138	-	1,2	75	3,2	3	0,36
Polyphenylene ether (PPE)	-	-	150-230	360	1,37	60	3,1	11	2,3
Polystyrene (PS)	A	85	50-70	90	1,05	42	3,3	1,5	<0,4
Polyetheretherketone (PEEK)	SCr	143	250	343	1,26-1,32	100	4,1	<60 / 5	0,5

continued on following page

Table 2. Continued

Material Type	Structure	T_g (^{0}C)	Service Temp Long Time (^{0}C)	T_m (^{0}C)	Density (g/cm^3)	Tensile Strength (MPa)	Tensile Modulus (GPa)	Elongation at Break (%)	Water absorption (%)
Polytetraflourethylene (teflon) (PTFE)	SCr	127	140-260	380	2,15	10-40	0,7	350	0,00
Polybenzimidazole (PBI)	A	-	260-400	>450	1.3	160	5,9	3	0,4
Polyethylene - Low Density (PE-LD)	SCr	-	35	120	0,92	5-25	0,1-0,3	>400	0,02
Polyvinylchloride (PVC)	A	-	50	80	1,4	60	~3	40	0,4
Ethylene Vinyl Acetate (EVA)	A	-	35	80	0,93	13	-	800	0,07
Acrylonitrile Butadiene Styrene (ABS)	A	-	90	105	1,05	29	-	20	0,27
Styrene Acrylonitrile (SAN)	A	-	85	115	1,08	0,01	3,4	4	-
Thermoplastic Polyurethane (TPU)	A	-	115	140	1,2	40	-	>500	-

Step2. It is necessary to bring all the attributes (having different units or measured on different interval scales) in the common range (0-1) by normalization. Construct normalized decision matrix 'R' from decision matrix 'D', where

$$r_{ij} = \frac{d_{ij}}{\left(\sum_{i=1}^{m} d_{ij}^2\right)^{1/2}} \quad (1)$$

where $i = 1, ..., m$; $j = 1, ..., n$ d_{ij} is an element of the decision matrix, **D**.

Step3. Form relative importance matrix 'N' = [n_{ij}], where the matrix element n_{ij} represents the importance of ith design attribute over jth resin attribute for given application. This is decided by a team of design experts on the basis of pair-wise comparison.

$$\text{where } n_{ij} = \frac{importance\ of\ i^{th}\ attribute}{importance\ of\ j^{th}\ attribute} \quad (2)$$

1. To overcome the effect of error introduced by pair-wise comparison, Eigen value formulation is introduced using AHP method. The methodology follows the below steps
   a. Calculating the geometric mean of ith row
   b. Normalizing the geometric means of rows in the comparison matrix

This can be represented as

$$GM_i = \left\{\prod_{j=1}^{N} a_{ij}\right\}^{1/N} \quad (3)$$

and

$$W_j = \frac{GM_i}{\sum_{i=1}^{N} GM_i} \quad (4)$$

The above equations derived from AHP is used to find out the relative normalized weights of the

attributes because of its simplicity and easiness to find out the maximum eigen value and to reduce the inconsistency in personal judgments.

2. Calculate matrix N3 and N4 such that N3 = N1 x N2 and N4 = N3/N2, where N2 = $\{w_1, w_2, ..., w_n\}^T$.
3. Find out the maximum Eigen value from Eigen spectrum as $\{\lambda_1, \lambda_2, ..., \lambda_{max}, ...,\lambda_n\}$.
4. Calculate the consistency index CI = $\frac{(\lambda_{max} - N)}{(N-1)}$. The smaller the value of CI, the smaller is the deviation from the consistency.
5. Obtain the random index (RI) for the number of attributes used in decision making.
6. Calculate the Consistency ratio CR = $\frac{CI}{RI}$. Usually CR $\leq$ 1is acceptable for best solution

Step4. Determine weighted normalized matrix 'V' using 'N' and 'W' as follows

$$V_{ij} = w_j * n_{ij}, \text{ where } i = 1,2,....., m \quad (5)$$

Step5. To find out an optimum solution, which is closest to the hypothetical best (ideal) resin system ***V**** and the farthest from the hypothetical worst (negative ideal) resin system ***V***$^-$, ideal and negative ideal resin system are generated from the V-matrix as follows

$$V^* = [(\max_j v_{ij} / j \in J), (\min_j v_{ij} / j \in J', i = 1, 2, \ldots, m)] = [v_1^*, v_2^*, \ldots, v_n^*]^T \quad (6)$$

$$V^- = [(\min_j p_{ij} / j \in J), (\max_j p_{ij} / j \in J', i = 1, 2, \ldots, m)] = [v_1^-, v_2^-, \ldots, v_n^-]^T \quad (7)$$

Where J = {j = 1,2,….,n}, j is associated with benefit/quality criteria, J ' with cost/error criteria.

Step6. Represent each design candidate system in n dimensional attribute space. Calculate separation measures S_i^* and S_i^- for each resin system alternative. This separation is measured by the n-dimensional Euclidean distance expressible as

Separation of ith resin system candidate from the ideal is given by

$$S_i^* = \left[\sum_{j=1}^{n} \left(v_{ij} - v_j^*\right)^2\right]^{1/2} \quad (i = 1,2,\ldots\ldots,m) \quad (8)$$

Separation of ith resin system candidate from the negative ideal is given by

$$S_i^- = \left[\sum_{j=1}^{n} \left(v_{ij} - v_j^-\right)^2\right]^{1/2} \quad (i = 1,2,\ldots\ldots,m) \quad (9)$$

Step7. A resin selection index RSI_i* (a single number evaluation measure of multiple attribute problem) is calculated from the formula for all the attributes related to several resin systems in the database

$$RSI_i^* = \frac{S_i^-}{S_i^* + S_i^-}, \text{ where } i = 1,2,..., m \quad (10)$$

Step8. Preferences rank the alternatives according to descending order of D_i*. This index represents relative closeness of the candidate resin system to the ideal solution. This index lies between 0 to 1, and is a measure of goodness of the resin system, for the chosen application on the basis of 'n' attributes selected for decision making. A resin system with the largest index is the optimum system for composite manufacturing. The candidate resin systems are arranged in the descending order of their indices. This order represents their ranking in order of their preference.

Stage 3. Optimum Selection: The final selection of the best possible resin alternative for the composite product design and development is done from the rank list considering the number of invisible attributes, like market availability, company & manufacturing strategies etc.

4.3. Ranking and Selection of the Resin System

The decision matrix along with normalized data matrix and weighted normalized data matrix are useful candidate matrices for selection of best resin system as well as selection of the positive benchmark system. A measure to compare the resin candidates with benchmark candidate resin is needed so that they can be ranked and selected. Let it be called as Resin Selection Index (RSI). The value of RSI is a positive fraction ($0 \leq RSI \geq 1$) and is a measure of the closeness of candidate resin system with the benchmark one. The candidates with RSI magnitude closer to unity are preferable, since it indicates the closeness to the positive benchmark resin system.

5. SELECTION OF THERMOPLASTIC RESIN FOR VACUUM INFUSED WIND TURBINE BLADE – AN ILLUSTRATIVE EXAMPLE

The motivation for this study stems directly from the needs of a designer, manufacturer and users, who want to select the suitable resin system, based on number of thermoplastic resins available in the market for vacuum infusion of thermoplastic composite wind turbine blades. This approach provides good insight into how the cost and manufacturing time are reduced and how the product quality and reliability are improved.

5.1. Identified Criteria for Resin Selection

The temperature is an important parameter in relation to the manufacturing process. The process temperature should be as low as possible in order to minimise degradation of fibre sizing, energy consumption and cost of accessories like vacuum bagging, sealants and moulds for high temperatures. After a thorough literature study of the various thermoplastic resins for vacuum infusion, candidate thermoplastic resin systems will be pre-selected based on the criteria listed.

The criteria for the pre-selection are:

- Viscosity of the neat resin should be less than 1 Pa·s (1000 cps) to enable VARIM processing
- T_g (glass transition temperature) of the neat resin should preferable be higher than 50-60°C
- The process temperature should be lower than 230°C, so that low cost accessories can be used
- The resin should have a long pot life
- Cost of the resin should be affordable
- Availability of basic knowledge and technology

Based on the above criteria's, the candidate resins which satisfy the VARIM process are listed below in Table 3. The values shown under '**cost**' column in the Table 3 are taken by various sources like published literature (Van Rijswijk et al., 2005b; Niccolo et al., 2006), discussion with industry (http://www.cyclics.com/pdf/CBT500_Composites.pdf), and literature available in the web (Van Rijswijk et al., 2005a; Van Rijswijk, 2007) (http://www.brueggemann.com/english/kunststoffadditive1.html).

5.2. Selection of Resin Based on Practical Approach

The group of experts in design and manufacturing of composites follow the below steps to select the resin material by evaluating the attributes using practical approaches.

The Resin viscosity is the important attribute to consider the resin selection, in particular to vacuum infusion process limits the maximum viscosity of the resin to 1 Pa·s. Impregnation of reinforcement is a critical issue for making a thick laminates, hence resin viscosity should be as low as possible to wet out the fibre layups. This limit is a value used in practice in order to infuse large composite parts in sufficiently short times. Reactive processing of TPU and PMMA commonly involves a pre-polymerization step, during which the viscosity becomes too high for vacuum infusion. Of the reactive thermoplastic oligomers, only PEK seems a feasible material system. The materials cost plays a significant role for developing big structures like wind turbine blade. The total weight of the blade consists of tonnes of resin and reinforcements, For example the recent largest blade in the world produced by LM Glasfiber A/S is 61.5m long, and the total weight of the blade is 17,740 kg. In general the blade consists of about 30% (by weight) of matrix material, which makes the costs of the polymer an important economical factor. Based on production volumes for the resin, one can imagine that it is

Table 3. List of resin materials selected based on the criteria for VARIM process

Sl. No	Thermoplastic polymer	Viscosity (Pa.s)	Processing temperature (^{0}C)	Cost (€/kg)	Availability / Vendor	Available processing knowledge	Glass transition temperature -T_g (^{0}C)
1	Polymethylmethacrylate (PMMA)	0.1	120 – 160	3.5 – 5	ESSTECH, Inc., USA	---	---
2	Polyamide 6 (PA 6)	0.01	140 – 160	2 – 3	Brüggemann Chemicals, Germany (DSM, Netherlands	Delft University, Netherlands	40 – 60
3	Polyamide 12 (PA 12)	0.05	180 – 245	20	EMS Chemicals, Switzerland	---	115 – 170
4	Polyethylene Terephtalate (PET)	0.95	250 – 325	2 – 4	PFG Chemicals Inc, CANADA	---	82
5	Thermoplastic Polyurethane (TPU)	0.8	300	8.5 – 20	Fulcrum Composites, USA	---	---
6	Polybutylene Terephtalate (PBT)	0.02	180 – 210	8.7 – 9	Cyclic Corporation, USA	Eire Composites, Ireland	55 – 60
7	Polycarbonate (PC)	0.7	250	4 – 6	Partial Available In the market	---	150
8	Polyether Ketone (PEK)	0.1	350	55 – 65	Partial Available In the market	---	120 – 160
9	Polyphthalamide (PPA)	1	200 – 290	5 – 6	EMS Chemicals, Switzerland	---	138

beneficial for the resin costs if the monomer for reactive processing is the same as the one that is used for the production of the equivalent polymer used in melt processing. This is the case for both polyamides (PA6 and PA12), whereas Cyclics and Fulcrum make use of a monomer specifically developed for reactive processing of their CBT and TPU, respectively (Van Rijswijk, 2007).

According to availability, based on literature and R&D perspective, there are large amount of resin materials available in the market for composite processing and characterization. Consequently, the matrix material should be sufficiently available and not just in lab scale quantities as stated by Van Rijswijk (2007). Depending upon the industrial needs, scaling up of the process and the actual manufacturing of large wind turbine blades in near future would benefit from a matrix material, which is already commercially available. Commercial available thermoplastic polymers suitable for resin infusion are listed in Table 4.

Availability of CBT Resins

Cyclics Corporation, USA offers a combined water-like viscosity with superior materials properties in its flagship product line of CBT resins (Table 1). The current line of resins includes CBT 100, CBT 160, CBT 500, and CBT XL 101. The most suitable grade for liquid composite manufacturing is CBT 500, which offers greater processing flexibility. The CBT 500 resin is effective in low pressure or vacuum assisted resin transfer moulding. The resin is compatible with all fibre types that are epoxy sized and offers superior wet out and high fibre loading with lower void content (http://www.cyclics.com/pdf/CBT500_Composites.pdf).

Availability of PA6 Resins

Brüggemann Chemical, Germany is now the distributor for DSM's flaked and liquid caprolactam for anionic polymerization (AP-Caprolactam). They supply raw materials for the production of cast Nylon by the process of Anionic polymerization of caprolactam. The product portfolio comprises the PA-6 monomer AP-Nylon caprolactam, including catalysts and activators under the brand name Bruggulen C catalysts, activators, and other additives (http://www.brueggemann.com/english/kunststoffadditive1.html). Brüggemann and Delft University have worked closely together to develop a material system which is suitable for large and thick structures, like wind turbine blades, and Delft University has some exclusive rights to this material system.

PA6 & PMMA have the *lowest processing temperatures* of all known reactively processable thermoplastics; see Table 5 and Figure 2. Costs also includes packing materials, tooling material, amount of heat or energy used in order to process the material around 230°C have major impact in selecting the processing temperature, hence this costs should be less. If the maximum acceptable

Table 4. Commercially available reactive thermoplastic precursors

Polymer	Trade Name	Company
PA6	AP Nylon	Brüggemann Chemical, Germany
		DSM Fibre Intermediates, The Netherlands
PA12	APLC12	EMS Chemical, Switzerland
PBT	CBT	Cyclics Corporation, USA
TPU	Fulcrum	Fulcrum Composites, USA
PMMA	X1270950	ESSTECH, Inc., USA
PPA	Grivory HT	EMS Chemicals, Switzerland

Table 5. Processing temperatures for some thermoplastic materials (Van Rijswijk & Bersee, 2007)

Thermoplastic matrix	Processing Temperature (^{0}C)		
	Melt processing	Reactive processing	Reduction
PA – 6	230-290	140-160	70-150
PA – 12	230-270	180-245	0-90
PBT	250-270	180-200	50-90
PMMA	220-260	120-160	60-140
PC	265-360	250	15-110
PET	265-325	250-325	0-15
PES	330-390	300	30-90
PPS	330	300	30
PEEK	380-390	350	30-40

process temperature is set to be 230°C for cost reasons, the only candidate materials are: PA6, PBT and PMMA. Table 5 also confirms that reactive processing in general result in a reduction in processing temperature compared to melt processing of the same polymer.

Similar to above practical analysis, the elimination of resin materials takes place step by step instead of considering the dependency of one

Figure 2. Melt viscosities and processing temperatures of various matrix materials for both reactive and melt processing (Van Rijswijk & Bersee, 2007)

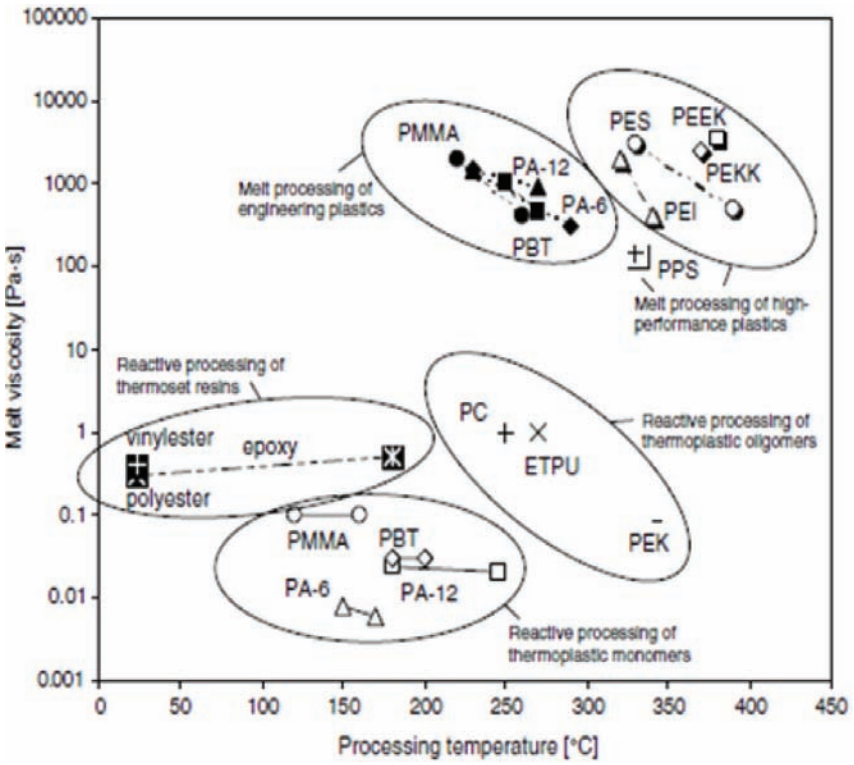


Table 6. Database matrix for the short-listed candidate resins

Sl. No	Attributes Material	Viscosity (Pa·s)	Processing temperature (^{0}C)	Cost (€/kg)	Availability
1	Polymethylmethacrylate (PMMA)	0.1	140	4	0.75 (good)
2	Polyamide 6 (PA 6)	0.01	150	2.5	1 (Highly available)
3	Polyamide 12 (PA 12)	0.05	220	20	0.75 (good)
4	Polyethylene Terephtalate (PET)	0.95	280	3	0.5 (Fair)
5	Thermoplastic Polyurethane (TPU)	0.8	300	10	0.75 (good)
6	Polybutylene Terephtalate (PBT)	0.02	200	9	1 (Highly available)
7	Polycarbonate (PC)	0.7	250	5	0.25 (Poor availability)
8	Polyether Ketone (PEK)	0.1	350	60	0.25 (Poor availability)
9	Polyphthalamide (PPA)	1	250	5.5	0.75 (good)

attribute over the other. Based on the practical approach, the ranking of resin system is as follows

PA6 - PBT - PMMA- PPA – PA12 – PET – PC - TPU – PEK

From the above section, it is clear that materials and processing technologies has got strong interrelationship, which hold the key to the future success of composites.

5.3. Selection of Resin Using Proposed Algorithm

The selection procedure of the combined MADM method for finding a right choice of resin from the available alternatives is explained below step-by-step:

From the thermoplastic resin database generated and after 'elimination search' manageable number of candidate resins and their pertinent attributes are tabulated in Table 6 (one can also add additional attributes if so desired). Attributes like viscosity, processing temperature and cost are non-beneficial attributes where low values are most desired. In other words, wind turbine blades is said to produce high quality blades with lost cost of materials, low cost of tooling and low viscosity. The quantitative data for these attributes are given in Table 6. Whereas the attribute like 'Availability' is subjective, based on resin vendor availability the values are defined as per the fuzzy numbers (Zadeh et al., 1996). The database matrix or also called decision matrix, 'D' i.e., the matrix which will contain all the magnitudes of attributes in actual units taken. The rows of the matrix are the candidate resins, with their attribute values listed in columns.

Construction of non-dimensional matrix [R] performed using Equation (1). This matrix helps to bring the data of various candidate resins having different dimensions under a uniform scale. Hence the matrix [R] is called as normalized database matrix.

$$R=\begin{bmatrix} 0.0572 & 0.1894 & 0.0612 & 0.3487 \\ 0.0057 & 0.2029 & 0.0383 & 0.4650 \\ 0.0286 & 0.2976 & 0.3062 & 0.3487 \\ 0.5435 & 0.3788 & 0.0459 & 0.2325 \\ 0.4577 & 0.4059 & 0.1531 & 0.3487 \\ 0.0114 & 0.2706 & 0.1378 & 0.4650 \\ 0.4005 & 0.3382 & 0.0765 & 0.1162 \\ 0.0572 & 0.4735 & 0.9185 & 0.1162 \\ 0.5721 & 0.3382 & 0.0842 & 0.3487 \end{bmatrix} \quad (11)$$

Using Equations (2) to (5), the weighted normalised matrix [V] calculated. The matrix is shown below helps for finding the best resins using the proposed methodology.

$$V = \begin{bmatrix} 0.0072 & 0.0150 & 0.0270 & 0.1235 \\ 0.0007 & 0.0161 & 0.0169 & 0.1646 \\ 0.0036 & 0.0236 & 0.1349 & 0.1235 \\ 0.0680 & 0.0300 & 0.0202 & 0.0823 \\ 0.0573 & 0.0321 & 0.0675 & 0.1235 \\ 0.0014 & 0.0214 & 0.0607 & 0.1646 \\ 0.0501 & 0.0268 & 0.0337 & 0.0411 \\ 0.0072 & 0.0375 & 0.4047 & 0.0411 \\ 0.0716 & 0.0268 & 0.0371 & 0.1235 \end{bmatrix} \quad (12)$$

The above weighted normalization matrix is all-inclusive matrix, which takes care of the attribute values and their relative importance. So this matrix will be able to provide good basis for comparison with each other and with the benchmark resins (optimum). Various methods, graphical and non-graphical as discussed previously can be applied for this comparison and ranking purposes.

5.3.1. Ranking Using Combined TOPSIS and AHP Method

The weighted normalized attributes for the Positive and Negative benchmark reinforcements can be obtained using Equation (6) *and* Equation (7) as follows

$$V^* = (0.0007, 0.0150, 0.0169, 0.1646) \quad (13)$$

$$V^- = (0.0716, 0.0375, 0.4047, 0.0411) \quad (14)$$

Relative closeness to the ideal solution is obtained using Equation (8) *through* Equation (10):

$$RSI^* = \frac{S_i^-}{S_i^* + S_i^-}, \text{ where } i = 1,2,\ldots, m \quad (15)$$

$$RSI_1^* = \frac{S_1^*}{S_1^* + S_1^-} = 0.9016$$

$$RSI_2^* = \frac{S_2^-}{S_2^* + S_2^-} = 0.9974 \quad (16)$$

$$RSI_3^* = \frac{S_3^-}{S_3^* + S_3^-} = 0.6986 \text{ etc., are defined in Table 7.}$$

5.3.2. Ranking Using Graphical Method

Here in graphical methods, used in this article is a method called spider diagram approach. For ranking various candidate resins we need to use the weighted normalized data matrix for plotting. The resin selection index (RSI) can be calculated from the above chart. The calculated RSI is tabulated as shown in Table 7.

The area under the graph (Figure 3) based on weighted normalized data matrix of the candidate resins and for optimum resin systems are V_2^L = 0.0032; V_{+B}^L = 0031609. The coefficient of similarity based on the weighted normalized data matrix of the first candidate resin is

$$RSI_1^{VL} = \frac{V_{+B}^L}{V_2^L} = 0.9878 \quad (17)$$

5.3.3. Optimum Selection

Materials of interest for the resin infusion process are listed in Table 7, where they are evaluated against the criteria for selecting the candidate resins. Only two materials are pre-selected as candidate materials, and these are PA6 and PBT.

6. CONCLUSION

A new decision making methodology named 'combined MADM approach' has been applied

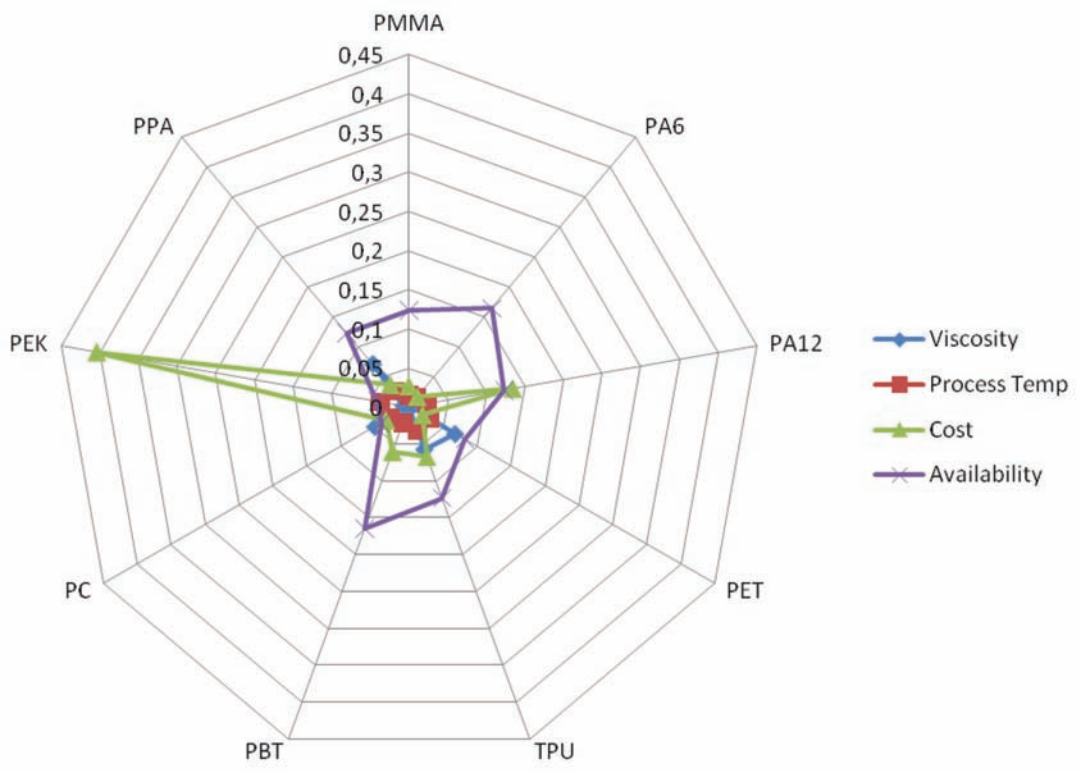
Table 7. Evaluation and ranking of the candidate reinforcement using various MADM methods

Resin Material	Eigen Value Solution Closeness to the +ve benchmark resin system RSI*	Rank based on RSI*	RSI Based on Spider diagram (RSI^{VS})	Rank based on RSI^{VS}
Polymethylmethacrylate (PMMA)	0.9016	3	0.5545	3
Polyamide 6 (PA 6)	0.9974	1	0.9878	1
Polyamide 12 (PA 12)	0.6986	8	0.1549	8
Polyethylene Terephtalate (PET)	0.7826	6	0.3193	4
Thermoplastic Polyurethane (TPU)	0.7979	5	0.1629	7
Polybutylene Terephtalate (PBT)	0.9037	2	0.6725	2
Polycarbonate (PC)	0.7342	7	0.2725	5
Polyether Ketone (PEK)	0.1365	9	0.0976	9
Polyphthalamide (PPA)	0.8155	4	0.1939	6

for evaluation, comparison and ranking of thermoplastic resins for a vacuum infusion process used today to build large composite structures. The contributions of the present research work are summarized as follows:

1. Various attributes like the quantitative and qualitative attributes are identified and discussed for the thermoplastic resin systems suitable for vacuum infusion process, which are available today in the market. These attributes form the basis for resin selection using the proposed decision making approach.
2. Combined MADM approach is the proposed model used to find out the best resin system for the vacuum infusion process. Elimination search in the proposed algorithm makes the method less time consuming and focused to a given application. This method is found to be effective as this method takes various attributes information into account for comparison, ranking and selection of resin system.
3. This method allows the user to specify the relative importance of one attribute with the other attributes of resin system for a given application. The relative importance of attributes can be changed based on the application or based on another criterion.
4. The methodology is versatile and comprehensive in nature and helps composite industry to build software coding that can include 'n' number of attributes for the available resins in the market (like both thermosetting and thermoplastic resins). Based on the database generated for software coding from various resin manufacturers, it can easily cope with the development of new products and processing techniques by analysing the attributes.
5. Ideal and negative ideal solutions are generated from the available attribute data for the alternatives.
6. The thermoplastic resins selected using the methodology is nearest to the hypothetical best solution and farthest from hypothetical worst solution.
7. Sensitivity analysis can be carried out on a set of pertinent attributes to find out their criticality for different product applications.
8. Based on resin attributes like viscosity, processing temperature, availability and

Figure 3. Resin selection chart based on weighted normalized data



material costs, decision making analysis results in two materials, which were pre-selected as candidate for vacuum infusion of wind turbine blades. The two candidates are PA6 and PBT, which are identified both by the practical approach and the modelling approach.

9. The PA6 material and the related technology are available through Brüggemann Chemical, Germany, and Delft University, The Netherlands. Whereas the PBT material and the related technology are available through Cyclics Corporation, USA and Europe, and Eire Composites, Ireland.
10. The proposed decision making methodology converts multiple attributes into single numerical index/attributes to assist designers to take a correct decision.

It is hoped that the decision making methodology will find acceptability among the design engineers of the composite industries, and will be a useful module in the development of more general and versatile computer aided material selection programme.

ACKNOWLEDGMENT

This work is a part of the 'BLADE KING' project supported by the Danish National Advanced Technology Foundation. The other project partners are LM Glasfiber A/S (Project leader), Comfil ApS, and Aalborg University (Department of Mechanical Engineering). Special thanks to the partners, for their support provided for our research studies at Risø National Laboratory for Sustainable Energy, Technical University of Denmark (Materials Research Division) within the Blade King Project.

The authors would also like to thank Dr Harald Bersee and Dr K. van Rijswijk, Delft University of Technology, Composite Material & Process Development for the detailed discussions on thermoplastic resin selection in their PhD thesis. The authors also would like to express sincere thanks to the material (resin) supplier Cyclic Corporation, USA and Johns Manville, USA for their support and useful discussion in carrying out this research study.

REFERENCES

Ahluwalia, J., Gupta, S. K., & Agrawal, V. P. (1993). Computer-aided optimum selection of roller bearings. *Computer Aided Design*, *25*, 493–500. doi:10.1016/0010-4485(93)90080-8

Baets, J., Dutoit, M., Devaux, J., & Verpoest, I. (2008). Toughening of glass fiber reinforced composites with a cyclic butylenes terephthalate matrix by addition of polycaprolactone. *Composites. Part A, Applied Science and Manufacturing*, *39*(1), 13–18. doi:10.1016/j.compositesa.2007.09.013

Brønsted, P., Lilholt, H., & Lystrup, A. (2005). Composite Materials for wind power turbine blades. *Annual Review of Materials Research*, *35*, 505–538. doi:10.1146/annurev.matsci.35.100303.110641

Chakladar, N. D., & Chakraborty, S. (2008). A combined TOPSIS-AHP-Method based approach for non-traditional machining processes selection. *Proceedings of the Institution of Mechanical Engineers. Part B, Journal of Engineering Manufacture*, *222*(12), 1613–1623. doi:10.1243/09544054JEM1238

Ciovacco, J., & Winckler, S. J. *(2000). Cyclic thermoplastic properties and processing.* In Proceedings of the 45th International SAMPE Symposium, *Long Beach, CA (pp. 13-16).*

Durai Prabhakaran, R. T., Babu, B. J. C., & Agrawal, V. P. (2006a). Optimum selection of a composite product system using MADM approach. *Materials and Manufacturing Processes*, *21*, 883–891. doi:10.1080/10426910600773472

Durai Prabhakaran, R. T., Babu, B. J. C., & Agrawal, V. P. (2006b). Structural modeling and analysis of FRP composite product subsystems-a systems approach. *Journal of Polymer Composites*, *27*, 681–698. doi:10.1002/pc.20244

Goren, A., & Atas, C. (2008). Manufacturing of polymer matrix composites using vacuum assisted resin infusion molding. *Archives of Materials Science and Engineering*, *34*(2), 117–120.

Hakme, C., Stevenson, I., Maazouz, A., Cassagnau, P., Boiteux, G., & Seytre, G. (2007). In situ monitoring of cyclic butylenes terephtalate polymerization by dielectric sensing. *Journal of Non-Crystalline Solids, 353*(47-51), 4362-4365.

Hwang, C. L., & Yoon, K. (1982). *Multiple attribute decision making – methods and applications- a state of the art survey (lecture notes in economics and mathematical systems)*. Berlin, Germany: Springer-Verlag.

Joncas, S., Rijswijk, V. K., Charron, J.-F., Bersee, H. E. N., & Beukers, A. *(2006). Interfacial shear strength properties of vacuum-infused anionic polyamide-6 glass-fiber composites. In* Proceedings of the 47th AIAA/ASME/ASCE/AHS/ASC Structures, Structural Dynamics, and Materials Conference, *Newport, RI (pp. 1-8).*

Khattab, A. (2005). *Exploratory development of VARIM process for manufacturing high temperature polymer matrix composites.* Unpublished doctoral dissertation, University of Missouri, Columbia, MO.

Khattab, A., & EI-Gizawy, A. S. (2008). Characterization of process-induced properties in vacuum assisted resin infusion molding of high temperature polymer composites. *Journal of Advanced Materials*, *40*(3), 51–68.

Luiser, A., Bourban, P. E., & Manson, J. A. E. *(1999). In-situ polymerization of polyamide 12 for thermoplastic composites. In* Proceedings of the 12th International Conference on Composite Materials, *Paris, France (pp. 33-45).*

Mallon, P. J., Dweib, M. A., Ziaee, S., Chatterjee, A., & Gillespie, J. W. (2003). VARTM and RTM processing of PBT and PA6 thermoplastic composites. *STAR*, *41*(4), 31–43.

Mohd Ishak, Z. A., Gatos, K. G., & Karger-Kocsis, J. (2006). On the in-situ polymerization of cyclic butylene terephthalate oligomers: DSC and rheological studies. *Polymer Engineering and Science*, *46*, 743–750. doi:10.1002/pen.20486

Niccolo, P., Zaniboni, C., Stephan, B., & Ermanni, P. (2006). Perspectives for reaction molding of PPA as matrix for high-performance composite Materials. *Journal of Thermoplastic Composite Materials*, *19*, 207–216. doi:10.1177/0892705706059738

Parton, H., & Verpoest, I. *(2003). Reactive processing of textile reinforced thermoplastics. In* Proceedings of the 14th International Conference on Composite Materials, *San Diego, CA (pp. 41-50).*

Parton, H., & Verpoest, I. (2005). In-situ polymerization of thermoplastic composites based on cyclic oligomers. *Polymer Composites*, *26*, 60–65. doi:10.1002/pc.20074

Ramesh, T., & Jan-Anders, E. M. (2000). Comprehensive composite materials: *Vol. 2*. *Polymer matrix composites*. Burlington, MA: Elsevier Science & Technology Books.

Rao, R. V. (2006). Machinability evaluation of work materials using a combined multiple attributes decision-making method. *International Journal of Advanced Manufacturing Technology*, *28*, 221–227. doi:10.1007/s00170-004-2348-4

Rao, R. V., & Davim, J. P. (2008). A decision-making framework model for material selection using a combined multiple attribute decision-making method. *International Journal of Advanced Manufacturing Technology*, *35*, 751–760. doi:10.1007/s00170-006-0752-7

Rudd, C. D., Long, A. C., Kendall, K. N., & Mangin, C. G. E. (1997). *Liquid moulding technologies*. Cambridge, UK: Woodhead Publishing. doi:10.1533/9781845695446

Ryan, A. J., Stanford, J. L., & Tao, X. Q. (1995). The processing, structure and properties of structural composites formed by reaction injection-moulding (SRIM). *Plastics Rubber and Composites Processing and Applications*, *23*(3), 151–159.

Selvum, P., Vaidya, U. K., & Janowski, G. M. (2005). Liquid moulding of carbon fabric-reinforced nylon matrix composite laminates. *Journal of Thermoplastic Composite Materials*, *18*(6), 509–527. doi:10.1177/0892705705054412

Shahzad, M. A., Steeg, M., & Mitschang, P. (2010). Development and characterization of glass fibre reinforced in-situ polymerized thermoplastic matrix composite material. In *Proceedings of the SAMPE Conference and Exhibition*, Seattle, WA (pp. 1-15).

Subramaniyan, A. K., & Sun, C. T. (2006). Enhancing compressive strength of unidirectional polymeric composites using nanoclay. *Composites. Part A, Applied Science and Manufacturing*, *37*(12), 2257–2268. doi:10.1016/j.compositesa.2005.12.027

Vaidya, U. K., & Chawla, K. K. (2008). Processing of fibre reinforced thermoplastic composites. *International Materials Reviews*, *53*(4), 185–218. doi:10.1179/174328008X325223

Van Rijswijk, K. *(2007).* Thermoplastic composite wind turbine blades – vacuum infusion technology for anionic polyamide – 6 composites. *Unpublished doctoral dissertation, Delft University of Technology, Delft, The Netherlands.*

Van Rijswijk, K., & Bersee, H. E. N. (2007). Reactive processing of textile fiber-reinforced thermoplastic composites - an overview. *Composites. Part A, Applied Science and Manufacturing*, *38*(3), 666–681. doi:10.1016/j.compositesa.2006.05.007

Van Rijswijk, K., Bersee, H. E. N., Jager, W. F., & Picken, S. J. (2006). Optimisation of anionic polyamide-6 for vacuum infusion of thermoplastic composites: Choice of activator and initiator. *Composites. Part A, Applied Science and Manufacturing*, *37*(6), 949–956. doi:10.1016/j.compositesa.2005.01.023

Van Rijswijk, K., Joncas, S., Bersee, H. E. N., & Bergsma, O. K. (2005). Vacuum infused fiber-reinforced thermoplastic MW-size turbine blades - a cost-effective innovation? In *Proceedings of the ASME Wind Energy Symposium*, Reno, NV (pp. 39-51).

Van Rijswijk, K., Joncas, S., Bersee, H. E. N., Bergsma, O. K., & Beukers, A. (2005). Sustainable vacuum -infused thermoplastic composites for MW-size wind turbine blades-preliminary design and manufacturing issues. *Journal of Solar Energy Engineering*, *127*(4), 570–580. doi:10.1115/1.2037107

Van Rijswijk, K., Lindstedt, S., Vlasveld, D. P. N., Bersee, H. E. N., & Beukers, A. (2006). Reactive processing of anionic polyamide-6 for application in fiber composites: A comparitive study with melt processed polyamides and nanocomposites. *Polymer Testing*, *25*(7), 873–887. doi:10.1016/j.polymertesting.2006.05.006

Van Rijswijk, K., Vlasveld, D. P. N., Bersee, H. E. N., & Picken, S. J. *(2003). Vacuum injection of anionic polyamide 6. In* Proceedings of the 4th ICCST Conference, *Durban, South Africa (pp. 23-28).*

Vlasveld, D. P. N., Rijswijk, V. K., Bersee, H. E. N., Beukers, A., & Picken, S. J. N. *(2003). Process considerations for liquid moulding of composites based on anionic polyamide 6. In* Proceedings of the 14th International Conference on Composite Materials, *San Diego, CA (pp. 23-38).*

Waigaonkar, S., Babu, B. J. C., & Durai Prabhakaran, R. T. (2008). A new approach for resin selection in rotational molding. *Journal of Reinforced Plastics and Composites*, *27*, 1021–1037. doi:10.1177/0731684407086629

Williams, C., Summerscales, J., & Grove, S. (1996). Resin infusion under flexible tooling (RIFT): A review. *Composites Part A*, *27*, 517–524. doi:10.1016/1359-835X(96)00008-5

Zadeh, L. A., Klir, G. J., & Yuan, B. (1996). *Fuzzy sets, fuzzy logic and fuzzy systems: Advances in fuzzy systems- applications and theory*. Singapore: World Scientific.

Zingraff, L., Bourban, P. E., Wakeman, M. D., Kohler, M., & Manson, J. A. E. *(2002). Reactive processing and forming of polyamide 12 thermoplastic composites. In* Proceedings of the 23rd Europe SAMPE Conference *(pp. 237-248).*

PATENTS

Fiber reinforced anionic polyamide composites for structural applications and the manufacturing there of. European Patent Application, EP1 975 191 A1, 2008.

This work was previously published in the International Journal of Manufacturing, Materials, and Mechanical Engineering, Volume 1, Issue 3, edited by J. Paulo Davim, pp. 31-52, copyright 2011 by IGI Publishing (an imprint of IGI Global).

Chapter 17
Reciprocating Wear Behaviour of Two Dimensionally Reinforced Carbon–Phenolic and Carbon–Epoxy Composites

Sourav Sarkar
Advanced System Laboratory, India

V.G. Sekaran
Advanced System Laboratory, India

E. Badisch
Austrian Center of Competence for Tribology, Austria

Manish Roy
Defence Metallurgical Research Laboratory, India

R. Mitra
Indian Institute of Technology, Kharagpur, India

ABSTRACT

A comparative study has been carried out on performance of two-dimensionally reinforced carbon/phenolic (C/P) and carbon/epoxy (C/E) composites, subjected to low amplitude reciprocating wear at different temperatures. The C/P composite has shown greater wear rate than the C/E composite, with the difference being modest at room temperature, and larger at 250 °C. The values of coefficient of friction, surface roughness, and depths of craters on worn surfaces have been measured, which along with surface morphologies examined by scanning electron microscope have been correlated to both amount of weight loss and mechanisms of damage by wear.

DOI: 10.4018/978-1-4666-1867-1.ch017

Copyright © 2013, IGI Global. Copying or distributing in print or electronic forms without written permission of IGI Global is prohibited.

1. INTRODUCTION

The tribological behaviour of the carbon fibre reinforced composites is believed to be influenced by the nature of matrix, microstructure and fibre architecture of the composites. Wear of components under oscillatory relative motion (either linear or torsional) with small amplitudes of displacement is termed as low amplitude reciprocating wear. Such short amplitude reciprocating sliding between contacting surfaces for a large number of cycles involves fatigue and is also termed as fretting wear. It has been shown that micro-movements involved in the process of reciprocating sliding motion are fundamentally associated with Hertzian contact subjected to a tangential force (Mindlin, 1949). One of the special characteristics of fretting is the prolonged retention of wear debris between the sliding surfaces, when amplitude of sliding is relatively small. It has been shown that such accumulation of debris can cause depressions on the surfaces by deformation (Colombie, Berthier, Floquet, Vincent, & Godet, 1984) due to the development of large contact stresses. Moreover, the temperature may affect the process of fretting in two ways: (12) corrosion and oxidation rates usually increase with temperature; and (ii) the mechanical properties of materials usually change with temperature.

Reinforced polymer based composites are frequently used to make components such as bearing's outer ring and housing, wire ropes, electrical switchgears, multiplayer leaf springs, palliatives, spline couplings, flanges, seals, riveted and pinned joints (Ohmae, Kobayashi, & Tsukizoe, 1974; Bill, 1985; Jocobs, Friedrich, & Schulte, 1991), where fretting wear is commonly observed. A survey of the literature (Chivers & Gordelier, 1984; Vishwanath & Rao, 1991; Sabota & Holy, 2000; Bijwe, Indumathi, & Ghosh, 2002; Bijwe, Indumathi, Satapathy, & Ghosh, 2002; Bijwe & Rattan, 2006; Xiang & Chuanjin, 2006; Rattan & Fahim, 2007; Shangguan & Cheng, 2007; Li & Cheng, 2008) suggests that research on the tribological behaviour of the continuous fibre reinforced composites has received significant attention. On account of their high strength and elastic modulus, corrosion resistance, good friction and wear properties and low thermal expansion, carbon fibres are widely used as fillers in advanced composite materials (Okabe & Takeda, 2002). However, limited information is available about the performance of carbon fibre reinforced composites with phenolic and epoxy matrices. In the present study, the response of two dimensionally (2D) reinforced carbon-fibre reinforced composites having different phenolic or epoxy matrices to reciprocating wear tests under two different test loads at either room temperature or 250 ^{o}C have been compared. These tests could not be carried out at higher temperatures such as 500 ^{o}C, because the rates of vaporization of phenolic and epoxy matrices have been found to be accelerated to an extent that damage by wear becomes less significant.

2. EXPERIMENTAL PROCEDURE

2.1. Processing of Materials

The carbon fibres used in preparation of the 2D C/P composite were PAN- type, and their properties are shown in Table 1. Composites having carbon fibres impregnated with phenolic resin were fabricated by stacking multiple plies in two directions (0° and 90°). The specified constituents and physical properties of the phenolic resin used in this study are shown in Table 2. To remove moisture, the carbon cloth was passed through a preheating chamber with temperature of ~100 ^{o}C. After passage through the preheating chamber, the cloth was fully dipped in the resin and then passed through a roller, where the excess resin was removed from the carbon cloth. Subsequently, the cloth was passed through the prepegging machine operated at controlled temperatures. Then, the prepregs were stacked with a polythene sheet

separating them, and rolled into bundles. Subsequently, these prepregs were cut to sizes and then arranged in a pre-designed layup. The lay-up was placed inside a bag having partial vacuum (pressure ≈ 0.088 MPa), and then subjected to curing in an autoclave. Carbonization of the as-cured composites was performed by heating at the rate of 2 °C/min to 1000 °C in nitrogen atmosphere, and holding there for 2 h. The carbon fibres were found to account for a volume fraction of ~60% in the finished 2D C/P composite.

The 2D C/E prepregs were prepared by a conventional hot-melt method (Cogswell, 1992; Ahn & Seferis, 1989; Lee, Seferis, & Bonner, 1986). In this method, the fabric composed of unidirectional fibre tows (6K) were impregnated with a desired amount of matrix resin at temperature and pressure of 80 °C and 0.784 MPa, respectively. The plies were prepared by cutting the fabric to required size. Subsequently, the prepreg was prepared by stacking the plies in two mutually orthogonal directions. The prepreg produced in this manner had 37 wt.% of resin and fibre mass per unit area of 145.3 g/m^2. In the next step, the prepregs were laid inside a mold, which was enclosed in a thin and flexible nylon vacuum bag (Airtech, WL7400). The entire assembly was placed inside a preheated autoclave for the purpose of curing. The two-stage cure cycle used for the preparation of C/E prepregs is shown schematically in Figure 1. The first stage in this cure cycle consisted of increasing the temperature at a heating rate of 0.5-3 °C/min up to 177 °C, where it was held for about 120-135 min, such that the minimum resin viscosity was reached. The gelation time at 177 °C was found to be ~16 min. During this period of heat treatment, the external pressure applied to the prepreg stack was 0.687 ± 0.098 MPa. At the end of the cure cycle, the temperature was slowly reduced to < 71 °C at the cooling rate of 3 °C/min, while the laminate was still under pressure. Subsequently, the laminate was removed from the vacuum bag. The glass transition temperature of the cured laminate was found as ~235 °C. The volume fraction of carbon fibres in the 2D C/E composite has been estimated as ~70%.

Table 1. Specified size and properties of PAN based carbon fibre

Sl. No.	Properties	Specifications
1	Density (g/cc)	1.75±0.05
2	Tensile strength (GPa)	3.5
3	Tensile modulus (GPa)	220
4	(%) Elongation	1.5±0.03
5	Tex value (weight per unit length, 1g/1000 m)	380±40

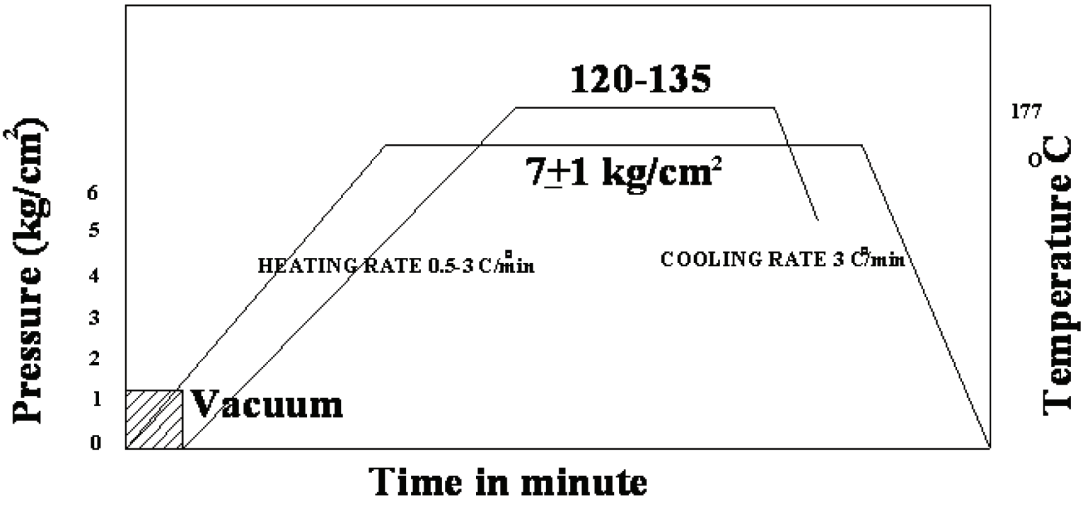
2.2. Reciprocating Wear Tests

Investigations on reciprocating wear behavior of the investigated C/P and C/E composites were carried out on a high reciprocating test rig, also known as SRV3© developed by Optimol Instruments (Optimol Instruments Prüftechnik, 2007) at the Austrian Center of Competence for Tribology (AC^{2}T), Wiener Neustadt, Austria. The experimental set-up used for these tests is schematically shown in Figure 2. These experiments involved the movement of a ball-bearing steel, 100Cr6 (hardness of ~60 HRC) of diameter 10 mm, which was oscillated against the test samples

Table 2. Specifications related to constituents and properties of phenolic resin

Sl. No.	Parameter	Nominal Values
1	Specific gravity (g/cc)	1.12 to 1.16
2	Viscosity at 308C (cp)	150 to 350
3	Point of trouble (ml of water)	6 to 8
4	Volatile content (%)	32 to 38
5	Solid content (%)	62 to 68.

Figure 1. Schematic illustration of the two stage cure cycle used for the preparation of the 2D C/E composite

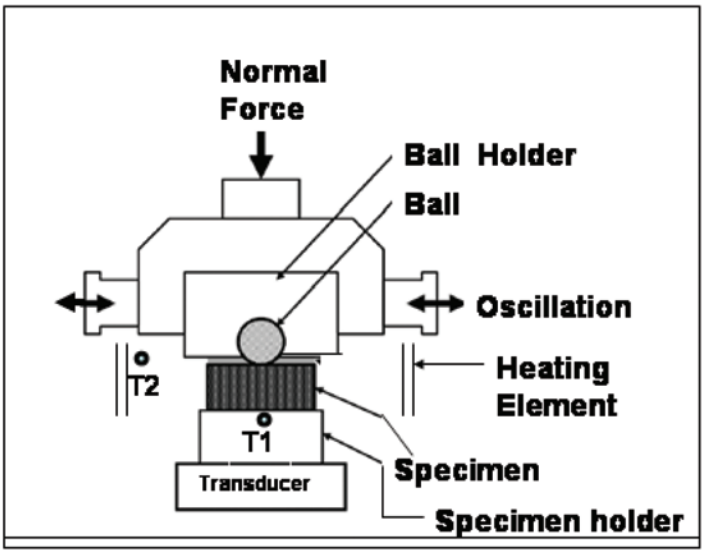


(20×20×5 mm) with a frequency of 20 Hz, with each stroke being 2 mm long. Furthermore, the experiments were carried out at two different temperatures, room temperature (25 °C) and 250 °C, and under two different normal loads, 100 and 200 N. The temperature was maintained with the help of two thermocouples, one which had its tip in contact with the specimen holder, and other placed near the heating element, as indicated in Figure 2. The maximum difference in temperature readings of these thermocouples was found as ≈20 °C. In course of each test, the coefficient of friction (C.O.F.) and its variation with time was continuously measured and recorded. Moreover, the weights of the samples were measured before and after the test using KERN EW620-3NM balance. The weight losses of the composite samples subjected to the tests were obtained by calculating the differences between the weights before and after the tests

2.3. Analysis of the Worn Surfaces

The depth of craters formed on the worn surfaces and their average roughness were evaluated using a confocal white light microscope (μ-surf, Nanofocus, Nanofocus AG, Stuttgart, Germany). For the purpose of these measurements, an illuminated pinhole was focused onto the surface to be measured, and the detector registered a surface signal, only if the focal plane matched with a real surface point. The objective was moved by small vertical steps, and the position of the objective was measured using a displacement transducer. Using an interpolation technique, a vertical resolution higher than ~10 nm was achieved. The measurements were carried out at four different locations on the bottom surfaces of the craters, and then averaged to get the depth of the crater. Four different measurements were performed to calculate the mean value of the wear depth. The surface roughness of the crater formed on the worn surface was evaluated using the confocal white light microscope in terms of the parameter, R_a, which is defined as the average of the peak heights and depths of the hills and valleys, respectively on the rough surface, measured from an arbitrary mean line defining a smooth surface.

Figure 2. Schematic illustration of the test-rig, which was used for the reciprocating wear tests. The positions of thermocouples for the control of temperature are indicated as T1 and T2



3. RESULTS AND DISCUSSION

3.1. Weight Loss

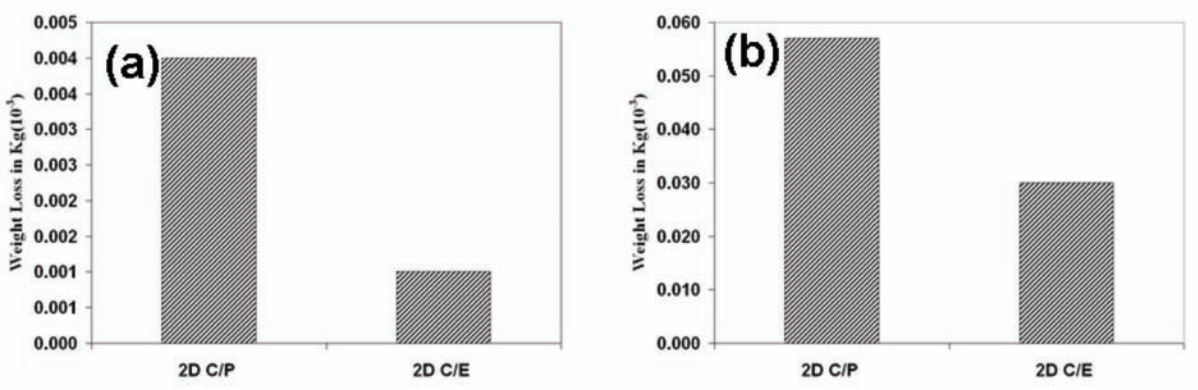
The weight loss has been found to be relatively insignificant during the tests carried out under the normal load of 100 N. But at the higher load (200 N), the weight loss has been found to be more significant. The data related to weight loss during the tests carried out under the normal load of 200 N at room temperature and 250 ^{o}C are shown using bar charts in Figures 3(a) and (b), respectively. From the results in these figures, it is inferred that at both the test temperatures, the C/E composite possesses higher wear resistance than the C/P composite. The lower weight loss observed for the C/E composite can be attributed to the higher volume fraction of the carbon fibres in this material, as well as strong fibre-matrix interfaces, both of which tend to restrict the weight loss significantly.

It may be noted that on increasing the test temperature from room temperature to 250 ^{o}C, the weight loss is increased by 15 and 30 times in case of 2D C/P and 2D C/E composites, respectively. In other words, the C/E composite is more adversely affected than the C/P composite at the higher temperature of test.

3.2. Size and Depth of Crater

Typical craters formed on the worn surfaces of C/P and C/E composites tested at the load of 100 N are shown in Figures 4(a) and (b), respectively. Examination of these images indicates that the craters are elliptical in shape. The lateral dimensions and depths of the craters are mentioned in Tables 3 and 4, respectively. Comparison of the results in these tables indicates that the sizes of the craters increase: (1) with increase in test temperature for tests carried out at a given normal load, and (2) with increase in the test load for tests carried out at a given temperature. Comparison of the results in the above-mentioned tables suggests that at room temperature, the dimensions and depths of craters formed on both the composites are comparable, while at 250 ^{o}C, the crater formed on the worn surface of the C/E composite is larger than

Figure 3. Bar charts depicting the weight loss due to the reciprocating tests carried out under the normal load of 200 N for the investigated composites at: (a) room temperature, and (b) 250 °C

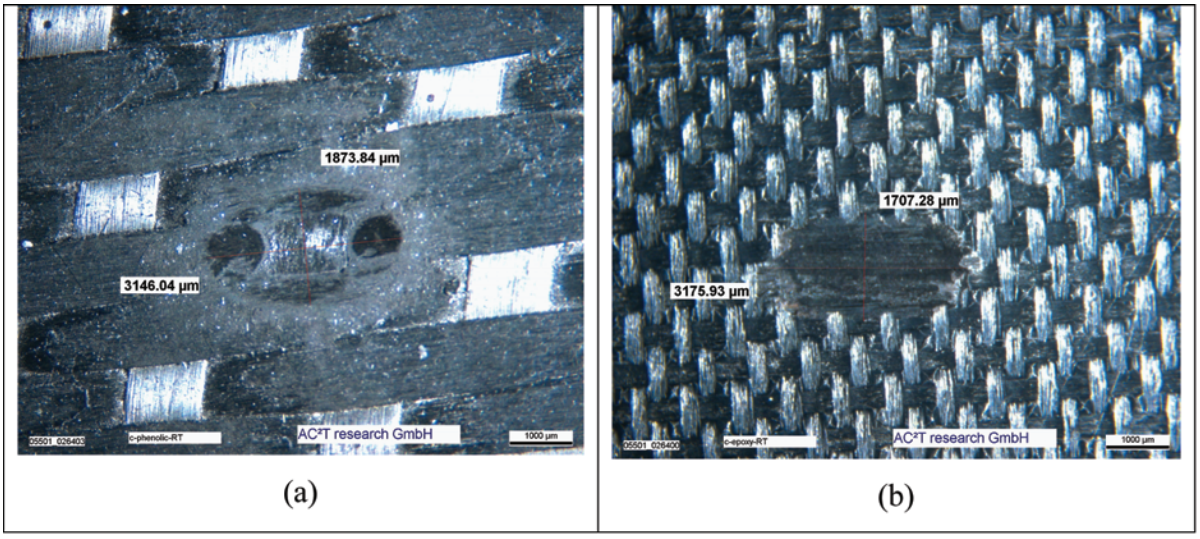


that on the C/P composite. This observation is somewhat unexpected considering that the weight loss observed for the C/P composite at 250 °C is greater than that recorded for the C/E composite, and also suggests that the depth of the crater may be quite non-uniform in case of the latter material. The variations in depth of crater at different locations have been quantitatively characterized through surface roughness measurements.

3.3. Surface Roughness

The values obtained from the surface roughness measurements for the craters formed on the worn surfaces of the investigated composites at the normal loads of 100 and 200 N are shown using bar charts in Figures 5 and 6, respectively. In each of these figures, (a) and (b) represent 2D C/P and 2D C/E composites, respectively. The results in these figures show that the surface roughness of

Figure 4. Shape of the craters formed on the worn surfaces after tests at 100 N load at room temperature on: (a) 2D C/P, and (b) 2D C/E composites



the crater formed on the 2D C/P composite decreases after the test at either room temperature or 250 °C [Figure 5(a)]. However, the surface roughness value for the crater formed on the 2D C/E composite is found to decrease after the room temperature test, but remain more or less unchanged after the test at 250 °C [Figure 5(b)]. However, for the experiments carried out under the higher normal load at either temperature, the surface roughness of the crater on the tested 2D C/P composite is found to be higher than that of the original surface [Figure 6(a)]. The results pertaining to tests under the load of 200 N at room temperature are much different for the 2D C/E composite, as much less roughness has been observed on the surfaces of the craters after tests compared to those on the original samples [Figure 6(b)]. This observation leads to the inference that uniform removal of fibres and matrix occurs in case of the C/E composite, while it is not so in case of the C/P composite for the tests carried out under the higher load.

The roughness values observed for the crater surfaces of the 2D C/E composite are higher for the tests at 250 °C than that for room temperature experiments, which suggests that there is enhancement in the differential wear of carbon fibre and epoxy matrix with increase in temperature, which is expected to involve the separation between fibre and matrix in the composite. In other words, fibre-matrix debonding is greater in the C/E composite than that in case of the C/P composite for tests carried out at 250 °C, contrary to the nature of behaviour found for tests at room temperature. High surface roughness observed in case of the C/E composite tested at 250 °C also leads one to infer that there are sharp variations in the depth of craters from one location to another, as has been suggested from analysis of the results reported in Section 3.3.

3.4. Morphology of Worn Surfaces

The SEM (SE) images depicting the surface morphologies of the craters formed on worn surfaces

Table 3. Shape and dimensions of craters formed on the worn surfaces of the investigated composites

Material	Condition	Shape	Crater Dimensions for Load = 100 n		Crater Dimensions for Load = 200 N	
			X (mm)	Y (mm)	X (mm)	Y (mm)
2D C/P	Room Temperature	Elliptical	3.146	1.874	4.458	3.354
	250 °C	Elliptical	3.564	2.354	4.959	3.759
2D C/E	Room Temperature	Elliptical	3.176	1.707	4.242	2.800
	250 °C	Elliptical	6.155	2.921	6.797	5.376

Table 4. Depth of the craters formed on the worn surfaces of the investigated composites

Material	Condition	Depth (mm) for Load = 100 N	Depth (mm) for Load = 200 N
2D C/P	Room Temperature	0.0968	0.284
	250 °C	0.1605	0.400
2D C/E	Room Temperature	0.0993	0.135
	250 °C	0.1643	0.678

Figure 5. Bar charts depicting the surface roughness (R_a) values obtained at the base of the craters formed during tests at 100 N load on (a) 2D C/P, and (b) 2D C/E composites

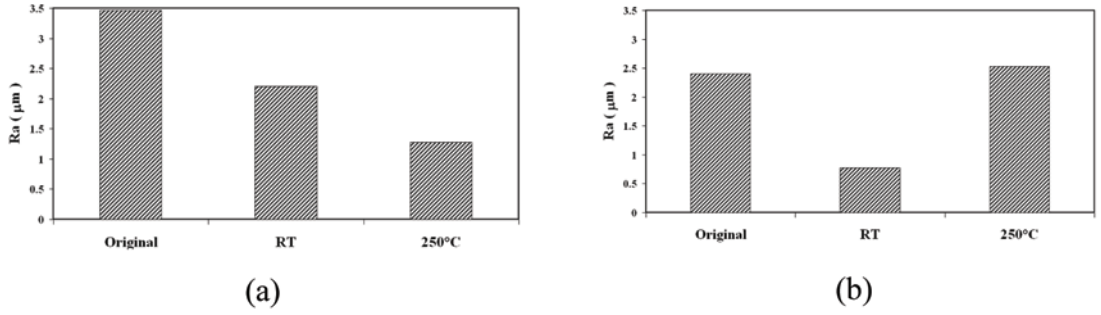
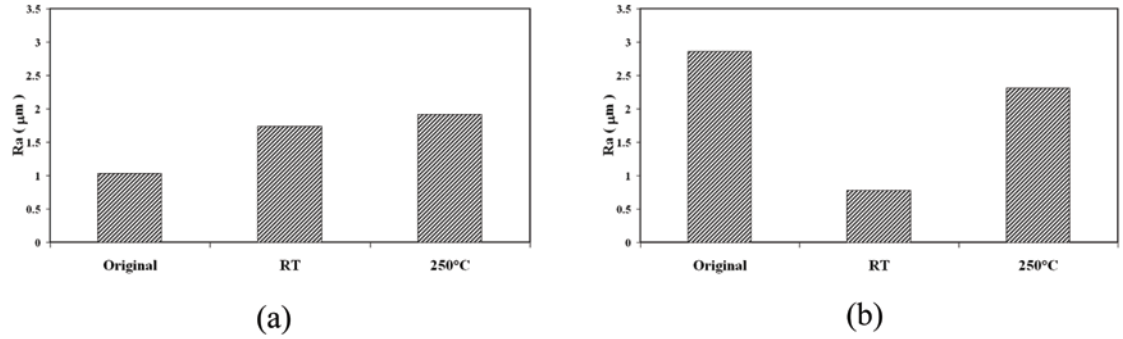


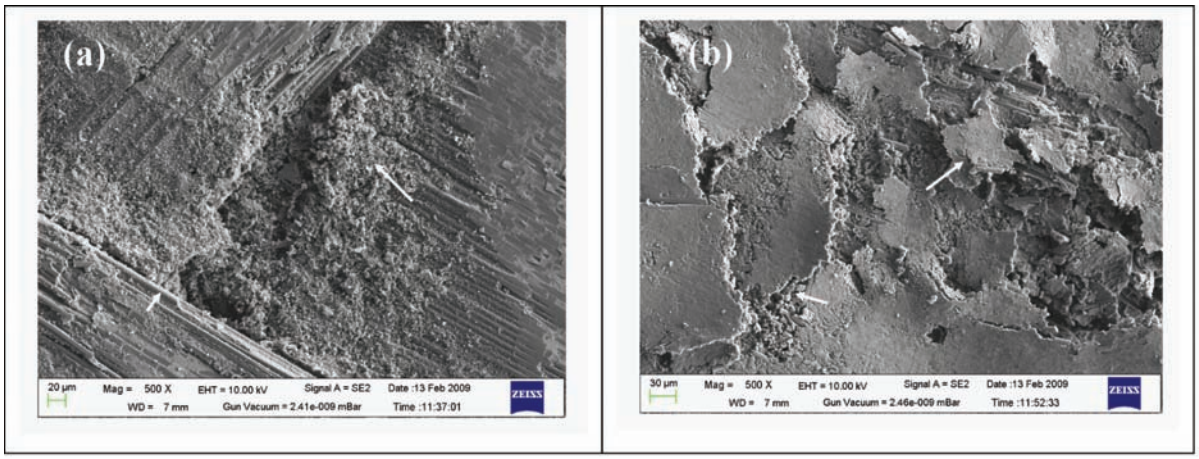
Figure 6. Bar charts depicting the surface roughness (R_a) values obtained at the base of the craters formed during tests at 200 N load on (a) 2D C/P, and (b) 2D C/E composites



of the investigated composites, subjected to reciprocating wear tests under both test load at 250 °C are shown in Figures 7 and 8, respectively. In these images, C/P and C/E composites are represented by (a) and (b), respectively. Examination of the images of the C/P composite shows that the carbon fibres are progressively exposed as the matrix is continuously removed in course of the wear tests. Comparison of the images shown in Figures 7(a) and 8(a) clearly indicates that the process of matrix removal accompanied by debonding and fracture of the carbon fibres is more prominent in case of the C/P composite subjected to tests at either temperatures.

Examination of the SEM (SE) images depicting the worn surface of the C/E composite tested at the load of 100 N shows the presence of a network of cracks located mostly in the matrix with broken fibres embedded in it [Figure 7(b)]. In such a situation, it is appropriate to infer that removal of matrix and fibres takes place in a more or less uniform manner. The observations of uniform removal of matrix and fibre in case of C/E composite and fibre-matrix debonding on the surfaces of the C/P composite are consistent with the greater amount of smoothness observed on the crater surface of the former material after the test at room temperature. However, the surfaces of C/E composite samples tested at room temperature shows the evidence of excessive damage along with evidence of a network of cracks in the matrix and a fairly large number of debonded fibres [Figure 8(b)]. The nature of observation recorded at 250 °C differs from that at room tem-

Figure 7. SEM images depicting the microstructures on the surfaces of craters on the worn surfaces of samples tested under 100 N load at 250 °C at room temperature: (a) 2D C/P, and (b) 2D C/E composites



perature, as there is extensive debonding of fibres from the matrix for the former condition of test.

3.5. Coefficient of Friction

The variation in the values of C.O.F. as measured for the investigated composites at different test temperatures under the loads of 100 and 200 N are shown in Figures 9 and 10, respectively. In these figures, the results obtained during the tests on C/P and C/E composites are shown in (a) and (b), respectively. Moreover, the range of C.O.F. values recorded for C/P and C/E composites along with their nature of variation are reported in Table 5. The results of the present study pertaining to the C.O.F. of C/P and C/E composites as shown in this table are in agreement with that reported by Kuo (2005), where these values have been found to vary in the range of 0.3-0.45 for different C/C composites impregnated with phenolic resin.

Figure 8. SEM images depicting the microstructures on the surfaces of craters on the worn surfaces of samples tested under 200 N load at room temperature: (a) 2D C/P, and (b) 2D C/E composites

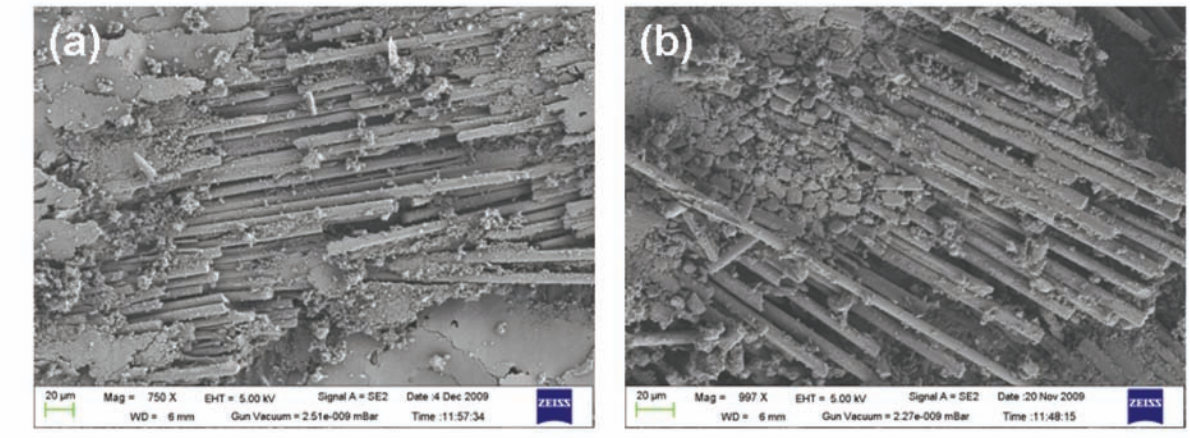


Figure 9. Variation of coefficient of friction with duration of tests under 100 N load at different temperatures on: (a) 2D C/P and (b) 2D C/E composites

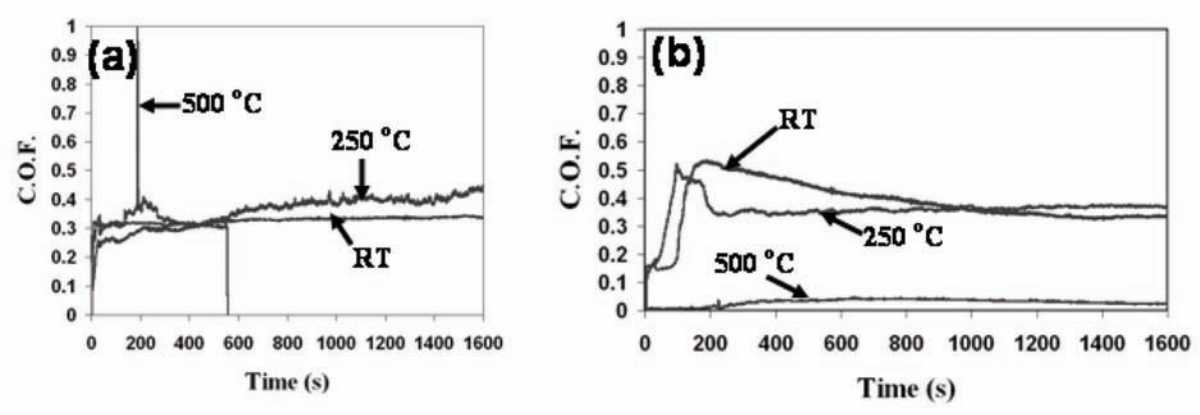
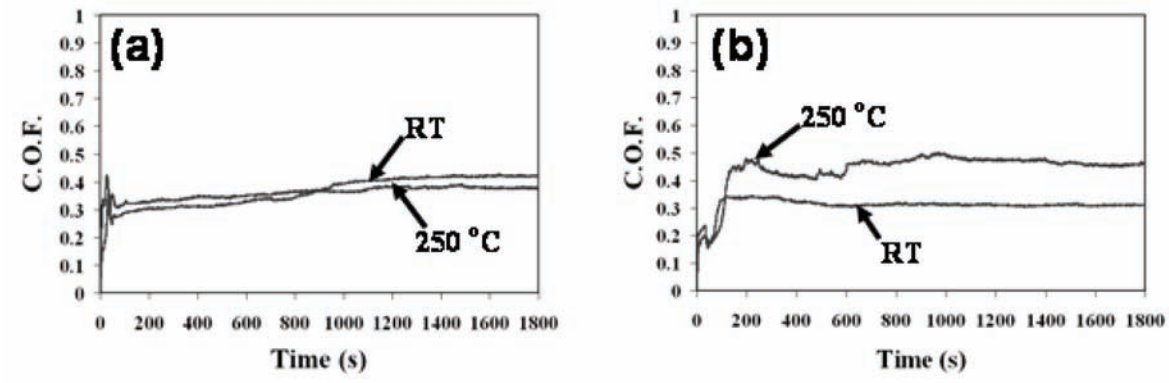


Figure 10. Variation of coefficient of friction with duration of tests under 200 N load at different temperatures on: (a) 2D C/P and (b) 2D C/E composites



Comparison of the ranges of C.O.F. values, as reported in Table 5, for the tests carried out at the load of 100 N on either C/P or C/E composite at room temperature and 250 °C are found to be more or less similar or comparable. In addition, it is noted from this table that for the tests carried out at the load of 200 N, the values of C.O.F. obtained at room temperature are close to those recorded at 250 °C in case of the C/P composites. However, in case of the C/E composite, the values of C.O.F. found through the tests at 250 °C appear to be almost consistently higher than that at room temperature, except in the initial stages. Furthermore, examination of the results shown in Figures 8 and 9 and those mentioned in Table 5 also indicate that the value of C.O.F. increases with time for the C/P composite, with the exception of the experiment at room temperature under lower load of 100 N. In contrast, the C.O.F. tends to become stable after an initial increase with decreasing trend for the C/E composite. Such a difference in variation of C.O.F. with time between C/P and C/E composites could be attributed to the higher wear rate of the former material.

Table 5. Range of coefficients of friction and nature of its variation recorded during reciprocating tests carried out at normal loads of 100 and 200 N for the investigated composites

Material	Condition	Load = 100 N		Load = 200 N	
		C.O.F	Tendency	C.O.F	Tendency
2D C/P	Room Temperature	0.31-0.34	Remain stable	0.26-0.42	Increasing
	250 °C	0.25-0.44	Increasing	0.31-0.38	Increasing
2D C/E	Room Temperature	0.33-0.53	Initial increase followed by decrease	0.31-0.35	Initially increases, and then stable
	250 °C	0.34-0.51	First Increasing, next decreasing, and then stable	0.41-0.50	Initially increases, and then stable

4. CONCLUSION

Based on the low amplitude reciprocating wear studies carried out on 2D C/P and 2D C/E composites under 100 or 200 N at room temperature or at 250 °C, the following conclusions may be drawn:

1. Much higher weight loss has been observed for the tests carried out on each of the investigated materials at the load of 200 N than that during tests at the lower load of 100 N. At both the test temperatures, the C/E composite has been found to be more wear resistant than the C/P composite, which is attributed to both higher carbon fibre volume fraction and strong fibre-matrix interfaces in the former material.
2. The craters formed on the worn surfaces of these composites have been found to be larger for the test at the higher temperature or greater load, and appear to be directly related to weight loss at least for the room temperature test.
3. The surface roughness values measured for the craters formed on the worn surfaces have been found to be related to both load and test temperature, depending on the type of material investigated.
4. The values of C.O.F. are found to be more or less similar for the tests carried out at room temperature and 250 °C on the C/P composite under both loads and on the C/E composite under 100 N. However, for tests carried out under the load of 200 N on the C/E composite, the values of C.O.F. obtained at 250 °C are higher than that recorded at room temperature.
5. Investigations of the morphologies of the worn surfaces have shown evidences of primarily fibre-matrix debonding in case of the C/P composite. In contrast, cracking of both fibre and matrix with much limited events of decohersion, followed by their removal appears to be the mechanism of wear in case of the C/E composite.

ACKNOWLEDGMENT

This work has been carried out at the "Austrian Center of Competence for Tribology". The authors are also grateful to Andreas Pauschitz for providing the facilities to carry out this work.

REFERENCES

Ahn, K. J., & Seferis, J. C. (1989). Prepreg processing science and analysis. In *Proceedings of the 34th International SAMPE Symposium* (pp. 63-70).

Bijwe, J., Indumathi, J., & Ghosh, A. K. (2002). Influence of weave of glass fabric on oscillating wear performance of polyetherimide composite. *Wear*, *253*(7-8), 803–812. doi:10.1016/S0043-1648(02)00167-9

Bijwe, J., Indumathi, J., Satapathy, B. K., & Ghosh, A. K. (2002). Influence of carbon fabric on fretting wear performance of PEI composites. *ASME Journal of Tribology*, *124*(4), 834–839. doi:10.1115/1.1456088

Bijwe, J., & Rattan, R. (2006). Influence of content of carbon fabric on the low amplitude oscillating wear performance of polyetherimide composites. *Tribology Letters*, *23*(3), 223–229. doi:10.1007/s11249-006-9060-5

Bill, R. C. (1985). Selected fretting wear resistant coatings for Ti-6 percent Al-4 percent V alloy. *Wear*, *106*(1-3), 283–301. doi:10.1016/0043-1648(85)90113-9

Chivers, T. C., & Gordelier, S. C. (1984). Fretting fatigue palliatives: Some comparative experiments. *Wear*, *96*(2), 153–175. doi:10.1016/0043-1648(84)90092-9

Cogswell, F. N. (1992). *Thermoplastic aromatic polymer composites* (pp. 44–58). Oxford, UK: Butterworth-Heinemann.

Colombie, C., Berthier, Y., Floquet, A., Vincent, L., & Godet, M. (1984). Fretting: Load carrying capacity of wear debris. *ASME Journal of Tribology*, *106*(2), 194–201. doi:10.1115/1.3260881

Kuo, H. H., Chern, Lin, J. H., & Ju, C. P. (2005). Tribological behavior of fast-carbonized PAN/phenolic-based carbon/carbon composite and method for improving same. *Wear*, *258*(10), 1555–1561. doi:10.1016/j.wear.2004.10.009

Lee, W. L., Seferis, J. C., & Bonner, D. C. (1986). Prepreg processing science. *SAMPE Quarterly*, *17*, 58–69.

Li, J., & Cheng, X. H. (2008). Friction and wear properties of surface-treated carbon fibre-reinforced thermoplastic polyimide composites under oil-lubricated condition. *Materials Chemistry and Physics*, *108*(1), 67–72. doi:10.1016/j.matchemphys.2007.09.003

Mindlin, R. D. (1949). Compliance of elastic bodies in contact. *Journal of Applied Mechanics*, *71*, 259–268.

Ohmae, N., Kobayashi, K., & Tsukizoe, T. (1974). Characteristics of fretting of carbon fibre reinforced plastics. *Wear*, *29*(3), 345–353. doi:10.1016/0043-1648(74)90020-9

Okabe, T., & Takeda, N. (2002). Size effect on tensile strength of unidirectional CFRP composites experiment and simulation. *Composites Science and Technology*, *62*(15), 2053–2064. doi:10.1016/S0266-3538(02)00146-X

Optimol Instruments Prüftechnik. (2007). *SRV operating instruction manual*. Munich, Germany: Optimol Instruments Prüftechnik.

Rattan, R., Bijwe, J., & Fahim, M. (2007). Influence of weave of carbon fabric on low amplitude oscillating wear performance of Polyetherimide composites. *Wear*, *262*(5-6), 727–735. doi:10.1016/j.wear.2006.08.005

Sato, J. (1988). Recent studies on fretting wear of polymeric materials. *Transactions ISLE*, *33*, 26–32.

Shangguan, Q.-Q., & Cheng, X.-H. (2007). Tribological properties of lanthanum treated carbon fibres reinforced PTFE composite under dry sliding condition. *Wear*, *262*(11-12), 1419–1425. doi:10.1016/j.wear.2007.01.020

Tai, N. H., Kuo, H. H., Chern, J. H., & Ju, C. P. (2002). Mechanical and tribological properties of 2-D carbon/carbon composites densified through pulse chemical vapor infiltration. *Journal of Materials Science*, *37*(17), 3693–3703. doi:10.1023/A:1016565426189

Vishwanath, B., Verma, A. P., & Rao, C. V. S. (1991). Effect of fabric geometry on friction and wear of glass fibre reinforced composites. *Wear*, *145*(2), 315–327. doi:10.1016/0043-1648(91)90139-L

Waterhouse, R. B. (1972). *Fretting corrosion* (1st ed.). Oxford, UK: Pergamon Press.

Xiang, D., & Gu, C. (2006). A study on the friction and wear behavior of PTFE filled with ultrafine kaolin particulates. *Materials Letters*, *60*(5), 689–692. doi:10.1016/j.matlet.2005.09.061

This work was previously published in the International Journal of Manufacturing, Materials, and Mechanical Engineering, Volume 1, Issue 4, edited by J. Paulo Davim, pp. 46-57, copyright 2011 by IGI Publishing (an imprint of IGI Global).

Chapter 18
Roughness Optimization of Electroless Ni–B Coatings Using Taguchi Method

Suman Kalyan Das
Jadavpur University, India

Prasanta Sahoo
Jadavpur University, India

ABSTRACT

In this paper, the authors present an experimental study of roughness characteristics of electroless Ni-B coatings and optimization of the coating process parameters based on L_{27} Taguchi orthogonal design. Three coating process parameters are considered viz. bath temperature, reducing agent concentration, and nickel source concentration. It is observed that concentration of reducing agent together with bath temperature play a vital role in controlling the roughness characteristics of the coatings. The analysis yields the optimum coating parameter combination for minimum roughness. A reduction of about 15% is observed in roughness at the optimal condition compared to the initial condition. The microstructure, composition, and the phase content of the coating are also studied with the help of scanning electron microscopes energy dispersive X-ray analysis, and X-ray diffraction analysis, respectively.

INTRODUCTION

In the middle of the last century, Brenner and Riddell (1950) discovered a revolutionary coating process, which does not need electricity and hence is popularized as electroless coating. Electroless plating is an autocatalytic process where the substrate develops a potential when it is dipped in electroless solution called bath that contains a source of metallic ions, reducing agent, complexing agent, stabilizer and other components. Due to the developed potential both positive and negative ions are attracted towards the substrate surface and release their energy through charge

DOI: 10.4018/978-1-4666-1867-1.ch018

Copyright © 2013, IGI Global. Copying or distributing in print or electronic forms without written permission of IGI Global is prohibited.

transfer process. The basic chemical reactions for electroless plating are given by the following expressions (Riedel, 1991):

$$R^{n+} \; R^{(n+z)} + ze$$

$$Me^{+z} + ze \; Me$$

where '*R*' indicates the reducing agent and '*Me*' indicates the metal to be deposited on a substrate.

Among the various types of electroless plating, electroless nickel has gained immense popularity due to its ability to provide a hard, wear resitant and corrosion resistant surface (Mallory & Hadju, 1991; Riedel, 1991). Hypophosphite reduced Ni-P coating (Agarwala & Agarwala, 2003; Hari Krishnan, John, Srinivasan, Praveen, Ganesan, & Kavimani, 2006; Sahoo, 2008) has already been widely accepted and the quest for achieving a superior hard and wear resistant surface has brought Ni-B coatings at the focus of research (Delaunois, Petitjean, & Lienard, 2000; Dervos, Novakovic, & Vassiliou, 2004; Krishnaveni, Sankara Narayanan, & Seshadri, 2005; Anik., Körpe, & Şen, 2008). Aerospace, automotive, chemical and electrical industries utilize electroless nickel–boron plating due to its good solderability and lubricity, high hardness, high wear and abrasion resistances (Mallory & Hadju, 1991).

For Ni-B deposition reducing agents such as sodium borohydride or dimethylamine are commonly used among which the reduction efficiency of the former is much higher. However the high reduction efficiency makes borohydride baths prone to instability particularly at lower pH. Hence borohydride baths are generally alkaline and the control of pH is very important to avoid the spontaneous decomposition of the bath solution. The properties of sodium borohydride reduced electroless nickel coatings are often superior to those of deposits reduced with other boron compounds or with sodium hypophosphite (Delaunois & Lienard, 2002). The principal advantages of borohydride-reduced electroless nickel deposits are its hardness and superior wear resistance in the as-deposited condition which increases even more with heat treatment (Delaunois & Lienard, 2002; Oraon, Majumdar, & Ghosh, 2008). Thermochemical and heat treatments ares also found to modify the electrochemical properties of Ni-B coatings (Kanta, Vitry, & Delaunois, 2009). The physiochemical properties of electroless Ni-B coatings have been considerably modified by the addition of ions like tungsten (Drovosekov, Ivanov, Krutskikh, Lubnin, & Polukarov, 2005). Search of improved tribological properties has lead to the formation of duplex coatings of Ni-P and Ni-B (Sankara Narayanan, Krishnaveni, & Seshadri, 2003) and three component coatings of Ni-B-P (Ivanov, 2000; Jiang, Xiao, Hu, Peng, Zhang, & Wang, 2009). Composite coatings with improved wear resistance have been formed by incorporating several particles in Ni-B coatings, viz. diamond, alumina and silicon carbide (Mallory & Hadju, 1991). When tribological characteristics are of primary concern the design engineer must find innovative methods for integrating a base material having certain bulk properties with a properly functioning surface and electroless Ni-B coating has proved to be a good tribological material.

The present study addresses the surface roughness characteristics of electroless Ni-B coatings. Roughness is a measure of the texture of the surface. Roughness plays an important role in determining how a real object will interact with its environment. Rough surfaces usually wear more quickly and have higher friction coefficients than smooth surfaces. Roughness is often a good predictor of the performance of a mechanical component, since irregularities in the surface may form nucleation sites for cracks or corrosion. It also affects other functional attributes of machine components like friction, wear, light reflection, heat transmission, lubrication, electrical conductivity, etc. Although roughness is usually undesirable, it is difficult and expensive to control the same in manufacturing. Decreasing the roughness of a surface will usually increase exponentially its

manufacturing costs. Thus an optimization of the controlling process parameters is generally suitable in obtaining surface finish of desired level. It is found from an extensive review of available literature that optimization of process parameters in minimizing roughness of electroless Ni-B coating has remain unaddressed. In the present study an attempt has been made in this direction. Taguchi method is applied to determine the suitable coating process parameters for optimum surface roughness in electroless Ni-B coatings.

TAGUCHI METHODOLOGY

Taguchi techniques were developed by Taguchi (Taguchi, 1990; Ross, 1996); these techniques have been utilized widely in engineering analysis to optimize the performance characteristics with the combination of design parameters. Taguchi technique is also a powerful tool for the design of high quality systems. It introduces an integrated approach that is simple and efficient to find the best range of designs for quality, performance, and computational cost (Montgomery, 2001).

In Taguchi technique, three-stages such as system design, parameter design, and tolerance design are employed. System design consists of the usage of scientific and engineering information required for producing a part. Tolerance design is employed to determine and to analyze tolerances about the optimum combinations suggested by parameter design. Parameter design is used to obtain the optimum levels of process parameters for developing the quality characteristics and to determine the product parameter values depending on the optimum process parameter values. The parameter design phase of the Taguchi method generally includes the following steps: (1) identify the objective of the experiment; (2) identify the quality characteristic (performance measure) and its measurement systems; (3) identify the factors that may influence the quality characteristic, their levels and possible interactions; (4) select the appropriate orthogonal array (OA) and assign the factors at their levels to the OA; (5) conduct the test described by the trials in the OA; (6) analysis of the experimental data using the signal-to-noise (S/N) ratio, factor effects and the analysis of variance (ANOVA) to see which factors are statistically significant and to find the optimum levels of factors; (7) verification of the optimal design parameters through confirmation experiment. In the present study, parameter design is used to achieve the optimum levels of coating process parameters leading to minimization of surface roughness (R_a) of electroless Ni-B coating. Based on orthogonal arrays, the number of experiments which may increase the time and cost can be reduced by using Taguchi technique. It employs a special design of orthogonal arrays to learn the whole parameters space with a small number of experiments only. Taguchi offers the use of S/N ratio to identify the quality characteristics applied for engineering design problems. The S/N ratio characteristics can be divided on the basis of three criteria: lower-the-better (LB), higher-the better (HB) and nominal-the best (NB). For the case of minimization of surface roughness, LB criterion needs to be used. Furthermore, a statistical analysis of variance (ANOVA) (Montgomery, 2001) is performed to find which process parameters are statistically significant. With the S/N ratio and ANOVA analysis, the optimal combination of coating parameters can be predicted. Finally, a confirmation experiment is conducted to verify the optimal process parameters obtained from the parameter design.

EXPERIMENTAL DETAILS

Coating Procedure

Mild Steel (AISI 1040) is used as the substrate material (square blocks of size 20 mm × 20 mm × 8 mm) for the deposition of Ni-B films. The substrates are carefully prepared so that their

Table 1. Bath constituents and ranges of values for electroless Ni-B coating

Parameters	Ranges of parameters
Nickel chloride	15 – 25 g/l
Sodium borohydride	0.6 – 1.0 g/l
Ethylenediamine	59 g/l
Lead nitrate	0.0145 g/l
Sodium hydroxide	40 g/l
Bath temperature	85 – 95°C
pH of solution	12.5

sizes are maintained with precision. Shaping, parting and milling operations are sequentially done to prepare the substrates. Finally the samples are subjected to surface grinding process. After preparation, the samples are cleaned of any foreign particles and corrosion products prior to coating. Then the samples are cleaned with distilled water. The specimens after thorough cleaning are given a pickling treatment with dilute (18%) hydrochloric acid for one minute to remove any surface layer formed like rust. Finally they are cleaned with distilled water prior to coating. A large number of trial experiments are performed before deciding on the bath composition with the ranges of the coating parameters. Table 1 indicates the bath composition and the operating conditions for successful coating of electroless Ni-B. Nickel chloride is used as the source of nickel while sodium borohydride is the reducing agent to reduce the nickel into its elemental form while itself getting oxidized. Since the reaction between nickel chloride and sodium borohydride is quite intense and fast, ethylenediamine is used as the complexing agent to slow down this reaction and make the process stable. Ethylenediamine forms metastable complexes with nickel ions and releases them slowly as required in the reaction. Although complexing agent stabilizes the reactions to a great extent but there is always a possibility for solution breakdown due to the formation of nickel borides and the subsequent chain reaction. Hence a stabilizer is needed so that deposition occurs at a predictable rate and on the substrate surface. In the present bath, lead nitrate plays the role of a stabilizer and prevents solution breakdown during the coating period. The pH of the solution is maintained around 12.5 by continuous monitoring with a pH meter. The cleaned samples are at first activated in palladium chloride solution kept at a temperature of 55°C. Then the activated samples are merged into the electroless bath and the deposition is carried out for 2 hours at a temperature of 85-95°C according to the orthogonal array. The setup used for the electroless Ni-B deposition is shown in Figure 1. The time for deposition is fixed so that we get a uniform thickness for the coatings. The range of coating thickness is found to lie between 20-25 microns. After deposition, the samples are taken out of the bath and cleaned using distilled water. As the positive influence of heat treatment on tribological properties is a known fact, some samples are subjected to heat treatment (annealing) in a box furnace. After heat treatment, the samples are slowly cooled to room temperature (about 25ºC).

There have been several propositions regarding the reaction mechanism of electroless Ni-B coatings but one of the mechanisms proposed by Gorbunova, Ivanov, and Moiseev (1973) is well supported by experimental evidence. The proposed scheme for the reaction mechanism of nickel boron plating consists of mainly three steps:

Reduction of nickel:

$$BH_4^- + 4H_2O \rightarrow B(OH)_4^- + 4H + 4H^+ + 4e^-$$

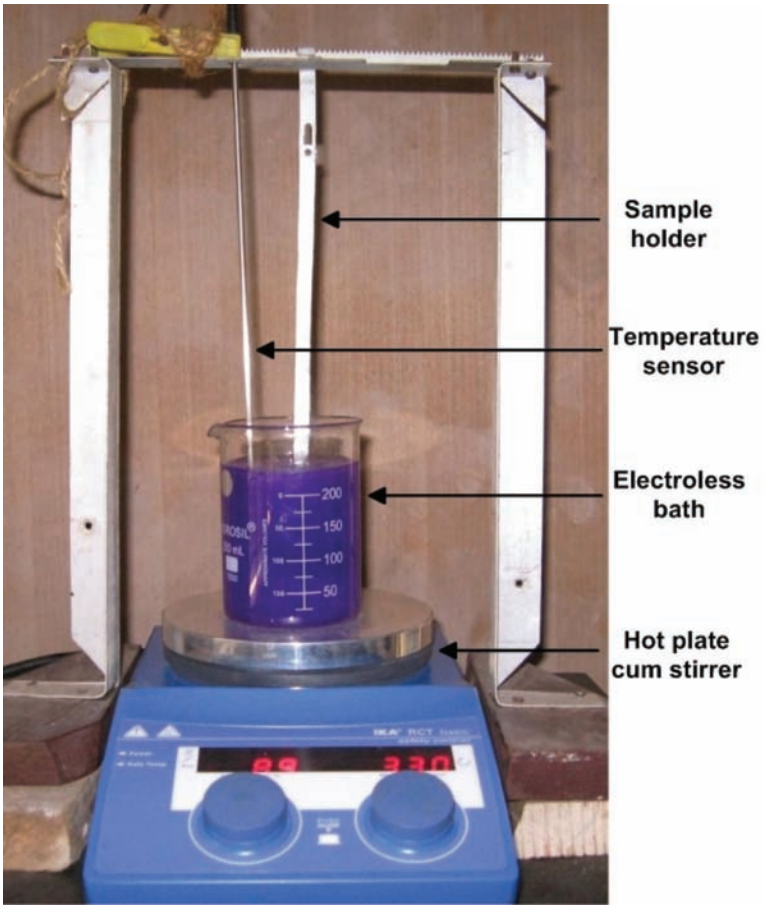
$$2Ni^{+2} + 4e^- \rightarrow 2Ni^0$$

$$BH_4^- + 2Ni^{+2} + 4H_2O \rightarrow 2Ni^0 + B(OH)_4^- + 2H_2 + 4H^+$$

Reduction of boron:

$$BH_4^- + H^+ \rightarrow BH_3 + H_2 \rightarrow B + \frac{5}{2}H_2$$

Figure 1. The electroless coating setup



Hydrolysis of borohydride:

$$BH_4^- + 4H_2O \rightarrow B(OH)_4^- + 4H + 4H^+ + 4e^- \rightarrow B(OH)_4^- + 4H_2$$

It is important to note that the present study does not consider the substrate roughness as the input variable. Thus it is essential that all samples after different stages of processing and prior to coating should have same roughness. But this is extremely difficult to achieve. Hence large numbers of samples are prepared and after all the processing prior to coating these are subjected to roughness evaluation (centre line average, R_a). Only those specimens that show insignificant variation (less than 0.1%) in roughness are used for coating deposition.

Choice of Design Factors

Even in a process as simple as electroless deposition, there are many factors which can impact the results such as bath temperature, reducing agent concentration, nickel source concentration, stabilizer concentration, pH of the solution, substrate, bath load, etc. In view of this it may be unreasonable to expect that all the factors be considered as this would make the experimental design complex and the analysis even more complicated. Based on an intensive literature review it is found that the three factors viz. bath temperature (A), concen-

Table 2. Design factors and their levels

Design Factors	Unit	Levels		
		1	2	3
Bath Temperature (A)	ºC	85	90[a]	95
Reducer conc. (B)	(g/l)	0.6	0.8[a]	1.0
Nickel source conc. (C)	(g/l)	15	20[a]	25

a: initial condition

tration of reducing agent (sodium borohydride) (B) and concentration of nickel source (nickel chloride) (C) are the mostly used ones by the researchers to control the properties of electroless nickel coating. Regarding the role of each factor it can be said that bath temperature initiates the reaction mechanism and thereby determines the rate of reaction by controlling the ionization and charge transfer process. Borohydride reduced plating baths are generally operated between 85-95ºC (Mallory & Hadju, 1991). Below 85ºC the plating rate is very slow but the rate increases exponentially with increase in temperature. Above 95ºC the bath is very much prone to instability. The plating rate is also affected by the concentration of sodium borohydride and it is generally observed that as the borohydride concentration increases, the plating rate increases but the bath stability decreases. Hence for a stable operation of the plating bath, sodium borohydride concentration is kept between 0.6 – 1.0 g/l. Nickel chloride is the source of nickel ions in the bath. Thus these three factors are considered as the main design parameters and their interaction effects are also investigated in the present study. Table 2 shows the design factors along with their levels.

Response Variable

The present study is carried out to consider the roughness characteristics of electroless Ni-B coating. Centre line average (R_a) is the most common roughness parameter used to study surface topography. Hence in the present study it is used as the response variable for surface topography characterization. Centre line average is defined as the arithmetic mean deviation of the surface height from the mean line through the profile while the mean line is defined so as to have equal areas of the profile above and below it. R_a may be expressed in the form:

$$R_a = \frac{1}{L}\int_0^L \left|Z(x)\right| dx \qquad (1)$$

where Z(x) is the ordinate of the profile curve, x is the profile direction and L is the sampling length. The unit of R_a is micrometer (μm). The coating process parameters are optimized with an objective to minimize R_a, i.e., to obtain smoother surface.

Design of Experiments

Design of experiments (DOE) is a technique to obtain and organize the maximum amount of conclusive information from the minimum amount of work, time, energy, money, or other limited resource. The DOE using Taguchi approach can economically satisfy the needs of problem solving and product/process design optimization projects in the manufacturing industry. By learning and applying this technique, it is possible to significantly reduce the time required for experimental investigations. As mentioned earlier Taguchi method uses an OA (orthogonal array) to reduce the number of experiments for determining the optimal process parameters. Orthogonal arrays allow one to compute the main and interaction effects via a minimum number of experimental trials (Ross, 1996). Taguchi has tabulated several standard OAs. The choice of a suitable OA design is critical for the success of an experiment and depends on the total degrees of freedom required to study the main and interaction effects, the goal of the experiment, resources and budget available and time constraints. In the present investigation, an L_{27} OA (Table 3) which has 27 rows corresponding

to the number of tests and 26 degrees of freedom (DOFs) with 13 columns at three levels is chosen. As per the Triangular Table for 3 level orthogonal array (Roy, 1990), 1st column is assigned to bath temperature (A), the 2nd column is assigned to concentration of reducing agent (sodium borohydride) (B), the 5th column is assigned to concentration of source of nickel (nickel chloride) (C), and rest of the columns are assigned to the two-way interactions of the factors and error terms. Degree of freedom (dof) refers to the number of fair and independent comparisons that can be made from a set of observations. In the context of DOE, the number of degrees of freedom is one less than the number of levels associated with the factor. In the present case since each of the main factors is associated with three levels, the dof of each of the factors is two. Again the number of dofs associated with an interaction is the product of the number of dof associated with each main effect involved in the interaction (Antony, 1998). In the present case each interaction is associated with four dofs (2×2). Therefore the total dof for the present case with three main parameter and three interactions is equal to eighteen (3×2 + 3×4). It is important to notice that the number of experimental trials must be greater than the total dof required for studying the effects. Hence L_{27} orthogonal array having twenty seven trials is suitably applied in the present case. Here each column represents a specific factor, each row represents an experimental run and the cell values indicate the factor settings for the run. The cell values in the main factor columns (A, B and C) indicate their levels (1, 2 and 3) while the same in the interaction indicate the combination of the levels of the main factors concerned. For example, the interaction between A and B (A×B) exists in columns 3 and 4, and for trial 1, the concerned cells show 1 in column 3 and 1 in column 4. Hence, interaction A×B has the value 11 which means it is the combination of level 1 of A and level 1 of B. Similarly, there are 9 such combinations (11, 22, 33, 12, 21, 23, 32, 13, 31) for A×B interaction in columns 3 and 4. The cell values in interaction columns and error columns are used in ANOVA for determination of their percentage contribution to the total effect.

Roughness Measurement

A stylus and skid type profilometer, Talysurf (Taylor Hobson, Surtronic 3+) is used to measure the roughness of the electroless Ni-B coatings. The instrument is set to a cut-off length of 0.8 mm, Gaussian filter and 4 mm evaluation length. The stylus traverses with a speed of 1 mm/s. Roughness measurement on the electroless Ni-B coatings is repeated four times and the average of the measurements is taken as the response for the actual experiment. The parameter evaluations are microprocessor based. The measured profile is digitized and processed through the dedicated advanced surface finish analysis software *Talyprofile* for evaluation of the roughness parameter R_a. A photograph of the actual profilometer along with the computer is given in Figure 2.

Surface Morphology and Composition Study

Scanning electron microscopy (JEOL, JSM-6360) is used to observe the surface morphology of the coating before and after heat treatment. This is done in order to analyze the effect of heat treatment on the Ni-B coatings. Energy dispersive X-ray analysis (EDAX Corporation) is made use of in order to determine the composition of the coating in terms of the weight percentages of nickel and boron. It has been demonstrated by previous studies (Watanabe & Tanabe, 1976) that the physical properties of the deposited film are greatly influenced by the concentration of boron in the film. This concentration in turn depends upon the amount of reducing agent added. Hence EDX analysis is done on the coatings developed from the bath consisting of different concentrations of sodium borohydride (reducing agent) in order to capture the range of boron content in the coatings. The different precipitated phases before and after

Table 3. L_{27} Orthogonal Array with design factors and interactions

	Column numbers												
Trial No.	**1 A**	**2 B**	**3 A×B**	**4 A×B**	**5 C**	**6 A×C**	**7 A×C**	**8 B×C**	**9 -**	**10 -**	**11 B×C**	**12 -**	**13 -**
1	1	1	1	1	1	1	1	1	1	1	1	1	1
2	1	1	1	1	2	2	2	2	2	2	2	2	2
3	1	1	1	1	3	3	3	3	3	3	3	3	3
4	1	2	2	2	1	1	1	2	2	2	3	3	3
5	1	2	2	2	2	2	2	3	3	3	1	1	1
6	1	2	2	2	3	3	3	1	1	1	2	2	2
7	1	3	3	3	1	1	1	3	3	3	2	2	2
8	1	3	3	3	2	2	2	1	1	1	3	3	3
9	1	3	3	3	3	3	3	2	2	2	1	1	1
10	2	1	2	3	1	2	3	1	2	3	1	2	3
11	2	1	2	3	2	3	1	2	3	1	2	3	1
12	2	1	2	3	3	1	2	3	1	2	3	1	2
13	2	2	3	1	1	2	3	2	3	1	3	1	2
14	2	2	3	1	2	3	1	3	1	2	1	2	3
15	2	2	3	1	3	1	2	1	2	3	2	3	1
16	2	3	1	2	1	2	3	3	1	2	2	3	1
17	2	3	1	2	2	3	1	1	2	3	3	1	2
18	2	3	1	2	3	1	2	2	3	1	1	2	3
19	3	1	3	2	1	3	2	1	3	2	1	3	2
20	3	1	3	2	2	1	3	2	1	3	2	1	3
21	3	1	3	2	3	2	1	3	2	1	3	2	1
22	3	2	1	3	1	3	2	2	1	3	3	2	1
23	3	2	1	3	2	1	3	3	2	1	1	3	2
24	3	2	1	3	3	2	1	1	3	2	2	1	3
25	3	3	2	1	1	3	2	3	2	1	2	1	3
26	3	3	2	1	2	1	3	1	3	2	3	2	1
27	3	3	2	1	3	2	1	2	1	3	1	3	2

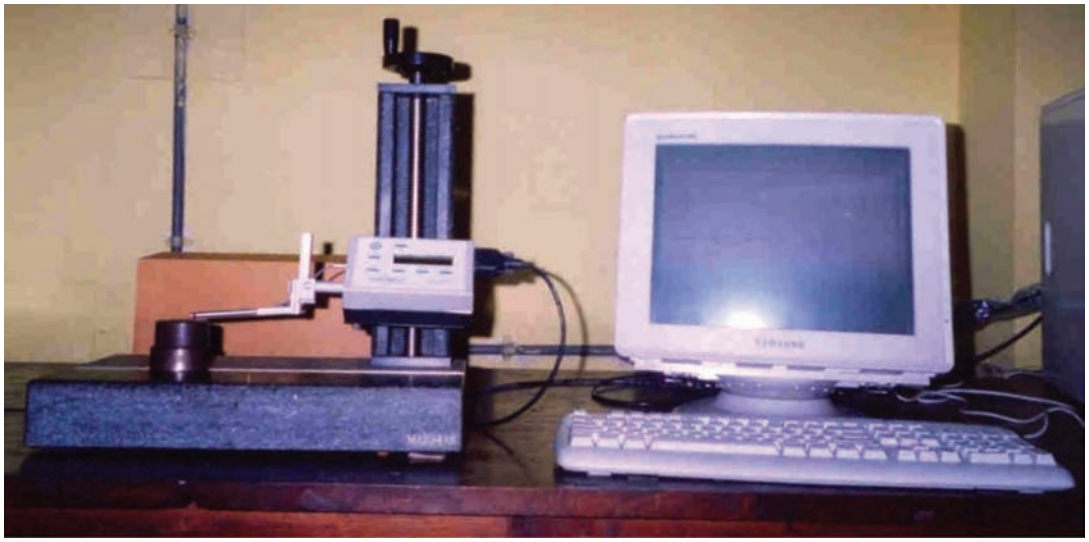
heat treatment are detected by using X-ray diffraction analyzer (Rigaku, Miniflex).

RESULTS AND DISCUSSION

Analysis of Signal to Noise Ratio

In Taguchi's parameter design, the basic objective is to identify the conditions which optimize process/product performance. In arriving at this optimal set of conditions, Taguchi advocates the use of signal-to-noise (S/N) ratio - the need is to maximize the performance of a system or product by minimizing the effect of noise while maximizing the mean performance. As an evaluation tool for determining robustness, the signal-to-noise S/N ratio is preferred to simple averages of results as the former can capture the variability of the results within a trial condition. The S/N is treated

Figure 2. Talysurf profilometer



as a response (output) of the experiment, which is a measure of variation when uncontrolled noise factors are present in the system (Antony & Kaye, 1999). Since the objective of the present work is to obtain a smooth surface by optimizing the coating parameters, the surface roughness parameter R_a needs to be minimized. Hence, in the present work S/N ratio analysis for R_a is done using LB (lower the better) criterion which is given by

$$S / N = -10 \log\left(\sum y^2 / n\right) \quad (2)$$

where y is the observed data and n is the number of observations. Table 4 shows the experimental R_a values along with their S/N ratio. As the experimental design is orthogonal, it is possible to separate out the effect of each coating parameter at different levels. For example, the mean S/N ratio for factor A at levels 1, 2 and 3 can be calculated by averaging the S/N ratios for the experiments 1–9, 10–18 and 19–27, respectively. The mean S/N ratio for each level of the other factors can be computed in a similar manner. The mean S/N for each level of the factors A, B and C is summarized in Table 5.

The response table shows the average of the selected characteristic for each level of the factors. The response table includes ranks based on Delta statistics, which compare the relative magnitude of effects. The Delta statistic is the highest average for each factor minus the lowest average for the same. Ranks are assigned based on Delta values; rank 1 is assigned to the highest Delta value, rank 2 to the second highest Delta value, and so on. The corresponding main effects and interaction effects plots between the process parameters are also shown in Figure 3 and Figure 4 respectively. In the main effects plot if the line for particular parameter is near horizontal, then the parameter has no significant effect. On the other hand, a parameter for which the line has the highest inclination will have the most significant effect. It is very much clear from the main effects plot that parameter B (concentration of reducing agent) is the most significant parameter while parameter A (bath temperature) also has a quite significant effect on the response. But parameter C (concentration of nickel source) has almost no effect. An interaction plot is useful in providing a rapid understanding of the nature of interactions. Interaction plots are constructed by plotting the

Table 4. Experimental results for surface roughness and S/N ratio

Sample	Surface roughness R_a (µm)	S/N ratio
1	0.623	4.099
2	0.393	8.101
3	0.447	6.993
4	0.715	2.913
5	0.713	2.938
6	0.756	2.429
7	0.910	0.814
8	0.864	1.269
9	0.979	0.177
10	0.309	10.17
11	0.405	7.845
12	0.371	8.600
13	0.485	6.271
14	0.420	7.535
15	0.467	6.613
16	0.887	1.041
17	0.480	6.375
18	0.804	1.892
19	0.343	9.281
20	0.357	8.928
21	0.270	11.366
22	0.374	8.542
23	0.402	7.904
24	0.356	8.958
25	0.403	7.877
26	0.666	3.527
27	0.798	1.959

average response values at each factor level combination. In case of interaction, parallel lines are an indication of the absence of interaction between the factors, while non-parallel lines are an indication of the presence of interaction between the factors. And if the lines intersect strong interaction is said to exist between the two factors. The intersecting lines in Figure 4 (b) reflect that strong interaction exists between factors A and C. This

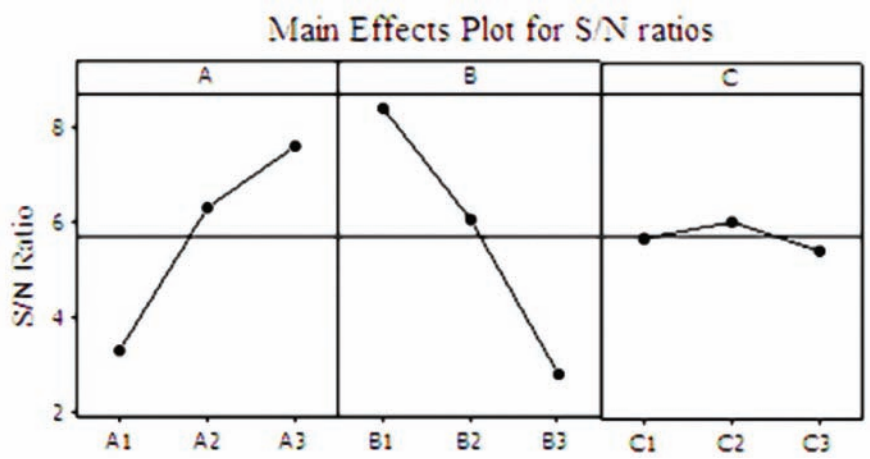
Table 5. Response table of mean S/N ratio for R_a

Level	A	B	C
1	3.304	8.377	5.669
2	6.262	6.012	6.047
3	7.594	2.771	5.443
Delta	4.290	5.607	0.604
Rank	2	1	3

The total mean S/N ratio = 5.719 dB

is indicative of the fact that bath temperature in some way influences the nickel ions participating in the reaction mechanism thus determining the smoothness of the Ni-B coatings. The non parallel lines in Figure 4 (a) and Figure 4 (b) indicate the presence of mild interaction between factors AB and BC respectively. Thus from the present analysis it is clear that the concentration of reducing agent (B) and bath temperature (A) are the most influencing parameters for R_a of Ni-B coatings. The optimal combination of parameters is obtained from the main effect plot of S/N ratio. Since higher S/N ratio indicates that the system tends towards optimality, the optimal condition for each parameter is taken at those points where the S/N ratio is found to be maximum. From Figure 3 it is seen that plot for parameters A, B and C reach maximum at levels 3, 1 and 2 respectively. Hence the optimal combination of coating process parameters is given as A3B1C2. It may be noted that quality of Ni-B deposits are very much affected by the ratio of concentrations of nickel and borohydride ions in the solution. An improper balance between the concentrations of nickel and borohydride can lead to poor and rough deposits (Mallory & Hadju, 1991). The optimal levels of nickel source (C2) and reducing agent (B1) obtained from the present study may be helping in striking a proper balance between the two (nickel and borohydride ions) for achieving smoother deposits. Moreover bath temperature increases the deposition rate by accelerating the reaction mechanism. Hence the thickness of the

Figure 3. Main effects plot for S/N ratios



coating deposited at a higher bath temperature is generally more than that deposited at a lower bath temperature. Now in the present study, smoother deposits are obtained at higher bath temperature. Thus, there may be a critical substrate roughness above which thicker deposits may actually be smoothening the surface. This idea may form part of a future study.

Analysis of Variance

In order to conduct an analysis of the relative importance of each factor more systematically, an analysis of variance (ANOVA) is applied to the data. The main objective of ANOVA is to extract from the results how much variations each factor causes relative to the total variation observed in the result. This indicates which of the process parameters significantly affect the performance characteristics. In the present case this is accomplished by separating the total variability of the S/N ratios, which is measured by the sum of the squared deviations from the total mean of the S/N ratio, into contributions by each of the process parameters and the error. In the present study ANOVA is performed using Minitab (Minitab User Manual, 2001). ANOVA results for R_a of electroless Ni-B coating is shown in Table 6.

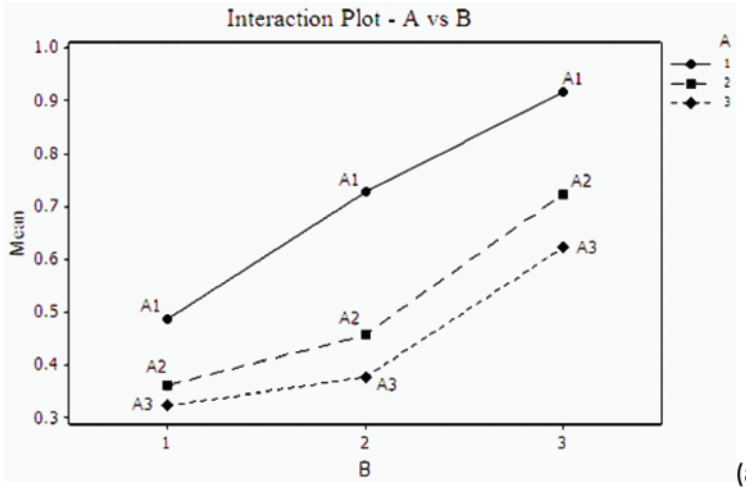
In ANOVA, a ratio called F-ratio, which is the ratio between the regression mean square and

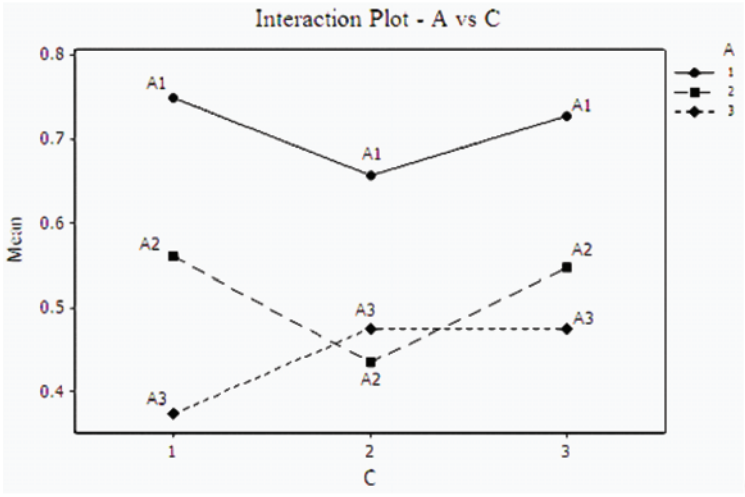
Table 6. ANOVA Table

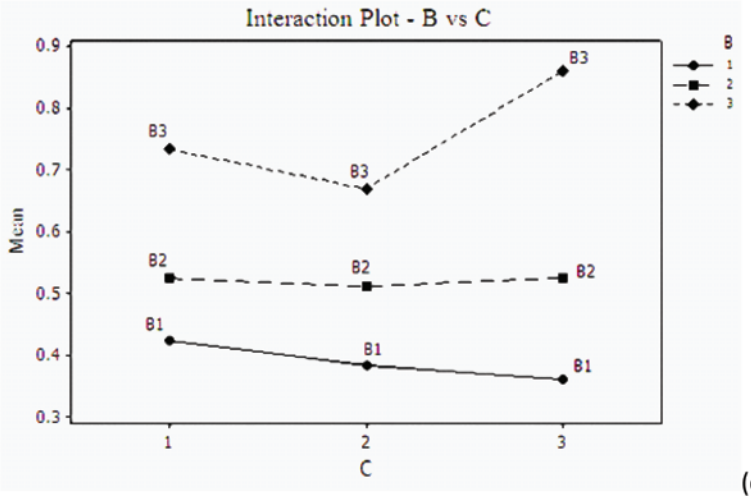
Source	DF	SS	MS	F	% contribution
A	2	86.769	43.385	11.70*	30.26
B	2	142.606	71.303	19.22*	49.74
C	2	1.675	0.838	0.23	0.58
A*B	4	5.065	1.266	0.34	1.76
A*C	4	11.036	2.759	0.74	3.85
B*C	4	9.866	2.467	0.67	3.44
Error	8	29.672	3.709		10.35
Total	26	286.690			100

* - Significant parameters and interactions ($F_{0.01,2,8} = 8.65$; $F_{0.01,4,8} = 7.01$)

Figure 4. Interaction effect plots for mean roughness: (a) A vs B, (b) A vs C and (c) B vs C







mean square error is used to measure the significance of the parameters under investigation with respect to the variance of all the terms included in the error term at a desired significance level, α. A calculated F-ratio which is higher than the tabulated F-ratio indicates that the factor is significant at a desired α level. ANOVA table also shows the percentage contribution of each parameter. It is seen that parameter B, i.e., concentration of reducing agent has got the most significant influence on roughness R_a at a confidence level of 99%. Bath temperature or parameter A is also found to be significant at the same level of confidence. None among the rest of the parameters or interactions are found to be significant enough to influence the roughness of Ni-B within the specific test range.

Confirmation Tests

Once the optimal level of the process parameters is selected, the final step of the Taguchi method is to predict and verify the improvement of the performance characteristic using the optimal level of the process parameters. The estimated S/N ratio, $\hat{\gamma}$ using the optimal level of the process parameters can be calculated as:

$$\hat{\gamma} = \gamma_m + \sum_{i=1}^{o}\left(\overline{\gamma}_i - \gamma_m\right) \quad (3)$$

where γ_m is the total mean S/N ratio, $\overline{\gamma}_i$ is the mean S/N ratio at the optimal level, and o is the number of the main design parameters that significantly affect the roughness of electroless Ni-B coating. Table 7 shows the comparison of the estimated S/N ratio with the experimental S/N ratio using the optimal parameters. The mid level combination of coating parameters i.e., A2B2C2 is considered as the initial condition for the present case. The increase of the S/N ratio from the initial condition to the optimal condition is found to be about 1.40 dB. This implies that the roughness of the coating surface generated using optimal combination of parameters is about 15% lesser than that generated using the initial combination of coating parameters.

Surface Morphology and Composition

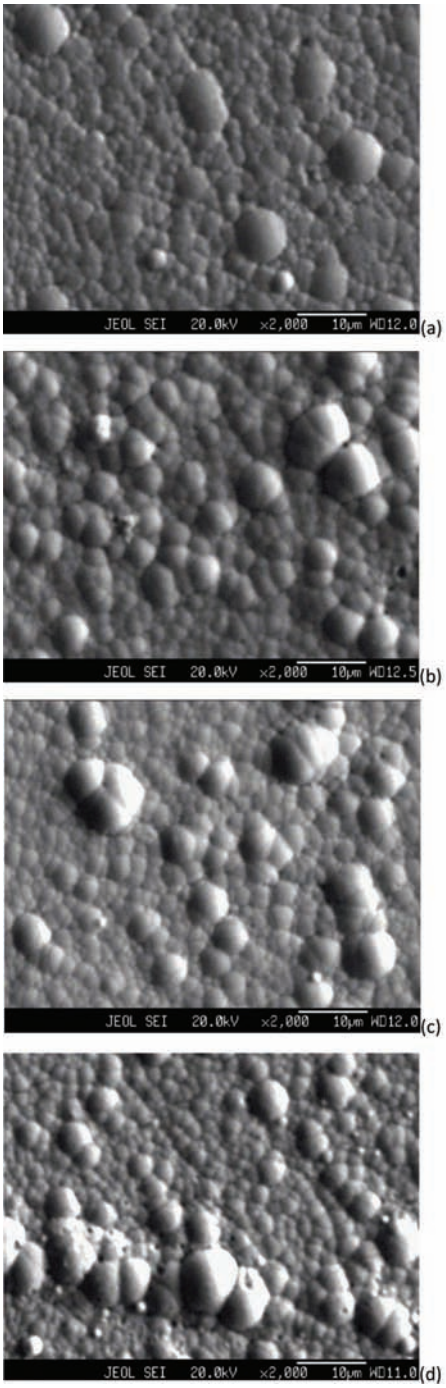
The SEM micrographs of the coating surfaces in as-deposited and heat treated (at 250°C, 350°C and 450°C for one hour) conditions are shown in Figure 5. The surface exhibits a cauliflower like structure which strongly points towards the coating possessing a lubricious behavior (Delaunois & Lienard, 2002). The surface of the Ni-B coatings appears to be dense and matte and grey in colour with low porosity. Energy dispersive X-ray analysis is performed with one of the newer EDX detector which does not contain any Beryllium window in order to detect light elements like boron. The Beryllium window if present absorbs all the soft X-rays thereby precluding the detection of lighter elements. The EDX plots are shown in Figure 6 and boron content in terms of weight percentages is found to be in the range of

Table 7. Confirmation tests

	Initial condition	Optimal condition	
		Prediction	Experimentation
Level	A2B2C2	A3B1C2	A3B1C2
R_a (μm)	0.420		0.358
S/N ratio (dB)	7.535	10.251	8.928

Improvement of S/N ratio = 1.393 dB

Figure 5. SEM micrographs of electroless Ni-B deposits: (a) as deposited, (b) heat treated at 250°C, (c) heat treated at 350°C and (d) heat treated at 450°C



5.72 - 7.46 while the remaining is mostly nickel. The XRD analysis (Figure 7) shows that the Ni-B film is almost amorphous in as- deposited phase but turns crystalline with heat treatment. This is evident from the presence of microcrystalline peaks in as-deposited phase whereas broad peaks of Ni, Ni_2B and Ni_3B are found in samples heat treated at 450°C.

Description of Optimized Coating Surface

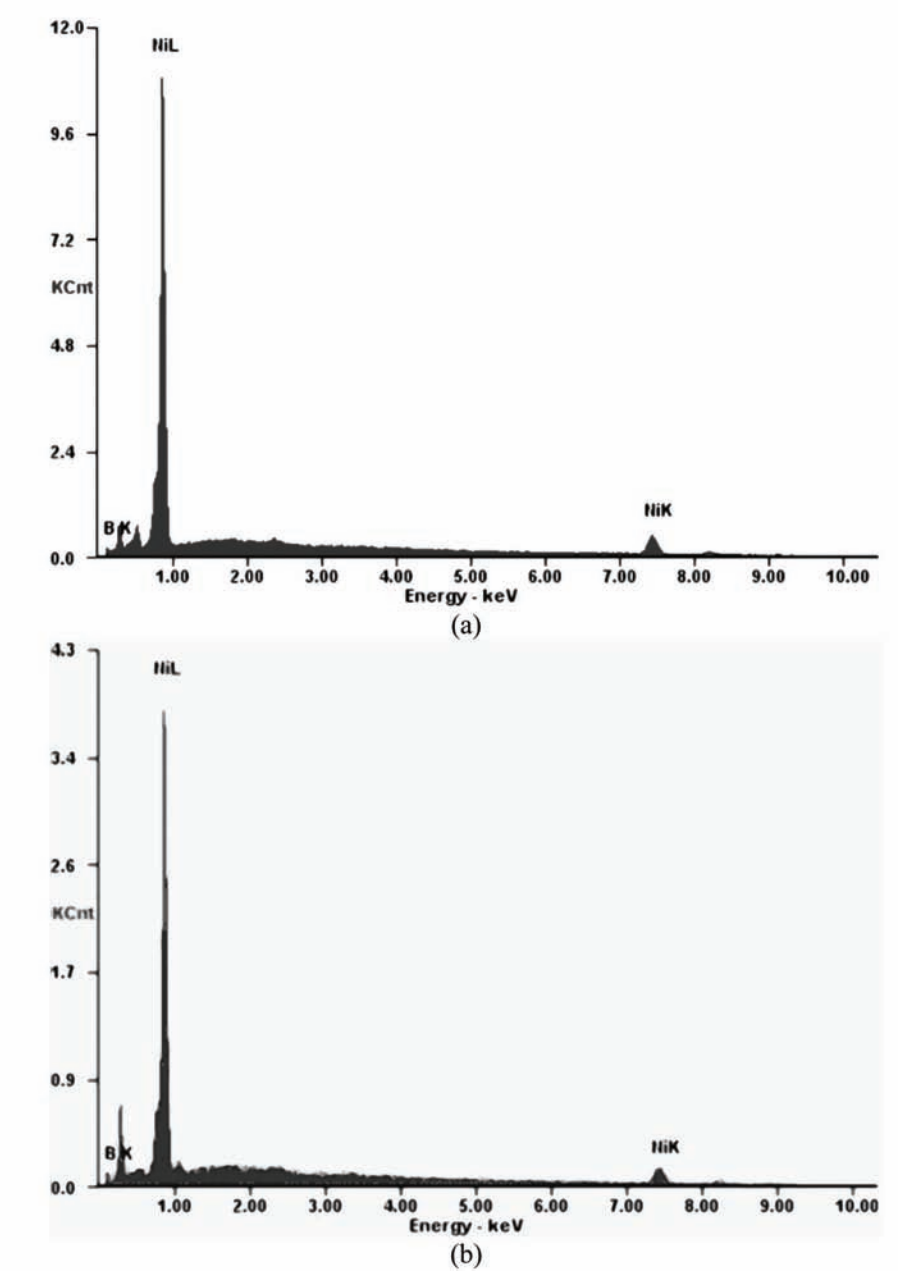
SEM is also performed on the coating obtained through the optimal combination of coating parameters to get a peek on the surface quality of the coating. The corresponding micrograph is provided in Figure 8. The colour of the coating appears matte grey in colour with low porosity, similar to the previous coatings. Moreover the optimized coating surface seems to be quite smooth in appearance with almost uniform distribution of Ni-B nodules. This is in conformation with the lower roughness (R_a) value of the surface.

CONCLUSION

In the present study, Taguchi orthogonal array is used to optimize the coating process parameters viz. bath temperature (A), concentration of reducing agent (B) and concentration of nickel source (C) in order to minimize the surface roughness (R_a) of electroless Ni-B coating. ANOVA is also performed to examine which of the factors or their interactions significantly affect the surface roughness of Ni-B coatings. Finally confirmation experimentation is done in order to validate the results obtained through the optimization. The following conclusions can be drawn:

- The optimal combination of coating parameters for minimum roughness is obtained as A3B1C2.

Figure 6. EDX spectra of the coating surfaces: (a) 0.6 g/l $NaBH_4$ concentration and (b) 1.0 g/l $NaBH_4$ concentration



- The ANOVA results indicate that the concentration of reducing agent (B) is the most important parameter along with bath temperature (A) that significantly affects the roughness of Ni-B at a confidence level of 99%.
- The confirmation test reveal that roughness of Ni-B coating developed at optimal condition (A3B1C2) is 15% lesser than that developed with the initial condition (A2B2C2).

Figure 7. XRD patterns of electroless Ni–B deposit in (a) as-deposited and (b) heat treated at 450ºC

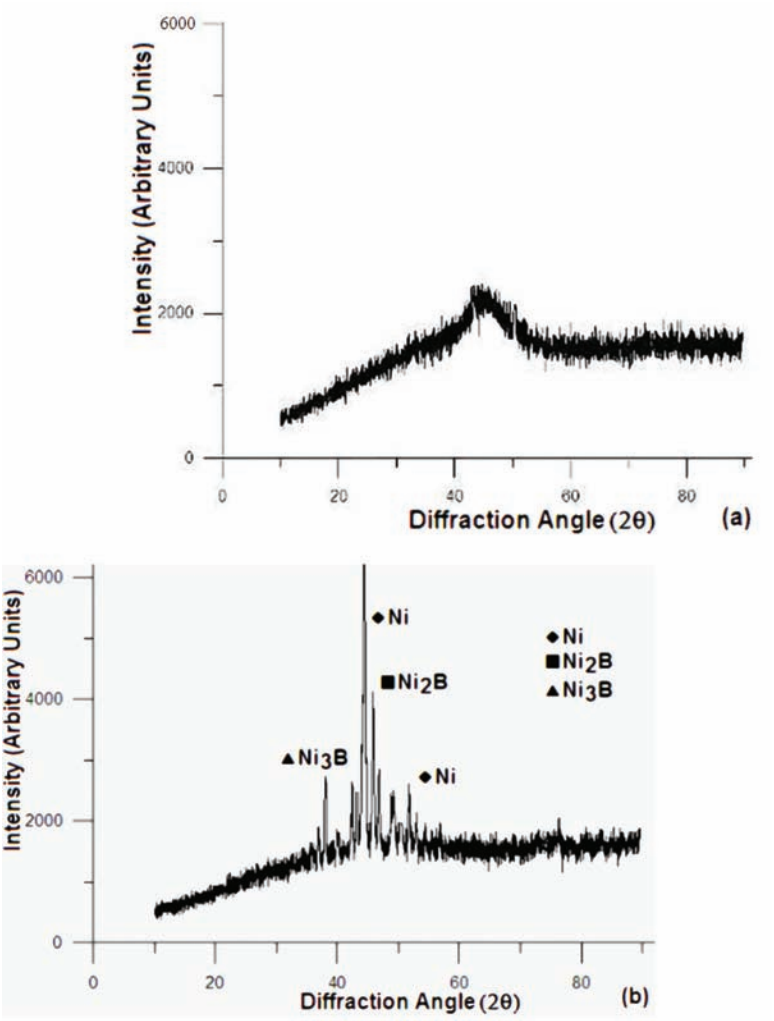
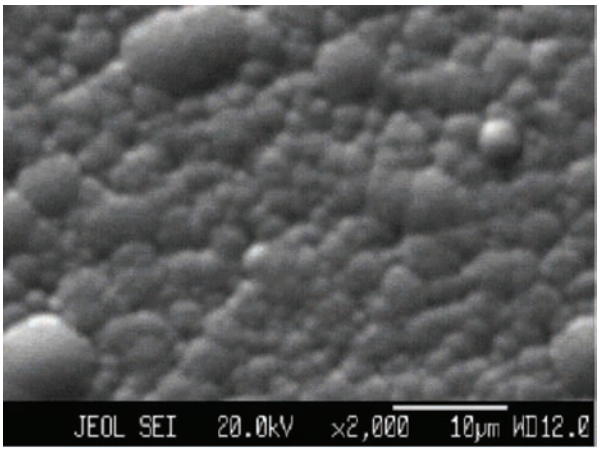


Figure 8. SEM micrograph of the optimized coating surface



The microstructure study through SEM micrographs reveals that the coating has a cauliflower like structure with no obvious surface damage. Also the coating is dense and grey in colour with low porosity. The boron content of the coatings is found to lie between 5.72-7.46%. In as deposited condition the coating is a mixture of amorphous and microcrystalline structure which gradually turns crystalline with heat treatment. This is confirmed by the presence of Ni, Ni_2B and Ni_3B peaks in the XRD plot of Ni-B coating annealed at 450°C.

ACKNOWLEDGMENT

One of the authors (SKD) would like to acknowledge the research support through Senior Research Fellowship provided by Council of Scientific and Industrial Research, Govt. of India: File No. 9/96(0621)2K10-EMR-I dated 05/03/2010.

REFERENCES

Agarwala, R. C., & Agarwala, V. (2003). Electroless alloy /composite coatings: A review. *Sadhana*, *28*(3-4), 475–493. doi:10.1007/BF02706445

Anik, M., Körpe, E., & Şen, E. (2008). Effect of coating bath composition on the properties of electroless nickel-boron films. *Surface and Coatings Technology*, *202*, 1718–1727. doi:10.1016/j.surfcoat.2007.07.031

Antony, J. (1998). Some key things industrial engineers should know about experimental design. *Logistics Information Management*, *11*(6), 386–392. doi:10.1108/09576059810242606

Antony, J., & Kaye, M. (1999). *Experimental quality - a strategic approach to achieve and improve quality*. Dordrecht, The Netherlands: Kluwer Academic.

Brenner, A., & Riddell, G. E. (1950). *U.S. Patent No. 2532282: Nickel plating by chemical reduction*. Washington, DC: U. S. Patent and Trademark Office.

Delaunois, F., & Lienard, P. (2002). Heat treatments for electroless nickel–boron plating on aluminum alloys. *Surface and Coatings Technology*, *160*, 239–248. doi:10.1016/S0257-8972(02)00415-2

Delaunois, F., Petitjean, J. P., Lienard, P., & Jacob-Duliere, M. (2000). Autocatalytic electroless nickel-boron plating on light alloys. *Surface and Coatings Technology*, *124*(2-3), 201–209. doi:10.1016/S0257-8972(99)00621-0

Dervos, C. T., Novakovic, J., & Vassiliou, P. (2004). Vacuum heat treatment of electroless Ni–B coatings. *Materials Letters*, *58*, 619–623. doi:10.1016/S0167-577X(03)00581-0

Drovosekov, A. B., Ivanov, M. V., Krutskikh, V. M., Lubnin, E. N., & Polukarov, Yu. M. (2005). Chemically deposited Ni-W-B coatings: Composition, structure, and properties. *Protection of Metals*, *41*(1), 55–62. doi:10.1007/s11124-005-0008-1

Gorbunova, K., Ivanov, M., & Moiseev, V. (1973). Electroless deposition of nickel-boron alloys mechanism of process, structure, and some properties of deposits. *Journal of the Electrochemical Society*, *120*, 613. doi:10.1149/1.2403514

Hari Krishnan, K., John, S., Srinivasan, K. N., Praveen, J., Ganesan, M., & Kavimani, P. M. (2006). An overall aspect of electroless Ni-P depositions- a review article. *Metallurgical and Materials Transactions A*, *37*, 1917–1926. doi:10.1007/s11661-006-0134-7

Ivanov, M. V. (2001). Electroless nickel-boron-phosphorus coatings: Protective and functional properties. *Protection of Metals*, *37*(6), 592–596. doi:10.1023/A:1012827932615

Jiang, B., Xiao, L., Hu, S., Peng, J., Zhang, H., & Wang, M. (2009). Optimization and kinetics of electroless Ni-P-B plating of quartz optical fiber. *Optical Materials*, *31*, 1532–1539. doi:10.1016/j.optmat.2009.02.016

Kanta, A. F., Vitry, V., & Delaunois, F. (2009). Effect of thermochemical and heat treatments on electroless nickel-boron. *Materials Letters*, *63*, 2662–2665. doi:10.1016/j.matlet.2009.09.031

Krishnaveni, K., Sankara Narayanan, T. S. N., & Seshadri, S. K. (2005). Electroless Ni-B coatings: Preparation and evaluation of hardness and wear resistance. *Surface and Coatings Technology*, *190*, 115–121.

Mallory, G. O., & Hadju, J. B. (1991). *Electroless plating: Fundamentals and applications*. Orlando, FL: AESF.

Minitab User Manual 13.2. (2001). *Making data analysis easier*. State College, PA: MINITAB Inc.

Montgomery, D. C. (2001). *Design and analysis of experiments*. New York, NY: John Wiley & Sons.

Oraon, B., Majumdar, G., & Ghosh, B. (2008). Improving hardness of electroless Ni-B coatings using optimized deposition conditions and annealing. *Materials & Design*, *29*, 1412–1418. doi:10.1016/j.matdes.2007.09.005

Riedel, W. (1991). *Electroless nickel plating*. Hertfordshire, UK: Finishing Publications.

Ross, P. J. (1996). *Taguchi techniques for quality engineering* (2nd ed.). New York, NY: McGraw-Hill.

Roy, R. (1990). *A primer on the Taguchi method*. Dearborn, MI: Society of Manufacturing Engineers.

Sahoo, P. (2008). Optimization of electroless Ni-P coatings based on surface roughness. *Tribology Online*, *3*(1), 6–11. doi:10.2474/trol.3.6

Sankara Narayanan, T. S. N., Krishnaveni, K., & Seshadri, S. K. (2003). Electroless Ni-P/Ni-B duplex coatings: Preparation and evaluation of microhardness, wear and corrosion resistance. *Materials Chemistry and Physics*, *82*, 771–779. doi:10.1016/S0254-0584(03)00390-0

Taguchi, G. (1990). *Introduction to quality engineering*. Tokyo, Japan: Asian Productivity Organization.

Watanabe, T., & Tanabe, Y. (1976). Formation and morphology of Ni-B amorphous alloy deposited by electroless plating. *Materials Science and Engineering*, *23*, 97–100. doi:10.1016/0025-5416(76)90175-0

This work was previously published in the International Journal of Manufacturing, Materials, and Mechanical Engineering, Volume 1, Issue 3, edited by J. Paulo Davim, pp. 53-71, copyright 2011 by IGI Publishing (an imprint of IGI Global).

Chapter 19
Al_2O_3 Nanobricks via an Organic Free Route Using Water as Solvent

M. A. Shah
King Abdul Aziz University, Saudi Arabia

ABSTRACT

The chemical synthesis of nanomaterials has been studied by few researchers, but innumerable improvements and better methods have been reported in the past few years. This new approach of preparing aluminum oxide (Al_2O_3) nanobricks is based on a soft reaction of aluminum powder and de-ionized (DI) water at 200°C without use of any additives or surfactants. Powder X-ray diffraction studies reveal that the as prepared nanobricks are highly crystalline in nature and by morphological investigations using FESEM, it was revealed that the bricks are rectangular in shape having width of 90±15nm and breadth of ~200nm, which was confirmed by high resolution TEM. The technique could be extended and expanded to provide a general, simple, and convenient strategy for the synthesis of nanostructures of other functional materials with important scientific and technological applications. The prospects of the process are bright and promising.

INTRODUCTION

Innovations at the intersection of medicine, biotechnology, engineering, physical sciences and information technology are spurring new directions in R&D, commercialization and technology transfer. The future of nanotechnology is likely to continue in this interdisciplinary manner. Nanotechnology is the next industrial revolution, and almost all industries will be radically transformed by it in a few years. Ceramics are regarded as versatile materials and aluminum oxide (Al_2O_3), one of the ceramic materials commonly known as sapphire is known to exist in a number of metastable

DOI: 10.4018/978-1-4666-1867-1.ch019

Copyright © 2013, IGI Global. Copying or distributing in print or electronic forms without written permission of IGI Global is prohibited.

polymorphs in addition to the thermodynamically stable α-Al_2O_3 or corundum form. Among which, α-Al_2O_3 is an important form of alumina because of its porous structure and high catalytic surface activity. This material has been widely used as catalysts, an adsorbent and as a support for industrial catalysis in hydrocarbon conversion (Lee & Crawford, 1987; Lee et al., 1997).

Various synthetic routes have been employed for the synthesis of Al_2O_3 nanostructures with various morphologies. Aside from nanorods, nanowires, nanobelts, nanotubes, limited studies have been made on nanobricks so far. The routes employed include the famous sol-gel chemistry, spray pyrolysis, precipitation, solovothermal, reverse micelles and physical approaches and have been well explained by Shah and Tokeer (2010). The chemical routes have attracted a great deal of attention and have been intensively studied in the recent years. These methods have the advantage of being used to produce α-form crystals at relatively low temperature but the starting materials are relatively expensive. The addition of catalysts or templates employed in other strategies involves a complicated process and may result in impurity in the products. Moreover, most of the pathways suggested for the synthesis of Al_2O_3 involve environmentally malignant chemicals which are toxic and not easily degraded in the environment. Organic solvents are practically problematic because many are toxic which makes the nanomaterials useless. Environmental friendly chemical synthesis requires alternative solvents such as ionic liquids, liquid and water. Water is particularly attractive because it is inexpensive, environmentally benign and bestowed with many virtues especially under supercritical conditions. In our preliminary studies reported earlier, we have obtained nanorods by varying the time and temperature of the reaction (Shah et al., 2009). It was proposed that the growth of nanostructures with different morphologies, sizes, compositions was mainly controlled by temperature and duration of reaction process. Encouraged by the results, the present studies have been carried out keeping the time and temperature constant.

Interestingly, almost uniform sized nanobricks were obtained by a simple reaction of aluminum powder and de-ionized water at very low temperature of 200°C and the reaction time was 24 hours. By morphological investigations, it was revealed that the bricks are rectangular in shape having width of 90±15nm and breadth of ~200nm. To the best of our knowledge, the synthesis of nanobricks without organics, catalyst and toxic solvents has not been reported so far. Detailed and systematic studies would be necessary to optimize the conditions for obtaining nanoparticles of desired dimensions.

EXPERIMENTAL

Aluminum foils as well as powder were used as a source of aluminum and were cleaned by ultrasonication in acetone and water for 20 minutes in each solvent. A closed cylindrical Teflon lined stainless steel chamber was used for the synthesis. De-ionized water was prepared in laboratory. Pure aluminum AR grade (Ranbaxy) with diameter of about 10μm was used as starting material. In the experiment, 2 mg of aluminum metal powder and 20ml of de-ionized water have been well sonicated in a glass vial for around 10 minutes. Few drops of ethylenediamine were added to avoid the agglomeration. After sonication, the reaction mixture was transferred to teflon-lined stainless steel chamber of 100ml capacity and has been kept at 200°C in an oven for 24 hours. After the desired time, the system was allowed to cool naturally. The reaction mixture was centrifuged to reclaim the precipitated sample and washed several times with DI water. The final product was air dried for few hours. A similar treatment was given to Al foils and the results were almost same.

Characterization of Samples

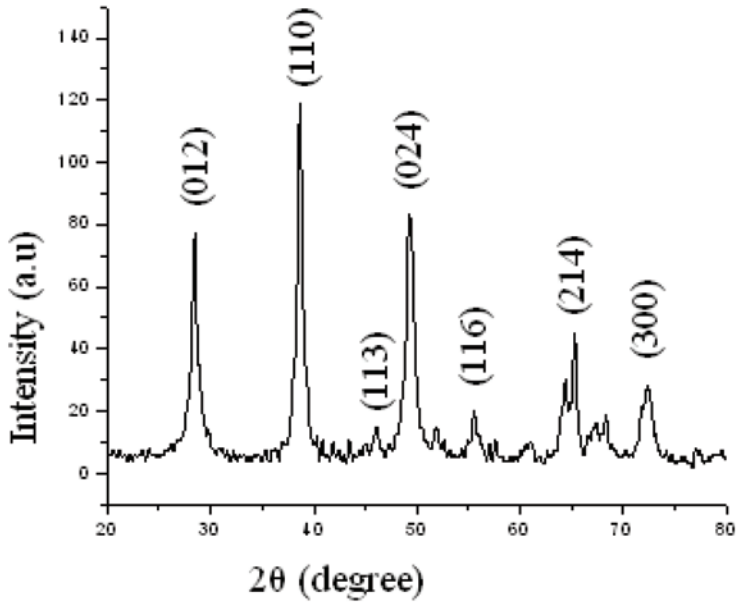
Phase structure and the purity of the as prepared samples were characterized by powder X-ray diffraction (XRD) taken on a Philips (X'Pert PRO PW-3710) diffractometer with 2θ ranging from 10-80°, using Cu Kα (λ =0.15141 nm) radiation operated at 40kV and 30mA. The morphology of the products was carried out using Field Emission Scanning Electron Microscope (FEI SEM, NNL 200, Japan), coupled with energy dispersive X-ray spectrometer EDX (Gensis). Transmission electron microscopy images were obtained on a high resolution transmission electron microscope HRTEM (JEOL JEM-2100F, Japan) at an accelerating voltage of 200kV to confirm the morphology of the products.

Results and Discussion

Phase Identification

The XRD patterns of the as-prepared samples synthesized at 200°C shown in Figure 1 reveals diffraction peaks of (012), (104), (110), (113), (024) and (214), which are characteristic of the α-Al_2O_3. Diffraction peaks of α-Al_2O_3 with lattice parameters a = 4.76Å and c = 12.99 Å (corresponding to JCPDS No. 46-1212) are identified unambiguously. The relative broad peaks suggest high crystallinity of the samples. The result is quite different from the traditional process in which only amorphous phase can be obtained from the precipitates derived by sol–gel process before calcinations and further higher temperature heat treatment is normally required to induce crystallization (Peng et al., 2002). Thus, this method, "the soft option of hydrothermal treatment" may be regarded as an alternative to calcinations for promoting the crystallization. The fact that no discernible peak was identified in the low range of 2θ = 1–10◦ has ruled out the existence of the amorphous structure. These results are in good agreement with those reported in the literature. Compared with the previous reports, the temperature applied in the synthesis is much lower and the results are much better. For example, Peng et al. (2002) reported Al_2O_3 nanowires using Al

Figure 1. The XRD pattern of the as synthesized sample



pieces and SiO_2 nanoparticles at 1200°C; Fang et al (2004) synthesized nanowires by using simple physical vapour evaporation of mixtures of Al and TiO_2 powders at 1150°C.

Morphology Examinations

After coating with 5nm thick gold, the morphology of the product was examined using FESEM. Figure 2 shows (a) low and (b) high-resolution FESEM images of nanobricks obtained by the reaction of aluminum metal powder with DI water at 200°C for 24 hours. The FESEM images confirm that the nanobricks are grown in a very high density. It was observed that the grown Al_2O_3 products revealed that the bricks are rectangular in shape having width of 90±15nm and breadth of ~200nm. The typical lengths of some of the grown nanobricks are about 1 μm. The size was also examined using TEM. Figure 3 shows the TEM image of the sample. It can be seen that uniform nanocrystalline Al_2O_3 nanobricks had rectangular shape with weak agglomeration. According to TEM image this preparation method successfully overcomes the problem of agglomeration.

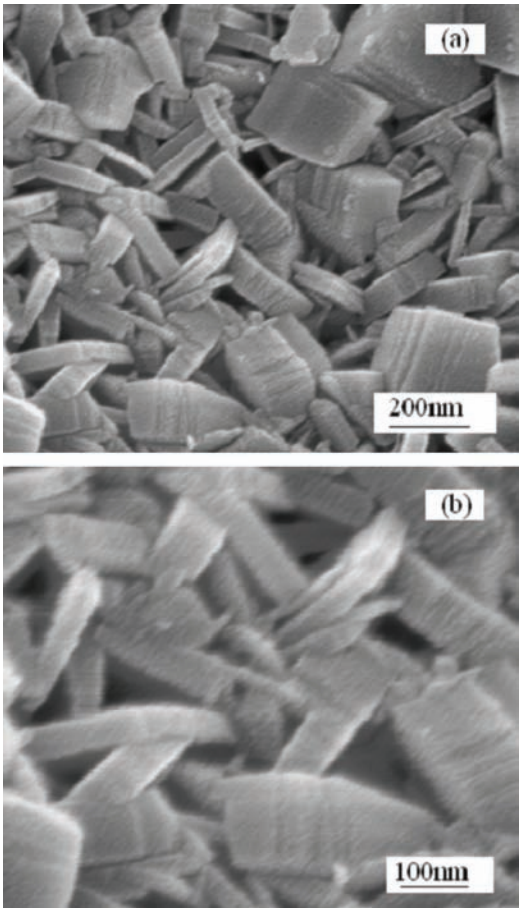
COMPOSITION OF SAMPLE

To check the composition of the as-grown materials, EDX analysis was performed and is shown in Figure 4. It is confirmed from the EDX analysis that the grown nanobricks are composed of aluminum and oxygen only. The molecular ratio of Al:O of the grown nanobricks, calculated from EDX and quantitative analysis data, is close to that of bulk (5% error is attributed to the analysis technique).

The Formation Mechanism

The formation of nanostructures by the reaction of aluminum metal with water can be explained as follows. During the reaction process, the aluminum ions react with water to form Al $(OH)_2$ colloids. As the concentration of the Al^{2+} and OH^- ions exceeds a critical value, the precipitation of aluminum oxide nuclei starts. The $Al(OH)_2$ can be transformed into the Al_2O_3 crystals via the simple chemical reactions mentioned below:

Figure 2. The typical (a) low and (b) high-resolution images of nanobricks obtained by the reaction of aluminum powder with water at 200°C for 24 hours.



$$2Al(OH)_2 \xrightarrow{\Delta} Al_2O_3 + 2H_2O$$

The precipitates of $Al(OH)_2$ are more soluble as compared to the aluminum precipitates, therefore, the formed $Al(OH)_2$ precipitates tend to continuously produce Al^{2+} and OH^- ions, which

Figure 3. The TEM micrograph of Al_2O_3 nanobricks

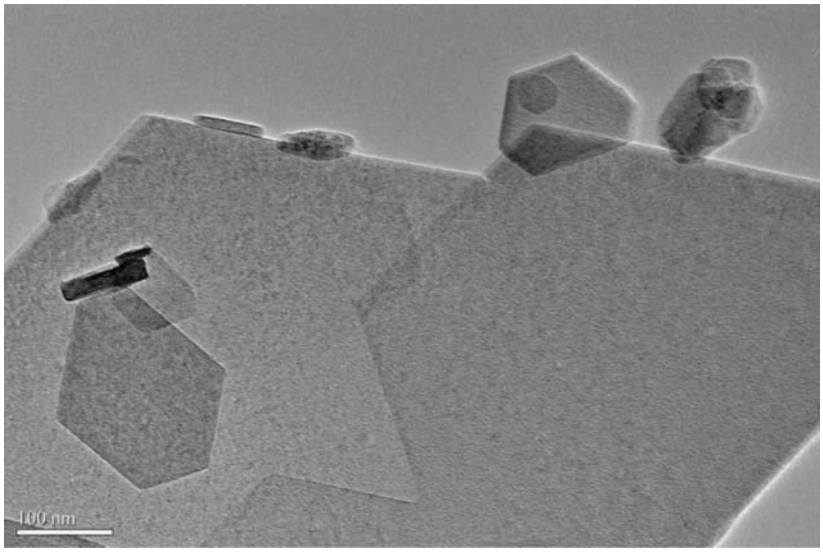
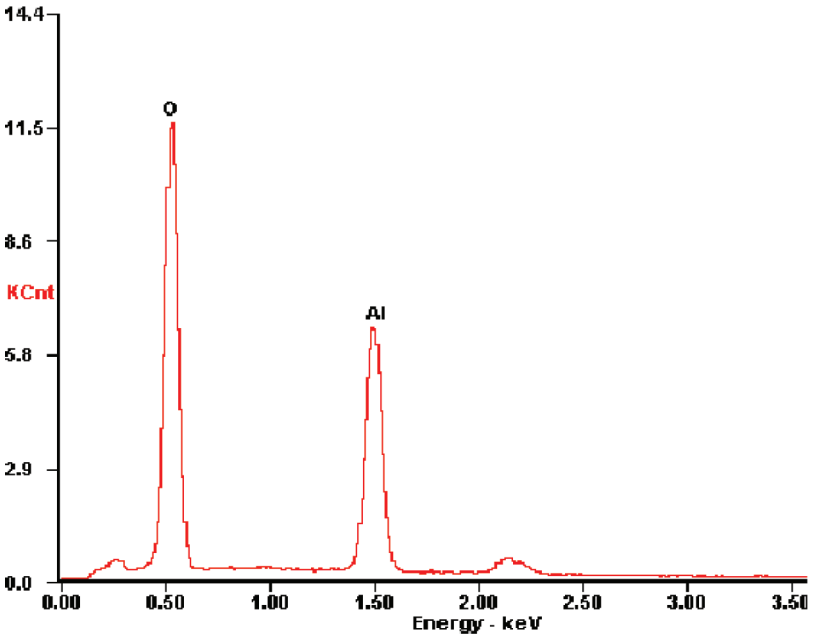


Figure 4. The EDX of pattern of as prepared samples showing Al and O of samples



form the Al_2O_3 nuclei. Aluminum metal also gives hydrogen on reaction with water. Water at elevated temperatures plays an essential role in the precursor material transformation because the vapour pressure is much higher and the state of water at elevated temperatures is different from that at room temperature. The solubility and the reactivity of the reactants also change at high pressures and high temperatures and high pressure is favorable for crystallizations. Earlier research groups have reported oxidation of nanoaluminum at temperatures of around 800K, which is below

the melting point of aluminum (Li et al., 2009). This is significantly different from our observations. These researches used dynamic thermal techniques, limitations to these techniques associated with heat and mass transfer are well known.

CONCLUSION

We report an organics free synthesis for nanobricks of α-Al_2O_3 by a simple reaction of Al and DI water at 200°C without any additives or catalyst. The mechanism for the formation of nanostructures is briefly described in accordance with decomposition of metal with water giving out hydrogen. The synthesis is non toxic without producing hazardous waste which could be used for number of applications.

ACKNOWLEDGMENT

KACST, Riyadh is acknowledged for characterization of samples.

REFERENCES

Fang, X., & Zhang, L. (2006). Controlled growth of one dimensional oxide nanomaterials. *Journal of Materials Science and Technology*, *22*(1), 1–18.

Lee, H. K., & Crawford, J. H. (1987). Additive coloration of sapphire. *Applied Physics Letters*, *33*, 273–275. doi:10.1063/1.90362

Lee, S., Bradbeck, C. M., & Yang, C. C. (1997). Dynamic nuclear polarization investigations of ESR and NMR strain-broadening effects in sapphire (Al_2O_3:Fe^{3+}). *Physical Review B: Condensed Matter and Materials Physics*, *15*, 69–2476.

Li, C., Huang, H., Yang, S., Zheng, R., Yong, Y., & Liu, Z. (2009). Controlled synthesis and characterization of 10nm thick Al_2O_3 nanowires. *Journal of Materials Letters*, *63*, 1016–1018. doi:10.1016/j.matlet.2009.01.072

Peng, X. S., Zhang, L. D., Meng, G. W., Wang, X. F., Wang, Y. F., & Wang, C. Z. (2002). Photoluminescence and infrared properties of α-Al_2O_3 nanowires and nanobelts. *The Journal of Physical Chemistry B*, *106*, 11163–11170. doi:10.1021/jp026028+

Shah, M. A. (2009). Aluminum oxide (α-Al_2O_3) nanorods prepared at low temperature without surfactant. *Physics Letters Part B*, *23*(13), 1–7.

Shah, M. A., & Towkeer, A. (2010). *Principles of nanoscience and nanotechnology*. New Delhi, India: Naroosa Publishing.

This work was previously published in the International Journal of Manufacturing, Materials, and Mechanical Engineering, Volume 1, Issue 2, edited by J. Paulo Davim, pp. 56-61, copyright 2011 by IGI Publishing (an imprint of IGI Global).

Chapter 20
Preparation of Copper Oxide (CuO) Nanoparticles and their Bactericidal Activity

F. M. Al-Marzouki
King Abdulaziz University, Saudi Arabia

O. A. Al-Hartomy
King Abdulaziz University, Saudi Arabia

M. A. Shah
King Abdulaziz University, Saudi Arabia

ABSTRACT

Single crystalline nanoparticles of copper oxide (CuO) having almost uniform particle size of ~40±10nm have been synthesized by a facile and versatile route. The technique employed is free from toxic solvents, organics, and amines, and is based on a simple reaction of copper powder and de-ionized water (DI) at very low temperatures of 180°C. The morphology, chemical composition, and crystalline structure of the nanoparticles were carefully investigated by the various characterization techniques. Besides simplicity, the advantages of producing nanoparticles by this method are that it is easeful, flexible, fast, cost effective, and pollution free. The synthesized nanoparticles are under investigations for various applications including their antibacterial activity.

1. INTRODUCTION

As a semiconductor with a narrow band-gap (Eg = 1.2eV), Copper oxide (CuO) is a unique monoxide compound (in monoclinic phase, different from normal rock salt type structure) for both fundamental investigations and practical applications. It has been used as heterogeneous catalysts in many important chemical processes, such as degradation of nitrous oxide with ammonia and oxidation of carbon monoxide, hydrocarbon and phenol in supercritical water. CuO can also be used as gas sensor, optical switch, magnetic storage media, lithium batteries and solar cells owing to its photoconductive and photochemical properties (Sambandan et al., 2005; Liu et al., 2006). It

DOI: 10.4018/978-1-4666-1867-1.ch020

Copyright © 2013, IGI Global. Copying or distributing in print or electronic forms without written permission of IGI Global is prohibited.

is well known that copper oxide have been used to disinfect liquids, solids and human tissue for centuries. Today it is used as water purifier, an algaecide, a fungicide and a nematocide as well as an antibacterial and antifouling agent (Ren et al., 2009).

It is well known that copper oxides can be conveniently obtained by thermal decomposition of copper salts (Han et al., 2008; Wang et al., 2002; Mang et al., 2008; Xu et al., 1999). However, it is too difficult to control the grain size of resulting copper oxide (CuO) particles through methods available, which is one of the essential requirements/conditions for the synthesis of nanomaterials. Moreover, the production in all cases required either elevated temperatures including prolonged reactions under special conditions or other tedious procedures in presence of harmful gases. In addition, most of the pathways suggested for the synthesis of CuO nanocrystals involve environmentally malignant chemicals and organic solvents which are toxic and not easily degraded in the environment. Environmental friendly chemical synthesis requires alternative solvents such as ionic liquids, liquid and water. Water is particularly attractive because it is inexpensive, safe, environmentally benign and bestowed with many virtues especially under supercritical conditions (Vostriko et al., 2009).

Encouraged by the interesting and useful results (Shah et al., 2009), we decided to apply the approach to copper metal. Interestingly, uniform sized nanoparticles were obtained by a simple reaction of copper powder and de-ionized water at very low temperature of 180°C. The diameter of nanoparticles ranges from 30-50nm with an average diameter of 40nm. The bactericidal efficacy of the as prepared nano-CuO against Escherichia coli (Grame negative) and Staphylococcus aureus (Grame positive) bacteria was investigated. The reported method besides being organics free is economical, fast, environmentally benign and free of pollution, which will make it suitable for large scale production. The aim of the study is to provide the feasibility of the simple route for the preparation of copper oxide nanostructures without additives and to test their antibacterial efficiency. The prospects of the process are bright and promising.

2. EXPERIMENTAL

2.1. Materials

Copper powder (Cu powder, Ranbaxy with diameter > 5μm) was used as a source of copper and was cleaned by ultra-sonication in acetone and water for 10 minutes in each solvent. The de-ionized water was prepared in the laboratory. Teflon lined stainless steel was used for preparation purpose.

2.2. Preparation

2 mg of copper powder was added to 20 ml of de-ionized water in a glass vial. Few drops of ethylenediamine (en) were added to reaction mixture to avoid agglomeration. The reaction mixture was sonicated for about 30 minutes in a glass veil, transferred into a stainless steel Teflon lined metallic bomb of 100ml capacity and sealed under normal conditions. The closed chamber was then placed inside a preheated box furnace and the mixture was heated slowly (2°C/min) to 180°C and maintained at this temperature for 12 hours. The furnace is allowed to cool after the desired time and the resulting suspension was centrifuged to retrieve the product, washed and then finally vacuum dried for few hours.

2.3. Characterization

The as synthesized powder was directly transferred to FESEM chamber without coating. The morphology and the size of the products were carried out using high resolution FE-SEM (FEI NOVA NANOSEM-600) coupled with energy dispersive x-ray spectrometer (EDX). The features

and shapes of the particles were also imaged by Transmission Electron Microscope (TEM) operated at 200kV. Structural information was given by powder X-ray diffraction (XRD) using a PAN analytical (X' pert PW 3710,) diffractometer with 2θ ranging from 10-90°, using Cu Kα (λ=0.15141 nm) radiation operated at 40kV and 30mA.

2.4. Antimicrobial Test

The antibacterial activity was tested against Grame positive Staphylococus aureus (S. aureus) bacteria and to Grame negative Escherichia coli (E.Coli) as well. The Staphylococus was resistant to gentamicine and to braymicine antibiotoxics. The second strain E.coil, Grame negative bacteria was resistant to chloromphenicol and tetracycline.

3. RESULTS AND DISCUSSION

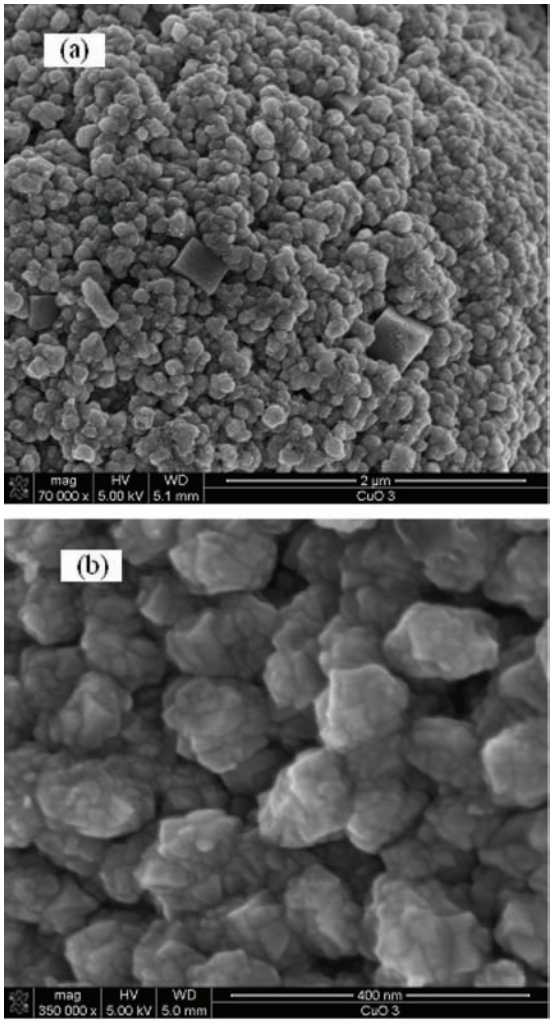
3.1. Morphology

Figure 1 (a) and (b) show the low and high magnification FESEM images of the nanoparticles and confirms that the nanoparticles are grown with well defined morphology. The nanoparticles are almost spherical in shape and have diameters varying between 30 to 50nm, with an average diameter of 40nm. The particle size was also examined using TEM. Figure 2 displays TEM micrographs of CuO revealing the average particle size is approximately 40nm. The influence of reaction conditions on physical properties of synthesized nanoparticles as well as mechanism is yet to be investigated.

3.2. Structural Characterization

To identify the crystallinity and crystal phases of the as-grown structures, X-ray diffraction (XRD) analysis was performed and shown in Figure 3. All the peaks could be clearly indexed to monoclinic phase with lattice constants a = 0.4675, b = 0.3418

Figure 1. Typical (a and b) low and (c and d) high-resolution FESEM images of CuO nanoparticles obtained by the reaction of copper metal powder with water at 180°C for 12h



and c = 0.5095 which were consistent with the literature (JCPDS-05-0661). The XRD diffraction peaks indicate small size of crystalline CuO particles. No diffraction peaks arising from any impurity can be detected in the pattern confirms that the grown products are pure. The result is quite different from the traditional process in which only amorphous phase can be obtained from the precipitates derived by solution process before calcinations and further higher temperature heat treatment is normally required to induce crystal-

lization (Yuan et al., 2007). Thus, this method, "the soft option of hydrothermal treatment" may be regarded as an alternative to calcinations for promoting the crystallization. The EDX pattern as shown in inset of Figure 3 confirms the composition of the sample shows no other peak for any other element has been found which again confirmed that nanoparticles are pure.

3.3. Bactericidal Tests

The antibacterial activity of CuO nanoparticles were tested by treating staph aerues and E.coli with $2mgmL^{-1}$ of the nanoparticles. The minimal inhibitory concentration (MIC) of these particles on staph aureus and E. coli strains was found in both cases to be 0.625mg mL-1. The test was carried out in nutrient broth as traditional MIC test for bacteria. The tests were performed while the bacteria were grown in their broth medium. The results of the treatment before and after are shown in Figure 4.

Overnight cultures of S. aureus and E. coli were grown on nutrient agar. These cultures were transferred into broth at pH 7, to final volume of 50ml, at an initial optical density of 0.1 and allowed to grow at 37°C and counted for viable bacteria by counting the colony forming units in each plate. Two controls were included in the experiment, one with the absence of bacteria and nanoparticles and second with bacteria but without the presence of bacteria.

3.4. Formation Mechanism

The formation of copper oxide nanoparticles by the reaction of copper with water can be explained by reaction mechanism. As initially, copper reacted with water and forms a protective hydroxide $Cu(OH)_2$ layer with dissolved hydroxide ions onto the surfaces of the Cu foil according to the following reaction mechanism:

$$Cu^{2+} + 2OH^- \rightarrow Cu(OH)_2(s)$$

As the concentration of the Cu^{2+} and OH^- ions exceeds a critical value, the precipitation of CuO nuclei starts. The $Cu(OH)_2$ can be transformed into the CuO crystals via the simple chemical reactions mentioned:

$$Cu(OH)_2(s) \xrightarrow{\Delta} 2CuO\ (s) + 2H_2O(l)$$

Figure 2. TEM micrograph of CuO nanoparticle

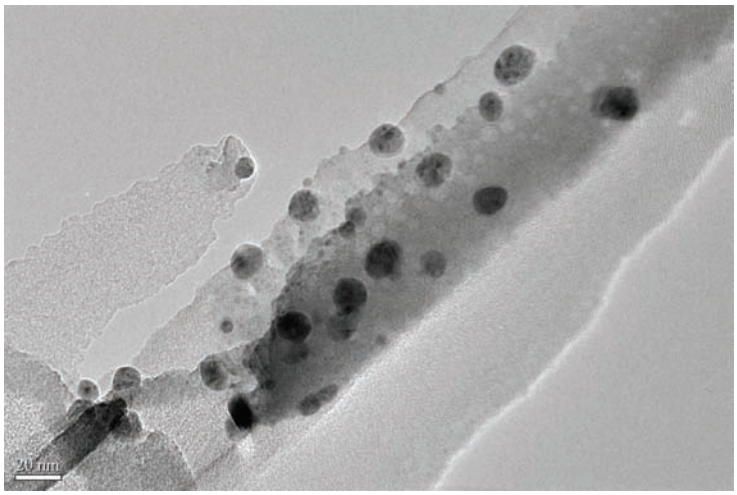


Figure 3. Corresponding XRD pattern of CuO nanoparticles. The inset shows the EDX pattern

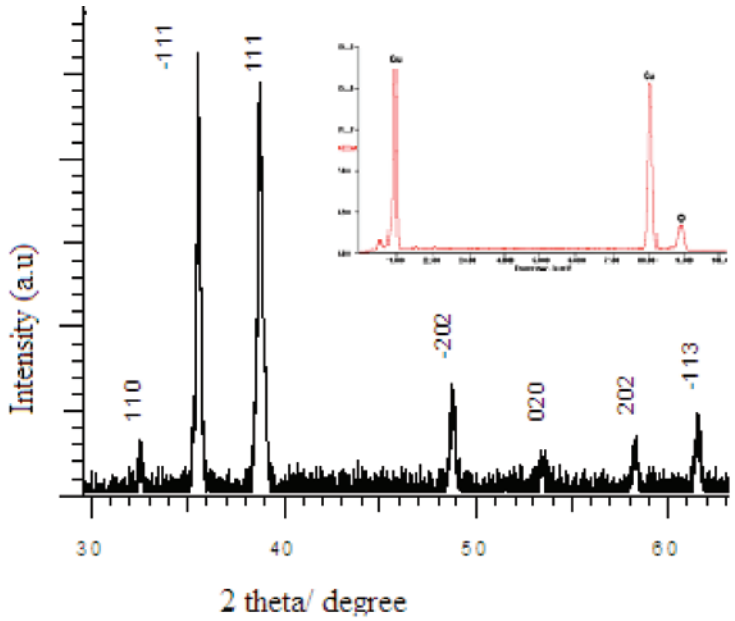
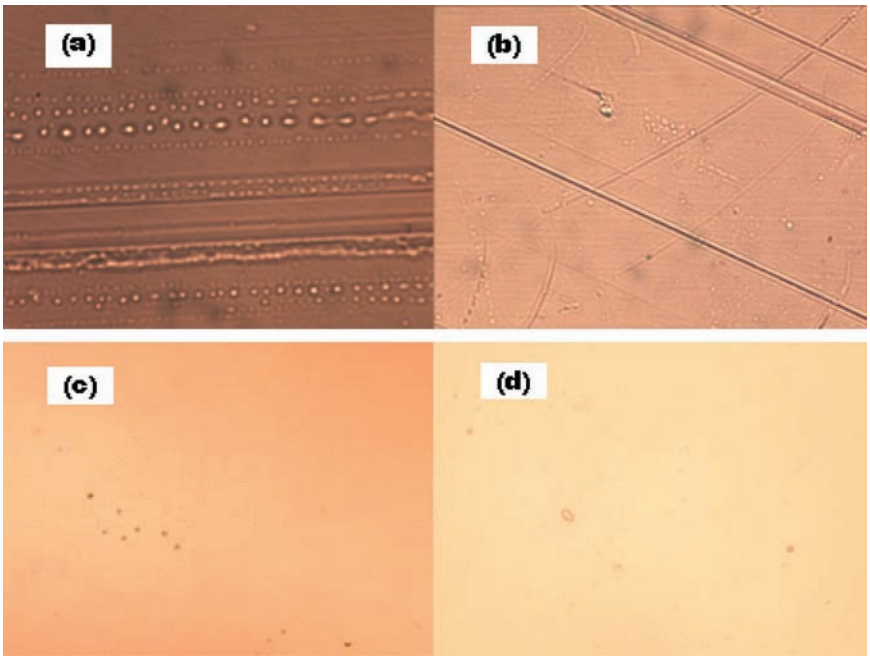


Figure 4. (c and d) Staphylococcus aureus (Grame positive) and Escherichia coli (Grame negative) bacteria before and after treatment of CuO nanoparticles respectively



The Cu metal on reaction with water slowly gives out hydrogen (g) and the liberated oxygen reacts with metal to give oxides as shown in the above reaction. The growth of nanoparticles could be occurring at the small oxide nuclei that may be present on the metal surfaces. Moreover, water at elevated temperatures plays an essential role in the precursor material transformation because the vapour pressure is much higher and the state of water at elevated temperatures is different from that at room temperature. The solubility and the reactivity of the reactants also change at high pressures and temperatures and high pressure is favorable for crystallizations (Wang et al., 2007).

Due to the temperature and pressure in the autoclave under the hydrothermal condition, a completely different reaction mechanism and formation sequence may be rationalized. The steam is generated under high temperatures to produce a hydrostatic pressure which in turn imposes a profound effect on the ultimate microstructure of the oxides thus prepared. This autogeneous hydrostatic pressure can be as high as 9 bars under a hydrothermal temperature of 180°C. Therefore, it can be said that in this aqueous system in the sealed autoclave, the temperature has much higher impact reaction rate, the morphology, as well as the reaction mechanism.

4. CONCLUSION

Uniform sized ~ 40±10nm particles of copper oxide were synthesized by a very versatile, non toxic and environmental friendly approach at 180°C without using any organics. The process is a simple, efficient and one step synthesis. It may be extended to fabricate other metal oxide nanomaterials. The mechanism of nanoparticle formation has been discussed in relation to the sample preparation conditions in detail. The performance of the as synthesized particles was investigated and their excellent bacterial effected demonstrated. These can be recommended for the purification of medical and food equipments.

ACKNOWLEDGMENT

The authors are thankful to the Deanship of research, KAU, Jeddah for financial support of this work. KACST, Riyadh is acknowledged for characterization of materials.

REFERENCES

Anandam, S., Wen, W., & Yang, S. (2005). Room temperature growth of CuO nanorods arrays on copper and their applications as a cathode in dye synthesized solar cells. *Materials Chemistry and Physics*, *93*, 35–40. doi:10.1016/j.matchemphys.2005.02.002

Han, D., Yang, H., Zhu, C., & Wang, F. (2008). Controlled synthesis of CuO nanoparticles using triton X-100 based water in oil reverse micelles. *Powder Technology*, *185*, 281–290. doi:10.1016/j.powtec.2007.10.018

Liu, Q., Ling, X., Liu, H., Hang, J., & Hu, Z. (2006). Solution phases synthesis of CuO nanorods. *Materials Chemistry and Physics*, *98*, 519–522. doi:10.1016/j.matchemphys.2005.09.073

Ren, G., Hu, D., Cheng, E. W. C., Vargas-Reus, M. A., Reip, P., & Allaker, R. P. (2009). Characterisation of copper oxide nanoparticles for antimicrobial applications. *International Journal of Antimicrobial Agents*, *33*(6), 587–590. doi:10.1016/j.ijantimicag.2008.12.004

Shah, M. A., & Quarshi, A. (2009). Novel surfactant free synthesis of MgO nanoflakes. *Journal of Alloys and Compounds*, *482*, 548–552. doi:10.1016/j.jallcom.2009.04.129

Vostrikov, A. A., Fedyaeva, O. N., Shishkin, A. V., & Sokol, M. A. (2009). ZnO nanoparticles formation by reactions of bulk zinc with H_2O and CO_2 at sub and super critical conditions. *Journal of Solid Supercritical Fluids*, *48*, 1554–160.

Wang, H., Zhang, J., Zhu, J. J., & Chen, H. Y. (2002). Preparation of copper oxide nanoparticles by microwave irradiation. *Journal of Crystal Growth*, *244*, 88–99. doi:10.1016/S0022-0248(02)01571-3

Wang, J., Yang, J., Sun, J., & Bio, Y. (2004). Synthesis of copper oxide nanocrystals and the growth mechanism of copper oxide nanorods. *Materials & Design*, *25*, 625–629. doi:10.1016/j.matdes.2004.03.004

Xu, F., Ji, W., Shen, Z. X., Tang, S. H., Ye, X. R., & Jia, Z. A. (1999). Preparation and characterization of CuO nanocrystals. *Journal of Solid State Chemistry*, *147*, 516–519. doi:10.1006/jssc.1999.8409

Yuan, G.-Q., Jiang, H.-F., Lin, C., & Lia, S.-J. (2007). Shape and size controlled synthesis of Cupperic oxide nanocrystals. *Journal of Crystal Growth*, *303*, 400–406. doi:10.1016/j.jcrysgro.2006.12.047

Zhang, M., Xu, X., & Zhang, M. (2008). Hydrothermal synthesis of sheaf like CuO via ionic solids. *Materials Letters*, *62*, 385–388. doi:10.1016/j.matlet.2007.05.046

This work was previously published in the International Journal of Manufacturing, Materials, and Mechanical Engineering, Volume 1, Issue 4, edited by J. Paulo Davim, pp. 58-64, copyright 2011 by IGI Publishing (an imprint of IGI Global).

Compilation of References

Abaqus v6.7. (2007). Simulia Inc., Dassault Systémes.

Abbe, B. Z. E. (1873). Theorie des Mikroskops und der mikroskopischen Wahrnehmung. *Archiv Microskop Anatomy*, *9*, 413. doi:10.1007/BF02956173

Agarwala, R. C., & Agarwala, V. (2003). Electroless alloy /composite coatings: A review. *Sadhana*, *28*(3-4), 475–493. doi:10.1007/BF02706445

Ahluwalia, J., Gupta, S. K., & Agrawal, V. P. (1993). Computer-aided optimum selection of roller bearings. *Computer Aided Design*, *25*, 493–500. doi:10.1016/0010-4485(93)90080-8

Ahn, K. J., & Seferis, J. C. (1989). Prepreg processing science and analysis. In *Proceedings of the 34th International SAMPE Symposium* (pp. 63-70).

Akarca, S. S., Song, X., Altenhof, W. J., & Alpas, A. T. (2008). Deformation behaviour of aluminum during machining: Modelling by Eulerian and smoothed-particle hydrodynamics methods. *Proceedings of the Institute of Mechanical Engineers –Journal of Materials: Design and Applications, 222*, 209-219.

Aksu, G. (1982). Free vibration analysis of stiffened plates by including the effect of inplane inertia. *Journal of Applied Mechanics Transactions of ASME*, *49*(1), 206–212. doi:10.1115/1.3161972

Aksu, G., & Ali, R. (1976). Free vibration analysis of stiffened plates using finite difference method. *Journal of Sound and Vibration*, *48*(1), 15–25. doi:10.1016/0022-460X(76)90367-9

Alexander, J. M. (1960). An approximate analysis of the collapse of thin cylindrical shells under axial loading. *The Quarterly Journal of Mechanics and Applied Mathematics*, *13*, 10–15. doi:10.1093/qjmam/13.1.10

Alexander, J. M., Brewer, R. C., & Rowe, G. W. (1987). Manufacturing Technology: *Vol. 2*. *Engineering Process*. London: Ellis Horwood Limited, England.

Al-Hassani, S., Johnson, W., & Lowe, W. T. (1972). Characterization of inversion tubes under axial loading. *Journal of Mechanical Engineering Science*, *14*, 370–381. doi:10.1243/JMES_JOUR_1972_014_046_02

Allan, T. (1968). Investigation of the behaviour of cylindrical tubes subject to axial compressive forces. *Journal of Mechanical Engineering Science*, *10*, 182–197. doi:10.1243/JMES_JOUR_1968_010_026_02

Allwood, J. (2005). *What is sustainable manufacturing?* Paper presented at the Sustainable Manufacturing Seminar Series. Retrived from www.ifm.eng.cam.ac.uk/sustainability/seminar/documents/050216lo.pdf

Almeida, B. P. P., Alves, M. L., Rosa, P. A. R., Brito, A. G., & Martins, P. A. F. (2006). Expansion and reduction of thin-walled tubes using a die: experimental and theoretical investigation. *International Journal of Machine Tools & Manufacture*, *46*, 1643–1652. doi:10.1016/j.ijmachtools.2005.08.018

Al-Qureshi, H. A., & Morais, G. A. (1976). Analytical investigation of thin wall tube expansion by the inversion process. In *Proceedings of the Design Engineering Conference* (ASME paper No. 76-DE-9).

Alves, L. M., Rodrigues, J. M. C., & Martins, P. A. F. (2003). Simulation of three-dimensional bulk forming processes by the finite element flow formulation. *Modelling and Simulation in Materials Science and Engineering – Institute of Physics, 11*, 803-821.

Alves, L. M., & Martins, P. A. F. (2009a). Cold expansion and reduction of thin-walled PVC tubes using a die. *Journal of Materials Processing Technology*, *209*, 4229–4236. doi:10.1016/j.jmatprotec.2008.11.015

Alves, L. M., & Martins, P. A. F. (2009b). Understanding invert forming of thin-walled polyvinyl chloride tubes using a die based on a mechanical flow formulation. *Materials and Manufacturing Processes*, *24*, 1398–1404. doi:10.1080/10426910902997530

Amabili, M. (2006). Theory and experiments for large-amplitude vibrations of rectangular plates with geometric imperfections. *Journal of Sound and Vibration*, *291*(3-5), 539–565. doi:10.1016/j.jsv.2005.06.007

Anandam, S., Wen, W., & Yang, S. (2005). Room temperature growth of CuO nanorods arrays on copper and their applications as a cathode in dye synthesized solar cells. *Materials Chemistry and Physics*, *93*, 35–40. doi:10.1016/j.matchemphys.2005.02.002

Andrade-Campos, A., Pilvin, P., Simões, J., & Teixeira-Dias, F. (2009). *Software Development for Inverse determination of constitutive Model Parameters* (Software Engineering and Development, Chapter 4). Nova publishers. ISBN: 978-1-60692-146-3

Andrade-Campos, A., Thuiller, S., Pilvin, P., & Teixeira-Dias, F. (2007). On the determination of material parameters for internal variable thermoelastic-viscoplastic constitutive models. *International Journal of Plasticity*, *23*, 1349–1379. doi:10.1016/j.ijplas.2006.09.002

Anik, M., Körpe, E., & Şen, E. (2008). Effect of coating bath composition on the properties of electroless nickel-boron films. *Surface and Coatings Technology*, *202*, 1718–1727. doi:10.1016/j.surfcoat.2007.07.031

Ansarifar, A., Wang, L., Osmani, M., & Pappu, A. (2009). Assessing effects of thermoset polyester resin waste powder on the processing and mechanical properties of natural rubber. *Journal of Rubber Research*, *12*(1), 12–26.

Ansys, I. (2007). *Release 11.0 Documentation for ANSYS*.

Antony, J. (1998). Some key things industrial engineers should know about experimental design. *Logistics Information Management*, *11*(6), 386–392. doi:10.1108/09576059810242606

Antony, J., & Kaye, M. (1999). *Experimental quality - a strategic approach to achieve and improve quality*. Dordrecht, The Netherlands: Kluwer Academic.

Argüelles, M., Benavides, C., & Junquera, B. (2006). The impact of economic activity in Asturias on greenhouse gas emissions: Consequences for environmental policy within the Kyoto Protocol framework. *Journal of Environmental Management*, *81*(3), 249–264.

Armstrong-Hélouvry, B., Dupont, P., & Canudas de Wit, C. (1994). A survey of models, analysis tools and compensation methods for the control of machines with friction. *Automatica*, *30*, 1083–1138. doi:10.1016/0005-1098(94)90209-7

Arnet, H., & Vollertsen, F. (1995). Extending laser bending for the generation of convex shapes. *Proceedings of the Institution of Mechanical Engineers. Part B, Journal of Engineering Manufacture*, *209*(No. B6), 433–442. doi:10.1243/PIME_PROC_1995_209_107_02

Arrazola, P. J., & Özel, T. (2008). Numerical modelling of 3-D hard turning using arbitrary Eulerian Lagrangian finite element method. *International Journal of Machining and Machinability of Materials*, *3*, 238–249.

Arrazola, P. J., & Özel, T. (2010). Investigations on the effects of friction modeling in finite element simulation of machining. *International Journal of Mechanical Sciences*, *52*, 31–42. doi:10.1016/j.ijmecsci.2009.10.001

Arrazola, P. J., Ugarte, D., & Domínguez, X. (2008). A new approach for friction identification during machining through the use of finite element modelling. *International Journal of Machine Tools & Manufacture*, *48*, 173–183. doi:10.1016/j.ijmachtools.2007.08.022

Arthur, A., & Dickens, P. M. (1998). The measurement of heat distribution in stereolithography electrodes during electro-discharge machining. *International Journal of Production Research*, *36*(9), 2451–2461. doi:10.1080/002075498192625

Arthur, A., Dickens, P. M., & Cobb, R. (1996). Using rapid prototyping to produce electrical discharge machining electrodes. *Rapid Prototyping Journal*, *2*(1), 4–12. doi:10.1108/13552549610109036

Ashby, M. F., Brechet, Y. J. M., Cebon, D., & Salvo, L. (2004). Selection strategies for materials and processes. *Materials & Design*, *25*, 51–67. doi:10.1016/S0261-3069(03)00159-6

Asokan, P., Osmani, M., & Price, A. (2009). Assessing the recycling potential of glass fibre reinforced waste in concrete and cement composites. *Journal of Cleaner Production*, *17*(9), 821–829. doi:10.1016/j.jclepro.2008.12.004

Asokan, P., Osmani, M., & Price, A. (2010). Improvement of the mechanical properties of glass fibre reinforced plastic waste powder filled concrete. *Construction & Building Materials*, *24*(4), 448–460. doi:10.1016/j.conbuildmat.2009.10.017

Astakhov, V. P., & Outeiro, J. C. (2008). Metal cutting mechanics, finite element modelling. In Davim, J. P. (Ed.), *Machining: Fundamentals and recent advances*. Berlin, Germany: Springer-Verlag.

Attanasio, A., Cerretti, E., Rizzuti, S., Umbrello, D., & Micari, F. (2008). 3D finite element analysis of tool wear in machining. *CIRP Annals - Manufacturing Technology, 57*(1), 61-64.

Aurich, J. C., & Bil, H. (2006). 3D finite element modelling of segmented chip formation. *Annals of the CIRP*, *55*(1), 47–50. doi:10.1016/S0007-8506(07)60363-1

Avitzur, B. (1980). *Metal Forming: the Application of Limit Analysis*. New York: Marcel Dekker, and Basel.

Ayres, R. U. (1997). Metals recycling: Economic and environmental implications. *Resources, Conservation and Recycling*, *21*(3), 145–173. doi:10.1016/S0921-3449(97)00033-5

Baets, J., Dutoit, M., Devaux, J., & Verpoest, I. (2008). Toughening of glass fiber reinforced composites with a cyclic butylenes terephthalate matrix by addition of polycaprolactone. *Composites. Part A, Applied Science and Manufacturing*, *39*(1), 13–18. doi:10.1016/j.compositesa.2007.09.013

Baker, M. (2003). An investigation of the chip segmentation process using finite elements. *Technische Mechanik*, *23*, 1–9.

Baker, M. (2005). Does chip formation minimize energy. *Computational Materials Science*, *33*, 407–418. doi:10.1016/j.commatsci.2004.08.007

Bäker, M. (2006). Finite element simulation of high-speed cutting forces. *Journal of Materials Processing Technology*, *176*, 117–126. doi:10.1016/j.jmatprotec.2006.02.019

Baker, M., Rosler, J., & Seimers, C. (2002). A finite element model of high speed metal cutting with adiabatic shearing. *Computers & Structures*, *80*, 495–513. doi:10.1016/S0045-7949(02)00023-8

Baker, M., Rosler, J., & Seimers, C. (2002). Finite element simulation of segmented chip formation of Ti6Al4V. *Journal of Manufacturing Science and Engineering*, *124*, 485–488. doi:10.1115/1.1459469

Basak, I., & Ghosh, A. (1997). Mechanism of material removal in electrochemical discharge machining: A theoretical model and experimental verification. *Journal of Materials Processing Technology*, *71*, 350–359. doi:10.1016/S0924-0136(97)00097-6

Bäuerle, D. (2000). *Laser processing and chemistry*. Berlin, Germany: Springer-Verlag.

Bedair, O. K. (1997). Analysis of stiffened plates under lateral loading using sequential quadratic program. *Computers & Structures*, *62*(1), 63–80. doi:10.1016/S0045-7949(96)00281-7

Bedair, O. K. (1997). Fundamental frequency determination of stiffened plates using sequential quadratic programming. *Journal of Sound and Vibration*, *199*(1), 87–106. doi:10.1006/jsvi.1996.0606

Bedair, O. K. (1998). A contribution to the stability of stiffened plates under uniform compression. *Computers & Structures*, *66*(5), 535–570. doi:10.1016/S0045-7949(97)00102-8

Bedair, O. K., & Troitsky, M. (1997). A study of fundamental frequency characteristics of eccentrically and concentrically simply supported stiffened plates. *International Journal of Mechanical Sciences*, *39*(11), 1257–1272. doi:10.1016/S0020-7403(97)00016-7

Beg, J., & Shunmugam, M. S. (2002). An object oriented planner for inspection of prismatic parts-OOPIPP. *International Journal of Advanced Manufacturing Technology*, *19*, 905–916. doi:10.1007/s001700200103

Belegundu, A. D., & Chandrupatla, T. R. (1999). *Optimization concepts and applications in engineering*. Upper Saddle River, NJ: Prentice-Hall.

Betzig, E., Trautman, J. K., Wolfe, R., Gyorgy, E. M., Finn, P. L., & Kryder, M. H. (1992). Near-field magneto-optics and high density data storage. *Applied Physics Letters*, *61*(2), 142–144. doi:10.1063/1.108198

Bhandarkar, M. P., & Nagi, R. (2000). STEP-based feature extraction from STEP geometry for agile manufacturing. *Computers in Industry*, *41*, 3–24. doi:10.1016/S0166-3615(99)00040-8

Bhaskara Reddy, S. V., Shunmugam, M. S., & Narendran, T. T. (1999). Operation sequencing using genetic algorithms. *International Journal of Production Research*, *37*(5), 1063–1074. doi:10.1080/002075499191409

Bhattacharyya, A. (2006). *Metal cutting theory and practice*. Calcutta, India: Central Book Publishers.

Bhattacharyya, B., Doloi, B. N., & Sorkhel, S. K. (1999). Experimental investigations into electrochemical discharge machining (ECDM) of non-conductive ceramic materials. *Journal of Materials Processing Technology*, *95*, 145–154. doi:10.1016/S0924-0136(99)00318-0

Bijwe, J., Indumathi, J., & Ghosh, A. K. (2002). Influence of weave of glass fabric on oscillating wear performance of polyetherimide composite. *Wear*, *253*(7-8), 803–812. doi:10.1016/S0043-1648(02)00167-9

Bijwe, J., Indumathi, J., Satapathy, B. K., & Ghosh, A. K. (2002). Influence of carbon fabric on fretting wear performance of PEI composites. *ASME Journal of Tribology*, *124*(4), 834–839. doi:10.1115/1.1456088

Bijwe, J., & Rattan, R. (2006). Influence of content of carbon fabric on the low amplitude oscillating wear performance of polyetherimide composites. *Tribology Letters*, *23*(3), 223–229. doi:10.1007/s11249-006-9060-5

Bil, H., Kılıç, S. E., & Tekkaya, A. E. (2004). A comparison of orthogonal cutting data from experiments with three different finite element models. *International Journal of Machine Tools & Manufacture*, *44*, 933–944. doi:10.1016/j.ijmachtools.2004.01.016

Bill, R. C. (1985). Selected fretting wear resistant coatings for Ti-6 percent Al-4 percent V alloy. *Wear*, *106*(1-3), 283–301. doi:10.1016/0043-1648(85)90113-9

Birkinshaw, M. (1998). *Some Advice on Minimization Routines (Internal Memo)*. AXAF Science Center.

Björke, O. (1992). *Layer manufacturing – a challenge of the future*. Trondheim, Norway: Tapir Academic Press.

Bjorkholm, J. E., Bokor, J., Eichner, L., Freeman, R. R., Gregus, J., & Jewell, T. E. (1990). Reduction imaging at 14 nm using multilayer coated optics: Printing of features smaller than 0.1 μm. *Journal of Vacuum Science and Technology*, *8*(6), 1509. doi:10.1116/1.585106

Black, J. T., & Huang, J. M. (1996). An evaluation of chip separation criteria for the FEM simulation of machining. *Journal of Manufacturing Science and Engineering*, *118*, 545–553. doi:10.1115/1.2831066

Bobbert, P. A., & Vlieger, J. (1986). Light scattering by a sphere on a substrate. *Physica A. Statistical and Theoretical Physics*, *137*(1-2), 209–242. doi:10.1016/0378-4371(86)90072-5

Bocking, C. E., Bennett, G. R., Dover, S. J., Arthur, A., Cobb, R. C., & Dickens, P. M. (1997). Electrochemical routes for engineering tool production. *The GEC Journal of Technology*, *14*(2), 66–74.

Brenner, A., & Riddell, G. E. (1950). *U.S. Patent No. 2532282: Nickel plating by chemical reduction*. Washington, DC: U. S. Patent and Trademark Office.

Brønsted, P., Lilholt, H., & Lystrup, A. (2005). Composite Materials for wind power turbine blades. *Annual Review of Materials Research*, *35*, 505–538. doi:10.1146/annurev.matsci.35.100303.110641

Brown, T. (2010). Sustainable manufacturing: Regeneration through remanufacture. *The Manufacturer, 13*.

Brubak, L., & Hellesland, J. (2008). Strength criteria in semi-analytical, large deflection analysis of stiffened plates in local and global bending. *Thin-walled Structures*, *46*, 1382–1390. doi:10.1016/j.tws.2008.03.013

Burmeister, F., Schafle, C., Keilhofer, B., Bechinger, C., Boneberg, J., & Leiderer, P. (1998). From mesoscopic to nanoscopic surface structures: Lithography with colloid monolayers. *Advanced Materials (Deerfield Beach, Fla.)*, *10*(6), 495–497. doi:10.1002/(SICI)1521-4095(199804)10:6<495::AID-ADMA495>3.0.CO;2-A

Burmeister, F., Schafle, C., Matthes, T., Bohmisch, M., Boneberg, J., & Leiderer, P. (1997). Colloid monolayers as versatile lithographic masks. *Langmuir*, *13*(11), 2983–2987. doi:10.1021/la9621123

Burnley, S. (2001). The impact of the European landfill directive on waste management in the United Kingdom. *Resources, Conservation and Recycling*, *32*(3-4), 349–358. doi:10.1016/S0921-3449(01)00074-X

Byrne, G., Dornfeld, D., & Denkena, B. (2003). Advancing cutting technology. *Annals of the CIRP*, *52*(2), 483–507. doi:10.1016/S0007-8506(07)60200-5

Cailletaud, G., & Pilvin, P. (1994). Identification and inverse problems related to material behaviour. In *Proceedings of the International Seminar on Inverse Problems*, Clamart, France (pp. 79-86).

Calamaz, M., Coupard, D., & Girot, F. (2008). A new material model for 2D numerical simulation of serrated chip formation when machining titanium alloy. *International Journal of Machine Tools & Manufacture*, *48*, 275–288. doi:10.1016/j.ijmachtools.2007.10.014

Cao, J., & Lin, J. (2008). A study on formulation of objective functions for determining material models. *International Journal of Mechanical Sciences*, *50*, 193–204. doi:10.1016/j.ijmecsci.2007.07.003

Carbon Trust. (2008). *Publically Avaliable Specification 2050 Briefing Document, BSI British Standards*. London, UK: The Carbon Trust.

Casamichele, L., Quadrini, F., & Tagliaferri, V. (2007). Process-efficiency prediction in high power diode laser forming. *Transactions of the ASME*, *129*, 868–873.

Ceretti, E., Braga, D., & Giardini, C. (2010). Optimization of process parameters and part geometry for high diameter tube hydroforming. In *Proceedings of the ESAFORM conference 2010 (CD-Rom)*, Brescia University, Italy (paper No. MS01-316).

Ceretti, E., Fallböhmer, P., Wu, W. T., & Altan, T. (1996). Application of 2D FEM to chip formation in orthogonal cutting. *Journal of Materials Processing Technology*, *59*, 169–180. doi:10.1016/0924-0136(96)02296-0

Ceretti, E., Lazzaroni, C., Menegardo, L., & Altan, T. (2000). Turning simulations using a three-dimentional FEM code. *Journal of Materials Processing Technology*, *98*, 99–103. doi:10.1016/S0924-0136(99)00310-6

Ceretti, E., Lucchi, M., & Altan, T. (1999). FEM simulation orthogonal cutting: Serrated chip formation. *Journal of Materials Processing Technology*, *95*, 17–26. doi:10.1016/S0924-0136(99)00261-7

Chakladar, N. D., & Chakraborty, S. (2008). A combined TOPSIS-AHP-Method based approach for non-traditional machining processes selection. *Proceedings of the Institution of Mechanical Engineers. Part B, Journal of Engineering Manufacture*, *222*(12), 1613–1623. doi:10.1243/09544054JEM1238

Chak, S. K., & Rao, P. V. (2007). Trepanning of Al_2O_3 by electro-chemical discharge machining (ECDM) process using abrasive electrode with pulsed DC supply. *International Journal of Machine Tools & Manufacture*, *47*, 2061–2070. doi:10.1016/j.ijmachtools.2007.05.009

Chan, J. W. K., & Tong, T. K. L. (2007). Multi-criteria material selections and end-of-life product strategy: a grey relational approach. *Materials & Design*, *28*, 1539–1546. doi:10.1016/j.matdes.2006.02.016

Chapman, A., Bartlett, C., McGill, I., Parker, D., & Walsh, B. (2009). *Remanufacturing in the UK: A snapshot of the remanufacturing industry in the UK in 2009*. Retrieved from: http://www.remanufacturing.org.uk/free-reuse-publication.lasso?report=342.

Chatterjee, P., Athawale, V. M., & Chakraborty, S. (2009). Selection of materials using compromise ranking and outranking methods. *Materials & Design*, *30*, 4043–4053. doi:10.1016/j.matdes.2009.05.016

Chen, C. J., Liu, W., & Chern, S. M. (1994). Vibration analysis of stiffened plates. *Computers & Structures*, *50*(4), 471–480. doi:10.1016/0045-7949(94)90017-5

Chen, D., Wu, S., & Li, M. (2004). Deformation behaviours of laser curve bending of sheet metals. *Journal of Materials Processing Technology*, *148*(1), 30–34. doi:10.1016/j.jmatprotec.2003.12.024

Chen, M. L., Jeswiet, J., Bates, P. J., & Zak, G. (2008). Experimental study on sheet metal bending with medium-power diode laser. *Journal of Engineering Manufacture*, *222*, 381–389. doi:10.1243/09544054JEM951

Chen, S. J., & Hwang, C. L. (1992). *Fuzzy multiple attribute decision making-methods and applications (LNEMS)*. Berlin: Springer Verlag.

Chiabert, P., Lombardi, F., & Orlando, M. (1998). Benefits of geometric dimensioning and tolerancing. *Journal of Materials Processing Technology*, *78*, 29–35. doi:10.1016/S0924-0136(97)00459-7

Childs, T. H. C. (2006). Friction modelling in metal cutting. *Wear*, *260*, 310–318. doi:10.1016/j.wear.2005.01.052

Childs, T. H. C., & Maekawa, K. (1990). Computer-aided simulation and experimental studies of chip flow and tool wear in the turning of low alloy steels by cemented carbide tools. *Wear*, *139*, 235–250. doi:10.1016/0043-1648(90)90048-F

Chimmalgi, A., Choi, T. Y., Grigoropoulos, C. P., & Komvopoulos, K. (2003). Femtosecond laser aperturless near-field nanomachining of metals assisted by scanning probe microscopy. *Applied Physics Letters*, *82*(8), 1146–1148. doi:10.1063/1.1555693

Chivers, T. C., & Gordelier, S. C. (1984). Fretting fatigue palliatives: Some comparative experiments. *Wear*, *96*(2), 153–175. doi:10.1016/0043-1648(84)90092-9

Chong, T. C., Hong, M. H., & Shi, L. P. (2009). Laser precision engineering: From microfabrication to nanoprocessing. *Laser and Photonics Reviews*, *4*(1), 123–143. doi:10.1002/lpor.200810057

Ciovacco, J., & Winckler, S. J. *(2000). Cyclic thermoplastic properties and processing.* In Proceedings of the 45th International SAMPE Symposium, *Long Beach, CA (pp. 13-16).*

Clarr, P. W., & Vogel, J. M. (1989). *Review of active suspension control for on and off highway vehicles.* Retrieved from http://papers.sae.org/892482/

Coelho, R. T., Ng, E.-G., & Elbestawi, M. A. (2006). Tool wear when turning AISI 4340 with coated PCBN tools using finishing cutting conditions. *Journal of Machine Tools & Manufacture*, *47*(1-2), 263–272.

Cogswell, F. N. (1992). *Thermoplastic aromatic polymer composites* (pp. 44–58). Oxford, UK: Butterworth-Heinemann.

Cohen, D. (2007). Earth's natural wealth: An audit. *The New Scientist Magazine*, *2605*, 34–41.

Cole, M. A., Elliott, R. J. R., & Shimamoto, K. (2005). Industrial characteristics, environmental regulations and air pollution: An analysis of the UK manufacturing sector. *Journal of Environmental Economics and Management*, *50*(1), 121–143. doi:10.1016/j.jeem.2004.08.001

Colombie, C., Berthier, Y., Floquet, A., Vincent, L., & Godet, M. (1984). Fretting: Load carrying capacity of wear debris. *ASME Journal of Tribology*, *106*(2), 194–201. doi:10.1115/1.3260881

Crandall, S. H. (1956). *Engineering analysis: A survey of numerical procedures*. New York, NY: McGraw-Hill.

Davim, J. P. (2008). *Machining: Fundamentals and recent advances*. Berlin, Germany: Springer-Verlag.

Davim, J. P., & Maranhao, C. (2009). A study of plastic strain and plastic strain rate in machining of steel AISI 1045 using FEM analysis. *Materials & Design*, *30*, 160–165. doi:10.1016/j.matdes.2008.04.029

Davim, J. P., Maranhão, C., Faria, P., Abrão, A., Rubio, J. C., & Silva, L. R. (2009). Precision radial turning of AISI D2 steel. *International Journal of Advanced Manufacturing Technology*, *42*, 842–849. doi:10.1007/s00170-008-1644-9

Davim, J. P., Maranhão, C., Jackson, M. J., Cabral, G., & Grácio, J. (2008). FEM analysis in high speed machining of aluminum alloy (Al7075-0) using polycrystalline diamond (PCD) and cemented carbide (K10) cutting tools. *International Journal of Advanced Manufacturing Technology*, *39*, 1093–1100. doi:10.1007/s00170-007-1299-y

Dearden, G., & Edwardson, S. P. (2003). Some recent developments in two and three-dimensional laser forming for 'macro' and 'micro' applications. *Journal of Optics. A, Pure and Applied Optics*, *5*, S8–S15. doi:10.1088/1464-4258/5/4/352

Defra. (2009). *2009 Guidelines to Defra / DECC's GHG conversion factors for company reporting* (Version 2.0). London, UK: AEA.

Delaunois, F., & Lienard, P. (2002). Heat treatments for electroless nickel–boron plating on aluminum alloys. *Surface and Coatings Technology*, *160*, 239–248. doi:10.1016/S0257-8972(02)00415-2

Delaunois, F., Petitjean, J. P., Lienard, P., & Jacob-Duliere, M. (2000). Autocatalytic electroless nickel-boron plating on light alloys. *Surface and Coatings Technology*, *124*(2-3), 201–209. doi:10.1016/S0257-8972(99)00621-0

Denkov, N., Velev, O., Kralchevski, P., Ivanov, I., Yoshimura, H., & Nagayama, K. (1992). Mechanism of formation of two-dimensional crystals from latex particles on substrates. *Langmuir*, *8*(12), 3183–3190. doi:10.1021/la00048a054

Dervos, C. T., Novakovic, J., & Vassiliou, P. (2004). Vacuum heat treatment of electroless Ni–B coatings. *Materials Letters*, *58*, 619–623. doi:10.1016/S0167-577X(03)00581-0

Dirikolu, M. H., Childs, T. H. C., & Maekawa, K. (2001). Finite element simulation of chip flow in metal machining. *International Journal of Mechanical Sciences*, *43*, 2699–2713. doi:10.1016/S0020-7403(01)00047-9

Dixit, P. M., & Dixit, U. S. (2008). *Modeling of metal forming and machining processes: By finite element and soft computing methods*. London, UK: Springer.

Dozio, L., & Ricciardi, M. (2009). Free vibration analysis of ribbed plates by a combined analytical–numerical method. *Journal of Sound and Vibration*, *319*, 681–697. doi:10.1016/j.jsv.2008.06.024

Drovosekov, A. B., Ivanov, M. V., Krutskikh, V. M., Lubnin, E. N., & Polukarov, Yu. M. (2005). Chemically deposited Ni-W-B coatings: Composition, structure, and properties. *Protection of Metals*, *41*(1), 55–62. doi:10.1007/s11124-005-0008-1

Duan, C. Z., Dou, T., Cai, Y. J., & Li, Y. Y. (2009). Finite element simulation and experiment of chip formation process during high speed machining of AISI 1045 hardened steel. *International Journal of Recent Trends in Engineering*, *1*(5), 46–50.

Dupont, P. (1993). The effect of friction on the forward dynamics problem. *The International Journal of Robotics Research*, *12*, 164–179. doi:10.1177/027836499301200205

Durai Prabhakaran, R. T., Babu, B. J. C., & Agrawal, V. P. (2006a). Optimum selection of a composite product system using MADM approach. *Materials and Manufacturing Processes*, *21*, 883–891. doi:10.1080/10426910600773472

Durai Prabhakaran, R. T., Babu, B. J. C., & Agrawal, V. P. (2006b). Structural modeling and analysis of FRP composite product subsystems-a systems approach. *Journal of Polymer Composites*, *27*, 681–698. doi:10.1002/pc.20244

Edwards, K. L. (2005). Selecting materials for optimum use in engineering components. *Materials & Design*, *26*, 469–473. doi:10.1016/j.matdes.2004.07.004

Edwards, W., & Newman, J. R. (1986). *Multiattribute Evaluation*. Cambridge, UK: Cambridge University Press.

Efimtsov, B. M., & Lazarev, L. A. (2009). Forced vibrations of plates and cylindrical shells with regular orthogonal system of stiffeners. *Journal of Sound and Vibration*, *327*(1-2), 41–54. doi:10.1016/j.jsv.2009.05.021

Ehmann, K. F., Kpoor, S. G., DeVor, R. E., & Lazoglu, I. (1997). Machining processes modeling: A review. *ASME Journal of Manufacturing Science and Engineering*, *119*, 655–663. doi:10.1115/1.2836805

Eimadany, M. M., & Abdlizabbar, Z. S. (1999). Linear quadratic Gausssian control of a quarter-car suspension. *Vehicle System Dynamics*, *32*, 479–497. doi:10.1076/vesd.32.6.479.4224

Ejday, M., & Fourment, L. (2010). Metamodel assisted evolutionary algorithm for multi-objective optimization of non-steady metal forming problems. In *Proceedings of the ESAFORM conference 2010 (CD-Rom)*, Brescia University, Italy (paper No. MS01-017).

El Kadiri, M., & Benamar, R. (2003). Improvement of the semi-analytical method, based on Hamilton's principle and spectral analysis, for determination of the geometrically non-linear response of thin straight structures. Part III: Steady state periodic forced response of rectangular plates. *Journal of Sound and Vibration*, *264*(1), 1–35. doi:10.1016/S0022-460X(02)01162-8

Elbastwani, M. A., Srivatava, A. K., & Wardany, E.-L. (1996). A model for chip formation during machining of hardened steel. *Annals of CIRP*, *45*, 71–76. doi:10.1016/S0007-8506(07)63019-4

Elbheiry, E. M., & Karnoop, D. C. (1996). Optimal control of vehicle random vibration with constrained suspension deflection. *Journal of Sound and Vibration*, *189*, 547–564. doi:10.1006/jsvi.1996.0036

El-Domiaty, A. (1997). Curling of thin tubes: analytical and experimental study. *Journal of Materials Engineering and Performance*, *6*, 481–495. doi:10.1007/s11665-997-0120-2

Erdel, B. P. (2003). *High-speed machining*. Toronto, ON, Canada: Society of Manufacturing Engineers.

Fang, X., & Zhang, L. (2006). Controlled growth of one dimensional oxide nanomaterials. *Journal of Materials Science and Technology*, *22*(1), 1–18.

Faraj, I. (2003). Manufacturing features: Verification interaction accessibility and machinability. *International Journal of Production Research*, *41*(10), 2249–2272. doi:10.1080/0020754031000090630

Fayazbakhsh, K., Abedian, A., Manshadi, B. D., & Khabbaz, R. S. (2009). Introducing a novel method for materials selection in mechanical design using Z-transformation in statistics for normalization of material properties. *Materials & Design*, *30*, 4396–4404. doi:10.1016/j.matdes.2009.04.004

Finn, M. J., Galbraith, P. C., Wu, L., Hallquist, J. O., Lum, L., & Lin, T.-L. (1995). Use of a coupled explicit-implicit solver for calculating springback in automotive body panels. *Journal of Materials Processing Technology*, *50*, 395–406. doi:10.1016/0924-0136(94)01401-L

Fourment, L., Balan, T., & Chenot, J. L. (1996). Optimal design for non-steady-state metal forming processes. II. Application of shape optimization in forging. *International Journal for Numerical Methods in Engineering*, *39*, 51–65. doi:10.1002/(SICI)1097-0207(19960115)39:1<51::AID-NME845>3.0.CO;2-#

Gao, B., Darling, J., Tilley, D. G., Williams, D. G., & Donahue, J. (2006). Control of a hydropneaumatic active suspension based on a non-linear quarter car model. *Journal of Systems and Control Engineering*, *220*(1), 15–31.

Gaoling, P., Wenjian, L., & Xutang, Z. (2005). An Internet-based system for setup planning in machining operations. In *Proceedings of the 10th IEEE International Conference on Engineering of Complex Computer Systems* (pp. 245-251).

Gaoling, P., Wenjian, L., & Yuru, Z. (2005). Intelligent setup planning in manufacturing by fuzzy set theory based approach. In *Proceedings of the IEEE International Conference on Automation Science and Engineering* (pp. 130-135).

Gavankar, S. P., & Henderson, R. M. (1995). Graph based extraction of two morphological features from boundary representation. *Journal of Intelligent Manufacturing*, *6*, 401–413. doi:10.1007/BF00124066

Geiger, M., & Vollertsen, F. (1993). The mechanism of laser forming. *CIRP*, *42*, 301–304. doi:10.1016/S0007-8506(07)62448-2

Gibson, P., Ismail, H. S., & Sabin, M. A. (1999). Optimisation approaches in feature recognition. *International Journal of Machine Tools & Manufacture*, *39*, 805–821. doi:10.1016/S0890-6955(98)00068-6

Goodall, R. M., & Kortum, W. (1983). Active control in ground transportation-a review of the state-of-art and future potential. *Vehicle System Dynamics*, *12*, 225–257. doi:10.1080/00423118308968755

Gorbunova, K., Ivanov, M., & Moiseev, V. (1973). Electroless deposition of nickel-boron alloys mechanism of process, structure, and some properties of deposits. *Journal of the Electrochemical Society*, *120*, 613. doi:10.1149/1.2403514

Goren, A., & Atas, C. (2008). Manufacturing of polymer matrix composites using vacuum assisted resin infusion molding. *Archives of Materials Science and Engineering*, *34*(2), 117–120.

Gouveia, B. P. P., Alves, M. L., Rosa, P. A. R., & Martins, P. A. F. (2006). Compression beading and nosing of thin-walled tubes using a die: experimental and theoretical investigation. *International Journal of Mechanics and Materials in Design*, *3*, 7–16. doi:10.1007/s10999-006-9009-8

Gray, C., & Charter, M. (2006). *Remanufacturing and product design, designing for the 7th generation*. Retrieved from www.cfsd.org.uk/Remanufacturing%20and%20Product%20Design.pdf

Gregory, M., Prisk, M., Lucas, I., & Thurso, J. (2009). *The annual manufacturing report* (pp. 3-60). London, UK: SayOne Media. Retrieved from http://www.themanufacturer.com/uk/reports.html

Grzesik, W. (2002). Developments in metal removal processes. In *Proceedings of the 4th International Scientific Conference on Development of Metal Cutting*, Kosice, Slovakia (pp. 103-110).

Grzesik, W. (2006). Determination of temperature distribution in the cutting zone using hybrid analytical-FEM technique. *International Journal of Machine Tools & Manufacture*, *46*, 651–658. doi:10.1016/j.ijmachtools.2005.07.009

Grzesik, W. (2008). *Advanced machining processes of metallic materials: Theory, modelling and applications*. Oxford, UK: Elsevier.

Guglielmino, E., & Edge, K. A. (1980). *A controlled friction damper for vehicle applications*. Bath, UK: University of Bath.

Guglielmotti, A., Quadrini, F., Squeo, E. A., & Tagliaferri, V. (2007, October 2-3). Solid-state foaming of thermosets. In *Proceedings of the Polymer Foam Conference*, Newark, NJ.

Guglielmotti, A., Quadrini, F., Santo, L., & Squeo, E. A. (2009). Double indentation of laser bended stainless steel sheets. *International Journal of Material Forming*, *2*, 665–668. doi:10.1007/s12289-009-0465-1

Guglielmotti, A., Quadrini, F., Squeo, E. A., & Tagliaferri, V. (2008). Diode laser forming of stainless steel tubes. *International Journal of Material Forming*, *1*, 1343–1346. doi:10.1007/s12289-008-0112-2

Guide, V. D. R. (2000). Production planning and control for remanufacturing: Industry practice and research needs. *Journal of Operations Management*, *18*(4), 467–483. doi:10.1016/S0272-6963(00)00034-6

Guist, L. R., & Marble, D. P. (1966). Prediction of the inversion load of a circular tube. In *TND 3622, NASA*.

Gungor, A., & Gupta, S. M. (1999). Issues in environmentally conscious manufacturing and product recovery: A survey. *Computers & Industrial Engineering*, *36*(4), 811–853. doi:10.1016/S0360-8352(99)00167-9

Guo, W., Wang, Z. B., Luk'yanchuk, B. S., Whitehead, D. J., Li, L., & Liu, Z. (2008). Generation of nano-bumps on transparent quartz glass surface under femtosecond laser irradiation. In *Proceedings of the 27th International Congress on Applications of Lasers and Electro-Optics*, Temecula, CA

Guo, W., Wang, Z. B., Li, L., Whitehead, D. J., Luk'yanchuk, B. S., & Liu, Z. (2007). Near-field laser parallel nanofabrication of arbitrary-shaped patterns. *Applied Physics Letters*, *90*(24), 3. doi:10.1063/1.2748035

Guo, Y. B., & Liu, C. R. (2002). 3D FEA modeling of hard turning. *ASME Journal of Manufacturing Science and Engineering*, *124*, 189–199. doi:10.1115/1.1430678

Habraken, A. M. (2004). Modelling the plastic anisotropy of metals. *Archives of Computational Methods in Engineering*, *11*, 3–96. doi:10.1007/BF02736210

Hakme, C., Stevenson, I., Maazouz, A., Cassagnau, P., Boiteux, G., & Seytre, G. (2007). In situ monitoring of cyclic butylenes terephtalate polymerization by dielectric sensing. *Journal of Non-Crystalline Solids, 353*(47-51), 4362-4365.

Han, D., Yang, H., Zhu, C., & Wang, F. (2008). Controlled synthesis of CuO nanoparticles using triton X-100 based water in oil reverse micelles. *Powder Technology*, *185*, 281–290. doi:10.1016/j.powtec.2007.10.018

Hao, N., & Li, L. (2003). An analytical model for laser tube bending. *Applied Surface Science*, *208-209*, 432–436. doi:10.1016/S0169-4332(02)01428-9

Hari Krishnan, K., John, S., Srinivasan, K. N., Praveen, J., Ganesan, M., & Kavimani, P. M. (2006). An overall aspect of electroless Ni-P depositions- a review article. *Metallurgical and Materials Transactions A*, *37*, 1917–1926. doi:10.1007/s11661-006-0134-7

Harik, I. E., & Guo, M. (1993). Finite element analysis of eccentrically stiffened plates in free vibration. *Computers & Structures*, *49*(6), 1007–1015. doi:10.1016/0045-7949(93)90012-3

Harsch, M., Karger-Kocsis, J., & Holst, M. (2007). Influence of fillers and additives on the cure kinetics of an epoxy/anhydride resin. *European Polymer Journal*, *42*(4), 1168–1178. doi:10.1016/j.eurpolymj.2007.01.025

Harun, W. A., & Case, K. (2000). Feature-based representation for manufacturing planning. *International Journal of Production Research*, *38*(17), 4285–4300. doi:10.1080/00207540050205091

Hedrick, J. K., & Wormely, D. N. (1975). Active suspension for ground support vehicles - a state-of-the-art review. *ASME Applied Mechanics Division Journal*, *15*, 21–40.

Heeds. (2009). *Professional Design Optimization Software*. Red Cedar Technology, Inc.

Hibbit, Karlsson and Sorens Inc. (2011). *HKS ABAQUS Theory manual* (version 6.7). Pawtucket, RI: Hibbit, Karlsson and Sorens Inc.

Hinkelmann, K., & Kempthorne, O. (2008). Design and analysis of experiments: *Vol. 1. Introduction to experimental design*. Hoboken, NJ: John Wiley & Sons.

Hoffman, M. C., & Joan-Arinyo, R. (1998). CAD and the product master model. *Computer Aided Design*, *30*(11), 905–918. doi:10.1016/S0010-4485(98)00047-5

Ho, K. H., & Newman, S. T. (2003). State of the art electrical discharge machining (EDM). *International Journal of Machine Tools & Manufacture*, *43*, 1287–1300. doi:10.1016/S0890-6955(03)00162-7

Hong, K. S., Sohn, H. C., & Hedrick, J. K. (2002). Modified skyhook control of semi-active suspensions-A new model, gain scheduling and hardware-in-the loop tuning. *Journal of Dynamics, Measurements and Control*, *124*, 158–167. doi:10.1115/1.1434265

Hong, M. H., Huang, S. M., Luk'yanchuk, B. S., & Chong, T. C. (2003). Laser assisted surface nanopatterning. *Sensors and Actuators. A, Physical*, *108*(1-3), 69–74. doi:10.1016/S0924-4247(03)00364-9

Hon, K. K. B., Li, L., & Hutchings, I. M. (2008). Direct writing technology-advances and developments. *CIRP Annals-Manufacturing Technology*, *57*(2), 601–620. doi:10.1016/j.cirp.2008.09.006

Hortig, C., & Svendsen, B. (2007). Simulation of chip formation during high-speed cutting. *Journal of Materials Processing Technology*, *186*, 66–76. doi:10.1016/j.jmatprotec.2006.12.018

Hsieh, H.-S., & Lin, J. (2004). Laser-induced vibration during pulsed laser forming. *Optics & Laser Technology*, *36*, 431–439. doi:10.1016/j.optlastec.2003.11.005

Hsieh, H.-S., & Lin, J. (2005). Study of the buckling mechanism in laser tube forming. *Optics & Laser Technology*, *37*(5), 402–409. doi:10.1016/j.optlastec.2004.06.004

Hu, G., & Bidanda, B. (2009). Modeling sustainable product lifecycle decision support systems. *International Journal of Production Economics*, *122*(1), 366–375. doi:10.1016/j.ijpe.2009.06.011

Hutton, D. V. (2004). *Fundamentals of finite element analysis*. New York, NY: McGraw-Hill.

Hu, Z., Kovacevic, R., & Labudovic, M. (2002). Experimental and numerical modeling of buckling instability of laser sheet forming. *International Journal of Machine Tools & Manufacture*, *42*(13), 1427–1439. doi:10.1016/S0890-6955(02)00075-5

Hwang, C. L., & Yoon, K. (1982). *Multiple attribute decision making – methods and applications- a state of the art survey (lecture notes in economics and mathematical systems)*. Berlin, Germany: Springer-Verlag.

Hwang, E.-H., & Jeon, J.-K. (2010). Preparation and mechanical properties of bulk molding compound composite prepared using recycled FRP waste powder. *Journal of the Korean Industrial and Engineering Chemistry*, *21*(2), 217–223.

Iakovakis, V., Kechagias, J., Petropoulos, G., & Maropoulos, S. (2009). Finite elements analysis of cylindrical copper shelled SLA electrodes. In da Silva Bartolo, P. J., Jorge, M. A., da Conceicao Batista, F., Almeida, H. A., Matias, J. M., & Vasco, J. C., (Eds.), *Innovative development in design and manufacturing* (pp. 651–656). Boca Raton, FL: CRC Press.

Ijomah, W. L., McMahon, C. A., Hammond, G. P., & Newman, S. T. (2007). Development of design for remanufacturing guidelines to support sustainable manufacturing. *Robotics and Computer-integrated Manufacturing*, *23*(6), 712–719. doi:10.1016/j.rcim.2007.02.017

Iordanova, I., Surtchev, M., Forcey, K. S., & Krastev, V. (2000). High-temperature surface oxidation of low-carbon rimming steel. *Surface and Interface Analysis*, *30*, 158–160. doi:10.1002/1096-9918(200008)30:1<158::AID-SIA744>3.0.CO;2-6

Iqbal, S. A., Mativenga, P. T., & Sheikh, M. A. (2008). Contact length prediction: Mathematical models and effect of friction schemes on FEM simulation for conventional to HSM of AISI 1045 steel. *International Journal of Machining and Machinability of Materials*, *3*(1-2), 18–32. doi:10.1504/IJMMM.2008.017622

Irani, S. A., Koo, H. Y., & Raman, S. (1995). Feature-based operation sequence generation in CAPP. *International Journal of Production Research*, *33*, 17–39. doi:10.1080/00207549508930135

Ito, T., & Okazaki, S. (2000). Pushing the limits of lithography. *Nature*, *406*(6799), 1027–1031. doi:10.1038/35023233

Ivanov, M. V. (2001). Electroless nickel-boron-phosphorus coatings: Protective and functional properties. *Protection of Metals*, *37*(6), 592–596. doi:10.1023/A:1012827932615

Iwata, K., Osakada, K., & Terasaka, Y. (1984). Process modeling of orthogonal cutting by the rigid-plastic finite element method. *ASME Journal of Engineering Materials and Technology*, *106*, 132–138. doi:10.1115/1.3225687

Jacobs, P. F. (1996). *Stereolithography and other RP&M techniques: From rapid prototyping to rapid tooling*. New York, NY: ASME Press.

Jahan, A., Ismail, M. Y., Mustapha, F., & Sapuan, S. M. (2010). Material selection based on ordinal data. *Materials & Design*. doi:10.1016/j.matdes.2010.02.024

Jain, V. K., Choudhury, S. K., & Ramesh, K. M. (2002). On the machining of alumina and glass. *International Journal of Machine Tools & Manufacture*, *42*, 1269–1276. doi:10.1016/S0032-3861(02)00241-0

Jain, V. K., Dixit, P. M., & Pandey, P. M. (1999). On the analysis of the electrochemical spark machining process. *International Journal of Machine Tools & Manufacture*, *39*, 165–186. doi:10.1016/S0890-6955(98)00010-8

Jalham, I. S. (2006). Decision-making integrated information technology (IIT) approach for material selection. *International Journal of Computer Applications and Technology*, *25*, 65–71. doi:10.1504/IJCAT.2006.008669

Japke, O. E. (2009). *Practical guideline: Development of a framework for assessing the economic benefits of remanufacturing*. Bedfordshire, UK: Cranfield University.

Jaspers, S. P. F. C., & Dautzenberg, J. H. (2002). Material behavior in conditions similar to metal cutting: Flow stress in the primary shear zone. *Journal of Materials Processing Technology*, *122*, 322–330. doi:10.1016/S0924-0136(01)01228-6

Jee, D. H., & Kang, K. J. (2000). A method for optimal material selection aided with decision making theory. *Materials & Design*, *21*(3), 199–206. doi:10.1016/S0261-3069(99)00066-7

Jiang, B., Xiao, L., Hu, S., Peng, J., Zhang, H., & Wang, M. (2009). Optimization and kinetics of electroless Ni-P-B plating of quartz optical fiber. *Optical Materials*, *31*, 1532–1539. doi:10.1016/j.optmat.2009.02.016

Jiang, Z. Y., Tieu, A. K., Sun, W. H., Tang, J., & Wei, D. B. (2006). Characterisation of thin oxide scale and its surface roughness in hot metal rolling. *Materials Science and Engineering A*, *435-436*, 434–438. doi:10.1016/j.msea.2006.07.070

Ji, Z., & Wu, S. (1998). FEM simulation of the temperature field during the laser forming of sheet metal. *Journal of Materials Processing Technology*, *74*(1-3), 89–95. doi:10.1016/S0924-0136(97)00254-9

Johnson, G. R., & Cook, W. H. (1983). A constitutive model and data for metals subjected to large strains, high strain rates and high temperatures. In *Proceedings of the 7th International Symposium on Ballistics*, The Hague, The Netherlands (pp. 541-547).

Johnson, G. R., & Cook, W. H. (1985). Fracture characteristics of three metals subjected to various strains, strains rates, temperatures and pressures. *Engineering Fracture Mechanics*, *21*(1), 31–48. doi:10.1016/0013-7944(85)90052-9

Joncas, S., Rijswijk, V. K., Charron, J.-F., Bersee, H. E. N., & Beukers, A. *(2006). Interfacial shear strength properties of vacuum-infused anionic polyamide-6 glass-fiber composites. In* Proceedings of the 47th AIAA/ASME/ASCE/AHS/ASC Structures, Structural Dynamics, and Materials Conference, *Newport, RI (pp. 1-8).*

Joshi, S., & Chang, T. C. (1988). Graph-based heuristics for recognitions of machined features from a 3D Solid model. *Computer Aided Design*, *20*(2), 58–66. doi:10.1016/0010-4485(88)90050-4

Kang, M., Han, J., & Moon, J. C. (2003). An approach for interlinking design and process planning. *Journal of Materials Processing Technology*, *139*, 589–595. doi:10.1016/S0924-0136(03)00516-8

Kannan, T. R., & Shunmugam, M. S. (2009). Processing of 3D sheet metal components in STEP AP-203 format. Part I: Feature recognition system. *International Journal of Production Research*, *47*(4), 941–964. doi:10.1080/00207540701510055

Kanta, A. F., Vitry, V., & Delaunois, F. (2009). Effect of thermochemical and heat treatments on electroless nickel-boron. *Materials Letters*, *63*, 2662–2665. doi:10.1016/j.matlet.2009.09.031

Karnoop, R. M., Crosby, R. A., & Harwood, R. A. (1974). Vibration control using semi–active force generators. *ASME Journal of Engineering for Industry*, *96*, 619–626. doi:10.1115/1.3438373

Kashani, R., & Strelow, J. E. (1999). Fuzzy logic active and semi active control of road-vehicle suspensions. *Vehicle System Dynamics*, *32*, 409–420. doi:10.1076/vesd.32.4.409.2075

Kato, J., Takeyasu, N., Adachi, Y., Sun, H.-B., & Kawati, S. (2005). Multiple-spot parallel processing for laser micronanofabrication. *Applied Physics Letters*, *86*(4), 3. doi:10.1063/1.1855404

Kechagias, J., Iakovakis, V., Katsanos, K., & Maropoulos, S. (2008). EDM electrode manufacture using rapid tooling: A review. *Journal of Materials Science*, *43*, 2522–2535. doi:10.1007/s10853-008-2453-0

Khabbaz, R. S., Manshadi, B. D., Abedian, A., & Mahmudi, R. (2009). A simplified fuzzy logic approach for materials selection in mechanical engineering design. *Materials & Design*, *30*, 687–697. doi:10.1016/j.matdes.2008.05.026

Khailash, S. B., Zhang, Y. F., & Fuh, J. Y. H. (2001). A volume decomposition approach to machining feature extraction of casting and forging components. *Computer Aided Design*, *33*, 605–617. doi:10.1016/S0010-4485(00)00107-X

Khan, A., Wang, Z., Sheikh, M. A., Whitehead, D. J., & Li, L. (2010). Parallel near-field optical micro/nanopatterning on curved surfaces by transported micro-particle lens arrays. *Journal of Physics. D, Applied Physics*, *43*(30), 305302. doi:10.1088/0022-3727/43/30/305302

Khattab, A. (2005). *Exploratory development of VARIM process for manufacturing high temperature polymer matrix composites*. Unpublished doctoral dissertation, University of Missouri, Columbia, MO.

Khattab, A., & EI-Gizawy, A. S. (2008). Characterization of process-induced properties in vacuum assisted resin infusion molding of high temperature polymer composites. *Journal of Advanced Materials*, *40*(3), 51–68.

Kim, Y. S., Wang, E., & Rho, H. M. (2001). Geometry-based machining precedence reasoning for feature-based process planning. *International Journal of Production Research*, *39*, 2077–2103. doi:10.1080/00207540110038513

Kinkead, A. N. (1983). Analysis for inversion load and energy absorption of a circular tube. *Journal of Strain Analysis*, *18*, 177–188. doi:10.1243/03093247V183177

Kirby, E. D., Zhang, Z., Chen, J. C., & Chen, J. (2006). Optimizing surface finish in a turning operation using the Taguchi parameter design method. *International Journal of Advanced Manufacturing Technology*, *30*, 1021–1029. doi:10.1007/s00170-005-0156-0

Kitamura, N. (1983). Tecnical report of joint project on material processing by high power laser. *JWES-TP*, *8302*, 359–371.

Klamecki, B. E. (1973). *Incipient chip formation in metal cutting- A three dimensional finite element analysis.* Unpublished doctoral dissertation, University of Illinois, Urbana, IL.

Kleinermann, J.-P. (2000). *Identification Parametrique et Optimisation des Procédés de Mise a Forme par Problemes Inverses*. Unpublished doctoral dissertation, University of Liege, Liege, Belgium.

Klocke, F., & Kratz, H. (2005). Advanced tool edge geometry for high precision hard turning. *Annals of the CIRP*, *54*(1), 47–50. doi:10.1016/S0007-8506(07)60046-8

Klocke, F., Raedt, H.-W., & Hoppe, S. (2001). 2D-FEM simulation of the orthogonal high speed cutting process. *Mining Science and Technology*, *5*, 323–340.

KNITRO Optimization software. (2007). Ziena Optimization Inc.

Koko, T. S., & Olson, M. D. (1991). Non-linear analysis of stiffened plates using super elements. *International Journal for Numerical Methods in Engineering*, *31*(2), 319–343. doi:10.1002/nme.1620310208

Koko, T. S., & Olson, M. D. (1992). Vibration analysis of stiffened plates by super elements. *Journal of Sound and Vibration*, *158*(1), 149–167. doi:10.1016/0022-460X(92)90670-S

Komvopoulos, K., & Erpenbeck, S. A. (1991). Finite element modeling of orthogonal metal cutting. *ASME Journal of Engineering for Industry*, *113*, 253–267.

Konig, W., Jinge, M. K., & Link, R. (1990). Machining with hardened steels with geometrically defined cutting edges. *Annals of CIRP*, *39*, 61–64. doi:10.1016/S0007-8506(07)61003-8

Korhonen, R., & Savolainen, I. (1999). Contribution of industrial and developing countries to the atmospheric CO_2 concentrations: Impact of the Kyoto protocol. *Environmental Science & Policy*, *2*(4-5), 381–388. doi:10.1016/S1462-9011(99)00035-0

Korte, F., Nolte, S., Chichkov, B. N., Bauer, T., Kamlage, G., & Wagner, T. (1999). Far-field and near-field material processing with femtosecond laser pulses. *Applied Physics. A, Materials Science & Processing*, *69*, 7–11.

Krishnaveni, K., Sankara Narayanan, T. S. N., & Seshadri, S. K. (2005). Electroless Ni-B coatings: Preparation and evaluation of hardness and wear resistance. *Surface and Coatings Technology*, *190*, 115–121.

Krzyzanowski, M., & Beynon, J. H. (1999). The tensile failure of mild steel oxides under hot rolling conditions. *Steel Research*, *70*, 22–27.

Krzyzanowski, M., & Beynon, J. H. (2002). Measurement of oxide properties for numerical evaluation of their failure under hot rolling conditions. *Journal of Materials Processing Technology*, *125-126*, 398–404. doi:10.1016/S0924-0136(02)00290-X

Krzyzanowski, M., Beynon, J. H., & Sellars, C. M. (2000). Analysis of secondary oxide scale failure at entry into the roll gap. *Metallurgical and Materials Transactions. B, Process Metallurgy and Materials Processing Science*, *31*(6), 1483–1490. doi:10.1007/s11663-000-0033-z

Kulkarni, A., Sharan, R., & Lal, G. K. (2002). An experimental study of discharge mechanism in electrochemical discharge machining. *International Journal of Machine Tools & Manufacture*, *42*, 1121–1127. doi:10.1016/S0890-6955(02)00058-5

Kuo, H. H., Chern, Lin, J. H., & Ju, C. P. (2005). Tribological behavior of fast-carbonized PAN/phenolic-based carbon/carbon composite and method for improving same. *Wear*, *258*(10), 1555–1561. doi:10.1016/j.wear.2004.10.009

Kyrsanidi, A. K., Kermanidis, T. B., & Pantelakis, S. G. (1999). Numerical and experimental investigation of the laser forming process. *Journal of Materials Processing Technology*, *87*, 281–290. doi:10.1016/S0924-0136(98)00367-7

Lawrence, J. (2002). A comparative investigation of the efficacy of CO_2 and high-power diode lasers for the forming of EN3 mild steel sheets. *Journal of Engineering Manufacture*, *216*, 1481–1491. doi:10.1243/095440502320783521

Lawrence, J., Schmidt, M. J., & Li, L. (2001). The forming of mild steel plates with a 2.5 kW high power diode laser. *International Journal of Machine Tools & Manufacture*, *41*, 967–977. doi:10.1016/S0890-6955(00)00117-6

Lee, H. K., & Crawford, J. H. (1987). Additive coloration of sapphire. *Applied Physics Letters*, *33*, 273–275. doi:10.1063/1.90362

Lee, S., Bradbeck, C. M., & Yang, C. C. (1997). Dynamic nuclear polarization investigations of ESR and NMR strain-broadening effects in sapphire (Al_2O_3:Fe^{3+}). *Physical Review B: Condensed Matter and Materials Physics*, *15*, 69–2476.

Lee, W. L., Seferis, J. C., & Bonner, D. C. (1986). Prepreg processing science. *SAMPE Quarterly*, *17*, 58–69.

Leissa, A. W. (1989). Closed form exact solutions for the steady state vibrations of continuous systems subjected to distributed exciting forces. *Journal of Sound and Vibration*, *134*(3), 435–453. doi:10.1016/0022-460X(89)90568-3

Li, C. L., & Hui, K. C. (2000). Feature recognition by template matching. *Computers & Graphics*, *24*, 569–582. doi:10.1016/S0097-8493(00)00059-5

Li, C., Huang, H., Yang, S., Zheng, R., Yong, Y., & Liu, Z. (2009). Controlled synthesis and characterization of 10nm thick Al_2O_3 nanowires. *Journal of Materials Letters*, *63*, 1016–1018. doi:10.1016/j.matlet.2009.01.072

Lieberman, K., Shani, Y., Melnik, I., Yoffe, S., & Sharon, Y. (1999). Near-field optical photomask repair with a femtosecond laser. *Journal of Microscopy-Oxford*, *194*, 537–541. doi:10.1046/j.1365-2818.1999.00547.x

Li, J., & Cheng, X. H. (2008). Friction and wear properties of surface-treated carbon fibre-reinforced thermoplastic polyimide composites under oil-lubricated condition. *Materials Chemistry and Physics*, *108*(1), 67–72. doi:10.1016/j.matchemphys.2007.09.003

Li, K., Gao, X.-L., & Sutherland, J. W. (2002). Finite element simulation of the orthogonal metal cutting process for qualitative understanding of the effects of crater wear on the chip formation. *Journal of Materials Processing Technology*, *127*, 309–324. doi:10.1016/S0924-0136(02)00281-9

Lima, J. G., Avila, R. F., Abrao, A. M., Faustino, M., & Davim, J. P. (2005). Hard turning: AISI 4340 high strength alloy steel and AISI D2 cold work tool steel. *Journal of Materials Processing Technology*, *169*, 388–395. doi:10.1016/j.jmatprotec.2005.04.082

Lin, A. C., Lin, S. Y., & Cheng, S. B. (1997). Extraction of manufacturing features from a feature-based design model. *International Journal of Production Research*, *35*(12), 3249–3288. doi:10.1080/002075497194066

Lin, C.-T., Chow, H.-A., Yang, L.-D., & Chen, Y.-F. (2007). Feasibility study of micro-slit EDM machining using pure water. *International Journal of Advanced Manufacturing Technology*, *34*, 104–110. doi:10.1007/s00170-006-0570-y

Lin, J., Cheong, B. H., & Yao, X. (2002). Universal multi-objective function for optimising superplastic-damage constitutive equations. *Journal of Materials Processing Technology*, *125-126*, 199–205. doi:10.1016/S0924-0136(02)00311-4

Lin, Z. C., & Lin, S. Y. (1992). A couple finite element model of thermo-elastic-plastic large deformation for orthogonal cutting. *ASME Journal of Engineering for Industry*, *114*, 218–226.

List, G., Sutter, G., & Bi, X. F. (2009). Investigation of tool wear in high speed machining by using a ballistic set-up. *Wear*, *267*, 1673–1679. doi:10.1016/j.wear.2009.06.018

Liu, G. R., & Han, X. (2003). *Computational Inverse techniques in Nondestructible Evaluation*. Boca Raton, FL: CRC Press. doi:10.1201/9780203494486

Liu, G. R., & Quek, S. S. (2003). *The finite element method: A practical course*. Oxford, UK: Butterworth Heinemann.

Liu, Q., Ling, X., Liu, H., Hang, J., & Hu, Z. (2006). Solution phases synthesis of CuO nanorods. *Materials Chemistry and Physics*, *98*, 519–522. doi:10.1016/j.matchemphys.2005.09.073

Liu, Z., & Wang, L. (2007). Sequencing of interacting prismatic machining features for process planning. *Computers in Industry*, *58*, 295–303. doi:10.1016/j.compind.2006.07.003

Liu, Z., Wei, Q., & Zhang, X. (2005). Surface plasmon interference nanolithography. *Nano Letters*, *5*(5), 957–961. doi:10.1021/nl0506094

Li, W., & Yao, Y. L. (2001). Laser bending of tubes: Mechanism, analysis, and prediction. *Journal of Manufacturing Science and Engineering. Transactions of the ASME*, *123*(4), 674–681.

Li, Y. H., Krzyzanowski, M., Beynon, J. H., & Sellars, C. M. (2000). Physical simulation of interfacial conditions in hot forming of steels. *Acta Metallurgica Sinica*, *13*, 359–368.

Lord Rayliegh. (1945). *Controlled suspensions. Theory of sound* (*Vol. 1-2*). New York, NY: Dover Publications.

Lorentzon, J., & Jarvstrat, N. (2009). Modelling chip formation of alloy 718. *Journal of Materials Processing Technology*, *209*, 4645–4653. doi:10.1016/j.jmatprotec.2008.11.029

Lothongkum, A. W., Nonthapone, R., Seangkiatiyuth, K., & Tanthapanichkoon, W. (2007). Powder characteristics and coating conditions of fresh and re-used polyester resins for electrostatic powder coating: powder recycling and loss prevention. *Advanced Powder Technology*, *18*(2), 175–186. doi:10.1163/156855207780208664

Luiser, A., Bourban, P. E., & Manson, J. A. E. *(1999). In-situ polymerization of polyamide 12 for thermoplastic composites. In* Proceedings of the 12th International Conference on Composite Materials, *Paris, France (pp. 33-45).*

Lu, Y. H. (2005). Study of perform and loading rate in the tube nosing process by spherical die. *Computer Methods in Applied Mechanics and Engineering*, *194*, 2839–2858. doi:10.1016/j.cma.2004.07.032

Mabrouki, T., Deshayes, L., Ivester, R., Regal, J.-F., & Jurrens, K. (2004, April 4-5). Material modeling and experimental study of serrated chip morphology. In *Proceedings of the 7th CIRP International Workshop on Modeling of Machining Operations* (pp. 53-66).

Mabrouki, T., Girardin, F., Asad, M., & Regal, J.-F. (2008). Numerical and experimental study of dry cutting for an aeronautic aluminum alloy. *International Journal of Machine Tools & Manufacture*, *48*, 1187–1197. doi:10.1016/j.ijmachtools.2008.03.013

Mabrouki, T., & Rigal, J.-F. (2006). A contribution to a qualitative understanding of thermo-mechanical effects during chip formation in hard turning. *Journal of Materials Processing Technology*, *176*, 214–221. doi:10.1016/j.jmatprotec.2006.03.159

Mackerle, J. (1962). Finite element methods and material processing technology, an addendum (1994–1996). *Engineering Computations*, *15*, 616–690. doi:10.1108/02644409810225788

Mackerle, J. (1999). Finite-element analysis and simulation of machining: A bibliography (1976-1996). *Journal of Materials Processing Technology*, *86*, 17–44. doi:10.1016/S0924-0136(98)00227-1

Mackerle, J. (2003). Finite element analysis and simulation of machining: An addendum a bibliography (1996-2002). *International Journal of Machine Tools & Manufacture*, *43*, 103–114. doi:10.1016/S0890-6955(02)00162-1

Mallon, P. J., Dweib, M. A., Ziaee, S., Chatterjee, A., & Gillespie, J. W. (2003). VARTM and RTM processing of PBT and PA6 thermoplastic composites. *STAR*, *41*(4), 31–43.

Mallory, G. O., & Hadju, J. B. (1991). *Electroless plating: Fundamentals and applications*. Orlando, FL: AESF.

Mamalis, A. G., Horvath, M., Branis, A. S., & Manolakos, D. E. (2001). Finite element simulation of chip formation in orthogonal metal cutting. *Journal of Materials Processing Technology*, *110*, 19–27. doi:10.1016/S0924-0136(00)00861-X

Mamalis, A. G., Kundrák, J., Markopoulos, A., & Manolakos, D. E. (2008). On the finite element modeling of high speed hard turning. *International Journal of Advanced Manufacturing Technology*, *38*(5-6), 441–446. doi:10.1007/s00170-007-1114-9

Maniatty, A. M., & Zabaras, N. (1996). Investigation of regularization parameters and error estimating in inverse elasticity problems. *International Journal for Numerical Methods in Engineering*, *37*, 1039–1052. doi:10.1002/nme.1620370610

Maniya, K., & Bhatt, M. G. (2010). A selection of material using a novel type decision-making method: preference selection index method. *Materials & Design*, *31*, 1785–1789. doi:10.1016/j.matdes.2009.11.020

Manshadi, B. D., Mahmudi, H., Abedian, A., & Mahmudi, R. (2007). A novel method for materials selection in mechanical design: combination of non-linear normalization and a modified digital logic method. *Materials & Design*, *28*, 8–15. doi:10.1016/j.matdes.2005.06.023

Maranhão, C., & Davim, J. P. (2010). Finite element modelling of machining of AISI 316 steel: Numerical simulation and experimental validation. *Simulation Modelling Practice and Theory*, *18*, 139–156. doi:10.1016/j.simpat.2009.10.001

Mark, R. (2001). Surface oxide formation and acid-descaling for stainless steel: Part 1. *Wire Industry*, *68*, 503.

Marquardt, D. W. (1963). An algorithm for least-squares estimation of non-linear parameters. *Journal of the Society for Industrial and Applied Mathematics*, *11*, 431–441. doi:10.1137/0111030

Marusich, T. D., & Ortiz, M. (1995). Modelling and simulation of high-speed machining. *International Journal for Numerical Methods in Engineering*, *38*, 3675–3694. doi:10.1002/nme.1620382108

Masuzawa, T., Fujino, M., Kobayashi, K., Suzuki, T., & Kinoshita, N. (1985). Wire electro-discharge grinding for micro-machining. *CIRP Annals: Manufacturing Technology*, *34*(1), 431–434. doi:10.1016/S0007-8506(07)61805-8

Mathematica. (2009). *Wolfram Mathematica 7*. Wolfram Research, Inc.

Mathew, J. (2005). *Thermo-mechanical analysis of metallized stereolithography EDM electrodes.* Retrieved from http://hdl.handle.net/10057/572

Matlab. (2007). The Language of technical Computing. In *User Manual* (Vol. R2007). The Mathworks, Inc.

Melton, T. (2005). The benefits of lean manufacturing: What lean thinking has to offer the process industries. *Chemical Engineering Research & Design*, *83*(6), 662–673. doi:10.1205/cherd.04351

Menezes, L. F., & Teodosiu, C. (2000). Three-dimensional numerical simulation of the deep-drawing process using solid finite elements. *Journal of Materials Processing Technology*, *97*(1-3), 100–106. doi:10.1016/S0924-0136(99)00345-3

Miller, G. (2003). *Tube forming processes: A comprehensive guide*. Dearborn, MI: SME-Society of manufacturing Engineers.

Mindlin, R. D. (1949). Compliance of elastic bodies in contact. *Journal of Applied Mechanics*, *71*, 259–268.

Minitab User Manual 13.2. (2001). *Making data analysis easier*. State College, PA: MINITAB Inc.

Mitra, S. (2007). Revenue management for remanufactured products. *Omega*, *35*(5), 553–562. doi:10.1016/j.omega.2005.10.003

Miyashita, K., Nishimura, S., Toyofuku, T., & Shirakashi, J.-I. (2009). Nanoscale patterning of NiFe surface by scanning probe microscopy scratch nanolithography. *Journal of Vacuum Science & Technology B Microelectronics and Nanometer Structures*, *27*(2), 953–957. doi:10.1116/1.3077488

ModeFrontier. (2008). *ESTECO ModeFrontier - multi-objective optimization and design environment software* (Vol. 4.0). ESTECO.

Mohd Ishak, Z. A., Gatos, K. G., & Karger-Kocsis, J. (2006). On the in-situ polymerization of cyclic butylene terephthalate oligomers: DSC and rheological studies. *Polymer Engineering and Science*, *46*, 743–750. doi:10.1002/pen.20486

Monk, D. (2010). Europe goes down under. *The Journal for Waste and Resource Management Professionals*, 42-43.

Montgomery, D. C. (2001). *Design and analysis of experiments*. New York, NY: John Wiley & Sons.

Morris, J. R., Phillips, P. S., & Read, A. D. (1998). The UK landfill tax: An analysis of its contribution to sustainable waste management. *Resources, Conservation and Recycling*, *23*(4), 259–270. doi:10.1016/S0921-3449(98)00037-8

Movahhedy, M. R., Altintas, Y., & Gadala, M. S. (2002). Numerical analysis of metal cutting with chamfered and blunt tools. *ASME Journal of Manufacturing Science and Engineering*, *124*, 178–188. doi:10.1115/1.1445147

Movahhedy, M., Gadala, M. S., & Atlantis, Y. (2000). Simulation of the orthogonal metal cutting process using an arbitrary Lagrangian Eulerian finite element method. *Journal of Materials Processing Technology*, *103*, 267–275. doi:10.1016/S0924-0136(00)00480-5

Mukherjee, A., & Mukhopadhyay, M. (1986). A review of dynamic behavior of stiffened plates. *Shock Vibration Digest*, *18*(6), 3–8. doi:10.1177/058310248601800603

Mukherjee, A., & Mukhopadhyay, M. (1988). Finite element free vibration of eccentrically stiffened plates. *Computers & Structures*, *30*(6), 1303–1317. doi:10.1016/0045-7949(88)90195-2

Mukhopadhyay, M. (1994). Stiffened plates in bending. *Computers & Structures*, *50*(4), 541–548. doi:10.1016/0045-7949(94)90024-8

Munther, P. A., & Lenard, J. G. (1999). The effects of scaling on interfacial friction of hot rolling of steels. *Journal of Materials Processing Technology*, *88*, 105–113. doi:10.1016/S0924-0136(98)00392-6

Murray, N. G. D., Schuh, C. A., & Dunand, D. C. (2003). Solid-state foaming of titanium by hydrogen-induced internal stress superplasticity. *Scripta Materialia*, *49*, 879–883. doi:10.1016/S1359-6462(03)00438-X

Nalbant, M., Gökkaya, H., & Sur, G. (2007). Application of Taguchi method in the optimization of cutting parameters for surface roughness in turning. *Materials & Design*, *28*, 1379–1385. doi:10.1016/j.matdes.2006.01.008

Nasr, E. S. A., & Kamrani, A. K. (2006). A new methodology for extracting manufacturing features from CAD system. *Computers & Industrial Engineering*, *51*, 389–415. doi:10.1016/j.cie.2006.08.004

Ng, E. G., & Aspinwall, D. K. (2002). Modeling of hard part machining. *Journal of Materials Processing Technology*, *127*, 222–229. doi:10.1016/S0924-0136(02)00146-2

Ng, E. G., Aspinwall, D. K., Brazil, D., & Monaghan, J. (1999). Modelling of temperature and forces when orthogonally machining hardened steel. *International Journal of Machine Tools & Manufacture*, *39*, 885–903. doi:10.1016/S0890-6955(98)00077-7

Ng, E. G., Tahany, I., Wardany, E.-L., Dumitrescu, M., & Elbestawi, M. A. (2002). Physics based simulation of high speed machining. *Mining Science and Technology*, *6*, 301–329.

Niccolo, P., Zaniboni, C., Stephan, B., & Ermanni, P. (2006). Perspectives for reaction molding of PPA as matrix for high-performance composite Materials. *Journal of Thermoplastic Composite Materials*, *19*, 207–216. doi:10.1177/0892705706059738

Norris, D. M., Morran, J. R. B., Scudde, J. K., & Quinones, D. F. (1978). A computer simulation of the tension test. *Journal of the Mechanics and Physics of Solids*, *26*, 1–19. doi:10.1016/0022-5096(78)90010-8

Nouari, M., & Ginting, A. (2004). Wear characteristics and performance of multi-layer CVD-coated alloyed carbide tool in dry end milling of titanium alloy. *Surface and Coatings Technology*, *200*(18-19), 5663–5676. doi:10.1016/j.surfcoat.2005.07.063

Oberg, E., Jones, D. F., Horton, H. L., & Ryffel, H. H. (2008). *Machinery's Handbook*. Industrial Press.

Obikawa, T., Sasahara, H., Shirakashi, T., & Usui, E. (1997). Application of computational machining method to discontinuous chip formation. *ASME Journal of Manufacturing Science and Engineering*, *119*, 667–674. doi:10.1115/1.2836807

O'Connell, C., Sherlock, R., & Glynn, T. J. (2010). Fabrication of a reusable microlens array for laser-based structuring. *Optical Engineering (Redondo Beach, Calif.)*, *49*(1), 4.

Ohbuchi, Y., & Obikawa, T. (2005). Adiabatic shear in chip formation with negative rake angle. *International Journal of Mechanical Sciences*, *47*, 1377–1392. doi:10.1016/j.ijmecsci.2005.05.003

Ohmae, N., Kobayashi, K., & Tsukizoe, T. (1974). Characteristics of fretting of carbon fibre reinforced plastics. *Wear*, *29*(3), 345–353. doi:10.1016/0043-1648(74)90020-9

Ojeda, R., Prusty, B. G., Lawrence, N., & Thomas, G. (2007). A new approach for the large deflection finite element analysis of isotropic and composite plates with arbitrary orientated stiffeners. *Finite Elements in Analysis and Design*, *43*, 989–1002. doi:10.1016/j.finel.2007.06.007

Okabe, T., & Takeda, N. (2002). Size effect on tensile strength of unidirectional CFRP composites experiment and simulation. *Composites Science and Technology*, *62*(15), 2053–2064. doi:10.1016/S0266-3538(02)00146-X

Oliveira, M. C., Alves, J. L., Chaparro, B. M., & Menezes, L. F. (2007). Study on the influence of work-hardening modeling in springback prediction. *International Journal of Plasticity*, *23*, 516–543. doi:10.1016/j.ijplas.2006.07.003

Olovsson, L., Nilsson, L., & Simonsson, K. (1999). An ALE formulation for the solution of two-dimensional metal cutting problems. *Computers & Structures*, *72*, 497–507. doi:10.1016/S0045-7949(98)00332-0

Optimol Instruments Prüftechnik. (2007). *SRV operating instruction manual*. Munich, Germany: Optimol Instruments Prüftechnik.

Oraon, B., Majumdar, G., & Ghosh, B. (2008). Improving hardness of electroless Ni-B coatings using optimized deposition conditions and annealing. *Materials & Design*, *29*, 1412–1418. doi:10.1016/j.matdes.2007.09.005

Östlin, J., Sundin, E., & Björkman, M. (2009). Product life-cycle implications for remanufacturing strategies. *Journal of Cleaner Production*, *17*(11), 999–1009. doi:10.1016/j.jclepro.2009.02.021

Özel, T. (2003). Modeling of hard part machining: Effect of insert edge preparation in CBN cutting tools. *Journal of Materials Processing Technology*, *141*, 284–293. doi:10.1016/S0924-0136(03)00278-4

Ozel, T. (2006). The influence of friction models on finite element simulations of machining. *International Journal of Machine Tools & Manufacture*, *46*, 518–530. doi:10.1016/j.ijmachtools.2005.07.001

Özel, T. (2009). Computational modeling of 3D turning: Influence of edge micro-geometry on forces, stresses, friction and tool wear in PcBN tooling. *Journal of Materials Processing Technology*, *209*, 5167–5177. doi:10.1016/j.jmatprotec.2009.03.002

Özel, T., & Altan, T. (2000). Process simulation using finite element method – prediction of cutting forces, tool stresses and temperatures in high-speed flat end milling process. *International Journal of Machine Tools & Manufacture*, *40*, 713–738. doi:10.1016/S0890-6955(99)00080-2

Ozel, T., & Zeren, E. (2006). A methodology to determine work material flow stress and tool-chip interfacial friction properties by using anaysis of machining. *ASME Journal of Manufacturing Science and Engineering*, *128*, 119–129. doi:10.1115/1.2118767

Özel, T., & Zeren, E. (2007). Finite element modeling the influence of edge roundness on the stress and temperature fields induced by high-speed machining. *International Journal of Advanced Manufacturing Technology*, *35*, 255–267. doi:10.1007/s00170-006-0720-2

Palmeri, P. S., Moschetti, A., & Gortan, L. H. (1995). *Infinity control for active suspension system*. Retrieved from http://www.papers.sae.org/950583

Park, J., Ryu, Y., Kim, H., & Yu, C. (2009). Simple and fast annealing synthesis of titanium dioxide nanostructures and morphology transformation during annealing processes. *Nanotechnology*, *20*(10), 105608. doi:10.1088/0957-4484/20/10/105608

Parton, H., & Verpoest, I. *(2003). Reactive processing of textile reinforced thermoplastics. In* Proceedings of the 14th International Conference on Composite Materials, *San Diego, CA (pp. 41-50).*

Parton, H., & Verpoest, I. (2005). In-situ polymerization of thermoplastic composites based on cyclic oligomers. *Polymer Composites*, *26*, 60–65. doi:10.1002/pc.20074

Patil, L., & Pande, S. S. (2002). An intelligent feature-based process planning system for prismatic parts. *International Journal of Production Research*, *40*, 4431–4447. doi:10.1080/00207540210155855

Patton, D., & Worthington, I. (2003). SMEs and environmental regulations: A study of the UK screen-printing sector. *Environment and Planning. C, Government & Policy*, *21*(4), 549–566. doi:10.1068/c0321

Peace, G. S. (1993). *Taguchi methods: A hands-on approach*. Reading, MA: Addison-Wesley.

Pena, A., Wang, Z. B., Whitehead, D. J., & Li, L. (2009). High speed laser micro-texturing of Si wafer for improved light trapping for photo-voltaic application. In *Proceedings of the 28th International Congress on Applications of Lasers & Electro-Optics*, Orlando, FL.

Peng, L. X., Liew, K. M., & Kitipornchai, S. (2006). Buckling and free vibration analyses of stiffened plates using the FSDT mesh-free method. *Journal of Sound and Vibration*, *289*(3), 147–164. doi:10.1016/j.jsv.2005.02.023

Peng, W. Y., & Liao, Y. S. (2004). Study of electrochemical discharge machining technology for slicing non-conductive brittle materials. *Journal of Materials Processing Technology*, *149*, 363–369. doi:10.1016/j.jmatprotec.2003.11.054

Peng, X. S., Zhang, L. D., Meng, G. W., Wang, X. F., Wang, Y. F., & Wang, C. Z. (2002). Photoluminescence and infrared properties of α-Al_2O_3 nanowires and nanobelts. *The Journal of Physical Chemistry B*, *106*, 11163–11170. doi:10.1021/jp026028+

Pickering, S. J. (2006). Recycling technologies for thermoset composite materials—current status. *Composites: Part A*, *37*, 1206–1215. doi:10.1016/j.compositesa.2005.05.030

Pinkerton, A. J. (2004). *A mathematical and experimental investigation of thin wall laser direct metal deposition*. Manchester, UK: UMIST.

Polak, E. (1997). *Optimization – Algorithms and Consistent Approximations*. New York: Springer Verlag.

Ponthot, J.-P., & Kleinermann, J.-P. (2006). A cascade optimization methodology for automatic parameter identification and shape/process optimization in metal forming. *Computer Methods in Applied Mechanics and Engineering*, *195*, 5472–5508. doi:10.1016/j.cma.2005.11.012

Prathap, G., & Varadan, T. K. (1978). Large amplitude flexural vibration stiffened of plates. *Journal of Sound and Vibration*, *57*(4), 583–593. doi:10.1016/0022-460X(78)90547-3

Press, W. H., Teukolsky, S. A., Vetterling, W. T., & Flannery, B. P. (2005). *Numerical recipes in Fortran 77* (2nd ed.). Cambridge, MA: Press Syndicate.

Quadrini, F., & Squeo, E. A. (2008). Solid-state foaming of epoxy resin. *Journal of Cellular Plastics*, *44*, 161–173. doi:10.1177/0021955X07082486

Quaglia, G., & Sorli, M. (1996). Analysis of vehicular air suspensions. In *Proceedings of the Fourth JHPS International Symposium on Fluid Power*, Tokyo, Japan (pp. 389-384).

Raczy, A., Elmadagli, M., Altenhof, W. J., & Alpas, A. T. (2004). An Eulerian finite-element model for determination of deformation state of a copper subjected to orthogonal cutting. *Metallurgical and Materials Transactions*, *35A*, 2393–2400. doi:10.1007/s11661-006-0219-3

Rahmani, K., & Arezoo, B. (2006). Boundary analysis and geometric completion for recognition of interacting machining features. *Computer Aided Design*, *38*, 845–856. doi:10.1016/j.cad.2006.04.015

Rakotomalala, R., Joyot, P., & Touratier, M. (1993). Arbitrary Lagrangian-Eulerian thermomechanical finite element model of material cutting. *Communications in Numerical Methods in Engineering*, *9*, 975–987. doi:10.1002/cnm.1640091205

Rall, L. B. (1981). *Automatic Differentiation: Techniques and Applications (LNCS)*. New York: Springer Verlag.

Rameshbabu, V., & Shunmugam, M. S. (2008). Hybrid feature recognition method for setup planning from STEP AP-203. *Robotics and Computer-integrated Manufacturing*, *25*(2), 393–408. doi:10.1016/j.rcim.2007.09.014

Ramesh, T., & Jan-Anders, E. M. (2000). Comprehensive composite materials: *Vol. 2*. *Polymer matrix composites*. Burlington, MA: Elsevier Science & Technology Books.

Rao, D. V., Sheikh, A. H., & Mukhopadhyay, M. (1993). A finite element large displacement analysis of stiffened plates. *Computers & Structures*, *47*(6), 987–993. doi:10.1016/0045-7949(93)90303-U

Rao, R. V. (2006). A material selection model using graph theory and matrix approach. *Materials Science and Engineering A*, *431*, 248–255. doi:10.1016/j.msea.2006.06.006

Rao, R. V. (2006). Machinability evaluation of work materials using a combined multiple attributes decision-making method. *International Journal of Advanced Manufacturing Technology*, *28*, 221–227. doi:10.1007/s00170-004-2348-4

Rao, R. V. (2007). *Decision making in the manufacturing environment using graph theory and fuzzy multiple attribute decision making methods*. London: Springer Verlag.

Rao, R. V. (2008). A decision making methodology for material selection using an improved compromise ranking method. *Materials & Design*, *29*, 1949–1954. doi:10.1016/j.matdes.2008.04.019

Rao, R. V., & Davim, J. P. (2006). A decision making methodology for material selection using a combined multiple attribute decision making method. *International Journal of Advanced Manufacturing Technology*, *35*, 751–760. doi:10.1007/s00170-006-0752-7

Rao, R. V., & Davim, J. P. (2008). A decision-making framework model for material selection using a combined multiple attribute decision-making method. *International Journal of Advanced Manufacturing Technology*, *35*, 751–760. doi:10.1007/s00170-006-0752-7

Rao, S. R., Sheikh, A. H., & Mukhopadhyay, M. (1993). Large-amplitude finite element flexural vibration of plates/stiffened plates. *The Journal of the Acoustical Society of America*, *93*(6), 3250–3257. doi:10.1121/1.405710

Rattan, R., Bijwe, J., & Fahim, M. (2007). Influence of weave of carbon fabric on low amplitude oscillating wear performance of Polyetherimide composites. *Wear*, *262*(5-6), 727–735. doi:10.1016/j.wear.2006.08.005

Reddy, T. Y. (1989). Tube inversion – an experiment in plasticity. *International Journal of Mechanical Engineering Education*, *17*, 277–291.

Reddy, T. Y. (1992). Guist and Marble revisited – on the natural knuckle radius in tube inversion. *International Journal of Mechanical Sciences*, *34*, 761–768. doi:10.1016/0020-7403(92)90040-N

Reidy, H. (2010). As good as new. *Professional Engineering and Manufacturing*, 23-24.

Ren, G., Hu, D., Cheng, E. W. C., Vargas-Reus, M. A., Reip, P., & Allaker, R. P. (2009). Characterisation of copper oxide nanoparticles for antimicrobial applications. *International Journal of Antimicrobial Agents*, *33*(6), 587–590. doi:10.1016/j.ijantimicag.2008.12.004

Reynolds, H. M. (1993). *Automotive ergonomics* (pp. 99–116). London, UK: Taylor and Francis.

Ribeiro, P. (2004). Non-linear forced vibrations of thin/thick beams and plates by the finite element and shooting methods. *Computers & Structures*, *82*, 1413–1423. doi:10.1016/j.compstruc.2004.03.037

Riedel, W. (1991). *Electroless nickel plating*. Hertfordshire, UK: Finishing Publications.

Rong, Y., Huang, S. H., & Hou, Z. (2005). *Advanced computer-aided fixture design*. London, UK: Elsevier Academic Press.

Rosa, P. A. R., Rodrigues, J. M. C., & Martins, P. A. F. (2003). External inversion of thin-walled tubes using a die: experimental and theoretical investigation. *International Journal of Machine Tools & Manufacture*, *43*, 787–796. doi:10.1016/S0890-6955(03)00062-2

Rosa, P. A. R., Rodrigues, J. M. C., & Martins, P. A. F. (2004). Internal inversion of thin-walled tubes using a die: experimental and theoretical investigation. *International Journal of Machine Tools & Manufacture*, *44*, 775–784. doi:10.1016/j.ijmachtools.2004.01.013

Rossow, M. P., & Ibrahimkhail, A. K. (1978). Constraint method of analysis of stiffened plates. *Computers & Structures*, *8*, 51–60. doi:10.1016/0045-7949(78)90159-1

Ross, P. J. (1996). *Taguchi techniques for quality engineering* (2nd ed.). New York, NY: McGraw-Hill.

Roy, R. (1990). *A primer on the Taguchi method*. Dearborn, MI: Society of Manufacturing Engineers.

Rubio, S., & Corominas, A. (2008). Optimal manufacturing-remanufacturing policies in a lean production environment. *Computers & Industrial Engineering*, *55*(1), 234–242. doi:10.1016/j.cie.2007.12.009

Rudd, C. D., Long, A. C., Kendall, K. N., & Mangin, C. G. E. (1997). *Liquid moulding technologies*. Cambridge, UK: Woodhead Publishing. doi:10.1533/9781845695446

Ryan, A. J., Stanford, J. L., & Tao, X. Q. (1995). The processing, structure and properties of structural composites formed by reaction injection-moulding (SRIM). *Plastics Rubber and Composites Processing and Applications*, *23*(3), 151–159.

Saaty, T. L. (2000). *Fundamentals of decision making and priority theory with AHP*. Pittsburgh, PA: RWS Publications.

Safdar, S., Li, L., & Sheikh, M. A. (2007). The effect of non-conventional laser beam geometries on stress distribution and distortions in laser bending of tubes. *Journal of Manufacturing Science and Engineering*, *129*, 592–600. doi:10.1115/1.2716715

Safdar, S., Li, L., Sheikh, M. A., & Zhu, L. (2006). Finite element simulation of laser tube bending: Effect of scanning schemes on bending angle, distortions and stress distribution. *Optics & Laser Technology*, *39*(6), 1101–1110. doi:10.1016/j.optlastec.2006.09.014

Saha, K. N., Misra, D., Pohit, G., & Ghosal, S. (2004). Large amplitude free vibration study of square plates under different boundary conditions through a static analysis. *Journal of Vibration and Control*, *10*, 1009–1028. doi:10.1177/1077546304038101

Sahoo, P. (2008). Optimization of electroless Ni-P coatings based on surface roughness. *Tribology Online*, *3*(1), 6–11. doi:10.2474/trol.3.6

Sakurai, H. (1995). Volume decomposition and feature recognition: Part 1-polyhedral objects. *Computer Aided Design*, *27*(11), 833–843. doi:10.1016/0010-4485(95)00007-0

Sankara Narayanan, T. S. N., Krishnaveni, K., & Seshadri, S. K. (2003). Electroless Ni-P/Ni-B duplex coatings: Preparation and evaluation of microhardness, wear and corrosion resistance. *Materials Chemistry and Physics*, *82*, 771–779. doi:10.1016/S0254-0584(03)00390-0

Sapountzakis, E. J., & Katsikadelis, J. T. (2000). Elastic deformation of ribbed plates under static, transverse and inplane loading. *Computers & Structures*, *74*, 571–581. doi:10.1016/S0045-7949(99)00066-8

Sapountzakis, E. J., & Mokos, V. G. (2008). An improved model for the dynamic analysis of plates stiffened by parallel beams. *Engineering Structures*, *30*(6), 1720–1733. doi:10.1016/j.engstruct.2007.11.016

Sapuan, S. M. (2001). A knowledge-based system for materials selection in mechanical engineering design. *Materials & Design*, *22*, 687–695. doi:10.1016/S0261-3069(00)00108-4

Sato, J. (1988). Recent studies on fretting wear of polymeric materials. *Transactions ISLE*, *33*, 26–32.

Schulz, H. (2001). *Scientific fundamentals of HSC*. Munich, Germany: Carl Hanser Verlag.

Schulz, H., & Moriwaki, T. (1992). High-speed machining. *Annals of the CIRP*, *41*(2), 637–643. doi:10.1016/S0007-8506(07)63250-8

Seitz, M. A. (2006). A critical assessment of motives for product recovery: The case of engine remanufacturing. *Journal of Cleaner Production*, *15*, 1147–1157. doi:10.1016/j.jclepro.2006.05.029

Sekhon, G. S., Gupta, N. K., & Gupta, P. K. (2003). An analysis of external inversion of round tubes. *Journal of Materials Processing Technology*, *133*, 243–256. doi:10.1016/S0924-0136(02)00438-7

Selvum, P., Vaidya, U. K., & Janowski, G. M. (2005). Liquid moulding of carbon fabric-reinforced nylon matrix composite laminates. *Journal of Thermoplastic Composite Materials*, *18*(6), 509–527. doi:10.1177/0892705705054412

Shah, J. J., & Mantyla, M. (1995). *Parametric and feature-based CAD/CAM*. New York, NY: John Wiley & Sons.

Shah, M. A. (2009). Aluminum oxide (α-Al_2O_3) nanorods prepared at low temperature without surfactant. *Physics Letters. [Part B]*, *23*(13), 1–7.

Shah, M. A., & Quarshi, A. (2009). Novel surfactant free synthesis of MgO nanoflakes. *Journal of Alloys and Compounds*, *482*, 548–552. doi:10.1016/j.jallcom.2009.04.129

Shah, M. A., & Towkeer, A. (2010). *Principles of nanoscience and nanotechnology*. New Delhi, India: Naroosa Publishing.

Shahzad, M. A., Steeg, M., & Mitschang, P. (2010). Development and characterization of glass fibre reinforced in-situ polymerized thermoplastic matrix composite material. In *Proceedings of the SAMPE Conference and Exhibition*, Seattle, WA (pp. 1-15).

Shangguan, Q.-Q., & Cheng, X.-H. (2007). Tribological properties of lanthanum treated carbon fibres reinforced PTFE composite under dry sliding condition. *Wear*, *262*(11-12), 1419–1425. doi:10.1016/j.wear.2007.01.020

Shang, Y. W., & Qiu, Y. H. (2006). A Note on the Extended Rosenbrock Function. *Evolutionary Computation*, *14*(1), 119–126. doi:10.1162/evco.2006.14.1.119

Shanian, A., & Savadogo, O. (2006a). A material selection model based on the concept of multiple factor decision making. *Materials & Design*, *27*, 329–337. doi:10.1016/j.matdes.2004.10.027

Shanian, A., & Savadogo, O. (2006b). A non-compensatory compromised solution for material selection of bipolar plates for polymer electrolyte membrane fuel cell (PEMFC) using ELECTRE IV. *Electrochimica Acta*, *51*, 5307–5315. doi:10.1016/j.electacta.2006.01.055

Shanian, A., & Savadogo, O. (2006c). TOPSIS multiple-criteria decision support analysis for material selection of metallic bipolar plates for polymer electrolyte fuel cell. *Journal of Power Sources*, *159*, 1095–1104. doi:10.1016/j.jpowsour.2005.12.092

Sharp, R. S., & Corolla, D. A. (1987). Road vehicle suspension design–A review. *Vehicle System Dynamics*, *16*, 169–192. doi:10.1080/00423118708968877

Sheikh, A. H., & Mukhopadhyay, M. (2000). Geometric non-linear analysis of stiffened plates by spline finite strip method. *Computers & Structures*, *76*(3), 765–785. doi:10.1016/S0045-7949(99)00191-1

Shen, H., & Vollertsen, F. (2009). Modelling of laser forming - An review. *Computational Materials Science*, *46*, 834–840. doi:10.1016/j.commatsci.2009.04.022

Shichun, W., & Zhong, J. (2002). FEM simulation of the deformation field during the laser forming of sheet metal. *Journal of Materials Processing Technology*, *121*(2-3), 269–272. doi:10.1016/S0924-0136(01)01241-9

Shi, G., Deng, X., & Shet, C. (2002). A finite element study of the effect of friction in orthogonal metal cutting. *Finite Elements in Analysis and Design*, *38*, 863–883. doi:10.1016/S0168-874X(01)00110-X

Shih, A. J. (1995). Finite element simulation of orthogonal metal cutting. *ASME Journal of Engineering for Industry*, *117*, 84–93. doi:10.1115/1.2803283

Shih, A. J. (1996). Finite element analysis of orthogonal metal cutting mechanics. *Journal of Machine Tools & Manufacture*, *36*, 255–273. doi:10.1016/0890-6955(95)98765-Y

Shi, J., & Liu, C. R. (2004). The influence of material models on finite element simulation of machining. *ASME Journal of Manufacturing Science and Engineering*, *126*, 849–857. doi:10.1115/1.1813473

Shirakashi, T., & Usui, E. (1974). Simulation analysis of orthogonal metal cutting mechanism. In *Proceedings of the First International Conference on Production Engineering, Part I* (pp. 535-540).

Shi, Y., Shen, H., Yao, Z., & Hu, J. (2007). Temperature gradient mechanism in laser forming of thin plates. *Optics & Laser Technology*, *39*(4), 858–863. doi:10.1016/j.optlastec.2005.12.006

Simo, J. C. (1998). A framework for finite strain elastoplasticity based on maximum plastic dissipation and the multiplicative decomposition. *Computer Methods in Applied Mechanics and Engineering*, *66*, 199–219. doi:10.1016/0045-7825(88)90076-X

Singh, Y. P., Jain, V. K., Kumar, P., & Agrawal, D. C. (1996). Machining piezoelectric (PZT) ceramics using an electrochemical spark machining (ECSM) process. *Journal of Materials Processing Technology*, *58*, 24–31. doi:10.1016/0924-0136(95)02102-7

Smith, S., & Tlusty, J. (1997). Current trends in high-speed machining. *ASME Journal of Manufacturing Science and Engineering*, *119*, 664–666. doi:10.1115/1.2836806

Srituravanich, W., Fang, N., Sun, C., Luo, Q., & Zhang, X. (2004). Plasmonic nanolithography. *Nano Letters*, *4*(6), 1085–1088. doi:10.1021/nl049573q

Steinhilper, R. (1998). *Remanufacturing the ultimate form of recycling*. Stuttgart, Germany: Fraunhofer IRB Verlag.

Strenkowski, J. S., & Carroll, J. T. (1985). A finite element model of orthogonal metal cutting. *ASME Journal of Engineering for Industry*, *107*, 346–354. doi:10.1115/1.3186008

Strenkowski, J. S., & Carroll, J. T. (1986). Finite element models of orthogonal cutting with application to single point diamond turning. *International Journal of Mechanical Sciences*, *30*, 899–920.

Strenkowski, J. S., & Moon, K.-J. (1990). Finite element prediction of chip geometry and tool/workpiece temperature distributions in orthogonal metal cutting. *ASME Journal of Engineering for Industry*, *112*, 313–318. doi:10.1115/1.2899593

Stribrsky, A., Honcu, J., Hyniova, K., & Kruczek, A. (2002). H-infinity control of active suspension systems. In *Proceedings of the Conference on Process Control*, Pardubice, Czech Republic (Vol. 35).

Suarez, L., Houbaert, Y., Vanden, X., & Colás, R. (2009). High temperature deformation of oxide scale. *Corrosion Science*, *51*, 309–315. doi:10.1016/j.corsci.2008.10.027

Subramaniyan, A. K., & Sun, C. T. (2006). Enhancing compressive strength of unidirectional polymeric composites using nanoclay. *Composites. Part A, Applied Science and Manufacturing*, *37*(12), 2257–2268. doi:10.1016/j.compositesa.2005.12.027

Sun, W. H. (2005). *A study on the characteristics of oxide scale in hot rolling of steel*. Unpublished doctoral dissertation, University of Wollongong, Australia.

Sundin, E. (2004). *Product and process design for successful remanufacturing.* Unpublished doctoral dissertation, Linkopings University, Sweden.

Sun, W. H., Tieu, A. K., & Jiang, Z. Y. (2004). Effect of rolling condition on mill load and oxide scale deformation in hot rolling of low carbon steel. *Steel GRIPS Journal of Steel Related Materials*, *2*, 579–583.

Sun, W. H., Tieu, A. K., Jiang, Z. Y., Lu, C., & Zhu, H. T. (2003). Surface characteristics of oxide scale in hot strip rolling. *Journal of Materials Processing Technology*, *140*(1-3), 77–84. doi:10.1016/S0924-0136(03)00823-9

Sun, Z., & Yang, H. (2002). Development of a finite element simulation system for the tube axial compressive precision forming process. *International Journal of Machine Tools & Manufacture*, *42*, 15–20. doi:10.1016/S0890-6955(01)00100-6

Sutherland, J. W., Adler, D. P., Haapala, K. R., & Kumar, V. (2008). A comparison of manufacturing and remanufacturing energy intensities with application to diesel engine production. *CIRP Annals:Manufacturing Technology*, *57*(1), 5–8. doi:10.1016/j.cirp.2008.03.004

Sutter, G., Ranc, N., Molinari, A., & Pina, V. (2008). Experimental measurement of temperature distribution in the chip generated during high speed orthogonal cutting process. *International Journal of Machining and Machinability of Materials*, *3*(1-2), 52–61. doi:10.1504/IJMMM.2008.017624

Taguchi, G. (1990). *Introduction to quality engineering*. Tokyo, Japan: Asian Productivity Organization.

Tai, N. H., Kuo, H. H., Chern, J. H., & Ju, C. P. (2002). Mechanical and tribological properties of 2-D carbon/carbon composites densified through pulse chemical vapor infiltration. *Journal of Materials Science*, *37*(17), 3693–3703. doi:10.1023/A:1016565426189

Tang, D. W., Wang, C. Y., Hu, Y. N., & Song, Y. X. (2009). Finite-element simulation of conventional and high-speed peripheral milling of hardened mold steel. *Metallurgical and Materials Transactions A*, *40*, 3245–3257. doi:10.1007/s11661-009-9983-1

Tay, A. O., Stevenson, M. G., & de Vahl Davis, G. (1974). Using the finite element method to determine temperature distribution in orthogonal machining. *Proceedings - Institution of Mechanical Engineers*, *188*(55), 627–638. doi:10.1243/PIME_PROC_1974_188_074_02

Tlusty, J. (1993). High-speed machining. *Annals of the CIRP*, *42*(2), 733–738. doi:10.1016/S0007-8506(07)62536-0

Tomesani, L. (1997). Analysis of a tension-driven outside-in tube inversion. *Journal of Materials Processing Technology*, *64*, 379–386. doi:10.1016/S0924-0136(96)02589-7

Torrez, J. B. (2007). *Light-weight materials selection for high-speed naval craft*. Unpublished doctoral dissertation, Massachusetts Institute of Technology, Cambridge, MA.

Trent, E. M., & Wright, P. K. (2000). *Metal cutting*. Woburn, MA: Butterworth-Heinemann.

Triantaphyllou, E. (2000). *Multi-criteria decision making methods: a comparative study*. London: Springer Verlag.

Tseng, Y., & Joshi, S. (1994). Recognizing multiple interpretations of interacting machining features. *Computer Aided Design*, *26*(9), 667–688. doi:10.1016/0010-4485(94)90018-3

Umbrello, D., Filice, L., Rizzuti, S., Micari, F., & Settineri, L. (2007). On the effectiveness of finite element simulation of orthogonal cutting with particular reference to temperature prediction. *Journal of Materials Processing Technology*, *189*, 284–291. doi:10.1016/j.jmatprotec.2007.01.038

Umbrello, D., M'Saoubi, R., & Outeiro, J. C. (2007). The influence of Johnson-Cook material constants on finite element simulation of machining of AISI 316L steel. *International Journal of Machine Tools & Manufacture*, *47*, 462–470. doi:10.1016/j.ijmachtools.2006.06.006

Usui, E., & Shirakashi, T. (1982). Mechanics of machining – from "descriptive" to "predictive" theory. In Kops, L., & Ramalingam, S. (Eds.), *On the art of cutting metals – 75 years later: A tribute to F. W. Taylor* (*Vol. 7*, pp. 13–35). New York, NY: ASME.

Vaidya, U. K., & Chawla, K. K. (2008). Processing of fibre reinforced thermoplastic composites. *International Materials Reviews*, *53*(4), 185–218. doi:10.1179/174328008X325223

van Luttervelt, C. A., Childs, T. H. C., Jawahir, I. S., Klocke, F., & Venuvinod, P. K. (1998). Present situation and future trends in modelling of machining operations. *Annals of the CIRP*, *47*(2), 587–626. doi:10.1016/S0007-8506(07)63244-2

Van Rijswijk, K. *(2007)*. Thermoplastic composite wind turbine blades – vacuum infusion technology for anionic polyamide – 6 composites. *Unpublished doctoral dissertation, Delft University of Technology, Delft, The Netherlands.*

Van Rijswijk, K., Joncas, S., Bersee, H. E. N., & Bergsma, O. K. (2005). Vacuum infused fiber-reinforced thermoplastic MW-size turbine blades - a cost-effective innovation? In *Proceedings of the ASME Wind Energy Symposium*, Reno, NV (pp. 39-51).

Van Rijswijk, K., Vlasveld, D. P. N., Bersee, H. E. N., & Picken, S. J. *(2003). Vacuum injection of anionic polyamide 6. In* Proceedings of the 4th ICCST Conference, *Durban, South Africa (pp. 23-28).*

Van Rijswijk, K., & Bersee, H. E. N. (2007). Reactive processing of textile fiber-reinforced thermoplastic composites - an overview. *Composites. Part A, Applied Science and Manufacturing*, *38*(3), 666–681. doi:10.1016/j.compositesa.2006.05.007

Van Rijswijk, K., Bersee, H. E. N., Jager, W. F., & Picken, S. J. (2006). Optimisation of anionic polyamide-6 for vacuum infusion of thermoplastic composites: Choice of activator and initiator. *Composites. Part A, Applied Science and Manufacturing*, *37*(6), 949–956. doi:10.1016/j.compositesa.2005.01.023

Van Rijswijk, K., Joncas, S., Bersee, H. E. N., Bergsma, O. K., & Beukers, A. (2005). Sustainable vacuum -infused thermoplastic composites for MW-size wind turbine blades-preliminary design and manufacturing issues. *Journal of Solar Energy Engineering*, *127*(4), 570–580. doi:10.1115/1.2037107

Van Rijswijk, K., Lindstedt, S., Vlasveld, D. P. N., Bersee, H. E. N., & Beukers, A. (2006). Reactive processing of anionic polyamide-6 for application in fiber composites: A comparitive study with melt processed polyamides and nanocomposites. *Polymer Testing*, *25*(7), 873–887. doi:10.1016/j.polymertesting.2006.05.006

Varadan, T. K., & Pandalai, K. A. V. (1979). Large amplitude flexural vibration of eccentrically stiffened plates. *Journal of Sound and Vibration*, *67*(3), 329–340. doi:10.1016/0022-460X(79)90540-6

Vaziri, M. R., Salimi, M., & Mashayekhi, M. (2010). A new calibration method for ductile fracture models as chip separation criteria in machining. *Simulation Modelling Practice and Theory*, *18*, 1286–1296. doi:10.1016/j.simpat.2010.05.003

Vaz, M. Jr, Owen, D. R. J., Kalhori, V., Lundblad, M., & Lindgren, L.-E. (2007). Modelling and simulation of machining processes. *Archives of Computational Methods in Engineering*, *14*, 173–204. doi:10.1007/s11831-007-9005-7

Vishwanath, B., Verma, A. P., & Rao, C. V. S. (1991). Effect of fabric geometry on friction and wear of glass fibre reinforced composites. *Wear*, *145*(2), 315–327. doi:10.1016/0043-1648(91)90139-L

Vlasveld, D. P. N., Rijswijk, V. K., Bersee, H. E. N., Beukers, A., & Picken, S. J. N. *(2003). Process considerations for liquid moulding of composites based on anionic polyamide 6. In* Proceedings of the 14th International Conference on Composite Materials, *San Diego, CA (pp. 23-38).*

Vollertsen, F. F. (1994). An analytical model for laser bending. *Lasers in engineering, 2*, 261-276.

Vollertsen, F., Komel, I., & Kals, R. (1995). The laser bending of steel foils for microparts by the buckling mechanism-a model. *Modelling and Simulation in Materials Science and Engineering*, *3*(1), 107–119. doi:10.1088/0965-0393/3/1/009

Voros, G. M. (2009). Buckling and free vibration analysis of stiffened panels. *Thin-walled Structures*, *47*, 382–390. doi:10.1016/j.tws.2008.09.002

Vostrikov, A. A., Fedyaeva, O. N., Shishkin, A. V., & Sokol, M. A. (2009). ZnO nanoparticles formation by reactions of bulk zinc with H_2O and CO_2 at sub and super critical conditions. *Journal of Solid Supercritical Fluids*, *48*, 1554–160.

Vyas, A., & Shaw, M. C. (1999). Mechanics of saw tooth chip formation in metal cutting. *Journal of Manufacturing Science and Engineering*, *121*, 163–173. doi:10.1115/1.2831200

Waigaonkar, S., Babu, B. J. C., & Durai Prabhakaran, R. T. (2008). A new approach for resin selection in rotational molding. *Journal of Reinforced Plastics and Composites*, *27*, 1021–1037. doi:10.1177/0731684407086629

Wang, H., Zhang, J., Zhu, J. J., & Chen, H. Y. (2002). Preparation of copper oxide nanoparticles by microwave irradiation. *Journal of Crystal Growth*, *244*, 88–99. doi:10.1016/S0022-0248(02)01571-3

Wang, J., Wilson, D. A., & Halikias, G. D. H. (2001). Robust-performance control of decoupled active suspension system based on LMI method. In *Proceedings of the American Control Conference*, *4*, 2658–2663.

Wang, J., Yang, J., Sun, J., & Bio, Y. (2004). Synthesis of copper oxide nanocrystals and the growth mechanism of copper oxide nanorods. *Materials & Design*, *25*, 625–629. doi:10.1016/j.matdes.2004.03.004

Wang, X., Lei, M. K., & Zhang, J. S. (2007). Surface modification of 316L stainless steel with high-intensity pulsed ion beams. *Surface and Coatings Technology*, *201*(12), 5884–5890. doi:10.1016/j.surfcoat.2006.10.040

Wang, Z. B., Guo, W., Pena, A., Whitehead, D. J., Luk'yanchuk, B. S., & Li, L. (2008). Laser micro/nano fabrication in glass with tunable-focus particle lens array. *Optics Express*, *16*(24), 19706–19711. doi:10.1364/OE.16.019706

Wang, Z. B., Hong, M. H., Luk'yanchuk, B. S., Lin, Y., Wang, Q. F., & Chong, T. C. (2004). Angle effect in laser nanopatterning with particle-mask. *Journal of Applied Physics*, *96*(11), 6845–6850. doi:10.1063/1.1786652

Watanabe, T., & Tanabe, Y. (1976). Formation and morphology of Ni-B amorphous alloy deposited by electroless plating. *Materials Science and Engineering*, *23*, 97–100. doi:10.1016/0025-5416(76)90175-0

Waterhouse, R. B. (1972). *Fretting corrosion* (1st ed.). Oxford, UK: Pergamon Press.

Wei, D. B., Huang, J. X., Zhang, A. W., Jiang, Z. Y., Tieu, A. K., & Wu, F. (2009a). Deformation of oxide scale and surface roughness transfer during hot rolling of stainless steel 304L. *International Journal of Surface Science and Engineering*, *3*, 459–470. doi:10.1504/IJSURFSE.2009.029141

Wei, D. B., Jiang, Z. Y., & Tieu, A. K. (2009b). *Study on friction in hot rolling of stainless steels, a progress report*. Gwynneville, Australia: University of Wollongong.

Williams, C., Summerscales, J., & Grove, S. (1996). Resin infusion under flexible tooling (RIFT): A review. *Composites Part A*, *27*, 517–524. doi:10.1016/1359-835X(96)00008-5

Williams, R. A. (1997). Automotive active suspensions. *Automobile Engineering*, *211*, 415–426. doi:10.1243/0954407971526551

Woo, Y., & Sakurai, H. (2002). Recognition of maximal features by volume decomposition. *Computer Aided Design*, *34*, 195–207. doi:10.1016/S0010-4485(01)00080-X

Wu, D. W., & Matsumoto, Y. (1990). The effect of hardness on residual stresses in orthogonal machining of AISI 4340 steel. *Journal of Engineering for Industry*, *112*, 245–252. doi:10.1115/1.2899582

Wu, H.-C. (2004). *Continuum mechanics and plasticity*. Boca Raton, FL: Chapman and Hall/CRC.

Wutzow, W. W., & Paiva, J. B. (2008). Analysis of stiffened plates by the boundary element method. *Engineering Analysis with Boundary Elements*, *32*, 1–10. doi:10.1016/j.enganabound.2007.06.005

Xiang, D., & Gu, C. (2006). A study on the friction and wear behavior of PTFE filled with ultra-fine kaolin particulates. *Materials Letters*, *60*(5), 689–692. doi:10.1016/j.matlet.2005.09.061

Xu, F., Ji, W., Shen, Z. X., Tang, S. H., Ye, X. R., & Jia, Z. A. (1999). Preparation and characterization of CuO nanocrystals. *Journal of Solid State Chemistry*, *147*, 516–519. doi:10.1006/jssc.1999.8409

Xu, H., Du, J., & Li, W. L. (2010). Vibrations of rectangular plates reinforced by any number of beams of arbitrary lengths and placement angles. *Journal of Sound and Vibration*, *329*(18), 3759–3779. doi:10.1016/j.jsv.2010.03.023

Yang, H., & Li, S. (1995). Process optimization of the inverting-forming of thin-walled tubes with radiused dies. *Journal of Materials Processing Technology*, *52*, 489–495. doi:10.1016/0924-0136(94)01621-7

Yang, H., Zhichao, S., & Yingjun, J. (2001). FEM analysis of mechanism of free deformation under dieless constraint in axial compressive forming process of tube. *Journal of Materials Processing Technology*, *115*, 367–372. doi:10.1016/S0924-0136(01)01018-4

Yang, W. H., & Tarng, Y. S. (1998). Design optimization of cutting parameters for turning operations based on the Taguchi method. *Journal of Materials Processing Technology*, *84*, 122–129. doi:10.1016/S0924-0136(98)00079-X

Yuan, G.-Q., Jiang, H.-F., Lin, C., & Lia, S.-J. (2007). Shape and size controlled synthesis of Cupperic oxide nanocrystals. *Journal of Crystal Growth*, *303*, 400–406. doi:10.1016/j.jcrysgro.2006.12.047

Yu, Y., & Lenard, J. G. (2002). Estimating the resistance to deformation of the layer of scale during hot rolling of carbon steel strips. *Journal of Materials Processing Technology*, *121*, 60–68. doi:10.1016/S0924-0136(01)01176-1

Zadeh, L. A., Klir, G. J., & Yuan, B. (1996). *Fuzzy sets, fuzzy logic and fuzzy systems: Advances in fuzzy systems-applications and theory*. Singapore: World Scientific.

Zerilli, F. J., & Armstrong, R. W. (1987). Dislocation-mechanics-based constitutive relations for material dynamics calculations. *Journal of Applied Physics*, *61*, 1816–1825. doi:10.1063/1.338024

Zhang, B., & Bagchi, A. (1994). Finite element formation of chip formation and comparison with machining experiment. *ASME Journal of Engineering for Industry*, *116*, 289–297. doi:10.1115/1.2901944

Zhang, C., Chan, K. W., & Chen, Y. H. (1998). A hybrid method for recognizing feature interactions. *Integrated Manufacturing Systems*, *9*(2), 120–128. doi:10.1108/09576069810202078

Zhang, J., Cheng, P., Zhang, W., Graham, M., Jones, J., & Jones, M. (2006). Effects of scanning schemes on laser tube bending. *Transactions of the ASME*, *128*, 20–33.

Zhang, L., Reutzel, E. W., & Michaleris, P. (2004). Finite element modeling discretization requirements for the laser forming process. *International Journal of Mechanical Sciences*, *46*(4), 623–637. doi:10.1016/j.ijmecsci.2004.04.001

Zhang, M., Xu, X., & Zhang, M. (2008). Hydrothermal synthesis of sheaf like CuO via ionic solids. *Materials Letters*, *62*, 385–388. doi:10.1016/j.matlet.2007.05.046

Zhang, P., Guo, B., Shan, D., & Ji, Z. (2007). FE simulation of laser curve bending of sheet metals. *Journal of Materials Processing Technology*, *184*(1-3), 157–162. doi:10.1016/j.jmatprotec.2006.11.017

Zhang, Y. F., Hu, W., Rong, Y., & Yen, D. W. (2001). Graph-based set-up planning and tolerance decomposition for computer aided fixture design. *International Journal of Production Research*, *39*(14), 3109–3126. doi:10.1080/00207540110056171

Zha, X. F. (2005). A web-based advisory system for process and material selection in concurrent product design for a manufacturing environment. *International Journal of Advanced Manufacturing Technology*, *25*(3-4), 233–243. doi:10.1007/s00170-003-1838-0

Zhu, H., & Menq, C. H. (2002). B-rep model simplification by automatic fillet/round suppression for efficient automatic feature recognition. *Computer Aided Design*, *34*, 109–123. doi:10.1016/S0010-4485(01)00056-2

Zingraff, L., Bourban, P. E., Wakeman, M. D., Kohler, M., & Manson, J. A. E. *(2002). Reactive processing and forming of polyamide 12 thermoplastic composites. In* Proceedings of the 23rd Europe SAMPE Conference *(pp. 237-248).*

Zorev, N. N. (1963). Inter-relationship between shear processes occurring along tool face and shear plane in metal cutting. In *Proceedings of the International Research in Production Engineering Conference* (pp. 42-49).

About the Contributors

J. Paulo Davim received his PhD degree in Mechanical Engineering from the University of Porto in 1997 and the Aggregation from the University of Coimbra in 2005. Between 1986/96, he was Lecturer in University of Porto. Currently, he is an Aggregate Professor at the Department of Mechanical Engineering of the University of Aveiro and the Head of MACTRIB - Machining and Tribology Research Group. He has more than 25 years of teaching and research experience in manufacturing, materials, and mechanical engineering with special emphasis in machining & tribology. He is the Editor in Chief of six international journals, Guest Editor of journals, books Editor, book Series Editor, and Scientific Advisory for many international journals and conferences. Presently, he is an Editorial Board member of 20 international journals and acts as reviewer for than 60 prestigious ISI Web Science journals. In addition, he has also published as author and co-author more than 40 book chapters and 300 articles in journals and conferences (more than 170 articles in journals indexed in ISI Web Science, h-index 23+).

* * *

Omar Al-Hartomy is a solid state physicist and has carried his entire studies in UK. A dedicated and a hard worker is a member of many societies besides occupying vital administrative post in Tabuk University in Saudi Arabia.

Fhad M Al-Marzouki has carried his studies including doctorate in UK and is working in King Abdul Aziz University, Jeddah, Saudi Arabia from the last three decades. He has been on various administrative posts from time to time and a reputed scientist. His interests include electrical measurements and application of materials in devices. To his credit are more than 50 peer reviewed papers, more than 100 in conference proceedings and is a member of many science academies.

Tom Løgstrup Andersen is currently working as a senior development engineer at Materials Research Division, Risø DTU, National Laboratory for Sustainable Energy, Technical University of Denmark. He received the B.Sc. from Danish Academy of Mechanical Engineering in 1989 and has been employed at Risø DTU since 1989. The main focus has been manufacturing technology for polymer fibre composites, documented fabrication of fibre composite specimens and characterization of material quality. He was honored with DTU´s Innovation price in 2008 for the work with new spin-off companies as well as the close collaboration with especially the windmill industry typically as confidential consultant work. His publications count 19 articles in international refereed journals as well as 3 patents and more than 50 confidential reports.

A. Andrade-Campos received his PhD in Mechanical Engineering from the University of Aveiro, Portugal in 2005. He is an Assistant Professor of Mechanical Engineering at the University of Aveiro, research collaborator of CEMUC (Mechanical Engineering Center from University of Coimbra, Portugal) and LiMATb (Laboratory of Materials Engineering of Brittany, France). His research interest includes inverse methods, identification and determination of constitutive model parameters, optimization methods, the use of optimization methods in mechanical systems and shape optimization in metal forming problems.

Michaela Appleby graduated from Lancaster University, in July 2009, with a BEng (Hons) degree in Sustainable Engineering. Since graduating, Michaela has continued her studies at Lancaster University and is currently undertaking a post-graduate MSc (by research) degree in Sustainable Manufacturing, with support from Lancaster Product Development Unit, based within the Engineering Department at the University. Michaela has a keen interest in sustainability, climate change and environmental policy, which has led her research into a variety of areas and topics, and is now investigating how to lower the carbon footprint of the manufacturing industry.

K.K. Appukuttan is working as senior professor in the department of mechanical engineering, National Institute of Technology Karnataka (NITK), Surathkal. He has published more than 200 papers in International and national Journals and conference proceedings. He has more than 25 years of teaching and research experience in Mechanical Engineering. So far he has supervised sixteen students for PhD. His area of interests are robotics, control engineering, vibration and noise control.

Ewald Badisch has a huge experience in abrasive wear and surface engineering. He has number of international paper on the field of tribology.

Adam Buckley is Head of Programmes for The Manufacturing Institute (TMI), in Manchester, Northwest England, which since 2002 has helped regional manufacturers generate financial savings of £670 million. Adam directs TMI's portfolio of education and training services, and is leading the launch of the internationally renowned Shingo Prize, which he was instrumental in bringing to the UK and Northern Ireland. Adam is also responsible for TMI's Make It in Manufacturing campaign, a charitable program aimed at attracting tomorrow's talent into the sector.

Nikolaos I. Galanis received his Ph.D. from the Laboratory of Manufacturing Technology at the National Technical University in Athens, Greece in 2011. His Ph.D. research has to do with the precision and ultra precision manufacturing of artificial biological hip joint implants.

S.V. Gorabal is an assistant professor at SKSVMA College of Engineering and Technology, Laxmeshawar, India. He obtained his ME in production management from B.E.C Bagalkot in the year 1998. Currently he is perusing his PhD at Research center of Visveswaraya Technological University at BEC Bagalkot. His research interests include mathematical and experimental modeling of Hydro pneumatic friction dampers. S.V. Gorabal is a Life Member of ISTE, India. So far, he has published 7 papers in the proceedings of National/International conferences.

Alessandro Guglielmotti graduated in Mechanical Engineering at the University of Rome 'Tor Vergata' in 2006. Since October 2006, he is a PhD student at the same university, his research doctorate is in Material Engineering. His scientific activity is mainly focused On metal and polymeric cellular structures and diode laser forming. These researches resulted in the production of five scientific papers published on proceedings of International journals and conferences.

Junxia Huang is a Research Engineer in Stainless Steel Technical Centre, Baosteel Research Institute (R&D Center). She is pursuing her PhD in Shanghai Jiaotong University. Her research areas include simulation of oxide scale deformation, the influence of rolling parameters on surface and properties of steels.

Vassilios Iakovakis is Assistant Professor and Head of the Laboratory of Machine Design at the Department of Mechanical Engineering, Technological Educational Institute of Larissa, Greece, since 1998. He received his Diploma in Mechanical Engineering from the Aristotle University of Thessaloniki, Greece (1985) and his Dr-Ing from the University of Braunschweig, Germany (1993). His interests revolve around machine design, computer aided design, and modelling and simulation.

M. S. Che Jamil is a final year Phd candidate in the Laser Processing Research Centre (LPRC) at The University of Manchester, UK. His research specialisation is on optimization of laser forming for metal tubes and plates. He obtained his first degree from Universiti Teknologi Malaysia (2002) in the field of Mechanical Engineering (majoring in automotive). After graduation, he worked as a Vehicle Architect Engineer at the Proton Holding (Malaysian car manufacturer). Then, he pursued the master's degree in Advanced Manufacturing Technology at UMIST in 2005. He then worked as a design engineer in an engineering consultancy firm, based in Rochdale, UK, where he carried out structural calculations and finite element analysis.

Zhengyi Jiang is currently a Professor in the School of Mechanical, Materials and Mechatronic Engineering, University of Wollongong. He received his PhD in Materials Processing Engineering from the State Key Laboratory of Rolling and Automation, Northeastern University in 1996, and was appointed as a Vice Director of the State Key Laboratory in 1996 and as a Professor of Materials Processing Engineering in 1998 at Northeastern University. He received two Australian Research Fellowship Awards from the Australian Research Council, in 2002 and 2008. His main research interests are computational mechanics, contact mechanics, and tribology of materials processing engineering, particularly in metal rolling.

Sihai Jiao received his PhD in Material Processing Engineering from Northeastern University, China in 1998. As the Principal Researcher of Baosteel Research Institute, he works in the field of rolling and heat treatment technologies, especially, the application of thermomechanical processing.

K. Kantzavelos is a mechanical engineer who concluded his diploma thesis in the Laboratory of Manufacturing Technology, National Technical University in Athens, Greece in 2009. His subject was the analysis of high speed machining with the Finite Element Method.

John Kechagias received his Diploma in Mechanical Engineering (1995), and his PhD (2001) from the Polytechnic School of the University of Patras, Greece. He is Assistant Professor and the Head of the Laboratory for Manufacturing Processes at the Department of Mechanical Engineering, Technological Educational Institute of Larissa, Greece, since 2004. His interests revolve around the investigation of conventional and non conventional manufacturing processes and machine tools.

Ashfaq Khan received the Bachelors of mechanical engineering from the National University of Sciences and Technology (NUST), Pakistan in 2007. He later received Master degree in manufacturing engineering from the same university in 2008. He is currently working towards the PhD degree at School of Mechanical, Aerospace and civil Engineering. His main research interests include laser surface nano/ micro patterning and Nano imaging.

Amandeep Kundal is a M.E. student, Mechanical Engineering Department, Punjab Engineering College; (Deemed University), Chandigarh-160012, India.

S.N. Kurbet is a professor of mechanical engineering at Basaveshwar Engineering College Bagalkot. He obtained his PhD from Indian Institute of Technology Madras. He has published more than 35 papers in International and National journals and in conference proceedings. He has more than 23 years of teaching and research experience in Mechanical Engineering. He has guided many students in ME Research), M.Tech, and PhD. His research activities are in robotics, thermal, vibration and control.

Chris Lambert is a Project Manager at Lancaster University, working specifically within the knowledge exchange team for the Engineering Department: Lancaster Product Development Unit. Chris has a keen interest in providing support to SMEs by identifying and helping to exploit opportunities presented by the climate change agenda. Chris has worked on several business support initiatives of this nature and has successfully engaged commercial entities with the academic knowledge base to bring about a range of benefits to the stakeholders concerned. Chris has worked on a range of regional, national and trans-national programmes funded from a variety of sources.

Lin Li is holding the post of Director of Research and Deputy Head of School, in the School of Mechanical, Aerospace and Civil Engineering, The University of Manchester, UK. He is also Director of Laser Processing Research Centre. Professor Li did PhD degree from Imperial College, London University in 1989 in Laser Engineering. He joined University of Manchester (formerly UMIST) in 1994 as a Lecturer. He established the first laser processing research laboratory at the university and in 2000 he was fast track promoted to a full professor and was appointed as the Director of Laser Processing Research Centre. Professor Li has published over 400 SCI and EI cited papers and is the inventor and co-inventor of over 40 patents. He has been awarded Charles Main Award from Institute of Mechanical Engineers for his contribution in laser engineering in nuclear industry.

Carmine Lucignano graduated in Mechanical Engineering at the University of Naples 'Federico II' in 2006. Since October 2009, he is a PhD in Material Engineering at the Department of Mechanical Engineering of the University of Rome 'Tor Vergata'. His scientific activity is mainly focused on manufacturing processes of polymer nanocomposites, manufacturing processes of functionally graded

materials, non-destructive and minimally invasive testing systems, thermosets recycling. These researches resulted in the production of about twenty scientific papers published on proceedings of international journals and conferences.

Aage Lystrup is currently working as a senior scientist at Materials Research Division, Risø DTU, National Laboratory for Sustainable Energy, Technical University of Denmark. He received the B.Sc. from Danish Academy of Mechanical Engineering in1972, and has been employed at Risø DTU since 1972. Since 1977 his main focus has been research and development of manufacturing technology of fibre composites. He is a member of the Research and Education committee within Danish Polymer Industry, Section for Composite Materials and has since 1986 worked as a project manager for more than10 larger public research programmes in collaboration with Danish and international industries. He has more than 50 publications and more that 100 internal project reports.

Alakesh Manna is an Associate professor, Mechanical Engineering Department, Punjab Engineering College, Chandigarh, India. His research areas include advanced manufacturing, production of MMC's and ceramics, traditional, on-traditional machining, advanced hybrid and micromachining etc. He has published 125 research papers in international and national journals and conference proceedings. He has attended 24 international and national conferences and presented the key notes, expert talk, and research papers including session chairmanship. He has guided number of M.E and Ph.D students. He is principal investigator of different project and scheme. He is recipient of gold medals for best and excellent teaching; and various medals, memento, certificates for his excellent past service.

Dimitrios E. Manolakos is Professor and Director of the Laboratory of Manufacturing Technology, National Technical University in Athens, Greece. He has published more than 180 papers in various areas of manufacturing technology and materials science.

Angelos P. Markopoulos received his Ph.D. from the Laboratory of Manufacturing Technology, National Technical University in Athens, Greece in 2006. His area of expertise is ultraprecision machining and micromachining processes.

Stergios Maropoulos received his BSc, MSc and PhD from the Department of Metallurgy, Manchester University, UK. He is an Associate Professor and Head of Department at the Department of Mechanical Engineering Dept., Technological Educational Institute of West Macedonia, Koila, Kozani 50100, Greece and Head of the Advanced Industrial Production Department, Centre of Technological Research of West Macedonia. His fields of interest are machining and forming processes, machine elements, materials technology, welding and non-destructive testing.

Anirban Mitra graduated from the Department of Mechanical Engineering, National Institute of Technology, Durgapur in the year 2006. Thereafter he completed his Master in Mechanical Engineering degree (Specialisation: Machine Design) from Jadavpur University in the year 2008. He is currently pursuing his PhD under the supervision of Prof. Kashinath Saha and Prof. Prasanta Sahoo in the Department of Mechanical Engineering, Jadavpur University. He is presently working as a senior research fellow (SRF) under the National Doctoral Fellowship (NDF) scheme of AICTE, India. His current area of research is large amplitude free and forced vibration analysis of stiffened plates in elastic and post-elastic regime.

Rahul Mitra has published more than 60 research papers on reputed international journals. He has obtained two patents from India. His work in the field of composite material is well known. He guided more than 10 people for obtaining PhD degree.

B. K. Patel received his BTech and MTech degrees from S.V. National Institute of Technhlogy, Surat, India. He has about 5 years of teaching and research experience. He is presently working as a senior research and his research interests include advanced manufacturing technology, production and operations management, and optimization techniques.

George Petropoulos received his BSc in Physics and PhD in Mechanical Engineering from the Aristotle University of Thessaloniki, Greece. He was Assistant Professor and Director of the Manufacturing Processes Laboratory, Department of Mechanical and Industrial Engineering, University of Thessaly, Greece (1996-July 2010). His interests revolved around theory and technology of machining (conventional and non conventional) processes, machining of composite materials, metrology, tribology (surface characterisation and modelling of lubricated contacts).

R. T. Durai Prabhakaran is currently working as a researcher in the Materials Research Division, Risø DTU, National Laboratory for Sustainable Energy, Technical University of Denmark. He received the B.Tech degree in Mechanical engineering from Sri Krishnadevaraya University, Ananthapur, Andhra Pradesh, India in 1997 and M.Tech degree in Design engineering from Indian Institute of Technology, New Delhi, India in 2001. He got his PhD in 2007 in the polymer composite field under BITS, Pilani, INDIA. He also worked as a faculty for 8 years, to teach undergraduate courses in Mechanical Engineering. His major research interests are Composite Materials Design, Finite Element Methods, Graph theory, Material Science. He has published 11 papers in Journals such as Journal of Composite Materials, Polymer composites, Reinforced Plastics and Composites, Materials and Manufacturing Processes etc.

Fabrizio Quadrini graduated with honours in Material Engineering at the University of Naples 'Federico II'. Since 2002, he has been a Researcher at the University of Rome 'Tor Vergata', where he teaches a course on Manufacturing Systems Technology. He has collaborated with several industrial partners to design and optimize new processes and products. He is the author of about a hundred papers accepted in international journals and conferences. He acts as referee for some international journals and has participated in scientific committees of international conferences.

R.V. Rao received his BTech from Nagarjuna University, his MTech from BHU Varanasi and his PhD from BITS Pilani, India. He has 20 years of teaching and research experience and is presently working as a professor in the department of mechanical engineering of S.V. National Institute of Technhlogy, Surat, India. His research interests include advanced manufacturing technology, CAD/CAM/Robotics, and fuzzy multiple attribute decision making. He has about 150 research publications to his credit.

Allan Rennie is the Head of Lancaster Product Development Unit, based within the Engineering Department at Lancaster University. The unit provides support to SMEs in the North West with issues ranging from design capability and 3D CAD through to manufacture. This is done through the delivery of a suite of European Funded Projects, which have been secured by Allan from various sources, including the European Regional Development Fund (ERDF), the European Social Fund (ESF), the North

West Development Agency (NWDA) and the Higher Education Innovation Fund (HEIF). Allan is also a co-organiser of the National Rapid Prototyping Conference, a conference used for the dissemination of rapid prototyping, tooling and manufacturing research in the UK.

Manish Roy worked as a scientist in DRDO for last 22 years in the field of tribology. He is working as a reviewer of number of reputed journals. He has published number of research papers on reputed international journals.

Kashinath Saha served Indian industry as design engineer in the sectors involving tea machineries, Industrial fan and air handling equipments and other heavy machinery components for five years. He joined academia as lecturer in the Department of Mechanical Engineering, Jadavpur University in 1987. He is pursuing teaching and research in the area of Machine Elements Design, Stress, deformation analysis and design of Structural Elements and Structural Stability Analysis. He has also carried out several experimental studies in the field of structural dynamics and supervised a number of post graduate thesis and research projects and has over 50 publications in international journals and conference proceedings.

Prasanta Sahoo is Professor at the Department of Mechanical Engineering, Jadavpur University, Kolkata, India. He received Bachelor of Mechanical Engineering from Jadavpur University and MTech and PhD in Mechanical Engineering from Indian Institute of Technology, Kharagpur, India. His research area is tribology and structural mechanics. He is the supervisor of 7 PhD theses and 16 Master's theses. He has authored a textbook on Engineering Tribology (Prentice Hall of India, 2005) and book-chapters in Tribology Research Advances (Nova Science, 2009) and Tribology for Engineers – a practical guide (Woodhead Publishing, 2010). He has co-authored more than 150 technical papers in international journals and conference proceedings. He is Associate Editor (computational mechanics and tribology) of International Journal of Engineering, Science and Technology (Multicraft). He is on the editorial board of Journal of Tribology Research (Serials), Journal of Tribology and Surface Engineering (Nova Science), International Journal of Manufacturing, Materials and Mechanical Engineering (IGI Global), Materials and Design (Elsevier).

Sourav Sarkar is experienced in the field of mechanical integration, testing of re-entry vehicle structure. Published 3 international journal paper and 2 international conference papers in the field of carbon composite materials.

V.G. Sekaran has a huge experience in large rocket motor in design, fabrication and execution. He worked as a scientist in DRDO for last 26 years.

M.A. Shah graduated from the University of Kashmir, Srinagar in 1994 and doctorate in Materials Science, from Jamia Millia Islamia, New Dehli. He joined National Institute of Technology, (Deemed University) Srinagar in September 1999. Established World Bank funded Sophisticated Instrumentation Centre which caters the needs of scientific fraternity of whole region and an author of "Principles of Nanoscience and Nanotechnology", a book for all. He is an explorer of a versatile technique "A Safe way to Nanotechnology" for the synthesis of oxide nanomaterials. Having recently joined Faculty of Sciences, King Abdul Aziz University, Jeddah, Saudi Arabia, Dr. Shah is a member of many science academies and societies.

Mohammed Sheikh obtained his PhD from the University of Sheffield in 1983 for his work on the development of novel boundary domain techniques for modelling of various physical processes. He is currently Reader in Mechanical Engineering in the school of mechanical, aerospace and civil engineering. His research centres on the development of numerical techniques, such as FEM and BEM, and their application to modelling of materials, their processing, and their integrity. His current areas of research are modelling of: material forming, laser material processing, thermal transport in composites, and high speed machining. He has published more than 140 technical papers and is a member of review committees of many international journals.

Xu Shi is an Engineer of Metallurgical Process Department, Baosteel Research Institute (R&D Center). She obtained her PhD in Material Processing Engineering from Northeastern University. Her research area is hot rolling process, and finite element simulation of rolling process.

Erica Anna Squeo graduated with honours in Mechanical Engineering at the University of Rome 'Tor Vergata' in 2005. She obtained her PhD in Engineering of Materials from the same university on 2009. At present, she is a Research Fellow of Manufacturing Processes at the University of Rome 'Tor Vergata'. Her scientific activity is mainly focused on manufacturing processes of high-performance polymers, non-conventional foaming of thermosets, non-destructive and minimally invasive testing systems and non-conventional joining, welding and forming processes. She has published about 30 papers in international journals and conferences.

A. Kiet Tieu is currently a Professor of Mechanical Engineering, and was Head of the School of Mechanical, Materials and Mechatronic Engineering, University of Wollongong. After graduating with an Engineer with BlueScope Steel for eight years, and then joined the University of Wollongong in 1982. His research interests are in tribology and computational mechanics in metal forming.

Zengbo Wang educated in a mixed background of physics (B.Sc. Physics 1997, M.Sc, Physics, 2001, China) and engineering (Ph.D in Electrical & Computer Engineering, 2005, NUS Singapore). He is a lecturer in the school of MACE. He has 10 years of research experience in the field of laser micro/nano-science and technology, particularly in the development of micro/nano fabrication techniques and modelling of nano-photonics, with over 70 publications. He also has extensive industrial experience laser processing, including, for example, laser cleaning for hard disk industry, laser surface treatment for biology and energy industries and laser fabrication for the MEMs industry. His current research interests include nanoscale optical imaging.

Dongbin Wei is a Research Fellow in the School of Mechanical, Materials and Mechatronic Engineering, University of Wollongong. He was awarded his PhD in Materials Processing Engineering from University of Science and Technology Beijing. His research areas of interest include modelling of metal forming process, tribology in metal forming and development of new metal forming technology.

Aiwen Zhang is a Senior Research Engineer of Baosteel Research Institute (R&D Center). He received his ME in composite material from the Southeast University, China in 1998. He works in the field of new steel grades development, rolling and heat treatment technologies.

Index

304L stainless steel 148, 240, 242, 244, 247-248
304 stainless steel 144, 146-147, 240-242, 244, 247-248

A

active suspension 62-63, 70-71
adiabatic shearing 192, 197, 200, 215, 220, 222-223
Al_2O_3-ceramics 167, 171
analysis of variance (ANOVA) 304, 312
analytical modelling 267
Analytic Hierarchy Process (AHP) 256, 269
antibacterial activity 326, 328-329
Arbitrary Lagrangian-Eulerian (ALE) analysis 180
Attributed Adjacency Matrix (AAM) 102, 107
Attributed Connectivity Matrix (ACM) 102, 104, 117, 119-120
backbone curve 25, 28, 34, 36, 40, 46, 50-51, 54
boundary element method (BEM) 26

B

Buckling Mechanism (BM) 142-143, 151, 153

C

carbon footprinting 73
chip morphology 178, 181, 186, 189, 198, 210-211, 214, 216, 221-222, 224
closed shell 109
coefficient of friction 64, 187, 207, 289, 292, 297-298
cold end forming 226, 231
composite foams 91, 93-94, 101
compression beading 227-228, 238
Computer Aided Design (CAD) 102
Computer Aided Manufacturing (CAM) 102
Computer Aided Process Planning (CAPP) 102
Computer Integrated Manufacturing system (CIM) 102
constitutive model parameters 2, 4, 22
Contact Particles Lens Arrays (CPLA) 130
copper powder 326-327
corrosion resistance 260, 274, 290, 319
CPLA deposition 130
critical instability load 228, 235, 237

D

DD3IMP 10, 15-16, 18, 22
de-ionized water 320-321, 326-327
Difference Method (FDM) 141
dry friction damping 64-65

E

ELECTRE 253, 263
electrical spark discharge (ESD) 168
electrochemically spark abrasive drilling (ECSAD) 168
electrochemical machining (ECM) 168
electroless 302-308, 312, 314-315, 317-319
end-of-life (EOL) disposal 74
EOL products 73, 75-78, 80, 86, 88
epoxy-polyester (EP-PE) powders 92
Extreme Ultra Violet lithography (EUV) 131

F

feature-based models 103
feature recognition 102-105, 107, 109-110, 114-115, 117, 122-126
Finite Element Method (FEM) 2, 6, 141, 159, 180, 198
first-order shear deformable theory (FSDT) 27
forced vibration 25, 27-29, 33-36, 38, 48, 50, 52, 54
forced vibration analysis 25, 27-29, 34-36, 38, 52

G

Geometric Dimension and Tolerance (GD&T) 102
geometric non-linearity 25
governing equations 25, 28, 33-35, 204, 209
gradient-based methods 3, 6-7, 10
Greenhouse Gas (GHG) emissions 74-75, 77, 81, 83-88

H

hardening model 1, 11, 15-16
harmonic excitation 25, 27-30, 33, 35-38, 40, 50, 52
High Power Diode Laser (HPDL) 140-142
High Speed Machining (HSM) 179
hot rolling 240-244, 247-250
hydro-pneumatic friction damper 62, 69

I

immune algorithms 3

L

laser beam forming 140-141
Liquid Composite Moulding (LCM) 269
lithography 131, 138
low amplitude reciprocating wear 289-290, 299

M

material removal rate (MRR) 168
mechanical bending 140-142
mesh-free Galerkin method 27
metal forming 1, 11, 16, 23-24, 140, 193, 231, 238, 240
Micro Lens Array (MLA) patterning 131
montmorillonite (MMT) nano-particles 93
multiple attribute decision making (MADM) 252-254

N

nanobelts 321, 325
nanobricks 320-321, 323-325
nano-clay 93
nanocrystals 327, 332
nanomaterials 320-321, 325, 327, 331
nanorods 321, 325, 331-332
nanotubes 271, 321
nanowires 321-323, 325
nature-inspired algorithms 3, 6
near-field enhancement 130-131
Newton-Raphson iteration technique 26
Ni-B coating 302-305, 307, 312, 314-316, 318
non-linear quarter car model 62, 70

O

object oriented models 103
operational deflection shape (ODS) 25, 42
original equipment manufacturers (OEMs) 76
oxide scale 240-244, 248-249

P

parameter identification 1-7, 11, 15-16, 22, 24
Particle on Surface (POS) model 132
PAS 2050 77-79, 81
passive suspension system 62
Plasmonic Lithography 131
plasticators 93
pneumatic friction damper 62, 67, 69
Polyamide 6 (PA 6) 269
Poly-Butylene Terephthalate (PBT) 271
Polymethylmethacrylate (PMMA) 273
Polyphthalamide (PPA) 272
powder coating 91-92, 101
preference selection index (PSI) 253
pressure regulation 62
process map development 78
Product Recovery 73, 75-78, 80-83, 85-90

R

rawstock 102-107, 109-110, 112, 120, 122-124, 127
recycling technology 91
remanufacturing 73, 76-80, 82-90
repairing 73, 76-78, 80, 83-84, 86-88
resin attributes 267, 274, 284
Resin Selection Index (RSI) 278, 283
ring-opening polymerization (ROP) 269

S

scanning electron microscopy 308
Scanning Probe Microscopy (SPM) 131
SDL optimization lab 2-3, 7-11, 22
secondary suspension system 63
Seeman Composite Resin Infusion Moulding Process (SCRIMP) 269
segmented chip 180, 182, 192, 197, 199-200, 212-223
SEM graphs 173
semi-active damping 63
semi-active suspension 63

sensitivity analysis 7, 10, 284
sequential quadratic programming (SQP) 26
shape optimization 1-3, 5-7, 11, 22-23
SIDOLO code 1, 3
Small and Medium-Sized Enterprises (SMEs) 73
solid-state foaming 91-92, 94, 101
Spectrophotometer 134-135
steel substrate 240-242, 248
stiffened plate 25-29, 32-34, 36, 44-45, 48, 50, 52, 54
stress-strain curve 98, 228
structural reaction injection moulding (SRIM) 269
surface roughness 194, 240-242, 244, 247-249, 289, 292, 294-296, 299, 303-304, 310-311, 315, 319
sustainable manufacturing 73-75, 80, 88-90

T

Taguchi Analysis 178
Taguchi Method 188, 194, 196, 302, 304, 307, 314, 319
Temperature Gradient Mechanism (TGM) 141-142, 151
tensile strength (TS) 260
thermoplastic polymers 267-268, 280
thermoplastic resins 268-269, 273-275, 278, 284
thermoplastics 93, 267-269, 271, 280, 287
thin-walled polymer tubes 228
topology optimization 1
Transmission Electron Microscope (TEM) 328
traveling wire electrochemical spark machining (TW-ECSM) 167-168, 173, 176
tube bending 140-142, 148-149, 152-156
tube end forming 226-232, 237

U

UK manufacturing industry 74
Upsetting Mechanism (UM) 142-143, 151, 154

V

vacuum assisted resin transfer moulding (VARTM) 269
variational method 25
vehicle suspension system 62
vibration isolation 62
volume decomposition 102-103, 126

W

waste management 74-76, 87-90
waste powders 92-93
Weldability 268, 274
welded thin-walled tubes 226, 228
wire electro discharge machining (WEDM) 168

X

X-ray diffraction (XRD) 322, 328
X-ray diffractometry 94

Y

Young’s modulus (YM) 258, 260